UCRL--53929-88

DE89 016960

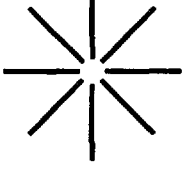

NUCLEAR TEST–EXPERIMENTAL SCIENCE

Annual Report
Fiscal Year 1988

Lawrence Livermore National Laboratory

University of California
Livermore, California 94551

UCRL-53929-88
Distribution Category UC-02

Acknowledgments

Robert W. Kuckuck is the Associate Director for the Nuclear Test–Experimental Science Directorate. Lawrence J. Ferderber is the Principal Deputy Associate Director, Frank R. Wondolowski is the Assistant Associate Director for Resources, and Lynda L. Yon is the NTES Staff Assistant. The four program leaders are: Richard J. Fortner, Prompt Diagnostics; Glenn L. Mara, Field Operations; Carl H. Poppe, Nuclear Chemistry; and Norman R. Burkhard, Containment.

The following people formed the publication staff for the FY88 Nuclear Test–Experimental Science Annual Report:

Scientific Editor	Gordon L. Struble
Publication Editor	Maureen L. Donohue
Editorial Coordinator	Carolin Middleton
Editors	Ginny Bucciarelli Maureen L. Donohue Jonathan D. Hymer Robert D. Kirvel Carolin Middleton Judy Prono Sondra Reid Barbara Strack
Designer	Frank Uhlig
Artists	Technical Information Department Art Division Quali-Type
Compositor	Marion Capobiance
Cover Photograph	Don Gonzalez

Special thanks to Mary Ann Esser for her guidance, suggestions, encouragement, and careful reading of the entire manuscript.

Contents

Nuclear Test–Experimental Science Overview 1

1 Prompt Diagnostics 4

Experimental Physics in FY88

Schellbourne X-Ray Spectrometers, Camera Systems, and Active Alignment Systems 6

Electron Beam Ion Trap 13

Fusion Gamma-Ray Experiments at the California Institute of Technology 19

Experimental Studies of Amplified Spontaneous Emission 22

Magnetically and Vacuum Insulated Transmission Line Experiments 28

Equation of State of Low-Density Materials 33

Material Behavior Calculations in Support of NTES 36

Streak-Camera Data Systems

Optical Streak Cameras and Their Test Program Applications 39

Streak-Camera Developments for NTES Applications 42

Streak-Camera Data Interpretation 47

Kernville Spectrometers: IBEX, VJACS, EODIX, and XPOLY 50

Electron Optics Modeling of Radiation-Induced Voltage Fluctuations on Streak Cameras 54

Calibration of Electro-Optic System for Underground Nuclear Tests 56

Detector Development

Time-Resolving Intensified Detectors for Low-Level X-Ray Detection 60

Neutron-Treated, Ultrafast Photoconductor Detectors 64

Fast *p-i-n* Diodes 68

Phosphors and Scintillators: Fabrication and Characterization 70

Radiation-to-Coherent-Light Converter 72

Optical Guided-Wave Devices for Single-Transient Instrumentation 75

Experiment Components

Characterization of Layered Synthetic Microstructures 80

Thin Vitreous Carbon/Silicon Carbide X-Ray Mirrors 83

Quartz Finger Mixers 86

A New Generation of Array Camera 88

Improving PINEX Shutters 89

High-Speed Digital Recorders 92

Fiber-Optic Fiducial System 95

Experiment Design, Analysis Codes, and Calibration Facilities

COG Monte Carlo Transport Code 97

Experiment Design and Data Analysis on the Macintosh II 99

Nuclear Test Image Processing 102

The X-Ray Calibration and Standards Facility 104

LEXIS: A Pulsed X-Ray Facility 108

New Directions in Development of Underground Weapons Physics

Measurement of Electron Temperature in a Nuclear-Driven Plasma 110

The LRACS/MIFFLEX Package for Measuring X-Ray Output Below the Spectral Peak 114

Fiber-Optic Alpha Measurement Development 118

Astrophysical Opacity Experiment 121

Coherent Microwave Generation Using an Intense Relativistic-Electron-Beam–Plasma Interaction 126

2 Field Operations 130

Improved Capabilities for Emplacing Complex Experiments at the Nevada Test Site 132

Digital Downhole Surveyor: A Nevada Test Site Logging Tool 133

Testing the Lightning-Invulnerable Device System 137

Environmental Control Systems for Nevada Test Site Experiments 141

Timing and Control System at Nevada Test Site 143

Kearsarge and Shagan: The Joint Verification Experiment 146

3 Nuclear Chemistry 150

Test Program Research

Development and Implementation of a Field Gamma-Ray Spectrometer for Onsite Core Analyses at the Nevada Test Site 152

A New Approach to Characterizing Nonlinearities in Multiplier Ion-Detection Systems 154

Variation of Fission-Product Yields with Neutron Energy 156

Calibration of Fission-Product Yields for ^{136}Xe and ^{85}Kr 159

Using Radiochemical Diagnostics to Evaluate Containment Performance 160

(n,2n) Cross-Section Measurements of Krypton and Xenon Isotopes 162

Analog (p,n) Cross Sections of the Zirconium Isotopes 164

Preliminary Results for the Excitation Functions of $^{151,153}Eu(p,n)^{151,153}Gd$ and $^{151,153}Eu(d,2n)^{151,153}Gd$: Measurements and Modeling 166

One- and Two-Step Direct Reactions in the Continuum 169

Calculation of a Study Set of Neutron Excitation Functions for Isotopes of Iridium 170

New Bomb-Fraction Tracer: ^{243}Am 174

Counting Facility Upgrade Project 175

NCD's Computer Capabilities in the Age of Information 179

GOSPEL: Our Third-Generation Radiochemical Diagnostics Code 182

Development of IBM PC Codes for Use in our Nuclear Cross-Section Calculational Effort 184

A Preliminary Evaluation of the 3×10^6-Year Isomeric State of ^{210}Bi in Astrophysical s-Process Nucleosynthesis 186

Spheromak Model of Planetary Nebulae 190

Measuring the Beta-Decay End Point of Atomic Tritium 193

Laboratory and Field Studies of Radionuclide Transport in Groundwater 195

Accelerator-Based Mass Spectrometry At LLNL 197

Accelerator Mass Spectrometry Measurements of ^{129}I and ^{36}Cl in Groundwater from the Nevada Test Site 202

Tritium Oxidation Kinetics 204

Weapons Supporting Research

Introduction 207

Primordial Noble Gases from Earth's Mantle 208

Subcrustal Sources for Basalts and Mantle Pyroxenites from Northern Mexico 210

Hydrolysis of the La[2.2.1] Cryptate 213

Measurement of the Enthalpies of Complexation of Thorium with Multiple Fluoride Ligands 216

Calorimetric Determination of the Enthalpies of Complexation of Thorium with Some Amine-N-Polycarboxylic Acids 219

Development of an Automated, Chromatographic Actinide Separation System 222

Monovalent Lawrencium is Unlikely 225

Neutron Emission as a Function of Fragment Energy in the Spontaneous Fission of ^{260}Md 227

Discovery of 5-ms ^{262}Nc and the Study of Its Spontaneous-Fission Decay Properties 229

Investigations of the Decay Properties of ^{263}[105] and ^{264}[105] 232

Half-Life Calculations for Actinide and Transactinide Nuclides 234

Actinide Cross Sections from the Reaction of ^{13}C Ions with ^{254g}Es 236

Possible Two-Phonon Octupole States in ^{96}Zr 238

Single-Proton Transfer Experiments on a ^{148}Gd Target 240

Measurement of Magnetic Dipole Ground-State Transitions in ^{148,150}Nd and ^{152}Sm by Using Inelastic Electron Scattering 242

The Nuclear Structure of Deformed Odd-Odd Nuclei: Experimental and Theoretical Investigations 243

Predictions of Nuclear Properties on the Astrophysical r-Process Path 247

Nuclear Structure of ^{200}Pt from In-Beam Conversion-Electron and Gamma-Ray Spectroscopy 249

The Study of Octupole Deformation in ^{227}Ac by Single-Proton Stripping Reactions: ^{226}Ra(α,t)^{227}Ac and ^{226}Ra(^{3}He,d)^{227}Ac 252

Conversion-Electron Experiment to Characterize the Decay of the ^{237}Np Shape Isomer 255

Fragmentation Studies Using Niobium + Gold Reactions at 50, 75, and 100 MeV/A 258

Fragmentation in Peripheral Collisions of Relativistic Heavy Ions 261

4 Containment 264

Measuring Cavity Pressure in Nuclear Tests 266

Adapting Carbon/Oxygen Logging for Use at the Nevada Test Site 268

Plug Evaluation Diagnostics Systems 271

Calculations of Underground Nuclear Explosions Using DYNA2D 273

Faster, More Efficient Data Processing from Converted Codes 275

Nuclear Test–Experimental Science

Overview

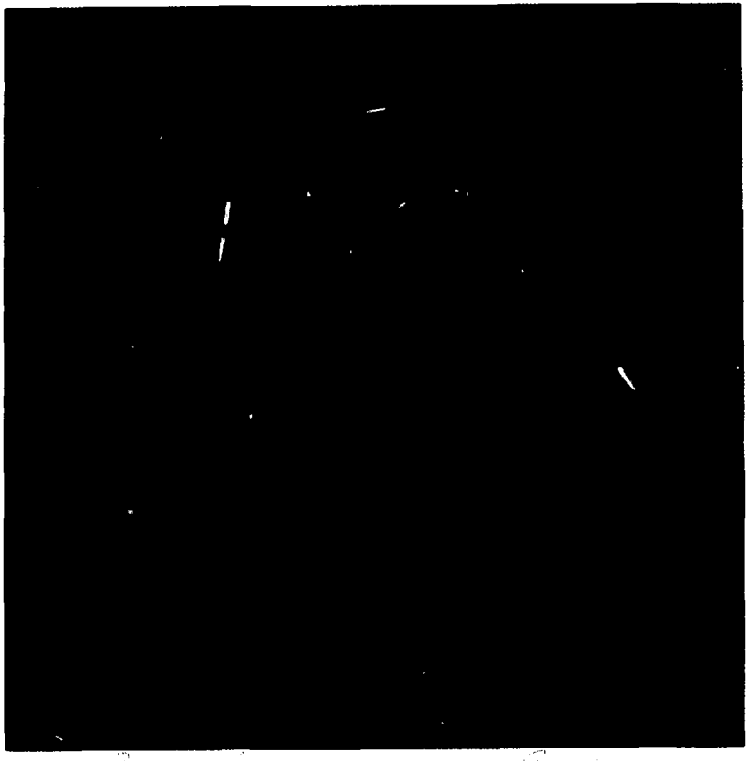

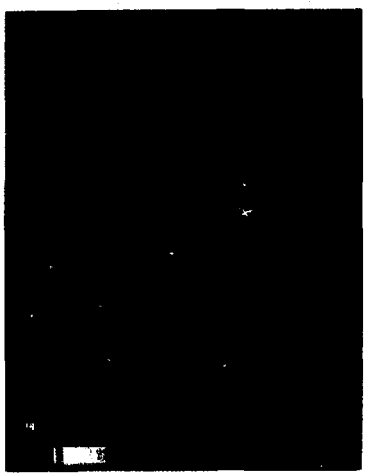

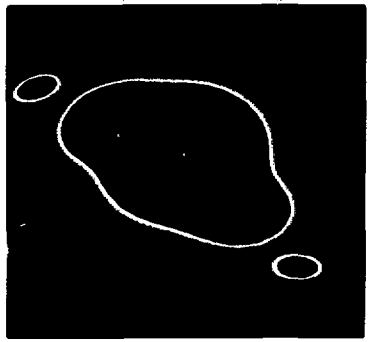

Fiscal year 1988 has been a significant, rewarding, and exciting period for Lawrence Livermore National Laboratory's nuclear testing program. It was significant in that the Laboratory's new director chose to focus strongly on the program's activities and to commit to a revitalized emphasis on testing and the experimental science that underlies it. It was rewarding in that revolutionary new measurement techniques were fielded on recent important and highly complicated underground nuclear tests with truly incredible results. And it was exciting in that the sophisticated and fundamental problems of weapons science that are now being addressed experimentally are yielding new challenges and understanding in ways that stimulate and reward the brightest and best of scientists.

During FY88 the program was reorganized to emphasize our commitment to experimental science. The name of the program was changed to reflect this commitment, becoming the Nuclear Test–Experimental Science (NTES) Program.

The NTES Program is the experimental component of nuclear-weapon design activities at LLNL. As such, NTES has both a programmatic and an institutional mission. The programmatic mission is to challenge and validate theoretical and calculational models of the physics phenomena associated with nuclear weapons. This mission includes responsibility, in the broadest interpretation, to test hypotheses developed in designing nuclear weapons and to solve the problems that occur in these designs. The institutional mission addresses broader and longer-term issues. It includes the responsibility to identify, develop, and apply expertise in cutting-edge technologies relevant to designing and testing nuclear weapons, as well as the responsibility to relate synergistically with other LLNL programs and technology needs.

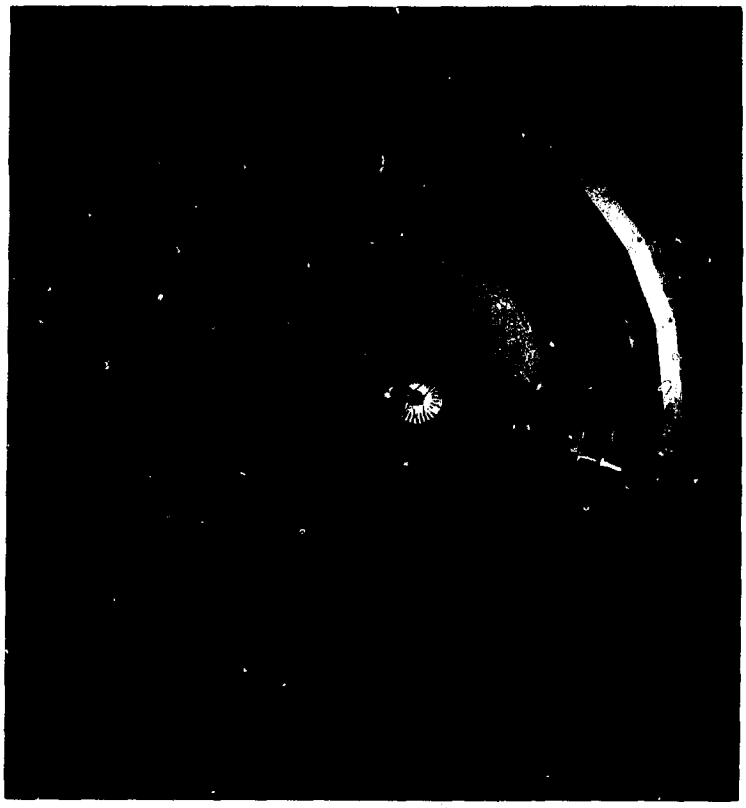

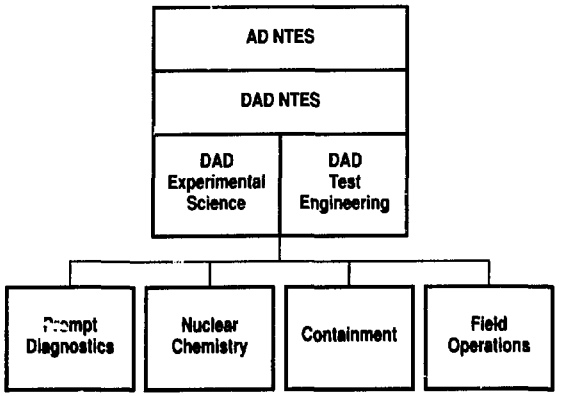

Figure 1.
Diagram of NTES organization.

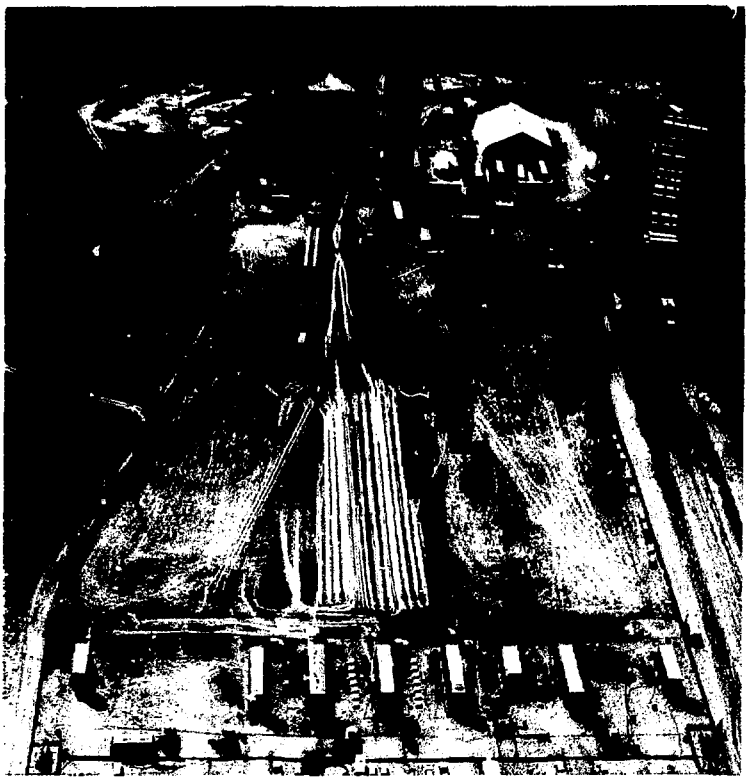

Implicit in these missions is the safe and efficient conduct of underground nuclear tests (UGTs), the development and maintenance of UGT engineering technologies, and the establishment of new and appropriate world-class facilities to support the quality of science and engineering required to execute our programs.

Our revitalization objective, when taken in the context of scarce resources and the national, DOE, and Laboratory commitments to higher standards of quality in environmental, safety, and security concerns, manifests itself into three components: enhanced science, enhanced efficiency, and enhanced quality. The first two of these components, *science* and *efficiency*, have been addressed in a reorganization and redirection of the program responsibilities. The third, *quality*, is being addressed through the line management and includes all aspects of our activities, particularly safety, security, environmental impact, and experimental results.

The NTES organization is shown in Fig. 1. The positions of Deputy Associate Director (DAD) for Experimental Science and for Test Engineering are new and are designed to place emphasis on addressing the enhanced science and efficiency objectives, respectively.

NTES is divided into four program elements that are responsible for the different aspects of the program. They are Prompt Diagnostics, Field Operations, Nuclear Chemistry, and Containment.

- The Prompt Diagnostics program develops methods to measure fast, time-dependent physics phenomena associated with nuclear explosions. The data obtained from these measurements are usually in the form of electrical or optical signals on cables.
- The Field Operations program is responsible for the engineering aspects of fielding and executing underground nuclear tests.

• The Nuclear Chemistry program develops nuclear chemistry techniques to measure the physics phenomena associated with nuclear explosions. The data obtained are usually in the form of radioactive products retrieved from post-shot drilling.

• The Containment program is responsible for the total underground containment of all products from nuclear explosions, particularly radioactive debris.

In FY88, NTES fielded several new measurement techniques with unprecedented success. The program also conducted many related experiments and studies both at LLNL and at other laboratories with which we collaborate. Our experiments have enabled us to explore, in considerable detail, areas of nuclear-weapons-related physics that, heretofore, have been addressed only by calculational approximations, assumptions, and extrapolations. The information obtained is critically impacting our calculational models and our understanding of nuclear-weapons performance. Although much of this information is classified, we provide illuminating examples of our work in this unclassified annual report in the Prompt Diagnostics and Nuclear Chemistry sections.

Also in this fiscal year, we successfully conducted several complex UGTs, which are our "laboratories" for acquiring our experimental data. These tests presented many very difficult fielding challenges including the need to tightly control the underground temperature and humidity surrounding critical experimental components; to dynamically control, *in situ*, the highly precise alignment of sensitive measurement systems; to handle, emplace, and bury highly delicate and sophisticated instrumentation packages weighing nearly 1,000,000 lb into holes up to 2000 ft deep; and to successfully contain underground all nuclear explosions, which are conducted in a variety of engineering and geological circumstances. Articles addressing the range of fielding challenges and accomplishments appear in the Field Operations and Containment sections of this report.

The NTES Program significantly broadened its expertise in several areas this past year, including atomic physics of highly ionized matter, high-resolution x-ray spectroscopy, imaging techniques, electro-optic technology, nuclear chemistry techniques, and synchrotron radiation. New facilities include an automated chemical separation and analysis laboratory, synchrotron radiation beam lines (at Stanford University), electron-beam ion trap (EBIT) for atomic physics studies, improved low-energy x-ray source (LEXIS) for instrumentation development and calibration, and an expanded control room at NTS to support highly complex and computer-controlled experiments. Other facilities also have been started: a dedicated (research) laser for plasma physics experiments, an enhanced EBIT, and a new office and laboratory facility, the Nuclear Test Technology Complex, to house most of the program.

Fiscal year 1988 has been a significant, rewarding, and exciting year for the NTES Program, with the predominant achievement being renewed emphasis and revitalization. This first-ever NTES annual report symbolizes and documents our efforts in this regard. Consequently, the report focuses predominantly on the science of the program, and highlights important aspects of our fielding and engineering activities. It draws from all programmatically supported activities in the following NTES Divisions: L Division, Nuclear Chemistry, Nuclear Test Engineering, Field Test Systems, and the Nuclear Test Operations Department, as well as from some groups in the Physics and the Earth Sciences departments. Other relevant work in these divisions that is supported by the Laboratory's Institutional Research and Development (IR&D) Program is reported annually by that program.

This report is somewhat constrained to keep it unclassified, but its utility as a tool in reaching out to broaden our interfaces and collaborations more than compensates for the constraint. We look forward to building on and further honing this tool in future years.

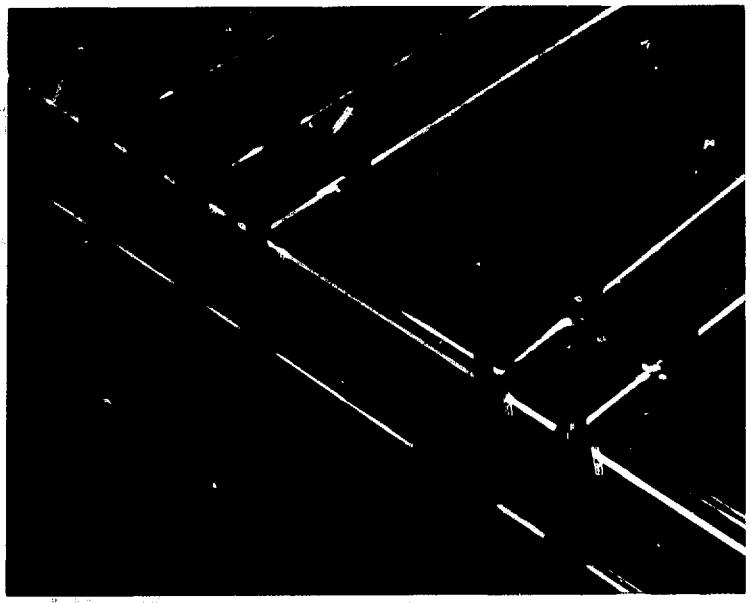

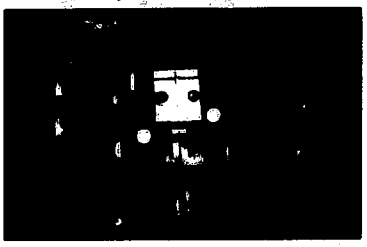

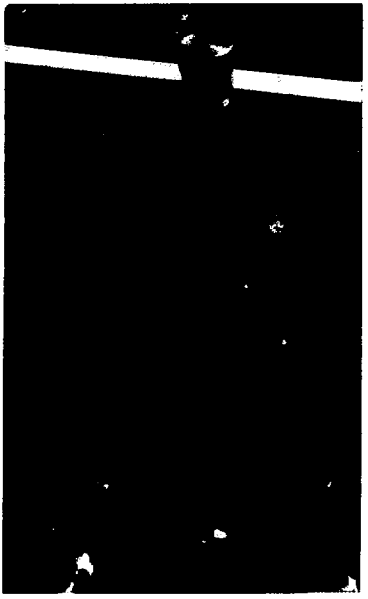

1

Prompt Diagnostics

The role of the experimentalist is to observe and provide data about physical processes in order to solidify our theoretical understanding. The Prompt Diagnostics Program is one of several groups of experimentalists who support weapons design and research at LLNL. Together with the other Nuclear Test–Experimental Science (NTES) groups, the Prompt Diagnostics Program performs measurements on underground nuclear tests. In addition, we conduct laboratory research on phenomena important to the performance of nuclear explosives. The specific direction for our experimental effort is determined by analysis of our ability to model critical phenomena of weapons physics. In conjunction with the nuclear design programs, we determine the sensitivity of an explosive's performance to variations of the process in question; identify appropriate observables; and invent measurement technologies.

Many of the measurement techniques used at the Nevada Test Site (NTS) have been standardized during the past decades, but new diagnostic inventions have been the key to an explosion of data in the past few years that has been fundamentally important to the weapons design process. This is particularly true in the development of the x-ray laser, where detailed x-ray spectral and imaging data have proved to be important model constraints. The instrumentation invented for these applications rivals the best quality available in the laboratory in spatial, energy, and time resolution. That we have been able to apply this instrumentation successfully in the underground environment is remarkable in itself; the quality and importance of the data returned cannot be overstated.

During FY88, our underground experiments also pushed the frontiers of high-bandwidth signal generation and recording with the use of small B-dot detectors and well-characterized oscilloscope systems to increase our understanding of the transient response of electronic circuits to pulsed radiation. We developed a method for shuttering image cameras that allows us to spatially measure the evolution of the fusion process in an explosive. We used high-resolution x-ray spectroscopy to make measurements of the emissivity of uranium, providing data that have proved provocative to the nuclear design and test communities.

We conducted laboratory experiments at the California Institute of Technology and on LLNL's electron beam ion trap (EBIT) with the goal of duplicating specific weapon-like phenomena on a small scale in order to obtain more detailed physics interpretations that we could use to help develop appropriate nuclear and atomic models for weapons applications. These experiments have contributed to advancements, which, in turn, have dramatically improved the quality of data output over previous measurements. We also sought appropriate optical analogs to x-ray laser phenomena in order to obtain the data necessary for easier evaluation of the models.

The objectives of most of the work of the Prompt Diagnostics Program are classified, as are the results obtained and the significance of those data for the Laboratory's mission. Where possible within the rules of classification, we have attempted here to give such technical assessments, but the bulk of this section deals with the technology of our experimental programs. The advances in and application of these technologies, as well as the data and their meaning, have been nothing less than spectacular.

Experimental Physics in FY88

Schellbourne X-Ray Spectrometers, Camera Systems, and Active Alignment Systems

J. Wobser, T. Perry, D. Hakala, and R. Quinuis

The Schellbourne Event was a multipurpose underground nuclear test that included several investigations of device design and physics, all details of which are classified. The Schellbourne Event was successfully executed on May 13, 1988. Prompt diagnostic measurements included three reaction-history measurements, two filtered-fluorescer (SPECTEX) measurements, one Dart measurement, three microchannel-plate active crystal spectrometer (MCPACS) measurements, and two taut-wire alignment gauge (TWANG) measurements. These experiments were arranged in a moderately complex diagnostic canister with seven lines of sight plus the TWANGs. The MCPACS spectrometers, together with their active alignment systems, were new and unproven designs, and most measurement systems returned data of generally high quality. In this article, we present the unclassified version of the MCPACS design and electronic readout system, current applications of the spectroscopy array camera (SPAC), and the design of the active downhole alignment system.

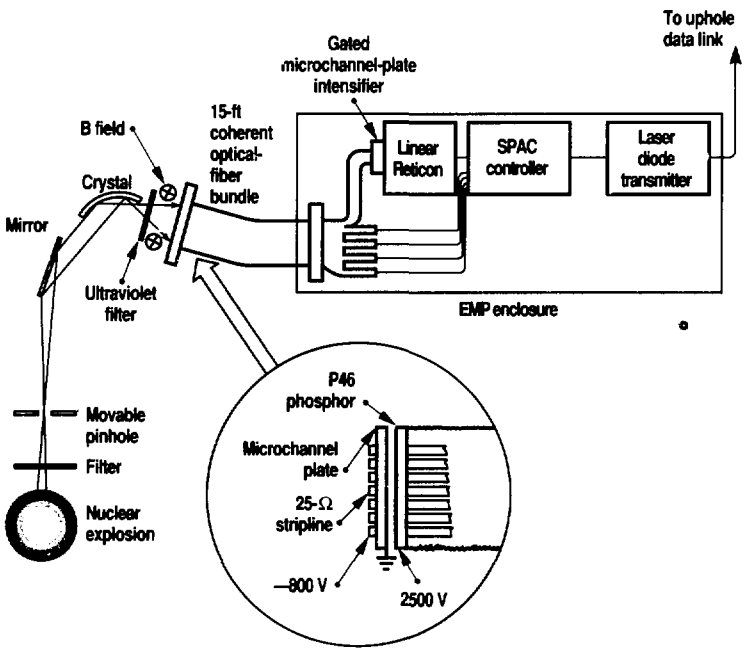

Figure 1. Diagram of the MCPACS spectrometers used on the Schellbourne Event.

Microchannel-Plate Active Crystal Spectrometer

Many physical processes occur during a nuclear explosion. While nuclear processes are responsible for the production of energy, we have become increasingly interested in the atomic physics that takes place in the hot, dense plasmas produced by these explosions. To investigate such processes, we have developed new, high-resolution x-ray spectrometers. For the physics of interest on the Schellbourne Event, we wanted to measure the x-ray spectrum between 1.9 and 4.0 keV with a spectral resolution of 1 eV. This is the largest spectral coverage, spanning over a factor of 2 in photon energy, of any high-resolution spectrometer fielded to date in the downhole nuclear test program.

We built three spectrometers to cover the spectral range. Due to budget and geometric constraints, we were unable to obtain 1-eV resolution over the entire spectral range. Instead, we compromised, with one spectrometer having 1-eV resolution and the others having poorer resolution but broader spectral coverage to cover the complete range. Table I shows the range covered by the three spectrometers.

Figure 1 shows a diagram of the spectrometers. Each spectrometer contained an x-ray mirror, curved diffraction crystal, and gated microchannel-plate x-ray detector. The detector output was transported through a coherent optical-fiber bundle to a downhole electronic camera system. This system, called the SPAC

system, is described in the next section. Components similar to those in our spectrometers had been tested in earlier events, but never in the configuration used for the Schellbourne Event. Thus, the MCPACS instruments were used for the first time on this event.

The purpose of the x-ray mirror was to act as a low-pass filter for the spectrometer, eliminating any confusion arising from possible higher-order reflections from the crystal. Mirrors in the different spectrometers reflected x-ray energies only up to approximately 120% of the upper-energy cutoff in Table 1. An x-ray mirror works because the index of refraction of materials in the x-ray region is slightly less than unity. Thus, x-rays striking a flat surface at a sufficient glancing angle are externally reflected. Unfortunately, the angles necessary to reflect kilovolt x-rays are small. The mirror angle for MCPACS 3 was only 0.7 degrees. This shallow angle necessitated a mirror 18 in. long that was flat across its surface to within a few thousand angstroms and that had a surface roughness of only a few angstroms. The x-ray mirrors were composed of a 2500-Å layer of Ni, vapor deposited on an optically flat glass substrate. The substrates were Pyrex glass bonded to Kovar bases. The adhesive had to be strong enough to withstand field environmental conditions but sufficiently flexible to compensate for the differential expansion between the two materials. An early design used a different bonding adhesive and a stainless-steel base. We discovered during a separate experiment that the original adhesive released, allowing the Pyrex mirrors to fall off. The same failure mechanism may have contributed to data loss on the Labquark Event. Since using a new adhesive and Kovar bases, we have experienced no further problems of that nature. However, during optical alignment of the spectrometer bodies with the mirrors in place, we have observed distortions in the images. We found that the mirror flatness distortion was caused by the bonding to the Kovar bases. Because our mirrors had been x-ray calibrated prior to this bonding, we had to resurface, nickel-plate, and calibrate all the mirrors after bonding to the bases and before proceeding with optical alignment. Filters in front of the mirror were designed to keep the temperature of the mirror cool so that its reflecting properties did not change during the experiment.

We used different crystals in each of the three spectrometers: mica, quartz, and fluorite (CaF_2). These crystals were chosen according to the energy coverage of each spectrometer. All three crystals were cylindrically curved, with the spatial direction along the axis of the cylinder and the energy diffraction along the radius.

Mica (002) crystals have been successfully fielded on spectrometers in the past. In our design, the approximately 0.004-in.-thick crystals were elastically bent around the crystal holder and attached at the edges. A test using a laser-beam reflection through the bend focus point indicated a uniform bend radius across the crystal surface, but the 0.010-in.-thick quartz crystal did not remain uniform when elastically bent. Thus, we used a Pyrex mandrel ground to the proper radius to support the crystal. Although this technique solved the problem of surface uniformity, it added significantly to the background intensity at the detector.

Our CaF_2 (111) crystal presented two problems. We had no previous experience with this type of crystal and had never attempted to bend a crystal to such a tight radius (2.7 cm). One crystal supply company agreed to bend these crystals to our specifications. After several months without meaningful results, we purchased a supply of 10-, 20-, and 40-mil-thick stock and attempted to bend some ourselves, but without success. Finally, a contractor successfully supplied three sets of 0.020-in.-thick crystals, which were inelastically formed by placing the crystals in a graphite fixture and heating them to 1000°C. One of these crystals broke months later over a weekend after the spectrometer had been x-ray calibrated. However, no other crystals have broken once installed and calibrated in their respective spectrometers.

Crystal calibration was done on the double-goniometer Henke facility, with cross calibration on the ion-accelerator (IONAC) and low-energy x-ray (LEX) facilities. Crystal heating was a more difficult problem than mirror heating. To achieve 1-eV resolution, the crystal temperature cannot rise by more than a few degrees. By proper selection of filters, we were able to keep the temperature low enough that spectrometer resolution was unaffected on MCPACS 1 and 3. On MCPACS 2, the resolution was degraded by about 50% during the experiment.

Our detector was similar in design to those used on the Orkney EDACS, Cottage KILOSPUD, and Delamar MCPOD experiments. The distinguishing feature of these detectors is the inclusion of a microchannel plate to obtain high sensitivity in the detector. High sensitivity is important because of the relatively low efficiency of the x-ray diffraction crystal. If a detector does not have sufficient sensitivity, the diffraction crystal starts to lose resolution due to heating before enough diffracted x rays reach the detector to produce a measurable signal. This is especially true in high-resolution experiments because the

Table 1. MCPACS specifications.

Spectrometer number	Energy coverage (keV)	Energy resolution (eV)	Mirror angle (degrees)	Crystal material (plane)	Crystal radius (cm)
1	1.9–2.6	2–4	1.0	mica (002)	17.0
2	2.5–2.8	1–2	1.0	quartz ($10\bar{1}0$)	17.0
3	2.7–4.0	5–9	0.7	fluorite (111)	2.7

available energy is divided into many spectral bins.

The detector contained a 40-mm-diam microchannel plate. The back side of the microchannel plate was uniformly conducting; the front side was coated with seven 3-mm-wide conducting strips separated by 2-mm gaps placed symmetrically on the microchannel plate. The photocathode surface for MCPACS 1 and 2 was Ni; for MCPACS 3 it was Au. X rays striking the photocathode produce electrons that enter the channels in the microchannel plate. If voltage is present across the microchannel plate, a cascade process multiplies the photoelectrons by several orders of magnitude. Electrons leaving the back of the microchannel plate are accelerated across a 0.5-mm gap to strike P46 phosphor coated on an optical-fiber faceplate. We selected P46 phosphor because its short decay ($1/e$ decay time = 70 ns) allowed most of the light from the detectors to be collected before the detectors had to be gated off because of neutrons arriving at the spectrometer. Light emission from P46 phosphor peaks at 530 nm and is easily transmitted through the coherent optical-fiber bundle.

The strips on the microchannel plate formed a 25-Ω stripline geometry and allowed us to take several time snapshots of the incident x-ray spectrum. For the experiment, each strip was turned on for 5 ns. The thickness of the strips is critical. The metal must be thick enough that the resistance remains small (about 1 Ω). High resistance would cause the electrical pulse to be attenuated while crossing the strip, resulting in nonuniform gain. On the other hand, a thick coating substantially reduces detector sensitivity.

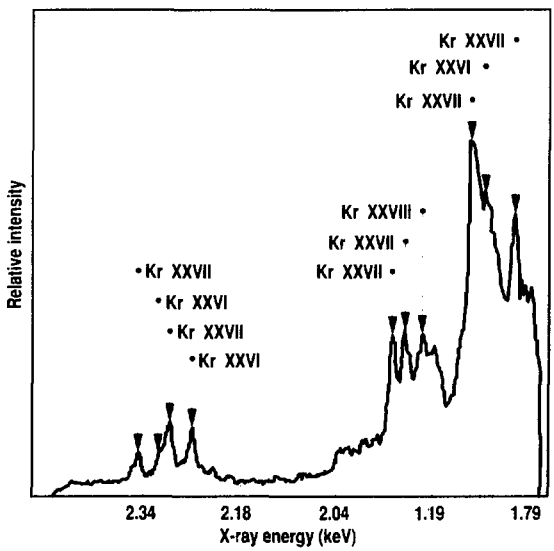

Figure 2. Spectrum of a Kr implosion taken with the MCPAC 1 device. This operation in a gated mode was done to ensure proper calibration. (Scale on the x axis is nonlinear.)

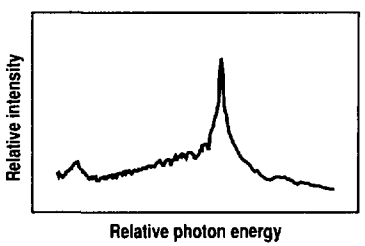

Figure 3. Example of data obtained by a MCPACS spectrometer during the Schellbourne Event.

One problem that arose during calibration of the detectors was that the P46 phosphor became charged as it was bombarded with electrons from the microchannel plate. The phosphor had been bonded to the optical-fiber faceplate using lacquer, and the phosphor-lacquer combination proved to be highly insulating. Sufficient charge accumulated on the phosphor to turn off the detector completely. The charge persisted unless the detector was brought up to air. We eliminated this charging problem by switching to potassium silicate as a bonding agent.

Because our detectors were calibrated in the dc mode, we wanted to ensure that the calibration was valid in a pulsed mode. The MCPACS 1 spectrometer was connected to the low-energy x-ray instrumentation system (LEXIS) machine, and the detector was operated in the gated mode. Figure 2 shows a spectrum obtained from Kr plasma.

We designed and built three pulsers to gate the microchannel-plate x-ray detectors. Our design was similar to that used on the EDACS experiment on Orkney and included a planar triode vacuum tube to produce high-current, high-voltage pulses. Each of the three pulsers had four 50-Ω outputs. Two outputs were combined prior to entering the detector to match the 25-Ω impedance of the striplines. The amplitude of the pulses could be varied between 500 and 1000 V, and the width of the pulses was 5 ns.

Pulsers were triggered by a signal from the device. The RF-19 trigger cables from the Compton diodes were run in a straight line through the center of the diagnostic canister to minimize trigger delay. The pulse from the pulser was sequentially sent through the strips on the detector. We obtained five time snapshots of the spectrum, each 5-ns long, with gaps between snapshots.

Figure 3 shows results from a portion of the spectrum from the Schellbourne Event. We obtained good data for all channels on MCPACS 1 and 3, but no data from MCPACS 2. The electromagnetic pulse (EMP) enclosure for the camera system for MCPACS 2 was located closer to the

device, and, apparently, the larger EMP signal at this location destroyed the electronics. Data from this experiment are still being analyzed. We believe this work represents a significant step forward in understanding the atomic physics of plasmas produced by nuclear explosions.

Spectroscopy Array Camera

Since its inception in 1984, the SPAC system[1] has developed into one of our most useful tools both in the laboratory and at the NTS. At the NTS, the SPAC system is used for calibrations and setup prior to an event and for data gathering during an event. This section details the changes made since 1985 and current applications for the SPAC system, including the fielding of 24 SPAC cameras on the Schellbourne Event.

The heart of the SPAC system is a Reticon 1024SF linear array (see Table 2). The size of the complete array is 25 by 2.5 mm, and the pixel area has a 100:1 aspect ratio. The resolution of the system has been increased due to a change from 10- to 12-bit A/D converters, and the typical dynamic range (peak signal divided by rms noise) is at least 4000:1 even at room temperature. Because the SPAC typically has a saturation energy on the order of 800 mergs/cm^2, a user can discern energy values on the order of 0.2 mergs/cm^2.

The SPAC system is typically connected to a microchannel-plate intensifier (MCPI) when light is not optically bright enough or else is at a wavelength such that the array is not responsive enough. In either case, the array has an optical-fiber window allowing for attachment of an MCPI. This helps increase the sensitivity to as low as 8 mergs/cm^2 at saturation; however, addition of the optical-fiber window degrades saturation exposure, quantum efficiency, and spectral response characteristics. The 12-μm-diam fibers in the window allow each pixel in the array to see at least two fibers in the narrow direction, with no degradation of the theoretical contrast transfer function (CTF) of 20 lp/mm. The component limiting the CTF is typically the MCPI and its interface to the array window. A CTF of 12.5 lp/mm at a light level of 20% of saturation is common.

Another significant improvement is that a new physical layout now allows for more versatile use of the array system. Individual arrays are now packaged in their own modules and can be used in different locations within the constraints of the 3- to 4-ft cable length. The signals from the array modules (cameras) are combined in the SPAC controller. Thus, a SPAC system is comprised of up to eight cameras and one controller. We typically use seven cameras for data gathering and one as a background reference to maintain continuity of the calibrations.

The SPAC system is read out in the laboratory by a stand-alone display and storage system, called the spectroscopy array camera display enhancement system (SPADES). SPADES is designed around an LSI-11/23 computer, which enables users to obtain a virtually real-time image of counts versus pixel position in the form of an easily read graph. The combined SPAC and SPADE systems enable users to view spectrometer data in real time and to correlate the number of counts back to an energy level that can be traced to a known quantity. This enables a user to determine the previously unknown energy level of x rays, for example, emanating from the source. The stand-alone capability of SPADES enables the system to be used in many different laboratories and in the NTS tower. An array module can also be used independent of the controller, if desired.

The system is also used to characterize optical-fiber arrays that transmit data from detectors to receivers. High resolution allows the checkout of these arrays in a fraction of the time required by film techniques. Storage and archive capabilities allow users to maintain a permanent file of all calibration data.

During the Schellbourne Event, 24 SPAC cameras were fielded in a downhole environment looking at a spectroscopy experiment. Event data were retrieved on disk upon the arrival of the recovery team. Sixteen of the 24 cameras functioned properly, and data were successfully gathered and processed. The remaining eight cameras appeared to be saturated, an unexpected result. The 16 functional cameras were located in a specially built module at the top of the diagnostic canister; the eight nonfunctional units were located in another module approximately 15 ft lower in the canister. All indications suggest an EMP effect; however, we have not yet been able to simulate this effect. The linear array is a silicon photodiode, which has been shown to be radiation resistant; thus, we conclude that the electronics were affected in an unknown manner. We have since used a tesla coil to generate shield currents and an electrostatic discharge gun to generate pulses to interrupt the system, but to no avail. Further studies should be done with a larger EMP generator.

Our future plans include streamlining the display system and developing a camera based on the Reticon 2048SF array. This array has 2048 pixels, with the same physical dimensions as the 1024SF, allowing a 5-cm-long array to be seen in one shot. We expect the prototype to be built by the summer of 1989.

Schellbourne Active Alignment System

In this section, we discuss alignment of the two spectrometer lines of sight (LOS 6 and 7) and the active downhole alignment system[2] used to maintain alignment of critical components in the

Table 2. Electrooptical characteristics of the Reticon 1024SF linear array at 25°C.

Center-to-center spacing (μm)	25
Aperture width (mm)	2.5
Responsivity [C/(J/cm^2) at 750 nm]	2.8×10^4
Nonuniformity of response (%)	±10
Saturation exposure (nJ/cm^2)	50
Saturation charge (pC)	14
Average dark current (pA)	5
Quantum efficiency (%)	75
Spectral peak response (nm)	750
Spectral response range (nm)	250–1000

spectrometer experiments. We also discuss the mini-TWANG system used to evaluate canister bending in the region of spectrometer housings during the Schellbourne Event. Figure 4 shows LOS 6 and 7 and the two TWANG systems. Our primary concern was that, if the diagnostic canister deflected during the stemming operation, then spectrometer data could be compromised.

From a physics point of view, each spectrometer had a field of view at the x-ray source, which originated at the detector, was geometrically projected through the various collimators and pinholes, and included the effects of crystal diffraction and mirror reflection. Each projected beam required tight alignment tolerances to achieve our objectives. Figure 5 shows the calculated field of view of the MCPACS experiments at a window 2.00 in. above the source. All three projected fields of view fit inside a 0.87-in.-diam circle, with only a portion of the MCPACS 3 footprint projected on the region of undoped material. LOS 7 viewed this window vertically, while LOS 6 viewed it at a slight angle (note the second view at the -2.00-in. elevation). MCPACS 2 and 3 not only shared the same pinhole, but the projection of MCPACS 3 had to go through the collimator and spectrometer housing of MCPACS 2. Alignment of critical components within spectrometer housings was done in the laboratory and maintained after installation in the diagnostic canister due to the rigidity of these housings.

We would have preferred total alignment tolerances of less than ±0.5 mm at the source with respect to material interface boundaries. Since we could only build the source with known boundary uncertainties of ±0.015 in., the spectrometer pointing alignment had to be within ±0.010 in. to achieve the overall criteria. The spectrometer bodies were to maintain an angular displacement or tilt less than 0.05 degrees with respect to the reference line established by the pinhole and entrance collimators to the spectrometer housing.

A two-wire system established the reference line between the working-point elevation and the entrance to MCPACS 1 and 3, with a detector station located on the same *x-y* positioning table as the pinhole collimators. The detector station consisted of two Kaman high-resolution proximity transducers[3] and a video camera located on the *x-y* axes of the diagnostic canister. The Kaman transducers provided relative motion measurements with uncertainties of ±0.0025 in.; the video camera provided redundancy in the event of transducer failure, but with a resolution of only ±0.040 in. Linear variable-displacement transducers (LVDTs) also monitored the translation of the *x-y* table.

We conducted a deflection test of the diagnostic canister (see Fig. 6) to understand the displacement relations between the relevant LOS to an applied side load. We also measured angular displacement of the MCPACS housings due to loading of the supporting bulkheads (tin-canning effect).

Our tests revealed a correlation between midspan canister deflection and movement measured by the Kaman sensors as well as *x-y* table translation indicated by the LVDT transducers. The bend test also allowed us to observe the responses of individual components and systems and allowed us to make changes that enhanced the field performance of the alignment system. We found that, if

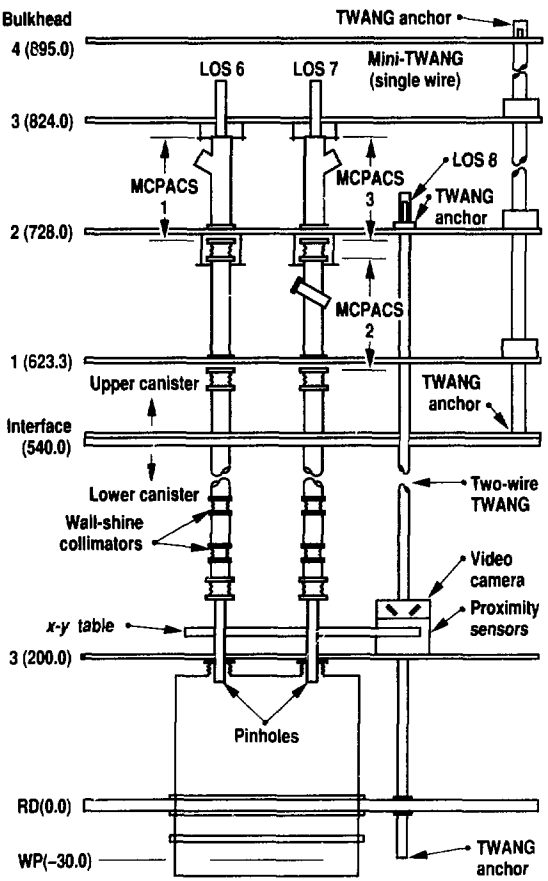

Figure 4.
Schematic of LOS 6 and 7 and the TWANG system. All dimensions are in inches.

the diagnostic canister deflected approximately 0.12 in. at midspan. MCPACS 2 would interfere with MCPACS 3 and affect critical data associated with spectrometer experiments. Thus, the MCPACS fields of view on LOS 7 were changed, as shown in Fig. 7.

We also established a correlation between the *x*-*y* table translation and angular displacement of the MCPACS housings (see Table 3). Any midspan deflection greater than approximately 0.25 in. would exceed the physics criteria of 0.05 degrees angular displacement. Our tests also showed that, when a downward load was applied to bulkhead 2 of the upper diagnostic canister, the alignment and angular displacement of MCPACS 1 and 3 remained unchanged. Thus, the issue of bulkhead tin-canning was put to rest.

At the NTS, the diagnostic canister and device pedestal were placed in a free-hanging, stable condition in the tower to prevent bending or movement of the canister due to forces exerted by tie-down restraints. An uninsulated tower allows sun-generated, side-to-side temperature gradients to distort the canister. Vertical temperature gradients also create light refraction in the lines of sight that can cause the alignment targets to wander when viewed through the alignment scope. Consequently, we monitored the Kaman sensors for several days to determine when the canister was thermally stable. We found that the best time of day to establish the TWANG reference line was from several hours before sunrise until one hour after sunrise.

The mini-TWANG implementation, a result of Kernville TWANG data, was added to quantify any large deflections believed to have occurred near the top of the Kernville diagnostic canister during the downhole stemming process. A single-wire TWANG system was installed in the upper diagnostic canister, consisting of three video stations mounted on bulkheads 1, 2, and 3, thus spanning the region containing all three MCPACS housings.

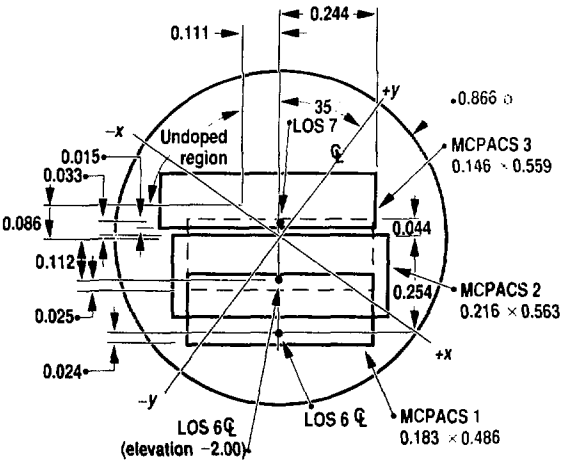

Figure 5.
Calculated field of view of the MCPACS experiments at a window 2.00 in. above the source. All dimensions are in inches.

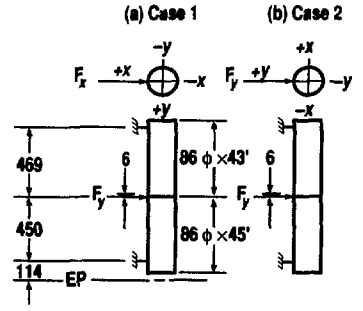

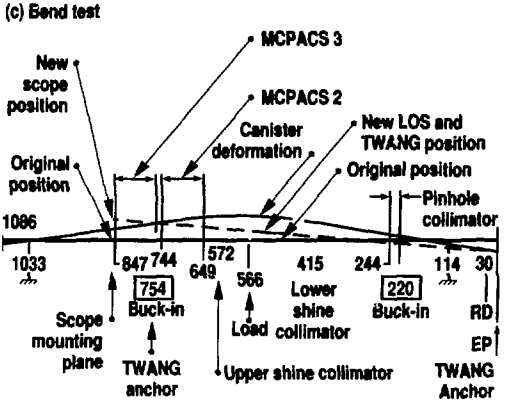

Figure 6.
Schematic diagram of the bend test. All dimensions are in inches unless otherwise noted.

Diagnostic and device canisters were emplaced in hole U2gf at the NTS and positioned in the center of a straight section of the hole. From historic data, placement in a straight section of hole would imply midspan deflections of <0.25 in. and, therefore, angular displacement of the spectrometer housings of <0.05 degrees. We also added Al doors and prestemming to stiffen the diagnostic canister and placed a foam cushion under the device canister to decrease compressional loading and to minimize deflection of both canisters.

During the stemming operation, the measuring system indicated that the pinhole collimators had moved from their original aligned position. The final Kaman sensor readouts indicated a displacement of $x = +0.005$ in. and $y = -0.031$ in. The x-y table was then translated until the Kaman sensors reached the null position. The LVDT readouts indicated that the table was displaced 0.005 in. in the $+x$ direction and 0.032 in. in the $-y$ direction, in agreement with the Kaman sensor readings. The translation of the table corresponded to approximately 0.240 in. of midspan deflection of the diagnostic canister and an angular displacement of the MCPACS experiments of 0.05 degrees. The video TWANG station, which was a backup to the proximity transducers, but with much less resolution, also recorded a deflection of the TWANG wire of the same order of magnitude.

Figure 8 was generated from the Kaman sensor readouts as the stemming material activated various stemming-switch elevations. These sensors indicated the direction the x-y table had to translate, which was the direction opposite to the deflection of the diagnostic canister. No deflection within the upper diagnostic canister was detected with the mini-TWANG. Because of these data and a reevaluation of Kernville data, we now believe that the upper canister structures with streak-camera modules are sufficiently rigid for most spectrometer designs.

Alignment of the MCPACS experiments was achieved and maintained despite the small fields of view of the MCPACS experiments, stringent alignment within each spectrometer housing, and all the external influences on the experiments (e g., bending of the diagnostic canister and downhole stemming). Data from the various alignment instruments indicated that the TWANG performed as expected. We found no changes between the first and last calibration check. The correlation between different transducers was also outstanding; there was no apparent electrical or mechanical drift in either system (LVDTs and Kaman transducers versus video camera). The mini-TWANG also performed as expected.

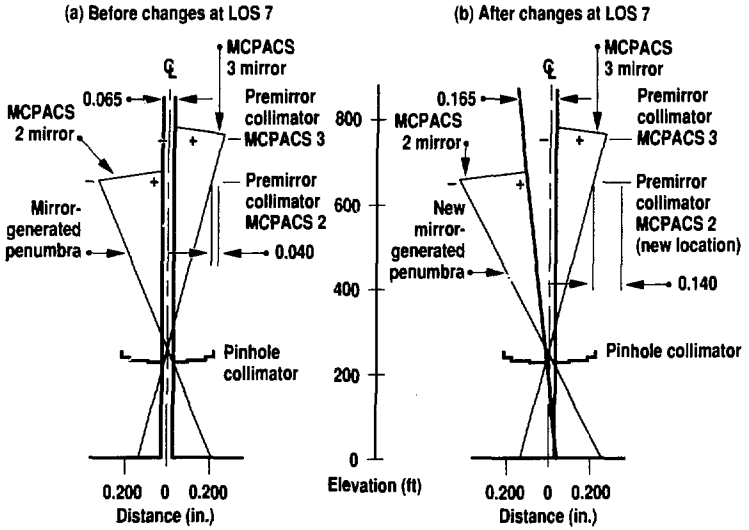

Figure 7. Changes made to the MCPACS experiments. All dimensions are in inches unless otherwise noted.

Table 3. Correlations among translation, deflection, and angular displacement.

Direction	Translation of x-y table (in.)	Predicted midspan deflection of diagonal canister (in.)	Predicted angular displacement of MCPACS (degrees) 1	2	3
	0.016	0.080	0.02	0.02	0.01
	0.031	0.160	0.03	0.03	0.03
x direction	0.046	0.240	0.04	0.04	0.04
	0.062	0.320	0.06	0.06	0.06
	0.076	0.400	0.09	0.08	0.08
	0.011	0.080	0.02	0.02	0.02
	0.021	0.160	0.03	0.04	0.03
y direction	0.031	0.240	0.03	0.05	0.05
	0.041	0.320	0.06	0.07	0.07
	0.053	0.400	0.07	0.08	0.09

Our conclusion is that canister bending was localized just below the lower and upper diagnostic canister interface, and the remainder of the canister remained essentially straight. Overall, we conclude that diagnostic canister bending did not compromise alignment of the MCPACS experiments and that our new active downhole alignment system was highly successful.

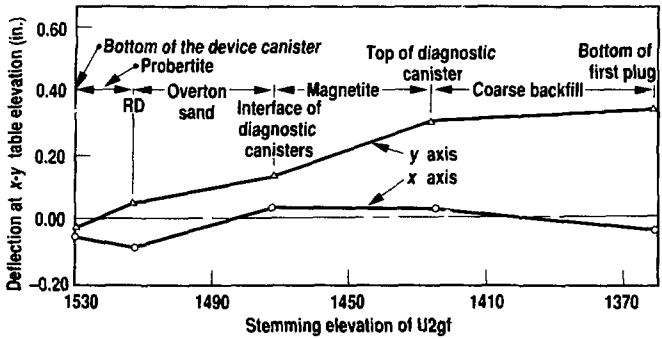

Figure 8. Plot of x-y table data points generated from Kaman sensor readouts.

References:

1. C. R. O'Brien, *Subnanosecond Spectroscopy using Stripline Microchannel Plates and Reticon 1024SF Linear Arrays*, Lawrence Livermore National Laboratory, Livermore, Calif., UCRL-50025-085-3 (1985).
2. R. Quibuis, *Schellbourne Active Alignment System Report*, EG&G/AVO, AVO/ME-008 (1988).
3. B. Costerus, *Quality Assurance Procedure for the Schellbourne TWANG Alignment System*, Lawrence Livermore National Laboratory, Livermore, Calif., memorandum to EG&G (August 20, 1987).

Electron Beam Ion Trap

M. B. Schneider

The electron beam ion trap (EBIT) is a new device designed to study x rays produced by highly charged ions when they interact with free electrons.[1–4] The ions are electrostatically trapped for minutes to hours in a narrow cylindrical region defined by biased electrodes in the axial direction and by a high-current-density electron beam in the radial direction. The energy of the electron beam in EBIT can be varied reliably from 2–25 keV, which is sufficient to strip elements up to Mo of all electrons (Q = +42), to make He-like Pb (Q = +80), and to make any naturally occurring element Ne-like (Q_{max} = +82).

Highly charged ions are ideally studied in EBIT for several reasons. First, processes crucial to understanding high-temperature plasmas (which are highly ionized) can be directly measured. These processes include electron-impact ionization, excitation, and recombination processes. EBIT is a major advance because, although a few measurements of ionization cross sections for charge states up to $Q \leq 50$ are available at present,[5,6] direct measurements of electron impact excitation (IE), dielectronic recombination (DR), and radiative recombination (RR) cross sections have been possible only for $Q \leq 6$ with previous techniques, such as crossed or merged beams.[7,8] Second, the physics in these ions is of interest. The electrons in such highly charged ions experience large electromagnetic forces from the nucleus; relativistic effects are important. In quantum-electrodynamic terms, the electron is in the strong field limit. These effects are probed by observing x rays from the inelastic collisions of trapped ions with electrons in the beam via a high-resolution, well-calibrated spectrometer.

Description of EBIT

As shown in Fig. 1, electrons from an electron gun are adiabatically compressed into a 70-μm-diam beam by following the magnetic field lines of 3-T superconducting Helmholtz coils. The beam is accelerated to kiloelectron volt energy by the drift tube (DT) assembly, and ions are trapped in the center of that assembly. The beam is then decelerated, spread out, and dumped into the collector assembly. The entire machine operates at ultrahigh vacuum pressures; however, because the magnet assembly and the center of EBIT are at liquid He temperatures (4 K), a much higher vacuum is attained in this region. A liquid N shield (77 K) surrounds the 4-K region. A 5-*mil*-thick Be window on the vacuum enclosure allows the transmission of hard x rays to external detectors. Ions are usually introduced into the trap axially by firing the metal-vapor vacuum-arc source (MEVVA)[9,10] that produces low-charged ions ($Q = +1$ to $+4$). This source works much like an automobile spark plug and produces ions from the material in the electrodes. The advent of long trap lifetimes for highly charged ions allows firing the MEVVA less often, so that a single unit can last for one month before refurbishing. We have also introduced ions by evaporation from the electron gun (Ba) and in a neutral beam through a side port (see Fig. 2). Table 1 lists the EBIT parameters.

Figure 2 shows the ion-trapping region. Three tubes make up the DT assembly. The central tube consists of four quadrants making up a Cu cylinder 10 mm in diameter; the two end tubes are Cu cylinders, which narrow to a 3-*mm* diameter 1.5 cm from the center of EBIT. X rays are observed at 90 degrees to the electron beam through the 2.5-mm-wide spaces between the quadrants of the central DT. The electron-ion interaction energy is determined by the output voltage of a precision high-voltage regulator that biases the DTs. An optical fiber controller allows biasing the end DTs with respect to the central tube by up to ±300 V, thus changing the axial trap voltage. Beryllium windows can be placed on the 4-K or 77-K shields (Fig. 1), and they can be removed for soft-x-ray or vacuum ultraviolet (VUV) spectroscopy.

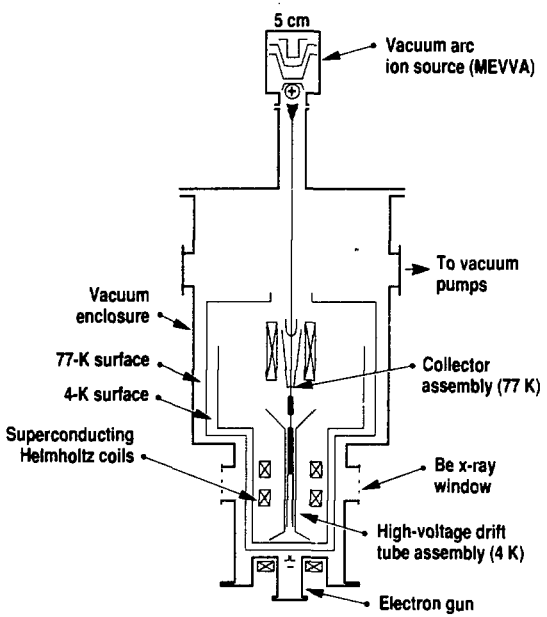

Figure 1. Diagram of EBIT.

Figure 3(a) shows a typical spectrum obtained from a solid-state detector with high detection efficiency but only moderate energy resolution. The spectrum is of near-Ne-like Au (Au^{69+}, Au^{68+}, Au^{67+}, . . .) at a beam energy E_e of 18 keV. An inelastic collision of an ion with an electron in the beam can excite one of the ion's bound electrons to a higher energy level (IE). X rays are often emitted as the electron falls back to the ground state ($n = 2$). The transition lines for $n = 3 \rightarrow 2$, $n = 4 \rightarrow 2$, $n = 5 \rightarrow 2$, . . . are shown, up to the series limit.

When an electron from the beam is captured (recombines) with an ion, an x ray with energy equal to the beam energy plus the binding energy of the shell that contains the captured electron is often emitted. These RR lines are the second typical feature of the spectrum. The lines for RR to $n = 3$, $n = 4$, . . ., up to the series limit at E_e, are shown. The RR cross section for electron capture into the ground state of an ion can be accurately calculated.[11] We use these calculations to fit the RR portion of the spectrum for the ionization balance among the various charge states. Measuring absolute electron-ion cross sections in EBIT is difficult because of the uncertainty in electron current density, solid angle of the detector, and number of ions trapped in

Table 1. Summary of operating parameters for EBIT.

Electron beam energy range (experimental) (keV)	2–25
Electron energy resolution (FWHM) (eV)	~60
Accessible ion-charge states (Q)	≤ +82
Peak magnetic field (T)	3
Electron current (mA)	≤150
Effective electron current density (A/cm^2)	≥2000
Electron beam diameter (μm)	~70
Central vacuum (Torr)	10^{-12}
Drift tube temperature (K)	4
Length of ion trapping region (cm)	~2
Electron gun voltage (kV)	3–4
Electron density (i_e = 100 mA) (cm^{-3})	2×10^{12}
Ion density (cm^{-3})	$4–10 \times 10^{9}$

the beam. Relative cross sections are obtained from the x-ray spectra alone. The cross sections are made absolute using RR spectra taken at the same time.[11]

Evaporative Cooling

EBIT was designed to operate at a central vacuum of 10^{-12} Torr to prevent neutral background gases from donating electrons to the ions and, thus, deionizing them (charge exchange). It soon became obvious that if the vacuum was too pure, the lifetime of highly charged ions in the trap was reduced.[1,12]

Elastic collisions between ions and the electron beam primarily increase the kinetic energy of the ions. This kinetic energy is partitioned in all directions and among all ions by ion-ion elastic collisions. The energy gain for ions is large enough that some begin to spend significant time outside the electron beam and eventually escape the trap, often before reaching the maximum ionization state possible for the energy of the electron beam. In evaporative cooling, a second species of lower-charged ions (LCIs) with a lower charge state q is continuously added to the trap containing the desired highly charged ions (HCIs). The LCIs are heated through ion-ion collisions with the HCIs until both species have approximately the same temperature or average kinetic energy. The LCIs with a lower charge need less energy per ion to escape the trap; thus, they evaporate, removing their kinetic energy from the trap. The continuous evaporation of LCIs cools the HCIs.

We modified one x-ray port to allow a steady flow of atoms or molecules into the center of EBIT for cooling. The LCIs are formed by ionization of neutrals as they pass through the electron beam. We have used both Ti from a hot Ti wire and N gas from a gas injector successfully. Figure 3 shows the dramatic success of evaporative cooling. Ions with $Q = 69$ have remained in the trap for hours.

Measurements of Impact Excitation

The IE cross section has been measured for five $n = 2 \rightarrow 3$ transitions in Ne-like Ba^{46+} (Refs. 2 and 3). Figure 4(a) shows a high-resolution spectrum of Ba^{46+} obtained with a Bragg diffraction spectrometer; Fig. 4(b) is an energy-level diagram of the relevant levels. The spectrometer contained a flat crystal for broad spectral coverage and a position-sensitive proportional counter. For a given line, the observed x-ray intensity is proportional to the IE cross section for exciting that energy level directly and the branching ratio for the level to decay radiatively to the ground state; it is inversely proportional to the feeding ratio of the level being directly excited to all other ways of populating that level. The feeding ratios in Fig. 4(b) are almost 100% for the five levels studied, and the branching ratio for two of the levels is 100%. The remaining three levels are forbidden to decay directly to ground state, but they are responsible for essentially all of the lowest-energy, strong x-ray line (at 4.568 keV) through their $\Delta n = 0$ decay to the level. We deduced absolute IE cross sections from the relevant line intensities using theoretical collision strengths,[13] radiative decay rates, and branching ratios shown in the figure, normalizing the line intensity to the RR line intensity, and using the calculated RR cross section.[11] The measured IE cross sections, which are the first for highly charged ions, support existing theoretical calculations.[13,14]

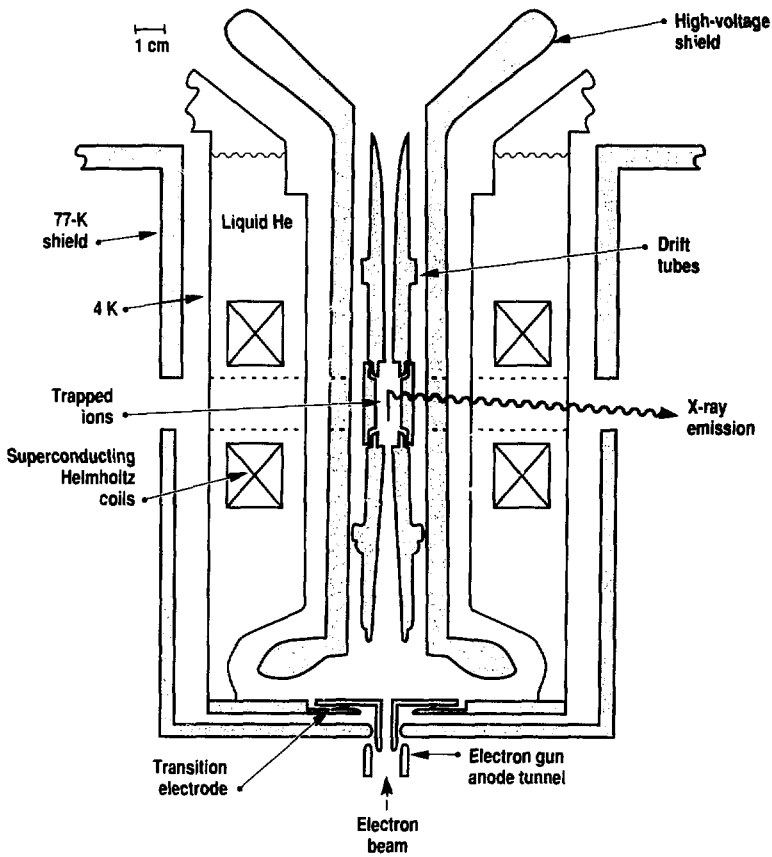

Figure 2. Schematic of the trapping region in EBIT.

Measurements of Dielectronic Recombination

In the DR process, an electron from the beam is captured by the ion of charge Q and excites one of the ion's electrons. Subsequent decay of the excited ion of charge $Q-1$ via an x ray makes the process measurable in EBIT. This process is resonant, occurring when the energy of the electron from the beam plus the binding energy to the shell captured equals the excitation energy of the core electron. The DR process is important in hot or highly ionized plasmas whose x-ray emission spectra contain satellite lines characteristic of DR. However, until EBIT, there were no detailed measurements of DR cross sections for the high ionization stages (such as He-like Fe^{24+} or Ni^{26+}), which are produced in tokamaks[15,16] and solar flares.[17] Because of the precise control of the electron beam energy in EBIT and the fine energy resolution, EBIT is a powerful tool for measuring a resonant process, such as DR. We have performed DR measurements for He-like ions (Ni^{26+} and Fe^{24+}) and Ne-like ions (Ba^{46+} and Au^{69+}).

In practice, the DR cross sections measured are quite large, and setting the electron beam energy on a DR resonance soon destroys the charge state being measured. We overcome this problem by rapidly switching the electron energy between the resonant energy and a higher nonresonant energy, which restores the ionization balance. At most, only 10%

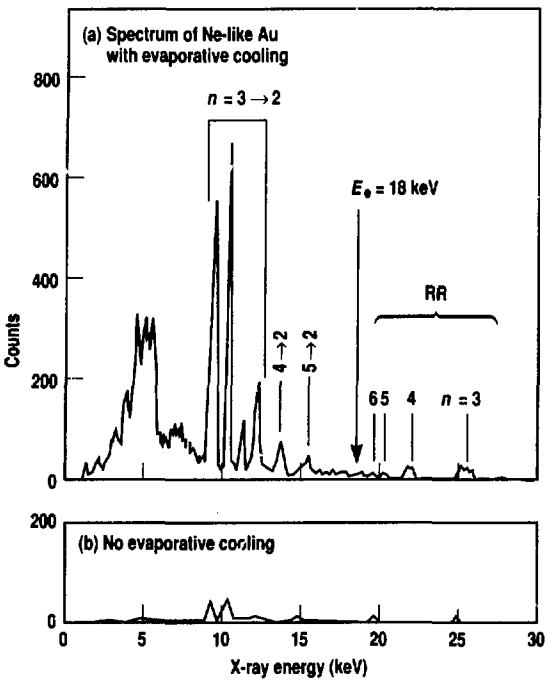

Figure 3. (a) Typical spectrum obtained with a solid-state detector. The spectrum is of near-Ne-like Au; the detector is an intrinsic-Ge detector. The excitation line series and the radiative recombination line series are also shown. Spectrum (a) is taken with evaporative cooling (Ti ions). The cooling is turned off by quickly (25 ms) placing a shutter in the path of the atomic beam. Spectrum (b) is taken for the same length of time (1 min). The count rate decreases when there is no evaporative cooling.

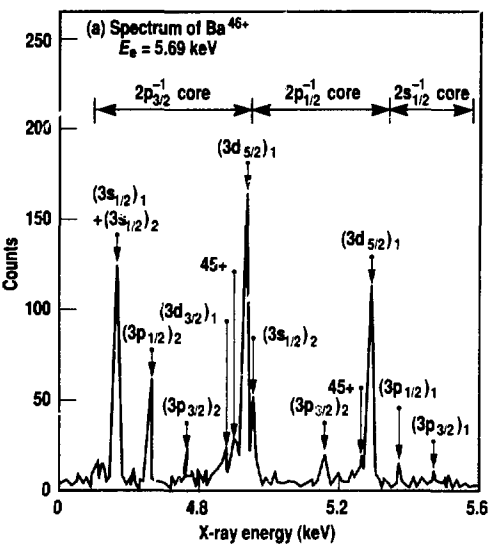

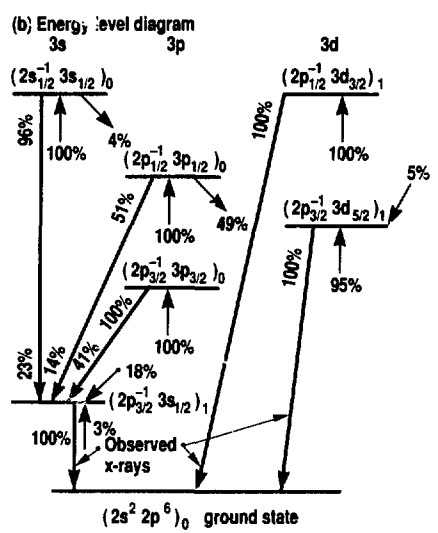

Figure 4. (a) High-resolution spectrum of Ne-like Ba^{46+} and (b) energy-level diagram. The decay branching ratios and feeding ratios shown for excited levels are derived from theoretical rates for electrons at 5.69 keV. Upward arrows indicate electron IE from the ground state. Downward arrows indicate cascade feeding and decay, which sometimes involve levels not shown. The electron beam energy was set to 5.69 keV to avoid resonances.

of the time is spent on resonance. Successive data runs are taken in which the lower electron energy (DR energy) is changed by a small amount.

For He-like Ni^{26+} target ions, Fig. 5 shows x-ray spectra taken at electron beam energies above the threshold for directly exciting the excitation lines, on a DR resonance, and at a nearby energy (but off resonance). The x-ray intensity in the line is plotted versus E_e to give the excitation spectra, shown in Fig. 6 for three different x rays.

The excitation spectra are fit using the theoretical positions and line strengths for resonances from a multiconfiguration Dirac-Fock calculation.[18] An absolute cross section is obtained by normalizing the x-ray counts in a resonant peak to a radiative recombination spectrum taken at a nearby energy but off resonance, and using calculated radiative recombination cross sections.[11] (Data analysis is complicated by correcting for the initial ionization balance and the change in the ionization balance during the DR process itself.) The Ni^{26+} results were in excellent agreement with theory.

Figure 7 shows an excitation spectrum for near-Ne-like Au. The system is more complex than a He-like system because there are many more resonant states. In EBIT, the ratio of Ne-like Au to all Au was, at best, 50%, far from the greater-than-90% ionization balance for He-like Ni.

Measurements of Precision Wavelength

The small diameter of the electron beam (60 μm) as it passes through the trapped ions in EBIT produces an ideal source for high-resolution-wavelength measurements using Bragg-diffraction crystals. We have constructed a Johann spectrometer, which enables measurement of soft x rays (~700 eV) and hard x rays (~8 keV). We are using this instrument to perform two different sets of measurements.

Lamb Shift in H-like High-Z Ions. Relativistic quantum mechanics predicts a splitting in a H-like system of the $2s_{1/2}$ and $2p_{1/2}$ levels from the $2p_{3/2}$ level.

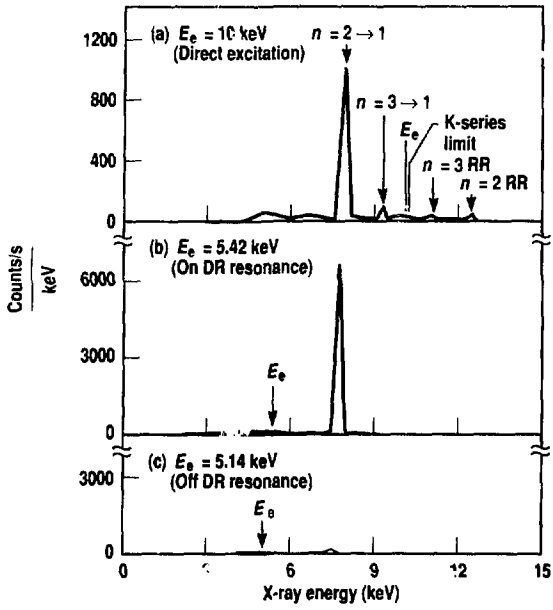

Figure 5. X-ray spectra from He-like-Ni^{26+} target ions at three different electron beam energies. (a) Above the $n = 1 \rightarrow 2$ direct-excitation threshold. (b) On resonance. (c) Off resonance.

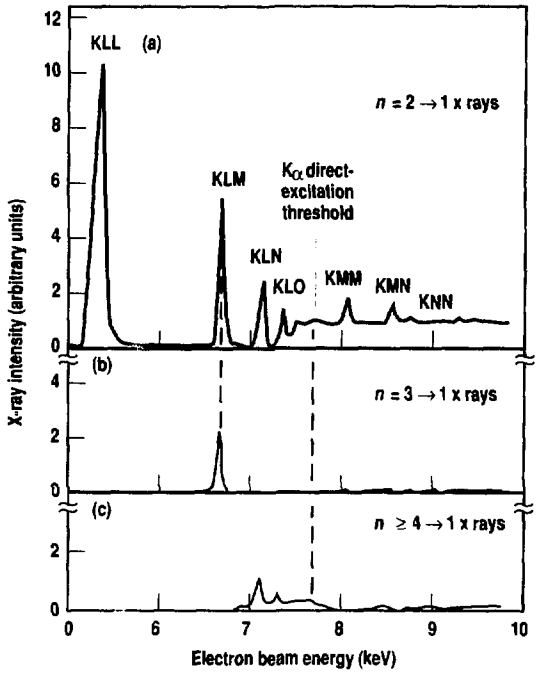

Figure 6. Measured DR electron excitation with He-like-Ni^{26+} target ions for three x-ray energy bands. Peaks above the direct-excitation threshold for $n = 2 \rightarrow 1$ x rays are due to resonant excitation (the electron from the beam is captured and excites a bound electron; it then autoionizes, and the remaining excited ion has the same charge as the original target ion).

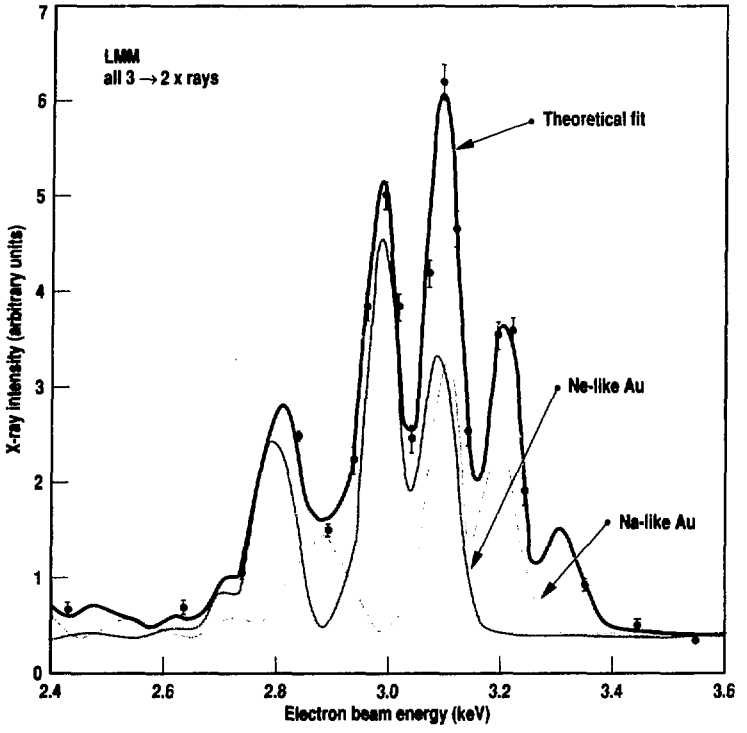

Figure 7. Measured DR electron excitation function for all $n = 3 \rightarrow 2$ x rays with near-Ne-like-Au target ions. The theoretical fit suggests contributions from 50% Ne-like, 34% Na-like, and 16% Mg-like Au (not shown).

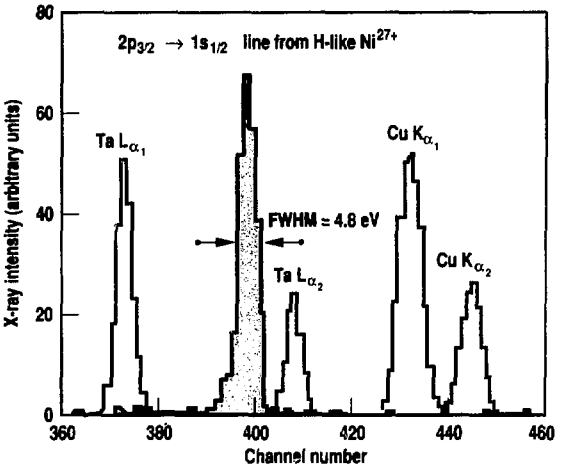

Figure 8. Lamb shift measurement from the Johann spectrometer. The $2p_{3/2} \rightarrow 1s_{1/2}$ line from H-like Ni^{27+} in EBIT is superimposed on the calibration lines. The x-ray energy range shown is approximately 8060–8170 eV.

Quantum electrodynamics has a "radiative correction" term, which further splits the levels and removes the remaining degeneracy (the Lamb shift); this term is large for high-Z ions. Any measurement of an exact energy level would test the theory. We have performed a preliminary experiment in EBIT by measuring the exact energy of the $2p_{3/2} \rightarrow 1s_{1/2}$ transition in H-like Ni^{27+} (Fig. 8). Our preliminary measurements are in agreement with theory and promise precision much better than that previously obtained for fast, high-Z ion beams produced at accelerators.

M-Shell Spectroscopy in High-Z Ions. The maximum beam energy obtainable with EBIT allows the production of Ne-like ions of any element in the periodic table. To measure the splitting of energy levels directly, we have begun a series of measurements of intrashell transition spectra of configurations close to the Ne like core for some of the heaviest elements. Figure 9 shows inner-shell transitions of Na-like and Mg-like Au. In addition to analogous effects (such as Lamb shifts) to the simple H-like ion, screening is important. Our theoretical understanding of these spectra is much less well founded than for the H-like or He-like charge states.

Conclusions

EBIT is now established as a unique tool for studying highly charged ions. The ionization stages available for x-ray spectroscopy with EBIT exceed those observed in the most advanced tokamaks and essentially match the highest charge states studied in beam-foil spectroscopy. Planned upgrades of the electron beam energy in EBIT will allow our x-ray measurements to be extended to H-like U.

References:

1. M. A. Levine, R. E. Marrs, J. R. Henderson, D. A. Knapp, and M. B. Schneider, "The Electron Beam Ion Trap: A New Instrument for Atomic Physics Measurements," *Phys. Scr.* **T22**, 157 (1988).

2. R. E. Marrs, M. A. Levine, D. A. Knapp, and J. R. Henderson, *Phys. Rev. Lett.* **60**, 1715 (1988).
3. R. E. Marrs, M. A. Levine, D. A. Knapp, and J. R. Henderson, *Electronic and Atomic Collisions*, H. B. Gilbody, W. R. Newell, F. H. Read, A. C. H. Smith, eds. (Elsevier Science, 1988) p. 209.
4. R. E. Marrs, C. Bennett, M. H. Chen, T. Cowan, D. Dietrich, J. R. Henderson, D. A. Knapp, M. A. Levine, M. B. Schneider, and J. H. Scofield, *International Conf. Physics Multiply Charged Ions International Workshop E.C.R. Ion Sources*, Grenoble, France, September 14–16, 1988.

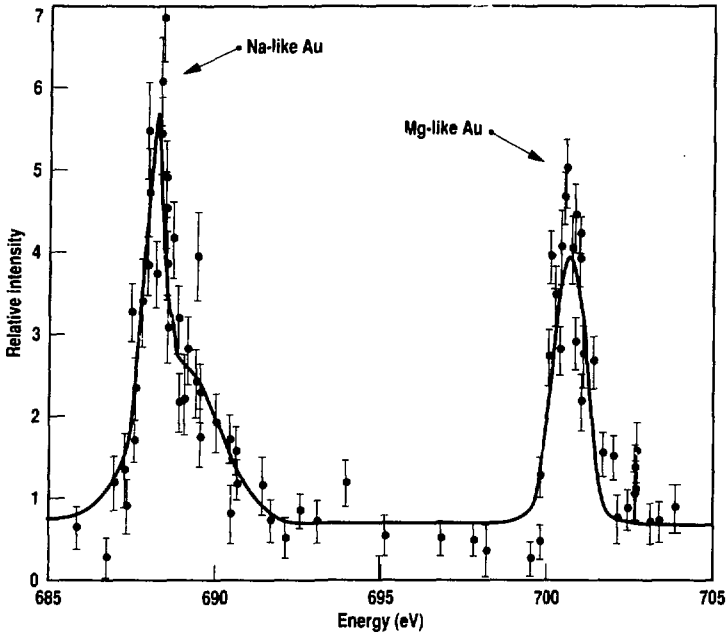

Figure 9. M-shell spectroscopy from the Johann spectrometer. The lines have been tentatively identified as 3p → 3s transitions in Na-like and Mg-like Au.

5. E. D. Donets, *Phys. Scr.* **T3**, 11 (1983).
6. E. D. Donets and V. P. Ovsyannikov, *Sov. Phys. JETP* **53**, 466 (1981).
7. D. Gregory, G. H. Dunn, R. A. Phaneuf, and D. H. Crandall, *Phys. Rev. A* **20**, 410 (1979).
8. P. F. Dittner, S. Datz, P. D. Miller, P. L. Pepmiller, and C. M. Fou, *Phys. Rev. A* **35**, 3668 (1987).
9. J. Faure, B. Feinberg, A. Cortois, and R. Gobin, *Nucl. Instr. Meth.* **219**, 449 (1984).
10. I. G. Brown, J. E. Galvin, R. A. MacGill, and R. T. Wright, *Appl. Phys. Lett.* **49**, 1019 (1986).
11. E. B. Saloman, J. H. Hubbell, and J. H. Scofield, *At. Data Nucl. Data Tables* **38**, 1 (1988).
12. M. A. Levine and M. B. Schneider, National Superconducting Cyclotron Laboratory Report MSUCP-47 (1987).
13. K. J. Reed, *Phys. Rev. A* **37**, 1 (1988).
14. H. Zhang, D. H. Sampson, R. E. H. Clark, and J. B. Mann, *At. Data Nucl. Data Tables* **37**, 17 (1987).
15. F. Bombarda, R. Giannella, E. Kallne, G J. Tallents, F. Bely-Dubau, P. Faucher, M. Cornille, J. Dubau, and A. H. Gabriel, *Phys. Rev. A* **37**, 504 (1988).
16. H. Hsuan, M. Bitter, K. W. Hill, S. von Goeler, B. Grek, D. Johnson, L. C. Johnson, S. Sesnic, C. P. Bhalla, K. R. Karim, F. Bely-Dubau, and P. Faucher, *Phys. Rev. A* **35**, 4280 (1987).
17. K. Tanaka, T. Watanaabe, K. Nishi, and K. Akita, *Appl. J.* **254**, L59 (1982).
18. M. H. Chen, *Phys. Rev. A* **33**, 994 (1986).

Fusion Gamma-Ray Experiments at the California Institute of Technology

J. E. Kammeraad, J. M. Hall, and K. E. Sale

We are conducting an experiment at the California Institute of Technology (CIT) to study the reaction $T(d,\gamma)^5He$, which is the radiative capture of a deuteron by a tritium nucleus, producing a 16.7-MeV gamma ray. This reaction has a small cross section compared to the well-known fusion reaction $T(d,\alpha)n$. We are measuring the so-called "branching ratio" (the ratio of cross sections) for the radiative capture reaction relative to the fusion reaction. An accurate knowledge of the branching ratio would provide us with an

important diagnostic tool for studying hot deuterium-tritium (DT) plasmas, such as those found in fusion reactors and certain nuclear weapons.

With accurate values for the branching ratio of T(d,γ)^{5}He relative to T(d,α)n, we could study the burn rate of DT plasmas by analyzing the emitted 16.7-MeV gamma rays instead of the 14-MeV neutrons. In certain situations, such as in underground weapons tests at the NTS, energy dispersion makes neutron data ambiguous by broadening the time history of the event (high-energy neutrons travel faster than low-energy neutrons). All gamma rays travel at the same speed, regardless of energy; thus, measurement of the 16.7-MeV gamma rays as a function of time would provide unambiguous data on how long the fusion reaction lasts and its development over time.

Figure 1 is a summary of measurements of the branching ratio reported by various investigators over the past three decades. The deuteron energy range of 10–120 keV is of particular interest because this range corresponds to DT plasma temperatures of 0.2–20 keV. In this region, the T(d,α)n reaction exhibits a single-level resonance; therefore, the branching ratio is expected to be independent of energy. The various measurements of the branching ratio in this region differ from each other by up to one order of magnitude. The most recent measurements from Morgan et al.,[1] Cecil and Wilkinson,[2] and our preliminary experiment are statistically consistent with each other and give a branching ratio between 5×10^{-5} and 8×10^{-5}.

In our experiment at CIT, a tritiated Ti target was bombarded with a deuteron beam. Alpha particles from T(d,α)n were detected in a surface-barrier detector located at 150 degrees relative to the beam direction. The 16.7-MeV gamma rays from T(d,γ)^{5}He were detected in a special detector located at 0 degrees relative to the beam direction (see Fig. 2).

Because the reaction produces more than 10,000 neutrons for each 16.7-MeV gamma ray, the challenge in our experiment was to measure gamma rays while ignoring the large background of 14-MeV neutrons. To do so, we use an array of seven hexagonal NaI detectors arranged in a honeycomb pattern (six around one). A lead collimator allows gamma rays from the target to reach the central detector but not the six outer detectors. The detector assembly was used as a pair spectrometer; that is, it was set to respond preferentially to any gamma ray that produced a positron-electron pair in the central detector. When the positron annihilates, two 0.511-MeV photons are created and may be detected in the outer detectors. The signature of a high-energy gamma ray is a triple coincidence in three detectors (the central detector plus two outer detectors) in which the two outer detectors each measure a 0.511-MeV photon. This system provided good discrimination between incident gamma rays and neutrons because neutrons do not undergo pair production, and it is highly unlikely that three neutrons would arrive simultaneously and deposit the correct energies to simulate a pair-production event.

For our experiment, the most important source of background is high-energy gamma rays from (n,γ) reactions (14-MeV neutron capture) produced in the target or detector. To reduce background gamma rays produced by the target, the structure was made of minimum-thickness (4-mg/cm^2) Ti evaporated onto 0.010-in.-thick Be, which was mounted on a 0.010-in.-thick Al vacuum barrier. To reduce the background gamma rays produced in the detector, 56 cm of polyethylene was interposed between target and detector. This material reduces incident neutron flux by a factor of about 500 while reducing incident gamma-ray flux

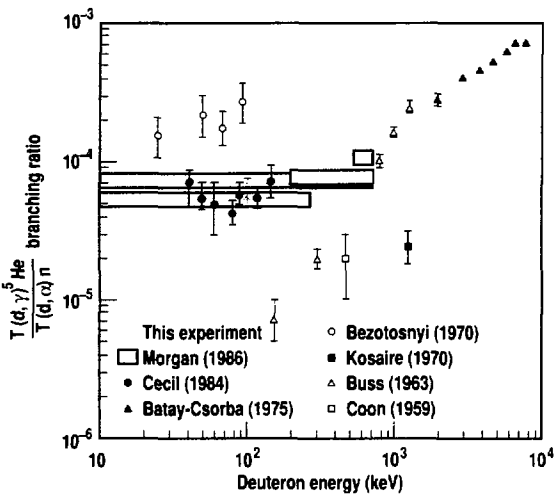

Figure 1. Measurements by various investigators over the past three decades of the ratio of the cross section of T(d,γ)^{5}He relative to T(d,α)n as a function of deuteron energy.

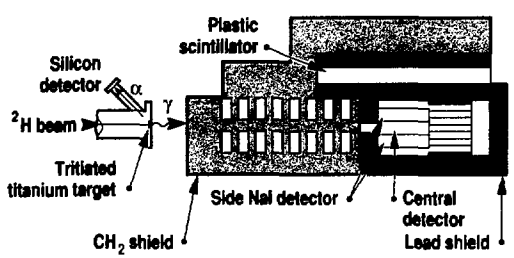

Figure 2. Schematic of the target and detector (side view).

by about a factor of 3. The entire detector assembly was shielded by at least 2 in. of Pb and 4 in. of B-loaded polyethylene. Three sheets of plastic scintillator were placed at the top and along two sides of the detector to reject cosmic rays.

We tested the response of the detector to high-energy gamma rays using 6.1-MeV gamma rays from $^{19}F(p,\alpha\ \gamma)$, 19.8-MeV gamma rays from T(p,γ), and 16.7-MeV gamma rays from D(^{3}He,γ). The first two reactions produce monochromatic gamma rays, allowing us to measure detector resolution and efficiency. The third reaction is the mirror reaction of T(d,γ), which is especially useful. A mirror reaction is one in which each particle is replaced by its mirror particle. (The mirror particle for a proton is a neutron and vice versa; thus, the mirror nucleus of the deuteron is itself, and the mirror nucleus for the triton is the ^{3}He nucleus.) Because the nuclear force is essentially charge-independent, the two reactions are expected to produce the same gamma-ray spectrum. The spectrum from D(^{3}He,γ), which has been extensively studied by Buss et al.,[3] displays two overlapping peaks, one at 16.7 MeV and a broad peak at about 11 MeV. The second peak results from a transition to the first excited state of ^{5}Li. Using this reaction, we can measure the detector response to the proper spectrum of gamma rays.

Figure 3 shows our results. The spectra obtained from T(p,γ) in Fig. 3(a) and $^{19}F(p,\alpha\ \gamma)$ (not shown) are well described by Monte Carlo calculations of the response of the detector to monochromatic gamma rays [see the solid curve in Fig. 3(a)]. Similar calculations for the D(^{3}He,γ) spectrum are in progress. To obtain a preliminary measurement of the branching ratio, we estimated the spectral shape and fit the spectrum for D(^{3}He,γ) with this shape plus an exponential background and a flat background [see Fig. 3(b)].

Figure 3(c) shows the spectrum obtained for T(d,γ) in a 33-hour run with a deuteron energy of 100 keV and beam current of 1.6 μA. With this small beam current, the total count rate in the detector was about 1 kHz, and pulse pile-up was negligible. We fit the spectrum for T(d,γ) with the estimated spectral shape for D(^{3}He,γ) plus an exponential to represent low-energy gamma rays, mainly from (n,n′γ) reactions, and a flat background to represent cosmic rays.

Because the branching ratio R is known for the D(^{3}He,γ) reaction, we can

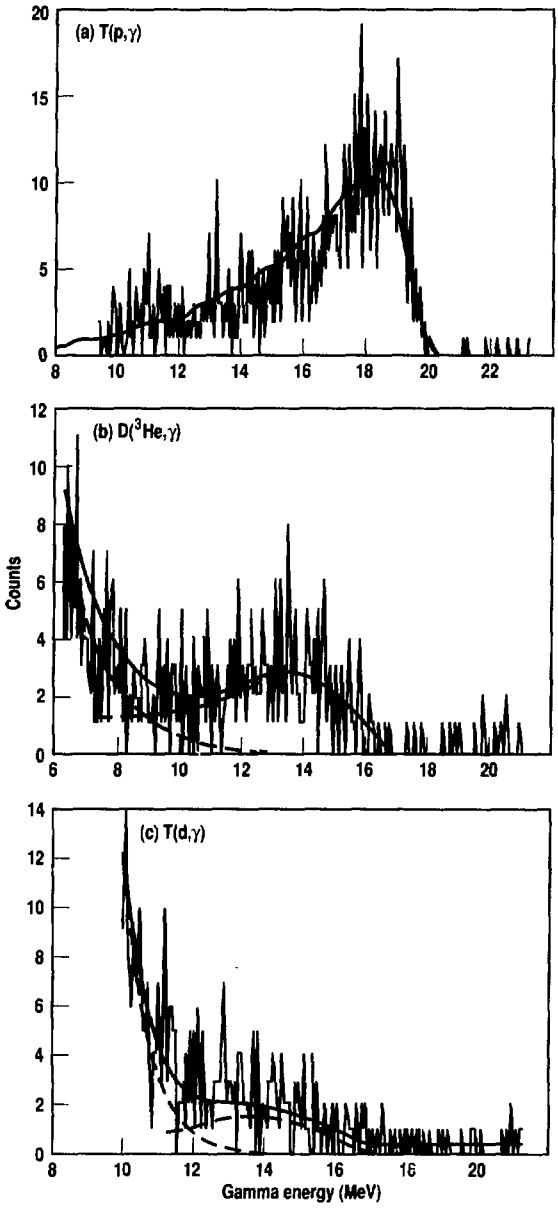

Figure 3. Measured gamma-ray spectra obtained with the pair spectrometer for three reactions. (a) T(p,γ) spectrum and Monte Carlo prediction. (b) D(^{3}He,γ) spectrum and fit to peak and background. (c) T(d,γ) spectrum and fit to peak using D(^{3}He,γ).

directly calculate the branching ratio for T(d,γ) as follows:

$$R_{DT} = R_{D^3He}\left(\frac{N^{\gamma}_{DT}}{N^{\gamma}_{D^3He}}\right)\left(\frac{N^{\alpha}_{D^3He}}{N^{\alpha}_{DT}}\right) \quad (1)$$

In this equation, $N\gamma$ is the number of gamma-ray counts, with background subtracted, in the energy region from 14 to 16.9 MeV, and $N\alpha$ is the number of alpha particles detected. Given that $R_{D^3He} = (2.5 \pm 0.5) \times 10^{-5}$ (the branching ratio for decay to the ground state in ^{5}Li), we obtain $R_{DT} = (5.8 \pm 1.9) \times 10^{-5}$ for the branching ratio for decay to the ground state in ^{5}He. The uncertainty in this measurement is due mainly to uncertainty in the background-subtracted gamma-ray counts for the T(d,γ) reaction.

Using the technique of comparing measured gamma-ray spectra from T(d,γ) to that from D(^{3}He,γ), we plan to obtain more data at 100-keV deuteron energy as well as at several other energies (probably 250, 350, 450, and 600 keV). We are currently analyzing data obtained at 175 keV. We hope to measure the branching ratio to an accuracy of 10–20%.

References:

1. G. L. Morgan et al., "Measurement of the Branching Ratio ^{3}H(d,γ)/^{3}H(d,α) Using Thick Tritium Gas Targets," *Phys. Rev. C* **33**, 1224 (1986).
2. F. E. Cecil and F. J. Wilkinson III, "Measurement of the Ground-State Gamma-Ray Branching Ratio of the DT Reaction at Low Energies," *Phys. Rev.* **53**, 767 (1984).
3. W. Buss, W. Del Bianco, H. Waffler, and B. Ziegler, "Deuteron Capture in ^{3}He," *Nucl. Phys.* **A112**, 47 (1968).

Experimental Studies of Amplified Spontaneous Emission

H. Nathel, J. C. Garrison, and R. W. Minich

The amplified spontaneous emission (ASE) laboratory was established to study fundamental phenomena associated with bright quasi-coherent light sources produced by the stimulated-emission process and also to provide a diversified data base covering all aspects of ASE. All x-ray lasers to date are ASE sources rather than conventional lasers that make use of cavity optics (lenses and mirrors) and that give longitudinal and spatial coherence as a result of their spectral- and spatial-mode selection abilities. Because x-ray laser cavity-optical component technology is still in its infancy, we are pursuing experiments concerning fundamental characteristics of ASE, or mirrorless, lasers, to expand our knowledge of ASE physics.

On the basis of a quantum theory of amplified spontaneous emission,[1] we performed a scaling analysis to demonstrate that a dye-laser medium could be used as an experimental analog for x-ray lasers. We formulated a second quantized theory of propagation in laser-active media and applied it to the description of quantum noise amplification for the case of a three-level (truncated from four levels) emitter in a rod-like geometry with an arbitrary Fresnel number. The characteristic fields and geometries resulting from the scaling analysis demonstrated that because the dye-laser medium could obtain very large gains (implying a high degree of saturation), use various geometries (implying varying Fresnel numbers), and had rapid dephasing times, it was, therefore, an appropriate x-ray laser analog.

We also chose a conventional dye-laser medium, operating at optical wavelength, because it was an accessible "tabletop" analog for modeling the x-ray laser. This means that we can produce experiments and data at a rapid rate, which we in turn use to verify computer codes to help us design and analyze x-ray laser experiments. Code verification is only one important aspect of the ASE project; we

are also testing new amplifier designs and architectures. Most important, we are investigating new physical phenomena associated with noise-amplifier physics that operate in regimes important to x-ray lasers (large degree of saturation, various Fresnel numbers). We must better understand all these phenomena, which can either promote or hinder x-ray laser operations, before x-ray laser experiments with their high cost and low data return take place. Understanding these phenomena, which are associated with spatial coherence and propagation issues, is the major pursuit of our laboratory.

ASE Laboratory

We are using instrumentation that measures spectral, spatial, energy, and coherence characteristics of ASE sources. To date, most experiments have been time integrated. However, in the near future, we will be using time-resolving diagnostics to measure the dynamic evolution of ASE characteristics as well as transient phenomena associated with ASE propagation.

A schematic of the ASE laboratory experimental setup is shown in Fig. 1. The 10-ns, 1064-nm output of a Q-switched, injection-seeded, Nd^{3+}:YAG laser-amplifier system is frequency doubled using second harmonic generation in a KD*P crystal. We use the resulting 532-nm pump-laser light to excite dye samples in a configuration that promotes light amplification of spontaneous emission. We use cylindrical input optics and adjustable slits to shape the 532-nm pump light to excite small aspect-ratio samples. The amplification proceeds via stimulated emission only along the longitudinal axis of the dye sample.

Use of transverse pumping to excite the dye samples results in counterpropagating ASE fields and allows us to take measurements on either output end, or both simultaneously, to diagnose the ASE output. The flexibility of the cells that hold our dye samples allows us to measure longitudinal-gain profiles by monitoring the transverse fluorescence along the amplifier (dye sample) axis.

Optics Experiments

To successfully use an ASE source, we must deliver the output radiation efficiently to a target. For ASE sources with Fresnel numbers ($\pi r^2/\lambda L$) greater than 1, the geometric divergence is determined by the geometric aspect ratio (d/L). For systems with Fresnel numbers less than or equal to 1, the divergence is limited by diffraction ($\lambda/\pi r$). X-ray lasers incorporate geometries that result in Fresnel numbers greater than 1. As a result of the geometric divergence, propagation of the output radiation causes a severe loss in light intensity. We, therefore, had to determine the best position to place the focus of a lens along the longitudinal axis of an amplifier to most effectively collimate its output radiation, which is difficult to determine because an amplifier cannot be considered a point source. Not only is this light source extended in the transverse dimension (for larger Fresnel number) but it is also distributed along the longitudinal axis.

The "placement" question was open when we started our studies of ASE. One idea was to place the focus of the lens at the point of origin of the intensity of the output radiation, which meant determining a "source function." The source function is a function of longitudinal position along the amplifier and is defined by:

$$\text{Source function} = \Delta z \times \left(\frac{1}{1+\frac{I(z)}{I_{sat}}}\right)\left(\frac{S_o}{I_{sat}}\right)\left(\frac{\Omega(z)}{4\pi}\right) \times \left\{\exp\left[\int_L^z dz\left(\frac{g_o}{1+\frac{I(z)}{I_{sat}}}\right)\right]\right\}, \quad (1)$$

where the first three terms define a spontaneous-emission noise source, the fourth term is a solid-angle fraction, and the fifth term is the integrated amplification that the noise term sees. In this equation, $I \equiv$ ASE intensity, $I_{sat} \equiv$ ASE saturation intensity, $S_o = Ah\omega N^*$, $\Omega(z)$ = solid angle, and g_o = unsaturated gain coefficient. A is the spontaneous-emission rate (Einstein A coefficient) and N^* is the excited-state density.

Figure 2 shows the source function for various gain-length (g_oL) products (determining the degree of saturation) from our laboratory studies. These plots show that the output radiation appears to originate from an extended region toward the back end of the amplifier. Thus, some thought that the focus of the lens should be placed there.

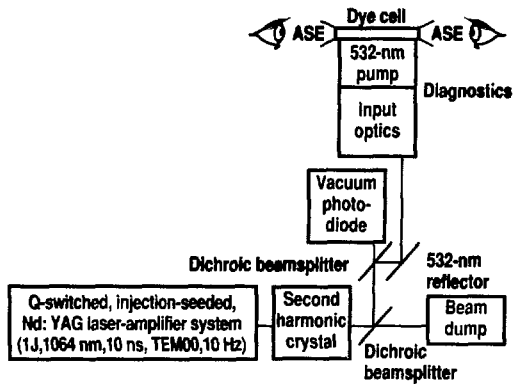

Figure 1. Schematic diagram of the ASE laboratory experimental setup.

However, when we conducted the experiment to determine optimum lens placement for the collimation of an ASE source with a Fresnel number of approximately 200 (see Fig. 3), we obtained disparate results. A 10-cm focal-length lens was translated so that we could position the focal point at various positions along the longitudinal axis. The light collected by the 10-cm lens was imaged onto a two-dimensional, solid-state TV camera through a C-mounted zoom lens focused at infinity. The image was viewed in real time, stored on a MAC II computer, and analyzed with LABVIEW software. We analyzed the intensity profile in two ways to determine the optimum collimation of the output radiation as a function of lens focus position along the longitudinal axis of the amplifier. We determined the maximum of the intensity distribution (denoted Max) and the width of the intensity distribution (denoted S). A maximum in S corresponds to a minimum in positional uncertainty of the intensity profile at the detector. D termination of where both figures of merit are maximum as a function of longitudinal amplifier position corresponds to optimum collimation of the amplifier output radiation.

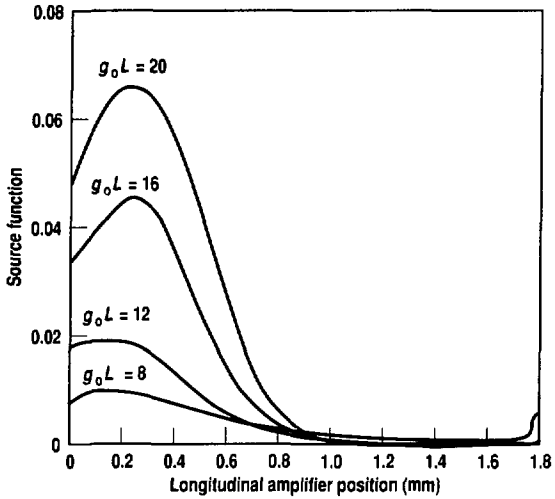

Figure 2. Plots showing the source function for various gain-length products studied in the laboratory. The output radiation appears to originate from an extended region toward the back end of the amplifier.

The experimental results for gain-length products of 8, 12, 16, and 20 are shown in Fig. 4. Saturation of the ASE source sets in at approximately g_0L = 12. Optimum collimation for all g_0Ls occurs when we place the focal point of the lens at the center of the amplifier. To reconcile this result with the preconceived notion that the maximum in the source function was the point of origin for the output radiation, we conducted the following experiment [see Fig. 5(a)]. We created an "incoherent" light source by placing an aperture with a diffuser in front of a light bulb. Using similar criteria to discover optimum lens positioning for collimation, we determined that the lens focus should be placed exactly at the source position for optimum collimation of the emitted light [Fig. 5(a)]. However, when we placed another aperture, equal in size to the first aperture, downline from the source [Fig. 5(b)], the lens focal position moved to the center of the two apertures for optimum collimation.

We can understand these results in terms of ray tracing or geometrical optics. For a source that is extended in the transverse dimension, the effective point source corresponds to the point along the longitudinal axis where the rays for the entire system have a maximum crossing rate. The notion that the effective point source for such a system is at the maximum ray-crossing position is demonstrated by the results shown in Fig. 5(b), (c), and (d), where we moved the maximum ray-crossing position by manipulating the size of the apertures.

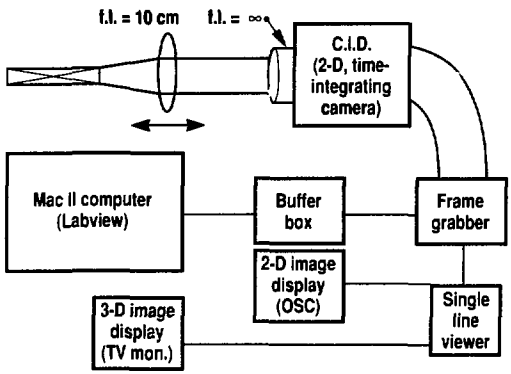

Figure 3. Experimental setup to determine optimum lens placement for collimation of output radiation from a large-Fresnel-number ASE source. A 10-cm focal length lens was translated so that we could position the focal point at various positions along the longitudinal axis. Light collected by the lens was imaged onto a two-dimensional, solid-state TV camera through a C-mounted zoom lens focused at infinity.

For the symmetrical case [Fig. 5(b)], the effective point source was in the middle of the two apertures. For the asymmetrical case [Figs. 5(c) and (d)], the effective point source moved to track the maximum ray-crossing points. The aperture systems serve as geometric analogs for the gain medium.

The results of our optical-collimation experiments on ASE sources imply geometrical divergence. The independence of the results on gain-length products indicates that geometry dictates the divergence for all systems we investigated.

Transverse-Fluorescence Experiments

Measuring the spatial distribution of the fluorescence (spontaneous emission) that is transverse to the ASE propagation direction (longitudinal axis) probes the excited-state distribution as a function of axial amplifier position.[2-4] In this way, we can measure the longitudinal-gain distribution, which is directly proportional to the excited-state distribution. We must fully understand the interaction of the pump field with the gain medium as well as the buildup of the ASE field from noise and its interaction with the gain medium for proper numerical modeling of this type of experiment. Agreement between experiment and simulation indicates complete comprehension of the microscopic physics of these systems.

A schematic representation of the transverse-fluorescence experiments is shown in Fig. 6. The dye concentration was fixed, and the gain was varied by adjusting the excitation rate (pump-laser intensity). The transmitted pump beam was filtered (blocked) from our detector by an OG570 filter. The fluorescence emission was collected by a C-mounted zoom lens and imaged onto a solid-state TV camera. We used the same equipment for data collection, storage, and analysis that we used in the optic experiments.

Results of the experiments are shown in Fig. 7. Increasing the incident pump intensity (from 1.07×10^5 to 4.65×10^6 W/cm^2) resulted in effective gain-length products ranging from 4.6 to 31.5 (going down each column). As the gain of the system is increased, the ASE intensities near both ends of the amplifier increase. Rapid depopulation of the excited state caused by higher stimulated-emission rates at the ends of the amplifier suppresses occupation of the excited state relative to the center of the amplifier. Therefore, the excited-state distribution peaks in the middle of the amplifier as the gain of the system increases.

We modeled this behavior using a homogeneously broadened, four-level description of the dye molecules.[1] The amplifier (dye sample) has a rod-like geometry. We calculated the gain as a function of pump intensity using a measured, stimulated-emission cross section of rhodamine 6G in DMSO solvent. Because we transversely pumped the dye sample from one side, we took into account the exponential decay in pump intensity across its radial dimension.

Figure 4. Experimental results for determining optimum focal-point positioning for collimation of the output radiation from a large-Fresnel-number ASE source. Saturation sets in at approximately $g_0 L = 12$. Optimum collimation occurs when focal point of lens is at center of amplifier. Max = maximum of the intensity distribution, S = width of the intensity distribution.

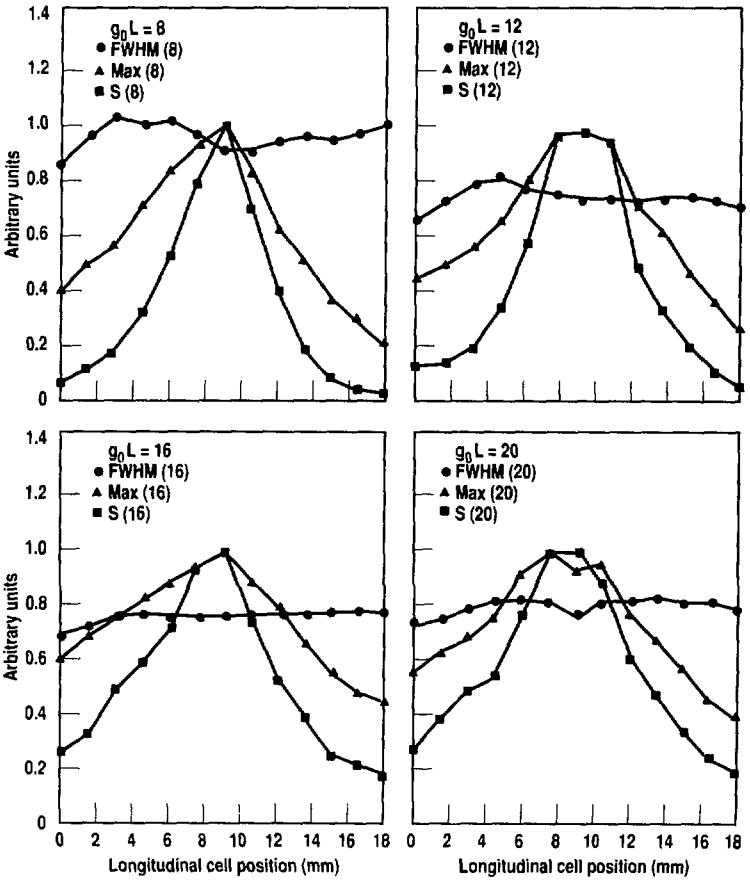

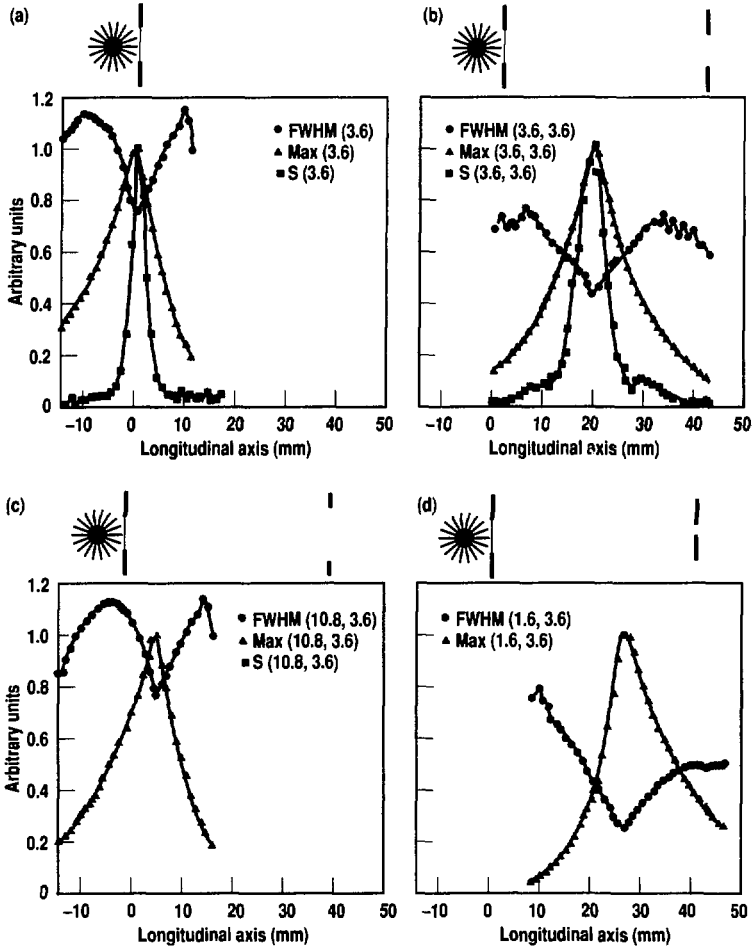

Figure 5. Results of luminous-disk imaging experiments. (a) Well-defined source along longitudinal axis. (b) Results of luminous disk with tube-like structure. (c) and (d) Imaging experiments and results of luminous disk with cone-like structures. Max = maximum of the intensity distribution, S = width of the intensity distribution.

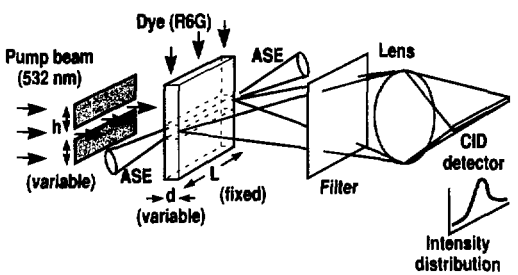

Figure 6. Schematic of transverse-fluorescence experiments. Dye concentration was fixed; gain was varied by adjusting the excitation rate. Transmitted pump beam was blocked from detector by OG570 filter.

Averaging the pump dependence of the gain across three absorption depths gave us excellent agreement with experiments. The ASE saturation intensity in our model is linearly dependent on the pump intensity. We fed results of the model into a photon-transport, ray-tracing code in the forms of a spontaneous-emission source term, a small signal-gain coefficient, and an ASE saturation intensity. The time-dependent code generated spontaneous emission from each longitudinal zone into flux tubes in straight lines. The ASE intensity was updated at each time step using the saturated gain.

The results of the simulation are overlaid on the experimental data in Fig. 7. The model and experiment are in excellent agreement except at very high pump intensity (high gain) where the experimental profiles appear slightly narrower than the simulations. Two possible explanations for the discrepancies are that our detection technique registers time-integrated values and that the homogeneously excited cylindrical geometry assumed in the model has not been realized experimentally. The raggedness in the experimental profiles compared to the simulated profiles results from imperfections in our pump profiles. It is also important to note that calculated ASE output intensities agree within the experimental uncertainties with the measured ASE output intensities. Improvements to the experiment and modeling, which are underway, consist of time-resolving the imaged fluorescence with a streak camera and including radial dependencies to source and gain terms, respectively.

By removing the OG570 filter and monitoring the spatial distribution of the transmitted pump beam, we observe a new optical phenomenon. When we overlay the transmitted pump-beam data on the fluorescence data and simulation, we see qualitative agreement in the shape of the transmitted pump beam and other quantities. The transmitted pump beam probes the ground-state population and, therefore, provides complementary

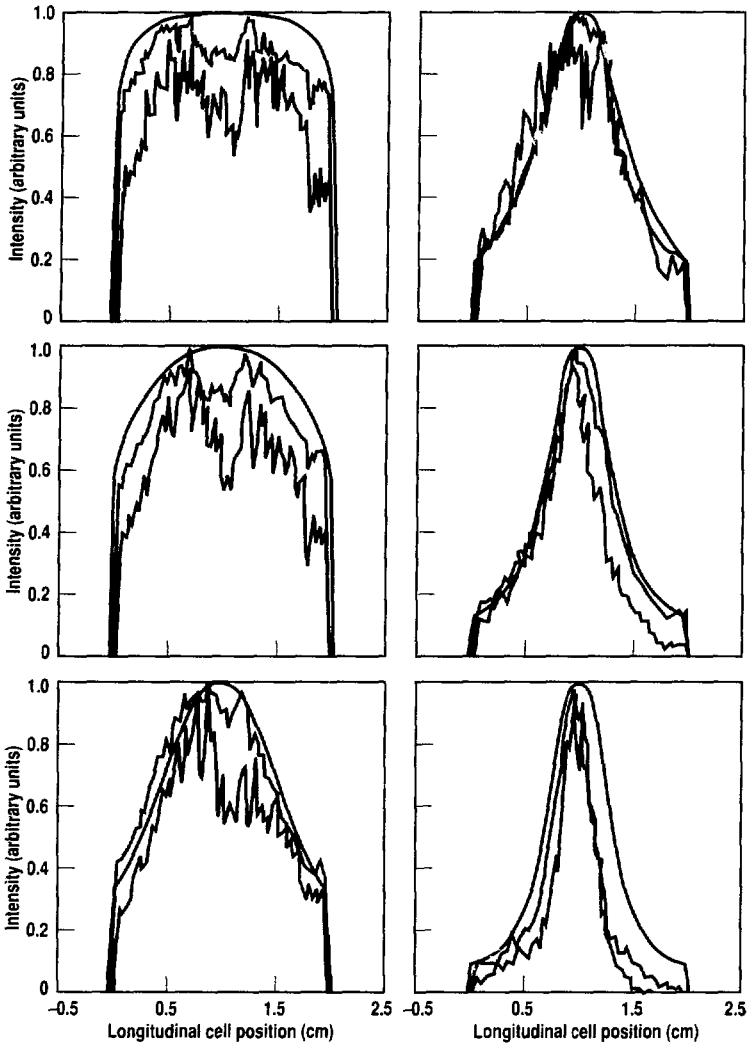

Figure 7. Results and simulation of the transverse-fluorescence experiments. Increasing the incident pump intensity resulted in effective gain-length products. Excited-state distribution peaks in the middle of the amplifier as the gain in the system increases. Nonsaturable absorption effect is also demonstrated by overlaying the transmitted pump data.

information to the transverse fluorescence. Absorption of the pump beam is enhanced by higher stimulated-emission rates (and, therefore, larger ground-state populations) near the ends of the amplifier. We effectively have a spatially dependent absorption depth along the amplifier axis because of the increased recycling of the dye molecules. When we ignore the occupation of the states, other than the upper-lasing state and ground state (due to rapid intramolecular vibrational-relaxation rates), the enhancement of the absorption of the pump is virtually nonsaturable, and the profiles of the fluorescence and the transmitted pump beam become identical.

References:

1. J. C. Garrison, H. Nathel, and R. Y. Chiao, "Quantum Theory of Amplified Spontaneous Emission: Scaling Properties," *J. Opt. Soc. Am.* **B5**, 1528 (1988).
2. J. W. Klüver, "Laser Amplifier Noise at 3.5 Microns in Helium-Xenon," *J. Appl. Phys.* **37**, 2987 (1966).
3. I. Keiskémety, Z. S. Bor, B. Rácz, and L. Kozma, "Spatially Inhomogeneous Saturation of Gain in Organic Solutions Caused by Amplified Spontaneous Emission," *Opt. Comm.* **21**, 25 (1977).
4. A. A. Hnilo, O. E. Martínez, and E. J. Quel, "Stored Energy in Pulsed Dye Laser Amplifiers," *IEEE J. Quantum Electron.* **QE-22**, 20 (1986).

Magnetically and Vacuum Insulated Transmission Line Experiments

L. G. Wiley, S. Arnold, and D. A. Goerz

High-voltage transmission lines that carry electrical pulses to remotely located diagnostic equipment may attenuate voltage peaks and distort rise times. Therefore, transmission line behavior must be accurately characterized if experimenters are to make meaningful use of the data transmitted. The main advantage of vacuum-insulated transmission lines (VITLs) is that they are high-impedance devices that do not load down voltage sources. However, because of their high-impedance, VITLs may perform poorly in high-radiation environments with copious supplies of scattered free electrons that can distort or completely short out the transmitted pulse. Their impedance can be lowered by bringing the electrode surfaces closer together, but the smaller vacuum area that results may lower the line's peak voltage-handling capability.

With very fast, high-voltage pulses, the line will undergo a process known as self-magnetic insulation. Strong electric fields cause electrons to be field emitted and create plasmas on the surfaces of the electrodes. Cathode surface plasmas become excellent sources of additional electrons, and the electron currents give rise to self-magnetic fields that can prevent these electrons from reaching the anode.[1–4] Lines that take advantage of self-magnetic insulation are called magnetically insulated transmission lines (MITLs). In some cases, however, a MITL may unacceptably load down a voltage source. Therefore, the specific experimental application will dictate which type of line is better.

Our overall experimental objectives were to characterize the propagation of high-voltage, fast-rise-time pulses through MITLs and VITLs more accurately than has been done in the past and to compare experimental results with computer predictions. Although MITLs have been studied as power transmission devices,[5] most recent research has focused on the terminating diodes used to absorb the power and to couple it efficiently into an intense electron or light-ion beam. Previous efforts to predict MITL performance have often relied on one-dimensional analyses and limited computer simulations at the injection and diode ends of the transmission lines. Although the concept of magnetic insulation is easily understood, experimental results have been difficult to predict with simple models. For example, current losses in uniform-geometry coaxial transmission lines

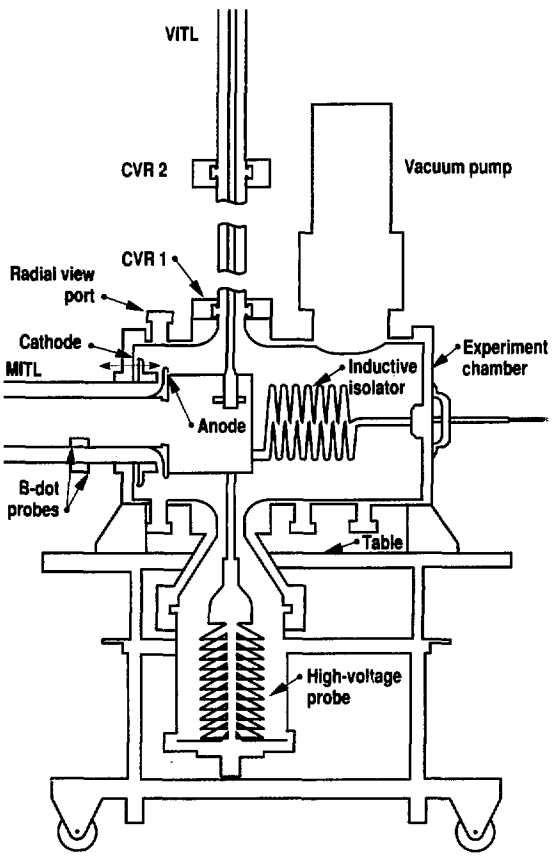

Figure 1. Laboratory setup for the MITL and VITL experiments.

have not been accurately calculated. Lumped circuit analysis is very useful if empirical conductance information is available, but truly predictive capability is limited. Also, much evidence supports the notion that substantial nonuniform electron-current flow exists even in simple, uniform geometries.

The pulse propagation characteristics we studied were sharpening of the pulse rise time, erosion of the leading edge, voltage attenuation, and onset of magnetic insulation (as measured by the difference between the anode and cathode currents). For MITLs, we compared our experimental results with those of CONDOR, a two-dimensional electromagnetic, fully relativistic, charged-particle computer code. (CONDOR predictions for the VITL were not made because the code assumes full space-charge-limited field emission from metal surfaces.) The experiments helped us determine when electron field emission from the cathode surface was sufficient to alter properties of the transmitted pulse. For MITLs, field emission determines the onset of magnetic insulation; for VITLs, it must be minimized. Field emission is a difficult process to control effectively and is dependent on the amplitude and temporal characteristics of the voltage pulse as well as on the properties of the cathode surface itself.

MITL Experiments

We used a pulse generator to produce a positive-polarity, 60-ns pulse of up to 1.2 MV into 2- and 3-m coaxial MITLs. A variable-impedance, annular electron diode dissipated most of the power from the pulse generator. A 20-cm-long coaxial line connected the anode to a resistive voltage probe. The movable cathode allowed us to vary the diode gap. Differential B-dot probes were placed at 60-cm intervals along the inner and outer conductors to measure the rate of change in the magnetic field at the conductor walls. A simplified diagram of the experiment in shown in Fig. 1.

The inner conductor (anode) probes measured field changes caused by total MITL current, while the outer conductor (cathode) probes measured a fraction of that field because of the free-electron current that flowed in the vacuum gap between the conductors. By integrating and comparing the time-dependent probe signals at each location, we could determine the fraction of total current carried by the free electrons as a function of distance along the MITL. This comparison provided us with evidence of the onset of magnetic insulation. Probe voltages were sent to oscilloscopes and digitized for measurement.

Figure 2(a) shows the rise time of the leading edge of the voltage pulse for both the 2- and 3-m MITLs. These rise-time measurements indicate the degree of pulse sharpening that occurs. The 3-m MITL produced 10–90% rise times of 2.6 ± 0.3 ns, compared with 10–80% rise times of 4–5 ns for the 2-m MITL.

From these data, we can also determine the degree of pulse erosion by comparing the output voltage with an input voltage that we infer by multiplying injected current by 6 Ω, the measured MITL impedance. For both output voltages in Fig. 2(a), a small prepulse is discernible at about 65 ns. This prepulse arrives before the magnetic insulation process

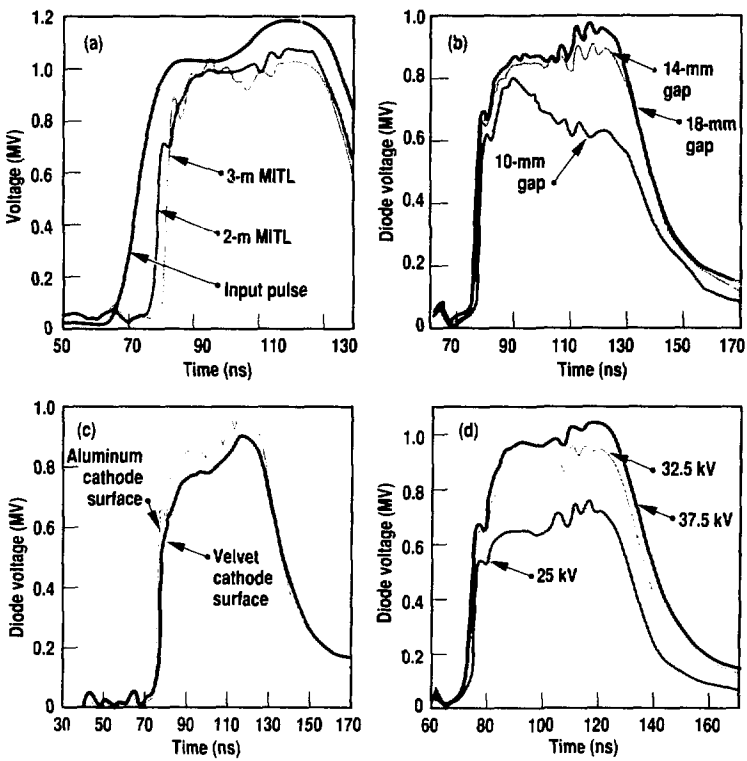

Figure 2. MITL experimental results. (a) Reduced voltage rise time for the 2- and 3-m MITLs compared with that of the input pulse. (b) Diode impedance was matched by varying the diode gap. (c) The velvet cathode produced a more uniform cathode emission, but the bare aluminum cathode gave a faster voltage rise time. (d) Diode voltages versus time for three injected voltage levels reveal that magnetic insulation was obtained even with the lowest charging voltage (25 kV).

has become fully established. The gap between the prepulse and main pulse represents erosion at the pulse front, which occurs when energy in the initial part of a fast-transient pulse is absorbed during the onset of magnetic insulation. Once magnetic insulation has been established, the remainder of the pulse propagates with little further attenuation.

Figure 2(b) through (d) shows our remaining MITL results. Again, we used the measured voltage across the voltage probe to infer the characteristics of the propagated pulse. Figure 2(b) shows how diode voltage is affected by variations in diode impedance caused by changes in the spacing of the anode-to-cathode gap. These impedance changes affect the point at which the diode voltage decays. The B-dot probes see current reflections as the MITL attempts to increase current to the diode. Cathode current is quite sensitive to any mismatch because the vacuum electrons see larger magnetic fields with the increase in total anode current. Improving magnetic insulation increases the MITL cathode current so that it more closely follows the total anode current. The dynamics of this process severely test our modeling capabilities.

In Fig. 2(c), we see how changing the surface material in the cathode from bare aluminum to velvet affects terminating diode voltage. Proper choice of surface material can enhance or delay plasma production and, hence, the onset of magnetic insulation. A bare metal surface delays the formation of uniform electron emission, while a velvet surface optimizes emission and reduces the electric field necessary to form a plasma. Our results showed that diode voltage and impedance were reduced with the velvet surface; indeed, impedance was reduced so much that we were unable to match to the MITL impedance simply by widening the diode gap. Also, the diode voltage was lower from the very outset of the pulse, indicating a more rapidly rising cathode current. The more uniform damage to the anode surface with the velvet cathode indicated a more uniform plasma formation on the cathode. However, the bare aluminum cathode gave the faster rise time and was the one we used for the remaining experiments.

Finally, Fig. 2(d) shows diode voltage versus time for three initial charging voltages (25, 32.5, and 37.5 kV). The waveform of the voltage pulses changes little as the amplitude increases. Magnetic insulation was observed even with the lowest injected voltage. Machine parameters did not allow us to reduce the injected voltage to the point where we could determine the magnetic insulation threshold.

CONDOR Modeling

Results from our CONDOR modeling showed some agreement with measured data; however, substantial differences were also apparent. We broke the modeling problem down into two parts. To simulate pulse propagation and determine pulse shape over the entire line, we first modeled a 4-m-long MITL terminated in an impedance-matched, coarsely zoned electron diode (4 zones across the gap). These long-MITL calculations were then used as input to a 1-m model terminated with a more finely zoned diode (10–20 zones). The finer zoning more accurately calculated diode impedance. Because propagation results obtained with the 1-m model were nearly identical to those with the 4-m model for a matched-impedance diode geometry, we felt justified in our two-step modeling approach.

CONDOR predicted that erosion of the pulse's leading edge would sharpen it. Figure 3(a) shows the calculated voltage pulse at various locations along the MITL. Leading-edge sharpening is quite apparent, as is a reduction in peak amplitude. The CONDOR model failed to calculate the prepulse, however, as shown in Fig. 3(b). Also, the rise time of the eroded pulse is faster in the calculations than in the measurement, and peak voltage levels differ. In both calculations and measurement, however, nearly all of the original pulse energy reaches the diode after its leading edge is eroded [see Fig. 2(a)].

Figure 4, a comparison of calculated and measured magnetic fields from the anode (total) and cathode currents, points up another important discrepancy

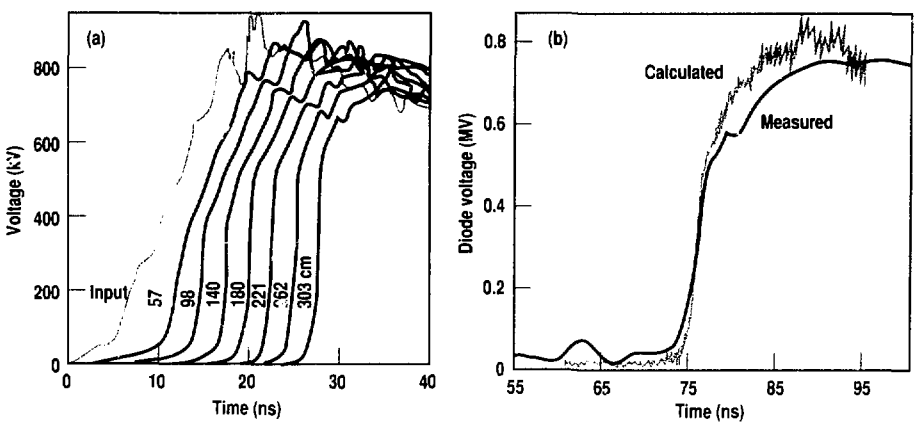

Figure 3. CONDOR calculations of MITL performance. (a) CONDOR predicted pulse erosion and reduced peak amplitude as a function of distance along the MITL. (b) For the 2-m MITL, CONDOR failed to predict the prepulse of diode voltage and calculates a faster rise time and higher peak voltage than measured.

between the CONDOR model and our measurements. CONDOR predicts a cathode current that is about 50% of the anode current. (Free electrons drifting in the vacuum gap account for the remainder.) However, our measurements indicate that nearly 80% of the current remains in the cathode, leaving only 20% to be carried by the free-electron current. These findings indicate that CONDOR by itself cannot adequately predict the onset of magnetic insulation, at least not until the assumption of space-charge-limited emission from cathode walls is modified. These discrepancies also suggest that models of more complex geometries should be viewed with caution.

VITL Experiments

Accurately characterizing the behavior of a VITL requires a pulse with a rise time on the order of 2–3 ns (faster than the 12–15 ns produced by our pulse generator). We, therefore, capitalized on the pulse-sharpening capabilities of the 3-m MITL to provide a voltage pulse with a 2.6 ± 0.3-ns rise time and a peak amplitude of 0.8–1.08 MV. In addition to dissipating power, the electron diode at the end of the MITL provided a low-impedance voltage source to the VITL.

Experiments were done on three 2.9-m-long coaxial aluminum VITLs, each of which was terminated with a resistive vacuum voltage divider to measure the voltage propagated to its end. The three VITL designs differed in the diameters of their inner conductors. This allowed us to vary the peak electric field applied to the anodized aluminum cathode; fields of 180, 250, and 320 kV/cm were applied. Current-viewing resistors (CVRs) at 5, 96, and 280 cm along the VITLs allowed us to determine current losses.

We wanted to determine the point at which electron field-emission effects became apparent and to measure the degree of rise-time and/or amplitude distortion from electron leakage currents. From our measurements, we conclude that no distinct electric-field threshold exists above which current loss is unacceptable. However, the degree of transmitted-pulse distortion caused by electron leakage currents varied from shot to shot for essentially identical initial conditions of VITL injected voltage. The minimum measured pulse voltage loss was 4.8%, and the maximum reached 40–50%. This variability makes predicting the outcome of such a measurement very difficult, as shown by the examples of Figs. 5 and 6.

Figure 5(a), in which diode voltage and VITL-transmitted voltage are plotted versus time, shows marginally acceptable voltage distortion. In this shot, the pulse rise time (measured at the 10% and 90% points) is degraded slightly from 2.6 ns at the input to 3.1 ns at the end of the VITL. Likewise, the peak amplitude is attenuated from 1.13 MV (250 kV/cm) to approximately 1.02 MV, for about a 10% voltage loss. The ±8% uncertainty in the voltage divider calibration may account for some of the apparent loss, while the remainder can be attributed to current loss. Figure 5(b) shows current measurements taken by the three CVRs. The total current loss indicated by CVR 1 (nearest the diode) is approximately 8 kA, or about 2% of full space-charge-limited field emission. Like the voltage loss, this current loss is marginally acceptable in a VITL measurement.

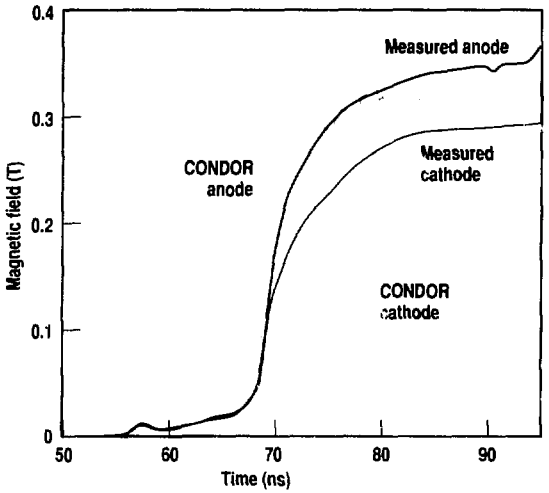

Figure 4. Comparison of measured and calculated magnetic fields at 190 cm indicates that CONDOR cannot adequately predict magnetic insulation.

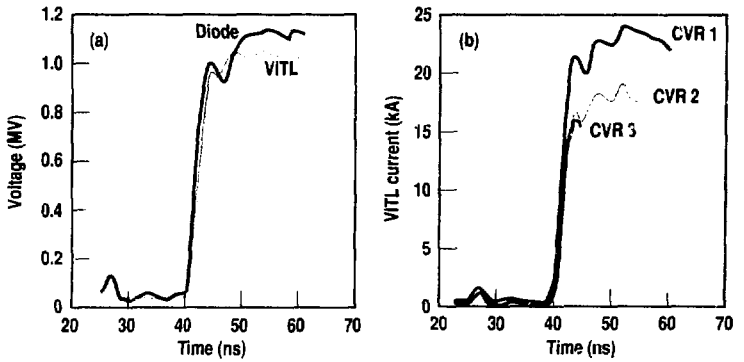

Figure 5. VITL experimental result showing (a) marginally acceptable voltage distortion and (b) current measurements at 5, 96, and 280 cm (CVR 1, 2, and 3) that indicate some current loss.

Figure 6(a), on the other hand, shows unacceptably large voltage distortion at the end of the VITL. Peak voltage is attenuated from 1.1 MV (320 kV/cm) to approximately 0.7 MV, or about 35–40%. Pulse rise time at the end of the VITL is little changed. The CVR current measurements of Fig. 6(b) indicate large, monotonically increasing currents in the VITL that bear little resemblance to the voltage waveform. Electron-current losses in the line create a lossy transmission line; associated magnetic fields are insufficient for magnetic insulation to occur. The remaining data we obtained show a trend toward larger losses at higher field strengths. However, no one-to-one correspondence exists between the current loss and the amplitude of the injected voltage.

Conclusions

Our experiments showed, first, that we could generate a 2.6-ns, 1-MV pulse using a 3-m MITL. We then used the MITL to study the propagation characteristics of the high-voltage pulse. In particular, we observed an initial voltage prepulse followed by the main pulse, whose leading edge was progressively eroded as the pulse propagated through the MITL. Onset of magnetic insulation was observed as the total current diverged from the cathode return current. The remaining current was carried by magnetically insulated electrons flowing in the vacuum gap.

CONDOR models of MITL behavior showed qualitative agreement with measured values of pulse sharpening, leading-edge erosion, peak amplitude attenuation, total current, and MITL operating impedance. Differences between the model results and the experiment were also apparent. The code does not predict the voltage prepulse and predicts significantly less cathode current than was measured. Both deficiencies reflect the CONDOR assumption of space-charge-limited field emission and the lack of an electric-field threshold for electron emission to start. To achieve a quantitative predictive capability, we must develop a physical model of electron emission that takes into account time- and electric-field-dependent emission.

The VITL experiments demonstrated that high-voltage pulses can be propagated over 2.9 m with small distortions in rise time and 10–15% distortion in peak amplitude. However, the results also showed significant shot-to-shot fluctuations in the amount of current loss along the VITL. Also, no distinct electron-emission threshold was observed even for electric-field strengths of 180–200 kV/cm. These results are consistent with a low level of electron emission even at low electric fields. For better reproducibility of results, we will need to better control the preparation of the cathode surface.

CONDOR could not simulate VITL behavior because it imposes the assumption of fully space-charge-limited field emission from metal surfaces. Although we could have arbitrarily limited field emission in the code to match our experimental results, the experimental conditions could not be controlled well enough to ensure that this CONDOR model could successfully predict the outcome of subsequent experiments. For both MITLs and VITLs, significantly better modeling capability than that now available will be needed if we are to use computer codes to predict transmission line behavior.

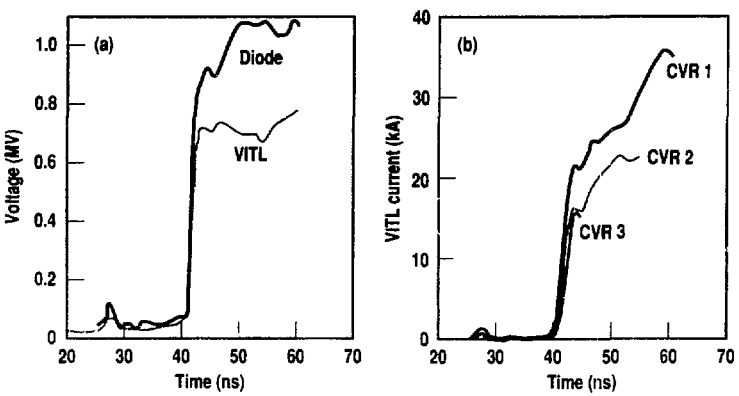

Figure 6. VITL experimental results showing (a) unacceptably high voltage distortion and (b) monotonically increasing currents that indicate significant current losses along the VITL.

References:

1. A. Ron, A. Modelli, and N. Rostoker, *IEEE Trans. Plasma Science* **PS-2**, 85 (1973).
2. J. Creedon, *J. Appl. Phys.* **48**, 1070 (1977).
3. K. Bergeron, *J. Appl. Phys.* **48**, 3065 (1977).
4. R. V. Lovelace and E. Oh, *Phys. Fluids* **17**, 1263 (1974).
5. M. DiCapua, D. G. Pellinen, P. D. Champney, and D. McDaniel, "Magnetic Insulation in Triplate Vacuum Transmission Lines," *Proc. Int. Topical Conf. High Power Electron and Ion Beam Research and Technology* (Cornell University, Ithaca, N.Y. 1977), pp. 781–792.

Equation of State of Low-Density Materials

N. C. Holmes

Low-density, expanded materials are used for a variety of applications. In the environment of a nuclear device, intense radiation heats these materials to high temperatures; high internal pressures result. Simulations of the hydrodynamic effects of this require accurate models of the equations of state (EOS) of these materials. While a number of theoretical EOS models exist, there is no experimental data to confirm the accuracy of these models. It is the goal of this project to determine the EOS of important low-density materials and to improve tabular equations of state for use in simulations.

We use the impact of high-velocity projectiles fired by LLNL's two-stage light-gas gun to generate strong shock waves in low-density materials. A series of such experiments at varying projectile velocities determines the principal Hugoniot of a particular material. The Hugoniot is not a thermodynamic path; it is the locus of final states achieved in shock-wave experiments of varying strength. The states, both before and after the shock passes in a material, are characterized by the Rankine-Hugoniot relations,[1] which express conservation of momentum, mass, and energy. For a sample initially at rest and with initial pressure P_0 and energy E_0, these equations are

$$P - P_0 = \rho_0 u_s u_p \,, \tag{1}$$

$$\rho = \rho_0 (1 - u_p/u_s)^{-1} \,, \text{ and} \tag{2}$$

$$E - E_0 = (P + P_0)(V_0 - V)/2 \,. \tag{3}$$

where ρ_0 ($\rho_0 \equiv 1/V_0$) is the initial density, u_p is the mass velocity behind the shock front, u_s is the shock velocity, and P, ρ, E are the final pressure, density, and energy behind the shock front. In the experiments described here, P_0 and E_0 are negligible. The mass velocity u_p is derived from the projectile velocity u_i and the known EOS of the Al impactor plate mounted on the face of the projectile.[1] Thus, we need only to measure ρ_0, u_s, and u_i to determine a point on the Hugoniot of a particular sample material.

Shock-wave techniques have several important advantages: the measurements are very precise, the shock wave generated is steady, and the shock is uniform and nearly planar over large dimensions.

The Hugoniot we measure is only a part of the overall EOS. To further constrain the EOS, we also will measure the shock temperature. This helps to determine the partition of the energy in the sample material. Furthermore, it will improve confidence when the EOS model is extrapolated over wide ranges of thermodynamic variables.

These experiments will characterize the following three materials: silica aerogel, which is a low-density, open-cell SiO_2 with very small cells (≈10 nm); TPX, which is a low-density CH_2 polymer foam; and CH (polystyrene) foam. Since the development of our technology base has accounted for most of our work so far, we are presenting data for aerogel samples only. To provide data that is most easily modeled to verify theoretical models, we have used very pure aerogel. Details of the preparation of the samples are described in detail below.

Experimental Methods

As noted above, we needed to measure ρ_0, u_i, and u_s to determine the Hugoniot point. The samples are simple stepped cylinders as depicted in Fig. 1. We determine shock velocity by measuring the transit time of the shock across the known height of the step. We use the light emitted by the shock front as it reaches the thin Au layer on the sample. The Au layer blocks the light until the shock arrives at the layer; otherwise, the brightness would reduce the contrast at arrival time. The Au layer also improves our ability to determine the sample dimensions.

An autofocus infrared-backscatter technique measures the overall sample thickness and step height and provides numerous measurements of the sample thickness over a grid pattern on the stepped surface of the target. To correct for any tilt of the target during the measurement, we use a least-squares fitting method to find the step height. The targets are measured across three diameters 120 degrees apart. We use the smoothest diameter for the calculation and the experiment; the deviation of the data from the fit serves as a measure of sample roughness. We weigh the sample prior to coating with Au so that the density is easily found.

Short-pulse x radiography of the projectile in flight measures the impactor velocity just prior to its impact with the sample.[2] This provides a typical accuracy of 0.1%.

The most challenging task is the measurement of the shock-transit time. We have developed an optical method of unprecedented accuracy for this purpose. In this technique, we use an electronic image-converter streak camera to record the arrival of the shock front along a diameter at the stepped surface of the sample and an achromatic lens system to form an image of the surface on the slit of the streak camera. We use electronic shorting pins mounted through holes in the sample to trigger the streak camera just prior to the arrival of the shock at the surface.

While electronic streak cameras have very high time resolution (about 0.1 ns for the camera we use), they all suffer from nonuniform streak rates; that is, the sweep rate (distance/time) varies across the length of the sweep. This variance can lead to large errors in shock-transit time measurements if uncorrected. We use a mode-locked Ar-ion laser to record a series of time markers on the streak record simultaneously with the shock-arrival signals. These time markers have a pulse width of about 150 ps and provide very precise marks at roughly 12 ns intervals. With this system, we can measure shock-transit times from about 0.1 to about 0.3%. Details of its use in the data analysis are given in the following sections. We use a multiple-shutter method to control the total time that the mode-locked pulse train is applied to the streak camera. This is necessary to limit the effects of secondary emission at the photoanode of the streak tube.

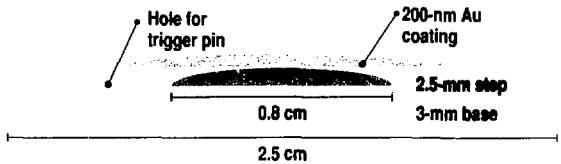

Figure 1. A cross-section view of a sample for a shock-velocity experiment. The overall diameter of the sample is 2.5 cm, and the diameter of the stepped section is 0.8 cm. The Au coating is used to prevent shock-front emission from being detected until the shock reaches the surface of the sample. Electronic shorting pins are used to trigger the streak camera.

Sample Preparation

We baked silica aerogel samples in air at 500°C for 5 hours to oxidize hydrocarbon impurities and desorb H_2O. Unbaked samples can contain as much as 5% C by weight; this amount is reduced to below 1% by the baking process. The goal of this step is to produce samples that are pure SiO_2. After bakeout, we weigh the samples with a sensitive balance. Then, we evaporatively coat the rear-stepped surface with Au to about a 200-nm thickness. We next measure the samples using the autofocus infrared-backscatter method and mount them into target bodies and evacuate them to about 10^{-4} Torr. The target bodies feature a remote-controlled front-gate valve. After we mount the targets in the two-stage gun-target chamber, we pump the chamber to roughly 10-μm Hg pressure. Just before we fire the gun, a pulse actuates the gate valve, exposing the aerogel surface for projectile impact.

Experimental Results

We performed six EOS experiments on silica aerogel: five on baked samples and one on an unbaked sample of similar

Table 1. EOS data for shock-compressed silica aerogel.

Experiment name	Impactor velocity (km/s)	Sample density (g/cm³)	Shock velocity (km/s)	Mass velocity (km/s)	Pressure (kbar)	Density (g/cm³)
Foam 11	5.160	0.1265	5.326 ± 0.038	4.944 ± 0.006	33.3 ± 0.24	1.76 ± 0.177
Foam 12	5.858	0.1289	6.036 ± 0.039	5.580 ± 0.007	43.4 ± 0.29	1.71 ± 0.148
Foam 13	6.757	0.1254	6.918 ± 0.026	6.407 ± 0.008	55.6 ± 0.23	1.70 ± 0.092
Foam 14	7.879	0.1289	8.186 ± 0.037	7.401 ± 0.010	78.1 ± 0.38	1.34 ± 0.066
Foam 15	4.153	0.1283	4.198 ± 0.016	4.010 ± 0.005	21.6 ± 0.09	2.87 ± 0.267
Foam 16[a]	5.944	0.1307	6.226 ± 0.023	5.651 ± 0.007	46.0 ± 0.19	1.41 ± 0.060

[a] Unbaked sample.

initial density. The results are tabulated in Table 1. Uncertainties are shown at the 2σ, or the 95% confidence level.

The analysis of the shock-velocity data requires additional explanation. The projectiles fired by the gun typically exhibit a small amount of parabolic distortion as a result of their rapid acceleration and also may be tilted slightly at impact. We must correct for these effects to achieve high accuracy so we use the time markers on the streak record for this purpose.

Figure 2(a) is the reproduction of a typical record. We measure the position of the shock-arrival signals at several points along the base of the step and again at several points on the step breakout signal. Using the time marks, we calculate the time at each point using either cubic spline or local quadratic interpolation between the time marks. We then use a four-parameter, least-squares calculation to find three parameters to account for the tilt and distortion and find the shock-transit time as the fourth parameter. We compare the results of such a fit to the experimental data in Fig. 2(b). In this fit, the shock-transit time is about 354 ns and the root-mean-square deviation of the points from the fit is only 0.25 ns, less than 0.1%.

We typically report the uncertainty in EOS data at 2σ, or the 95% confidence level. If the root-mean-square deviation of the step-dimension measurements is δh and the scatter of the time measurements is δt, for a shock-transit time Δt, then the overall uncertainty in the shock velocity is given by

$$\delta u_s/u_s = 2\,[(\delta t/\Delta t)^2 + 2(\delta h/h)^2]^{1/2}\,, \qquad (4)$$

where h is the height of the step and $u_s = h/\Delta t$. To find the total uncertainty in the pressure, density, and energy, we use the method previously described by Mitchell and Nellis,[1] which takes into account the uncertainty in initial density, impactor velocity, and the EOS of the Al impactor.

The shock-velocity data for pure, baked aerogel fit the relation $u_s = C + Su_p$ for $C = -0.046 \pm 0.011$ and $S = 1.163 \pm 0.021$. This kind of linear relationship is common to most materials. The fit and the data are shown in Fig. 3, which also includes data for three unbaked samples. We can use this fit to display the data in the pressure-volume plane shown in Fig. 4. The relatively large uncertainties in the final densities are a direct result of the large compressions achieved. For shock-wave experiments, the uncertainty in the final density varies as $(\eta - 1)\delta u_s/u_s$, where η is the compression ($\eta = \rho/\rho_0$). Since the samples have a distribution of initial densities, the shaded band indicates the spread of final densities using the linear fit shown in Fig. 3. The results are compared in Fig. 4 with the best tabular EOS for pure SiO_2. The unbaked samples lie consistently to the left of the shaded band and demonstrate the importance that impurities, especially H_2O, can have on the compression properties.

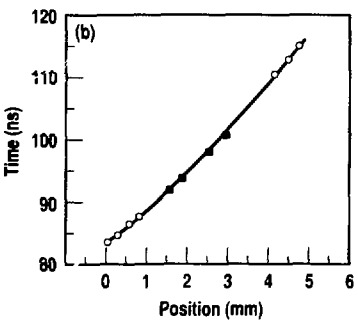

Figure 2. (a) Streak-camera record. Time is increasing to the right in the figure, and the distance from top to bottom is proportional to the distance along a target diameter. The line of dots at the top of the streak record is the mode-locked, laser-timing marks. The bright area just below the streak near the left edge results from photoanode scattering from the time-mark pulse train before the camera is triggered. (b) Results of a four-parameter fit to the shock-arrival-time data for this record. The circles are the shock-arrival times for the base of the target; the solid squares are the arrival-time data for the top of the step and have been corrected to the curve by subtracting the calculated shock-transit time. For this record, the shock-transit time is 354 ns, and the standard deviation of the scatter about the fit is 0.27 ns.

Future Work

We plan to perform similar experiments on pure TPX and CH. Since we carry out many NTS applications in an $N/Ar/H_2O$ atmosphere, we will also test these samples in this atmosphere. We expect the addition of H_2O vapor to silica aerogel to have a significant effect. To do this, we must enclose the samples within a vacuum-tight sample holder filled with $N/Ar/H_2O$. Now, the aerogel will be in contact with an Al plate to seal the impact side of the target body. When the shock passes from the Al into the low-density samples, the shock pressure

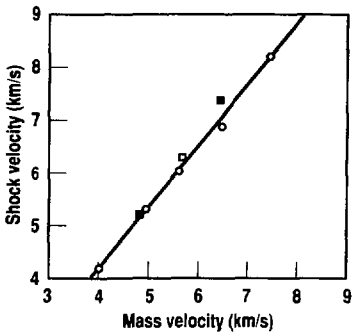

Figure 3. The solid line is a linear least-squares fit to the data for baked silica aerogel (open circles). The unbaked samples are shown by squares: the open square is Foam 16 (see Table 1), and the solid squares indicate data from previously reported experiments.

will decrease as the Al plate undergoes an isentropic release into the foam samples. The release properties of Al have not been measured. We will characterize this process using the shock pressure generated in aerogel.

A new, fast, fiber-optic-coupled optical pyrometer is now nearing completion. We will use it to measure the shock temperature in silica aerogel (baked and unbaked) as well as in TPX and CH. This system uses six time-resolved, narrow-wavelength-band optical channels as well as a spectrograph to record the emission spectrum of the shocked samples. We will fit the data from the time-resolved channels to a grey-body spectrum. Since the system will be absolutely calibrated against the National Institute of Standards and Technology's traceable standard, we can find both temperature and emissivity in such experiments. This is a relatively straightforward measurement in a transparent medium such as aerogel.[3] However, TPX and CH are translucent because the pore size is much larger than optical wavelengths. Initial experiments show that we can detect the shock-front emission when the shock front moves to within about 1.5–2 mm from the rear surface. Since it is possible to measure the absorption and scattering response of the samples, we are confident that the measurements will determine the true shock temperature.

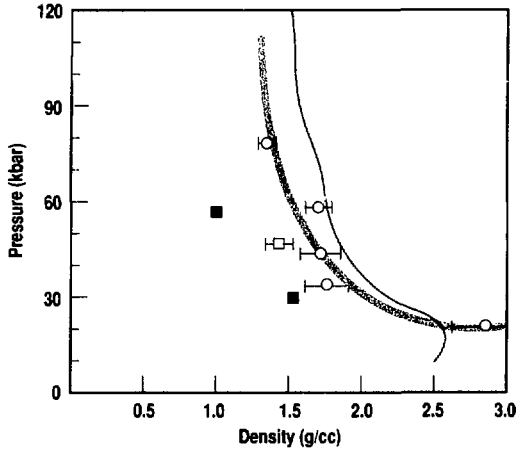

Figure 4. Summary of pressure-volume data for shock-compressed silica aerogel. The open circles are for baked aerogel, and the squares indicate points for unbaked samples. The shaded band is derived from the linear fit shown in Fig. 3 for the range of initial densities of the samples. The blue curve is calculated from the best tabular EOS for silica with $\rho_0 = 0.128$ g/cm^3.

References:

1. A. C. Mitchell and W. J. Nellis, "Shock Compression of Aluminum, Copper, and Tantalum," *J. Appl. Phys.* **52**, 3363 (1981).
2. A. C. Mitchell and W. J. Nellis, "Diagnostic System of the Lawrence Livermore National Laboratory Two-Stage Light-Gas Gun," *Rev. Sci. Instrum.* **52**, 347 (1981).
3. N. C. Holmes, H. B. Radousky, M. J. Moss, W. J. Nellis, and S. Henning, "Silica at Ultrahigh Temperature and Expanded Volume," *Appl. Phys. Lett.* **45**, 626 (1984).

Material Behavior Calculations in Support of NTES

C. E. Frerking

During the past decade, NTES has become increasingly interested in performing device diagnostics using the low-energy x-ray region (<1–20 keV) of the photon spectrum. In the past, most measurements used high-energy gamma rays or neutrons, both of which are deeply penetrating and neither of which is affected by small amounts of material obstructing a line of sight (LOS). In the case of low-energy x rays, however, a measurement can be seriously impaired, or even rendered meaningless, if even a small bit of ablated or vaporized material moves into an LOS. Our ability to perform low-energy x-ray experiments in the field has required that we find new techniques to model material behavior that can affect the viability of an experiment. Using the LLNL hydrodynamics codes to model such behavior, we have recently been able to design more-reliable experiments and to understand problems where possible material effects are displayed.

Typically, x-ray measurements use either a small pinhole (<0.5 cm diam) or a slit that isolates a spatial region of an emitting source. The behavior of

material that has been heated to between a few electron volts and a few hundred electron volts ("warm material") leads to a class of phenomena that can cause problems to device diagnostics measurements. Those effects include the blow-in of debris on x rays being viewed through an LOS, changes in scattering and transmission properties through x-ray filters and scatterers, changes in the reflective properties of x-ray mirrors as heating occurs, and effects on the degree of heating of LOS components from the reradiation of hot elements in the LOS. During the past year, experiments that viewed various forms of low-energy x rays on the Schellbourne and Comstock events demonstrated the importance of being able to model warm-material behavior, both to predict that an experiment is safe and to verify that such behavior has affected a measurement.

On Schellbourne, we modeled warm-material behavior using the LLNL hydrodynamics code LASNEX to determine whether the pinhole would survive on low-energy x-ray experiments (Fig. 1).

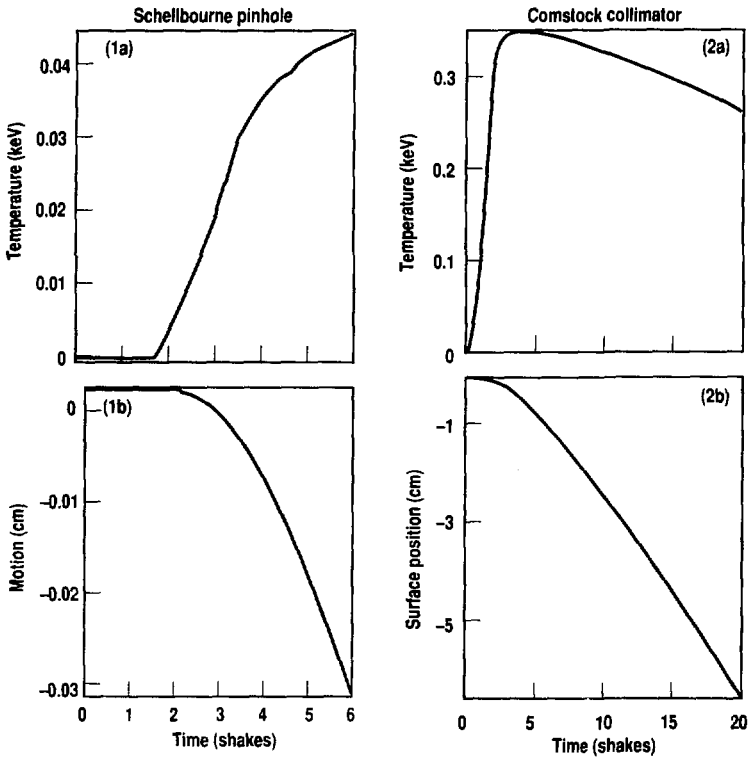

Figure 1. (a) LASNEX calculation showing the temperature of the inner zone of a Schellbourne pinhole as the material heats and ablates. During the time of interest, the material heats to about 45 eV. (b) The same calculation also shows the amount of movement that can be expected for the same heated material. Given the narrow aperture (1.1 mm), this movement represents a closure of about 50% during the time of interest. (c) The closure-versus-time streak calculation of the slit using a postprocessor with LASNEX. The original one-dimensional cold slab starts at the 0.2-cm position at zero time. Material ablates to the left as time progresses, obstructing the slit.

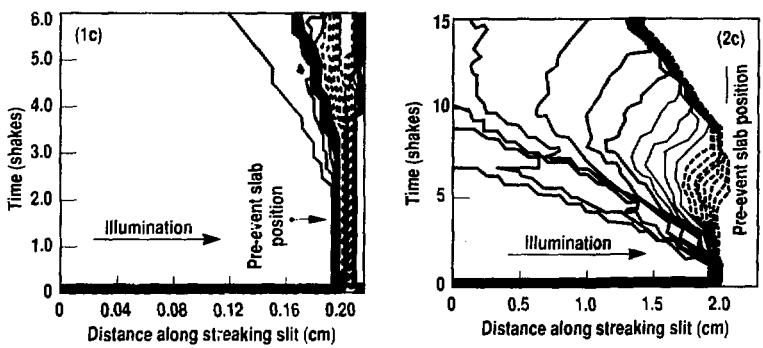

Figure 2. (a) LASNEX calculation for the front zone of the Comstock collimator shows a much higher degree of heating and more substantial ablation rate than shown in Fig. 1(a). (b) Position of the front surface demonstrates the high probability that closure was indeed seen on event measurements. (c) A streak calculation of the collimator closure using a post processor with LASNEX. The original one-dimensional cold slab starts at the 2 cm position at zero time. With illumination from the left, material ablates to the left as time progresses, obstructing the collimator view.

The pinhole we used was a 2.5- × 1.1-mm rectangular aperture, smaller than the pinholes customarily used in other x-ray experiments. The pinhole material consisted of 1 mil of Cu sandwiched between 1-mil layers of Be. The pinhole was also filled with Be to provide a tamper to impede closure. Farther up the LOS was a filter, consisting of 62 mil of Ca backed with 1 mil of Be, that provided a spectral window to a spectrometer. After this had been run as a two-dimensional problem for several shakes, the accrued velocities and motion showed that the material behavior was marginally safe but could easily introduce the need to make corrections to closure during the later times of interest. This result was verified with a one-dimensional problem that modeled the pinhole materials as a slab that is exposed to the source directly from the front. After reviewing these results, we initiated another LASNEX problem to determine whether the pinhole would remain cooler if the Ca filter, initially located above the pinhole, were moved below. Results showed that the Ca-Be filter would stop a significant fraction of the flux heating the pinhole, removing all doubt regarding the viability of the pinhole. Further calculations using LASNEX and the HOPE opacity code allowed us to check the transmissive properties of Ca at the elevated temperatures to ensure that the filter would not change its characteristics during the measurement in the x-ray energy range of interest.

During FY88, we were also able to verify that material closure was an observed effect on an x-ray experiment on the Comstock Event. Canister prints revealed that, within an LOS that included several collimated beams, the beam arrangement passed relatively close to the pipe wall. This experiment was somewhat unusual because the amount of energy entering the LOS was much larger than normal, and the pipe walls at the bottom of the LOS could directly view a portion of the source, causing reradiation higher into the LOS. A one-dimensional LASNEX problem that modeled the pipe material and the source (Fig. 2) verified that material could easily have intruded into the LOS fast enough to affect the measurement.

Optical Streak Cameras and Their Test Program Applications

J. J. Ronchetto

The increasing amount of high-bandwidth data generated during field tests has spurred the development of optical streak-camera systems with multiple channels. Multichannel systems can be much smaller than conventional systems based on wideband oscilloscopes and have made it possible to measure downhole phenomena that would not otherwise be feasible. Because our experiments are done underground, we rely primarily on downhole systems, although we have fielded uphole systems for specialized diagnostics measurements.

Downhole Systems

We have developed a 6-ft³ downhole streak-camera system that can gather data from more than 100 individual channels over a period of 30 ns with a temporal resolution of less than 1 ns and an intensity range of 100:1. Because of the prodigious number of channels required, data acquisition with other techniques would be severely limited by the large number of signal cables required. The smaller streak-camera system readily lends itself to downhole use and permits the acquisition of an enormous amount of time-dependent data. In a recent field test, we obtained streak-camera data from approximately 1450 channels.

Figure 1 shows the major components of a typical downhole streak-camera system such as those used on low- and high-energy spectrometers to view time histories of spectral outputs and, on imaging experiments, to view time histories of one-dimensional images.

The nuclear phenomena to be investigated are first converted into light by means of a scintillating material mounted at the detector within the vacuum of the line-of-site pipe. Two different methods are used for this conversion. The first converts the radiation directly when it strikes a scintillating material. The second, more sensitive, method involves an active detector that converts the radiation to photoelectrons, which are then focused (and in some cases intensified) and accelerated before striking the scintillating material. In both cases, the emitted light is coupled out of the vacuum area by means of a fiber-optic faceplate and transmitted via a bundle of optical fibers directly to the streak camera's photocathode. This bundle contains approximately 100 individual 50- to 300-μm-diam fibers that are laid by hand in a predetermined matrix. Each end of this fiber link can have a different style array head or heads, and individual fibers can be in different positions at the two ends. This type of optical fiber bundle can be produced in any reasonable length and has relatively low light loss.

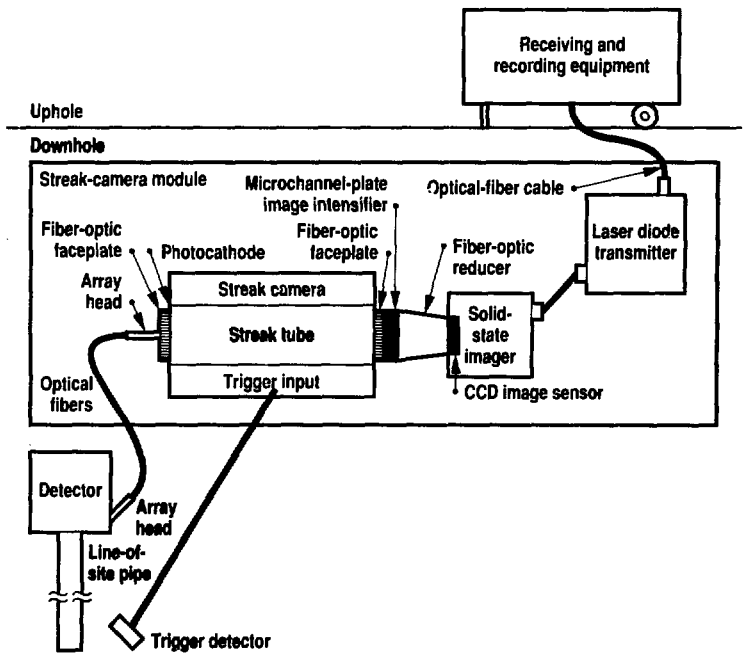

Figure 1. Typical downhole streak-camera system.

The streak-camera system itself is enclosed within an electromagnetic interference (EMI) proof module located from 15–60 ft above the detectors at the top of the downhole canister. This position is necessary because it allows time for the streak-camera systems to accumulate and read out their data before the shock wave arrives and destroys both the module and the enclosed equipment. We can measure, transmit, and record the data uphole in less than 3 ms.

Within the streak camera, the streak tube detects, amplifies, and folds the signals into a two-dimensional image. The microchannel-plate image intensifier further amplifies the outputs from the streak tube. A fiber-optics reducer is needed to reduce the image size from the intensifier to match a solid-state two-dimensional imager. The system components are packaged with precise, contiguous coupling by means of fiber-optic faceplates to minimize transmission losses and image degradation between components. The solid-state imager contains a CCD image sensor with an array of 122 by 380 pixels and converts the image into digital information, which is serialized and transmitted uphole at a 180-mHz rate through a single optical-fiber cable driven by a laser diode transmitter. Uphole is a receiving and recording apparatus for these digital light signals. The serial data are detected by a photodiode, then captured and stored in solid-state nonvolatile memory. The data are later transferred by hand to a removable hard disk for analysis.

We developed a downhole streak camera capable of activating in response to the triggering signal in only a few nanoseconds. This system has served well in a variety of downhole applications, all requiring especially fast and precise triggering and timing control. However, the trend of moving the instrumentation as close as possible to the signal source (i.e., the nuclear device) to enhance measurement sensitivity and minimize signal distortion further reduces the time available for the streak-camera system to accept data and process and transmit them uphole. Therefore, an ongoing research goal is to improve the speed and precision of the system and the amount of data it can collect.

Figure 2 depicts a new mode of streak-camera operation, which has been successfully applied on two field tests. This system incorporates and builds on our earlier advances in the control of the photoelectronic signal (a stream of photocathode-generated electrons) as it passes through the streak tube. The circuitry controlling the gating electrode and the deflection plates (which, in synchronization, control the rate and direction of the electron beam) had already been developed but had to be improved to allow for fast, time-stable gating and good sweep ramp linearity. This improved control and an innovative idea made it possible to increase the number of input arrays to two or more, with a corresponding increase in the number of image areas at the output end of the tube. The advantage of this arrangement, called spatial multiplexing, is that it multiplies the input signal population. With this technique, we obtain more data channels per streak camera and thereby reduce both the cost per data channel and the physical size of the downhole instrument.

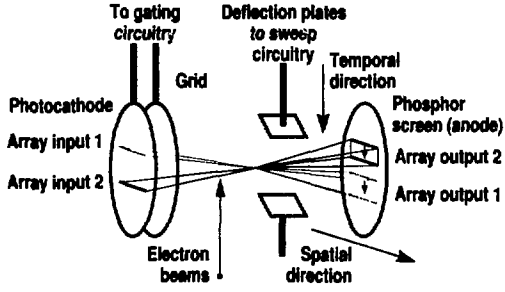

Figure 2. Spatial multiplexing, a new mode of streak-camera operation.

There is an inherent timing difficulty in triggering very-high-bandwidth systems, such as oscilloscopes and streak cameras, that have limited temporal viewing windows within which the signal of interest must occur. The window for streak-camera systems is determined by a combination of the streak camera's gate and sweep timing. The signals we wish to record are on the order of 5 ns wide and require a temporal resolution of less than 1 ns. This limits, for resolution reasons, the maximum streak-camera sweep time for each array to about 60 ns (30 ns when spatially multiplexed by two). Thus, any data to be acquired must fall within this small time window.

The signals that we wish to study are created by the interactions of the radiation emitted from the device's secondary. Triggering of the primary and the radiation output of the secondary can have ±25 ns of timing uncertainty or jitter, which may move the desired data out of the preselected time window. It is, therefore, necessary to trigger the streak cameras from a detector whose output is related to the timing of the device's secondary. The timing problem occurs because all of the reactions after the secondary trigger occur very rapidly, and the signals to be viewed travel at the speed of light in vacuum while the trigger signal, which was transmitted by means of coaxial cable, travels at a slightly slower speed. Also, the circuitry internal to the streak camera requires time to start and become stable. This late-triggering dilemma is solved by using any or all of three different techniques.

- Air coax can be used in our triggering path since its velocity of propagation is close to that of the speed of light in vacuum.
- The bundle of optical fibers is made longer, which delays the signal we wish to view with respect to the trigger.

• The third technique is used only with spatial multiplexing. In this case, the start of the time window is determined by the start of the sweep while the end of the window is determined by the end of the streak-camera gate pulse. We can, thus, use a bi-stable gate circuit that opens early with a trigger from the device's primary and closes with a slightly delayed trigger from the fast secondary. The undelayed secondary signal also triggers the sweep circuitry, which responds very quickly.

We use streak tubes that were designed with a computer simulation code. These tubes give better resolution than was previously available. The fabricator of the tube is able to create the photocathodes by a deposition process outside of the tube, allowing the photocathode faceplate to be mounted cleanly inside the tube. Formerly, this deposition was done *in situ* with some resultant contamination of other elements of the tube from the photocathode material being deposited on them. This change in manufacturing process has improved the tube's signal-to-noise ratio.

The new tube also incorporates a near-ultraviolet transmissive faceplate as the entrance window. At a wavelength of 380 nm, the new tube's sensitivity is comparable to that of a glass-window tube, but the advantage of a fiber faceplate is retained. It has in the past been necessary, when viewing near-ultraviolet light signals, to use a glass entrance window and a fore-optics system of various lens to focus the array image on the photocathode. This new faceplate eliminates the bulky fore-optics previously required to view the color of our present fast-response scintillators and allows a further reduction in the size of the streak-camera system.

The new streak tubes are also more resistant to damage from vibration during transportation and handling, from extreme temperatures, from high altitude at the NTS, and from voltage breakdown from the high voltages (up to 15 kV) in use. The 23.5-cm-long by 10.8-cm-diam glass tubes are now potted with a rubber material inside a solid fiberglass housing and have ridged mounting flanges on both ends for easier mounting. These are simple steps, but because of the unique application and exceptionally hostile physical environment, they are very important.

Uphole Systems

Uphole streak-camera systems for the Prompt Diagnostics Program differ from the downhole systems because of the dissimilar operating environments and the different measurement requirements.

We presently have two uphole streak-camera designs. Uphole cameras are designed and packaged with "ease-of-use" features such as dial-adjustable photonic system gain and sweep speed. They also usually require improved performance in one particular parameter while another parameter may be relaxed. Some experiments require very wide bandwidths and, thus, the temporal resolution becomes very important; others require wide dynamic range.

Since the uphole system is not immediately destroyed after acquiring data as is the downhole system, the data can be read out much slower or recovered directly. The fast downhole solid-state imager and the associated fiber-optic reducer are, therefore, replaced with either a film pack or a commercial high-resolution imaging system. Either alternative possesses higher spatial resolution (in both the temporal and spatial directions of the streak camera output image) and a wider dynamic range than does the downhole imager.

The light signals we are interested in uphole are predominantly at the red end of the optical spectrum (as opposed to the very blue signals, which are of interest downhole), and uphole cameras are not spatially multiplexed because of the difficulty in bringing each individual data channel uphole on a separate optical fiber. This fact also keeps the signal population on the photocathode low, which is beneficial when trying to optimize other streak-camera parameters.

One of our uphole cameras, which uses a streak tube similar to the downhole tube, differs mostly in its spectral sensitivity and photocathode layout. This camera also contains a feature that places a digital image on film for the labeling of data. The other uphole camera contains a streak tube developed by EG&G that is capable of slightly improved spatial and dramatically improved temporal resolution. This tube is also available with either the blue- or red-sensitive photocathode. We have obtained an impulse response of less than 50 ps with this camera.

Summary

Prompt Diagnostics Program is successfully fielding exceedingly complex state-of-the-art streak-camera systems downhole. The vital physics data are obtained in a magnitude that would be impossible to obtain with more conventional data-acquisition techniques.

We are also fielding uphole systems that have proven to be very effective for specialized diagnostics measurements. Both uphole and downhole systems have been miniaturized with substantial benefits for data recording. We are continuing our efforts to improve data quality, data quantity, and (because of the financial impact) data population for our streak-camera systems.

Streak-Camera Developments for NTES Applications

M. Lowry and J. Bonlie

High-fidelity measurements of single-transient events are one of the most challenging measurement problems. An important aspect of these measurements is temporal fidelity. Single-shot or single-transient events—such as nuclear weapons tests, high-power laser-produced plasmas, or chaotic behavior in photonic devices—cannot be usefully studied by repetition. Sampling or correlation techniques provide very high temporal resolution. However, these techniques generally can measure only those phenomena that are identically repeatable, and many single-transient events are not.

Our high-fidelity instrumentation must be single transient; that is, it must gather a large amount of information per unit of "real" time. Ideally, the instrumentation produces a series of snapshots that provide a "movie" of the relevant physical observables. This movie must have good resolution temporally, spatially, and often spectrally. Thus, very-high-bandwidth time-resolved imaging is required.

In general, a figure of merit for such a system can be given by:

$$M = (1/\Delta t)NdL(s/n)\,, \qquad (1)$$

where Δt is the temporal impulse response, N is the number of independent channels, d is the dynamic range, L is the usable record length (measured in units of Δt), and s/n is the signal-to-noise ratio averaged over the dynamic range. The figure of merit reflects that, in general, we value the overall fidelity—how well the record of the event corresponds to the event—rather than one factor of Eq. (1) over another.

To date, the recording tool that best serves as our high-bandwidth single-transient movie camera is the imaging-tube streak camera. Accordingly, we have concentrated our research on developing large-format (many channel) streak-camera systems with high dynamic range and good temporal response. The streak camera differs from more conventional oscilloscope recording techniques in that an incoming optical signal modulates the intensity (z-axis) rather than the deflection (y-axis) of the electron beam. Electrons in the image tube are swept across a screen that senses the intensity of the electron-beam signal as a function of position on the screen. Then by precisely knowing the sweep velocity, we can translate the screen position into time.

Streak-Camera System

The physical concepts of an imaging-tube streak camera are straightforward. Photons strike the tube's photocathode (Fig. 1), and the "footprint" of the incident photons is translated into a photoelectron footprint. The photoelectrons, which are accelerated away from the photocathode by the fields produced by the electron-imaging electrodes, are imaged on the phosphor screen of the tube. With a streak tube that has been properly designed and set up, this image at the phosphor screen accurately represents the input photon footprint. The phosphor screen lights up in proportion to the local electron-beam intensity. Then, by applying complementary voltage ramps to the internal deflection plates, we can sweep or "streak" the image across the phosphor screen. Thus, the temporal evolution of the input photon footprint appears as a streak of light at the phosphor; variations in the intensity of the streak along the streak direction reflect any changes with time of the input photon-footprint intensity. This phosphor streak decays quickly, typically in a few hundreds of microseconds, but the optical output is sufficient to be

recorded on film or, more important, with an electronic focal plane array (FPA). To boost the sensitivity, we often use a microchannel-plate image-intensifier (MCPII) tube at the output of the streak tube's phosphor screen to amplify the streaked image.

The temporal response is composed of two portions: that due to the imaging point-spread function (PSF) of the tubes and that due to dynamic effects. The PSF is the spatial impulse response of the imaging system measured full width at half maximum (FWHM). This response is determined by measuring the image transfer quality of the tube, or of the cascaded imaging tubes when an MCPII is used. The PSF not only affects the temporal response, but, because it is the spatial resolution of the camera, it also affects N, the number of channels that the camera can record. The PSF also may be a function of optical intensity, particularly at high intensities as a result of the space charge effects in the streak tube and the saturation effects in the MCPII.

The principal dynamic temporal broadening is caused by transit-time broadening of the photoelectron pulse. This contribution to the time response is given by:[1]

$$\Delta t = 3.37 \times 10^{-8} \times \frac{\Delta\varepsilon}{E} \quad , \qquad (2)$$

where $\Delta\varepsilon$ is the photoelectron energy spread in eV, and E is the electrical field in the region of the photocathode in V/cm. Thus, by applying a large accelerating voltage to the photoelectrons, we can dramatically improve the time response. Operation of the streak tube in this mode is sometimes called "extraction" mode. Nevertheless, even with extraction mode operation, the time response is limited when input photon densities are sufficiently high to produce dense photoelectron packets that screen the applied field and decrease the effective E, thus increasing the time response.

For many years, the streak camera was successfully employed using film as the recording medium. However, the addition of an electronic FPA in the form of a charge-coupled device (CCD) to the output of the streak-camera phosphor (or MCPII) is probably the most significant streak-camera development since the invention of the electronic streak tube. In NTES, we use a CCD camera as the readout of a streak-camera system in both downhole and uphole recording systems (Fig. 2). In downhole applications, the readout of the camera must occur in a relatively short time. A major factor in the fidelity of the system with current CCD technology is the time available to read out the CCD chip. The fast-readout CCD chips of the downhole streak-camera system, in general, yield much less fidelity than the slow-readout CCD cameras.[2] However, using the downhole CCD readout, we can field multichannel experiments of unprecendented complexity and high data return that cannot presently be done otherwise. With the improved fidelity of the slow-readout (low-noise) CCD system used on our uphole and laboratory streak cameras, we have made significant advances in our understanding of the streak camera itself and have begun developing very-high-fidelity instrumentation systems.

Our CCD/computer readout systems can generate comparatively high-fidelity data at such a high rate that it has put a commensurate burden on the data analysis effort. Software development has proceeded synergistically with improved laboratory characterizations.[3] Thus, characterizations of streak cameras are much more thorough than was possible with the laborious and imprecise film recording methods.

Streak Camera R&D Facilities

NTES has expanded and improved the LLNL Streak Camera Research and Development (R&D) Laboratory, where we perform many of the calibrations, characterizations, and evaluations of streak cameras both for field and laboratory

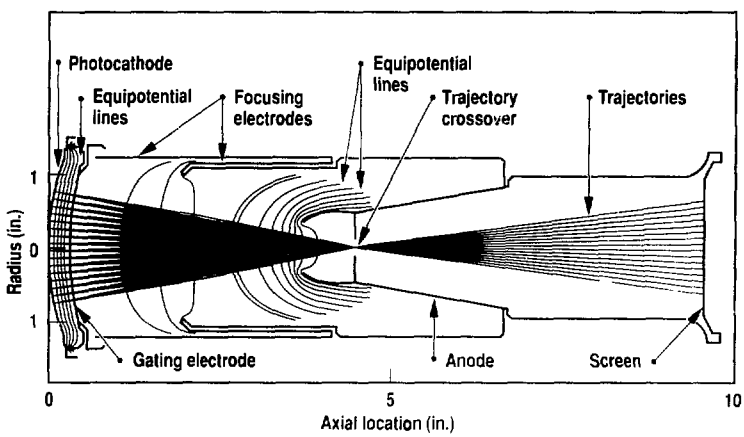

Figure 1. Plot of selected trajectories, equipotential lines, and electrode profiles in the optimized streak tube design. Electrode shape and location are shown by thick lines. The trajectories trace the focusing of the electron optics as the image is formed. The trajectory lines demonstrate a tight, well-defined crossover near the anode aperture as well as a curved field focus profile near the screen. (Adapted from C. C. Lai, *Design and Development of a New Streak Tube*, Lawrence Livermore National Laboratory, Livermore, Calif., UCAR-10159, 1986).

applications. This facility has several optical sources, including flash-lamp-pumped mode-locked dye laser systems, N_2-pumped dye laser systems, opto-liner imagers, Xe flash-lamp flat-field instruments, various optical components, and numerous types of modulated laser diodes. We use high-fidelity CCD camera systems and computers to process the data gathered in each streaked record. We also environmentally test camera designs at the R&D Laboratory to ensure field compatibility. We also have expanded the NTES Photonics Laboratory to develop extremely well-characterized and sophisticated optical sources and to improve our characterization techniques. We work in these laboratories to advance current camera designs and, thus, find more efficient methods to record and analyze single-transient experiments.

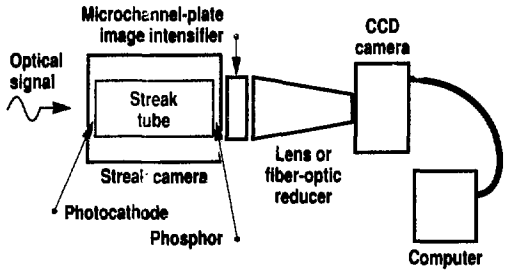

Figure 2. Streak-camera/CCD readout system. For uphole and laboratory applications, the computer is located near the CCD camera. In downhole applications, the CCD camera is connected to the computer by a digital data link about 1 km long.

Recent Performance Advances and Characterization Techniques

As noted, a revolutionary improvement over previous streak-camera systems is the addition of the high-fidelity CCD camera to read out the streak camera. Using the CCD camera and a very stable laser source (developed in NTES for the integrated-optical modulator project[4]), we demonstrated a nearly tenfold increase in the signal-to-noise ratio of the streak-camera system.

We found that much of the "noise" in the streak-camera record was apparently reproducible,[5] but this fixed structure had been masked by film noise in previous systems. With our stabilized laser sources, by single-shot triggering the optical source and recording this nominally constant optical carrier several times using the streak-camera system of Fig. 2 (with high-fidelity CCD readout), we explored the reproducibility of the measurement system. Figure 3 summarizes such a measurement.[6] The top trace is the average of four individual single-shot streaks; the reproducible structure in the readout is evident. The low spatial frequency shading is mostly due to

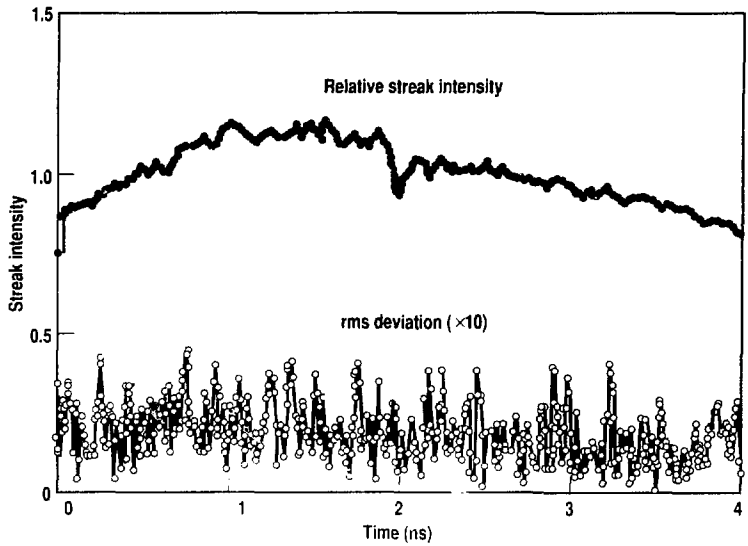

Figure 3. Results of streak-camera reproducibility studies using a very stable laser source. The top trace is a normalized average of four single-shot streaks. The bottom is the rms deviation about the average.

coupling-lens vignetting, while the higher-frequency structure is attributed to several causes: spatially dependent sensitivities of the streak tube phosphor, spatially dependent gain in the MCPII, and streak velocity variations. However, by calculating the root-mean-square (rms) deviation of each of the individual streaks about the average, we can quantify the level of precision for the system. This rms deviation is plotted in the lower trace of Fig. 3. Note that these values have been multiplied by 10 for ease of viewing. Thus, the rms deviation of the stabilized laser streak-camera system for mid-level intensities is 2.2%, averaged over all pixels of the record.

With this precision, we began to notice new details of streak-camera performance. For example, earlier sweep circuit designs—for slower streak speeds than those in Fig. 3—using avalanche transistor strings yielded unacceptably high streak velocity variations. This characteristic is revealed by illuminating the photocathode with temporally constant (on the timescale of the streak) light from a flash-lamp source. When the streak velocity slows, the electron beam spends more time on a given pixel, causing an erroneously large intensity signal in that region. These apparent intensity deviations can be as large as a factor of 2. By redesigning the sweep circuitry to incorporate field-effect transistors, we greatly minimized this problem for the slower sweep speeds typically used in downhole experiments.

To increase the efficiency and cost effectiveness of downhole streak-camera experiments, we increased the number of channels per streak camera by streak multiplexing. The technique exploits the fact that the streak tube is, first, a two-dimensional imaging tube (it has two spatial dimensions and one intensity dimension). Two tiers of input optical channels are stacked in what is normally considered the temporal direction.[7] Thus, by applying the sweep ramps, we can streak both tiers of input simultaneously. The spatial offset between the tiers effectively creates two streak records where previously there had been only one. This twofold increase in channel density reduces the temporal impulse response to slightly less than half of the nonmultiplexed configuration; thus, M of Eq. (1) is slightly diminished. However, in sophisticated downhole imaging applications, we value channel density more highly than other streak-camera characteristics.

This conceptually simple solution for doubling the number of streak-camera channels created some significant technical hurdles. Chief among them was the need to quickly gate the streak tube on and off, for which the tube was not designed. We solved this problem by creating a gating circuit that can be turned on relatively quickly while driving a highly reactive load. After being turned on, the circuit must hold the photocathode bias at a stable tube-open voltage, and the gate must close quickly so the first tier of channels does not write over the second tier. The new gating circuitry successfully accomplishes this. Also, with the streak camera downhole, the sweep circuits must deflect the imaged electrons with very little timing delay. Therefore, we designed the sweep circuit to have an extremely short turn-on delay and to operate in a linear mode a few nanoseconds after being triggered.

Streak multiplexing creates interesting challenges for system characterization, as well. In normal streak-camera applications, the electron beam is initially held off the phosphor window until the sweep velocity reaches a nearly constant value. However, when characterizing the sweep flat field with a multiplexed configuration, we cannot turn on the optical source and allow it to stabilize ahead of the streak sweep. If the optical source is on during the sweep start-up phase, photoelectrons pile up at one point on the phosphor screen, causing the streak image to bloom intensely at zero time. This causes serious loss of flat-field information in that region of the sweep. We solved this problem by creating two high-quality optical Heaviside-function (step-function) inputs. One source quickly turns on a laser diode. The second source, which uses a long-lifetime phosphor pumped with a short-pulse N_2 laser, allows us to make *in situ* flat-field calibrations as well as calibrations of many downhole streak-camera experiments. The first source is used primarily as a timing mark generator, while the second is used as a system flat-field calibration source.

In FY88, we also extended the usefulness of our streak tube by successfully operating it far beyond its original design voltages in the extraction mode. In extraction mode operation, a very large extraction field is created at the output surface of the photocathode. This field quickly accelerates the photoelectron packet, minimizing transit-time spread [Eq. (2)] and space charge effects. The streak tube has a demonstrated temporal response of 10 ps over the lower signal intensities and a temporal response no worse than about 30 ps over a signal range of about 1000. Previous large-format streak cameras had a temporal response of 90 ps at best. This markedly improved temporal response has no significant deleterious effect on other important system characteristics—e.g., there is no significant degradation in spatial resolution.

Some of our new characterization facilities were brought to bear on the problem of understanding the multichannel performance of these new extraction-mode streak cameras. A new capability in the Prompt Diagnostics photonics lab is the mode-locked yttrium-aluminum-garnet (YAG) laser characterization facility (Fig. 4). The 1.06-μm YAG output is frequency doubled and used to synchronously pump the dye laser. This dye laser output consists of a mode-locked train of pulses at about 600 nm, 5–10 ps FWHM separated by 12 ns. We also added a 1.06-μm pulse compressor (not shown in Fig. 4); with this element in the system, the dye laser pulse width can be as short as 500 fs. The pulse train is passed through an etalon to create an exponentially decaying series of pulses, typically covering a factor of 1000 or

greater in dynamic range and temporally spaced a known amount. The beam is symmetrically expanded and collapsed to a line focus with a cylindrical lens. This line focus is manipulated onto a mask affixed to the streak-camera photocathode. The mask, which has precisely defined openings, simulates a string of evenly spaced optical inputs that would be optical fibers in typical applications. Figure 5 shows the data density we achieve with this system. In each single shot, we have information about the temporal impulse response, the dynamic range, and the spatial resolution of the camera. We collected the data in Fig. 5 with the new zero-temporal-magnification streak camera developed by EG&G (Pleasanton, Calif.).

We further exercised our characterization facilities by comparing the NTES extraction mode tube with the EG&G camera. The new EG&G tube appears to have temporal response characteristics that are as good as those of our tube with slightly better dynamic range; however, the spatial resolution is somewhat reduced. Figure 6 shows a temporal profile of one input channel from the EG&G tube, using data similar to those shown in Fig. 5. The data for Figs. 5 and 6 were taken with the system shown in Fig. 4.

We also measured the electromagnetic interference characteristics of downhole streak cameras, in agreement with computer modeling predictions.[8]

Current Agenda

In FY89, we plan to improve our streak-camera diagnostic systems. A project is under way to further characterize this new generation of streak cameras. We are experimenting with a low-noise image-reducing tube that may be used to couple a streak tube to a CCD camera. We also are

Figure 4.
Multichannel streak-camera characterization system.

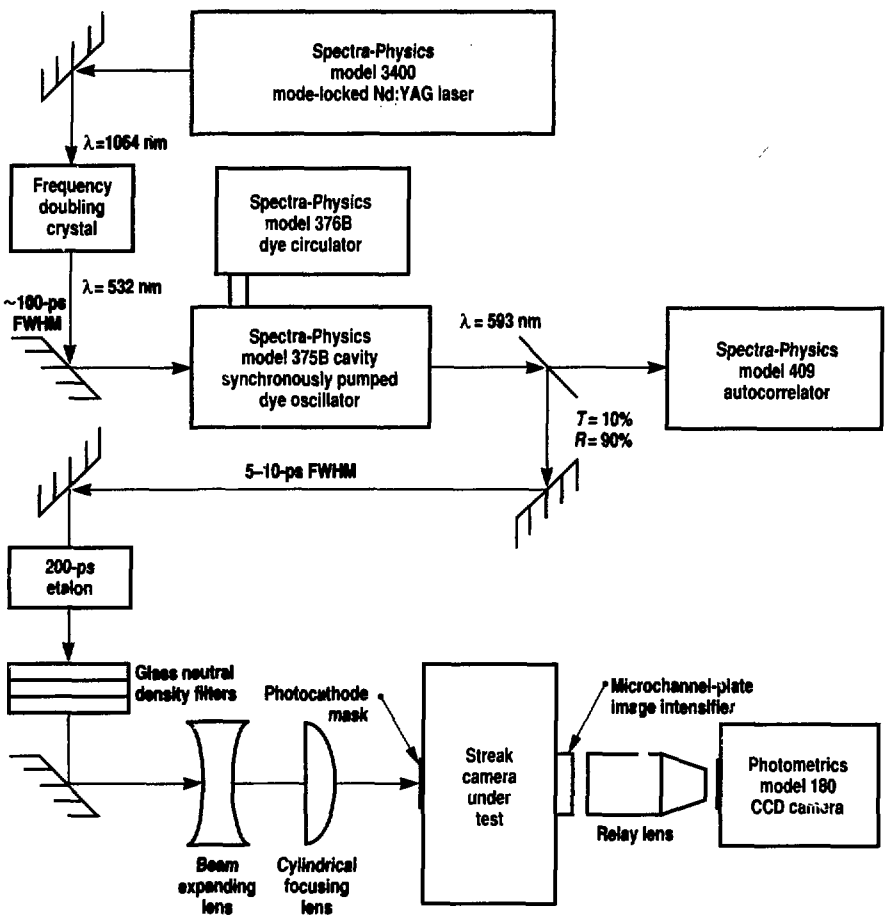

developing an advanced time-based generator and new data analysis techniques, and we are evaluating a new streak tube design.

References:

1. I. P. Csorba, *Image Tubes* (Howard W. Samms Co., Indianapolis, Ind., 1985).
2. M. Lowry and B. Jacoby, "Ultra-High Speed Single-Shot Electronic Imaging," *Proc. SPIE*, Critical Reviews of Technology: Electronic Imaging (January 1989).
3. E. Frerking, "Nuclear Test Image Processing," this publication, p. 102.
4. M. Lowry, "Optical Guided-Wave Devices for Single-Transient Instrumentation," this publication, p. 75.
5. National Laboratories' Photonics Workshop, Berkeley, Calif., hosted by L Division, NTES, Lawrence Livermore National Laboratory, Livermore, Calif., (June 1988).
6. M. Lowry, G. Lancaster, R. T. Peterson, B. Kidd, D. Nelson, and F. Roeske, "Analog High Bandwidth Single-Shot Data Link Using Integrated-Optical Modulators and a High Fidelity Optical Streak Camera," *Proc. SPIE* **987**, 68 (1988).
7. J. Ranchetto, "Optical Streak Camera and its Test Program Applications," this publication, p. 39.
8. M. Bower, "Electron Optics Modeling of Radiation-Induced Voltage Fluctuations on Streak Cameras," this publication, p. 54.

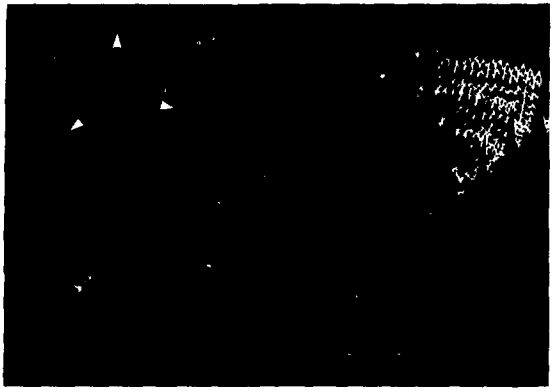

Figure 5. Multichannel streak-camera data from the system shown in Fig. 4.

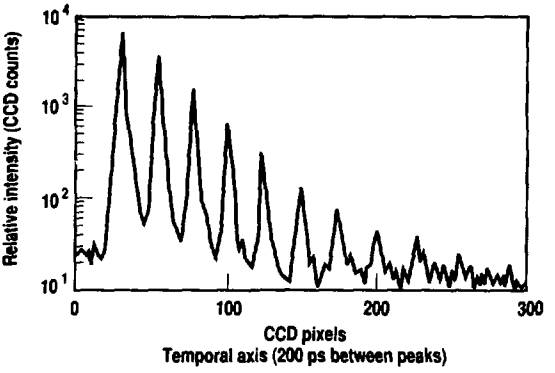

Figure 6. Temporal profile of one input channel using data similar to those shown in Fig. 5.

Streak-Camera Data Interpretation

B. A. Jacoby

In our current x-ray imaging experiments with streak cameras, optical mixers are used between a uniform linear imaging detector and a fiber array that is intended to sample the detector output in a nonuniform manner. Mixers are optical elements that consist of 30–100 rectangular slivers of glass, with varying widths, stacked together in a row. Each sliver takes light from a detector incident on one end, propagates that light down its length, and homogenizes it over the area at the other end where it enters one or more fibers. For a uniformly illuminated detector, the fibers transmit different light intensity because the mixers have a varying size in the imaging direction and, therefore, sample varying areas of the detector. We put the best resolution, the most fibers, and the smallest mixer elements in the center of the streak camera. We put the fewest fibers and the largest mixer elements at the edges of the field of view. Because we place a premium on the streak-camera

photocathode area, the technique of varying mixer-element size is important, as is the ability to separate and define signals coming from individual fibers.

We determined two problems in defining the light intensity from each fiber. The first was that the charge-coupled device (CCD) camera used to image the streak camera output imposes digitation on the data. This camera uses a CCD chip with 380 pixels in the spatial direction and 122 pixels in the temporal direction. We needed to distinguish the streak record for each fiber in the spatial direction. Currently, the fibers have a core/clad diameter of 200/240 µm. The downhole streak camera/CCD systems give only 2.5 samples over the core diameter of each fiber, which is adequate to avoid aliasing[1] but makes it difficult to follow a signal that varies greatly in intensity from fiber to fiber. We needed to find a means to overcome this digitization and to return as closely as possible to the initial analog signal seen by the CCD camera.

The second problem was that we had to eliminate the cross talk between adjacent sweeps on the output phosphor of the streak tube. The streak-camera system's relatively poor spatial-frequency response combined with the small distance between each fiber is the cause of this smearing. At the photocathode of the streak camera, the fibers lie side by side with only 40 µm separating each fiber from its neighbor. In one attempt[2] to calculate the spot size or spatial-impulse response of the streak-camera system, we found that the streak width for a point input was about 140 µm. Thus, the 40 µm that separated each fiber was not sufficient to prevent light from neighboring fibers from affecting and adding to the light produced and measured by an individual fiber. In our experiments, we learned to quantify and eliminate this cross talk and to isolate the signal from each single fiber.

Digitization

Figure 1 shows six square-wave inputs that simulate the light distribution from six optical fibers onto the photocathode. Superimposed is the spatial variation in intensity at the phosphor in which the sharp input has been smeared by the camera's spatial frequency response. The effect of digitization caused by the finite sampling pixels of the CCD imaging camera is shown in Fig. 2. Our challenge was to return to the analog signal shown in Fig. 1 before the digitization took place in order to identify the individual fibers and their peak signals. We used a technique outlined for the construction of a two-dimensional image:[3] an interpolating function, which turned out to be a sine function. We found the value of a point $I(x)$ at a position x by performing the following:

$$I(x) = \sum_{i=1}^{n} I_s(i\Delta) \times \sin\{\pi(x - i\Delta)/\Delta\}/\{\pi(x - i\Delta)/\Delta\}, \quad (1)$$

where $I_s(i\Delta)$ was the sampled data for the ith point, n was the number of samples, and Δ was the sample step size. In Fig. 3, we show the result of using this algorithm on the mock data in Fig. 2. We also show the original, presampled streak-system data in the Fig. 3 graph where the two curves overlay quite well.

Cross Talk

The plot in Fig. 4 illustrates the cross-talk problem. This plot shows measured light intensities from a calibration array made from polymicro fibers that have a 200/240-µm core/clad ratio. The array consists of a rectangular block of fibers bunched together on one end (not coherently arranged) and laid side by side on the streak-camera end. We used the labsphere as the source light to illuminate the rectangular end. Because of the random nature of the fibers at the rectangular end, individual random fibers could be illuminated by masking a portion of that array with tape. We took one streak using this masked array and arbitrarily selected row 60 of the recorded streak image for analysis, which produced the bottom set of individual and clumped

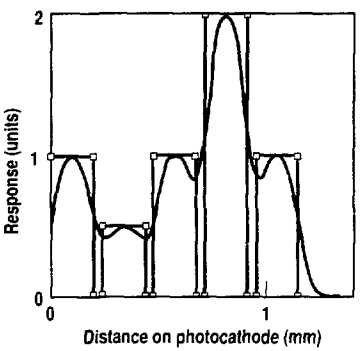

Figure 1. A square-wave input simulating optical-fiber signals shown with the streak-system response. Response effect is to smear signals.

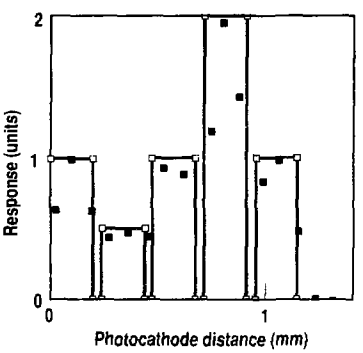

Figure 2. An event showing the effect of a digitized signal on the analog signal. In this example, the return to the square-wave analog signal was easily achieved.

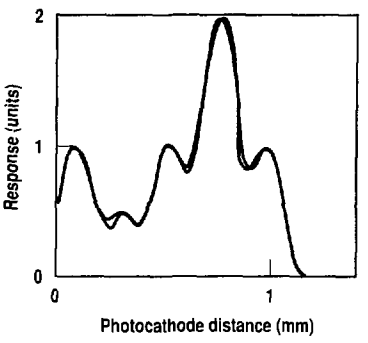

Figure 3. Results of reconstructed data using Eq. 1 on the mock data in Fig. 2 along with the original, presampled, streak-system data. The two curves overlay quite well.

fiber signals. We then took one streak with the array unmasked and again selected row 60 from the resulting image, which produced the top curve in the Fig. 4 plot. The labsphere produced light that was within 4% for the two shots. Without cross talk, the peaks of the masked-array data should have matched the level of the unmasked data. However, they did not, except for the peak from the clump of fibers around the pixel value of 200. We sent the same amount of light into both arrays. However, the number of signal counts was lower in the fibers that we taped and isolated. Without correction, one would deduce that the amount of light sent into the masked fiber array was lower when actually it was the same as that for the unmasked array.

We used the following equation to correct the problem, assuming that a fixed percentage of the peak signal would spill over to adjacent fibers:

$$I(n) = I_0(n) - pI(n-1) - pI(n+1) . \quad (2)$$

In this equation, $I(n)$ is the actual peak light out of the nth fiber into the streak system before it is contaminated by its neighbors, $I_0(n)$ is the peak signal recorded by the streak system with the additional light, and p is the fraction of the peak signal that spills over to the adjacent fiber. When we iterate Eq. (2), the results converge to the contaminated signal.

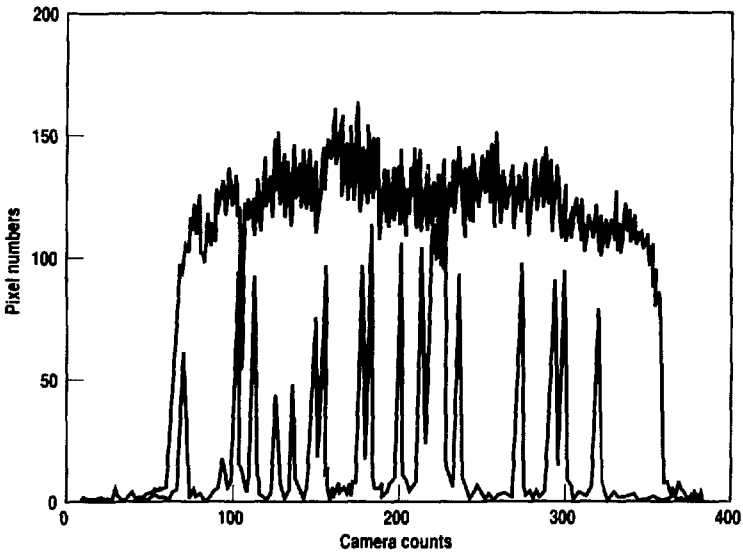

Figure 4. Calibration arrays from polymicro fibers that have a 200/240-μm core/clad ratio. Array consists of a rectangular block of fibers bunched together on one end and laid side by side on the streak-camera end. Figure shows results of streaks taken of both masked and unmasked arrays.

Conclusions

We corrected the data from our current fiber-optic streak systems by first running it through Eq. (1) to produce clearly discernable peak-intensity values for individual fibers. We then took the resulting peak fiber signals and corrected them for cross talk, using Eq. (2). The value for p had been previously determined from calibration data. We completed these experiments by using an array of some 50–70 fibers placed next to one another on the streak-camera end and separated by 0.1 cm from each other on the rectangular end. In addition, we used a mask that blocked out every other fiber or every two fibers. The masking created additional distance between fibers conducting light and made it possible to isolate the signal recorded by the streak-camera system for an individual fiber and to produce a peak value of that signal, uncontaminated by signals from adjacent fibers. We determined the appropriate values of p for the streak camera by using this array and mask.

References:

1. A. V. Oppenheim and R. W. Schafer, *Digital Signal Processing* (Prentice-Hall, Inc., New York, 1985), p. 28.
2. B. A. Jacoby, "Streak Camera Data Interpretation," Lawrence Livermore National Laboratory, Livermore, Calif., XRS-88-48 (1988).
3. B. A. Jacoby, "Reconstruction of the Analog Image from Its Sampled Image," Lawrence Livermore National Laboratory, Livermore, Calif., COL-81-63 (1981).

Kernville Spectrometers: IBEX, VJACS, EODIX, and XPOLY

D. Clark, R. Heinle, R. Stewart, D. Price, P. Springer, and G. Shimkaveg

During FY88, we conducted several programmatically important x-ray spectroscopic measurements at NTS. Spectrometers on the Kernville Event returned almost overwhelming amounts of high-resolution data. These data give us a better understanding of the ionization processes and atomic kinetics of systems of interest to the test program. The four instruments discussed here are second-generation spectrometers whose performances were enhanced by significant evolutionary improvements in design.

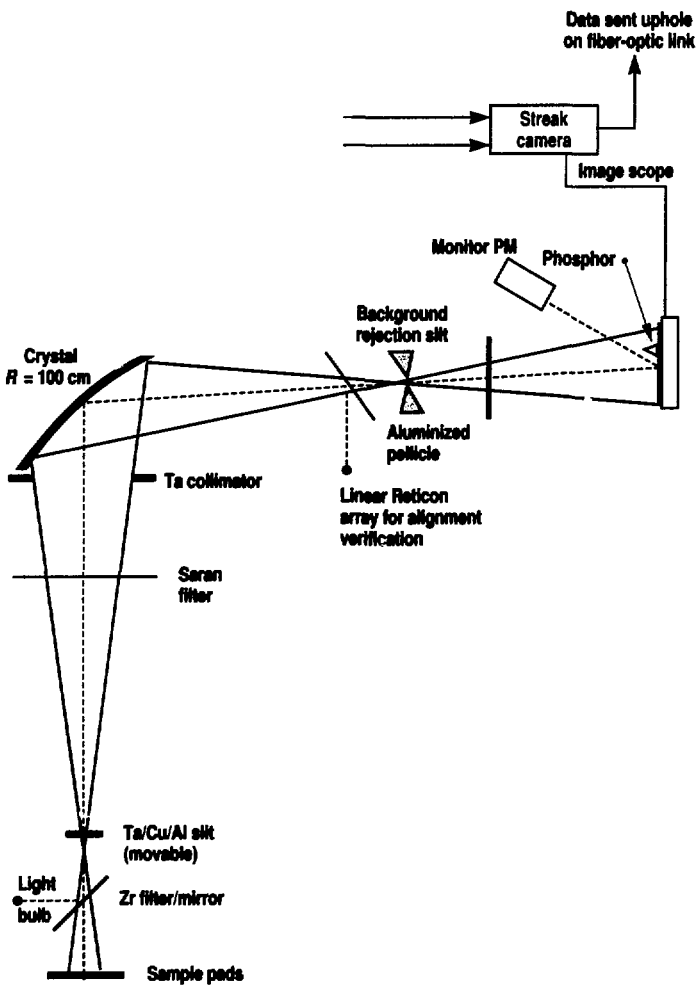

Figure 1. Schematic drawing of the IBEX spectrometer.

Each crystal x-ray spectrometer was designed to cover one part of a spectral region with different energy resolution. These spectrometers operate according to the same general principle. Background ultraviolet (UV) excitation is avoided on the spectrometers by two UV filters located before the phosphor. X rays diffracted by the crystal strike a WL1198 phosphor (CdS:In), which emits green light (520 nm) when excited. Light at this frequency is easily transmitted through fiber optics. The light from the phosphor carries the x-ray spectral data as a linear image of varying intensity. The light is optically coupled to a coherent array of fiber optics. The fiber-optic array "pipes" the light to the photocathode of one or more streak cameras, where the time-dependent (and energy-dispersed) x-ray spectral data are recorded using standard streak-camera technology. The signal from the streak camera is recorded on a solid-state camera, and the picture is digitized and transmitted to the recording station.

IBEX

The IBEX spectrometer (Fig. 1), fielded for the second time on the Kernville Event, was designed to look at a moderate intensity of multikilovolt x rays with 3-eV resolution over a 2000-eV range. IBEX achieved a resolving power of about 10^4 by using a spherically curved crystal in the x-ray line of sight (LOS). The spherical geometry gives focusing in the direction normal to the dispersion of the crystal, concentrating the desired x rays through a collimator and, thus, increasing the signal about three orders of

magnitude over the background scattered signal from the crystal. This geometry also allows focusing in one direction by using the astigmatism present in spherical optics to separate the tangential (energy-dispersing direction) focus from the sagittal (intensity-direction) focus. The crystal (5 × 10 cm and 0.025 cm thick) was shaped by being pressed between precise convex and concave mold halves that were formed by optical grinding technology. It was then glued to the concave mold as a substrate to maintain its final shape. The crystal figure was maintained to a precision of four fringes of sodium light per inch, or about 10-μm variation over the entire crystal surface.

Installed alignment of the spectrometer was verified by substituting a light source for the x-ray source and observing where the optical pattern focused. (The optical pattern mirrors the x-ray signal when the crystal surface and the correct crystal plane are aligned.) This optical signal is reflected out of the spectrometer by an Al-coated pellicle mounted at 45 degrees behind the crystal but before the two UV filters. The spectrometer-focused optical image strikes a one-dimensional Reticon detector array (1 × 1024 elements) that allows verification of the location of the spectrometer focus after the stemming process has distorted the spectrometer's LOS. With this downhole optical verification, the calibration of the spectrometer can be adjusted to account for alignment changes after stemming downhole.

The energy calibration and resolution of the IBEX spectrometer was verified using an intense x-ray source emitting characteristic monoenergetic "lines" from several x-ray cathodes. We verified these calibrations in the field by placing the x-ray machine at the bottom of the LOS and taking long exposures using film at the detector plane in lieu of the phosphor. By indexing the film to the phosphor, the exact location of each x-ray line could be transferred to a corresponding point on the phosphor and, hence, to its streak-camera signal location.

VJACS

The VJACS spectrometer (Fig. 2) was fielded for the first time on Kernville. Based on a successful prototype spectrometer (MCPOD) that incorporated many of the same principles, VJACS

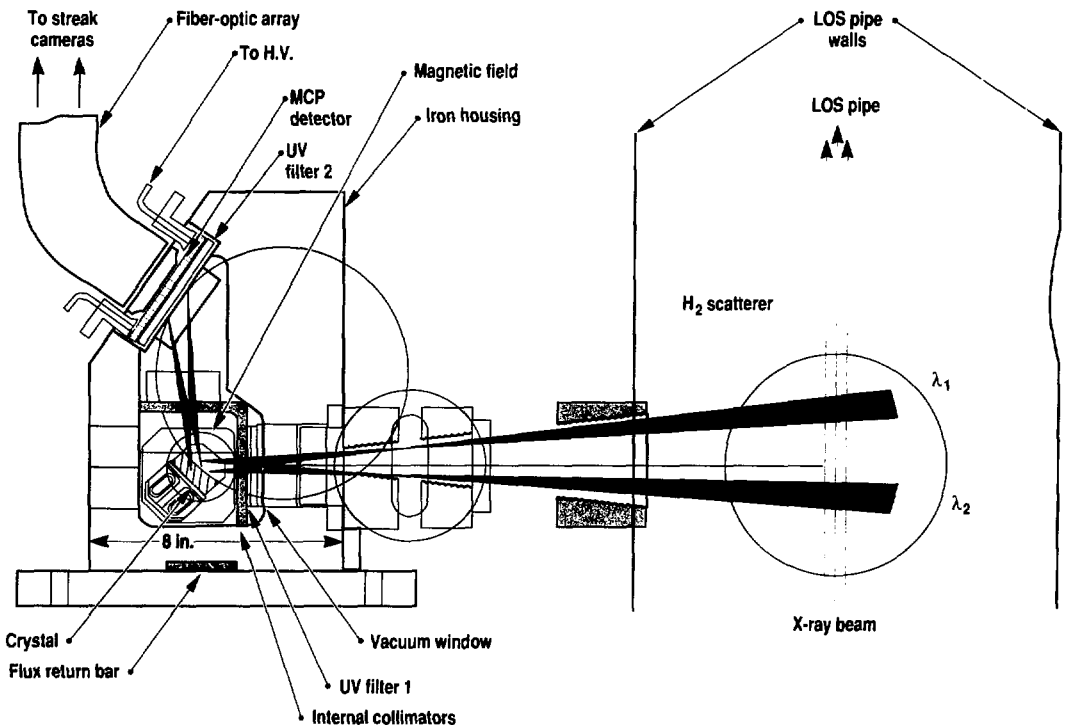

Figure 2. Side view of a VJACS spectrometer, showing the relationships among hydrogen-scattering volume, crystal, active detectors, and fiber optics.

was designed to measure the spectral content of several bright sources. For Kernville, each VJACS spectrometer was designed to analyze two sources using a single crystal.

The VJACS spectrometer design places the diffraction crystal outside the LOS. X rays are scattered from hydrogen gas in the LOS onto the crystal. VJACS is a Johann-geometry spectrometer using a cylindrically curved crystal (5 × 10 cm) that "views" the scattering volume of hydrogen gas. Collimators in front of the crystal confine the scattered x rays to the center of the crystal. Keeping the crystal out of the direct x-ray flux in the LOS avoids crystal heating due to excessive irradiation, which can change (during the measurement) the crystal layer spacing and, hence, the crystal diffraction properties. Hydrogen is an ideal scatterer because it emits no secondary radiation in the x-ray region of interest. The effective energy resolution of the VJACS is about 2.0 eV, its total energy coverage is about 110 eV, and its resolving power is about 640.

Unlike the other spectrometers, x rays Bragg-reflected off the VJACS spectrometer crystal strike an active detector that amplifies the x-ray signal.[1] The detector uses a 40-mm microchannel plate (MCP) coated with four 3-mm-wide strips of a layered Cu, Au, and CsI photocathode. These strips run along the energy-dispersive direction of the spectrometer. X rays incident on the photocathode release electrons that are accelerated into the pores of the MCP. Detector gain is realized as secondary electrons are released from the walls of the microchannels. This gain can be varied to meet different signal-strength requirements by varying the bias across the MCP. Electrons exiting the back of the MCP are electrostatically focused in the nondispersive direction of the detector and are accelerated to a higher energy. This energetic, concentrated electron beam, carrying x-ray spectral information in its spatial intensity profile, is then directed onto a phosphor. The subsequent light is transported by fiber array for streak-camera recording. Energy calibration of the VJACS spectrometer was performed in the laboratory and the field by putting an x-ray source in the hydrogen-scattering location and verifying where the location of each x-ray line corresponded to the streak-camera signal.

Figure 3. Isometric view of the EODIX spectrometer, showing the Be scatterer in the line of sight and the crystal looking at low-intensity scattered signals.

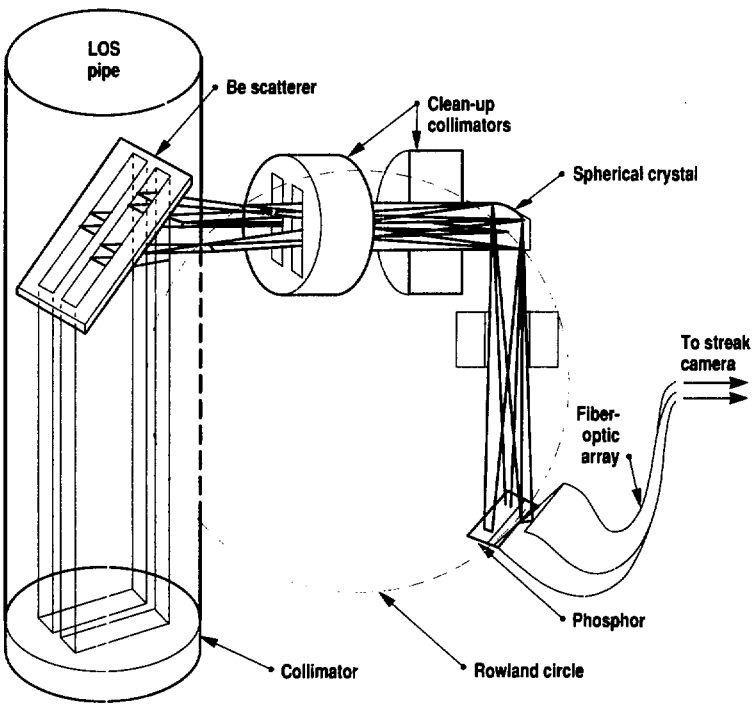

EODIX

The EODIX spectrometer (Fig. 3) is a prototype spectrometer first used on Kernville to measure sources in high resolution. The EODIX spectrometer uses a spherically bent crystal (2 × 2 cm), mounted on the Rowland circle, to obtain a total energy coverage of about 160 eV and a resolution of about 1.5 eV. A Be scatterer located in the LOS coherently scatters x rays into the spectrometer. As it does for VJACS, keeping the crystal out of the direct x-ray flux in the LOS avoids crystal heating due to excessive irradiation and subsequent change in the two-dimensional spacing of the crystal. Energy calibration was performed in the laboratory and the field by putting an x-ray source at the bottom of the LOS and verifying where the location of selected x-ray lines corresponded to the location of streak-camera signals.

XPOLY

The XPOLY spectrometer (Fig. 4) is a second-generation spectrometer modified for even higher resolution. Designed to record the time history of a single line, it uses a doubly curved crystal (5 × 10 cm) in toroidal (modified unfocused Von Hamos) geometry, with a crystal mounted in the

LOS. Two nearly identical spectrometer channels were built in the same housing, each with slightly different coverage and directed toward different sources. Instead of using a substrate, the doubly bent, free-standing crystals were shaped by a special crystal-holding fixture that "torqued" the crystal into the requisite shape. The total energy coverage of this spectrometer is very small, only 30–35 eV. A special slit, located 15 m below the instrument, serves as the defining aperture for the instrument's field of view. In the XPOLY spectrometer, x rays are focused sagittally through background rejection slits and are allowed to diverge slightly before the x rays hit the WL1198 phosphor.

To verify downhole alignment and recalibrate the instrument, we used an optical alignment system much like that used on IBEX. However, because of the narrow energy coverage of the XPOLY spectrometer, the crystal mount was designed to remotely rock the dispersing crystal's Bragg angle to allow downhole recalibration of the spectrometer after canister bending. This recalibration allowed the instrument to maintain its correct energy coverage. In addition, because the field of view of the crystal as projected to the source is so critical, we designed the slit so it can be adjusted downhole—that is, the slit can be repositioned after the canister is stemmed downhole. For source-intensity adjustment and UV background rejection, an additional filter was required above the slit that was opaque to visible light; hence, we remotely inserted this filter in the LOS after the optical alignment was complete. Energy calibration of XPOLY was performed in the laboratory and the field by putting an x-ray source at the bottom of the LOS and verifying where the location of a selected x-ray line corresponded to the location of a streak-camera signal.

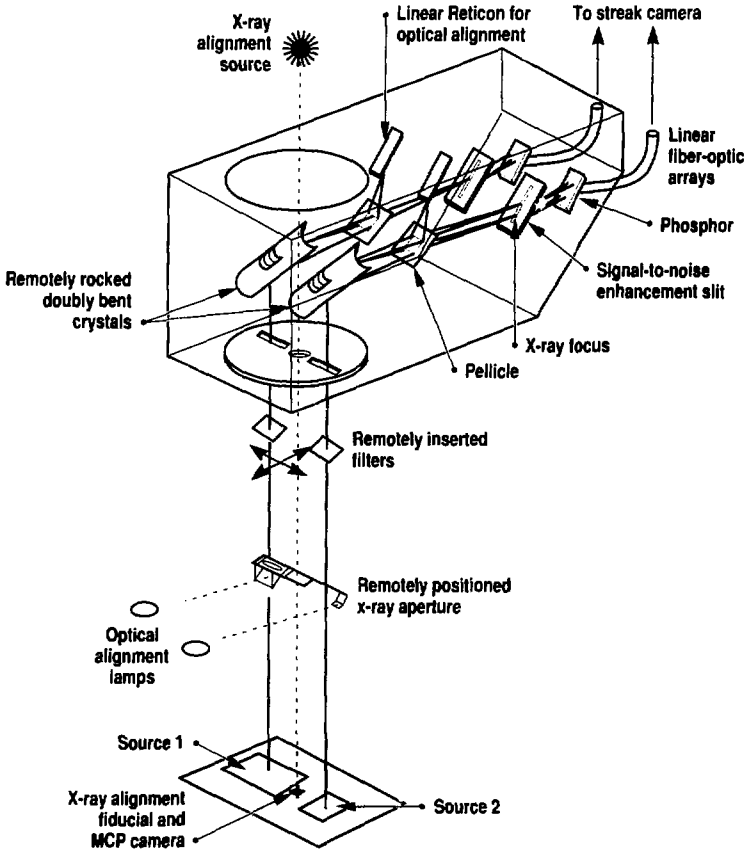

Figure 4. Isometric schematic of the XPOLY spectrometer, showing dual spectrometers looking at different sources through different slits.

Reference:

1. R. E. Stewart, M. R. Carter, and D. F. Price, *Time-Resolving Intensified Detectors for Low-Level X-Ray Detection*, this publication, p. 60.

Electron Optics Modeling of Radiation-Induced Voltage Fluctuations on Streak Cameras

M. W. Bowers

On the Kernville Event at NTS, four streak cameras used for the IBEX experiment were affected by electromagnetic radiation. A streak camera incorporates a photocathode to emit electrons when excited by light; electrodes that accelerate, focus, and sweep the electrons; and an output phosphor to convert the electron energy back to light. The output from a streak camera has a spatial line that is swept in time to produce an image of a fast, transient event. On the Kernville Event, radiation produced an electric field near the photocathodes of the four streak cameras, which distorted the sweep trace. Normal streaks would have been straight and uniform, as shown in Fig. 1(a). However, on photographs from the Kernville Event, the streaks were distorted in the spatial direction, as shown in Fig. 1(b), with the distortion becoming worse as the camera moved farther from the center of the tube. When we inspected the temporal comb—a fast light marker used for timing on streak cameras—we found that the timing of the sweep had been distorted as well. Spatially multiplexed cameras have produced streaks that deviate in the spatial direction as the photocathode potential was gated off; therefore, we believed a transient variation in the photocathode potential may have caused a similar variation in the sweeps obtained on the Kernville Event. To obtain reliable data for this event, we needed to straighten the bends and correct for temporal deviations.

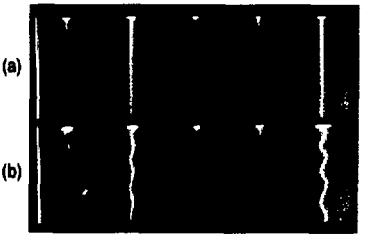

Figure 1. *(a)* Normal streaks and (b) distorted streaks.

Theoretical Modeling

To understand the electrical characteristics of the streak tube, we used an electromagnetic modeling code called EBQ. The streak tube was modeled in its normal operating condition to test the validity of the code. Then voltage on the photocathode and other electrodes in the tube were varied to determine how they affect electron trajectories.

To find the type of voltage variation that occurred on the Kernville Event, we simulated the spatial deviation that appeared on the streaks. This variation was measured as a function of distance from the center of the tube, which ranged from 0 mm at the center to 7 mm at the edges. A current deviation on the photocathode of +25 V out of 15,000 V caused a spatial deviation of 2.5 mm on the streak tube phosphor, 15 mm off-center. Figure 2 shows an electron trajectory model of a tube with a 25-V variation on the photocathode of the streak tube. The model shows a 180-degree phase shift on each side of the center of the tube. The deviation from normal operation varied linearly from the center of the tube toward its edges. Therefore, a sinusoidally varying voltage of ±25 V at a frequency of about 100 MHz produced the same spatial deviations that appeared on the streaks obtained for the Kernville Event.

Having determined the voltage variation on the photocathode of the streak tubes, we modeled the temporal fluctuations in the sweep speed. We again used a 25-V variation on the photocathode voltage, with electrons exiting from several positions on the surface. We positioned the gating grid slit—a small aperture in the first electrode of the streak camera—off-center to simulate the configuration of the spatially multiplexed camera. As shown in Fig. 3, the voltage on the electron trajectories varies in the

temporal direction. When this deviation is swept, a temporal deviation becomes apparent. More electron modeling showed that the temporal deviations in the electron path were dependent not only on the variation in voltage but also on the position of the electrons in relation to the gating electrode slit and the slit position in the tube. Figure 3 shows the electron paths when the gating grid slit is above the center of the tube axis. The upper electrons are deflected higher with a 25-V potential drift than with the normal photocathode voltage. The lower electrons are deflected downward. When they are swept, the upper electrons appear to slow down as the voltage is increased, while the lower electrons speed up. At a point between the lower edge of the slit and the center of the slit, the electrons do not deviate with these fluctuations in the voltage. If the slit were positioned on the lower side of the camera, the reverse would be true—the lower electrons would slow down and the upper electrons would speed up. Therefore, to deduce the proper timing for each channel, we must know where all channels are input to the streak camera. Also, we cannot determine the correct timing information only from the spatial deviations or from the fluctuations in voltage on the photocathode.

Experimental Verification

Four streak cameras were used on the Kernville Event: one Kentech camera and three LLNL-designed cameras, two containing RCA tubes and the third an ITT tube. We performed laboratory tests on these cameras to verify the spatial and temporal variations observed on field data and predicted by the electron modeling code. The photocathode voltage was varied by capacitively coupling a radiofrequency (rf) or pulse signal to the photocathode.

Capacitive coupling to the photocathode was achieved by using a 2-in.-diam copper plate terminated in 50 Ω and placed 1.5 in. from the photocathode. A Delrin spacer, inserted between the plate and the photocathode, held the fiber-optic inputs and prevented high-voltage breakdown. The capacitance between the plate and the photocathode was approximately 3 pF. A grid dipmeter was used to determine any resonance conditions for the four cameras. Figure 4 shows some results from this experimental procedure.

Streaks produced with the ITT tube, which had a spatial multiplexing gating board, showed a strong resonance at about 77 MHz. Streaks from the other tubes showed no strong resonances. Data from all four camera tubes showed spatial and temporal deviations that matched well with the theory. Each camera tube had a different coupling coefficient and, therefore, a different amplitude of spatial and temporal deviations. The RCA tube with the special

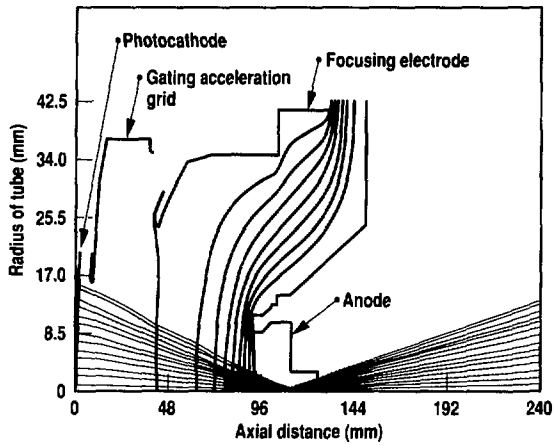

Figure 2. Internal structure of a typical streak camera that incorporates a gating grid structure. The operating voltages are photocathode, −15 kV; gating grid, −14.854 kV; focusing electrode, −13.310 kV; and anode, 0 V. The cross section is shown in the spatial direction of the tube. Vertical lines are equipotential lines. Solid horizontal lines are electron trajectories with a photocathode voltage of −15 kV; dashed lines are trajectories with a photocathode voltage of −14.975 kV.

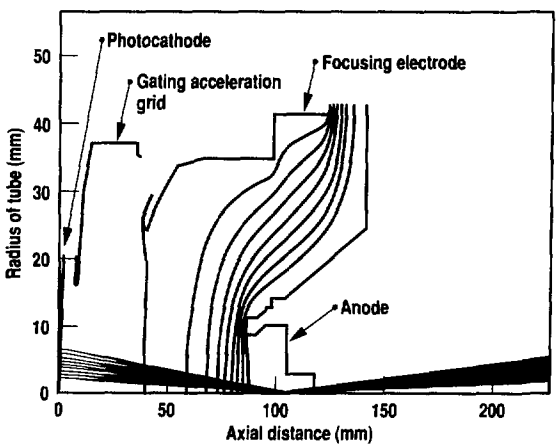

Figure 3. Internal structure of a typical streak camera where the temporal slit is off-axis. The deviation of the electron orbits is nonsymmetric about the center of the slit in the gating grid.

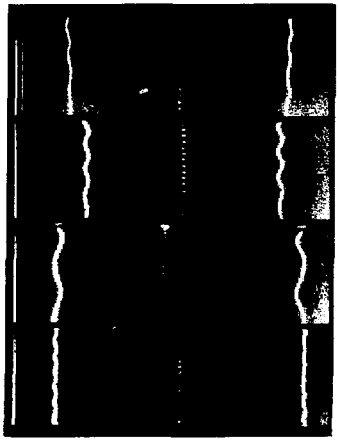

Figure 4. Streak distortions resulting from external voltage modulation. (a) ITT tube, 50-V peak, 100-MHz voltage modulation; (b) Kentech tube, 50-V peak, 120-MHz voltage modulation; (c) RCA tube, 32-V peak, 63-MHz voltage modulation; (d) RCA tube, 48-V peak, 100-MHz voltage modulation. All sweeps are 30 ns, shown in the vertical direction.

gating board for spatial multiplexing had the largest coupling coefficient; therefore, its spatial variation had the largest amplitude. All of the tubes were frequency sensitive in their coupling coefficients.

Pulsed input induced ringing at a fixed rate for each cameras. The ringing period and duration did not seem to be a function of the input pulse duration. They remained nearly constant on all cameras for about 7–8 ns, regardless of the input pulse amplitude or duration.

The streak camera incorporating the spatial multiplexing gating board exhibited several other problems that were not seen on records from the Kernville Event, nor could they be modeled with the electron trajectory code. A sweep speed deviation of a factor of 2, sweep start time variations, and an inhibited sweep trigger all occurred over certain rf ranges and amplitudes. We determined that trigger grounds picked up the rf signal, thus causing the sweeps to trigger improperly. By shortening the trigger leads and looping them through ferrite beads, we eliminated these irregularities. The other tubes tested were not affected by this problem.

Solution

Although we do not know how radiation entered the streak camera module, we believe it caused the distortions on the four streak cameras used in the IBEX experiment on the Kernville Event. To obtain reliable data from these images, we needed to straighten the bends and correct for temporal deviations. The electron modeling showed that the spatial direction could be fixed with a linear rescaling for each horizontal scan line. The temporal deviations were not linear, nor were they the same for each input channel. In addition, we lost many of the reference points from the timing comb off the edge of the picture. Therefore, accurate timing could not be made for these images.

On future events, the comb markers will be moved away from the edges to reduce the risk of losing them. If we can keep both left and right comb signals, a linear timing algorithm between the two could restore the correct timing information, assuming the array location is accurately known in reference to the slit on the gating electrode.

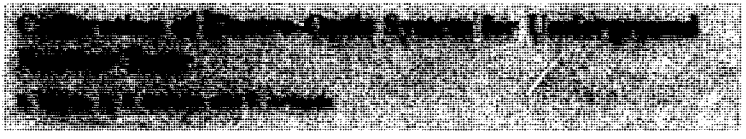

Nuclear Test Program experimenters use x-ray detector-spectrometer systems in underground tests to measure time- and energy-resolved x-ray fluxes. Calibrating such a system is a multistep process because, between the x-ray detector and the system output (at the charge-coupled device, or CCD, camera), the system may include three photocathodes, two microchannel plates, three phosphors, three electronic imagers, six fiber-optic faceplates, six optical interfaces, a set of optical mixers, a coherent linear fiber-optic array, a fiber-optic reducer, and a CCD imager—all in a single series path! We characterize each discrete element of this system individually, then characterize appropriate subsystems.

The precision and accuracy of any measurement or diagnostic device can be ascertained only after individual components and the overall system are checked, characterized, and calibrated against standard measurements. Because NTES

increasingly relies on fiber optics for transmitting data signals from detectors to electronic analysis equipment, we are developing new instrumentation and optical techniques to calibrate complex and precise fiber-optic systems. Here we report on calibration techniques developed for upcoming events.

Calibration Traceability

In the last ten years, we have increasingly used fiber-optic arrays to transmit data signals from radiation detectors to sophisticated electro-optical devices such as electronic streak cameras, spectrophotometers, and silicon detectors, all of which are calibrated by radiometric and photometric measurements. Only if each component calibration is traceable to primary standards can we assume that the data gathered during an experiment or nuclear test accurately represent physical phenomena. Our group is responsible for calibrating electro-optic equipment efficiently and economically, with demonstrated traceability to primary standards.

The foundation of a traceable measurement is a simple quantity measured at the National Institute of Standards and Technology (NIST, formerly the National Bureau of Standards) or at DOE's primary standards facility at Sandia National Laboratory, Albuquerque. The Opto-electronic Calibration Facility (OCF) at LLNL serves as a secondary standards laboratory and can calibrate measurement devices with traceability to NIST or Sandia. OCF devices can, in turn, be used to calibrate other devices or systems. Establishing OCF as a single point of secondary standards has provided better coordination of measurement and calibration between LLNL and our subcontractor, EG&G, and has assured traceability for calibration devices.

For example, for the Contact Event, OCF calibrated a Carey 2390 dual-beam spectrophotometer for wavelength and transmittance measurements with NIST-calibrated bandpass, neutral density, and holmium-oxide glass filters. The instrument measured the set of NIST primary standards several times, and statistically compared OCF and NIST measurements for transmission or wavelength accuracies and for the repeatability of OCF measurements. These comparisons are performed periodically to ensure proper instrument operation. It is then possible to use the Carey 2390 to calibrate other bandpass or neutral-density filters, provided the filters are used consistently with respect to temperature, spectral band shape or size, beam size, and beam collimation.

Through this chain of comparisons, we calibrated new diagnostic systems for the Contact Event, which will have six separate experiments using 27 fiber bundles (a total of 4852 fibers) for calibration, timing, and data transmission. Although the longest fiber is only 22.8 m, a total of 76.597 m of quartz fiber will be used on this event. The fibers are contained in 123 separate input and output arrays with seven different types of fiber configuration to match the specific experimental requirements. Noncoherent (not in a specific order) fiber bundles with a round configuration will be used for timing, and square-configured fiber bundles will be used for simultaneity measurements. Data will be transmitted between detectors and analysis equipment by coherent fiber arrays of varied spatial arrangements.

Streak Cameras

A major path of data transmission is from radiation detectors to streak cameras. A streak camera has two input arrays, each of which may have 118 abutted fibers in a coherent linear pattern coming from several detector heads. Detector heads have many different fiber configurations including 219 double-row close-packed fibers used for the HYJACS (HYdrogen Johann Active Crystal Spectrometer) spectrometers, and single- and double-row spaced fibers apart from one another. By using fibers in pairs, we can double-sample each location in the detector recording plane and connect separate fibers to low- and high-gain streak cameras, thus extending the dynamic range of the system.

Between the detector and these paired fibers is a mixer made up of square quartz rods with width:length ratio of at least 1:10. This optical device has two functions:

- Define the sampling region at the detector.
- Distribute light coming from any point in this defined region uniformly over the output area sampled by the fiber pair.

We are currently preparing for the Contact Event, which requires 28 fiber-array–mixer assemblies with elements ranging from 0.5–127 mm in length. Some mixer assemblies have 58 elements of three different sizes. To keep the fibers mated to the small elements (0.2-mm core fiber and 0.5-mm mixer elements), mechanical tolerances must be kept within 0.05-mm (nonaccumulating) error on both the fiber array and mixer. The fiber arrays and mixer arrays are located within their housings to 0.05 mm.

We developed instrumentation and techniques to optically calibrate the bundles and mixers. When the bundles arrived, they were given a general inspection followed by specific tests, including measuring the physical length, locating the various detector groups in the streak-camera heads, establishing that the fibers were located in the correct sequence and were all transmitting, measuring the width of the streak-camera array, measuring transmission variation, and making photomicrographs where necessary.

The mixers were mechanically inspected before the following optical measurements were made: numerical aperture of the elements, transmission versus input angle, transmission variation from element to element, spectral transmission, output variation across the output face of a single element, and cross-talk from an element to its neighbors. Photomicrographs were made where necessary to document anomalies.

Figure 1 shows the instrumentation for calibrating the combination of bundle,

mixer, and fiber-optic faceplate. The integrating sphere is a uniform radiator used to simulate a fluor, and the bundle/mixer/faceplate combination is configured as it will be for the experiment. First, the optical radiation coming from the port of the integrating sphere is measured using a calibrated radiometer in $W/cm^2/sr$. Then the fiber-optic components are inserted, and the power out of each fiber is simultaneously measured with a calibrated solid-state-array camera. This allows us to relate measured signal to absolute input intensity.

With accurately known pulsed and steady-state light sources available, the detector system shown in Figure 1 is temporarily disconnected in appropriate places to determine its response. Initially, most components are characterized separately, and then built up section by section and tested for subsystem integrity and response. A final end-to-end check will be done with low-level steady-state x rays used at the detector input. Both the streak camera and the CCD camera will be operated in continuous mode. The CCD image array will integrate its input signal for approximately 5 ms and then transfer the resulting image to a special image processor designed to repetitively sum the digitized image in a summing image plane. The technique is essentially a signal-averaging scheme that can recover a low-level signal buried in noise. The current system, called a Z-box, is an improved version of one used only once before for a similar purpose. It is expected that this approach will further improve the accuracy of the spectrometric measurements.

Silicon Photodetectors

Using a similar chain of comparisons, the OCF uses other NIST secondary standards to calibrate radiometers, photomultiplier tubes, and silicon photodetectors by a substitution method. For example, scanning and filter monochrometers are calibrated with NIST-traceable spectral line sources, neutral density and bandpass filters, and electrometers. The flux per unit wavelength for a particular monochrometer experimental configuration is measured by a silicon photodetector secondary standard and then the silicon photodetector to be calibrated. The current from the device to be calibrated is measured and, because the flux as measured by the standard detector is known, a simple equation gives the spectral response for the instrument under test. When using NIST-supplied radiometers for error analysis of the OCF calibration system, we found errors of 2% or less.

These calibrated devices had several important functions. Calibrated silicon detectors were provided to EG&G for acceptance and characterization testing of all streak cameras, MCPIs (microchannel plate intensifier), fiber-optic reducers, and CCD cameras. A second set of calibrated silicon detectors was provided to LLNL and EG&G Atlas for the calibration and characterization of the optoliner and integration-sphere calibration light sources. These calibration light sources, as previously discussed, have significant impact on the new electro-optic diagnostic systems because of their use in streak-camera, SPAC (SPectroscopy Array Camera), and CCD camera calibrations. Finally, a radiometer and calibrated SPAC camera were used to calibrate coherent fiber-optic bundles and mixers.

We will soon be able to verify our component calibrations by coupling the complete system and performing a single calibration from the x-ray input to digital bit-stream output. This single calibration has been impossible because appropriately strong pulsed x-ray sources were unavailable in the laboratory. We are now testing a special time-integration scheme that should circumvent this problem. The technique requires a light source with a specified spectral bandwidth and an accurately known and controllable output so

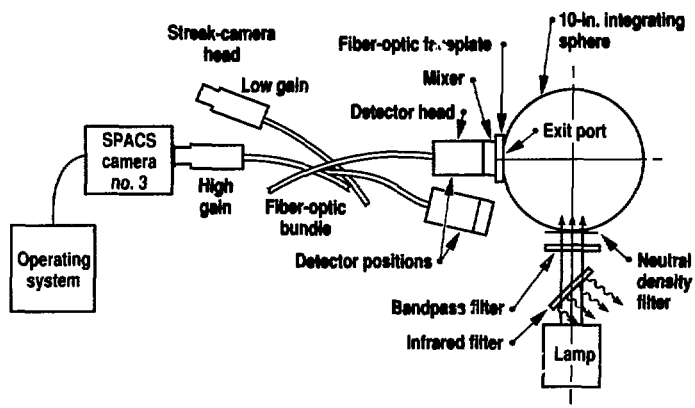

Figure 1. Fiber-optic calibration set up.

that the detector components are calibrated by what is essentially a signal-averaging scheme that can recover a low-level signal buried in noise. Two types of instrument are used.

The first type is a collimated source called an optoliner. A removable hemispherical diffused surface is illuminated either with a shrouded annular-pulsed xenon light source or a series of incandescent lamps spaced in a similar annular shroud. Reflected light from the hemisphere passes through a bandpass filter, one or two neutral density filters, and, if required, a precision transparency slide with an appropriate resolution chart or other image-forming pattern. A flat-field lens assembly collimates the light and forms an image of the slide at a focal plane a short distance beyond the front of the lens barrel assembly. The lens has adjustments for both focus and focal length. The complete unit is designed to have a flat-field illumination coverage within ±1%. Calibration involves placing a silicon photodiode detector with known response in the output image plane of the optoliner with only the bandpass filter in place. (The photodiode calibration traceability is established and maintained by the OCF.) Once the maximum light output of the optoliner is determined, it can be reduced in precise amounts by insertion of OCF-calibrated neutral-density filters.

The second type of light source is an integrating sphere with similarly interchangeable pulsed or steady-state light sources. Because this source is not collimated, only bandpass and neutral density filters are in the path from the light source to the sphere. At the plane of the integrating sphere exit port, light exits uniformly throughout virtually the complete 2π solid angle. This instrument is calibrated in a similar fashion, except that a collimated field radiometer (also calibrated by OCF) measures the light flux at the sphere exit port.

In summary, our efforts to streamline the calibration of an electro-optic system are making it more efficient and economical to produce reliable data from underground nuclear tests.

Time-Resolving Intensified Detectors for Low-Level X-Ray Detection

R. E. Stewart, M. W. Bowers, M. R. Carter, and D. F. Price

In recent years, increasing sophistication of high-density plasma experiments at NTS required the development of new low-energy x-ray detectors capable of sensing low-level signals in a hostile environment while simultaneously maintaining high-imaging fidelity and subnanosecond time resolution. In response, we have developed a new generation of fast x-ray detectors specifically designed to meet the challenges of underground test applications. The detectors are based on microchannel-plate (MCP)–intensified detectors previously developed at LLNL for time-resolved measurements of x-ray emission from electrical gas-discharge plasmas and laser-produced plasmas.[1] We built and successfully fielded a detector with a continuous time resolution of about 400 ps. The detector converts x-ray flux into an optical signal 1000 times brighter than the incident x-ray signal. This conversion efficiency is nearly a million times greater than that of the passive phosphors and scintillators used previously for x-ray detection in this energy range. By electrically gating the MCP, this detector achieves time resolutions of 100 ps for specialized applications. The use of efficient fast phosphors, such as In-doped CdS WL1198 or Ga-doped ZnO WL1201 (described elsewhere in this report), make the detector sensitive enough to detect single photons while maintaining subnanosecond time resolution.

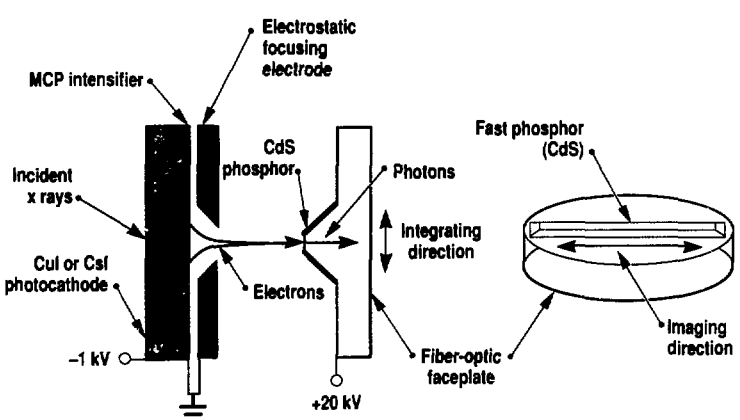

Figure 1. Schematic of an MCP-intensified x-ray detector with an x-ray photocathode to convert incident x rays to photoelectrons; an MCP to amplify a photoelectron; a fast phosphor to convert the electron's kinetic energy to light, and a fiber-optic faceplate to transmit the light out of the vacuum system. The electrostatic-focusing electrodes compress the electron current out of the MCP in one dimension while preserving spacial resolution in the other.

Detector Description

We use x-ray detectors for field applications to convert incident x-ray signals into optical signals, which we then record and digitize by conventional, visible electro-optical devices such as optical streak cameras and charge-coupled-device cameras. Since electro-optical devices are fairly sensitive to the kinds of electromagnetic pulses and nuclear radiation backgrounds that commonly exist in our experiments, they are located in heavily shielded and electrically isolated enclosures as far away from the experiment as possible. Coherent fiber-optic arrays link the x-ray detectors and convert the signals to optical light at the site of the experiment to the streak cameras. These fiber-optic links are inefficient compared to typical laboratory apparatus because of large optical-insertion losses at interfaces and bulk-glass transmission losses. Thus, the field detector must provide more optical signal per x-ray photon in order to transfer the signal to the streak cameras without more loss of information than a detector built for laboratory applications.

A schematic diagram of the basic detector that we have developed is shown in Fig. 1. The detector consists of an x-ray photocathode to convert incident x rays to photoelectrons, an MCP to amplify a photoelectron incident on its input surface into as many as 10,000 electrons on its back surface, electrostatic-focusing electrodes, a fast phosphor to convert the electron's kinetic energy to light, and a fiber-optic faceplate to transmit the light out of the vacuum system. The electrostatic-focusing electrodes shown in Fig. 1 compress the electron

current out of the MCP in one dimension (the integrating direction) while preserving spatial resolution in the other (the imaging direction). The electrons are typically compressed to strike the phosphor on a narrow strip corresponding to the entrance slit of an optical streak camera. The compression direction is the direction of the time sweep in the camera, and the size of the compressed image in this direction determines the ultimate time-revolution element in the streaked image.

We achieve imaging in the unswept direction by accelerating the electrons emitted by the MCP at the site of an incident photoelectron. We accelerate them so rapidly that they cross the gap to the anode-phosphor surface before they can move laterally across the imaging direction (proximity focusing). We use a static accelerating field of 60–70 kV/cm generated by applying 20 kV between the MCP and the anode. This voltage is much larger than the 2–3 kV used in conventional, laboratory x-ray detectors and helps to increase the optical gain of the detector by increasing the kinetic energy of the electrons hitting the phosphor. The large field strength employed in the detector and the MCP (20 kV/cm) make this system quite insensitive to stray field effects and electromagnetic pulses. We can operate the detector with reduced sensitivity as a two-dimensional imaging device by removing the focusing electrode. The phosphor is overcoated with a thin layer of Al (about 1000 Å), which allows us to apply voltage to the phosphor and to block background light.

We have developed several other versions of this detector, including a detector without the electron-focusing electrodes and one without an MCP. Many variations of this generic detector are possible, depending on the incident x-ray flux levels and the particular application. The detector shown in Fig. 1 was successfully operated in an underground test environment.

To make the MCP an efficient x-ray detector, we first coat it with an electrical conductor so we can apply bias voltage to the plate. We then vapor-deposit 0.2 μm of Au on both the front and back surfaces of the MCP—on the front surface at a grazing angle of 15 degrees to prevent the Au from traveling down the microchannels and on the back surface at a 45 degree angle. We use an x-ray photocathode to convert the incident photons to electrons. We vapor-deposit the photocathode directly on the Au on the front surface of the MCP by using the technique developed for CsI by Whiteley et al.[2] We have tried several x-ray photocathodes, including Au, CuI, and CsI. A typical thicknesses for both CuI and CsI is about 1000 Å. We deposit the photocathode on the front of the MCP at a 45-degree angle.

We also tested a version of this detector without the MCP. In this test, we deposited 0.1 μm of Al on a 0.5-μm polypropylene substrate. We then vapor-deposited 0.1 μm of either CsI or CuI over the Al. Incident x rays passed through the polypropylene and the Al and interacted with the photocathode. A photoelectron was emitted and accelerated directly into the phosphor.

Back-surface quantum yields for CsI are quite similar to the front-surface yields used in the MCP-based detector. We must take into consideration the x-ray transmission of the polypropylene and the Al when we determine the effective quantum yield. In the transmission-photocathode version, the electrons can be accelerated into the phosphor either by biasing the photocathode to a negative potential and grounding the phosphor or by biasing the phosphor positive and grounding the photocathode. We can reduce efficiencies of the transmission-photocathode version from the MCP version by approximately the gain of the MCP.

Electron Focusing and Spatial Resolution

The focusing electrode shown in Fig. 1 enhances the the sensitivity of the detector by compressing the electron current from the back of the MCP in one dimension. We modeled the electron trajectories between the MCP and the phosphor for various electrode geometries. Figure 2 shows a typical set of electron orbits between the MCP and the phosphor-coated fiber faceplate. In this case, we grounded the back of the MCP and the focusing electrodes and we biased the faceplate to +20 kV. The electric field between the focusing electrode and the faceplate is about 65,000 V/cm. We assumed the electrons were emitted from the MCP normal to the surface with energy of 75 eV. For this geometry, we found that we could collect electrons from a 4.7-mm-wide area of the MCP onto the 500-μm-wide area on the faceplate, which corresponded to a compression ratio of 9.4. We also studied the electron trajectories for more realistic initial conditions, including variations in initial energy and angle. We found these effects to be relatively small over typical ranges expected for the output of the MCP.

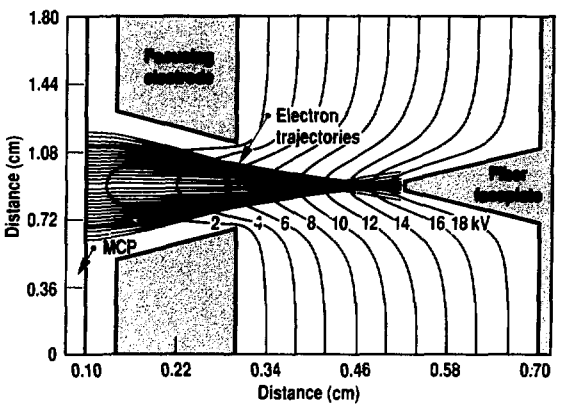

Figure 2. A typical set of electron orbits between the MCP and the phosphor-coated faceplate. Back of the MCP and focusing electrodes are grounded. Phosphor-coated faceplate is biased to +20 kV. The electric field between faceplate and focusing electrode is about 65,000 V/cm.

We can estimate the loss of spatial resolution in the direction perpendicular to the compression direction by calculating the transit time of the electrons from the MCP to the phosphor, assuming an initial direction and velocity, and by calculating how far the electron travels in the resolution direction from the time it leaves the MCP until it strikes the phosphor. Typical initial angles are less than or equal to 10 degrees, and initial energies are typically less than 100 eV, which corresponds to a displacement of about 100 μm. The spatial resolution of the detector full width at half maximum, shown in Fig. 2, should be on the order of 200 μm. In general, the spatial resolution depends on the compression ratio of the detector because the MCP anode spacing and the electron flight time increase with increasing compression. Our present applications require detector spatial resolution ranging from 100–500 μm and electron-compression factors of 5–10.

Spatial resolution in electro-optic devices typically degrades in pulsed operation because of distortions in the focusing optics and space-charge repulsion of the electrons in the output signal. We measured the pulsed spatial resolution of one of our detectors with a compression ratio of about 5 by placing a 50-μm-wide slit just in front of the MCP. A pulsed 300-ps electron source illuminated the detector through the slit, which was oriented perpendicular to the imaging direction. We recorded the spatial profile of the output light with photographic film. The detector was illuminated with electrons of sufficient intensity to totally saturate the detector MCP by depleting the stored charge in channel walls of the MCP. The spatial profile of the detector output under these conditions, which represent the most severe space-charge degradation possible of the detector's spatial resolution under normal operating conditions, was about 130 μm.

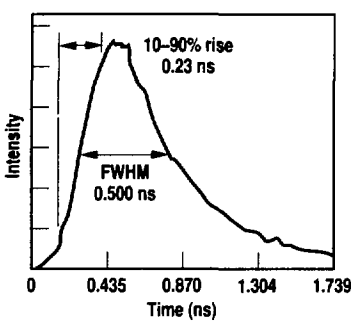

Figure 3. Detector time response calculated by the streak camera from data in the figure. The response time (500 ps) calculated by subtracting the modal dispersion in the fibers and the finite-incident pulse width in quadrature. The measured time response thought to be a function of phosphor decay time.

Time Response

We measured the time response of our detector using a WL1198 phosphor screen at the Janus laser facility at LLNL. The Janus laser is a frequency-doubled YAG laser with output energies in the range of 0.01–10 J at 532 nm and focused to a spot 70 μm in diameter to create a intense burst of x rays. We measured the x-ray pulse at 215 ps full width at half maximum with a 125-ps optical pulse from the laser. In our measurement, the output of the detector resulting from the x-ray pulse was sent to a streak camera through a 10-ft-long quartz-fiber array. The modal dispersion in the quartz-fiber array degraded the system time resolution. It was measured at 250 ps. The streak camera has a time resolution of 9 ps. The detector response time measured by the streak camera is shown in Fig. 3. The measured rise time (10–90%) was about 230 ps. The full width at half maximum was 500 ps. We calculated the response time from this data by subtracting the modal dispersion in the fibers and the finite-incident pulse width in quadrature, yielding a detector response time of about 500 ps. The measured time response is thought to be largely a function of the phosphor-decay time.

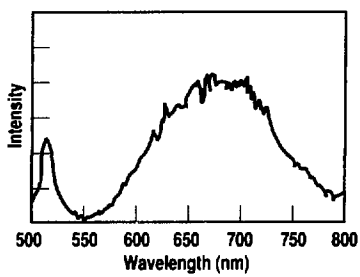

Figure 4. Spectral output of small grain-sized, In-doped CdS. The output spectrum in the red (about 700–800 nm) agreed well with previous measurements of this phosphor. Green component showed at 520 nm. Work done with the smallest particles (diameters less than 10 μm) in a batch of In-doped CdS. Significant red emissions resulted because particles not properly doped with In. By selecting only CdS particles larger than 10 μm, we were able to eliminate the red emission, which is slow compared to the green at 520 nm.

We used two subnanosecond phosphors developed by W. Lehman[3] with this detector when continuous time resolution was required. One is ZnO (WL1201), which emits at 390 nm (blue). The other is In-doped CdS (WL1198), which has a characteristic fast emission at 520 nm (green). Single-crystal CdS has been shown to emit in the red with a characteristic time of about 5 μs, but the red emission is suppressed for properly-prepared In-doped CdS. By selecting only the smallest particles (diameters less than 10 μm) in a batch of In-doped CdS, we created a phosphor with a fast green component (500 ps, 520 nm) and a slow red component (5 μs, 700 nm). Figure 4 shows the spectral output of small grain-sized, In-doped CdS. The output spectrum in the red agreed well with that measured in previous work with this phosphor.[4] In addition to the red emission, we saw the green component at 520 nm. By selecting only CdS particles larger than 10 μm, we found that we could eliminate the red emission. The resulting phosphor had a time response of about 500 ps. Our speculation is that the smaller particles were not properly doped with In, which resulted in significant red emission.

Efficiency

We defined the efficiency of the detector as the ratio of the output fluence of the phosphor (into 4π) to the input x-ray fluence:

$$e = E_{out}/E_{in}\,, \qquad (1)$$

where E_{out} = output fluence into 4π and E_{in} = incidence fluence.

We also measured the efficiency of the same detector used in the time-resolution measurement at Janus. For this measurement, the x rays emitted by the laser plasma were reflected from a carbon mirror (1.9 degree incident angle) and passed through a filter set containing either Be, Fe, or Al filters. Transmitted x rays with energies of 750eV (± 50 eV) were incident on the detector. The incident x-ray fluence is measured just in front of the detector with a solid-state *p-i-n* diode calibrated to 0.29 A/W/cm^2 for 700-eV x rays. Since the solid-state *p-i-n* diode does not have sufficient time response to follow the incident x-ray pulse, we had to integrate the total current output from it to determine the total x-ray fluence incident on the detector. We could then calculate the input x-ray flux (in W/cm^2) by dividing the total energy deposited by the x-ray pulse as measured by a fast x-ray diode or x-ray streak camera. We measured the output of the detector with an MCP-intensified optical streak camera. The output light of the phosphor was collected by a coherent fiber-optic faceplate (NA = 0.66). The light out of the faceplate was transferred to the streak camera through a 200-μm-core quartz fiber (NA = 0.27).

We calculated the output energy of the phosphor from energy collected by the streak using the following expression:

$$E_{sc} = E_{out}\,(4\pi)\,(\mathrm{NA})^2\,A_{fiber}$$

$$= E_{out}\,(4\pi) \times 1.145 \times 10^{-5}\,, \qquad (2)$$

where E_{sc} is the energy (in ergs) recorded by the streak camera, E_{out} is the output fluence (in erg/cm^2), NA is the numerical aperture of the quartz fiber (0.27), and A_{fiber} is the active area of the fiber (3.14×10^{-4} cm^2). In Eq. (2), we neglected any losses in the optical chain and assumed the output of the phosphor was Lambertian.

Figure 5 shows the measured detector efficiency, as defined in Eqs. (1) and (2), at various MCP voltages for both CuI and CsI photocathodes. For this data set, the phosphor voltage was held constant at 17 kV. We found that the detector efficiency increased by about a factor of 2 for every 50-V increase in the MCP voltage. We attained peak efficiencies of 1000 with the CsI photocathode. Since the x-ray scintillators previously used to convert x rays of this energy to optical light have conversion efficiencies of about 0.001, this increase represents a potential million fold effective increase in conversion and detection efficiency, which is so large an increase in brightness that excitation of the channelplate by a single photoelectron can be recorded on a remote streak camera through the fiber-optic link. The sensitivity of the detector is thus limited by the quantum photo-conversion efficiency of the photocathode, which can be of the order of 30% for low-energy x rays of interest in our experiments.

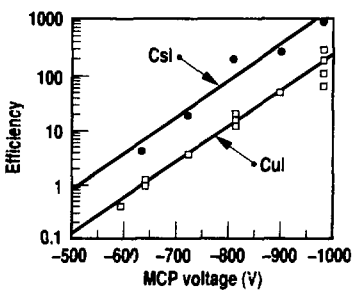

Figure 5. Measured detector efficiency with pulsed 750-eV x-ray excitation for CsI and CuI photocathodes vs MCP voltage. For this data set, the phosphor voltage was held at 17 kV. Detector efficiency increased by about a factor of 2 for every 50-V increase in the MCP voltage.

We also measured the variation of detector efficiency with phosphor voltage. We found that the efficiency varies linearly with phosphor voltage above a threshold of about 9 kV. This threshold was caused by electron-energy deposition in the Al layer overcoating the phosphor.

Conclusions

We have developed an imaging x-ray detector with subnanosecond time response, high efficiency, and good spatial resolution. The detector is rugged, resistant to electromagnetic-pulse effects, and creates sufficiently high-intensity fast signals to drive remote electro-optical instrumentation through long-length fiber-optic links with single-photon sensitivity. These characteristics have made a critical improvement in our ability to diagnose high-energy density experiments.

Acknowledgments

The authors thank Mark Bowers, Carl Bruns, George Cameron, Mark Eckart, Richard Fortner, Mark Rotter, and Jim Swain for their help in this research.

References:

1. B. K. F. Young, J. Bailey, R. E. Stewart, and J. G. Woodworth, "Experimental Demonstration of a 100-ps MCP Framing Camera," *Rev. Sci. Instrum.* **57**, 2729 (1986).
2. M. J. Whiteley, J. R Pearson, G. W. Fraser, and M. A. Barstow, "The Stability of CsI-Coated MCP X-ray Detectors," *Nucl. Inst. Meth.* **224**, 287 (1984).
3. W. Lehman, Lawrence Livermore National Laboratory, Livermore, Calif., private communication (1986).
4. M. R. Rotter, F. Roeske, P. M. Calavan, and S. S. Lutz, "Radiation-to-Light Converters for Nuclear Environments—Deep Red Emitters," *Proc. SPIE* **296**, 183 (1981).

Neutron-Treated, Ultrafast Photoconductor Detectors

C. L. Wang and P. T. Springer

It has been observed that the resolving time of photoconductive detectors decreases dramatically after irradiation with reactor neutrons.[1] However, not much is known about the mechanism of this phenomenon. This effect is intriguing because irradiation with gamma rays and even with high-energy Ar ions does not reduce the resolving time drastically.

Since the energy and fluence of the reactor neutrons used in our earlier photoconductive-detector experiments[1,2] were not well characterized, we decided to study the effect of 14-MeV neutrons on Cr-doped and undoped GaAs and Fe-doped InP as a first step to understanding the mechanism of neutron irradiation. This paper presents the temporal response and sensitivity of photoconductive detectors to electrons, x rays, and a laser as functions of neutron fluence. We show that the detector resolution is reduced to less than 30 ps after irradiation with approximately 1×10^{15} n/cm^2 (Ref. 3).

Photoconductor Chips and Neutron Irradiation

We fabricated GaAs, GaAs:Cr, and InP:Fe detector chips with homogeneous, photoconductive semiconductors. Each chip was 1 mm long, 2.5 mm wide, and 0.4 mm thick. We deposited thin electrodes with ohmic contact on both ends of the top surface, leaving an active area 1×2.5 mm at the center. We placed the chips for irradiation 10–200 cm from the rotating-target neutron source at LLNL and accumulated fluences from 1×10^{12} to 5×10^{15} n/cm^2. After the irradiation, we cooled the chips for about 2 weeks. We then inserted them into a 50-Ω stripline with coaxial cables connected to both ends and took the signal from one end while applying the bias voltage at the other.

Measurement of Detector Response

We measured the temporal response and sensitivity of the photoconductors to electrons and x rays using EG&G's 17-MeV linear accelerator (linac) at Santa Barbara. The shortest pulse one can obtain from this linac occurs at a low-electron current (approximately 100 mA). In earlier experiments with a Cerenkov detector coupled to a streak camera, the linac staff estimated that the length of the electron pulse was greater than 30 ps.

We recorded the signals from our photoconductors with a sampling oscilloscope that averaged 20 linac pulses. Figure 1(a) and (b) shows the response of GaAs:Cr to electron pulses. Figure 1(a) shows the detector response with and without 1.8×10^{12} n/cm^2 irradiations. We observed no significant change at this fluence. Note that the response has a rather long tail, which negates the usefulness of the detector for high-bandwidth application. In Fig. 1(b) through (f), we see a dramatic improvement of the detector response as the fluence is increased from 1.6×10^{13} to 3.4×10^{15} n/cm^2. The long tail is entirely eliminated at approximately 1×10^{15} n/cm^2 irradiation. The shortest pulses ranged from 41–48 ps. Taking the electron pulse to be 30 ps and the sampling-scope response to be 25 ps, we estimated the detector resolution to be 12–28 ps (i.e., less than 30 ps).

Figure 2(a) restates the information of Fig. 1(a) and (b) in graphic form. Since the pulse width and amplitude are proportional to the charge-carrier lifetime and mobility, respectively, both lifetime and mobility decrease rapidly for fluences over 1×10^{14} n/cm^2. Figure 2(b) is a similar plot for undoped-GaAs detectors. The bias voltages on GaAs:Cr and GaAs detectors were 300 and 150 V, respectively. Hence, to compare the amplitudes

with and without doping, we multiplied the scale of Fig. 2(b) by a factor of 2. We observed that Cr doping reduced the amplitude as well as the pulse width.

We obtained similar data with bremsstrahlung x rays generated by stopping 17-MeV electrons. In these experiments, however, the electron current had to be high (approximately 100 A), which made the pulse length longer (approximately 100 ps). The detector quickly reached the system response, limiting the usefulness of the time-resolution measurement below 100 ps.

Carrier Mobility

We measured the carrier mobility of these photoconductors using a YAG laser with a pulse compressor and a KDP frequency doubler that provided 3- to 6-ps pulses at 532 nm. We focused the beam down to fill the active area of the detector (1 × 2.5 mm) so that we could measure the incident power accurately. A sampling oscilloscope recorded the detector output.

The effective carrier mobility, accounting for both free-electron and hole conduction, is given in Eq. (1), from Ref. 4, as

$$\mu_{\text{eff}} = \frac{L^2 h\nu}{e E (1-\gamma)} \frac{I}{V}, \qquad (1)$$

where $L = 1$ mm is the detector length, $h\nu$ is the photon energy, e is the electron charge, E is the incident optical energy, $\gamma \approx 0.34$ is the surface reflectance, I is the observed peak current, and V is the bias voltage.

Figure 3 shows the result of the measured carrier mobility for Cr-doped and undoped GaAs as a function of the neutron fluence. As expected, the effective mobility decreased monotonically as the fluence increased. The Cr doping reduced the effective mobility because photogenerated carriers were scattered with Cr impurities.

Detector Characterization with Low-Energy X Rays

We will use an array of discrete photoconductor detectors, similar to those

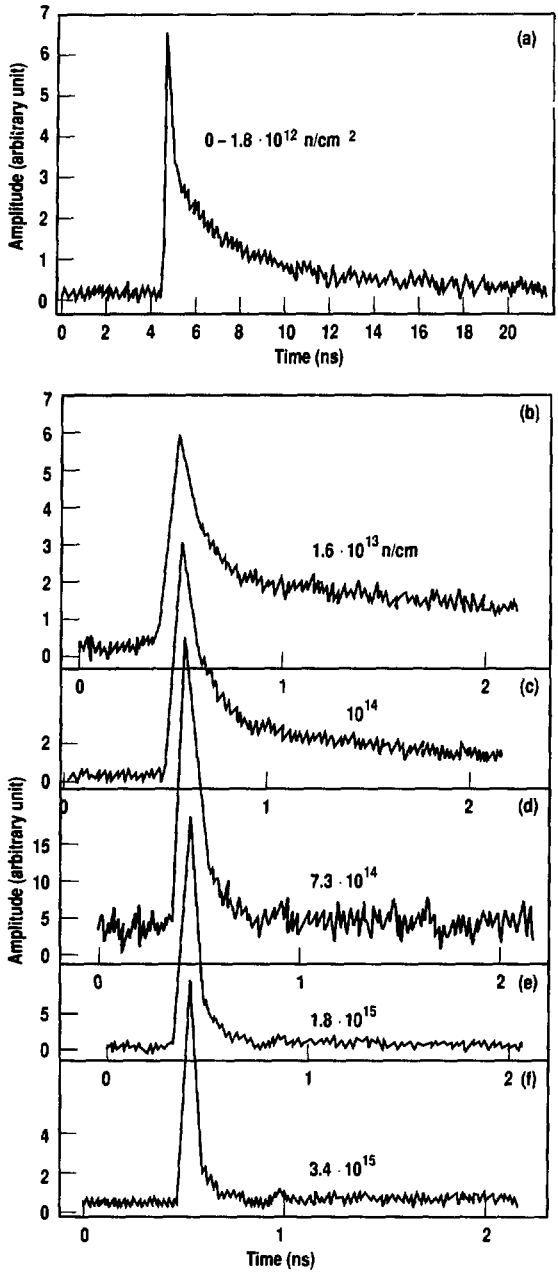

Figure 1.
(a) GaAs:Cr response to electrons with and without 1.8×10^{12} n/cm^2 irradiation. (b–f) Improvements of GaAs:Cr response as a function of neutron-irradiation fluence.

described earlier in the paper, as a fast and reliable readout of an x-ray spectrometer. We now use a spherically curved crystal to Bragg-reflect and image x rays from several different sources simultaneously. On the spectrometer-output plane, the spectra from the different sources are spaced by only 0.2 cm, requiring the use of small, sensitive, and finely positioned readout detectors. Although we do the primary spectrometer readout with a fast phosphor and an optical streak camera, we will use the photoconductive detectors as a redundant diagnostic.

The GaAs pieces with ohmic contacts were neutron damaged in the Omega West Reactor of Los Alamos. We surrounded the pieces with B_4C and In foil to capture thermal neutrons and placed them in close proximity to the reactor core for a sufficient duration to give response times of about 150 ps. With higher neutron doses, the detectors will have faster response times but lower sensitivities. Heavy neutron damaging was not desirable for the x-ray spectrometer application, since a 150-ps response time is adequate and the highest sensitivity is desired. We cooled the chips until they were safe to handle, then polished the x-ray entrance side.

We mounted the 1- × 1- × 0.5-mm, neutron-damaged GaAs detectors in an end cap that fits at the end of a 5-cm piece of 0.141-in.-diam Cu-coaxial cable. We made connections to the GaAs crystal using Ag epoxy. Spring bellows connected one side of the crystal to the center conductor of the coaxial cable, and a protecting end cap connected the other side of the crystal to ground. An SMA connector terminated the 0.141-in. Cu jack. When assembled, we could bias the detectors to about 1 kV, which we applied through a high-bandwidth coupling can.

As a check to verify that the detectors functioned and had adequate time response, they were biased to 1 kV and excited with 55-ps pulses of 800-nm light from a GaAs laser diode. The detectors showed a time response of approximately 150-ps full width at half maximum and exhibited no long-lived tail.

We calibrated the detectors for sensitivity using two different techniques. The first technique used pulsed x rays from a laser-produced plasma. The second technique used direct-current x-ray sources. The pulsed calibration used x rays with a mean energy of 2 keV, a pulse duration of about 200 ps, and peak intensity of 1.1×10^4 W/cm^2. We performed the direct-current calibrations to obtain the correct range of x-ray energies of interest in the spectrometer application.

We used the Janus laser facility at LLNL to produce a 200-ps pulse of x rays. We frequency doubled the doped-glass laser and operated it with a pulse duration of 100 ps. We focused the laser to a spot size of about 30 μm onto a Ti foil, placed a filter of 1.27 μm Be filter on a 50-ps, 8201 x-ray diode, and recorded the x-ray pulse using a 50-ps Tektronics 7250 oscilloscope. The observed x-ray pulse had a full width at half maximum of 225 ps. The pulsed x rays excited the photoconductive detector, and the energy deposition of the x-ray pulse was determined using two calibrated Si *p-i-n*-diode detectors. One *p-i-n* diode had a filter identical to the photoconductive detector and measured the x-ray intensity behind 1.27 μm of Be. The other *p-i-n* diode had an x-ray filter of 5.08 μm of Be, which we used to determine the mean energy of the x rays, approximately 2 keV. The photoconductive signal, shown in Fig. 4, has a full width at half maximum of 475 ps, close to the bandwidth limit of the Tektronics 7104 oscilloscope used to record the signal. The oscilloscope was used to record a 60-ps pulse from the pulse generator, and the full width at half maximum of the observed trace was approximately

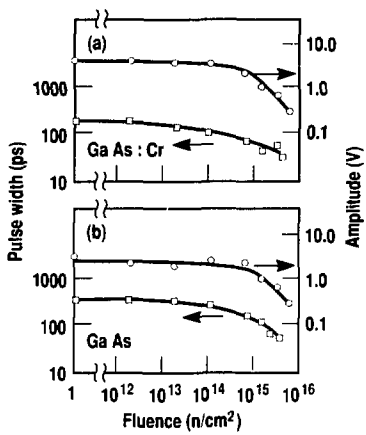

Figure 2. Pulse widths and amplitudes of (a) GaAs:Cr and (b) GaAs detectors as a function of neutron-irradiation fluence.

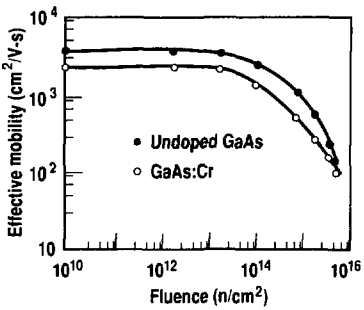

Figure 3. Effective carrier mobility of free electrons in Cr-doped and undoped GaAs as a function of neutron-irradiation fluence.

400 ps. The 475-ps width of the observed photoconductive signal was a combination of the photoconductive response time, the 225-ps time duration of the x-ray pulse, and the 400-ps oscilloscope response time. The observed trace was consistent with a photoconductive time response of about 150 ps, as it was with the GaAs laser diode.

Because the *p-i-n* diodes and photoconductive detectors both have similar, flat, x-ray spectral responses in the 1- to 3-keV x-ray region, we can relate the sensitivities of the photoconductive detector to those of the *p-i-n* diodes without a detailed knowledge of the incident x-ray spectrum. The *p-i-n*-diode signals imply a total of 294 μJ/sr of x rays behind the 1.27-μm Be filter and a total of 648 μJ/sr behind the 5.08-μm Be filter for the laser shot of 2.64 J. The total charge collected from the photoconductive response to the measured x-ray energy deposition implies a sensitivity of 7.1 mC/J.

The theoretical efficiency of the photoconductive detector is given by

$$\eta_{pcd} = ev\tau/wE_{eh} . \qquad (2)$$

Here, e is the electron charge, v is the carrier drift velocity, τ is the carrier recombination time, $w = 0.05$ cm is the gap width, and $E_{eh} = 5$ eV is the energy per electron-hole pair in GaAs. The measured efficiency implies a value of 1.78 μm for the product $v\tau$. The detector has only 3.6% of the intrinsic efficiency because of the neutron damaging. With an estimated $1/e$ recombination time of 120 ps, based on the pulsed-laser excitation data, the drift velocity is about 1.48×10^7 cm/s. This value is below that of intrinsic GaAs biased at 2×10^4 V/cm. The carrier mobility μ is 741 cm²/V·s at this bias level.

The second technique for calibrating the detectors is to use x rays from standard x-ray tubes. When we bias the GaAs detectors, they have a leakage current of about 1 μA caused by the resistance of GaAs. This leakage current far exceeds the typical currents (100 pA) induced by laboratory x-ray tubes. To extract the small x-ray-induced detector current, we chop the x-ray beam at a 1-kHz rate and use a phase-lock amplifier to extract the x-ray-induced detector current. We can extract a current as low as 1 pA using this method. Preliminary calibrations show that the detectors have a reduced sensitivity of 2.4 mC/J to 25-keV x rays. The large difference in penetration depth may cause the observed difference in sensitivity to 700 eV- and 25-keV x rays. We will perform a similar measurement using low-energy x rays, and we will investigate the pulsed versus direct-current response using optical excitation.

Discussion

Ultrafast GaAs and GaAs:Cr semiconductor detectors can be produced with 14-MeV neutron irradiation. We also obtained InP:Fe detectors of similar speed using the same process. However, InP detectors often exhibit a substantial increase in dark current, which indicates that more delicate control of the InP is required. For this reason, GaAs is usually preferred to InP.

As mentioned earlier, irradiations with gamma rays and high-energy Ar ions (1.1 GeV/nucleon) did not change the carrier lifetime substantially. Since the main energy-loss mechanism of these particles in matter is ionization, electromagnetic interaction appears ineffective in controlling the carrier lifetime. On the other hand, the interaction for neutrons is virtually all caused by strong interaction. In 14-MeV *n*-Ga or *n*-As interactions, although the elastic cross section is somewhat larger than the nonelastic cross section, the elastic scattering plays only a minor role in the energy transfer from neutrons to atoms. This is because, in these two-body collisions, the neutron is much lighter than the target atom, and the differential cross section is peaked forward. The dominant energy transfer is through nonelastic channels, and the resulting large number of atomic displacements is responsible for changing the carrier lifetimes and mobilities.

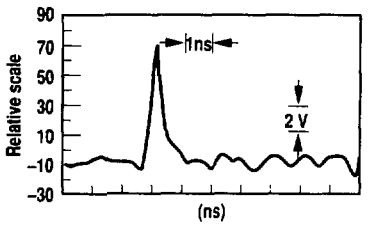

Figure 4. The photoconductive signal from the Janus x-ray pulse as recorded by a Tektronix 7104 oscilloscope.

Acknowledgments

We thank Mike Pocha and Jeff Morse for fabricating the detector chips; Mike Singh and Ed Ambrose for their assistance in neutron irradiation; Paul Nash, Ken Moi, Steve Iverson, and the linac crews of EG&G Santa Barbara for their invaluable contributions; and Bill Brazes and Don Jander for their help in running the short-pulse laser.

References:

1. R. B. Hammond, Los Alamos National Laboratory, Los Alamos, N.M., private communication (1985).
2. C. L. Wang, J. D. Eckels, W. V. Morgan, M. D. Pocha, D. R. Slaughter, B. A. Davis, D. R. Kania, and R. S. Wagner, "Photoconductor X/γ-ray Detectors and X-Ray Bolometers," *Rev. Sci. Instrum.* **57**, 2182 (1986).
3. C. L. Wang, M. D. Pocha, J. D. Morse, and M. S. Singh, "Neutron-Treated, Ultrafast, Photoconductor Detectors," *Appl. Phys. Lett.* **54**, 1451 (1989).
4. G. Mourou and W. Knox, "High-Power Switching with Picosecond Precision," *Appl. Phys. Lett.* **35**, 492 (1979).

Fast *p-i-n* Diodes

C. L. Wang and J. E. Findley

We now know how to make fast radiation detectors by radiation treatment of photoconductors.[1] The treatment consists of generating crystal defects, which serve as charge-carrier traps and fast recombination centers, by shortening the carrier lifetime. Thus, the fast response is obtained by quickly eliminating the charge or at the expense of detector sensitivity.

Fast photoconductive detectors are sensitive enough for many applications, such as x-ray, gamma-ray, neutron-, proton-, and electron-flux measurements. They are, however, not sensitive enough for certain x-ray measurements requiring <300-ps resolution. We therefore undertook to develop fast positive-intrinsic-negative (*p-i-n*) diodes that are much more sensitive than photoconductor detectors. In general, *p-i-n* diodes consist of a Si wafer with a *p* layer and an *n* layer sandwiching an intrinsic layer, the *i* region. *P*-type conductivity is associated with holes in the semiconductor, which are equivalent to positive charges. *N*-type conductivity is associated with electrons in a semiconductor.

Sensitivities of *p-i-n* Diodes and Photoconductor Detectors

Both *p-i-n* diode and photoconductor detectors operate under the same principle. They collect charge carriers generated in the solid by incident radiation to the electrodes connected to an external circuit. The sensitivity S of both detectors is given by

$$S = \frac{E}{w}\,\eta \qquad (1)$$

where E is the energy of the radiation absorbed, w is the average energy required to generate an electron-hole pair, and η is the collection efficiency defined as the fraction of the generated carriers collected by the electrodes before recombination.

For Si *p-i-n* diodes, $w = 3.67$ eV and $\eta = 1$. The 2.5-ms carrier lifetime is much longer than the collection time so that all charges are collected. Consider a flux of low-energy x rays totally absorbed in the depletion region. The dead layer at the entrance window can be made quite thin (~0.1 μm) so that the attenuation can be neglected. The calculated sensitivity is $S = 4.4 \times 10^{-17}$ C/keV = 270 mA/W.

For a photoconductor, we adjust the carrier lifetime τ by radiation damage to match the desired detector speed. To calculate the charge-collection efficiency, consider an electron generated at a distance x from the anode. The probability for the electron to reach the anode is $e^{-t/\tau}$, where $t = Lx/\mu V$ is the transit time of the electron, L is the gap between the electrodes, μ is the electron mobility, and V is the applied bias. The collection efficiency is then given by

$$\eta = \frac{1}{L}\int_0^L e^{\frac{-L}{\mu V \tau}}\,x\,dx$$

$$= \frac{\tau}{T}\left(1 - e^{-\frac{T}{\tau}}\right) \approx \frac{\tau}{T} \text{ for } \tau \ll T, \qquad (2)$$

where $T = L^2/\mu V$ is the transit time for an electron to cross the gap. For $\tau = 200$ ps, $L = 1$ mm, and $V = 500$ V, the value of T is 16.7 ns assuming $\mu = 1200$ cm²/V·s for neutron-damaged GaAs (Ref. 1). The collection efficiency is only 1.2%, and the calculated sensitivity is $S = 4.8 \times 10^{-19}$ C/keV = 3 mA/W assuming $w = 4$ eV. Thus, a 200-ps neutron-damaged GaAs detector is about 100 times less sensitive than a Si *p-i-n* diode.

It is instructive to visualize the insensitivity of the fast-photoconductor detector by calculating the distance x

the electron moves during the 200-ps lifetime. Thus,

$$x = \mu \frac{V}{L} \tau = 12\ \mu\text{m}. \quad (3)$$

Only electrons generated within 12 μm of the anode are collected. The effective length of the detector shrinks from 1 mm to 12 μm.

Resolving Time of the *p-i-n* Diode

It is clear from the above analysis that a *p-i-n* diode is indispensable when the radiation flux is low. Unfortunately, it is not easy to make *p-i-n* diodes fast. In fact, if fast *p-i-n* diodes of reasonable size had been available in the past, development of the fast photoconductor may not have been necessary.

The response of the *p-i-n* diode is controlled by the rise and decay time. To make the rise time fast, carriers need to be collected quickly. We can reduce the transit time by making the depletion depth thin. A depletion layer that is too thin, on the other hand, is detrimental to the decay time, which is determined by the RC constant of the circuit. The load impedance R is usually 50 Ω. The term C is the capacitance of the *p-i-n* diode, which is effectively a capacitor with the depletion layer as the dielectric. Clearly, it is necessary to optimize the rise and decay times.

Another consideration for low-energy x-ray detection is that the entrance window should be of *p*-type Si. Because x rays are absorbed near the entrance window, slow holes with one-third the mobility of electrons need not travel far before reaching the anode. We let the fast electrons cross the depletion layer to reach the cathode. Note that the *p-i-n* diode is reverse-biased. By convention, the anode collects the holes and the cathode collects the electrons, contrary to the vacuum-tube diode in which electrons are collected by the anode.

For a 20-μm depletion depth d, the electron transit time is 200 ps. Here, we apply a sufficiently high bias voltage and use the scattering-limited velocity 10^7 cm/s as the saturation velocity. For a diode with an area A of 1 mm², the capacitance C is given by $\varepsilon\varepsilon_0 A/d = 5.2$ pF, where $\varepsilon = 11.7$ is the dielectric constant of Si, and $\varepsilon_0 = 8.854 \times 10^{-14}$ F/cm is the permittivity of free space. The decay time is then 260 ps.

Experiments

Three *p-i-n* diodes with a 1-mm² sensitive area, 0.6-μm entrance dead layer, 18-μm depletion depth, and 30-μm exit layer were fabricated by Quantrad Corporation. Their standard technique provided an *n*-type, rather than *p*-type, entrance window that is desirable for low-energy x-ray detection, as mentioned earlier. We measured the response of these *p-i-n* diodes at a 200-V bias with a 100-ps pulse of 820-nm laser light. As shown in Fig. 1, the best rise time t_r was 195 ps, and the FWHM was 450 ps. It appears that the diode size needs to be reduced to attain a 300-ps resolution with this type of construction.

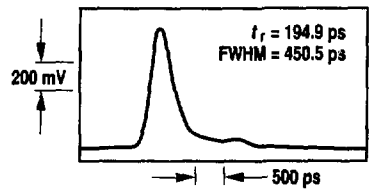

Figure 1. Response of a Quantrad 1-mm² *p-i-n* diode to a 100-ps, 820-nm light pulse.

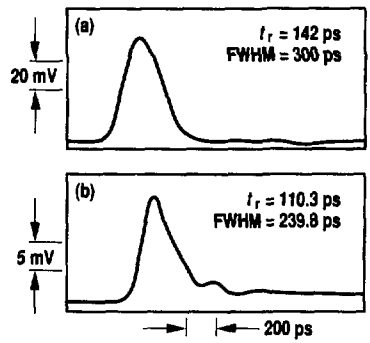

Figure 2. Response of a United Detector Technology 1.27- × 2.54-mm² *p-i-n* diode to an 80-ps, 532-nm laser beam collimated to (a) 1 × 2.1 mm² and (b) 1-mm diameter.

In our search for a commercially available diode with a *p*-type entrance window, we found a planar diffused *p-i-n* fabricated by United Detector Technology with an area of 1.27 × 2.54 mm² and a depletion depth of 10 μm. The *p-i-n* structure is isolated from the polysilicon substrate by a SiO_2 insulator. Although this *p-i-n* diode was not intended for high-speed applications, such a dielectric insulation may prevent carriers from slowly diffusing into the sensitive volume from surroundings; therefore, it can be helpful for fast detector response. We tested some samples provided by the manufacturer. To our surprise, the detector response was quite fast. The diode was biased at 40 V and placed in a 80-ps, 532-nm laser beam. Because the penetration depth of 532-nm light in Si is 1 μm, this was an excellent simulation for low-energy x rays. *P-i-n* diodes with the *p*-type entrance layer should yield the best results. When the beam was collimated to 1 × 2.1 mm² and a 1-mm diameter to avoid illuminating the electrode wire bond, we obtained a FWHM of 300 and 240 ps, as shown in Fig. 2(a) and (b), respectively. Rise times

were fast as well, with values of 142 and 110 ps, respectively.

It is not easy to understand why such good-sized *p-i-n* diodes are so fast. The calculated capacitance of 33 pF is in agreement with the measured value of 32 pF at a 40-V bias. The RC decay time is then 1.6 ns. That the decay time does not adhere to the RC constant and is not independent of the beam size clearly defies the conventional wisdom that a *p-i-n* diode is effectively a capacitor in the circuit analysis. We will attempt to solve this mystery in the future. Meanwhile, new *p-i-n* diodes of 0.25, 1, and 4 mm^2 and of 1 cm^2 are being fabricated using the dielectric insulation technique. These diodes will be mounted on high-bandwidth connectors and may be biased to a higher voltage of up to 300 V. We are hopeful that fast (<300-ps) and sensitive (300-mA/W) x-ray *p-i-n* diodes of reasonable size may become available in the near future.

Reference:

1. C. L. Wang, M. D. Pocha, J. D. Morse, and M. S. Singh, *Appl. Phys. Lett.* **54**, 1451 (1989).

Phosphors and Scintillators: Fabrication and Characterization

T. F. Perry, G. A. Baughman, and B. A. Jacoby

A considerable effort has been made at LLNL, Los Alamos, and EG&G to find and produce fast, bright phosphors and scintillators for use as radiation-to-light converters for the Nuclear Test Program. We are constantly looking for improved converters and striving to improve our understanding of the properties of the materials we now have. In the past few years, we have discovered two new phosphors with subnanosecond time response, WL1201 and WL1198.[1] In FY88, we continued our investigations with two major activities: We built a facility for synthesizing fast phosphors, and we characterized the temporal response of several plastic scintillators.

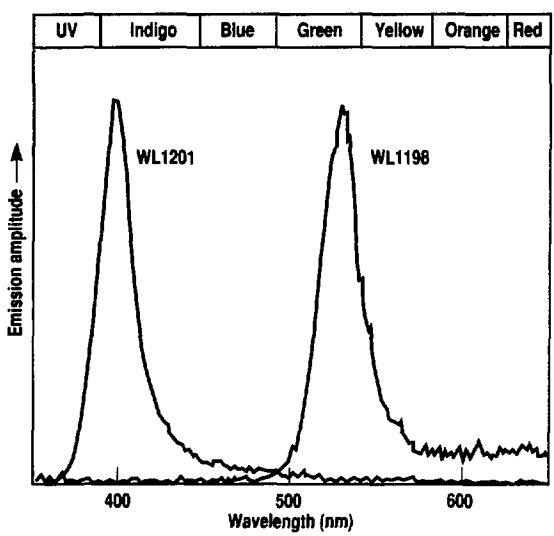

Figure 1. Emission spectra of WL1198 and WL1201. Amplitudes are normalized for comparison; WL1198 is about 25% as efficient as WL1201.

Phosphor Synthesis

Phosphors WL1201 (ZnO doped with gallium) and WL1198 (CdS doped with indium) were developed for Westinghouse Corporation by W. Lehman. Because they were not commercially available, we hired Lehman in 1987 as a consultant to help us fabricate enough of these phosphors for immediate test program needs. To ensure a continuing supply, we began construction of a fabrication facility at the EG&G laboratories in Santa Barbara, where the first batches of WL1201 have been produced during the past year under the direction of D. Turley. These batches were found to have a sensitivity and time response identical to those of the WL1201 produced at LLNL under Lehman's direction.

The facilities for producing these phosphors consist essentially of a chemistry laboratory, a high-temperature furnace, and a gas-handling system. The phosphors are manufactured in two steps. First, the appropriate chemicals are combined, and the resulting mixture is heated to 900–1100°C for about an hour. Next, after the mixture is cooled and broken down to form a fine powder, it is heated to 600–800°C under a reducing atmosphere. For WL1201, this atmosphere consists of slowly flowing hydrogen gas; for WL1198, hydrogen sulfide gas is used. Safety is of obvious concern at this stage, as both gases are extremely flammable, and hydrogen sulfide is toxic. Therefore, great care is taken to ensure that the facilities for fabricating these phosphors are safe. After the second firing, the phosphor is cooled (still in the reducing atmosphere) and then tested for appropriate luminescence spectrum. Figure 1 shows the emission spectrum for the two phosphors.

Since having our own production facility, we have been able to tailor the characteristics of the phosphors we produced to suit individual experiments. For example, we compared the light outputs that resulted from varying the rough firing temperature (see Table 1) and discovered that a firing temperature of 850–950°C is necessary for maximum light output. We next plan to measure the light output and time response as a function of dopant level.

Table 1. Luminescence properties of ZnO:Ga samples.

Rough firing temperature (°C)	Peak position (nm)	Luminescence amplitude[a]
800	385	17
850	390	44
900	389	34
950	390	45
1000	390	2

[a] Amplitude relative to pure ZnO at wavelength 384 nm.

We are currently expanding the EG&G facility for the manufacture of WL1198, which is faster than any other phosphor or scintillator we have used for Nuclear Test Program measurements. Having our own production facility will again allow us to vary the properties of the phosphor in the hope of making WL1198 still brighter and/or faster.

Temporal Response of Plastic Scintillators

Plastic scintillators have been routinely used in the Nuclear Test Program to measure short bursts of x rays, and the temporal response and saturation properties of the detectors that use them have been well studied. In a standard detector configuration, a plastic scintillator in front of a fast photodiode is connected to an oscilloscope via a coaxial cable. These plastic scintillators are relatively thick, about 1/8-in. thick in the thinnest direction. We have recently begun to use plastic scintillators in the form of thin films, often only a few microns thick, for increasing the resolution in high-resolution imaging experiments and (because they discriminate against higher-energy backgrounds) for measuring subkilovolt x rays. We contracted with the Applied Physics Laboratory at the Lockheed Research and Development Division in Palo Alto to investigate the temporal response of thin-film scintillators. Lockheed also investigated whether the heat generated during the process of evaporating a thin coating of aluminum on the front of some of the scintillators to increase light collection may also affect the characteristics of the scintillator. Time-response measurements were made using their pulsed Nd:glass laser facility.

Figure 2 shows the experimental configuration we used for measuring the prompt-to-total fluorescence ratio. A 3-ns pulse from the Nd:glass laser was focused onto a copper target, and the resulting x rays were passed through a Be filter onto the scintillator being measured. The x-ray spectrum peaked at about 1200 eV, with a full width at half maximum of a few hundred electron

Figure 2. A schematic representation of the experimental configuration.

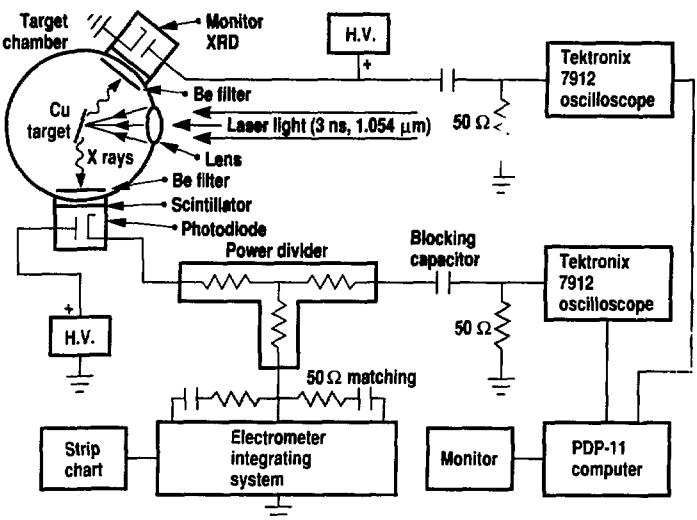

volts. Light from the scintillator was collected by a photodiode (ITT F4014, with an S-20 photocathode). The signal from the photodiode was collected by two recording systems. One was a fast oscilloscope (Tektronix 7912 digital) that recorded the prompt signal from the scintillator, the other an electrometer that integrated the total charge out to several seconds. Because of the blocking capacitor in front of the oscilloscope, the electrometer collects all the charge emitted by the photodiode. This arrangement is particularly ingenious in view of the different time scales involved. The oscilloscope measures the time behavior on a nanosecond time scale, while the time scale of the electrometer is in seconds—a factor of a billion difference. Moreover, this information is recorded simultaneously for both the short-term and the long-term fluorescence on every laser shot.

An x-ray diode (XRD) detector was also mounted on the laser chamber to monitor the x-ray output on each shot so that absolute sensitivities of the different scintillators we investigated could be compared. Data collection was controlled by a PDP-11 computer. All cables were coaxial cables of high quality, and the entire system was closely matched to 50 Ω. Care was taken to prevent leakage from the photodiode power supply into the electrometer and the escape of charge stored in the electrometer. We tested the system by replacing the scintillator photodiode with an XRD. This measurement gave a prompt-to-total ratio of unity, an expected result given that an XRD is known to have no long-term fluorescence.

The several scintillators we studied included plastic scintillators from Bicron Corporation (BC-418, BC-422, and BC-430), plastic scintillators from Nuclear Enterprises (NE-111, NE-111A, and Pilot-U), and inorganic phosphors (WL1198 and WL1201). The results of the measurements on the majority of the thin plastic scintillators were very close to those on the thicker plastic scintillators used in the past. For instance, previous measurements on BC-422 had indicated a ratio of the prompt to total fluorescence yield of 68%. The ratios of four of the seven thin film samples tested were within 2% of this value. Unfortunately, the ratios of the other three were significantly lower—59%, 55%, and 32%. Had we calibrated the sample that tested at 32% on a dc x-ray source only and then applied the standard correction factor to obtain a prompt sensitivity, its calibration would have been off by a factor of 2. This implies that a pulsed calibration will be necessary whenever we use thin plastic scintillators. The results of the measurements on the inorganic phosphors WL1198 and WL1201 were more encouraging. Their prompt-to-total fluorescence ratio of unity indicates that these phosphors can be calibrated equally well on dc and pulsed machines.

Reference:
1. "Fast Green Phosphor for Spectroscopy," *Energy and Technology Review*, Lawrence Livermore National Laboratory, Livermore, Calif., UCRL-52000-88-7,8 (1988), 25.

Radiation-to-Coherent-Light Converter

C. L. Wang, J. E. Flatley, and P. H. Stewart

For high-speed x-ray spectroscopy or imaging with ≤200-ps resolution that requires sending analog signals to a distant fast recorder, development of an array of radiation-to-coherent-light converters (RCLCs) appears necessary. Converting radiation to coherent light allows one to take advantage of optical fibers' high transmission bandwidth. Optical signals can be transmitted over long fibers (on the order of kilometers) with a multigigahertz bandwidth; this is virtually impossible with a conventional electric pulse via coaxial cables. As a first step toward developing such an array, we designed, built, and tested a single RCLC.

RCLC Design

The feasibility of making an RCLC became clear after our recent development of ultrafast, GaAs, photoconductive radiation detectors.[1] By using radiation damage to generate crystal defects that shorten the carrier lifetimes, we have made GaAs detectors with 30-ps resolution. With chromium

doping, these detectors have 200-ps resolution. Because semi-insulating GaAs is routinely used as a substrate for high-speed GaAlAs laser diodes,[2] building a monolithically integrated RCLC is thus possible.

Our RCLC consists of a chromium-doped GaAs (Cr:GaAs) detector and a GaAlAs laser diode integrated on a single semiconductor chip.[3] Part of the Cr:GaAs photoconductor has two gold electrodes and functions as a high-speed radiation detector; the other part serves as the substrate for a GaAlAs laser diode. The detector and diode are connected in series, as shown in Fig. 1.

The laser is biased by an injection current beyond the lasing threshold in the linear region. When irradiated, the photoconductor becomes a variable resistor, allowing extra current to be injected into the laser cavity, thus modulating the optical output. The photoconductor is operated in a linear region in which the induced current is proportional to the energy of the absorbed radiation. In other words, the modulated optical signal is proportional to the radiation pulse. Our RCLC is, thus, a two-step device that converts a radiation pulse to an electric pulse and then to a light pulse.

Figure 1 also shows a schematic of our integrated detector-laser and a photograph of the fabricated RCLC mounted on a copper block. Wire bonds at points 1, 2, and 3 on the electrodes connect to the power supplies and to ground. The device is 750 μm long and 250 μm wide. The area between electrodes 1 and 2 is sensitive to radiation. The connection between electrode 2 and the *p*-side of the laser is done at the wafer level (i.e., without a wire bond). The laser diode is 25 μm wide with a 2-μm-wide cavity.

The Cr:GaAs detector is simply a bulk photoconductive crystal with two ohmic contact electrodes. Electrons and holes created by the incident radiation are collected by the electrodes, which generate an electric pulse. This detector has a stripline geometry to assure a fast rise time. Its decay time depends on the carrier lifetimes, which can be controlled by radiation treatment or, to some extent, by impurity doping.[1]

The high-speed GaAlAs laser is a state-of-the-art "buried heterostructure window laser," so named because numerous heterojunctions (junctions of different material compositions) bury one another. These heterojunctions

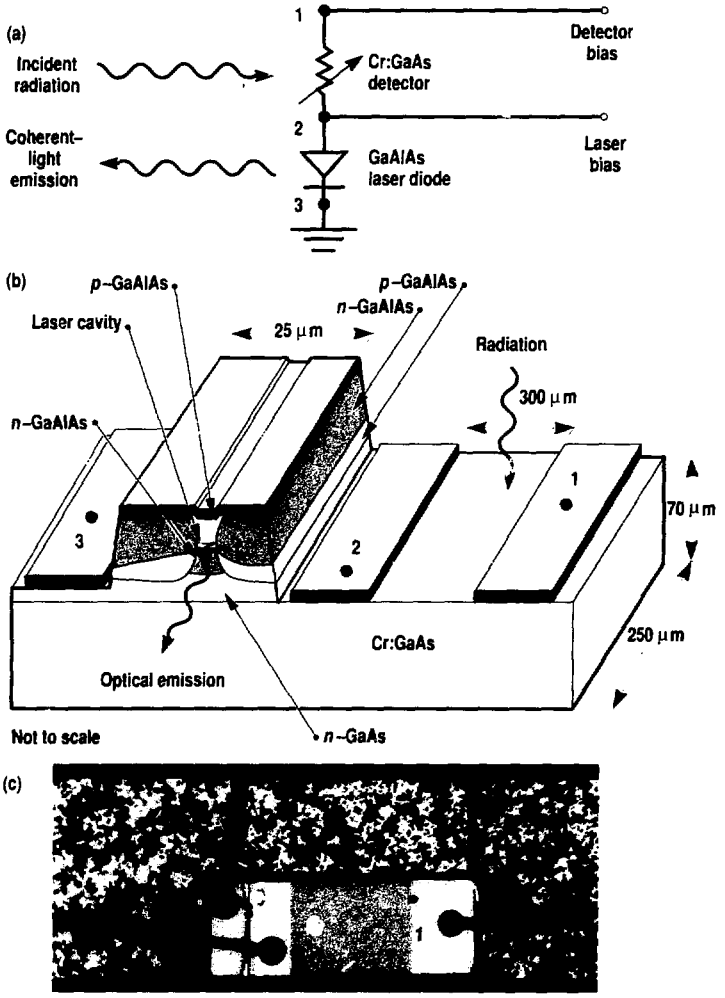

Figure 1. Integrated detector-laser chip as an RCLC: (a) circuit diagram, (b) schematic, and (c) photograph. The chip is 750 μm long, 250 μm wide, and 70 μm thick. Points 1, 2, and 3 are wire bonds on the gold electrodes. The *p*-side of the laser is connected to electrode 2 at the wafer level (no wire bond). The RCLC is mounted on a copper block in the photograph.

confine electrons and light to certain regions, where they can interact efficiently for maximum conversion of electrons to light. The window refers to the narrow transparent layer of unpumped GaAlAs at the end region near the crystal facets. This layer protects the laser mirror and allows a high optical-power capability. The modulation speed of this laser can reach 10 GHz (see Ref. 2 for more details on the fast laser diode).

After the RCLC chip was fabricated, we tested the photoconductor detector and the laser separately—the detector with a short optical pulse to confirm its function, and the laser by measuring its light output as a function of injection current. The diode's low lasing threshold (<20 mA) alleviates the heat-sink problem usually associated with these devices. The pure, single, longitudinal mode of the optical spectrum is important for fiber-optic transmission because it eliminates material dispersion, thereby allowing high-bandwidth and long-distance transmission.

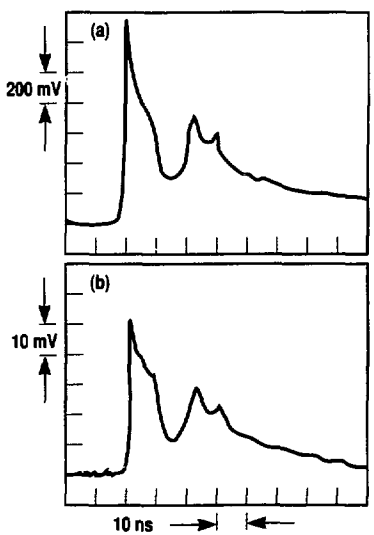

Figure 2. Comparison of (a) the x-ray pulse observed with the Cr:GaAs detector and (b) the laser pulse detected by a *p-i-n* diode. Their fidelity is remarkably good.

Experiment

We tested our RCLC with 16-MeV electrons from a linear accelerator and low-energy (keV) x rays from a z-pinch plasma source. We mounted the chip inside an rf shield to reduce the rf noise in the accelerator environment and the electromagnetic-pulse background near the plasma source. For the 16-MeV electrons, the RCLC was tested in air. To detect a low-energy x-ray pulse from the z-pinch plasma, the RCLC was tested in vacuum. We placed an x-ray filter in front of the radiation-entrance hole to block the visible light from the plasma source.

The RCLC laser emits at 90 degrees to the incident radiation; this light output is collimated with an aspheric lens with a 4.6-mm focal length and a numeric aperture of 0.55 and is then focused onto a 50-μm fiber with another lens. The detector and laser biases are supplied through semirigid coaxial cables, which are brought to within about 3 mm of the chip to minimize the impedance mismatch.

We determined that the impulse response of our RCLC to a 50-ps electron beam was 170 ps. The laser output pulse was transmitted with an optical fiber to a fast positive-intrinsic-negative (*p-i-n*) diode and analyzed with a sampling scope. We also used a coupling capacitor to monitor the impulse response of the Cr:GaAs detector to the electron beam. This turned out to be 200 ps FWHM, somewhat longer than the laser pulse. Preliminary investigation indicates that a possible low-impedance reflection may exist in the laser bias lead, shortening the laser pulse.

Figure 2(a) shows the x-ray pulse observed with the Cr:GaAs detector; Fig. 2(b) shows the laser pulse detected by the *p-i-n* diode. The fidelity of the two pulses is remarkable. A little more noise appears in the coaxial-cable than in the fiber-optic transmission.

Discussion

We are aware of concern regarding radiation damage to the laser diode in the integrated RCLC. For highly penetrating radiations like gamma rays or high-energy electrons, the energy loss in the thin laser cavity is so small that no damage is expected. No radiation damage was observed throughout our experiment with the 16-MeV electron beam. For low-energy x rays, the electrode can be made thick enough to keep x rays from reaching the laser cavity, thus preventing radiation damage. No radiation damage was observed during our experiment with keV x rays either.

Our RCLC functioned reasonably well for a first attempt. In the absence of a single-step, x-ray-pumped laser, it appears to be the first integrated device that can efficiently convert x rays or other radiations into coherent light. It opens up the possibilities of one- or two-dimensional RCLC arrays and large-scale integration.

Acknowledgments

We thank R. Baltrusaitis, N. Bar-Chaim, T. Davies, B. Davis, S. Iversen, K. Y. Lau, B. R. Marshall, M. C. Thomas, I. Ury, and P. A. Zagarino for their contributions during the fabrication and test phases of the experiment.

References:

1. C. L. Wang, M. D. Pocha, J. D. Morse, M. S. Singh, and B. A. Davis, "Neutron-Treated, Ultrafast, Photoconductor Detectors," *Appl. Phys. Lett.* **54**, 1451 (1989).
2. K. Y. Lau, N. Bar-Chaim, I. Ury, and A. Yariv, "11-GHz Direct Modulation Bandwidth GaAlAs Window Laser on Semi-Insulating Substrate Operating at Room Temperature," *Appl. Phys. Lett.* **45**, 316 (1984).
3. C. L. Wang et al. "Radiation to Coherent Light Converter," *Appl. Phys. Lett.* **54**, 1498 (1989).

Optical Guided-Wave Devices for Single-Transient Instrumentation

M. Lowry

In FY88, we developed a single-channel integrated-optical (IO) modulator/streak-camera system (Fig. 1). The electrical input to the IO modulator is supplied by a "conventional" fast radiation-to-electrical detector through a short run of high-bandwidth coaxial electrical cable, and the optical carrier is supplied by a laser diode pigtailed with polarization maintaining optical fiber.

For nuclear weapons testing, the highest fidelity recordings are obtained when the streak camera is remotely located from the phenomena under study. However, the optical information must then travel a significant distance from the event to the recording streak camera (typically about 1 km). Thus, single-mode optical fiber is required for the fiber link from the modulator to the streak camera, to preserve signal bandwidth.

External Modulator (EXMOD) System

Spectral instabilities and large-signal frequency bandwidth limitations result from directly encoding an electrical signal by modulating the laser diode injection current.[1,2] These instabilities lead to unacceptable signal distortion through the chromatic material dispersion of silica-based optical fiber. At 800 nm, the material dispersion is approximately 100 ps/nm-km. Thus, for a spectral instability of 10 nm for a 1-km fiber run, the signal could suffer a temporal distortion of 1 ns. Externally modulating the laser light does lead to significant advantages in spectral stability and large-signal frequency bandwidth; however, injection current modulation is not the only cause of spectral instabilities in laser diode output. Reflections as slight as 10^{-4} to 10^{-6} of the output optical power that are coupled back into the laser diode cavity may cause significant spectral instability.

These optical reflections can arise from any discontinuity in the index of refraction along the optical path of the signal. Typically, fiber-fiber junctions and device-fiber pigtails are the biggest offenders. Optical reflections also create significant intensity instabilities in laser diodes—in some cases, the relaxation oscillation resonance of the laser can be so effectively excited that the depth of modulation of the intensity instability may approach 100%. Thus, to optimize the system performance, we must take extraordinary care in evaluating the components used.

A significant complication in this evaluation process is that both the intensity and spectral instabilites are not identically reproducible; rather, they are chaotic. Therefore, single-transient techniques must be used even in evaluating our components—no sampling or time-integrated techniques are valid. A simple solution to the problem is shown in Fig. 2, where a high-resolution spectrometer is coupled to an NTES extraction-mode streak camera.[3] The spectrometer spectrally disperses the output of the component or subsystem under test along the spatial direction of the streak-tube photocathode. With this single-transient spectrometer, we can monitor the real-time power and spectral characteristics of the optical carrier. By making these unique single-transient measurements,

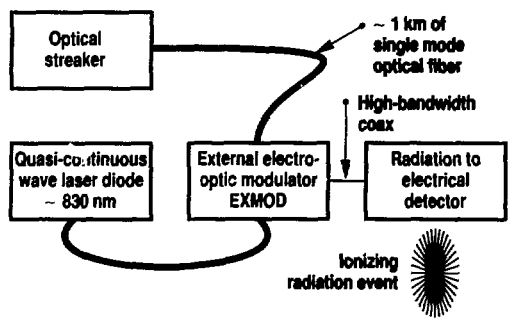

Figure 1. Single-channel integrated optic streak camera data link.

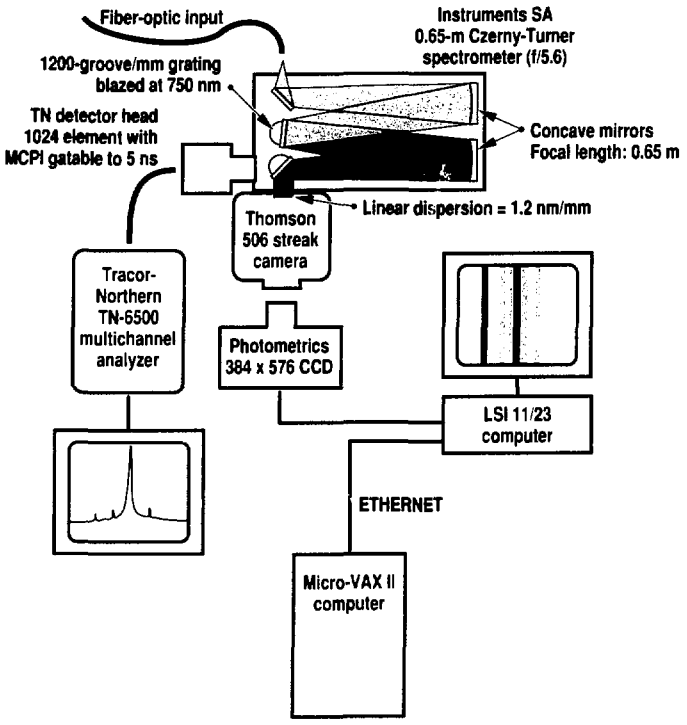

Figure 2. Single-transient spectrometer.

we also become significant contributors to the strategically important photonic device technologies.

Figure 3(a) illustrates the type of spectral instabilities that can occur if excessive optical feedback couples to the laser diode cavity; several laser spectral modes are evident. Fortunately, by using special slant-polished connectors (available from Radiall, Inc.) for fiber junctions, slant-polished device-fiber pigtail interfaces, and carefully engineered laser diode pigtail interfaces, these spectral instabilities can be effectively eliminated. In Fig. 3(b), we see that the laser is multimode at the turn-on time and stabilizes to a single mode relatively quickly. Also, these antireflection measures usually increase the laser diode power stability significantly.

Thus far, we have not always succeeded in stabilizing the optical power output without using a Faraday rotation isolator—a component that is not readily available in fieldable form at 800 nm. However, an IO modulator with dual, complementary optical outputs, such as the directional coupler modulator (DCM), has two signal outputs that, when summed, serve as a monitor of the optical carrier. We use this carrier monitor to normalize the raw modulated signal and extract a closer approximation to the true modulated signal. Our early work with

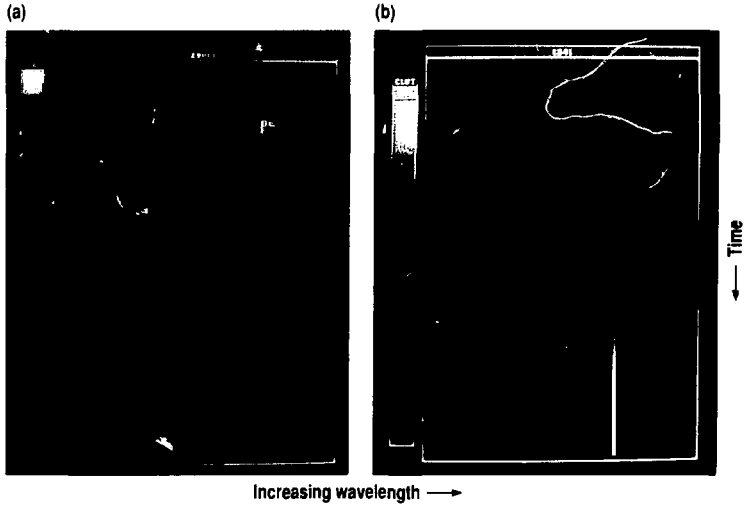

Figure 3. Single-transient laser diode time-resolved spectra. Wavelength of emission is 820 nm. (a) Sweep length is 100 μs, and spectral coverage is 26 nm. (b) Sweep length is 20 μs, and spectral coverage is 26 nm.

DCMs allowed us to demonstrate this technique effectively on the first IO/streak-camera system like that of Fig. 1. This system was fielded on the Phoenix Laser as an x-ray diagnostic.[4]

The x-cut 2 × 2 modulator [Fig. 4(a)] also has dual complementary signal outputs. In addition, the 2 × 2 has greater dynamic range than the conventional DCM but has lower bandwidth than the z-cut traveling-wave DCM.[4] The 2 × 2 modulator comprises three basic components: (1) a tunable directional coupler, (2) a Mach-Zehnder (MZ) interferometric electro-optic modulator, and (3) a second tunable directional coupler.

The operation of the 2 × 2 can be qualitatively understood by considering an optical beam of power P_0 that is perfectly coupled into the single-mode optical waveguide [Fig. 4(a)]. As this beam propagates down the first directional coupler, a fraction of its power couples into the lower waveguide through evanescent coupling. The directional coupler is designed so that, as the two beams emerge from the directional coupler, their powers are approximately equal; any as-fabricated inequality can be tuned out by adjusting the bias voltage, V_b. As these equal beams propagate into the MZ region, their relative phases are determined by the voltages applied to the signal electrodes, V_s. The phase changes are created by opposing changes in the indices of refraction of the waveguides through the electro-optic effect. These relative phases at the exit directional coupler then determine the power distribution in the two output waveguides. For a top launch, the output waveguide on top is called the straight-through or bar leg, and the bottom waveguide is called the cross leg. The two outputs, for a 2 × 2 that has been perfectly tuned, are described by:

$$P_{bar} = P_0 \sin^2\left(\frac{\pi V_s}{2V_\pi} + \phi\right),$$

$$P_{cross} = P_0 \cos^2\left(\frac{\pi V_s}{2V_\pi} + \phi\right), \qquad (1)$$

where V_π is the voltage required to modulate from a fringe minimum to the next maximum, and ϕ is a phase constant.

Equation (1) describes the way in which the electrical signal transfers information to the optical domain; thus, it is called the transfer function (TF) of the device.

Examples of the 2 × 2 measured TF are shown in Fig. 4. Figure 4(b) shows both legs of the Crystal Technology, Inc. (CTI) 2 × 2 device, serial number (s/n) 4, from –20 to 20 V of applied modulation signal. The complementary sinusoidal behavior is evident. Figure 4(c) demonstrates the very high optical extinction obtained near 0 V for the bar ouput of the CTI device, s/n 2. We arbitrarily shifted the voltage scale by a small constant to facilitate this log-log plot. The data were obtained with an automated TF measurement system developed at NTES.[5] With the TF system, we can measure 1024 points of a device TF in approximately 1 min. This level of automation and convenience has proved essential in understanding the modulator responses to a variety of parameters, including temperature and photorefractive damage.[5,6] As we move into multichannel applications, these automated characterization facilities are critically important.

In general, for the CTI 2 × 2s that we measured, the attainable extinction ratios for the bar leg were about 30 dB (power). Given the current state of the art in streak-camera recording,[3] we estimate that the single-fringe dynamic range of this modulator used with streak-camera recording would be about 50. If the modulator is driven over many fringes as well, the dynamic range could be 2000–4000 for a single modulator.

We evaluated the IO modulator/streak-camera combination by pulsing the IO modulator with a known well-characterized electrical pulse within the 3-GHz frequency response of the device.[7] The optical response was recorded on the streak camera. Then we corrected for the streak-camera flat-field response, following the techniques discussed elsewhere in this report.[3]

Figure 5(a) demonstrates the complementary modulation action of the two outputs from 2 × 2, s/n 2. A considerable timing offset occurs between the output of the two legs. To take advantage of the built-in optical carrier monitor of this system, we corrected the timing discrepancy by adjusting the data in time by a discrete number of time elements without interpolation.

Figure 5(b) demonstrates typical results of performing the timing shift to obtain the carrier monitor signal, and compensating the data for fluctuations in the optical carrier. We did not filter the data—all

Figure 4. (a) 2 × 2 integrated-optical modulator. (b) 2 × 2 modulator transfer function. (c) 2 × 2 modulator, bar leg dynamic range.

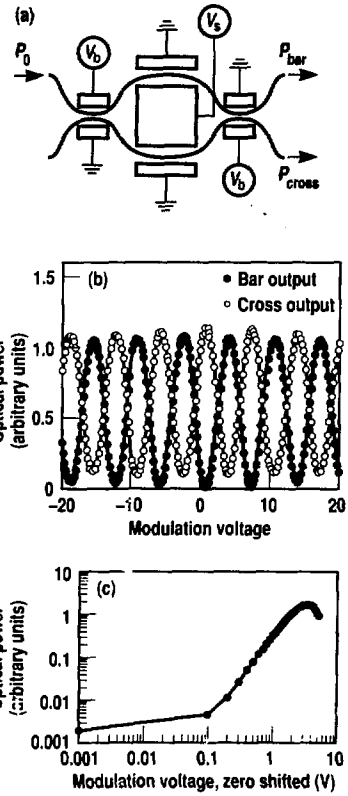

frequency components are still present. The upper trace shows the response of the cross leg of 2 × 2, s/n 2, to an 18-V, 270-ps electrical pulse. The 18-V pulser drives the 2 × 2 through several fringes of the TF. The bottom trace is the same data after division by the carrier monitor signal. Thus, the utility of the two complementary outputs is clear: it affords us the capability of readily compensating for the optical intensity fluctuations that often appear with present fieldable 800-nm laser diode source technologies.

Using the data analysis techniques previously described, we accumulated signal traces of three independent shots using the 18-V, 270-ps pulser. To compensate for the significant timing jitter, we compared the two lagging signals to the leading signal on the computer as the relative timing was artificially adjusted. The differences were observed and minimized as a function of the timing delay. After the timing was adjusted, we examined the root-mean-square (rms) deviation of the three signals relative to their average value. The top trace of Fig. 6 shows the average of the three signals shifted up by 6000 counts for clarity. The bottom trace shows the fractional rms deviation of the three independent shots with respect to the average. Note that the fractional rms deviation has been multiplied by 10 for clarity. Thus, the rms deviation of the three signals is less than 5% and is usually about 3% less.

Figure 6 shows that the largest rms errors occur where the streak-camera record has its highest frequency signal components; this observation is consistent with a streak sweep velocity that fluctuates slightly at high frequency. Since our current method of compensating for streak nonlinearity uses an optical-comb pulse train with only 3 data points/ns, we cannot compensate accurately for these nonlinearities. Work in progress on using the modulators to generate timing fiducials that are temporally very dense shows much promise of correcting even these small deviations. With the appropriate time corrections, we expect the precision of the system to be limited by the streak-camera recording system at approximately 2% at the midlevel intensities.

Also, our analysis of the system reproducibility necessarily includes the pulse-to-pulse variability of the electrical pulser. This pulser output was not measured single-shot, so the reproducibility is unknown. Therefore, the IO/streak-camera system error may be overestimated by an amount equal to the deviations of the pulser added in quadrature, although we expect that error to be small.

The commercially available external modulators have a somewhat limited frequency response—from dc to 3 GHz. NTES is developing extended frequency response modulators using traveling-wave electrode structures developed here (see cover photo). Preliminary measurements indicate the frequency response will extend past 10 GHz. These new designs will be measured extensively in FY89.

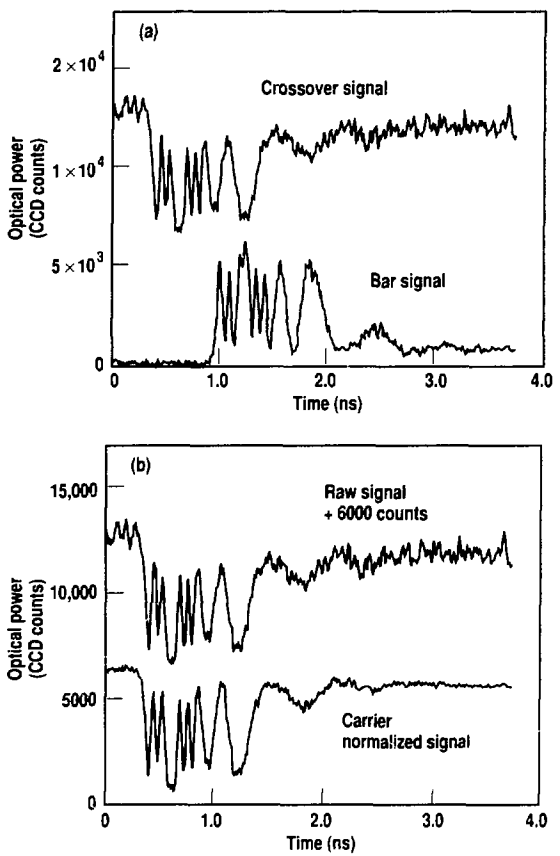

Figure 5. 2 × 2 modulator impulse response: (a) raw data and (b) time shifted and carrier normalized.

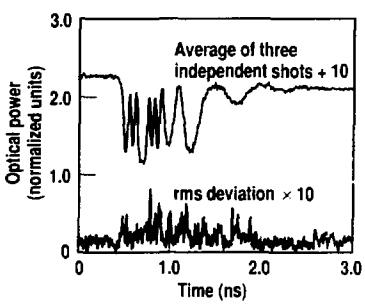

Figure 6. Total IO modulator/streak-camera system reproducibility.

Radiation-Pumped Integrated Optics

The conventional integrated-optics EXMOD approach relies on translating the ionizing radiation information into an electrical signal before the signal can be transformed into the optical domain. We have done some preliminary work on the direct conversion from ionizing radiation to an optical signal that is optimized for single-mode fiber transmission over long distances.

Direct-bandgap semiconductors can be used to fabricate semiconductor laser diodes. They are recognized as perhaps the next material class for integrated-optic device development. At NTES, single-mode waveguides have been fabricated in GaAs. In FY88, we performed initial experiments to study the interaction of single-mode waveguide structures with ionizing radiation, using a GaAs single-mode waveguide package that was pigtailed with single-mode optical fiber on both the input and output. A wavelength tunable optical carrier signal was launched into the input fiber, while the GaAs waveguide was irradiated with ionizing radiation from a Febetron 706 electron beam. The resulting optical signal was recorded on an optical streak camera.[8]

A remarkable feature of the output signal from the device was the intensity of the signal from the single-mode fiber output pigtail (Fig. 7). Other radiation-to-light schemes that use the fluorescence of materials fail to couple significant optical power into a single-mode fiber. In this case, because of the waveguide and stimulated emission within the GaAs, large amounts of optical power can be coupled into single-mode optical fiber. Before these devices can be used as remote radiation detectors, however, much work must be done to understand the spectral characteristics of the emission and the linearity of the optical output with respect to the input radiation signal.

Conclusion

The communications industry has spent billions of dollars developing single-mode fiber communications systems. Our work on single-mode optical guided-wave devices has allowed us to leverage this huge investment and efficiently develop new technologies for application to our single-transient measurement problems.

We developed the necessary characterization techniques to thoroughly understand the components of these new sophisticated instrumentation systems. We can now evaluate the single-transient laser carrier spectrally and temporally and understand the effects that other system components have on the laser diode output. We also can precisely measure the relationship between the electrical signal input and the optical output. On-going work to extend the bandwidth of these modulators shows early promise for increasing the usefulness of this generation of guided-wave devices. Our initial radiation-pumped integrated-optics developments show promise for the next generation of optical guided-wave measurement systems.

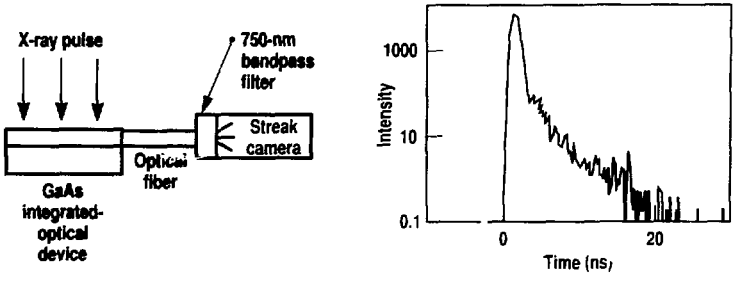

Figure 7. GaAs integrated-optical radiation detector.

Acknowledgments

Without the expert and dedicated assistance of L Division Photonics Laboratory personnel, Greg Lancaster, Dan Nelson, and Dick Peterson, these accomplishments would not have been possible. Glen McWright of LLNL's Engineering Research Department and Richard Becker of Integrated Optical Circuit Consultants provided expertise on the critical integrated optics fabrication.

References:

1. K. Y. Lau, N. Bar-Chaim, I. Ury, Ch. Harder, and A. Yariv, "Direct Amplitude Modulation of Short-Cavity GaAs Lasers up to X-Band Frequencies," *Appl. Phys. Lett.* **43**, 1 (1983).
2. K. G. Hagans, R. E. Haigh, and H. O. Francis, "Use of Laser Diodes for Analog Fiber Optic Diagnostic Systems," *Proc. SPIE* **987**, 56 (1988).
3. M. Lowry and J. Bonfie, "Streak Camera Developments for NTES Applications," this publication, p. 42
4. M. Lowry, D. Jander, G. Lancaster, P. Kwiat, G. McWright, R. T. Peterson, W. Tindall, and F. Roeske, "Lithium Niobate Directional-Coupler Modulators for High-Bandwidth, Single-Shot Instrumentation Systems Operating at 800 nm," *Proc. SPIE* **835**, 142 (1987).
5. M. Lowry, G. Lancaster, R. T. Peterson, G. McWright, D. Nelson, and B. Kidd, "Precision Transfer Function Measurements of Integrated Optical Modulators," *Proc. SPIE* **994**, 205 (1988).
6. M. Lowry, D. Jander, B. Kidd, P. Kwiat, R. Peterson, G. McWright, and F. Roeske, "A Study of the Photorefractive Effect in $LiNbO_3$ by Using Pulsed Illumination at 810 nm," *Proc. SPIE* **720**, 105 (1986).
7. M. Lowry, G. Lancaster, R. T. Peterson, B. Kidd, D. Nelson, and F. Roeske, "Analog High Bandwidth Single-Shot Data Link Using Integrated-Optical Modulators and a High Fidelity Optical Streak Camera," *Proc. SPIE* **987**, 68 (1988).
8. G. McWright, M. Lowry, E. Behymer, W. Brazes, G. Lancaster, and F. Roeske, "Gallium Arsenide Integrated Optical Devices in Adverse Environments," *Proc. SPIE Int. Symp. Tech. Optoelectronics* (Cannes, France, 1987).

Characterization of Layered Synthetic Microstructures

F. Wittmayer, R. Ernst, J. Hughes, and P. Waide

Early in 1988, we recognized the need for improving our x-ray-characterization capabilities for layered synthetic microstructures (LSMs). An LSM is a multilayer thin-film structure that acts as an efficient Bragg diffractor for x rays. To meet the calibration demands for current experiments, we required new x-ray-measuring techniques along with reference standards for LSMs. Our supplier of multilayers was Ovonyx Synthetic Materials Co. (Troy, Michigan).

Four x-ray systems within our facilities are capable of making the necessary x-ray diffraction measurements. Each is equipped with a theta, two-theta x-ray goniometer. These facilities are:

- The ion-accelerator (IONAC) subkilovolt x-ray facility, with seven selectable targets providing energies of 100–1000 eV.
- The Henke spectrometer facility, with interchangeable anodes and energies of 500 eV to 10 keV.
- The low-energy x-ray (LEX) facility, with selectable targets and energies from 1.5–8.0 keV.
- The Rigaku rotating-anode x-ray unit, with three anodes providing energies of 5.41, 8.04, and 17.48 keV.

The IONAC, LEX, and Henke x-ray systems all operate in a vacuum and use Siemens goniometers. The Rigaku x-ray generator operates in air and is equipped with a Rigaku x-ray diffractometer and a

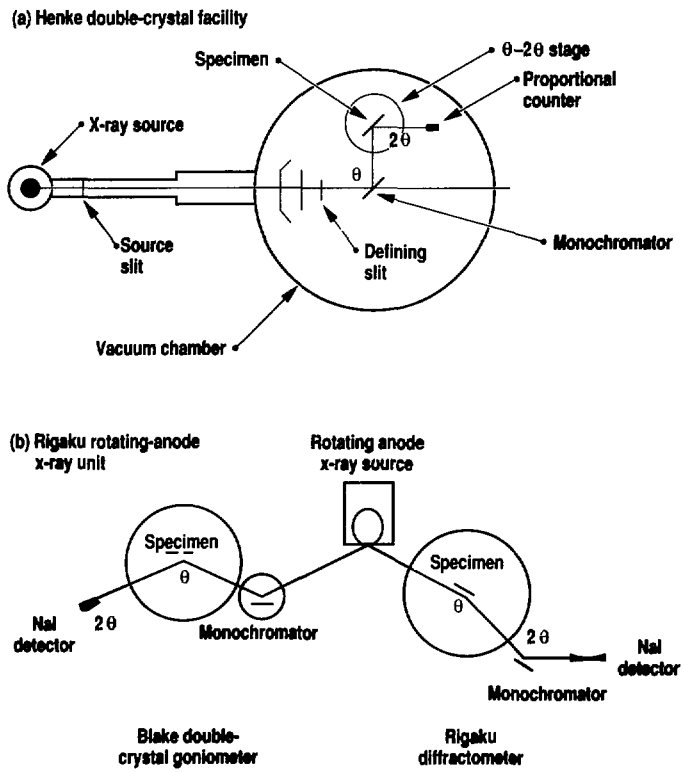

Figure 1. Goniometer geometries used on the (a) Henke and (b) Rigaku x-ray systems.

Blake double-crystal goniometer. The primary x-ray facilities for our measurements were the Henke facility at 704 eV and the Rigaku unit at 8 keV. We performed some cross-calibration checks on the IONAC at 932 eV. Figure 1 shows the goniometer geometries used on the Henke and Rigaku x-ray systems.

Characterization Standards

Three tungsten/silicon (W/Si) LSMs from Ovonyx became our standards. Ovonyx measured 2d spacings at 704 and 932 eV and supplied us with the results of their x-ray measurements. Because one W/Si LSM measured by Ovonyx showed a d spacing a few percent larger than the other two, this multilayer became helpful in determining our ability in measure small differences in d spacing. We measured the structures on the Henke (704-eV) and IONAC (932-eV) systems and compared our results with the Ovonyx measurements (Table 1). These three LSMs, along with single crystals of potassium acid phthalate (KAP) (001) and rubidium acid phthalate (RAP) (001) with 2d spacings of 26.63 and 26.12 Å, respectively, became our controls. For quality assurance, we remeasured LSMs from previous shipments when new shipments were received.

Using the Rigaku system, we mapped entire LSMs in terms of 2d spacing and reflectivity values, using as many as 25 different points on a given multilayer. The purpose of this work was to establish 2d variation so that we could select like areas of a given LSM and then cut out and assemble up to three tiles together on a substrate that would meet a d-spacing tolerance of ±1%. Figure 2 shows examples of various mounts for LSMs, and Fig. 3(a) shows the mapping pattern for a 25-point scan.

Some multilayer assemblies consisted of three 1.5- × 1-in. tiles epoxied on a single mount [Fig. 2(a)]. A ±1% tolerance in d spacing over the total length of the assembly was necessary because the device was to be used in an imaging system. These assemblies were to be measured for peak reflectivity, absolute-angle, full width at half maximum (FWHM), and uniformity of d spacing, all to better than ±1% (see Fig. 4). Thus, it became necessary to develop procedures and to design the hardware to complete measurements that would meet these specifications. The tile assemblies consisted of a substrate made from 4-in.-diam, 0.030-in.-thick Si wafers that were selected by the manufacturer (Monsanto) for flatness (2-μm rms or better). Tungsten/carbon (W/C) multilayers (usually 20-layer pairs) were then fabricated onto the Si wafers. Each 1.5-in. × 1-in. tile was cut from the best portion of the 4-in.-diam wafer. Although Ovonyx was pessimistic about meeting our tolerance of ±1%, the final d spacing was acceptable. We then measured the FWHM and scanned the devices for uniformity.

Table 1. Ovonyx, IONAC (932-eV), and Henke (704-eV) measurements of 2d spacing in three multilayer W/Si structures used as standards.

Sample number	Ovonyx (Å)	IONAC (Å)	Henke (Å)
1	45.93	45.99	45.55
2	45.96	46.46	46.04
3	47.72	47.27	47.10

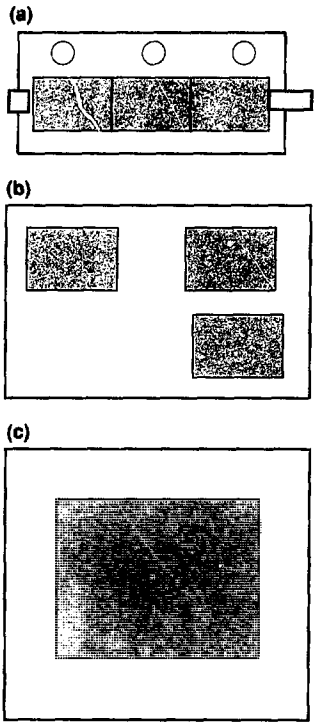

Figure 2. Three sample mounts for multilayer tile assemblies accommodated on various x-ray machines. (a) A tile device including KAP crystals on both ends. (b) Large-format assembly containing three 1.5- × 1-in. tiles epoxied on a single mount. (c) Single tile mounted on a single, larger substrate.

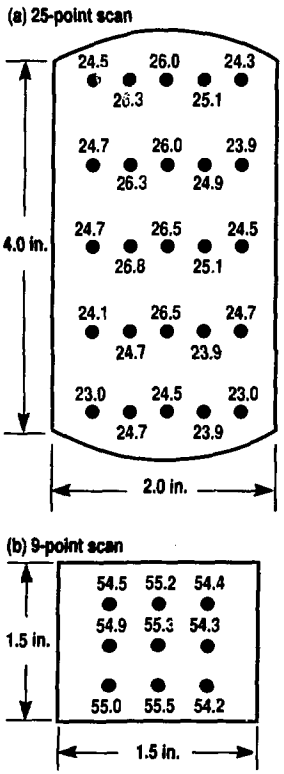

Figure 3. Mapping pattern for (a) a 25-point scan (W/C multilayer measuring 2.0 × 4.0 in.) and (b) a 9-point scan (W/C multilayer measuring 1.5 × 1.5 in.). Values shown are in Å.

Rigaku 2d Mapping

We used the Rigaku 8-keV source primarily for quality control of multilayer uniformity. This source was equipped with a Blake double-crystal goniometer, which contains a quartz monochromator on the primary goniometer, with a horizontal stage mounted on the theta axis of the secondary goniometer. After sampling multilayers from each shipment and performing the first 2d mappings, we discovered nonuniformity problems across many of the vendor-fabricated multilayers. A 2d variation of 2% over a 1.5-in. sample was typical. We mapped larger samples to determine which sections had the smallest 2d variation so that a smaller sample subsequently could be removed from that area.

In the Blake double-crystal goniometer, the stage provides linear motion across the face of an LSM and enough movement to map samples as large as 4 in. in diameter. We obtained vertical motion through manual repositioning. The beam spot on the face of an LSM was 0.25 × 0.50 in. to cover as much area as possible in each scan. We made our initial alignment with a KAP crystal, and we periodically reinstalled both the KAP crystal and a standard multilayer to verify alignment. The number of points required for mapping varied from three to 25, depending on the size of a given LSM (see Fig. 3). We ran a rocking curve at each point to calculate peak reflectivity and the corrected 2d spacing. After characterizing several samples, we sent them to the Henke facility to be scanned at 704 eV.

Henke Facility Calibrations

Our calibrations at 705 eV on the Henke facility included measuring d-spacing uniformity. To map d-spacing uniformity and integrated reflectivity across the surface of our multilayers, we built a remote-translation system for the Henke double-crystal facility. The system consisted of two Klinger translation stages assembled in an x-z configuration. This assembly was mounted on the theta stage of the secondary goniometer. Chamber size and beam placement limited our scan area to 6 × 0.75 in.

Operation of the stages was done by one 4-axis controller. Given a 0.75-in. vertical scan range and vertical x-ray collimation of 0.5 in., we were able to sample the entire surface of most LSMs without any repositioning. We had to reposition some of the larger pieces once for a complete scan. We selected a beam cross section of 0.050 × 0.500 in. to simulate the pixel resolution on the MIRREX experiment.

Integrated reflectivity can be determined by measuring peak reflectivity and width of the rocking curve. Our early measurements showed that the rocking-curve width of a given multilayer was fairly constant over the entire surface. For each sample, we measured the rocking curve at the center of the sample and at two points near its perimeter. Measurement of peak reflectivity was complicated by a drop in d spacing from a maximum near the center. By making linear scans across a sample at several different angles, we were able to build a composite profile of the uniformity in peak reflectivity.

We have found good agreement among the measurements obtained at the Henke, Ovonyx, and Rigaku facilities. The Blake facility can quickly and accurately determine 2d uniformity for any given size of multilayer. The close agreement between the results obtained by Ovonyx and our two machines (see Table 2) gives us added confidence in our data and will allow us to proceed in this our first major use of multilayers as a diagnostic tool.

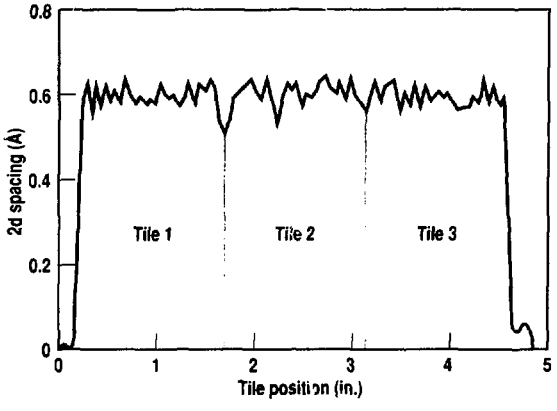

Figure 4. Measured 2d spacing across three sample tiles as a function of multilayer position.

Table 2. Comparison of Ovonyx, Rigaku, and Henke 2d-spacing measurements on ten 20-layer multilayers. The batch-to-batch tolerance is acceptable.

Multilayer number	Ovonyx (Å)	Rigaku (Å)	Henke (Å)
1	48.2	48.1	48.1
2	48.7	48.5	48.0
3	48.4	48.1	48.3
4	48.2	48.5	47.9
5	48.0	48.2	48.0
6	48.4	48.5	48.0
7	48.2	48.6	48.1
8	48.0	48.2	48.0
9	48.4	48.5	48.0
10	48.0	48.3	47.9

Thin Vitreous Carbon/Silicon Carbide X-Ray Mirrors

E. Bergin, G. Bergmyer, and B. Jacoby

At LLNL, we use x-ray mirrors for spectral and spatial diagnosis of pulsed x rays with energies below a few kilovolts.[1,2] X rays are totally reflected when they cross from one medium to another at less than the critical angle. However, the refraction index for x rays is less than one, so the reflection occurs external to the denser medium—in this case, the mirror material. X rays that strike the mirror at more glancing angles than the critical angle are totally reflected. If the absorption of x rays in the mirror material is low, the change in reflectivity across the critical cutoff energy at a particular mirror angle is quite sharp (about 0.1 keV) and can be used to resolve x-ray spectra. Consequently, mirrors have the uncommon but useful characteristic of behaving as efficient low-pass filters. The mirror also redirects x rays below the cutoff energy out of regions of high background, thus improving the signal-to-background ratio of the measurement.

We fabricated a grazing incidence x-ray mirror (Fig. 1) with low surface distortions and roughness. The mirror has a surface figure of less than 2 waves (measured with a Zygo interferometer) and a surface roughness of less than 5 Å rms (measured with a Sommargren profilometer). Both measuring systems used He-Ne light at a 6328-Å wavelength. The mirror's reflective area is 5.5 × 8.0 in., and its maximum thickness is 0.355 in. The reflectivity of the mirror matches theoretical predictions (Fig. 2), and the spatial distortion of the reflected x rays is less than 0.005 degrees (Fig. 3).

In our application, we use numerous x-ray beams in the detector area, so we needed a mirror with a relatively thin cross section and a large reflective area. Previous x-ray mirrors relied on thicker substrates, typically 1.625-in. Pyrex, and a hard, high-strength bonding adhesive to achieve an equivalent surface figure. Our approach overcomes warpage and distortion by using the high strength of the thick base material to dictate the figure and form to the weaker and thinner reflective surface.

Because the figure of a mirror surface improves as the mirror stiffness is increased, we tried to make the mirror as stiff as possible within the system space constraints. The deflection of a mirror on kinematic three-point mounting is proportional to the inverse of the product of Young's modulus of elasticity and the cube of the thickness (from the moment of inertia):

$$\text{Deflection} \propto \frac{1}{Et^3}, \qquad (1)$$

where E = modulus of elasticity and t = thickness.

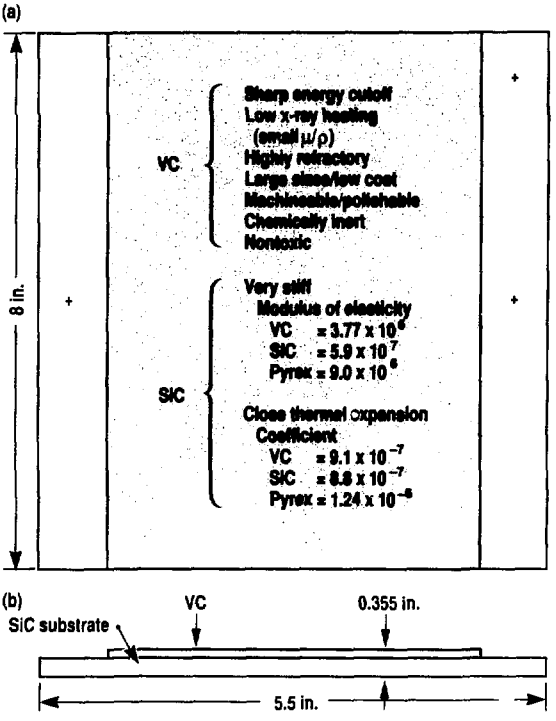

Figure 1. Schematic of our thin vitreous-carbon/silicon-carbide (VC/SiC) x-ray mirror: (a) top view and (b) end view. Plus signs show where the spring, ball-type plungers contact the mirror.

Additionally, the stiff base material must be compatible with the reflective surface and bonding material at the interface because stresses and loads by and through the bond—mainly from thermal expansion differences—could affect the final figure of the mirror. We wanted to use the maximum allowed thickness of the stiff base material to increase stiffness, which is related to surface flatness, and minimize the reflective layer thickness to its minimum safe value for x-ray source interaction. Therefore, the stiff base material dictates surface figure to the less stiff reflective area. Our final design (Fig. 1) is a 9-mm-thick mirror consisting of a 0.040-in. reflective layer of vitreous carbon (VC) bonded to a SiC substrate using an adhesive that cures at room temperature.

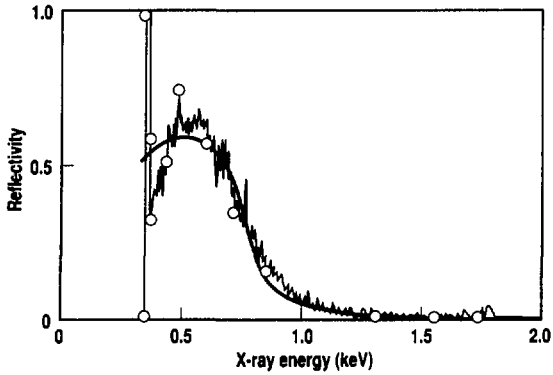

Figure 2. The measured reflectivity curve of the mirror as a function of x-ray energy with the mirror angle at 2 degrees. The theoretical curve is superposed for comparison. The x rays (continuum radiation from a tantalum anode in a Henke source) were detected in a proportional counter, and the curve was generated by dividing the reflected spectrum by the direct spectrum.

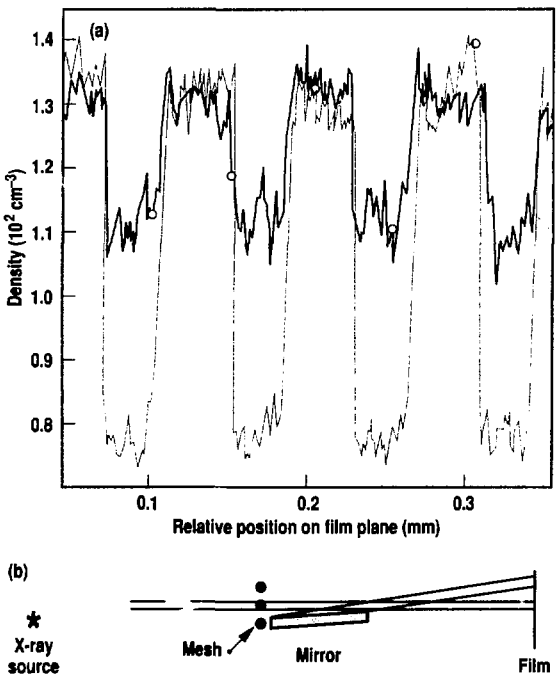

Figure 3. (a) Direct (blue rule) and reflected (solid rule) shadow-screen x-ray images of a mesh mounted in front of the mirror. Images were densitometered and superposed to compare sharpness. (b) Schematic of the experiment. X rays were generated by a point source far from the mirror.

Vitreous carbon, the reflective surface on our x-ray mirror, is a highly pure, nontoxic material with a high degree of surface chemical inertness, including low porosity and gas permeability, and a high specific heat and sublimation temperature. It can be ground and polished like optical glass and is available in large sizes at low cost. It also has a low x-ray absorption cross section, which sharpens the reflection cutoff and minimizes x-ray heating, and it has a very-low-energy K-absorption edge, which permits low-energy x-ray reflection above 0.300 keV. Vitreous carbon is obtained from pyrolysis of an organic polymer (a phenolic resin), which produces random glass-like bonding between the carbon atoms. For the x-ray mirror, we used Sigradur-K, a VC that we purchase in 3-mm-thick sheets.

We chose SiC for the substrate material because its thermal expansion is compatible with the reflective surface layer of VC. SiC is a stiff material (modulus of elasticity = 5.9×10^7) with high strength and hardness. It can be used in a vacuum and resists chemical attack. For the x-ray mirror, we used Hexoloy SA—a pressureless sintered alpha crystal, single-phase silicon carbide with no free silicon.

Mirror Fabrication

Before bonding the VC plate to the SiC plate, we used a blanchard-grinding process to smooth the joint surfaces to a flatness of less than 0.001 in. We grind the sheets on both sides in an iterative process—grinding one side and then the other. To reduce thermal expansion distortions, we chose a soft bond adhesive (TRA-CON 2135D) that cures at room temperature. A tensile test of 1-in. samples showed that the adhesive strength of the bond was >450 psi and that the VC is possibly weaker than the bond.

To bond the materials, we applied a drop of adhesive in the center of each plate and slowly pressed the plates together, allowing the adhesive to spread toward the edges of the plates without forming air bubbles. Then we uniformly added 1-psi loading over the entire bonding area, which produced a bond line of slightly less than 1 mil. This load was removed after 16 hours, and the bond was allowed to cure for three days. Then the bond material was continuously cycled in an oven for two days, with temperature cycles of 20–150°F changing 10°/hour. Temperature cycling at the maximum temperature excursions to which the mirror may be exposed is very important to hold the surface figure and must be done before the mirror is polished. Our studies showed that surface distortions occurred mainly during the first temperature cycle, but no additional distortions occurred in subsequent cycles

After the temperature cycles, we polished the mirrors. The polishing process required precise materials and methods to obtain the desired results. First, the VC thickness was reduced by blanchard grinding from 3 mm to about 1.02 in. For the final grinding, we used 30-μm Al_2O_3 followed by 9-μm Al_2O_3 to remove the subsurface damage done by the blanchard grinding process. The VC was polished in two steps—first with 6-μm diamond powder on pitch, then with 0.25-μm powder.

The pitch lap was 12 in. in diameter, and the method in which the diamond was applied to the lap was of critical importance to the quality of the surface finish. The polishing was done with a Strasbaugh over-arm oscillating machine, and the mirror extended slightly over the edge of the lap with each stroke to remove its convex shape. The mirror was polished on the machine's slowest speed, and the speed of the eccentric was set to keep the parts rotating at the same speed as the lap. Throughout the polishing process, we periodically checked the figure of the mirror and did not cut the mirror significantly until we obtained a good fit between the mirror and lap. The surface figure and surface roughness affected each other in that acceptable surface finish (<5 Å) was only obtained when a surface figure near the requirement (<2 waves) was maintained.

The mirrors were very stable during polishing and seemed to be more stable than VC/Pyrex mirrors, perhaps because SiC and VC are a better thermal match (thermal expansion coefficients = 8.8 and 9.1×10^{-7}, respectively) than are Pyrex (thermal expansion coefficient = 1.24×10^{-6}) and VC. Prototype mirrors tested over a temperature range of 70–110°F showed surface distortion of 0.75 waves, which is acceptable for our purposes. The peak to valley distortion over the full surface of the finished mirrors ranged from 0.5 to 1.2 waves (He-Ne laser with 6328-Å wavelength), and the average rms surface roughness was 2.2–3.9 Å for the eight mirrors we fabricated.

We also designed a compact kinematic mirror holder (Fig. 4) to maintain alignment despite vibration and rough handling. The holder minimizes the distortion of the mirror surface and allows us to position the mirror precisely each time we use it. To hold the mirror in place, we put three spring ball-type plungers into ultrasonically machined slots in the SiC substrate (Fig. 1). Each plunger is sufficiently compressed with a 10-lb load, so the mirror is precisely positioned against the stops. The mirror is free to move under force and can be mounted in any orientation. The kinematic features of the mirror mount are placed directly into the SiC substrate without an interfacing material or part, thus making the assembly extremely compact. The mirror surface was distorted only 0.04 waves by mounting, and angular movement during a rough-handling and vibration test was less than 1 arc-s.

One month after the final mirror fabrication, we conducted a long-term temperature test. The two-week test consisted of a continuous temperature cycle of 20–150°F changing 10°F/hour. The resulting shift in the surface of the mirror was measured at 0.095 waves, but we may be approaching the repeatability limits of the interferometer.

We also performed a standard outgassing test for high vacuum compatibility on the mirror. After 1.9 hours, the gas load was 8×10^{-5} Torr-L/s, a[illegible]ter 189 hours, 4×10^{-7} Torr-L/s. Water vapor accounted for most of the gas evolved. This gas load is typical for the materials used, and we found no unaccountable gas species.

To measure the spatial distortion of x rays reflected by the mirror, we transmitted a broad parallel beam of subkilovolt x rays through a mesh mounted in front of the mirror, so that part of the beam was reflected by the mirror and part passed directly onto x-ray film (Fig. 3). The direct and reflected beams were recorded side by side on the same piece of film so any distortion in the reflected image is apparent. Figure 3 shows a section of the densitometered reflected image (the smaller-amplitude signals) superposed on a section of the direct images. Equivalent sharpness can be observed (to about 1 mil in Fig. 3) to the reflected and direct images of the edges of the mesh, demonstrating that the mirror is not distorting the x-ray image within the resolution of the measurement (0.9 mil or 0.005 degrees).

Figure 4.
Photograph of the VC/SiC x-ray mirror in the kinematic mirror holder assembly.

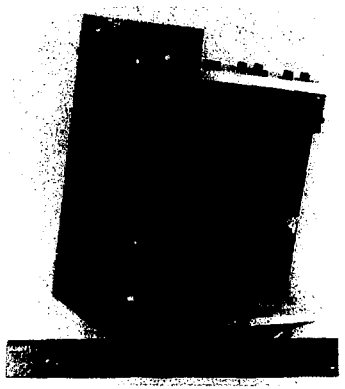

The mirrors have been calibrated in our x-ray system and have matched predicted calculations, indicating that the mirror is functioning properly at our energy levels.

References:

1. J. P. Stoering, R. Crabb, M. E. McGee, and G. Burginyon, "Double Reflection X-Ray Spectrometer for Pulsed Source Diagnostics," *Rev. Sci. Instrum.* **52**, 825 (1981).
2. G. A. Burginyon, J. P. Stoering, R. W. Hill, and L. V. Singman, *J. Appl. Phys.* **49**, 513 (1978).

Quartz Finger Mixers

B. A. Remington, G. Burginyon, and D. L. Anderson

We are working to improve the sensitivity of spatial-pattern measurements in our experiments. Our principal effort is in developing microchannel-plate detectors. These detectors have several orders of magnitude gain in signal output light over conventional passive fluor detectors. However, because the microchannel-plate detectors are expensive and complicated compared to fluor detectors, we created a new fluor geometry and achieved an order of magnitude gain in their signal output light.

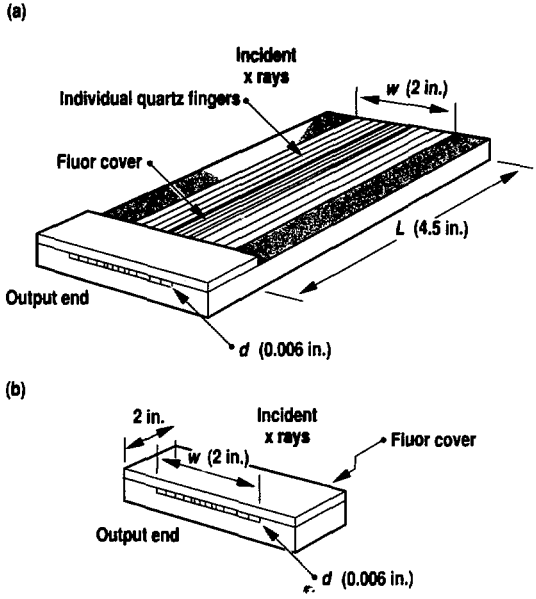

Figure 1.
Comparison of (a) new quartz finger mixer with (b) conventional quartz mixer. In (a), the incident x rays strike the side (Lw) with its larger area of fluor and create a magnitude of gain in signal output light. In (b), the incident x rays strike the smaller area (dw) and produce less signal output light.

Description of Geometry

Figure 1 illustrates how we achieved the gain for the fluor detector. First, we constructed a test quartz finger mixer [Fig. 1(a)] using 50–70, 0.03-cm-wide quartz fingers that we bonded together with epoxy. This bonding created new detector dimensions—length 4.5 in., width 2 in., and depth 0.006 in. The original fluor detector [Fig. 1(b)] measured only 2 in. long, 2 in. wide, and 0.01 in. deep. As with the original fluor detector, we attached an optical fiber to the opposite end of x-ray incidence on each finger. But instead of attaching the thin, 3.5-μm sheet of fluor over the end of the detector, we attached it over the entire side area. Next, instead of having the x rays strike the end piece (only 0.01×2 in. in the conventional fluor detector), we had the x rays strike the larger side area, now 4.5×2 in.

In the end-entry geometry of the conventional fluor detector, the x rays excited only a small area of fluor given by dw in Fig. 1. The quartz bounced the light created by the interaction between the x rays and the fluor and homogenized it at the fiber location on the other end of the detector. Each optical fiber sampled the light over the area (πr^2) at its face. Thus, for an x-ray flux given by dE/dA, or energy per area, the fiber saw a light signal proportional to

$$(dE/dA)(dw)(\pi r^2/dw)\,,$$

where d is the depth and w is the width of an individual quartz finger within the detector. On the other hand, with the improved side-entry geometry and longer and thinner quartz fingers of the new detector, we could generate light over a larger exposed area of fluor, which is shown in Fig. 1 as Lw. The quartz homogenized the light over the output area of dw so that the fiber saw a light signal proportional to

$$(dE/dA)(Lw)(\pi r^2/dw) .$$

The gain over the end-entry geometry was L/d. In other words, we got ten times as much light emission from the optical fibers with the new side-entry, quartz-finger-mixer geometry as we did with the end-entry geometry in the conventional fluor detector.

Fluor-Quartz Coupling

Problems still exist that prevent us from achieving the full gain of L/d when we couple the fluor with the quartz fingers because fluor and quartz have different indices of light refraction. Each medium creates a different distribution of light with respect to solid angle. Light generated in the fluor alone is distributed uniformly in all angles; however, light coupled to quartz is not.

Using Snell's law, the distribution of light in the quartz is proportional to

$$\cos\theta/\{1 - [n_q/n_f)^2 \sin^2\theta\}^{1/2} ,$$

where θ is the angle between the normal to the face of the fluor-quartz interface and the incident ray of light. The angles that are collected by the fiber are close to 90 degrees. Unfortunately, the fraction of light available is low, around 90 degrees, and is in fact zero at 90 degrees because of the cosine factor. The gain is reduced by a factor of 0.154 for the value of 1.58 for the index of refraction for the fluor (n_f), 1.46 for the index of refraction for the quartz (n_q), and 0.2 for the numerical aperture of the optic fiber typically used. This reduction is derived by integrating the angular distribution over the angle accepted by the fiber. The numerical aperture of the fiber determines the limits on such an integral. Thus, in coupling light from the fluor to the quartz, almost an order of magnitude gain is lost.

Experimental Results

We tested the new quartz-finger-mixer design using the side-entry configuration. The individual quartz elements had the following dimensions: $L = 0.73$ in; $d = 0.08$ in; and $w = 0.059$ in. The individual quartz fingers were both bonded and isolated from one another with a special epoxy used in cladding optical fibers. This epoxy has a refraction index of 1.42 for light. Since the refraction index for quartz is greater than this, total internal reflection takes place and prevents the light from escaping and reaching neighboring quartz fingers.

We next used a 3.5-μm-thick piece of BC422 fluor, which has a peak emission at 370 nm. This piece was hand laid on the side of the quartz finger mixer and then smoothed flat to ensure surface contact. We measured this assembly at the Low-Energy X-Ray Facility and produced Al k_α radiation at 1.487 keV. We placed a fiber on one element of the quartz-finger-mixer array and ran it to a cooled photomultiplier tube with a GaAs photocathode. We operated the detector in the counting mode so we could detect single photons emitting from the fiber.

In addition, we measured for several end-entry cases using the new quartz-finger-mixer array. In the first experiment, we removed the fluor from the side and placed it over the end of the array. This placement produced an end-entry geometry with the same mixer assembly and allowed us to compare the gain. In the second experiment, we placed Al foil over the end of the quartz finger mixer. In earlier calculations, we only included the angular spaces producing light rays that propagated in the direction of the fiber. In this test, we found that a simple factor of 2 can be had from the rays propagating in the angular space away from the fiber. We set up a third experiment with a mirror on the end of the quartz finger mixer. We predicted that the rays that shot in the opposite direction from those that reached the fiber could be collected once they hit the mirror and reversed their direction. With this concept, the predicted gain for the mirror assembly was

$$2(0.154)(L/d) = 2.8 .$$

The actual gain factor, however, was 3.05, showing that the concept worked.

Conclusions

The quartz-finger-mixer concept has been tested on four spatial measurements. The value for L for this field unit was 10 cm, while the value for d was 60 mil. These values produced a gain of 10 over the previous end-entry geometry. In recent tests at the ion-accelerator facility, we measured and confirmed this factor. Thus, by creating a side-entry geometry with increased dimensions, we have produced an order of magnitude improvement in sensitivity for the passive fluor detector.

A New Generation of Array Camera

N. C. Lau

Our current downhole imaging system for PINEX (Fig. 1) is the Reticon 100 × 100 array camera. This device uses a metallic cable that is capable of carrying an image at a rate of 45 Mbit/s to the uphole Image Data Acquisition (IDA) system. A four-row add system of the Fairchild 380 × 488 charge-coupled device (CCD) array camera is periodically fielded with the streak camera. An image of 380 × 122 pixels is transmitted uphole to the IDA system. As the prompt diagnostic becomes more sophisticated, the array camera system must collect more data with greater accuracy in less time. During this fiscal year, we completed the design of the Reticon 128 × 128 camera system, redesigned the Fairchild 380 × 488 camera, investigated speeding the readout of the Fairchild 380 × 488 array sensor at 40 instead of 20 MHz, and signed a development contract with Kodak for a high-performance 512 × 512 CCD array sensor.

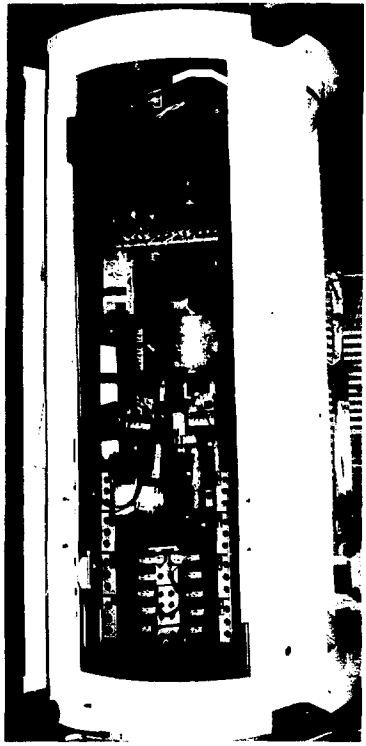

Figure 1. PINEX module. The camera fits inside this unit.

Reticon 128 × 128 Camera

The new Reticon 128 × 128 solid-state image sensor array (Fig. 2) is similar to that of the Reticon 100 × 100 sensor except that over 60% more photodiodes are arranged into 128 × 128 matrixes. The camera design uses programmable read-only memory (PROM) and surface-mount technologies so that the overall size is small and the camera is easy to field. As a result of multilayer printed circuit (PC) technology, the noise level of the camera is low, and the dynamic range is greater than 500 at 760 nm and greater than 300 at 520 nm.

Data from the camera are transmitted uphole through a coaxial cable with a transmission rate of 72 Mbit/s. The frame readout time is less than 2.4 ms. We have modified the Fairchild (180-MHz) bit-sync module for use in the Reticon 128 × 128 camera IDA system. We are also developing common bit-sync and frame-sync modules for the Reticon 100 × 100, Reticon 128 × 128, and Fairchild II cameras. The Reticon 100 × 100 sensor will operate in the Reticon 128 × 128 camera with a frame readout time of about 1.5 ms.

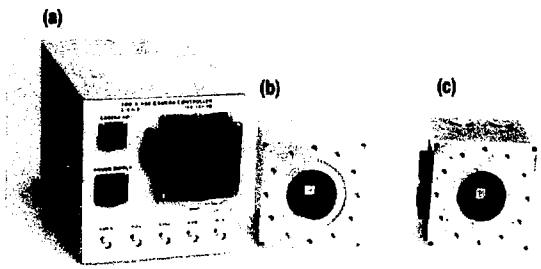

Figure 2. (a) and (b) The 100 × 100 array camera. (c) Our new 128 × 128 camera is far more compact and is housed in a single module.

Fairchild II Camera

The Fairchild II camera is a redesign of the previous Fairchild 380 × 488 camera. The Fairchild II design uses PROMs, a slim dual line-in package (DIP), and multilayer PC technologies to reduce the overall size, to eliminate most adjustments, to recover more data columns, and to reduce electronic noise to the floor level. The resultant dynamic range is about 150 of ×4 from blooming (or 200 of ×3 from blooming). We improved the contrast transfer function (CTF) to an average of 75% by adding a video peak-stretching circuit so that the timing of the A/D converting pulse is not critical.

Data for the Fairchild II camera are transmitted uphole through an 820-nm fiber cable with a data transmission rate of 180 Mbit/s. The frame readout time is about 2.5 ms for a four-row add system. The data transmission system remains the same, except that we will replace the current optical transmitter with a MA/COM, Inc., transmitter module.

Fairchild III Camera

The design for a Fairchild III camera is currently in the research phase. We cannot yet project how much performance we can obtain from the Fairchild CCD 222 by clocking at a video rate of 40 MHz. The video rate of the Fairchild II is 20 MHz although the specification is 7.16 MHz. Data will be transmitted uphole through a 1300-nm fiber cable with a data transmission rate of 360 Mbit/s. The frame readout time is about 1.3 ms for a four-row add and 2.5 ms for a two-row add system.

While designing the data-link system for the Fairchild III camera, we intend to look at two similar links. The first link will operate at up to 360 Mbit/s for the Reticon 100 × 100 and 128 × 128 cameras and the Fairchild II and III cameras. The optical transmitter, receiver, and clock-recovery circuit must be inexpensive (<$1000). The second link will operate at up to 1 Gbit/s for the Kodak camera.

Kodak 512 × 512 Camera

We have signed a contract with Kodak to develop a solid-state, 512 × 512 array sensor with a dynamic range of not less than 1000 to 1. This device will have over 70% CTF at 20 line pair/mm and blooming suppression well in excess of 8×. The sensor will be segmented into 16 outputs to meet our specification of a 2.5 ms readout time. If two optical-fiber links are used to carry the image uphole with eight outputs multiplexing into one, then we will require a data link of greater than 700 Mbit/s. By multiplexing four outputs into one, the 360-Mbit/s data link may be used. If, on the other hand, all 16 outputs are multiplexed into one data link, then a 1.4-Gbit/s data link will be required.

Improving PINEX Shutters

S. W. Thomas

Image-intensifier tubes are electro-optical devices used to detect, intensify, and shutter optical images from the near-ultraviolet to the near-infrared regions of the electromagnetic spectrum. They are used to intensify weak images for night vision, astronomy, electron microscopy, medical research, and radiology, and as high-speed light shutters. In our PINEX work, they are used to intensify an image and as an active light shutter, permitting very short exposure times.

We have been working to improve the shuttering time of the image-intensifier tubes used in our PINEX cameras. Several approaches were investigated in FY88. Of these, nickel-plating the cladding glass of the cathode substrate has resulted in subnanosecond shuttering times, a ten fold improvement over current shutter times.

Shuttering an Intensifier

Our intensifier tube consists of an image sensor (a photocathode) that converts an incident radiant image to a low-energy electron image, a proximity focusing lens that focuses the electron image, a microchannel plate (MCP) that amplifies the electron image current, and, finally, a second proximity focusing lens and a phosphor screen that convert the electron image to a light image. When the cathode is forward biased, the intensifier tube is gated on and amplifies light. Reverse-biasing the cathode with respect to the MCP input repels the electrons emitted from the photocathode and shuts the tube off.

The cathode is formed on a conductive substrate, usually nickel or some other metal with low resistance. The gating voltage is applied at the edges of the cathode and MCP and propagates inward. Thus, the outside edge of the tube turns on first, and this "on" state propagates inward to the tube's center. The period from application of the gating voltage until the tube reaches its normal operating condition is called the irising time. Figure 1 shows the intensity distribution from the output of an 18-mm image tube after the gating voltage has been applied for 1 ns. The irising effect is seen in the tube's edges coming on before its center.

We measure irising time at EG&G's Amador Valley Office (AVO) facility, using a frequency-doubled, 30-ps-FWHM YAG laser. A small portion of the laser pulse is tapped off to trigger an electrical gating-pulse generator. The main part of the laser pulse is passed through an adjustable delay and then introduced to the cathode of the tube under test. Changing the arrival times of a sequence of laser pulses allows us to make a record of the intensifier tube's output rise time on film or with a CCD array camera. The computer-generated representation of intensity, shown in Fig. 1, is based on data from a CCD array camera.

Irising time, which ranges from several microseconds to <1 ns, is controlled by the electrical time constant of the cathode substrate's distributed resistance and by the distributed capacitance of the gap between the cathode and MCP surfaces. Capacitance is fixed by tube geometry and impacts other tube parameters if changed. It ranges from 20 to 30 pF for the 18-mm tubes used in our PINEX cameras. Our efforts to shorten irising time have thus centered on reducing the cathode substrate's resistance. We have investigated several approaches.

Heavy Underlay

Substrate resistance can be lowered by applying a conductive coating to the cathode faceplate before forming the cathode. A 50-Å-thick coat of nickel will produce an irising time of 1 ns, but the input light will be attenuated by about 50% because of absorption by the nickel. A 5-ns irising time can be achieved with about 20% absorption. Intensifiers using this approach are available commercially from ITT and Varo, but their reduced light transmission is a serious drawback.

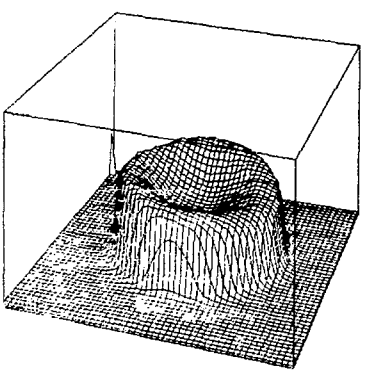

Figure 1. Isotrace of the output intensity distribution from an 18-mm intensifier tube 1 ns after the gate-on voltage was applied. The irising effect is shown by the greater brightness at the edge as compared to the center.

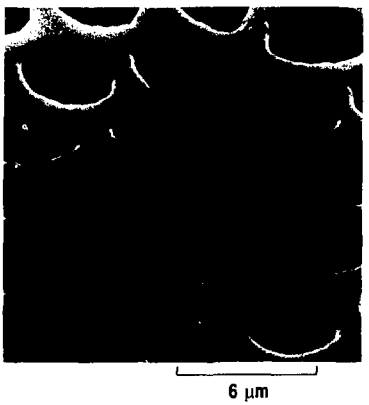

Figure 2. Electron microscope photograph of a fiber-optic faceplate with 1.2 µm of nickel deposited on the webbing. The active fiber diameter is about 5 µm, with a center-to-center spacing of about 6 µm.

Wire Mesh

A wire mesh of about 80% transmission can be cemented to the outside of the cathode surface. A pulse of about 1500 V is then applied between this mesh and the screen electrode. Capacitive voltage division of the pulse occurs among all of the tube's elements so that the required 200-V pulse is produced between the cathode and MCP input. The remainder of the pulse is shared among the MCP, the MCP-to-screen gap, and the input fiber-optic faceplate, with most of the voltage being dropped across the latter. Irising times of 120 ps have been achieved with this wire-mesh approach. Intensifier tubes with the mesh are commercially available from Grant Applied Physics, Inc., but they are very expensive.

Strip-Line Structure

We also investigated the feasibility of building the cathode-to-MCP input into a strip-line structure of constant impedance. Combined with a low cathode substrate resistance (like that possible with the plated webbing described below), this approach would allow subnanosecond gating, limited only by the ability to generate the electrical gating pulse. The width of the active area to be gated would determine the structure impedance, which would be about 6 Ω for a 12-mm width.

The most difficult part of this approach is to maintain uniform impedance from the input leads or tabs, through the tube body walls, to the cathode-MCP gap. Both dielectric constants and electrode spacing change during this transition. Because of the difficulty of implementing this approach, we concluded that its pursuit is not warranted at this time.

Plated Webbing

Theoretically, the cladding glass in a fiber-optic plate transmits no light and can be metalized to lower effective substrate resistance without reducing the plate's transmission. The process involves several steps. First, a 336-Å nickel layer is evaporated over the inside surface of the

cathode's fiber-optic faceplate. Next, positive photoresist is applied over this layer and then exposed through the faceplate and nickel, using the plate as a self-aligning mask for the active fiber area. Only the core glass area is exposed, leaving the photoresist over the cladding, or webbing, unexposed. Next, the photoresist is developed and washed off, exposing the nickel that covers the core fibers. This exposed nickel is removed in a dilute nitric acid or ferric chloride bath. The remaining photoresist, which covers the webbing, is then removed, leaving only the nickel covering the webbing. The final step is to electroplate this nickel seed layer to a thickness of about 1 μm.

Figure 2 shows an electron microscope photograph of a fiber-optic faceplate with a 1.2-μm layer of nickel plated over the webbing. We have just concluded a joint project with ITT to develop this process. LLNL applied the nickel to the webbing of several faceplates, and ITT incorporated them into intensifier tubes. RCA and Varo have also shown interest in the process.

Electroplating the nickel seed layer to increase its thickness and lower its resistivity has presented challenges. As yet, we have been unsuccessful in producing consistently good results; however, three tubes with just the evaporated 336-Å nickel layer have been constructed and are being tested. The irising time measured for these tubes is so much shorter than the rise time of the electrical gating pulse that an accurate measurement is not possible. Our gate-pulse generator has an output impedance of 50 Ω, which limits the theoretical electrical rise time to about 2.2 ns because of the tube's 20-pF input capacitance. However, since the tube is initially reverse biased by about 50 V and comes on before the gating pulse has reached its peak, the effective gating rise time is significantly less than 2 ns.

Figure 3 shows the output intensity of one of these tubes as a function of time. The tube output is dark when turned on (0 ps), starts to be discernible at 267 ps, and is nearly fully on at 467–533 ps. This turn-on time is mostly due to the pulser's 5-ns rise time. Because the irising period is shorter than the test system's resolution, it is barely discernible in these photographs. However, we estimate it to be in the 250- to 300-ps range.

We have just received a Grant Applied Physics pulser with a 200-ps rise time and have built a matching transformer that will reduce the gating pulse-source impedance to 1.6 Ω. These additions to our test station at AVO will allow us to measure irising times of 100 ps accurately.

Mesh Underlay

For quartz cathode faceplates, the plated webbing process obviously cannot be applied, since there is no webbing. However, a mesh or grid can be applied to produce the same effect, using many of the same steps as for plated webbing. In the process we have chosen, 0.5 μm of nickel is evaporated on the cathode side of the faceplate. Next, photoresist is applied and exposed through a photolithographic mask with 3-μm-wide lines separated by 98 μm. The exposed photoresist is developed and washed off, and the exposed nickel is removed by etching, leaving a 100-μm grid of 2-μm-wide wires, half a micrometer thick.

We are currently fabricating two mesh-underlay tubes (we are forming the mesh on vendor-supplied faceplates) and will compare them with two similar heavy underlay tubes being produced by Hamamatsu. This testing will be done in FY89.

Summary

We have explored several ways to shorten irising time and have demonstrated that subnanosecond shuttering can be economically achieved using a plated webbing technique. In FY89, we will compare the heavy underlay technique with that of a mesh underlay for use with quartz windows, as needed for infrared response. We will also improve our ability to measure irising time.

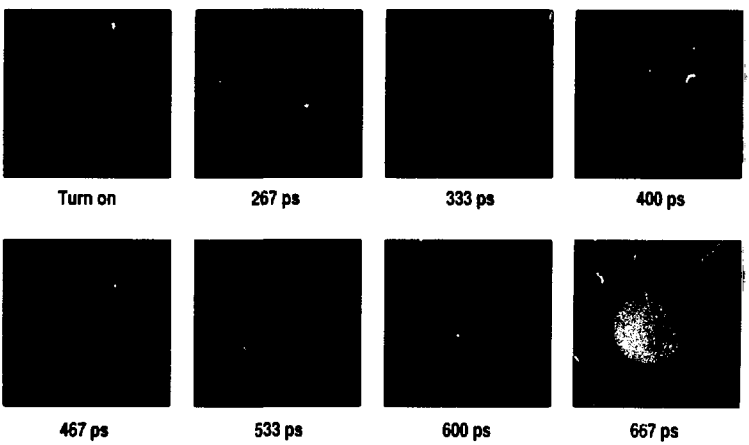

Figure 3. Turn-on characteristics of an 18-mm intensifier tube with a 330-Å-thick plated webbing underlay. The tube is just starting to turn on at 267 ps and is fully on by 533 ps. Irising time, displayed as amplitude shading from center to edge, is a fraction of the turn-on time.

High-Speed Digital Recorders

D. N. Hunt

The oscilloscope is our standard instrument for recording fast analog signals at the NTS. A camera is placed on the face of the scope, and the signal from the experiment is recorded on film. This film is later developed, digitized, and analyzed with software tools available on our computer systems. We have used this methodology for the past 30 years, and it is well understood by operational personnel, data analysts, and experimental physicists. The results produced are trusted and agree with computer models of the devices tested.

Two concerns have arisen with our standard system. The fielding of the current system is labor-intensive. In addition, we have a space problem due to the limited number of recording instruments that can fit in an equipment rack. With the camera on the face of the oscilloscope, the usual number of recording instruments in a 6-ft rack is four and the maximum number is five. Both problems can be addressed through the use of digital recorders. Two to six times the number of digitizers can be fielded in the space occupied by oscilloscopes. If all oscilloscopes on applicable signals were replaced with digital recorders, it would be possible to eliminate one trailer on some shots and thereby generate substantial savings. As computer-based tools used to control digital recorders improve, increasing support for automated operation of such equipment will emerge. Automation will decrease the labor required for setup and trial runs.

High-Speed Digital Recorders

Digital recorders sample an analog signal at fixed time intervals. Each sample is presented to an analog-to-digital converter (ADC), which produces a binary value proportional to the amplitude of the original signal. This binary number is stored in digital memory, and the next sample is processed. Digitizers of interest include those with sample frequencies of from 100 megasamples/s (Msamples/s) to 2 gigasamples/s (Gsamples/s). Digitizers with a sample rate much higher than 2 Gsamples/s are of great interest; however, such devices are currently unavailable commercially.

No ADCs are available that sample at a 2-Gsample/s rate and that also produce 8 to 12 bits of resolution. One technique is to demultiplex the analog signal into several slower sample streams that are then presented to an ADC running at a slower rate. Data from each ADC are stored in memory. Separate data streams are recombined as they are read from digital memory. Another technique is to demultiplex the analog signal into several banks

Table 1. Summary of available digital recorders.

Vendor and model	Sample rate	Resolution (bits)	Maximum memory (samples)	Effective bits
LeCroy 8818	100 Msamples/s	8	2 M	7.2
LeCroy 8828	200 Msamples/s	8	2 M	6.3
LeCroy 6880	1.35 Gsamples/s	8 or 11	10 k	6.1
HP 54111D	1 Gsamples/s	6	8 k	5.5
Tektronix 11602	2 Gsamples/s	8	32 k	6.9
Sequence 3100	1 Gsamples/s	10	1 k	6.2
DSP 2301	200 Msamples/s	8	1 M	—
Analytek An2000	2 Gsamples/s	11	8 k	—

of analog storage at the sample rate of the recorder. Once the recorder has gathered all samples for which it has storage, the analog samples are multiplexed back into a signal stream. This stream is fed to a single, high-resolution ADC at a slower rate and then to digital storage.

Matching the data from the multiple data streams can be a problem. Data from each of the multiple ADCs, sample-and-holds, and analog storage cells must be matched to the data from all other streams. The most common method for matching data streams is to characterize each one with known analog signals. The known signal is passed into the digital recorder being characterized. Actual values recorded in memory are compared to each other, and several parameters are calculated from the results. Passing the acquired data through compensation algorithms using the calculated parameters produces results that match the data from the multiple data streams. These parameters are stored in memory in the digital recorder. Upon acquisition of experimental data, the stored parameters are used with the compensation algorithms on the recorded raw data to produce processed data.

Table 1 shows eight of the more applicable digital recorders and their specifications. A reasonable selection in sample rate, memory length, and resolution is available. Nonvolatile memory is one of our major requirements because we have no guarantee that the main power to recording trailers will continue to operate after ground shock from an event. We also require digitizer sample rates in the range from 100 to 300 Msample/s as well as rates in the Gsample/s range. Our user community is also interested in rates 1 to 2 orders of magnitude higher.

In addition to the advantages already discussed, digital recorders have a long record, a convenient data format, and reasonably low cost per channel. The long record length and constant time resolution are both useful. (On an oscilloscope, as sweep length increases, time resolution drops.) The digital format of data saves steps in the data-reduction process. The low cost per channel, compared to an oscilloscope, addresses one of our most important issues, that of cost effectiveness. Digital recorders that have the best channel-to-space ratio also have the lowest cost per channel.

Equipment Evaluation

Our primary goal is to select a set of standard units. The units of interest will be evaluated both in the laboratory environment and in the field. Laboratory evaluation is performed first against signals produced by a signal generator. Resultant data are compared against the ideal waveform. The differences measured between the recorded and ideal signal are used to calculate such characteristics as differential nonlinearity, missing codes, aperture uncertainty, and effective bits.

A second set of laboratory tests consists of checking the response of digital recorders against the response of our standard oscilloscope/film recording system. The signals used in these tests are more representative of signals expected in the field environment. Such tests provide a better measure of how a digital recorder will perform on actual experiments at NTS. We are working with personnel from Los Alamos and EG&G on these tests.

Once a recorder performs well in the laboratory, we conduct tests in a field setting. The goal of field tests is to measure the unit's response to actual experimental signals and to determine its fieldworthiness. Most digital recorders can be controlled via the IEEE standard general-purpose interface bus (GPIB). In addition, most vendors provide IBM PC-based tools for control. The first fieldings of a recorder make use of these tools and operate the digital recorder in a configuration similar to that shown in Fig. 1. The bunker PC is used for dry-run support, equipment setup, and data archiving. The PC at the control point is used to calibrate, set up, and arm units before the start of automated countdown.

Two of our four digitizers operate in the 1-Gsample/s range: the LeCroy 6880 series gathers 10,016 eight- or eleven-bit samples at 1.3 Gsamples/s; the Sequence 3100 collects 1000 ten-bit samples at 1 Gsample/s. The other two units are the LeCroy 8828, a 200-Msample/s, eight-bit recorder that can gather up to 2 Msamples, and the LeCroy 8818, a 100-Msample/s version of the 8828. Three units have been fielded on several

Figure 1. Digital recorder configuration for initial field trials.

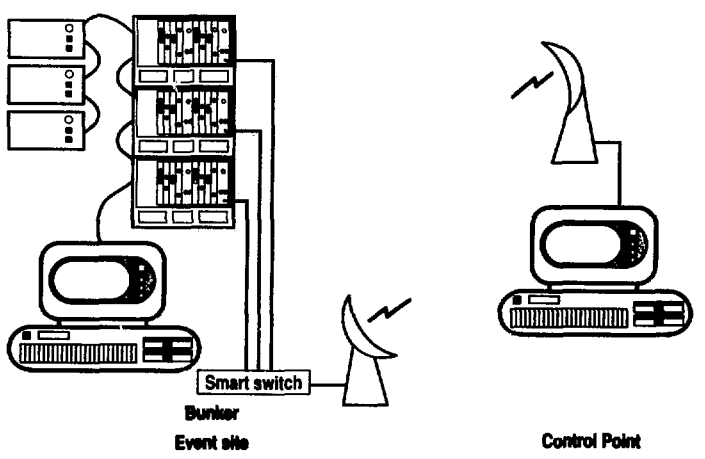

tests. The 8828 has been used to record slower signals related to the HE portion of the device under test. These units have performed quite well in this application. We have used the Sequence 3100 and the LeCroy 6880 to measure various portions of the alpha curve. While these units have proved to be somewhat useful in the low-frequency portions of this curve, they are useless in high-frequency portions. We have also used the LeCroy 6880 to measure Nuex and Captain data. In this application, the digital recorders have proved quite useful. The data are a reasonable match for oscilloscope data, and the long record length has helped analysts to measure and compensate for unexpected system responses. We are continuing to evaluate the applicability of these units.

We have begun to integrate the 6880s and 8828s into the standard data acquisition system, called the Integrated Data Acquisition (IDA) system. IDA is built around LSI-11 microcomputers housed in computer automated measurement and control (CAMAC) crates. This system is hierarchical, with the user interface at the highest level, a ROM-based computer controller at the next level, and data acquisition equipment at the lowest level.

Figure 2 shows the configuration planned for the digital recording system. The master system provides the user interface and the majority of application software. The user interface is built around a VT-100 terminal equipped with a Carrol touch panel. The master provides support for equipment setup, archiving of data, and display and simple reduction of data. The slave computer is a ROM-based controller optimized for reliable acquisition of data. The ROM in the slave is constructed to control data acquisition under the command of the automated countdown system. The slave is capable of data acquisition without the master and can support the downloading of diagnostic software from the master.

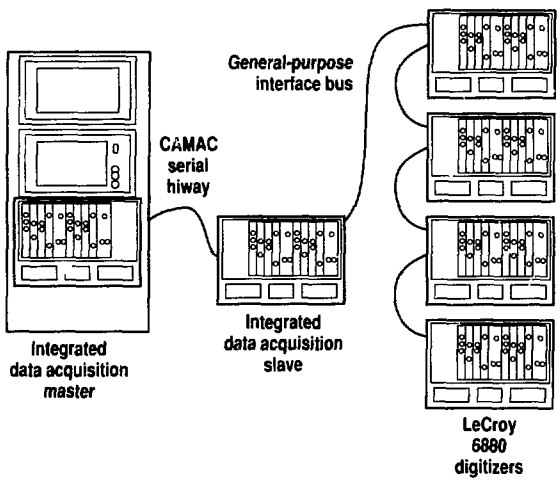

Figure 2. Planned configuration for the digital recording system.

Diagnostics support troubleshooting, special setup routines, and system checkout.

The digital recorders represent the lowest level of the support hierarchy. In the case of the 6880, a single slave system will support up to four CAMAC crates of 6880s. Each crate is capable of supporting six 6880s; however, our standard crates can support only four. The software system to support the fielding of the 6880 recorders has been in development since the spring of 1988. This system is nearing completion, and should be tested in a field environment in the second quarter of FY89.

Future Plans

Next year, we will perform additional evaluations, make further additions to the IDA acquisition suite, and do additional work in integrating data from digital recorders into the normal data-reduction process. We are expecting several new digital recorders this year.

Our goal in the IDA environment for next year is field test the 6880 system and to use it for prime data acquisition. We will then add the LeCroy 8828 and 8818 recorders to the IDA suite. As we complete evaluations of other applicable recorders, we will add them to the IDA system, as well. One of our major needs is the integration of digitizer data into the standard data reduction and analysis process. While data paths for moving data from the test site to the data-reduction sites are well defined, methods for passing digitizer data into the data-reduction process require additional development. Unlike the relatively smooth data produced by the film-reading system, digitizer data are relatively noisy and have comparatively fewer samples per unit time. Work is thus needed on the analysis tools required to efficiently process these data.

Fiber-Optic Fiducial System

D. A. Seligmann

The Diagnostics Instrumentation Group of the Field Test Systems Division has designed and field certified a fiber-optic fiducial pulse system for use at NTS. Six systems are now operational, representing a three-year joint development and test project with Sandia National Laboratory.

The fiducial pulse is a high-voltage (3- to 6-kV) pulse from a fire set, called the X unit, that initiates detonation. It is used as a time mark and trigger for many systems that collect data from a nuclear test. The fiducial system used in the past was simply a step-down isolation transformer connected directly to the X unit's load ring, with a secondary winding connected to a coaxial cable that ran to the front-end diagnostics trailer. From this trailer, the signal was then distributed to the experiments. This electrical system was simple, reliable, and allowed detailed analysis of the X unit's waveform to characterize the detonation devices.

Several years ago, however, a safety study at NTS determined that a lightning strike to the fiducial cable could carry large amounts of electrical energy directly to the high-explosive system. To eliminate this hazard, the Laboratory decided to replace the coaxial cables with fiber-optic ones. Because of the fiducial signal's importance and the potential complexity of a linear optical transmitter and receiver system, we spent several years designing and field testing the new system.

The system consists of a downhole transmitter and dry-run test pulser, an uphole receiver that includes the test pulser control circuits, and the fiber-optic cable (see Fig. 1). The electro-optic converter or fiducial transmitter (TC 995) was designed by LLNL and Sandia. Sandia is responsible for this unit and has contracted with General Electric in Florida to build and test it. The fiducial receiver chassis (LEA-87-1702) was designed and is being built by LLNL. We have installed six uphole receiver chassis in trailers at NTS; five more chassis are being built.

Both the uphole and downhole systems have two independent channels for redundancy; a total failure of one channel will not cause a loss of the fiducial pulse. Only one channel is shown in the schematic of Fig. 1, but both channels can be seen in the photograph of the transmitter.

The transmitter is very simple, consisting of a resistor divider driving an 820-nm light-emitting diode (LED). The transmitter is driven by a step-down isolation transformer similar to the original transmitter. The peak current into the LED is calibrated to be about 250 mA, and the transfer characteristic is about 0.5 μW of light coupled to the fiber optic per milliamp of input.

To calibrate, test, and routinely verify the integrity of the fiducial system and its fiber-optic cables, we developed a test pulser. A laser diode in the uphole chassis transmits 820-nm, 25-mW, square-wave light pulses downhole, where they are received by a photovoltaic *p-i-n* diode. The output voltage of this diode is stepped up about 40:1, rectified, and regulated to 5.5 V dc. This current then charges a small pulse storage capacitor. When a test pulse is desired, a trigger laser in the uphole chassis transmits a very narrow, high-power pulse to activate the downhole pulser "switch." This switch dumps all the pulse capacitor's stored energy into the transmitter's LED. The resulting current is very similar to the actual fiducial pulse, allowing accurate calibrations and diagnostic tests.

The uphole receiver has three separate amplifier stages to convert the received optical pulse into an 80-V output. The

first stage consists of a high-speed *p-i-n* diode as a receiver and a wide-bandwidth amplifier to convert the low optical power (~30 μW) into a 100-mV signal. The amplifier's gain is set electronically using an external potentiometer on the front panel of the chassis. The second amplifier stage is simply a wideband amplifier with a fixed gain to bring the output up to the 3- to 5-V level required to drive the output amplifier. This last amplifier uses a field-effect transistor (FET) output circuit to amplify the signal to 80 V into 50 Ω.

The system's fiber-optic cable (designated FO8) was designed for the NTS program. It consists of three 100/140 (i.e., 100-μm-diam core and 140-μm-diam cladding) multimode, graded-index fibers in an armored and gas-blocked jacket. Two of these fibers are for the test pulser; the third is for the fiducial signal.

This new fiber-optic fiducial system is now the only one used downhole at NTS by LLNL. The signal from it looks just like the old one [see Fig. 1(b)], and no changes to any other experimental or diagnostic systems have been required to accommodate it. Setup time in the field is minimal (1–2 hours), and now that the system has been fielded several times, minimal monitoring is required.

Figure 1. New fiber-optic fiducial pulse system at NTS. (a) Schematic of downhole transmitter unit with test pulser and uphole receiver chassis; (b) fiducial pulse produced; and (c) photograph of receiver chassis (note dual channels for redundancy).

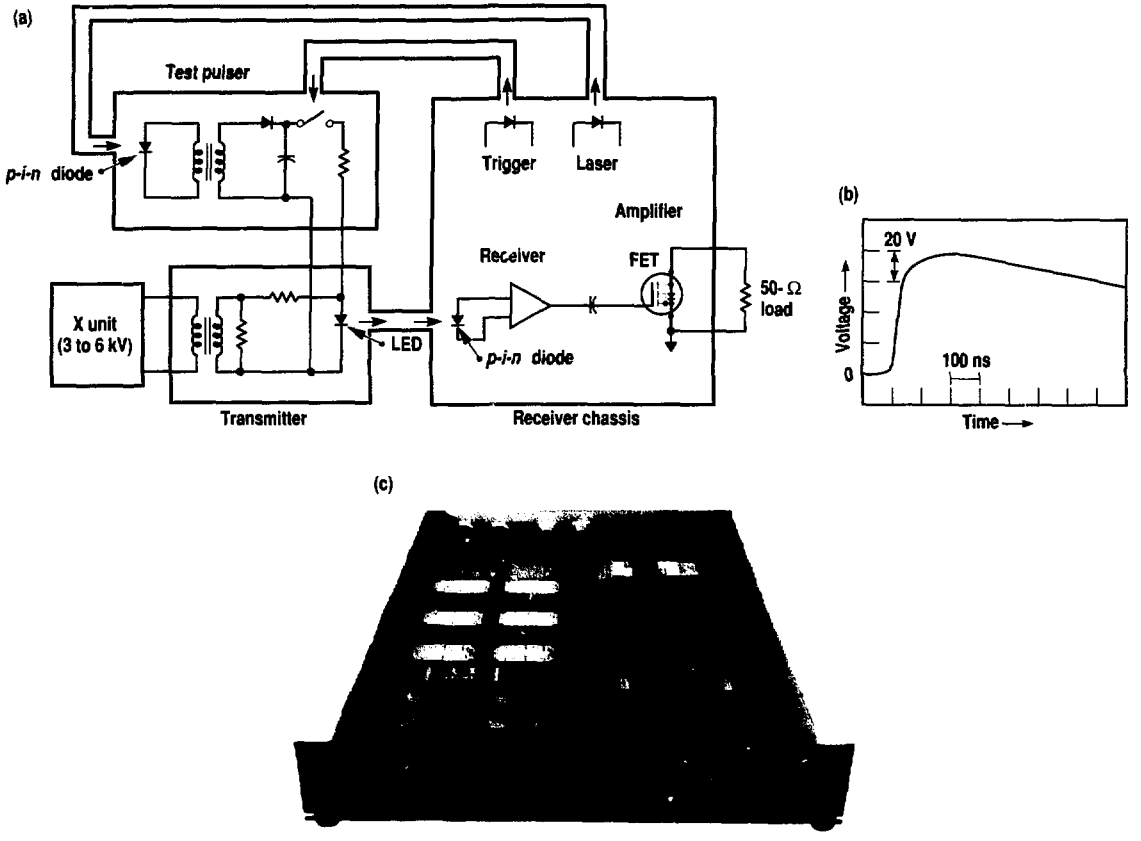

Experiment Design, Analysis Codes, and Calibration Facilities

COG Monte Carlo Transport Code

T. P. Wilcox and E. M. Lent

We have expended several man-years of effort over the last five years on developing a computer code to accurately calculate neutron and photon fields in the regions around nuclear tests. This work was substantially completed in 1987. Our efforts in 1988 have been directed toward educating physicists and engineers in the proper use of the new techniques that are now available.

The COG Transport Code

Our code, called COG, solves the Boltzmann transport equation using the Monte Carlo method. Unlike other LLNL codes that use this method, COG embodies special techniques that are applicable when the points at which answers are required have low probabilities of encountering a source-generated particle. For codes used in weapon design, approximately one-half of the source particles may be tallied at any given point. Within a typical test program problem, on the other hand, only one particle in 100,000 may reach points of interest. The normal Monte Carlo code achieves optimal operation by using sophisticated programming techniques, such as vectorization, to reduce computing times. The deep-penetration (or shielding) code must use biasing techniques adapted to each problem by the user. A user must therefore be adequately instructed regarding COG both through interaction with those who understand such techniques and by prompts from the code itself.

COG was designed to be state of the art both as to the methods employed in radiation transport and in its interaction with users. We also felt that the techniques employed should not include methods that limit the accuracy of calculations. A common fallacy is to replace the correct physics of a code with alternate methods that run faster and produce acceptable results for problems currently being considered. Later, when approximations have been forgotten and different problems are run, incorrect results are often obtained without users being aware of the inherent inaccuracies. COG uses pointwise cross sections, both in energy and scattering angle, with the same interpolation scheme as that employed by the evaluator of physical data. Errors associated with group-averaged cross-sectional data are, therefore, not evident in COG calculations.

Within the test program, problems in radiation transport are rarely simple with respect to the geometrical definitions that must be used to describe an entire canister, a single line of sight, or even one experiment. Past experience suggests that a researcher attempting to use one of the older calculational tools spends most of the available time in defining the geometry in terms that the code can understand. We used special techniques in COG to eliminate many of these problems. Surfaces are now defined in a consistent manner and without the requirement that a user understand analytic geometry. Many surface descriptions in the code embody several analytic surfaces in their definition without the necessity for a user to be aware of the multiple surfaces involved. For example, a six-sided box can be treated as easily as a single sphere. Entire units, such as a single line-of-sight pipe, can be defined along their own axes, rotated, and translated into proper position with a single input statement. Figure 1 shows one example of a complex geometry treated by COG.

To be useful, a code of this magnitude must facilitate interactions with users. Most users run few COG problems and then only in connection with their work

Figure 1. A small part of a complex geometry treated by COG. The shielding pieces shown here were added to a complex experiment (not visible in this drawing) to protect detectors and cables.

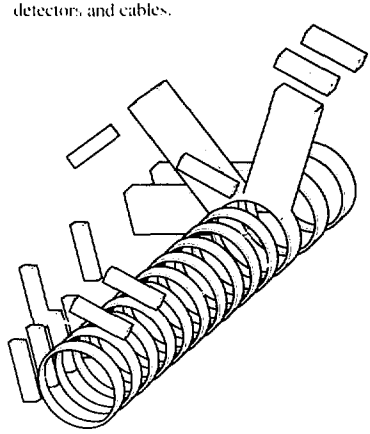

on a given nuclear test. In the intervening months, many users may forget how to employ the code. We have provided many checks of input data through extensive use of graphic output and by incorporating such output into printed text so that the two must be looked at together. For example, the source description in energy is plotted for the user. Thus, a misplaced point becomes immediately evident, and many pictures of the geometry can be drawn so that errors are obvious.

Developers of codes for radiation transport have long sought the ultimate code—one that would learn from experience with a given problem and automatically reset biasing parameters to achieve optimum performance. This ideal has only been achieved for very simple problems and with codes developed for only one type of problem. The size of a general code using such techniques and the complexity of equations that would require solution to achieve such an end preclude development until larger and faster computers are available. Even then, it may not be possible ever to reach the ideal code. In COG, we have taken a different approach. COG provides a user with information about the transport of particles in a problem that has been run. It then allows this information to be entered into a subsequent problem to achieve a more optimal solution. In this way, the expertise of a user is exploited, and a better understanding of the problem and its solution is obtained.

Both COG developers and users have now gained extensive experience. We have analyzed many experiments within the Corsair program and have developed shielding criteria to protect cables within experimental containers as well as shielding requirements external to such containers. This work involved calculations with geometries in complicated arrangements and mock-ups of several experimental lines of sight in tunnel configurations. Our work for R Program included calculations for many different shots to determine background signals. One such calculation included signals on cables running parallel to a line-of-sight pipe and established the feasibility of performing a desired experiment. We also performed a benchmark calculation that compared favorably to experimental results. Several detectors in different shots have been calculated to increase our understanding of how these devices work and to explain observed signals. Electron-generation terms added to the code to improve our understanding of these detectors have found additional use in providing source terms to other divisions working with EMP signals. Users outside our program have used COG to perform shielding-design studies for the Laser Isotope Separation (LIS) project and to evaluate shipping casks for storage and transport of spent-fuel elements. We also performed reference calculations to guide developers of the Superconducting Super Collider in their preliminary shielding designs. The criticality option, which was added to the code after its initial completion, has enabled two groups at LLNL concerned with reactor fuel element safety to use COG and to run almost 100 known criticality benchmark problems. Their work, which included both high- and low-enriched systems, indicated that COG provided better results than any other code currently used in the criticality safety community.

Although we tend to think of COG as a single, unchanging computer code, it is actually a framework within which frequent changes are made. When a problem is being studied for the first time, it is often necessary to develop an entirely new scheme of biasing or a new method of obtaining required results from random-walk histories. Last year, we added several new techniques to the code. Such additions become possible because the code was specifically written to facilitate changes. Our present work includes adding the ability to perform charged-particle transport within the framework of the existing COG.

Two COG user manuals are now available. The first volume provides formats of inputs to the code and includes suggestions on how to run a problem to secure the correct result.[1] The second volume describes work done to benchmark the code for deep penetration problems.[2] Work is currently underway on two additional volumes that will provide users with additional documentation on techniques for proper solutions.

References:

1. T. P. Wilcox, Jr. and E. M. Lent, *COG User Manual—Volume I*, Lawrence Livermore National Laboratory Report M-221-1, Livermore, Calif. (1989).
2. T. P. Wilcox, Jr. and E. M. Lent, *COG User Manual—Volume IV*, Lawrence Livermore National Laboratory Report M-221-4, Livermore, Calif. (1988).

Experiment Design and Data Analysis on the Macintosh II

R. M. Baek

Computer workstation technology has had a dramatic impact on the scientific use of computers by NTES. In the past two years, program scientists have gone from complete reliance on Octopus supercomputers to the use of office personal computers (sometimes called "workstations") for 80% of their computer-related tasks. This radical change has brought substantial gains in scientific productivity.

In the mid-70s, the VAX 780 was a standard, departmental, time-shared minicomputer system typically serving 40 users at a cost of about $200,000. Now, personal-computer systems, providing several times the VAX 780 performance, are available to the individual user for under $10,000 so that using remote time-shared computers is no longer a cost advantage. In addition, the advantages inherent in local computing make the choice of the personal-computer system compelling. For scientific use, its primary advantages are high interactivity, high-resolution graphics, and configuration flexibility.

Interactivity describes the response of the computer system to input from the user. A remote, time-shared system generally accepts input only from the user's keyboard. It responds (e.g., sends the user a message acknowledging that input was received) only when the processor is free from other tasks, which depends on the number of users simultaneously running on the system. Several studies of the effects of response time on user productivity show that delays of more than a second or two cause the user to lose concentration. Where time-shared systems generally have low interactivity, the personal computer interacts with only a single user and is ready to respond to commands within milliseconds. The user is never kept waiting because of system delays; concentration and productivity are greatly enhanced.

High-resolution graphics are essential in engineering and scientific applications where computer-modeling studies or analyses of data are frequently reported as graphs. Even low-cost personal computers can now generate high-resolution color images (512×512 picture elements per screen, with eight bits of color information). Users can update screens so fast that true animation is possible; for example, a user can show the rotation of a perspective view of a computer-generated mechanical model.

Configuration flexibility refers to the ease with which a computer system can be customized. A personal computer typically has several expansion slots attached to its input/output and memory buses. The user can add boards to these expansion slots that perform a variety of new tasks such as controlling laboratory instruments, acquiring and processing data, exchanging files with other computers over a network, and attaching various disk files, magnetic tapes, monitors, digitizing scanners, and other peripheral devices.

In the past, two barriers existed to the widespread introduction of workstations at the NTES: the difficulty of the command-oriented operating systems and the high cost and lack of workstation software. Early workstations, such as those vended by Apollo, Sun, and Dec, operated with a large set of commands and a complex command syntax. The systems were most often based on UNIX, which has a notoriously terse and cryptic command set that we did not want our users to have to learn and relearn. Furthermore, most workstations were software-poor; few vendors for office software (spreadsheets, word-processing, databases, graphics) existed and costs were high because the market was small. We wanted a system that would have the powerful processing and graphics

capabilities of the workstation combined with good, inexpensive office software and an easy-to-learn computer interface.

The Apple Macintosh II computer meets all our requirements. This computer is based on the Motorola 68020 central processing unit, which has demonstrated a computational performance equivalent to that of our time-shared Control Data Corporation 7600. It offers high-resolution color graphics, and its distinctive "mouse-driven" graphic interface allows the user to operate the computer and application codes by pointing to the displayed choices and clicking them on without using keyboard commands. The large Macintosh market offers an abundance of office software at low prices as well as peripheral hardware, such as removable-cartridge hard-disk drives. The evolutionary trend in Apple computers over the past several years, from the original Mac to the more powerful Mac II, and the announcement of yet more advanced central processing units in the 68000 family, such as the 68030 and the 68040, indicate that upgrades will be available to current Macintosh users whenever they wish to take advantage of new technology. Consequently, we chose to make the Macintosh II the standard NTES workstation, one that handles both interactive scientific computations and office tasks. In the past year, we have acquired a Macintosh II computer for every staff scientist.

A typical Macintosh station includes a Macintosh II with 5 Mbyte of memory, a SuperMac 16-in. color monitor, two floppy-disk drives, and two Mass Micro, external, hard-disk drives with removable 45-Mbyte cartridges. These cartridges allow users to work with classified data. At the end of the day, they can remove all such data from the system and secure the cartridges in a repository. Our experience with cartridge drives indicates that their reliability is good after a shakeout period of a month or two.

User acceptance of the Macintosh II has been very good, as it allows a scientist to design an experiment, control instruments in his laboratory, record data, analyze the data extensively and rapidly, and produce working documents and final reports. Additionally, the Macintosh II serves as a terminal into the Octopus system, which runs large Cray codes. The gains in user productivity have been major, approaching an order of magnitude in some typical cases. Previously, an experimenter had to transfer data taken on a laboratory device to a smaller computer that wrote a disk file, take the disk file to another computer, read it in, and then transport it to the Octopus system where the data was finally processed and the results graphically displayed. Only after all this work could the experimenter evaluate the data, several hours to a day or two after it was taken. With the Macintosh II for both data acquisition and analysis, data evaluation can take place in a few minutes at most.

In addition to productivity increases, we see significant collateral benefits associated with ownership of local systems. With the Octopus system, software and hardware changes are frequently made at the request of a large Octopus customer. Even though many of these changes offered no advantages to small users like NTES, it was necessary for us to take time to accommodate them in our codes in order to maintain code functionality. With individual workstations, each user decides if and when to provide system upgrades.

Developing software for the Macintosh posed new challenges to NTES developers accustomed to the Octopus system. In comparison to the Octopus and UNIX environments, relatively few programming tools (languages, debuggers, editors, design programs) were available until last year. To make their codes "Mac-like" (i.e., to use the innovative Mac graphics interface of icons, menus, windows, etc.), developers had to learn the Macintosh toolbox of built-in ROM subroutines, which number in the hundreds and take a five-volume set of manuals to describe. Another unfamiliar concept was the "event-loop" routine, which checks for user input (via key presses and mouse clicks on menus and windows) and which forms the main code of most Macintosh applications. Because system memory is not protected, a "buggy" code undergoing development can corrupt the system and cause crashes; locating the errors can be time consuming.

However, the payoff for our developmental work has been substantial. Our users can now effectively use a fully Mac-like application with little training or reference to the instruction manuals. All the codes' commands are displayed in "pull-down" menu form so they can easily browse to determine what the code can do. Selection of a command leads to a display of "dialogues," windows that briefly explain the command function and request necessary user input. Because all Mac-like codes use the same toolbox of user-interaction routines, procedures learned in the context of one code are likely to apply to all codes. This consistency is a major advantage to our users, many of whom are not computer experts.

Our choice of code development tools was constrained by the large body of existing Fortran codes that we wished to convert to the Macintosh. We chose the Absoft compiler system because it fully supported ANSI-standard Fortran 77. It also generated code for the 68020 central processing unit and the 68881 floating-point coprocessor, was fast in compilation and execution, had a source-level debugger, and provided run-time linking. This last feature allows a code to be run as a library of unlinked subroutines, speeding up the code-development cycle and permitting the development of applications like SODA, which can invoke user-developed ancillary subroutines at execution time.

In general, converting of codes from the Cray to the Macintosh was straightforward and speedy. However, special efforts were required to add Mac-like features and to provide for two-dimensional plotting. This task was eased by the development of a standard plot shell that allowed our application codes on any computer to plot via simple TV80-like subroutine calls to the shell. We implemented the shell on the Cray, VAX, Apollo, and Macintosh computers using

the native graphics package on each machine (Graflib, GKS, GPR, and QuickDraw, respectively).

Our shift in operations from the Octopus system to individual Macintosh IIs is nearly complete. With the exception of a few large Octopus codes that are best suited for mainframe computations, all of our interactive codes are now fully implemented. In the past year, we have developed or added new capabilities to these Macintosh codes: the CDG plotter (new) makes overlay data plots; SODA adds Fourier analysis and parameter elimination; ROSSI adds more Mac-like window features; GNARM adds plotting capability; TCAL (new) processes streak-camera timing traces; and StreakPro (new) provides a variety of streak-camera image operations, including automated streak extraction and correction of camera distortion. Figure 1 depicts a simulated oscilloscope trace produced by the ROSSI code on a laser printer. This realistic simulation allows the experimenter to adjust his recording system so that important signal regions will appear in the most readable areas of the oscilloscope.

In addition to mainframes, the Octopus system provides services such as file storage, file sharing, and electronic mail that our workstation users also need. We are in the process of duplicating these by linking the individual systems via a PhoneNet AppleTalk network to a set of VAX minicomputers and a [illegible] farm. When completed, this network will supply services such as electronic mail, exchange of data files and codes between users, file exchange with the Octopus system, transmission of draft documents to secretaries, output to laser printers and color printers, and secured storage of classified data to our Macintosh users. We chose Pacer software to link the Macintosh workstations to the VAX; Pacer provides a simple, Mac-like interface for file storage, transfer, and execution. The VAX appears to the user as an external hard disk to which he can apply standard Mac operations for creating, copying, and deleting files. File-transfer rates approximate those of floppy-disk operations.

Next year we plan to supply image-processing software to handle images generated by NTES instruments such as neutron pinhole-experiment images and time-resolved spectral measurements recorded by digital cameras. We have demonstrated that the Macintosh II is an excellent image-processing workstation for standard field images. For images larger than 1000×1000 picture elements, we may need Macintosh accelerator boards to provide acceptable processing times.

In summary, we have replaced our dependence on the remote computers of the Octopus system with individual Macintosh II personal computers. These computers give us large productivity gains in experiment design, data analysis, and signal processing. As NTES advances further into high-bandwidth optical-recording technology, we expect to increase our use of these workstations as image-processing systems for camera evaluation, calibration, and data analysis.

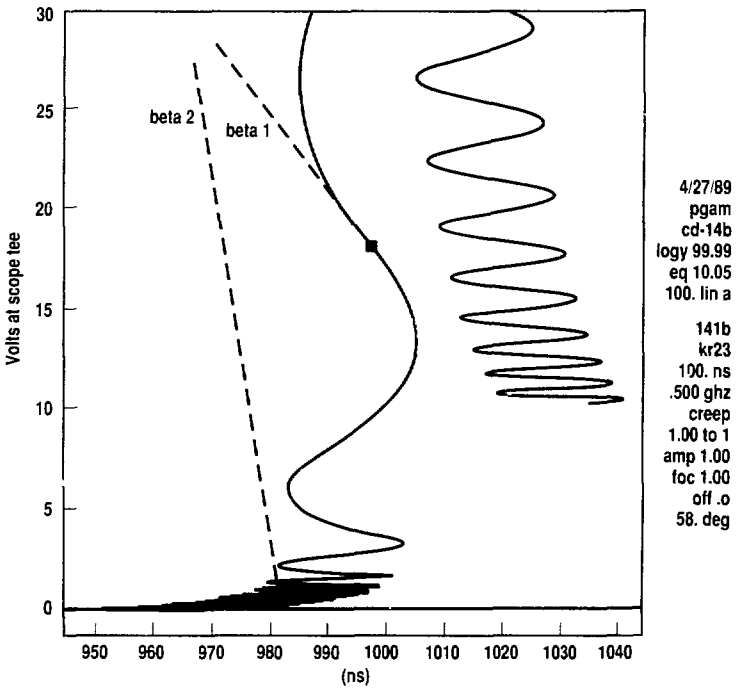

Figure 1. Macintosh II printout depicts a simulated oscilloscope trace produced by the ROSSI code on a laser printer. Realistic simulation allows the experimenter to adjust recording system so that important signal regions will appear in the most readable areas of the oscilloscope.

Nuclear Test Image Processing

C. E. Frerking

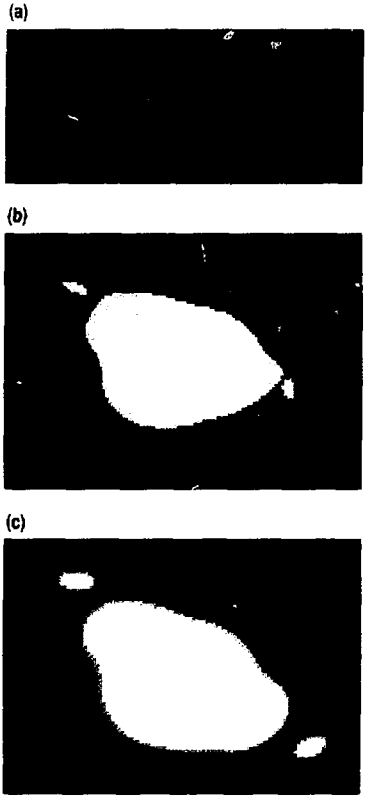

Figure 1. Our technique for "sliding" images into registration. (a) Two images of the same phenomenon, viewed from slightly different perspectives, have been rotated and translated with respect to each other. (b) The two images have been superimposed. Above a threshold value, one image displays as red, the other as green; where they overlap, they show as white. By controlling the translation and rotation, successive displays show success or failure. (c) The two images are in registration, their edges aligned and one completely contained by the other.

The Nuclear Test Program has been involved with the development of image processing techniques since the invention of the ELectronic PINEX (EL-PINEX) experiment in 1977. Fielding that experiment has created a number of related efforts, which range from camera construction and characterization to calibration and data acquisition and final processing—all of which require imaging equipment and techniques.[1] These related components have been developed over the years as parts of a major system that is flexible and relatively easily extended to include new types of data-acquisition hardware and methods. In FY88, we enhanced our ability to process data from the EL-PINEX experiment by improving our methods of comparing images from several cameras and developing a new standard format for displaying data.

The EL-PINEX Experiment

EL-PINEX uses a specially built pinhole that can project neutrons from a nuclear explosion to a fluorescent material at an image plane in the same way an ordinary pinhole can generate an image with light. The fluorescent material then emits light in proportion to the number of neutrons striking that neighborhood, rendering an image of the neutron source to shielded cameras located in a standard camera bay below the fluor. The active elements of these solid-state cameras are two-dimensional chips that are sensitive to the light from the fluor. These chips come in various sizes. Although our standard image consists of 100×100 picture elements representing a selected portion of the fluor, we have also developed cameras for 128×128 and 400×200 picture elements. Each element generates a digitized number that is proportional to the amount of light by which that element was illuminated. Using a high-speed communication line (cable or fiber optic), the datum for each element is sent uphole, where it is captured and stored in a nonvolatile memory to await storage, retrieval, preliminary processing at the NTS, and more detailed processing at the L-Division Image Research Laboratory (LIRL).

Image Comparisons

Because we are now able to control the time during which a camera views an incoming image, we can infer information about the time dependence of the images on the fluor by measuring differences between images. Since the several cameras that are installed on an event are all viewing the image from different perspectives, however, much processing work needs to be done before different views can be compared.

This past year, we developed a procedure for preliminary processing that begins with calibrating the raw data from the cameras to uniform physical units. Typically, the cameras are configured to maximize the probability of attaining data that will account for the possible signal intensities the source might emit given minimal, nominal, and maximal source behavior. Thus, the raw data on one camera must account for the details of how the camera was integrated into the experimental system before they can be directly compared to the raw data on another. Calibration to physical units is performed on a pixel-by-pixel basis from a set of ten flat-field images that were acquired from the camera during its construction and characterization by EG&G facilities in Pleasanton and Las Vegas. Because these flat-field images are taken at known exposure intensities, they provide both a conversion to real physical units and a linearity curve for each picture element.

Spatial distortions can also appear in a typical image. In particular, because the pinhole is very long (usually about 3 cm), any off-axis source particles undergo a

penumbral shading effect, which we routinely correct as required.

Once preliminary corrections have been performed, the images must be translated and rotated so that they are properly aligned before a difference can be taken. We have developed a method by which two images are displayed together by applying a threshold to each image so that all pixels above that threshold are shown with a specific color. Where those images overlap, a third color is displayed. This presentation allows the user to move and rotate one image relative to the other until a "best overlap" is found, a process analogous to manually sliding and rotating two pieces of film past each other until a best fit is achieved. Figure 1 is a simulated set of images that illustrates this concept.

A New Standard Display

In another addition to our repertoire of processing methods, we designed a "standard presentation" for displaying our EL-PINEX data consistently. We have learned the value of using several different representations for interpreting data, as any single representation can emphasize important information in an image and, likewise, can conceal information that is then easily overlooked. Our standard picture for simulated data is shown in Fig. 2.

Because the eye is accustomed to perceiving gray-scale information, we can quickly relate data intensities to the gray-scale view (Fig. 2, upper right). Small differences are not easily seen in the gray-scale picture, however, because there is little contrast between pixels of nearly the same value. As shown in Fig. 2 (upper left), a pseudo-color picture, where each pixel intensity is assigned a specific color, can present the data with more contrast between nearby values than a gray-scale picture, even though the information the color picture presents is not as easily interpreted by sight. Figure 2 (lower left) also shows a color mapping we apply that causes image contours to appear in such a way that the direction of intensity gradients can be determined. The colors chosen for contour mapping simulate the contour images presented in the standard Los Alamos display. The scale we include immediately makes an image visually comparable with other images from related events. Since defining this standard image, we have retrieved and archived all of our past EL-PINEX images and have reprocessed them to our standard display format. Those pictures now fill several books and provide a set of viewgraphs for use in talks.

Conclusion

Over the past decade, the ability to acquire data in the form of images and the ability to process such data in varied ways have become increasingly important to the Nuclear Test Program. We now have a complex array of equipment and methods available that allows us to capture and analyze data we could only dream about a few years ago. As equipment becomes more sophisticated, less expensive, and more powerful, it will become easier and faster to add new processing techniques. That still-greater flexibility will allow new experiments to answer yet a new generation of puzzling questions about the physics of nuclear designs.

Reference:

1. "Imaging in the Nuclear Test Program," *Energy and Technology Review*, Lawrence Livermore National Laboratory, Livermore, Calif., UCRL-52000-88-10 (1988), 30.

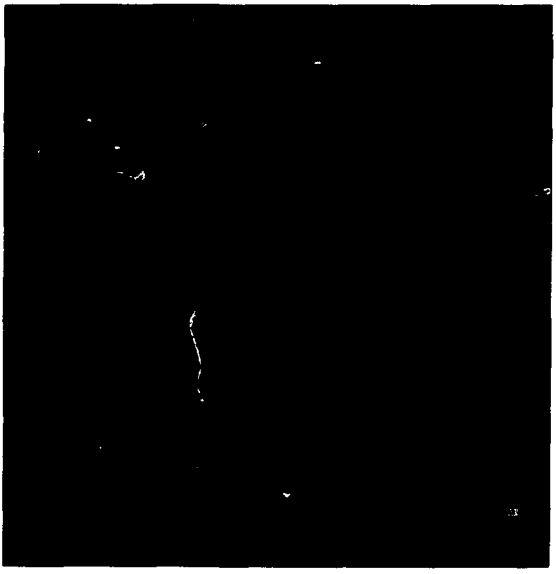

Figure 2. The "standard EL-PINEX image" includes (upper left) a pseudo-color representation that emphasizes small changes in amplitude; (upper right) a gray-scale image such as we are accustomed to viewing; and (lower left) a color contour image, which displays absolute amplitudes. The scale is included for comparison purposes.

The X-Ray Calibration and Standards Facility

C. E. Page, S. V. Kuhlmann, K. G. Tirsell, L. C. Wilson, M. J. Moran, N. A. DeGrande, and R. D. Lear

The X-Ray Calibration and Standards Facility (XCSF) project was undertaken to provide electromagnetic radiation that is substantially more intense than is available from conventional laboratory sources. To provide intense beams of photons or x rays in the 8–35,000 eV range, we have built two new beam lines (Fig. 1) on the Stanford Positron-Electron Asymmetric Ring (SPEAR) at the Stanford Synchrotron Radiation Laboratory (SSRL).

The project began in 1982 when a participating research team (PRT)—consisting of representatives from LLNL, Los Alamos, Sandia, and the University of California—was formed to design and construct two new beam lines at SSRL. Conventional facilities were constructed by the end of 1984, all beam lines were performing within specifications by February 1988, and initial experiments were begun soon afterward. Although LLNL was the lead laboratory for design and construction, the beam lines are available to all members of the PRT.

Description of the Beam Lines

The source of photons is the synchrotron radiation produced either at one of the bending magnets (beam line VIII) of the storage ring or from a wiggler inserted directly in a straight section of the ring beam line. The wiggler causes the beam to oscillate without any net deflection, producing radiation that can be several orders of magnitude more intense or brilliant than radiation from bending magnets.

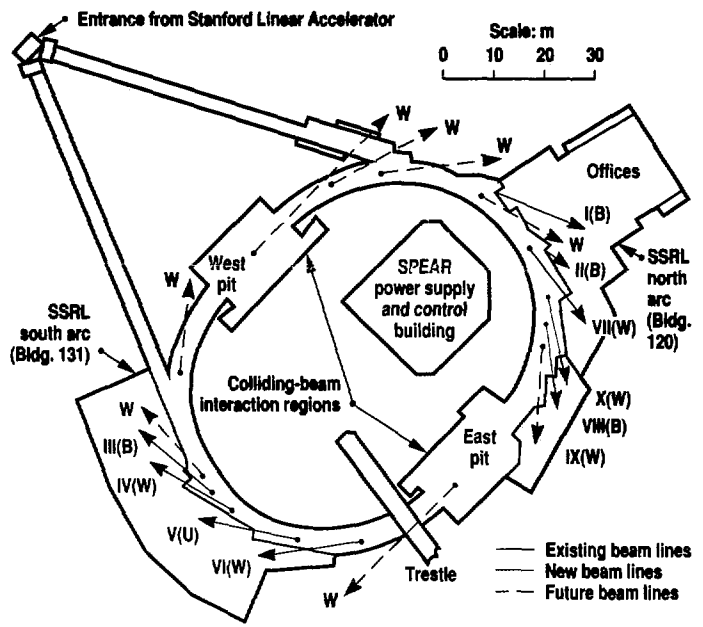

Figure 1. Site plan for the Stanford Synchrotron Radiation Laboratory, showing the Stanford Positron-Electron Asymmetric Ring and the location of beam lines VIII and X of the X-Ray Calibration and Standards Facility. Beam lines are identified by B (bending magnet), W (wiggler), and U (undulator).

Figure 2 shows the configuration of these two beam lines and the two branch lines of beam line VIII. The vacuum ultraviolet (UV) branch (beam line VIII-1) was operational in November 1986, and the soft-x-ray branch (beam line VIII-2, the wiggler line) was completed in November 1987. Beam line X is designed to accept two additional branch lines in the future, one for soft x-ray and one for experiments requiring high-intensity, broad-spectrum radiation. Table 1 summarizes the key features of the existing branch lines.

The nominal size of the beam is defined both horizontally and vertically by the source (either bending magnet or wiggler), the SPEAR operating parameters, and the dimensions of a fixed mask. The photon beam spreads out horizontally into a fan of 23 mrad for beam line VIII and 5 mrad for beam line X. Mirrors and masks further divide the fan for each beam line. Grazing-incidence optics are used to collect the fan of radiation and focus it on the target sample. Although the target spot size is determined by the optics configuration and quality (control of aberrations) and the electron beam cross section, diameters of 10 μm or less are achievable, but perhaps at the cost of some beam intensity.

As shown in Fig. 3(a), a cylindrical grazing-incidence mirror collects 12 mrad of the horizontal fan of radiation leaving the bending magnet. The first mirror deflects the vacuum UV photons upward by an angle of 12 degrees and focuses the beam horizontally onto the entrance slits of the vacuum UV monochromator. Located beyond the first mirror, a second, spherical mirror deflects the beam by an additional 12 degrees and focuses it vertically onto the entrance slit. The toroidal diffraction gratings of the monochromator image its entrance slit onto a movable exit slit, and a bent-cylinder mirror focuses the emerging monochromatic light onto the sample. This mirror's long radius of curvature is adjustable to compensate for the change of focus with grating angle. Because of the 24-degree net deflection of this branch line, the monochromator, refocusing mirror, and sample chamber are located on the XCSF mezzanine [Fig. 2(b)].

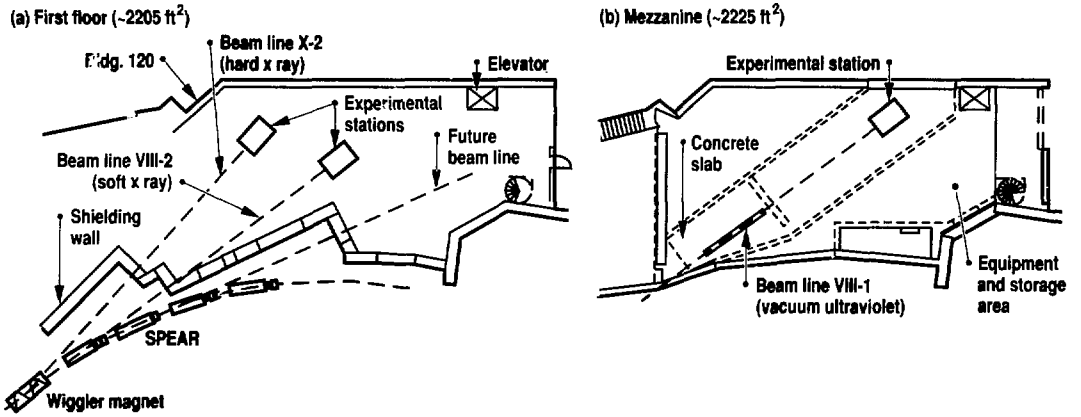

Figure 2. Floor plans of (a) the first floor and (b) the mezzanine of the Stanford Synchrotron Radiation Laboratory. Portions of the Stanford Positron-Electron Asymmetric Ring and the sources for beam lines VIII and X are shown.

Table 1. Key features of the existing branch lines at the X-Ray Calibration and Standards Facility.

Branch	Nominal energy range (eV)	Monochromator	Experimental stations
VIII-1: vacuum ultraviolet (bending magnet)	8–185	Toroidal grating	Photoemission, photoabsorption
VIII-2: soft x ray (bending magnet)	60–1,100	Spherical grating	Photoemission, photoabsorption
X-2: hard x ray (wiggler)	3,000–35,000	Double crystal	Spectroscopy and diffraction (in tandem)

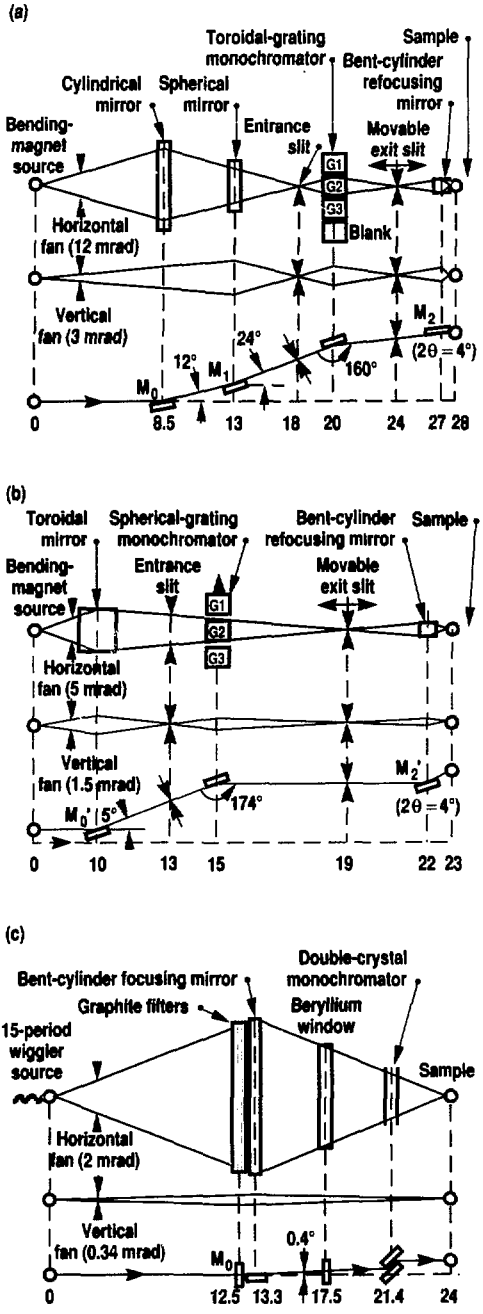

Figure 3. Optics showing beam-line elevations for the three beam-line branches: (a) beam line VIII-1, the vacuum UV branch (8–185 eV); (b) beam line VIII-2, the soft-x-ray branch (60–1100 eV); and (c) beam line X-2, the hard-x-ray branch (3–35 keV). The horizontal axis represents beam-line component positions, with values expressed in meters. Diagrams are not to scale.

On the soft-x-ray branch, shown in Fig. 3(b), the first mirror (which has a toroidal surface) collects 5 mrad of the fan of radiation, deflects the beam by a total angle of 5 degrees above the horizontal plane, and focuses the beam horizontally onto the soft-x-ray monochromator exit slit and vertically onto its entrance slit. The monochromator gratings are spherically configured to focus the beam vertically onto the exit slit. The exit slit is movable along the beam-line axis, and a bent, cylindrical refocusing mirror forms the image of the exit slit on the sample.

The wiggler beam-line optics are illustrated in Fig. 3(c). The bent-cylinder, double-focusing mirror collects 2 mrad of the beam, deflects it 0.4 degrees to the horizontal, and focuses it on the sample. The remainder of the fan is reserved for future branches. This mirror has a cutoff energy of 20 keV but is also retractable, thus providing the total spectrum of wiggler radiation for the beam line when necessary. The low-energy cutoff of this beam line is set at 3 keV by the beryllium window located just in front of the monochromator. The beam line has recently been modified to replace the beryllium window with a differential pumping section to allow the monochromator on this line to operate at 10^{-6} Torr. Modification of the monochromator for vacuum operation is planned for the summer of 1989. Once the present monochromator is modified to operate under vacuum, the spectral range of this beam line will be extended to below 1 keV. Thus the XCSF beam lines will provide continuous spectral coverage from 8–35,000 eV.

Because the synchrotron radiation is so intense, heat dissipation in the masks, beam stoppers, and optical elements is a major problem. The resulting distortion of the mirror can seriously degrade the quality of the beam, substantially reducing the useful photon flux delivered to the sample. This problem has been solved by using silicon carbide with a platinum coating for the first mirrors. Silicon carbide is less affected by thermal distor ion

than other mirror materials, and its stiffness, yield strength, and hardness allow a novel mirror holder and cooling scheme design. With the mirror loaded mechanically at the base, heat transfer is increased, and thermal distortions are compensated for so that the mirror maintains its unstressed position under operational thermal loads. The first successful chemical-vapor-deposited (CVD) silicon carbide mirrors for synchrotron beam lines in the United States were fabricated for the XCSF project and had surface finish roughnesses of less than 0.5 nm rms, the best reported surfaces for x-ray mirrors of CVD silicon carbide in the world.

Monochromators

Each monochromator in the vacuum UV and soft-x-ray branches uses three interchangeable, fused-silica gratings that are holographically produced, ion etched, platinum coated, and mounted for use in an ultrahigh-vacuum chamber. The toroidal gratings on the vacuum UV branch cover 7–140-nm wavelengths, corresponding to an energy range of 8–185 eV. On the soft-x-ray branch, the gratings are spherical and provide photons in 0.8–22-nm wavelengths, corresponding to energies of 60–1100 eV.

Wiggler

The wiggler for beam line X is a 15-period, variable-gap, permanent-magnet and steel hybrid designed and fabricated at LBL. Table 2 summarizes the parameters of the beam line X wiggler. Neodymium-iron-boron was selected as the permanent-magnet material because it is superior to rare-earth cobalt and less expensive. For an electron energy of 3 GeV, the wiggler at peak field will radiate 3 kW into a 5-mrad horizontal fan. This intensity makes it one of the brightest continuous hard-x-ray sources available.

Initial Experiments

We have begun initial experiments on all of these branch lines. Photo absorption and photon scattering are the main processes by which photons interact with matter, with photoabsorption dominating below 1 keV. We are measuring absolute photoabsorption experimental cross sections (APECS) to improve our understanding of photon interactions with matter by improving the atomic physics databases used in the design and analysis of x-ray experiments and by testing the predictive capabilities of our computer models. We have used XCSF beam lines to take data on many elements, including beryllium, chromium, iron, nickel, titanium, uranium, and vanadium. We have compared these data with a variety of theories to help us understand both atomic vs solid effects and the various atomic resonance phenomena and coupling schemes.

Of perhaps greatest significance are the new resonant and/or enhancement structures we have found at virtually every inner-shell (absorption-edge) threshold. A good example is shown in Fig. 4. Our APECS measurements show a sharp $1s$–$2p$ autoionizing resonance near the K absorption edge, followed by a broadened, atomic-like feature above the K-shell ionization threshold for solid beryllium. The theoretical interest created by these newly discovered features, which are unrepresented in current calculational

Table 2. Parameters of the beam line X wiggler.

Parameter	Value
Magnetic-period length	12.85 cm
Number of complete periods	15
Peak magnetic-field range	0.01–1.4 T
Peak-to-peak field uniformity	≤2% at minimum gap[a]
Operational magnetic-gap range	2.1–20.0 cm
Beam vertical aperture	1.8 cm
Pole width	7.5 cm
Transverse-field requirement	$\Delta B/B \leq 3\%$ (over 2.4 cm)
Effective magnetic length	202.4 cm

[a] Measured to be <0.24%.

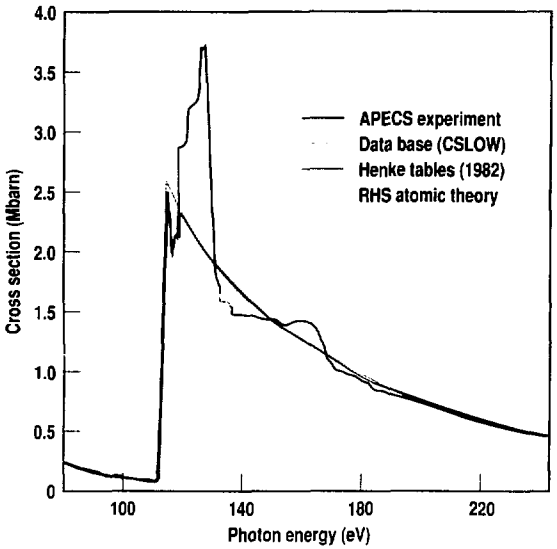

Figure 4. Absolute photoabsorption experimental cross sections of beryllium, showing resonance behavior near the 1s (K-edge) threshold. Preliminary APECS result obtained at the XCSF is compared with CSLOW (low-energy cross-section data base), tables compiled by Henke,[1] and RHS (relativistic Hartree-Slater) atomic theory.[2]

models, may well lead to developments that will improve the general theoretical basis for opacity calculations. Some general areas of Laboratory-wide interest include experiments on high-temperature semiconductor materials, x-ray absorption fine structure through detection of optical fluorescence, and x-ray tomographic-imaging techniques. XCSF beam lines have been used for EXAFS and x-ray absorption near edge structure (XANES) studies of materials in several areas. We have used optical emission of materials excited by soft x rays (10–1200 eV) to measure x-ray absorption edges and fine structure, and we have examined several crystalline and amorphous materials having either intrinsic luminescence or luminescence from transition metals and organic dyes present as dopants. This work has demonstrated the versatility of the optical emission method for both soft- and hard-x-ray regions. We have used this technique to study rare-earth materials and specialized glass materials.

The performance of all components of the XCSF project meets or exceeds our expectations. Initial experiments on all branch lines are returning data of importance to NTES and to the general weapons program.

References:

1. B. L. Henke et al., "Low-Energy X-Ray Interaction Coefficients: Photoabsorption, Scattering, and Reflection," *Atomic Data and Nuclear Data Tables* **27** (1), 1 (1982).
2. J. H. Scofield, Lawrence Livermore National Laboratory, Livermore, Calif., private communication (1987).

LEXIS: A Pulsed X-Ray Facility

V. W. Slivinsky and A. F. Clark

The low-energy x-ray illumination system (LEXIS) is a *Z*-pinch plasma source, manufactured by Maxwell Laboratory, designed to emit intense pulses of soft x rays. In FY88, we developed this source into a pulsed x-ray calibration facility to complement the continuous-current x-ray machine used at LLNL. LEXIS provides sufficient power to calibrate the most insensitive diagnostic systems used at NTS. It is easy to operate and can be pulsed once a minute for rapid use.

Figure 1. The LEXIS facility. This compact machine has 15 calibration ports that can accommodate various configurations of detectors and instruments. The screen room on the left protects sensitive recording instruments from electromagnetic backgrounds. The completed system used to operate LEXIS is shown in front of the screen room.

The LEXIS facility (Fig. 1) has 15 calibration ports that can accommodate various configurations of detectors and instruments. The machine is very compact and fits into the far side of room 1214 in building 121. The beam pipes built onto the machine are used to mount detectors and instruments to be calibrated. The screen room on the left protects sensitive recording instruments from electromagnetic backgrounds. The completed system used to operate LEXIS is shown in front of the screen room.

From a stored energy of 4000 J, about 1000 J of x rays with a blackbody shape and an effective temperature of 30–40 eV are emitted from the plasma source. However, for our calibrations, we use higher-energy emission lines characteristic of the particular gas used in the pinch. The Ne and Ar spectra from a similar machine are shown in Fig. 2.

In FY88, we used the Ne gas pinch almost exclusively. Neon provides

about 5 J in the helium-like line at 920 eV (see the $1s^2$–$2s2p$ line in Fig. 2). We effectively isolated this line with an x-ray filter.[1] The x-ray energies outside a small energy region at 920 eV are heavily attenuated by a 1.3-μm-thick Cu filter. We used Cu because it has an absorption edge at 930 eV, which is just above the region of interest. The temporal profile varies considerably from shot to shot as does the x-ray intensity. The x-ray pulse characteristics must be carefully monitored on each shot with standard x-ray detectors to account for the variations.

Other x-ray lines can be used by loading different gases into the machine. Krypton L lines at 1.8 keV and Ar K lines at 3.3 keV are most commonly used because diagnostics calibrations are often required in this energy region. Other x-ray energies could be provided by exploding wires instead of gases. However, the wires must be replaced after each shot, which increases the turnaround time to about 20 min.

A pinhole picture of the actual x-ray source shows a filament about 1 mm wide and 2 cm long with the most intense portion near the cathode and hot spots along the filament length.

We operate LEXIS using a computer-automated measurement and control (CAMAC) system. With this digital system, we can collect data from a Tektronix 7912 oscilloscope or, if we need measurements with a faster response time, from a Tektronix 7104 oscilloscope.

During FY88, we developed the LEXIS machine into an absolutely calibrated, pulsed, monoenergetic x-ray facility. LEXIS now provides an inexpensive, easy-to-use x-ray source for NTS instrument calibrations.

Reference:

1. A. Clark and C. Wong, *LEXIS Calibrations*, Lawrence Livermore National Laboratory, Livermore, Calif., internal memo IMG-88-19 (August 1988).

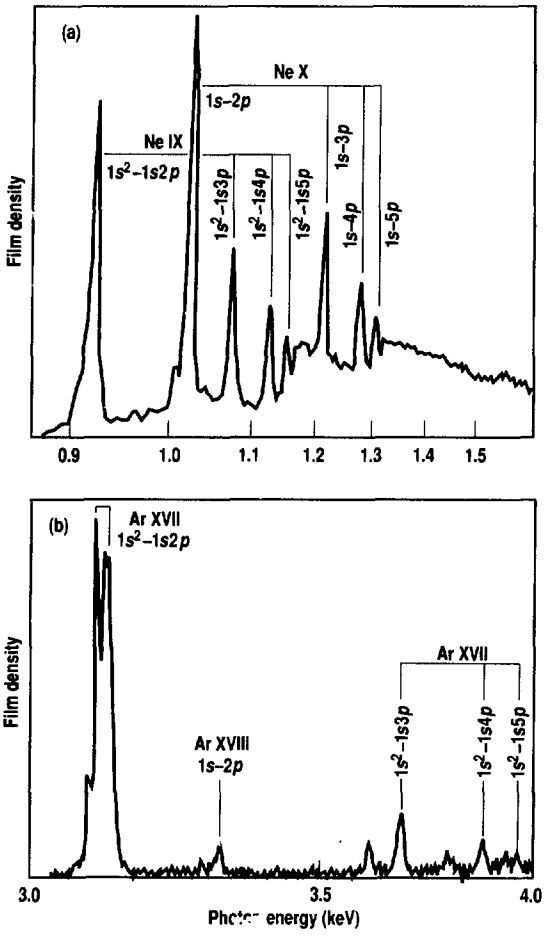

Figure 2. Spectra from a LEXIS machine: (a) neon K-shell spectra; (b) argon K-shell spectra.

New Directions in Development of Underground Weapons Physics

Measurement of Electron Temperature in a Nuclear-Driven Plasma

P. T. Springer

In this article, we report on the design of an experiment that will determine the electron temperature in a nuclear-driven plasma using free-bound x-ray emission from mid- to high-Z dopant ions. We require accurate knowledge of electron temperature for atomic-rate modeling and to design systems that are hydrodynamically stable when heated. We describe *ab initio* calculations of plasma temperature, which incorporate known heating and cooling mechanisms. For H-like, K-shell systems, we derived analytical expressions for the dependence of the free-bound x-ray spectrum on electron temperature, and we describe an extension to L-shell systems. The actual electron temperature of three nuclear-driven samples, including both K- and L-shell systems, will be determined experimentally using a high-resolution bent-crystal imaging spectrometer with subnanosecond resolution.

We performed our *ab initio* calculations of electron temperature using the atomic rate code XRASER. This code uses detailed atomic models for ions in their possible ionization states, and it accounts for known atomic processes and interactions with both x rays and electrons. Driven by a specified time- and frequency- (energy-) dependent x-ray intensity, XRASER determines plasma evolution, plasma temperature, nonlocal-thermodynamic-equilibrium-(NLTE)-level populations and intralevel transition rates, and the generation and transport of radiation within the plasma. The temperature is determined from known plasma heating and cooling mechanisms. Auger processes, photoionization, electron collisional excitation and ionization, and bremsstrahlung. For the x-ray-driven plasmas of interest, the dominant heating mechanism is from photoionization; the dominant cooling mechanism is from bremsstrahlung. Heating and cooling from Auger processes and electron-ion collisions are also important for high-Z systems.

We will experimentally determine the temperature of plasmas using x rays emitted from radiative recombination with highly stripped ions. In radiative recombination, a free electron makes a transition into a bound level of an ion, emitting an x ray. For recombination into the ground state of an ion, the x-ray energy is higher than the energies of all bound-bound transitions. The rate of x rays of a particular energy is related to the density of electrons having a particular energy, since the x-ray energy is the sum of the initial electron energy plus the ionization potential. X rays just above the continuum threshold are from recombination of electrons having a kinetic energy close to zero. Thus, the radiative recombination spectrum is related, in part, to the electron-energy distribution, or temperature. The spectrum also depends on the energy variation of the recombination cross section, which can be predicted using atomic theory. With a proper understanding of the atomic physics of the recombination cross section and plasma opacity effects, the free-bound-continuum x-ray spectrum can be used to measure the electron energy distribution and to infer plasma temperature.

Theory of Radiative Recombination for H-Like Systems

The plasma emissivity $\varepsilon_i(E)$ due to radiative recombination into a particular bound level i is given by

$$\varepsilon_i(E) = EJ_e N_i \sigma_{rec} , \qquad (1)$$

where E is the x-ray energy, J_e is the electron flux, N_i is the density of ions in

the appropriate ionization state, and σ_{rec} is the recombination cross section. Using time-reversal invariance, the cross section for radiative recombination can be related to its inverse process, photoionization. For the H-like ground state,

$$\sigma_{rec} = \sigma_{ph}\, 2k^2p^{-2}\,. \qquad (2)$$

where σ_{ph} is the photoelectric cross section, k is the photon momentum, and p is the electron momentum. In general, photoionization cross sections for ions of arbitrary ionization are calculated numerically using fully relativistic Dirac-Hartree-Fock wave functions. For nonrelativistic H-like ions, however, the photoelectric cross section can be expressed analytically, as follows:

$$\sigma_{ph} = \frac{2^9\pi^2}{3}\,\alpha\left(\frac{a_0}{Z}\right)^2\left(\frac{I}{E}\right)^4 \times \frac{\exp(-4\eta\,\cot^{-1}\eta)}{1-\exp(-2\pi\eta)}\,, \qquad (3)$$

where a_0 is the Bohr radius, Z is the nuclear charge, and the Sommerfeld parameter $\eta = (2mI/p^2)^{1/2}$. The photon and electron momenta are related by

$$E = ck = I + \frac{p^2}{2m}\,, \qquad (4)$$

where I is the ionization potential. Because of the fast electron-collision time, the electron-energy distribution should be Maxwellian, and the distribution of electron momenta should be given by

$$J_e = N_e\,\frac{p}{m}\,4\pi\,(2\pi mT)^{-3/2} \times \exp\left(\frac{-p^2}{2mT}\right)p^2\,dp\,, \qquad (5)$$

where N_e is electron density, m is electron mass, and T is electron temperature. Thus, the x-ray emission resulting from recombination with bare ions, producing the H-like free-bound continuum, is given by

$$\varepsilon_H(E) = N_e\,N_{bare}\,8\pi c(2\pi mc^2T)^{-3/2} \times \exp\left[\frac{-(E-I)}{T}\right]\sigma_{ph}\,E^3\,dE\,. \qquad (6)$$

For an optically thin plasma when the energy variation of $\sigma_{ph}E^3$ is removed, the emission has a simple exponential falloff characteristic of the electron temperature. The intensity of the free-bound continuum spectrum depends strongly on plasma density, temperature, and ionization state; however, the spectral shape depends mainly on electron temperature. Interpretation of the spectral shape becomes more complex when other states of ionization are considered and the effects of plasma opacity are examined.

Radiative Recombination in Complex Atomic Systems

The radiative recombination into excited levels and into ions with an arbitrary degree of ionization can be described in a manner similar to the expression for radiative recombination of free electrons into the ground state of a H-like ion. The observed spectrum will be a sum over all possible excited levels and all degrees of ionization. Provided that the electron temperature is small relative to the ionization energy, the radiative recombination spectra corresponding to recombination into different atomic shells K, L, . . . can be spectrally resolved. It is often difficult to resolve the radiative recombination into a given shell from ions with differing states of ionization. The continuum threshold energies of H-like and He-like K-shell recombination differ, and the recombination continua may overlap. Likewise, the continuum threshold energies of Li-like through Ne-like L-shell recombination differ, and the recombination continua may overlap. In the region of continuum thresholds of a given shell, the emission spectrum is complex, containing free-bound emission from lower states of ionization and high Rydberg bound-bound transitions from higher states of ionization. Above the highest-energy continuum threshold, the recombination spectrum will again have a simple exponential falloff indicative of the electron temperature. In this region, the net recombination spectrum is a sum of the form

$$\sum_i A_i \exp\left[\frac{-(E-I_i)}{T}\right]\sigma_{ph_i}\,E^3\,, \qquad (7)$$

where values of A_i depend on plasma ionization state, density, and temperature. In general, the photoionization cross sections have a simple energy dependence of the form $E^{-\alpha i}$ where the exponent α_i is nearly identical for all states in a given subshell (1s, 2s, 2p, . . .) regardless of the level of ionization. Thus, aside from a complicated normalization factor, the energy dependence of the recombination emission behaves as $E^{3-\alpha}\exp(-E/T)$, and α ranges from 2.5 to 2.8.

If the value of α is uncertain by $\delta\alpha$, then the effect on the derived temperature is of the order $\delta\alpha\, E/I$. Typically, the ionization potential is much greater than the electron temperature, and this uncertainty is small. For K-shell systems, the uncertainty in the value of α is on the order of 0.01. In K-shell systems, α can be calculated accurately and is nearly identical for both H-like and He-like ions, eliminating any dependence of α on ion balance. For L-shell systems, the uncertainty in α is on the order of 0.1. Although calculations of α are accurate and the value does not have a strong dependence on the ion species, the value of α for photoionization of 2s and 2p electrons differs. Thus, the L-shell population distribution plays a role in determining the admixture of recombination into 2s levels.

Because measurement of electron temperature depends on an accurate understanding of the free-bound emission spectrum, we must apply corrections for the spectral distortions due to plasma opacity. For a plasma of physical depth L with an x-ray mean free path given by $\lambda(E)$, the effective plasma depth is given by

$$L_{eff} = \lambda(E)\,\{1-\exp[-L/\lambda(E)]\}\,. \qquad (8)$$

If the plasma is optically thin, then $L_{eff} = L$. If the plasma is optically thick, then $L_{eff} = \lambda(E)$, which scales with x-ray energy as E^{α}. The spectrum of x rays that escape the plasma is given by the

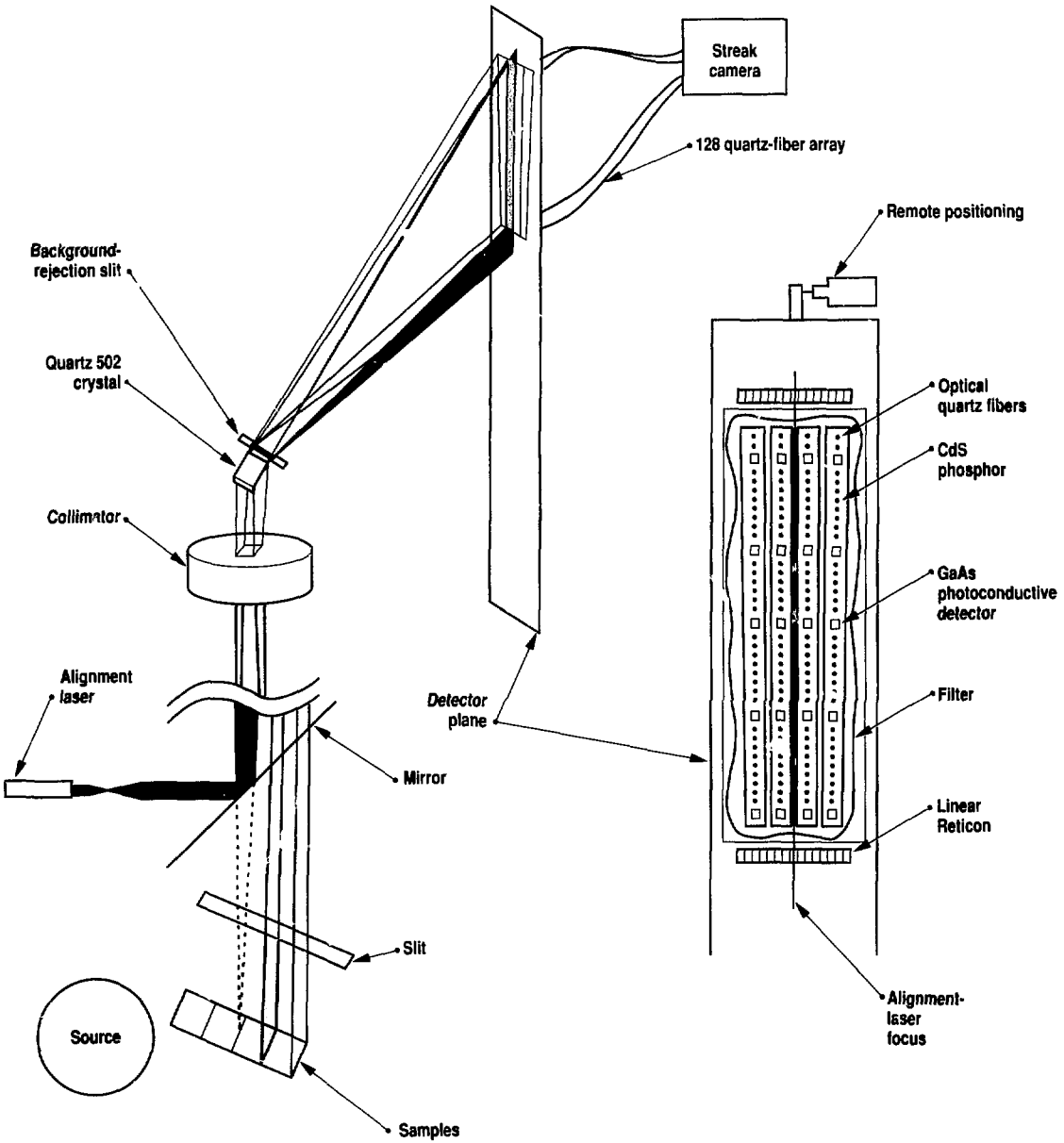

Figure 1. Setup for the electron temperature experiment. The curved-crystal spectrometer is designed to include spatial and spectral imaging of four samples, redundant x-ray-detection systems, downhole timing to the x-ray drive, and active alignment. Other features shown in this diagram are described in more detail in the text.

product of effective plasma depth and plasma emissivity. Thus, the observed spectral shape behaves as $E^3 \propto \exp(-E/T)$ for an optically thin plasma, and as $E^3 \exp(-E/T)$ for an optically thick plasma. In our experiment, the largest possible opacity correction is on the order of 35%. The samples we will use in the electron temperature experiment are nearly optically thin, and the opacity corrections are under 10%. Plasma opacity will be modeled using XRASER, and corrections for plasma opacity will be applied. The uncertainty in electron temperature as a result of plasma opacity should be less than 5%.

Electron Temperature Experiment

Figure 1 shows the setup for our electron temperature experiment. We will measure the free-bound continuum spectrum in several samples simultaneously. Three of the four samples, made of low-density foam and shown at the bottom of Fig. 1, will be doped with a mid-Z ion, a high-Z ion, and a mixture of mid- and high-Z ions. One sample will remain undoped to measure the source-scattered background for subtraction from other spectra. All four samples will have a hydrodynamic tamping pad with low x-ray emission in the spectral region of the experiment.

We chose the mid-Z and high-Z ions as complementary K- and L-shell systems. The K-shell ionization potential of the mid-Z ion lies slightly above the highest-energy (Li-like) L-shell continuum threshold of the high-Z ion. Thus, the free-bound spectral regions are similar, and the elements can be mixed with no spectral interference. The K-shell spectra are easiest to interpret and can be used to determine the electron energy distribution without the assumption that it is Maxwellian. We predict that the mid-Z sample will strip well into its K shell, with peak ionization in H-like. We predict that the high-Z sample will strip well into its L shell, with peak ionization in C-like.

A curved-crystal spectrometer with redundant x-ray detection systems will provide both spatial and spectral imaging of the four samples with subnanosecond resolution. The experiment will be timed downhole to the x-ray drive using a source-x-ray-driven, phosphor-light marker. Other experiments will characterize the source intensity and spectrum versus time.

A thin, optically flat quartz 502 crystal shown at the left in Fig. 1 is attached to a Cu-plated Pyrex substrate, which is diamond-turned with optical tolerances to a 20-in. radius. The use of Cu on the substrate significantly reduces x-ray-scattered background from the crystal. X rays from the samples will pass through filters of V and fused silica to eliminate low-energy x rays. X rays from different samples will be Bragg-reflected, passed through a narrow background-rejection slit, and focused at different positions on the detector plane. X rays will deposit their energy in the subnanosecond phosphor-indium-doped cadmium sulfate. Light will be transmitted via a discrete quartz-fiber array to two optical streak cameras. The streak cameras will provide a dynamic range of over 500, which is needed to record the large signal variations both in x-ray spectrum and over time. In addition to the streak camera readout, responses from a discrete array of neutron-damaged GaAs photoconductive detectors will be recorded via cable and oscilloscope to provide an approximate but redundant measurement of the x-ray spectrum.

The energy resolution of the spectrometer is set at approximately 10 eV by an entrance slit. The spatial resolving power is smaller than 200 μrad. To accurately align the spectrometer to the samples so that Bragg-reflected x rays strike the fiber arrays, we will use an active alignment system. A He-Ne laser located about 10 ft from the samples will simulate a point source of light in the center of the samples. This laser light will reflect from the crystal, exit the vacuum through a transparent fused-silica vacuum window, which also serves as an x-ray filter, and be focused onto the detector plane. Two Reticon cameras with a resolution of 0.001 in. will measure the focus sharpness and the centroid of the light focus. The cameras are mounted on an Al bar, which defines the detector plane and holds the phosphor and fiber arrays. The bar can be pivoted about the center of curvature of the crystal using a remote-controlled stepping motor. As a result of stresses introduced in the canister as it is buried, it will bend, and spectrometer pointing will, thus, be compromised. Using the laser light as a reference, the detector bar can be readjusted to bring the spectrometer back into proper alignment.

Calibration

It is difficult to calibrate our spectrometer system as a whole because readily available laboratory x-ray sources yield x-ray fluxes that are 10^{18} times weaker than x-ray fluxes expected during our experiment. Because x-ray imaging properties and crystal efficiency depend on having the x-ray source far from the spectrometer, the available intensities are weak. We could use photon-counting techniques to bridge this gap; however, because of backgrounds, such techniques are difficult to perform reliably. Instead, our spectrometer calibration is performed with both line emission and continuum bremsstrahlung from laboratory x-ray tubes. Pulsed and dc x-ray sources determine the phosphor efficiency versus energy and incident angle. We use pulsed, Lambertian light sources of the correct color to determine the fiber's transmissions and streak camera efficiency. These results are then married.

A solid-state Ge(Li) detector measures the spectrometer's x-ray spectral efficiency. With an x-ray tube placed at the appropriate source-to-spectrometer distance, a Ge(Li) detector measures the incident x-ray spectrum and intensity. The same detector measures the spectrum and intensity of x rays that Bragg-reflect and pass through a slit on the

detector plane. The spectral purity of the Bragg-reflected x ray is high, indicating that the alignment of the crystal is such that reflections from other crystal planes are not intense. We have measured the spectrometer x-ray efficiency versus energy to an accuracy of a few percent over the entire spectral region.

Calibration of the phosphor samples is performed using an 8-A, 50-kV, 200-ps pulse of electrons striking selected foil targets to produce x rays. X-ray filters then make the spectrum more nearly monochromatic. The x-ray-induced phosphor output is measured with a calibrated microchannel-plate-intensified photomultiplier tube and a sampling storage oscilloscope. An Si *p-i-n* diode determines the incident x-ray intensity. These measurements complement the dc x-ray calibrations using laboratory x-ray fluorescent sources and photon counting techniques. The phosphor emission is strongly self-absorbed, and the output is related to the x-ray energy deposition close to the optical-fiber faceplate on which it is deposited.

When our calibrations are complete, we will have characterized the efficiency versus x-ray energy of our spectrometer system with an accuracy on the order of 5% over the entire spectral range. This level of accuracy should enable us to measure electron temperature versus time with an accuracy on the order of 5%. A comparison between the experiment and code predictions should lead to improvements in our understanding of radiation-driven plasmas. The resultant data will be used as a benchmark to predict the behavior of both simple and complex atomic systems and will improve our ability to design nuclear-driven plasma structures that are hydrodynamically stable.

The LRACS/MIFFLEX Package for Measuring X-Ray Output Below the Spectral Peak

S. Ault

We routinely obtain moderate spectral resolution of the absolute output from nuclear explosives for photon energies in the range of 0.7–4.0 times the spectral peak. We make such measurements using filtered-fluorescer techniques. Measured and calculated values show good agreement at higher photon energies; however, we find increasing disparity for energies at or just below the peak. We now seek a better understanding of the lower-energy portion of the x-ray spectrum. To test the accuracy of calculated values, we must extend our measurements to the region well below the spectral peak.

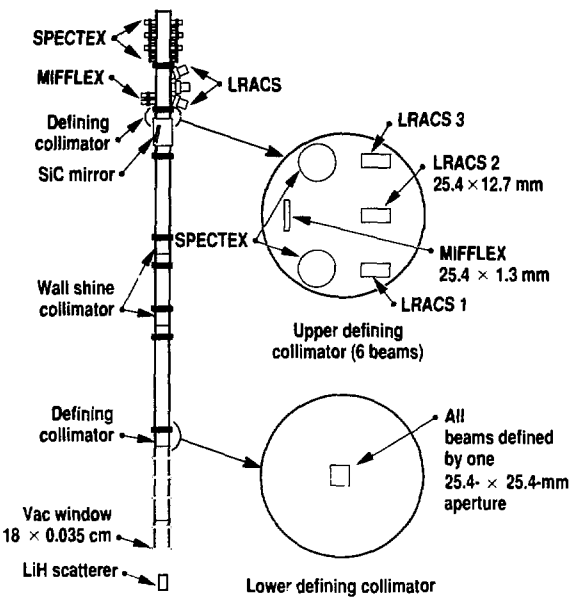

Figure 1. LOS layout and collimation for LRACS and MIFFLEX.

Filtered fluorescers do not work well in the low-energy region because the filter foil cannot stop photons with energies more than about twice the absorption-edge energy of the filter. This fact, coupled with space limitations inherent in underground nuclear tests, prompted us to design an experimental package containing two types of measurement techniques suitable for use well below the spectral peak. The first is the mirror filter-fluorescer experiment (MIFFLEX), which uses a grazing-incidence x-ray mirror as a low-pass filter in front of filtered fluorescers to cover the energy range of 1.5–4 keV. The second is a low-resolution active-crystal spectrometer (LRACS), which uses the first- and

second-order Bragg reflections from LiF crystals to form six energy bins covering the range of 3.5–14 keV. On the upcoming test for which our experimental package was designed, we expect to measure the absolute spectral power from 2 to 14 keV with an experimental uncertainty of about 16–18%.

Line-of-Sight Design

Figure 1 shows the layout of the line of sight (LOS), the location and collimation for LRACS and MIFFLEX, and the 10- to 60-keV filtered-fluorescer instrument, SPECTEX. X rays travel through a square hole with 2.54-cm sides in the lower defining collimator at an elevation of 302 cm from the source. An upper collimator located at elevation 1031 cm defines six beams: one for MIFFLEX, three for LRACS, and two for SPECTEX.

The experiment was designed to measure x rays emitted from a nuclear device and Compton scattered at 90 degrees from a scatterer. With suitable modifications, our package could also be used to directly view the device. Because programmatic considerations required the use of a scatterer for this event, low-density (0.1 g/cm^3) LiH foam suppresses thermal emission from the scatterer with respect to Compton-scattered emission. The use of a scatterer, especially at 90 degrees, placed constraints on the orientation of the entire package due to polarization of scattered x rays. For best performance, the package should be oriented so that the LRACS detector arms are coplanar with those x rays that travel from the center of the device to the center of the scatterer and up the LOS centerline. Such orientation will ensure that the polarization of beams incident on the crystals is correct for efficient Bragg scattering (i.e., beams will be σ polarized with respect to the crystals).

The lower defining collimator is heated during measurement by both the relatively hard-x-ray spectrum of Compton-scattered x rays coming directly from the scatterer and by the "soft" spectrum generated by diffusion of energy up the LOS pipe. Hard x rays come only from the scatterer; thus, their effect is minimized by use of a stack of increasing-Z materials, with each material shielded from hard x rays by materials below. Softer x rays come from all the walls in the lower part of the LOS pipe and, thus, represent a 2π source. The aperture is lined with 0.5 mm of high-purity graphite, which acts as a tamper to prevent blow-in. Carbon that blows into the aperture is of low density and is completely ionized on a short time scale; thus, it is transparent to the radiation of interest.

Heat loading of the upper defining collimator is much less severe and consists entirely of the Compton-scattered spectrum. A stack of materials similar to the one used on the lower defining collimator prevents blow-in by keeping all materials below their vaporization temperatures. No C liner is necessary because the LOS pipe is cooler at this elevation; hence, there is no wide-angle source of soft x rays.

MIFFLEX Design

Figure 2 shows the MIFFLEX concept. X rays from the scatterer strike a SiC mirror at an angle of 0.5 degrees. Those x rays having energies below about 4 keV are reflected into a 0.019-mm-thick Saran ($C_2H_2Cl_2$) foil. X rays above 2.819 keV cause K-shell fluorescence of the Cl in the Saran. These characteristic Cl x rays excite the NE-111 scintillator in the fluor-photodiode detector, causing the generation of an electrical signal, which is recorded uphole on oscilloscopes. This channel measures the power in a bin from 2.819 to 4 keV. Most x rays below the Cl K-edge pass through the Saran and strike a 0.019-mm-thick Al foil. The Saran foil acts as a K-edge filter, and the Al K-edge is at

Figure 2. The LRACS and MIFFLEX experimental package.

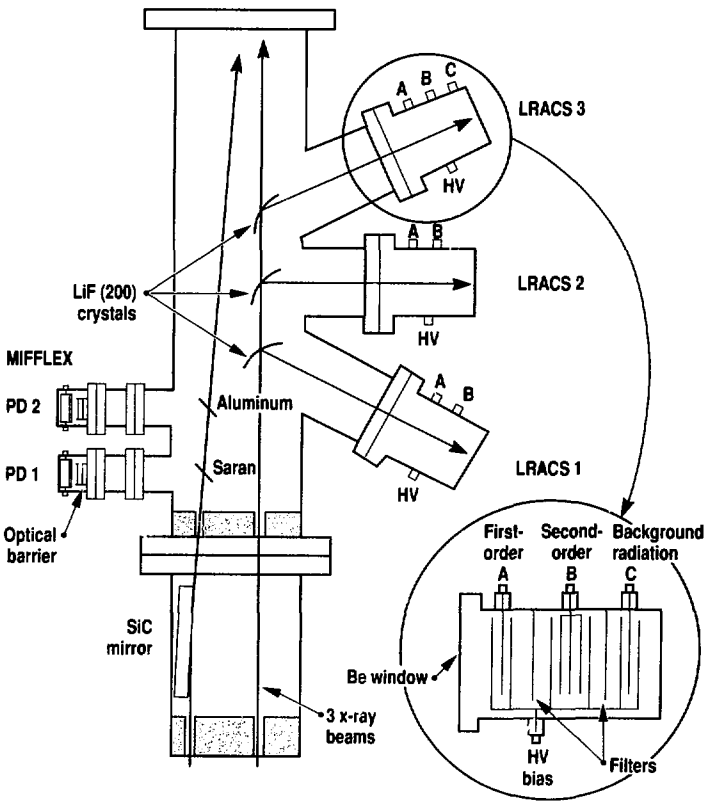

1.559 keV; therefore, the fluor-photodiode detector in this channel yields a signal that is proportional to the power contained in a bin from 1.559 to 2.819 keV.

The mirror is a 30-cm-long, 5-cm-wide, 5-cm-high blank of sintered SiC. Because this sintered material is not suitable for polishing, the reflective surface was coated with SiC by chemical-vapor deposition to form a hard, polishable surface with a density of 3.1 g/cm^3. The resulting mirror offers several advantages over metallic mirrors. The SiC substrate is hard and stable, and it has a low coefficient of thermal expansion. The reflective SiC coating has the same thermal properties as the substrate, thus minimizing thermally induced stress and deformation. The low mass-absorption coefficient of SiC results in a lower absorbed dose per gram than for metals; thus, the material stays cooler. In addition, SiC is a ceramic and can withstand a much higher specific dose than metals (860 cal/g for SiC versus 190 cal/g for Ni). Three kinematic mount points incorporated into the substrate provide a robust mounting system to prevent distortion of the mirror over the temperature range encountered in fielding the experiment.

The area of the beam striking the MIFFLEX foils is small (2.54 × 0.264 cm) because of the small projected area of the mirror in the beam direction. As a result, total power onto the foils is relatively small, leading to the requirement of detectors more sensitive than x-ray diodes. We, thus, selected commercial fluor-photodiode detectors, which view a 1.0-mm-thick piece of NE-111 scintillator. Electrons and ultraviolet photons from the LOS are prevented from reaching the scintillator by two thin, foil barriers consisting of 0.6-μm polypropylene coated with 0.1-μm Cu and 0.1-μm Al. The detectors are vented to the LOS vacuum through a labyrinth of low optical reflectivity, eliminating the need for a vacuum barrier. Figure 3(a) shows the channel response functions (sensitivity as a function of energy) for MIFFLEX.

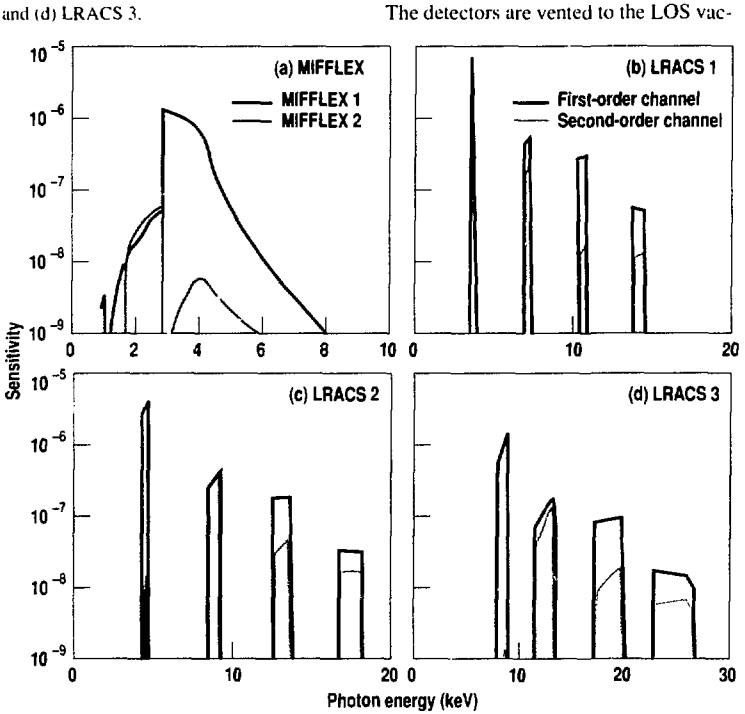

Figure 3. Channel responses for (a) MIFFLEX, (b) LRACS 1, (c) LRACS 2, and (d) LRACS 3.

LRACS Design

Figure 2 also includes a schematic drawing of the LRACS. X rays from the scatterer are collimated into three 1.27- × 2.54-cm beams, each striking the concave side of one of the three cylindrically bent LiF (200) crystals. Various filters in the beams, with K- and L-edges chosen to optimize signal levels, reduce heating of both the defining collimation and the crystals. The three crystals are set at different angles of incidence, thus defining different energy bins by virtue of the Bragg condition for x-ray diffraction. LRACS 1 is set at 60 degrees, LRACS 2 at 45 degrees, and LRACS 3 at 30 degrees. X rays striking the crystal at the Bragg angle appropriate to their energy are reflected, pass through a slit collimator and into a multi-element x-ray-diode detector, and produce electrical signals recorded uphole on oscilloscopes.

The material of choice for the crystals was LiF because it is available in large sizes, is stable and fairly easy to handle, has high reflectivity, and has no high-Z elements, thus eliminating the problem of secondary emission (fluorescence). Scattering and fluorescence from the mounting hardware are prevented by holding the crystals at their edges so that beams strike only LiF. The radii of curvature of the crystals were chosen so that the reflected beams, which converge to a crossover point and then diverge, would fall within the active area of detectors placed as near as practicable to the crystals. Lead slit collimators placed at the crossover points provide background suppression.

Each of the three LRACS detectors has a Be vacuum window to stop electrons and ultraviolet photons, and two sets of active elements: one set is selectively sensitive to first-order reflections and the other to second-order reflections. The active elements of the detectors are

thin foils of Be coated with layers of various materials. The coatings are optically thin to the x rays being detected so that both sides of the foils contribute to the signals. One of the detectors has an additional set of elements sensitive only to nuclear background radiation. Table I shows the coatings used on the elements in the detectors.

Because it is instructive to examine how selectivity is achieved, we use LRACS 2 as an example. The first-order range of energies reflected by the LRACS 2 crystal is 4.17–4.6 keV, the second-order range is 8.34–9.20 keV, and the third-order range is 12.51–13.8 keV. The first sensitive element in the LRACS 2 detector is coated with Ag, which has L-absorption edges around 3.8 keV, i.e., just below the range of the desired first-order channel. The coating is about 2 electron ranges thick for 4-keV electrons so that sensitivity is maximized for the first-order x rays. However, because the electron range is much shorter than the mean free path of an x ray of the same energy, the detector element is optically thin to all x rays striking it. The sensitivity of this element falls off as roughly E^{-3}, where E is photon energy; thus, this element is about 12% as sensitive to second order as to first order, and about 4% as sensitive to third order. This fact, coupled with the fact that higher-order reflections from the crystal become progressively weaker than first-order reflections, results in a channel that is predominately sensitive to first-order x rays. Ideally, the first-order channels would respond only to first-order x rays, but such ideal selectivity cannot be realized in practice. On the nuclear test for which LRACS was designed, the signal on the first-order channel will consist of 73% first-order x rays, 15% second-order x rays, and 10% third-order x rays. The remaining, small percentage of the signal is due to scattering from the crystal and other components. These percentages depend on the spectral shape.

The second set of active elements in the detector must be sensitive to second-order x rays and reject all other orders. First-order x rays are removed partly by the first active detector element, whose absorption edge is just below the first-order energy. Additional filtering is provided by a foil, in this case Zn, with an absorption edge at 9.66 keV. The Zn foil resides between the first and second set of active elements and is chosen to have an absorption edge just above that of the second-order channel. This filter tends to pass second-order reflections while eliminating some third-order and most first-order x rays. By selecting a coating for the second set of active elements that has an absorption edge just below the second-order energy (in this case, Ni at 8.3 keV), a channel is created that responds almost exclusively to second-order x rays. The expected signal on the upcoming test will consist of 88% second-order, 1% first-order, and 5% third-order x rays.

The required filtration for selectivity takes its toll on second-order x rays. Therefore, the set of elements that detects second-order x rays consists of two identical foils electrically connected in parallel, as shown in Fig. 2. This design nearly doubles the size of the detected signal on the second-order channel. Figure 3(b) through (d) shows the response functions for all six channels of LRACS.

Table 1. Coatings for elements in LRACS detectors.

Element number	Function	Coatings LRACS 1	LRACS 2	LRACS 3
1	Anode	none	none	none
2	Cathode (first order)	1200-Å Rh	2000-Å Ag	4000-Å V
3	Anode	none	none	none
4	Filter	20-μm Ni	40-μm Zn	65-μm Y
5	Anode	none	none	none
6	Cathode (second order)	7000-Å Ti	5500-Å Ni	10,000-Å Cu
7	Anode	none	none	none
8	Cathode	7000-Å Ti	5500-Å Ni	10,000-Å Cu
9	Anode	none	none	none
10	Filter	—	—	60.0-mil Ta
11	Anode	—	—	none
12	Cathode (background)	—	—	2-mil Ta
13	Anode	—	—	none

Data Analysis and Error Budget

The selectivity of LRACS channels is not ideal (i.e., the first-order channel has some sensitivity to higher orders, and the second-order channel has some sensitivity to first- and third-order x rays). Although this circumstance is inconvenient, it is possible to easily unfold the correct spectral shape algebraically because the channel-response functions of LRACS are small everywhere except within the energy bins defined by the crystal. Thus, the voltage on detector element $i = 1, 2$ can be expressed as $v_i = \sum_j S_{ij} P_j$, where S_{ij} is the sensitivity of element i to jth-order x rays, and P_j is the spectral power in jth order. If we use only the first and second order, we obtain a closed set of equations, which can be solved for P_1, P_2. Higher orders can be included if we use SPECTEX data in the analysis.

Using reasonable values for uncertainties in the upcoming test yields values for experimental uncertainty in spectral power of about 18% for the first-order channel and 16% for the second-order channel. Use of a harder x-ray spectrum results in values of 30% uncertainty in first-order power and 16% in second-order. This result is due to a larger second-order x-ray contribution to the first-order channel signal with a harder x-ray spectrum.

Fiber-Optic Alpha Measurement Development

B. L. Pruett

Fiber-optic alpha measurement (FOAM) is a technology we use on NTS events to measure fast gamma-ray (reaction history) signals that we cannot adequately diagnose with slower, conventional cable-oscilloscope systems.[1] FOAM couples high-bandwidth fiber-optic cable with state-of-the-art streak cameras. A distinct advantage of FOAM is that the downhole components are totally passive.

The availability of a new streak tube made by ITT greatly enhances the data quality that we can obtain and is a definite improvement over the RCA tube that we previously used. The ITT tube increases sensitivity to output signals and also permits use of a new, compact detector module and a new spectral equalizer. These advances result in less susceptibility to radiation damage in the detector fiber and improved time response.

Typical System Description

The traditional FOAM system (Fig. 1) uses a nominal 1-km fiber run and has a −1.5-dB optical-frequency response (equivalent to −3 dB electrical) in the 0.6-GHz range. It is representative of several systems we have used on NTS events over the past few years. We place a converter plate in a diagnostic-canister line of sight. When gamma radiation strikes the converter plate, the plate emits Compton electrons. We place an optical fiber in contact with the exit face of the converter so that, when the electrons strike it, they produce Cherenkov light in the fiber. We transmit this light uphole to a spectral equalizer and then to a streak camera for recording.

The converter plate is a slab of polyethylene about 1 cm thick that we place in the gamma-ray beam at 45 degrees to the beam direction. Polyethylene satisfies the necessity for a low-Z material that maximizes the fraction of the electron flux that strikes the detector fiber at the proper angles. Beryllium is a slightly better material but is much more expensive and difficult to fabricate.

We place a 100-μm-diam, step-index optical-detector fiber on the back side of the converter. The sensitivity of the converter-fiber combination is about 5×10^{-23} μW/(γ-MeV cm^{-2} s^{-1} nm cm) after adjustment for the amount of light coupled into a 50-μm-diam uphole transmitting fiber. The detector fiber has a pure SiO_2 core to minimize light attenuation caused by radiation damage. We keep the length of fiber from the detector point to the uphole fiber connection to less than 4 m to minimize the effects of modal dispersion (about 65 ps/m) typical of step-index fiber.

The uphole-transmission fiber cable is standard FO-2, which contains eight multimode fibers with 50-μm-diam graded-index cores. The fiber is specified to have a a bandwidth-length product of 1.3 GHz-km for a 2-nm spectral bite at about 800 nm.

We use an equalizer between the uphole-fiber termination and the streak camera to permit the use of a 40-nm-wide bandpass without the penalty of excessive material (chromatic) dispersion. This device employs an optical grating and a fiber-array scheme in conjunction with the streak camera to use the 40-nm-wide bandpass but limit the dispersion to that of a 2-nm bandpass. The equalizer insertion loss is about 6.5 dB.

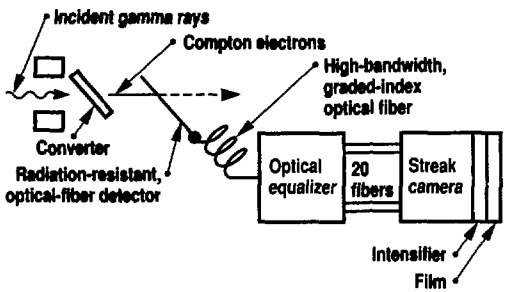

Figure 1. The fiber-optic diagnostic system, consisting of a detector, a high-bandwidth optical fiber, a spectral-streak equalizer, and a streak-camera recording system. Gamma rays from a nuclear source are converted into high-energy Compton electrons that generate light in a radiation-resistant optical fiber. The light is transmitted through a long graded-index fiber to the spectral-streak equalizer.

The streak-camera system, which records FOAM signals, has an RCA streak tube with a quantum efficiency of about 0.4% at 800 nm. This sensitivity allows us to record input signals that range from a few microwatts up to about 1 mW. Typical sweep lengths are 15 and 60 ns. All these systems use photographic film as the recording medium.

New Components

Four new components are available that can improve the FOAM experiments. The size of the observed source area and the canister line-of-sight geometry can place severe limitations on the detector collimator diameters. We have designed a new compact detector module to replace reaction-history doghouses and filter boxes (Fig. 2). We have reduced the separation between detector stations from 1 to about 0.3 m, which permits us to use smaller collimator diameters and shorter exposed fiber lengths than we could with the old hardware. The new module also reduces installation efforts. We have designed a new spectral equalizer[2] to accommodate four signal channels instead of one for each optical grating. This equalizer can also use up to forty 1-nm spectral bites instead of twenty 2-nm bites. The equalizer can reduce the effects of material dispersion in the uphole fiber by a factor of 2 with no additional loss of signal. The ITT streak tube has a quantum efficiency of about 4.8% at 800 nm, more than an order of magnitude greater than the old RCA tube. In addition, the new streak tube improves both temporal and spatial resolution, and other performance characteristics are at least equal to the RCA tube. New, charge-coupled-device camera-readout systems, which replace film recording, offer improved data quality and greater efficiency in the data-reduction process.

Time Response

We have significantly reduced the FOAM-system time response by taking advantage of the increased sensitivity of the ITT streak tube and the smaller dimensions of the new detector module. We have shortened the length of the detector fiber in the Compton electron field with a linear reduction in the time smear that is caused by the velocity mismatch between gamma and optical photons. The shorter module minimizes the length of step-index fiber needed to reach the FO-2 connection point and, therefore, reduces the modal dispersion in the step-index fiber.

The chromatic dispersion that takes place in the FO-2 fiber is about 105 ps/nm-km. Using the new equalizer, we have reduced the chromatic dispersion from about 210 to about 105 ps for a 1-km fiber run. Unfortunately, we cannot reduce the modal dispersion in the FO-2 (about 275 ps/km), which ultimately limits the FOAM-system time response.

The ITT streak tube, which has a nominal 0.3% of sweep-length response time compared to about 0.5% for the RCA tube, provides the final improvement to the system. By adding the time-response elements in quadrature, we demonstrate that we can reduce the system response time from about 510 to about 345 ps (full width at half maximum) when we use a 1-km cable.

Fiber-Radiation Damage

The increased recording-system sensitivity allows us to use less gamma

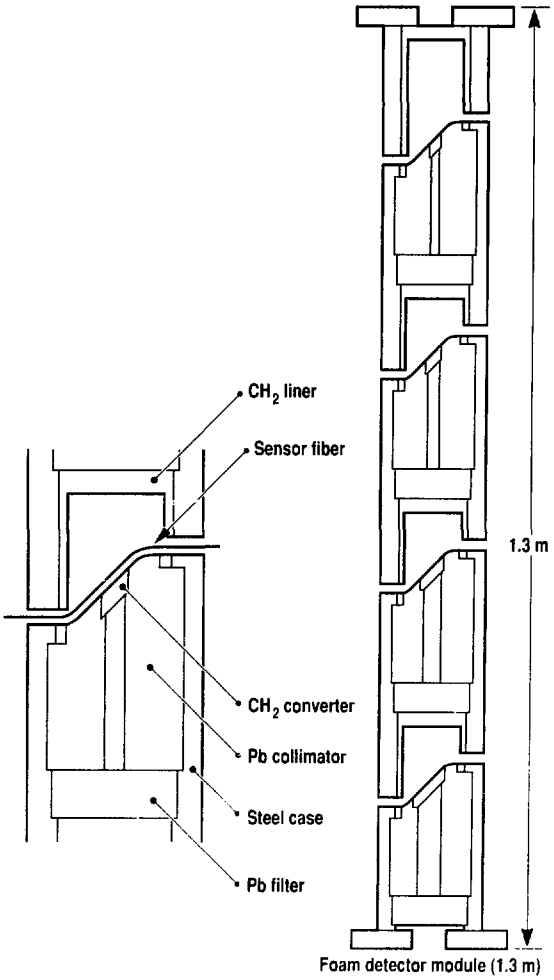

Figure 2. A cross section of the FOAM-detector module that is installed in a diagnostic-canister line of sight. The module has four fiber-detector stations with intervening Pb filters to obtain extended dynamic range. The CH_2 liners minimize the effects of electron backscatter. The overall length of the module is about 1.3 m.

radiation to produce a usable signal in the detector fiber. We can now record signals over a greater dynamic range or over longer time periods before the integrated-radiation dose to an optical fiber that has a fixed radiation-damage threshold becomes critical. Also, the effects of radiation damage are reduced when we shorten the detector-fiber length to improve time response.

Optical-Band Selection

The new optical equalizer has advantages. However, if it is not necessary to improve system time response, it should be possible to eliminate the equalizer altogether and instead use a narrow-band filter for band selection. If we use a 2-nm-wide filter with a 3-dB insertion loss in conjunction with the ITT streak tube, it gives us about the same signal-amplitude coverage that we obtain with the old FOAM system. Elimination of the custom-fabricated equalizers, which are matched to each fiber, would result in significant cost and effort savings. We could also use a monochromator in place of the equalizer, but it would probably have an insertion loss of about 6 dB.

System Comparisons

Table 1 summarizes time-response estimates (full width at half maximum) for a typical baseline system that we previously fielded and for three possible variations that we can now field using the newer technology. The response time for the new FOAM system, using a 1-km fiber run, has decreased from about 510 to about 344 ps. Its gamma-ray sensitivity is now double that of the baseline system. With a shorter (but often reasonable) fiber run of 0.67 km, the new FOAM system has an approximate 270-ps response time. A system using a narrow-band filter to replace the equalizer performs comparably to the baseline system.

Table 1 also illustrates how the FO-2 modal dispersion limits the ultimate time response. For example, the modal-dispersion time for the new 1-km system is about 80% that of the entire system response time. Therefore, any further improvements in the other elements would not be significant.

Table 1. Estimated response times for a typical baseline FOAM (fiber-optic alpha measurement) system and three variations.

	Baseline FOAM system	Upgraded FOAM system	FOAM system with shorter fiber run	Narrow-band filter system
System				
Fiber run (km)	1	1	0.67	1
Spectral bites	20	20	20	1
Bite width (nm)	2	1	1	2
Streak tube	RCA	ITT	ITT	ITT
Active sensor fiber				
Length (cm)	13	4.3	4.3	13
Response (ps)	234	77	77	234
Jumper fiber				
Length (m)	4	1	1	1
Response (ps)	252	63	63	63
FO-2 fiber				
Modal dispersion (ps)	272	272	182	272
Material dispersion (ps)	209	105	70	209
Streak camera				
Sweep (ns)	15	30	30	30
Response (ps)	145	154	154	154
System response				
FWHM (ps)	507	344	268	447
[illegible] (ps)	363	246	192	320
1.5-dB bandwidth (GHz)	0.62	0.91	1.17	0.70
3.0-dB bandwidth (GHz)	0.87	1.28	1.65	0.99
Relative sensitivity	1	2	2	1

Summary

New FOAM-system components with 1.0- and 0.67-km cable runs have rise times of about 245 and 195 ps, respectively, and their −1.5-dB optical bandwidths are about 0.9 and 1.2 GHz, respectively. The previous FOAM system, at 1 km, had a rise time of about 365 ps and a bandwidth of about 0.6 GHz. Cable-oscilloscope systems generally do not have rise times of less than 450 ps nor bandwidths greater than 0.5 GHz.

The new FOAM system offers significantly improved data quality, less cost, and less fielding effort. It also retains important features that are traditional for FOAM, such as multichannel recording by the streak camera.

References:

1. F. Roeske, D. Smith, B. Pruett, and R. Reedy, "A High-Bandwidth Multichannel Fiber Optic System for Measuring Gamma Rays," *SPIE Volume 506, Fiber Optics in Adverse Environments II, 1984* (The International Society for Optical Engineering, Bellingham, Wash., 1984), vol. 506, pp. 29–35.
2. R. P. Reedy, "Multichannel Fiber-Optic Spectral-Streak Equalizer," *SPIE Volume 720, High Bandwidth Analog Applications of Photonics, 1986* (The International Society for Optical Engineering, Bellingham, Wash., 1986), vol. 720, pp. 38–47.

Astrophysical Opacity Experiment

R.T. [redacted], T.S. [redacted], B.A. [redacted], C. [redacted], R.J. [redacted], and C.A. [redacted]

We have designed and propose to perform a detailed spectroscopic measurement of the opacity of a local thermodynamic equilibrium (LTE) sample with conditions close to stellar temperature, density, and composition. The experimental goal is to provide high-resolution, multifrequency opacity data to test and improve our understanding of the physics governing ions in hot dense plasmas. This should allow more accurate calculations of average opacities, such as the Rosseland mean opacity, used in the predictions of radiation flow through matter. The data should allow us to test details of the opacity theories including the following: atomic structure, resonance and satellite line strength, excited state occupation number, density dependence of the plasma ionization state, density dependence of line-broadening mechanisms, and effects of continuum lowering.

Plasma Samples

The plasma samples will be iron doped in a low-Z material at different doping concentrations for the different spectral regions covered, to give optical depths that can be accurately probed experimentally. Driven by radiation from a nuclear test, the samples will come to equilibrium with the radiation field at a temperature near 300 eV. The samples are predicted to have uniform densities that vary in time during the experiment from 1 to 0.1 gm cm^{-3}, as the samples expand. At these temperatures and densities, the iron in the samples is stripped well into the L-shell, giving a rich and complex bound-bound and bound-free structure, which dominates the plasma opacity.

The plasma absorption will be measured by backlighting a portion of each sample with a bright continuum emission from an optically thick plastic backlighter at a temperature of approximately 600 eV that is placed approximately 1 m behind the 300-eV samples. An imaging, bent crystal spectrometer will be used to spatially resolve the different samples and the backlit portions of each sample, also giving high-resolution spectral measurements of the plasma emission, the plasma absorption of the backlighter x rays, and the backlighter spectrum. The spectral coverage will include portions of the iron L-shell 3–2, 4–2, and 5–2 bound-bound manifolds and also the free-bound continuum. Sample temperature will be measured using the iron free-bound continuum spectrum, and sample density versus time will be measured using time-resolved radiography. The schematic of the experimental setup in Fig. 1 shows the placement of the spectrometer, opacity samples, and backlighter. Additional samples will be used for the temperature and density measurements as described below.

Modeling of Plasma Conditions

A dynamic simulation of the experiment is performed using the computer code LASNEX to predict radiation drive, sample temperature, ionization state, and densities versus time for a particular geometry. Since plasma conditions will be measured experimentally, it is important only that the temperature be sufficiently high that the samples are not too opaque.

Modeling of Opacity

Calculations of the opacity of ions in a hot dense plasma are complex, requiring knowledge of the detailed atomic structure of multiply ionized atoms as well as the effects of ion-plasma interactions. In a Saha-Boltzmann description of the plasma equilibria, an *ad hoc* cutoff in the number of bound Rydberg levels is employed to account for the continuum lowering due to Debye screening.

Rogers et al. have developed a more rigorous method employing a many-body expansion of the Coulomb interaction in the grand canonical ensemble. With parametric potentials and configuration interaction term splitting, the atomic structure and the bound-bound and bound-free cross sections are calculated for all levels of the ion in its different states of ionization. In determining the occupation of the atomic excited states, effective one- and two-body interactions in the many-body expansion are employed. Line profiles are then calculated using Doppler and Stark broadening mechanisms.

Figure 2 shows the calculated opacity of 1:200 (by weight), iron-doped samples

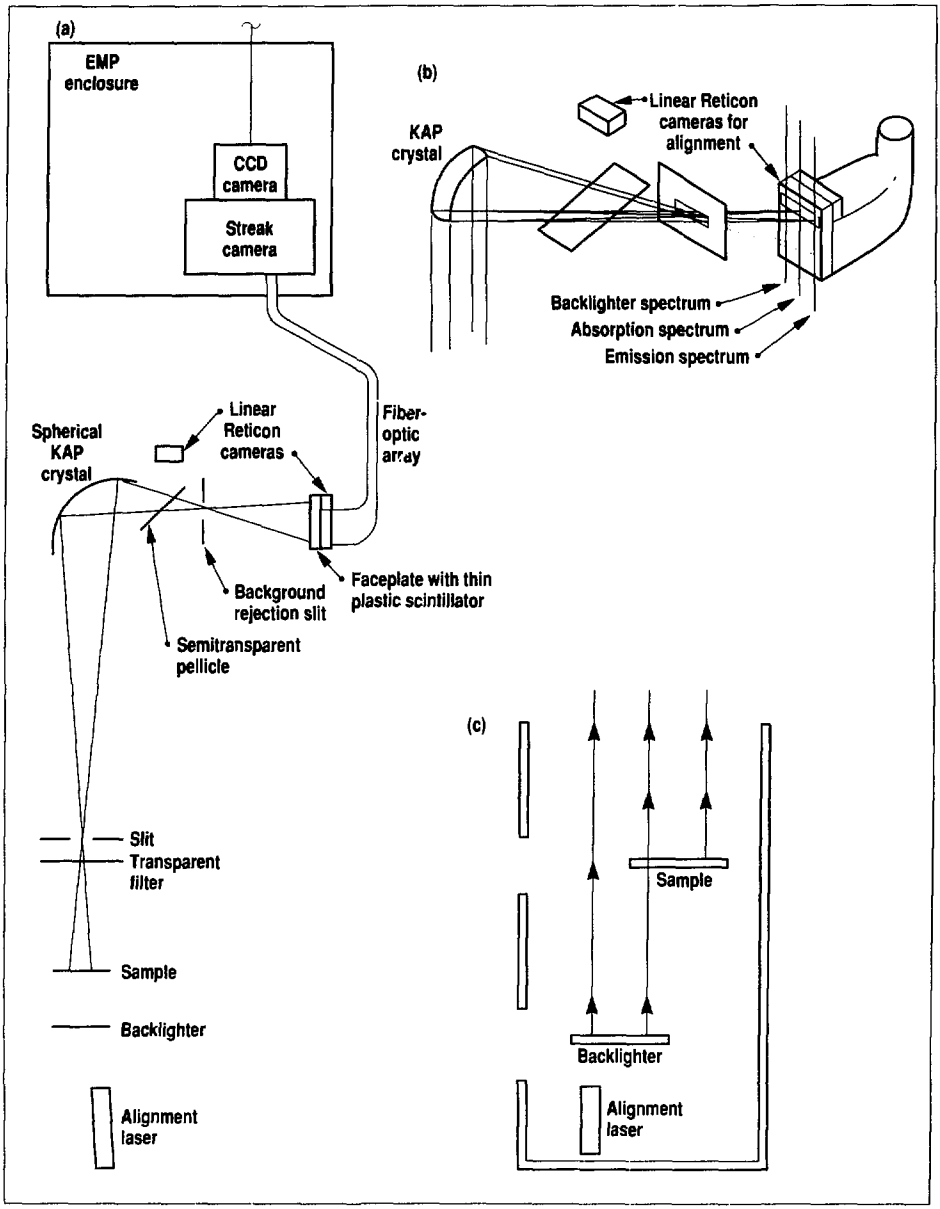

Figure 1.
Schematic of the experimental setup for spectroscopic measurement of the opacity of an LTE sample at nearly stellar condition. (a) The iron opacity experiment will use an imaging spectrometer. (b) A spherical crystal will allow imaging of different source regions. (c) Three source regions will be obtained by offsetting the source and backlighter.

at 300 eV and densities of 1.0, 0.3, and 0.1 gm cm^{-3}. Figure 3 shows the calculated opacity at a density of 0.3 gm cm^{-3} and temperatures of 270, 300, and 330 eV. Since the opacity depends critically on both the temperature and density, these parameters must be accurately determined if comparisons with the code predictions are to be meaningful. Although the plasma temperature is predicted to remain fairly constant during the experiment, the density of the sample changes as the sample expands. During this tenfold expansion, the average ionization state of the iron changes from nitrogen-like to beryllium-like. In the 3–2 manifold near 1 keV, the ionization change is reflected in the shift from a predominance of subkilovolt lines at high densities to supe-kilovolt lines at lower densities. The 3–2 emission spectrum can be used to determine the mean plasma ionization state. Stark broadening of the high Rydberg transitions can be used to determine the plasma density as is illustrated in the calculations, whereas, at high densities, the 4–2 and 5–2 manifolds seem to blend into the continuum. The measured line widths can be used as a density diagnostic. However, the density dependence of the line widths depends on the model used, and there are density-independent line broadening mechanisms, such as the lines' optical depth and satellite structure, for which corrections must be applied.

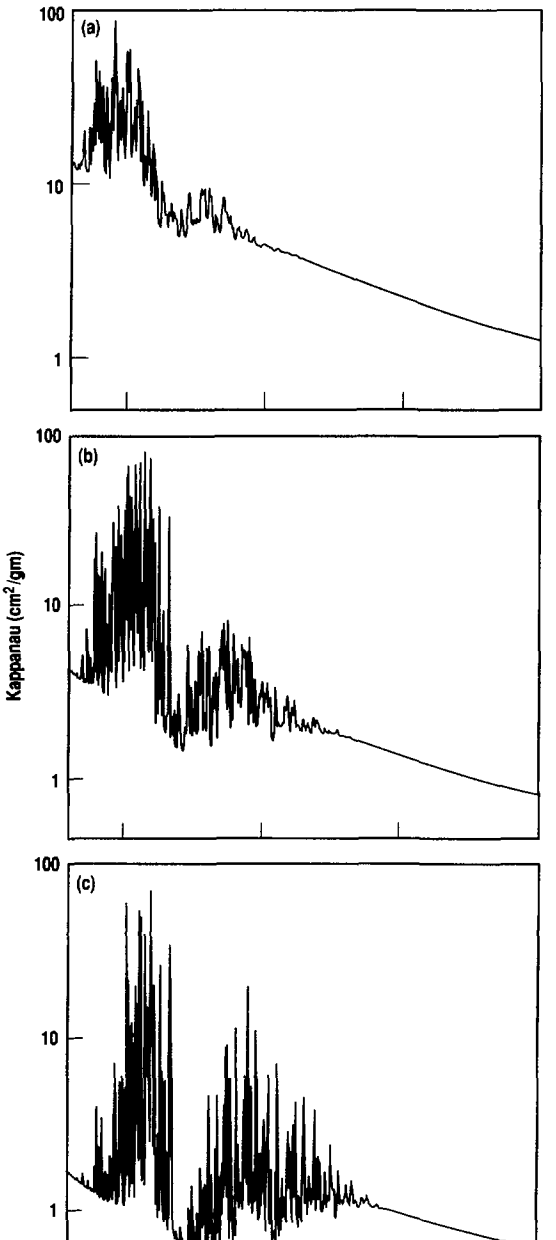

Figure 2. Calculated opacities of iron-doped samples at temperature of 300 eV and densities of (a) 1.0, (b) 0.3, and (c) 0.1 gm/cm^3.

LTE, Emission, and Absorption Opacities

In an LTE plasma of opacity K_ν, if we assume an index of refraction of unity, the emission spectrum is given by

$$\varepsilon_\nu = B_\nu(T)\,[1 - \exp(-K_\nu \rho L)]\,,$$

where $K_\nu \rho L$ is the plasma optical depth at frequency ν, and $B_\nu(T)$ is the blackbody brightness:

$$B_\nu(T) = 2h\nu^3 c^{-2}\,[\exp(h\nu/T) - 1]^{-1}$$

$$\times\ (\text{erg cm}^{-2}\,\text{s}^{-1}\,\text{ster}^{-1}\,\text{Hz}^{-1})\,.$$

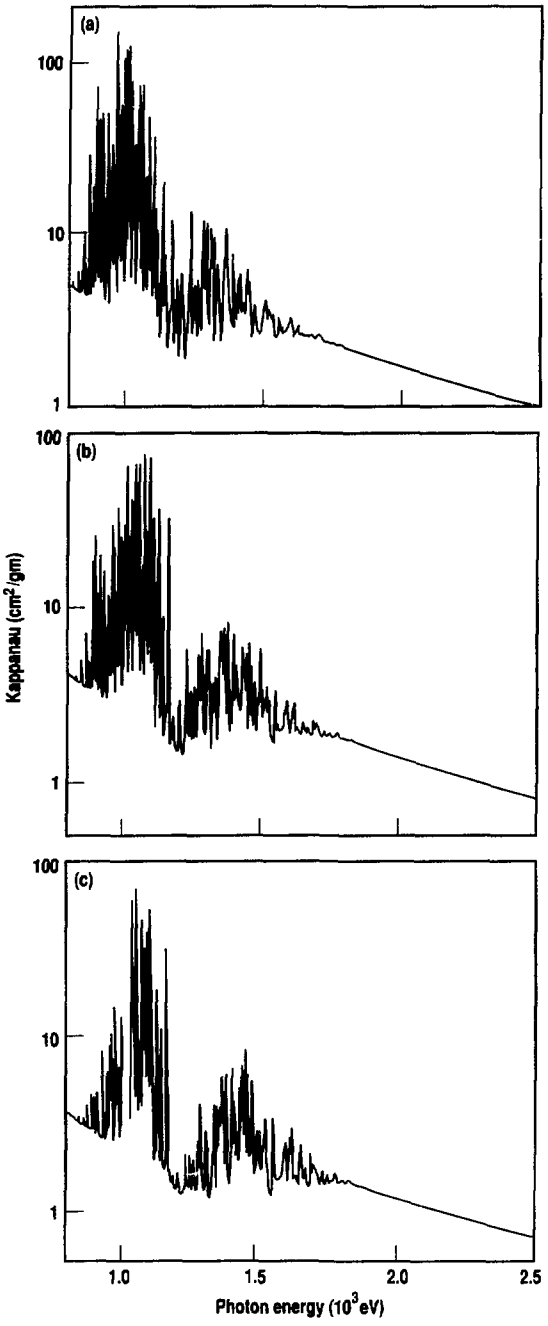

Figure 3.
Calculated opacities of iron-doped samples at density of 0.3 gm/cm^{-3} and temperatures of (a) 270, (b) 300, and (c) 330 eV.

The backlighter is an optically thick plastic sample designed to reach a temperature of T_b = 600 eV, which should have a spectrum given by:

$$\varepsilon_\nu B.L. = B_\nu(T_b) .$$

The sample emission spectrum at a temperature T_s = 300 eV is given by:

$$\varepsilon_\nu S = B_\nu(T_s)\,[1 - \exp(-K_\nu \rho L)] .$$

Because of its higher temperature, the backlighter emission is much brighter than the sample emission. For a spectral coverage from 0.8 to 2.5 keV, the brightness contrast ranges from a factor of 4.8 to 65.

The spectrum from the sample emission with backlighter absorption is given by:

$$\varepsilon_\nu \text{Abs.} = B_\nu(T_b) \exp(-K_\nu L) + B_\nu(T_s) \times [1 - \exp(-K_\nu L)] .$$

Experimental Accuracy

In the experiment, we simultaneously measure the spectra from the sample emission, the backlighter emission, and the sample emission with backlighter absorption. Experimentally, the opacity is obtained by subtracting the measured backlighter absorption spectrum from the measured sample emission spectrum and dividing by the measured incident backlighter spectrum. Thus, the opacity is given by:

$$K_\nu = (\rho o L)^{-1} \ln[\varepsilon_\nu B.L./(\varepsilon_\nu \text{ Abs.} - \varepsilon_\nu S)] .$$

Because all the spectra are measured on the same spectrometer and subject to the same instrumental response, the measurement is subject to little if any experimental systematic uncertainty. With care, a spectrometer can be calibrated in relative efficiency across the entire spectrum with an accuracy of about 5%. For an optically thin plasma, the sample emission and absorption spectra have nearly equal intensity, and the accuracy of the measured ratio should be less than 10%. Thus, it would be very difficult to measure opacities with an optical depth

through the sample of less than 0.1. For portions of the spectra that are very optically thick, the sample absorption spectrum is nearly equal to the sample emission spectrum. The subtraction can be performed to an accuracy of about 10% of the sample emission intensity. Because it is difficult to measure opacities if the attenuation is more than 10 times the contrast between the brightness of the sample and backlighter spectra, the sample optical depths should be less than about 4–5.

The plasma temperature will be determined from the shape of the emission spectrum above the highest-energy L-shell ionization potential, which is 2.05 keV for photoionization of lithium-like iron. In this case, opacity results mainly from photoionization of L-shell iron, and there are no bound-bound contributions from any ion. This measurement is possible only if the sample imaged has an iron-doping density to give an optical depth of about 1 at the free-bound continuum threshold. This sample will also play a role in the density measurement described below. In the spectra region corresponding to the free-bound continuum, the sample is nearly optically thin, and the emission spectrum is proportional to $[1 - \exp(-K_\nu \rho L)]$ $\exp(-h_\nu/T)$. Although the intensity of the free-bound continuum is determined by the plasma ionization state, which is a strong function of both plasma temperature and density, the shape of the spectrum is determined mainly by the plasma temperature. When the energy variation of the plasma opacity is removed, the emission spectrum falls exponentially with x-ray energy, and the plasma temperature then determines the falloff rate. The energy variation of the plasma opacity can be determined accurately because the variation of the photoionization cross sections with x-ray energy can be precisely calculated and because the plasma opacity and its energy variation are measured in the experiment. The uncertainty in the plasma temperature will be limited by the fidelity of the characterization of the spectrometer response, which should give a temperature measurement with an accuracy of about 5%.

The plasma density will be determined using time-resolved radiography. A sample similar to the opacity sample will be viewed edge-on and tamped on its ends with a low-Z material. In this way, the hydrodynamic expansion of the iron-doped part is not influenced by the blowoff of the ends but undergoes one-dimensional expansion. While the hydrodynamic expansion of the thin opacity sample does not affect the column density seen by the backlighter x rays, the expansion of the sideways sample reduces the column density, which affects the x-ray transmission. The x-ray transmission of the sideways sample will be measured in the region of the iron L-shell free-bound continuum, above 2 keV, where the opacity is dominated by the iron. Therefore, the thickness of the tamper needed to ensure one-dimensional expansion should not significantly influence the x-ray transmission. The transmission of the sideways sample will be given by $\exp(-K_\nu \rho H)$, where H, which is approximately 1 cm, is the thickness of the iron-doped region. The value of K_ν will be obtained from the backlit sample used in the temperature measurement, which should have an accuracy of about 10%. Providing that the samples are all heated with the same efficiency by the 300-eV radiation field and that the effects of the sample geometry and different iron-doping densities can be minimized, this method should provide a nearly model-free diagnostic of the plasma density with an accuracy of about 10%.

It is important for the spectrometer to image the thin sample even at early times in order to resolve the x-ray transmission of the iron portion of the tamped sample. As the sample expands, the imaging becomes easier to perform. An accurate determination of the density at late times, in conjunction with an accurate determination of the plasma temperature, can be used to reliably model the density versus time. Still, the spectrometer must be able to resolve objects on a scale of a few millimeters. The dynamic range (about 200) required of the instrument is set by the emission brightness of the samples and the backlighter. The spectral resolution will be about 1.5 eV, and the imaging resolution will be about 1 mm at the sample. The time resolution will be approximately 1 ns, and the total coverage time will be about 30 ns.

Approximately 4 spatially multiplexed streak cameras are required for a total of 16,000 resolvable data elements. Most of the camera coverage would be concentrated in the regions of the L-shell bound-bound manifold. The backlighter and free-bound continuum spectra do not require extensive spectral coverage because they are smooth.

Reference:

1. C. A. Iglesias, F. J. Rogers, and B. G. Wilson, *Astrophys. J. (Lett.)* **322**, L45 (1987).

Coherent Microwave Generation Using an Intense Relativistic-Electron-Beam–Plasma Interaction

B. Chang, B. Poole, and F. Camacho

High-current electron beams moving at speeds close to that of light have enormous amounts of kinetic energy. Our goal is to investigate the possibility of converting some of the energy into coherent microwave radiation. A high-power microwave source could have applications in the Strategic Defense Initiative (SDI), in lethality-vulnerability tests of electronic hardware, and even in nonmilitary areas, such as telecommunications.

The generation of microwaves by a beam-plasma instability is an easy concept to understand. Injecting an electron beam into a waveguide, which is filled with a plasma, excites the normal modes of the coupled plasma-waveguide system. The excitation occurs at the beam front where the beam comes into contact with the plasma and is caused by the Coulomb interaction of electrons in the beam with electrons in the plasma. As the beam gives off energy to the plasma, waves set up in the plasma by the excitation are amplified. Because the plasma waves are coupled to the TM modes of the electromagnetic field by the waveguide, microwaves are generated as the result of the excitation of waves in the plasma. It is a slight misnomer to call the excitation process a "beam-plasma instability," inasmuch as the beam actually excites plasma-electromagnetic waves, which are partly plasma and partly electromagnetic. We use the term "instability" because the plasma-electromagnetic waves grow as they gain energy from the beam.

Development of an efficient (>10%), high-power (1-GW), and coherent microwave source from a beam-plasma instability, which is driven by an intense (10-kA), relativistic (0.94 c) beam, is difficult. Many physical processes occur in the operation of a beam-plasma generator, and each must be understood and controlled before the concept can be made into a practical device. The most important issue is beam transport. At high currents, the beam induces a magnetic field that is so strong it pinches off the beam. Consequently, the beam is not likely to travel far into the plasma and interact with it. An issue almost as important as beam propagation is the extraction of microwave energy. Although this issue is primarily an engineering problem rather than a physics issue, we must, nevertheless, consider an efficient way to couple the microwave source to an antenna for energy extraction. Less critical issues that must also be addressed pertain to energy optimization, mode competition, and mode selectivity in the device. We have mounted an integrated experimental, theoretical, and computational effort to examine these problems.

Status

Our project was initiated in FY86. The work was motivated by findings from University of California (UC) Irvine researchers of broadband emissions in the frequency range of 1–100 GHz when a dense beam was injected into a plasma-filled lucite tube.[1,2] In the UC Irvine experiment, the density of electrons in the beam was closely matched to the density of electrons in the plasma. According to their theory, microwaves are generated by an electrostatic two-stream instability in which the beam and return current induced by the beam interact. We undertook a similar experiment to verify the UC Irvine results. Microwave emission was much lower than expected.[3] From current measurements taken by Rogowski coils placed along the tube, we also found that the beam did not propagate to the end. We concluded that a magnetic field was needed to aid beam transport.

We realized that the crucial ingredient missing from the UC Irvine experiment

was a metallic waveguide. For amplification to occur, the beam, plasma, and radiation field must travel synchronously over a long distance so that they have an opportunity to interact. Keeping them together over a long interaction region is unlikely in a lucite tube because the dielectric wall of the lucite is transparent to microwaves. On the other hand, the perfectly conducting walls of a metallic waveguide confine microwaves in the interaction region by reflecting them back into the beam and plasma. As a result of the reflection, energy is fed back into the beam, which causes the beam to bunch. The bunching of the beam amplifies microwaves to higher power levels. Thus, we have an explanation for the Livermore results and a theory for producing microwaves from a beam-plasma instability. However, our experimental results and theory remained at odds with the UC Irvine findings. We learned later in FY88 that the UC Irvine team had over-reported the emitted microwave power because of poor diagnostics.

Encouraged by the simulation results from CONDOR, a relativistic-particle–electromagnetic code, we proceeded with our conjecture long before the group at UC Irvine retracted their results. As a first step toward proving our conjecture, we added a 1.8-kG magnetic field to our experimental apparatus in FY88. We did not install a waveguide at this stage of our study so that we could study the issue of beam transport in isolation. The question addressed in this experiment was as follows: If the beam does not pinch off, then could the UC Irvine apparatus produce microwaves? Figure 1 is a representation of our experiment designed to answer this question. The four 16-in.-diam coils used to produce an axial magnetic field was a major modification of the experimental apparatus, and their installation required a great deal of effort. Replacement of the lucite tube with a metallic waveguide for the next set of experiments will be trivial in comparison. Our diagnostics consisted of a streak camera and Rogowski coils for beam-transport measurements and a microwave spectrometer for recording microwave emissions.

We found that the magnetic field modified the operation of our plasma source. Unlike the case for a zero magnetic field, in which plasma filled the entire lucite tube more or less uniformly, the plasma now was constricted to a column whose radius was that of the plasma source (2.5 cm). We concluded that the plasma column was constricted by observing the afterglow (no other measurement was made). Electrons tended to stay on the magnetic field lines on which they were born. This constriction of plasma may present serious problems to beam transport and to microwave production.

The presence of the axial magnetic field did not yield any noticeable improvements in plasma generation over past performance without the field.[4] Figure 2 shows a typical plot of microwave emission in the 6- to 7-GHz band. We concluded that beam-plasma interaction must take place within a waveguide for significant and efficient microwave generation.

Calculations and Additional Theory

Our calculations beginning in FY87 addressed two issues: the nature of the transport of a relativistic beam in a plasma and an understanding of the various instabilities associated with our physical system. These issues require a balance of analytic computations and particle-in-cell simulations. In FY88, we developed an analytical model to help interpret the simulation results.[5,6]

In contrast to low-current beams, an intense beam can modify zero-order solutions of the coupled particle-field equations in the sense that the solutions are no longer homogeneous or stationary. For example, an intense beam can initiate return currents[7,8] in the plasma so that a zero-order solution consisting of a stationary plasma is no longer a proper description of the plasma. Current density and velocity of the plasma return current are sensitive to the current density of the beam and the rise time of the injection of the beam into the plasma-waveguide system. These return-current parameters are important because the growth rate and

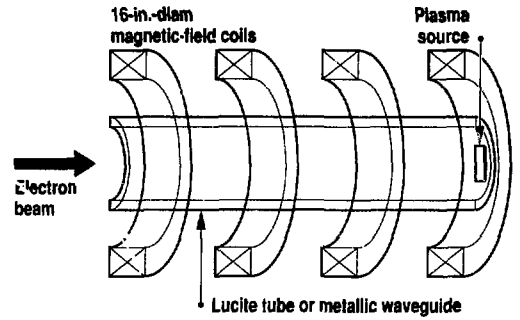

Figure 1.
Experimental setup. The axial magnetic field modifies operation of the plasma source by constricting plasma to a column with a 2.5-cm radius.

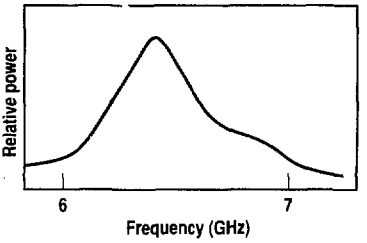

Figure 2.
Microwave emission from a plasma-filled lucite tube.

frequency-wavelength characteristic of microwave emission depend on them through an equation called a dispersion relation. However, these parameters can be ascertained with accuracy only by simulation. We have no analytical model to predict the return-current parameters reliably; thus, such prediction remains an active area of research.

The strength of the external magnetic field is another important parameter. In the limit of an infinite magnetic field, electron motion becomes one-dimensional along the axial magnetic field direction, and only the TM modes of the plasma-filled waveguide are excited. However, for finite magnetic fields, electrons in the plasma and in the beam can gyrate about the magnetic field direction. The effect of the cyclotron motion is to couple the TM modes to the TE modes. Furthermore, a magnetic field opens another avenue for the plasma to absorb energy from the electron beam, and this new mode can compete with the two-stream instability for energy in the beam. This additional mode, called electron-cyclotron resonance, can also be a source for microwave generation.

We have investigated extensively the large ($\omega_c >> \omega_p >> \omega_b$) magnetic field regime in which beam flow is predominantly one-dimensional. We feel that the motion of the beam in the z direction is responsible for efficient transfer of energy from the beam to the microwave-plasma oscillations. For this problem, the dispersion relations for all the modes (one of which is the beam-plasma instability) are determined simultaneously from a 14th-order polynomial. (Note that the term "dispersion relation" is used to denote both the equation and its roots.) This is, at best, a complex problem to understand. In FY88, we developed a code to determine the complex frequencies (roots) of a simplified version of the dispersion relation. The simplification is the assumption that the magnetic field strength is infinite. Figure 3 shows a typical plot of the complex dispersion relation. The real part of the dispersion relation [see Fig. 3(a)] gives the frequencies of the instability as a function of k_z, the z component of the wavevector. The imaginary part [see Fig. 3(b)] gives the growth rate of the instability as a function

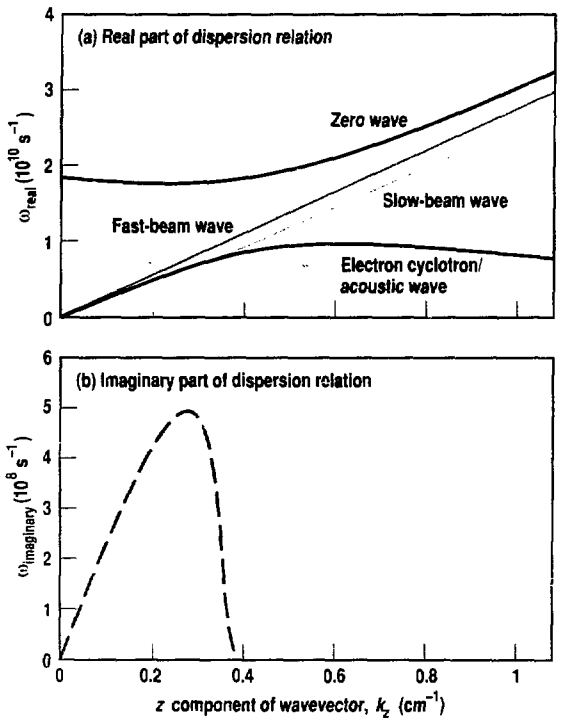

Figure 3. (a) Real and (b) imaginary plots of dispersion relation.

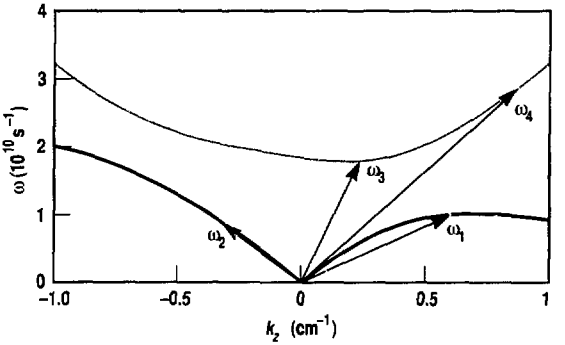

Figure 4. Possible wave-mixing processes. At first, $\omega_3 = \omega_1 + \omega_2$ and $k_3 = k_1 + k_2$; then $\omega_4 = \omega_1 + \omega_3$ and $k_4 = k_1 + k_3$ plus further cascading.

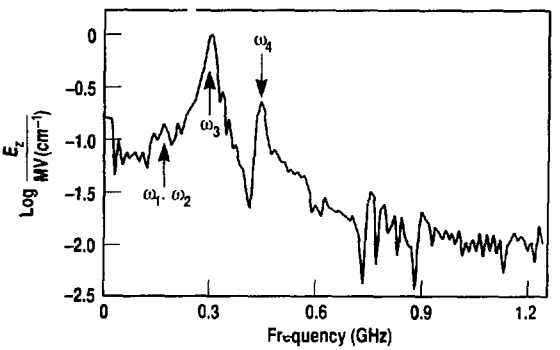

Figure 5. Fourier transform of electric-field amplitude. More power is contained in the third wave than in the forward wave.

of k_z. Notice that the nonzero imaginary part occurs over a band of wave numbers. Microwaves having these wave numbers are unstable and are the microwaves emitted by the device. Therefore, we expect to see a narrower band of microwaves than that predicted by the UC Irvine theory. The dominant frequency in the emission band is the microwave with the largest growth rate.

Using CONDOR to simulate the experiment, we found a nonlinear instability, which involved a three-wave mixing process.[5,6] Intense beam interactions caused the nonlinear instability, which could not be predicted from a linear theory, such as the dispersion relation result. Simulation results show that a high-current beam piles up electrons in front as it plows into the plasma. The pileup moves at a velocity less than that of the beam. At some point downstream, it grows so large that it backscatters the unstable wave. Three-wave mixing occurs when the backscattered wave mixes parametrically with the forward wave to form a third wave whose frequency and wavevector are the sum of the frequencies and wavevectors of the backscattered and forward waves, respectively. The process is shown in Fig. 4. More microwave power appears to be produced by the nonlinear instability than by the linear beam-plasma instability. This result is shown (see Fig. 5) in the Fourier transform of the electric-field amplitude. More power is seen in the third wave (higher frequency) than in the forward wave (lower frequency). Further mixing can occur between the third wave and the backscattered wave to form a fourth wave, and the process can continue to form the nth wave. Mixing stops when energy in the nth wave falls below a threshold value. Therefore, we would expect to see narrow bands of upconverted frequencies, rather than the continuous, broadband emission spectrum that the UC Irvine theory predicts.

Future Research

In FY89, we plan to carry out a proof-of-principle experiment for our generator. We must increase the magnetic field to 5.5 kG (a factor of 3) to ensure that the beam flow is laminar enough to allow for coherence in the emissions. We must also design a new plasma source so that the waveguide can be filled entirely with plasma. We must also design diagnostics to measure the mode character of emissions. To boost the efficiency of this generator, we envision a two-stage device in which the first stage acts as an oscillator and the second stage acts as an amplifier. Our most important issue for FY89 is to determine how to extract the microwaves.

References:

1. K. Kato, G. Benford, and D. Tzach, *Phys. Rev. Lett.* **50**, 1587 (1983).
2. K. Kato, G. Benford, and D. Tzach, *Phys. Fluids* **26**, 3636 (1983).
3. M. S. DiCapua, J. F. Camacho, E. S. Fulkerson, and D. Meeker, *IEEE Trans. Plasma Sci.* **16**, 217 (1988).
4. J. F. Camacho, B. R. Poole, B. Chang, and D. Meeker, *Bull. Am. Phys. Soc.* **33**, 1959 (1988).
5. B. Poole, B. Chang, and J. F. Camacho, *IEEE Conf. Rec. Abs.* 88CH2559-3 (1988).
6. B. Poole, B. Chang, J. F. Camacho, and D. Meeker, *Bull. Am. Phys. Soc.* **33**, 1959 (1988).
7. R. B. Miller, *Physics of Intense Charged Particle Beams* (Plenum Press, New York, 1982).
8. R. Lee and R. N. Sudan, *Phys. Fluids* **14**, 11213 (1971).

2

Field Operations

The principal role of the Field Operations Program is to ensure that underground nuclear tests and related experiments at the Nevada Test Site (NTS) are executed safely to meet the experimental objectives of the Nuclear Test–Experimental Science Directorate. Field Operations is predominantly an engineering organization that comprises several engineering groups, including the test directors, field engineering and construction, device systems, and timing, control, and communication systems. We are specifically responsible for selecting and preparing the site; drilling emplacement, satellite, and post-shot holes; emplacing the device and diagnostics; back-filling (stemming) the hole(s); detonating the device; and cleaning up the site after detonation.

Each event conducted by the Laboratory is overseen by a test director who coordinates the many activities involved in setting up and detonating an underground nuclear test. One of the most important responsibilities of the test director is to ensure the safe handling of the device and the safety of personnel while at the same time ensuring that all systems operate reliably as specified. This aspect of the test director's job is particularly important because Field Operations deals with large and complex engineering hardware that must be carefully handled to work reliably and to minimize the risk of injury to personnel or damage to the environment, experiments, or equipment.

Once the device has been installed and the hole stemmed, the test director works closely with DOE's test controller to coordinate detonation. The test controller gives the test director permission to fire after ensuring that all operational and weather conditions on the day of the test are favorable and that the entire NTS is secure (for example, that no unauthorized personnel are onsite). Once the countdown has begun, the test director alone controls the test and is the only person at that point with the authority to stop detonation.

Our field engineering and construction personnel are responsible for activities at ground zero (GZ), including erecting GZ facilities; constructing shock-mitigation frames on the nearby recording trailers; emplacing the experiment; and stemming the hole. They are also accountable to the test director for the following of established safety and operational procedures.

Device systems engineers design, fabricate, and assemble the device support hardware as well as any special engineering systems associated with the device, such as instrumentation to control temperature or humidity. They are then responsible for delivering, installing, and arming the device. After detonation, a reentry party returns to GZ for various inspections and data recovery.

Nuclear Test–Experimental Science personnel are continually exploring and expanding our knowledge of the physics of nuclear weapons and have dramatically escalated new diagnostics concepts in recent years. Each advancement in weapons technology challenges our field and engineering personnel to meet new experimental demands for more and better data with improved efficiency and productivity, without compromising our high safety standards.

The following articles highlight several recent advances in the Field Operations Program and illustrate the diversity of our technology base and the creativity of our engineers, designers, and technicians. In addition, we describe the historic Kearsarge and Shagan events, which were detonated in August and September 1988, respectively, in conjunction with Los Alamos National Laboratory and scientists, engineers, and technicians from the Soviet Union as part of continuing negotiations toward ratifying the Threshold Test Ban Treaty and Peaceful Nuclear Explosions Treaty. These events are described in this section because the Laboratory's primary activity in these experiments was to execute the field operations for Kearsarge. Our containment responsibilities and contributions to the CORRTEX achievements for Kearsarge are discussed in the Containment section of this report.

Improved Capabilities for Emplacing Complex Experiments at the Nevada Test Site

J. W. Miller and E. W. Christensen

. The Laboratory's Nuclear Test–Experimental Science Directorate has been conducting underground experiments that use increasingly larger, heavier, and more delicate equipment and instrumentation. To enable Field Operations to emplace these experiments with the required care and speed, we have recently acquired two major pieces of hardware and their supporting systems, described below.

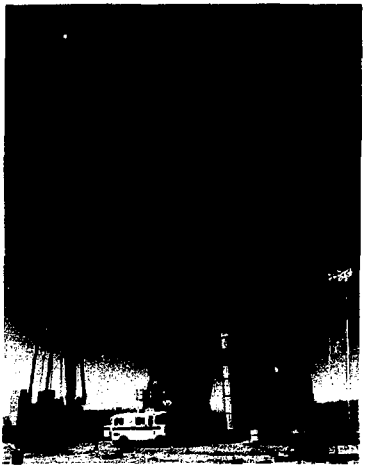

Figure 1. The Lampson Heavy-Lift Attachment on the Manitowoc 6000 crane, shown lifting 1060 tons during acceptance load testing.

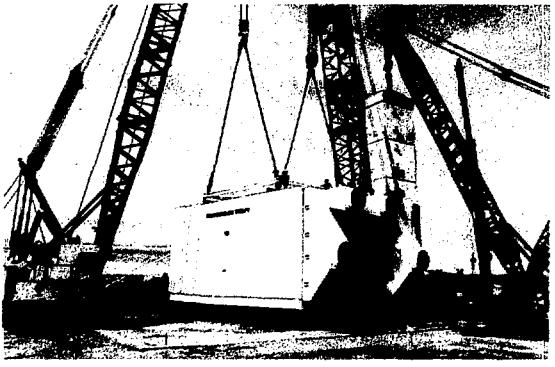

Figure 2. The Field Metrology Facility being moved into place at an event site.

LTL-800

The purchase of a Lampson Heavy-Lift Attachment, called the LTL-800 (see Fig. 1), for the Manitowoc 6000 crawler crane has greatly increased the limit for downhole loads, from 500 to 900 tons.

This increase in load capacity results primarily from the additional leverage provided by extending the point of the boom's hinge 60 ft forward of the original position. The location of the new boom attachment is supported by an 1800-ton-capacity crawler-type transporter, which is connected to the Model 6000 Crane by a pipe section called a stinger. The stinger ties the two crawlers together, enabling the machine to travel as one unit while carrying rated loads. All hoisting, booming, and swinging operations are performed from the control cab in the crawler crane. Before we acquired the LTL-800, the largest crane capacity for nuclear emplacement was 417 tons; maximum crane capacity has now been increased to 750 tons.

To take full advantage of this increase in load-carrying capacity, we are in the process of upgrading several support systems. For example, a new, stronger subbase—a two-story steel platform for use during downhole operations—is being built with a delivery date of September 1989. In addition, new, heavier pipe is on site with an emplaced load capacity of 1.04 million pounds and a stemmed load capacity (after the emplacement hole has been filled with various layers of concrete and gravel plugs) of 1.56 million pounds. Tools to handle the new pipe are on order to be delivered in 1990.

Field Metrology Facility

Field Operations' second recent acquisition is the Field Metrology Facility

(FMF). This 32-ft × 52-ft × 30-ft portable building (see Fig. 2) is necessary to make very precise measurements on certain experimental components that must be assembled on site before they can be installed inside the device canister. The FMF comprises an office, a receiving room, and a work room. The work room contains a 15-ton granite block on which is mounted the Coordinate Measuring Machine, which provides very precise (±0.5-micron accuracy) measurements in three axes (width, height, and depth).

Enclosing the FMF is a 90-ft × 90-ft tent to assist in maintaining the strict environmental standards required for the FMF. The separately attached environmental system, shown in Fig. 3, provides a temperature of 70°F (±0.5°F) at 10% (±1%) relative humidity. Within the FMF are nine temperature sensors, one pressure sensor, and one differential pressure sensor. These sensors plus the sensors on the air conditioners, heaters, dehumidifier, and humidifier, are monitored in the control trailer. The dehumidifier moves 9000 scfm of air, removing 40–300 pounds of water per hour.

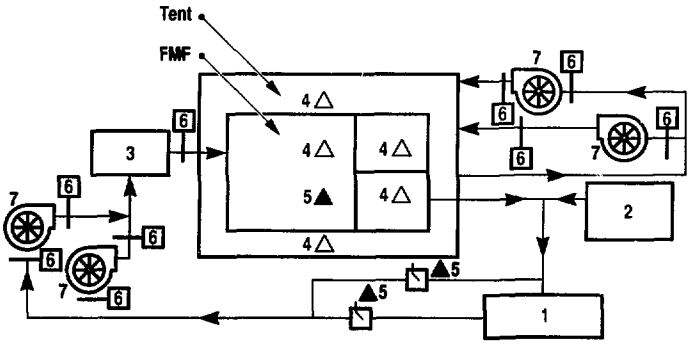

Figure 3. The environmental systems for the FMF (not all sensors are shown): (1) dehumidifier, (2) humidifier, (3) heater, (4) temperature sensors, (5) humidity sensors, (6) damper control, (7) air conditioners.

Digital Downhole Surveyor: A Nevada Test Site Logging Tool

V. P. Brugman and M. E. Kinkenon

Since the atmospheric test ban in 1963, nuclear explosives have been tested in underground tunnels or vertically drilled shafts. The use of vertical shafts led to the development of wire-line instruments similar to those used in oil and gas well logging. Exploratory holes were drilled and logged to locate sites for the larger, steel-lined emplacement holes. Because of the cost of encasing these holes, in the late 1960s, the Laboratory decided to leave them uncased, except for the surface casing. This made it necessary to routinely log 8- to 10-ft-diam holes to learn their geology and geometry. Routine logging of such large holes is done only at NTS.

A major thrust of the Laboratory's in-house development of logging instruments at NTS involved downhole cameras. Downhole Robotics Operation Nevada Experimental (DRONE) was begun in 1970 as a modular wire-line camera system suited to a multitude of downhole operations but used primarily to gather data. The DRONE system is still used as a photographic and video camera; it also serves as a testbed for experimental downhole gadgets. New modules have been added to it as needed.

In 1980, we added a laser range finder. It used simple triangulation to map large washouts, or cavities, created in the course of drilling an emplacement hole. A laser beam was projected horizontally at the wall. A closed-circuit video camera, mounted 3 ft above the laser, scanned the wall. The spot at which the laser appeared on the TV screen corresponded to a given hole radius. This

range finder was modified and used about once a year. After using it on the Agrini Event reentry in 1984, we decided to build an instrument optimized for routinely surveying emplacement holes. That instrument became the Digital Downhole Surveyor (DDS).

Digital Downhole Surveyor

The DDS surveys the entire emplacement hole, gathering 300,000–400,000 data points at a rate of over 10 ft/min. All data are referenced to the center of the top of the hole. The DDS is lowered on a steel-armored multiconductor cable (Fig. 1). Directly beneath the connector is a flux-gate north seeker to provide azimuth data to the computer. The computer and power supplies are beneath the north seeker. Next is the gyro and helium-neon laser. The laser beam is directed down through safety-interlocked shutters, a hollow slip-ring assembly, and the drive assembly to the rotating module. The drive assembly includes a rotary angle encoder to provide a reference between the rotating module and the north seeker.

In the rotating module (see Fig. 1 inset), a pentaprism directs the laser beam horizontally toward the drill-hole wall. A 50-mm lens reimages the laser spot on a linear photodiode array. Each photodiode corresponds to a radial distance. The angle between the array and the lens allows the laser image to stay in sharp focus from 7 in. to 70 ft even when the lens is wide open.

The DDS uses the same triangulation principle as does the DRONE laser range finder; however, the geometry of its optical system allows us to calibrate over the radial-distance range of from 7 in. to 70 ft. Triangulation is inherently nonlinear, which works to our advantage. Where the hole drifts out of plumb toward the DDS, we have higher resolution and the data (taken every 2 degrees) are at closer intervals. Precise measurements are needed at such points to determine if the wall will interfere with lowering the canister package. Where large washouts occur, resolution is reduced. However, we need only measure the washout's perimeter to determine the stemming volume required to fill it. The 4096-pixel photodiode array of the DDS gives much higher resolution than is possible with the DRONE camera.

Since the detector is digital, data can be processed as recorded. Data processing is done at Mercury at NTS on a Sun 3 Fileserver. The data-reduction software addresses a variety of issues related to an emplacement hole's geometry. Thus, the suitability of a hole for a particular experiment can be determined within hours of logging.

One option of the DDS software is to simulate a mandrel run (i.e., the lowering of a fixture resembling the canister package) to determine if a specific canister package will fit in the hole and at what depths its position must be adjusted to avoid contact with the wall. The mandrel-run option models the canisters as two right circular cylinders, one on top of the other. If the simulation shows that a canister will not fit in the hole in an upright position, another option simulates the canister sliding down the hole. These simulation techniques have successfully modeled downhole emplacements since 1986.

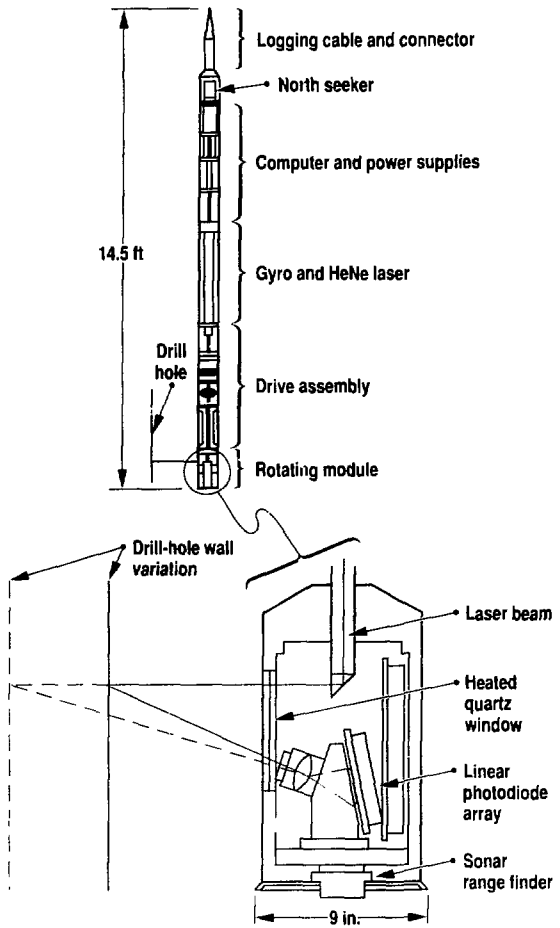

Figure 1. Main components of the DDS. Inset shows details of the rotating module used to determine an emplacement hole's diameter.

FY88 Developments

Kearsarge. We made several improvements to the DDS during FY88. To meet constraints in the Kearsarge Event, we enhanced the data-reduction software. When we encountered magnetic field deviations in logging a hole for the Comstock Event, we added an azimuth gyro to complement the flux-gate north seeker of the DDS. Finally, we automated the DDS calibration technique.

The canister package for Kearsarge consisted of a 6.8-ft-high, 88-in.-diam device canister, a 12.25-ft-high, 45-in.-diam diagnostics canister, and brackets to hold the CORRTEX cables extending a total of 476 ft above the diagnostics canister [see Fig. 2(a)]. The cable brackets were to be about 8 degrees apart; the first set was 71.4 in. and the second 28 in. in diameter. Our initial modeling of this package showed that the brackets would hit the hole for the first 350 ft if their rotation was ignored. The interference resulted because the cable brackets made the package much larger than normal, and the hole was nearly 1.5 ft out of plumb in the first 200 ft. Because these brackets could not be subjected to any significant lateral force, they could not be allowed to hit the wall. Further, the cable brackets extending above the diagnostics canister for the first 214 ft had to be at least 35.7 in. in radius; reducing their size was not an option.

To find a way to lower the package, we had to consider the brackets' rotation. We developed software to find the plane in the hole where the larger brackets would have maximum clearance [see Fig. 2(b)]. We considered the (x,y) offset position of the canister's center relative to the center of the top of the hole, along with the rotational position of the cable brackets. We determined the canister's position with a general mandrel-run simulation. This yielded a list of moves to get everything but the cable brackets in the hole, thereby defining the canister's (x,y) offset position at any depth.

The next step was to find the plane where the cable brackets would have maximum clearance given this offset

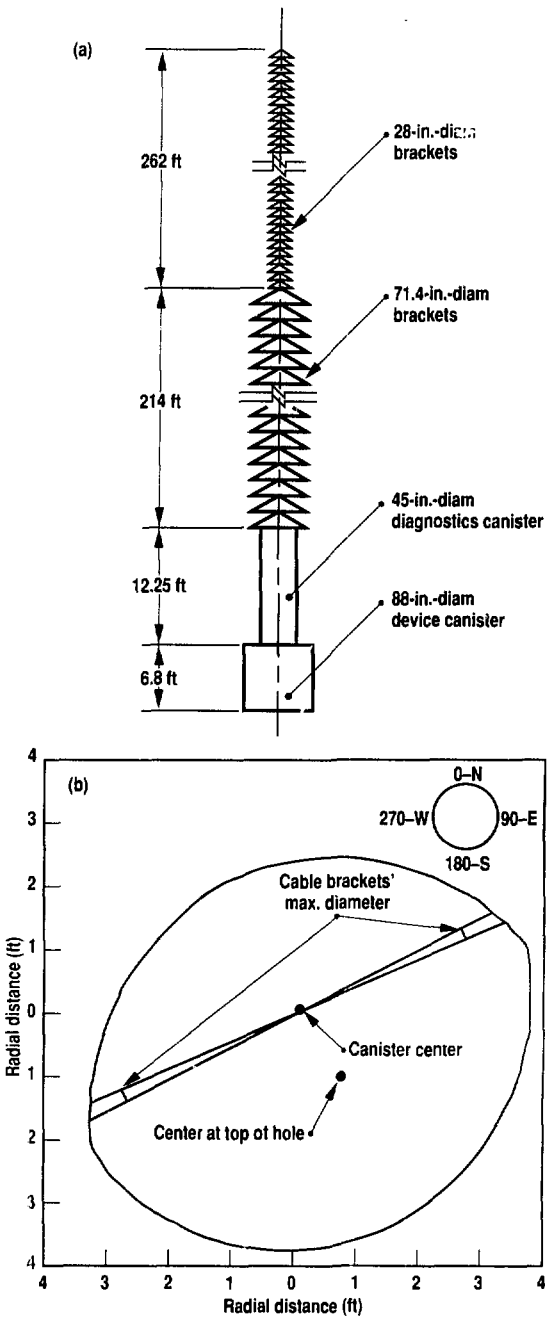

Figure 2. Kearsarge downhole package. (a) Components and (b) calculated plane of maximum clearance for the cable brackets within a compressed view of the hole's minimum radius over its entire length.

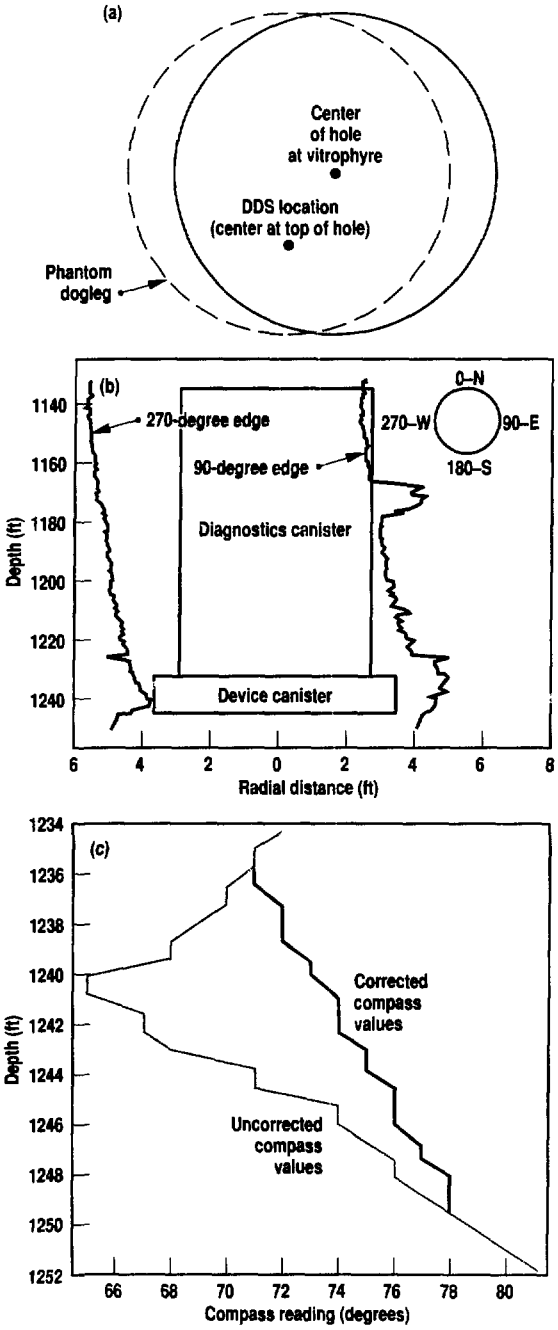

Figure 3. Effect and correction of phantom dogleg in Comstock emplacement hole. (a) Phantom dogleg. (b) Calculated lack of clearance for canister given erroneous compass readings. Edge angles are with respect to the canister's center, which is 9.04 in. E and 24.74 in. S of the top of the hole. (c) Erroneous and corrected compass values.

position. To do this we modeled the brackets 8 degrees apart and rotated them through each 8-degree plane in 2-degree increments. We modeled the full length of the brackets as they extended up the pipe string from the canister. The plane that allowed the greatest clearance from the wall was chosen as the most desired plane for the cable brackets. We repeated this calculation for every interval in the hole where the brackets' rotation had to be controlled.

Canister Centering. General concerns about canister distortion due to uneven stemming distribution made it necessary to use DDS data to compute the optimum canister position. Uniform stemming distribution was desired as the annulus (i.e., the clearance between the canister and the hole) was stemmed. We developed software to measure the volume of the annulus in each quadrant and compare the four quadrants. These volumes were computed for all possible canister positions and the distributions then ranked from best to worst regarding their uniformity.

Clear Line-of-Sight Plots. We also added a feature to the DDS data-reduction software that computes the clear line of sight for the entire hole. This line of sight can then be superimposed on any cross-sectional plot of the hole to determine the latter's relationship to the cross section of the overall hole. This is especially useful in quickly assessing the hole's overall straightness.

Improved Azimuth Data. The fluxgate north seeker used for azimuth data in the DDS is convenient because it is self-aligning, eliminating the need to survey a north reference during the logging process. We correct for the known magnetic deviation at NTS so azimuth data reference true north. We discovered that some holes on Pahute Mesa pass through a vitrophyre formation that has a magnetic field which is not parallel with surface magnetic north. The first time this became obvious was while logging a hole for the Comstock Event.

The hole deviated significantly from plumb at the vitrophyre because the drill

bit had skated off the latter into a softer surrounding formation. The DDS (being centered on the top of the hole) was, thus, closer to the vitrophyre side of the hole. The deviation of the magnetic flux lines resulted in artificial rotation of the data 15 degrees around the DDS, which generated a phantom dogleg [see Fig. 3(a)]. The mandrel-run simulations [Fig. 3(b)] then indicated a no-go at this dogleg. The package, which consisted of a 97-ft-high, 68-in.-diam diagnostics canister and a 13-ft-high, 86-in.-diam device canister, lacked clearance for lowering and would have to slide.

A series of tests using azimuth gyros simultaneously with flux-gate north seekers verified the magnetic field deviation. As a result, we added an azimuth gyro to the DDS. The gyro data are recorded and plotted differentially against the north-seeker output during the standard data-reduction procedure. Magnetic deviations stand out prominently and can be corrected using the gyro data. Figure 3(c) shows the erroneous readings that created the phantom dogleg in Comstock and their corrected values. However, we continue to use the north seeker as our primary reference to avoid surveying time at the top of the hole and avert concerns about gyro drift rates.

Automated Calibration. We calibrate the DDS by recording data as a neutral gray target card is placed at gradually increasing distances from the package. Any shifts resulting from differences are characterized by doing the same tests with a flat white and a flat black card. We used to do this by manually moving the target along a scale, which was time consuming and tedious. Our automated system automatically positions a target wheel to within 0.0001 in. This system also rotates the wheel to allow calibration against gray, black, and white at each point. The system interacts with the DDS computer to allow faster and more accurate calibrations with no chance of random human error.

Future Developments

The increasing use of DDS data has led us to consider building a second detector that will incorporate a number of technology improvements. Solid-state laser diodes are now available with collimating optics that project a smaller-diameter beam than does our current helium-neon laser. These diodes are more powerful, allowing us to consider pulsing the diode to reduce the integration time, hence reducing the arc-segment length represented by each measurement. A recently introduced linear photodiode array has 6000 pixels in the same sensor length as our current 4096 array. Incorporating these components with modified optical geometry in a new detector should allow us to improve its accuracy significantly. This opens the possibility of increasing standard canister sizes without increasing hole diameters. The current DDS would then become a backup instrument.

Testing the Lightning-Invulnerable Device System

R. T. Kuhrcuck

To ensure that lightning cannot accidentally detonate a nuclear-explosive test device at NTS, we have developed and tested a prototype lightning-invulnerable device system (LIDS). Although the probability of a lightning-induced detonation is considered "vanishingly small" (less than one in a million), such an accident would be absolutely unacceptable. In 1983, the lightning vulnerability of device systems at NTS was investigated by LLNL with the cooperation of Sandia National Laboratory, Albuquerque. This study led to our development of the LIDS concept to protect safety-critical device components from the effects of a direct lightning stroke.[1] Both simulated and rocket-triggered lightning tests in 1986 demonstrated that the LIDS concept provided lightning protection. It is now being implemented on all of the Laboratory's nuclear test device systems at NTS.

In evaluating lightning as a threat to nuclear devices, we decided that only the effects of a severe (full threat-level) stroke should be taken into account. Industry and military standards presently define such a stroke as one that lowers negative charge, leading to a peak current of 200 kA and/or a maximum current rise rate (di/dt) of 200 kA/μs. In addition, the energy input or action integral for such a stroke has a value of 1.5×10^6 $A^2 \cdot s$. These conditions occur in less than 1% of all lightning strokes.

LIDS Design

A nuclear test device system is considered most vulnerable to lightning while it

is suspended above its emplacement hole, just before being lowered into the ground. The cables that connect the instrumentation and control electronics to the device system could be struck by lightning, exposing the system to dangerously large electrical currents.

In principle, LIDS surrounds the device system with a "fortress," a topologically closed metallic skin (i.e., a Faraday cage). In practice, this fortress must be penetrated to accommodate power, instrumentation, and control lines. The penetrating electrical conductors are protected externally by overall shields and internally by transient limiters. The shields are terminated at the skin's outer surface with 360-degree backshell (i.e., EMI/RFI) connectors, which mate with bulkhead-mounted feedthrough connectors. Figure 1 shows a simplified version of the prototype LIDS design.

If the cables are struck by lightning, the current will divide among the shields and be conducted via the lowest impedance path between ground (earth) and the lightning channel. If the strike point is relatively close to the LIDS and the latter is near the ground, arcing to the nearest grounded object will occur. Most of the current will then flow through the fortress skin. A small portion (10–20%), carried within the fortress by the penetrating conductors, will pass through the transient limiters that are located immediately behind the feedthrough connectors. The limiters will conduct most of this residual lightning current, reducing to safe levels any transient voltages and currents that reach device system components.

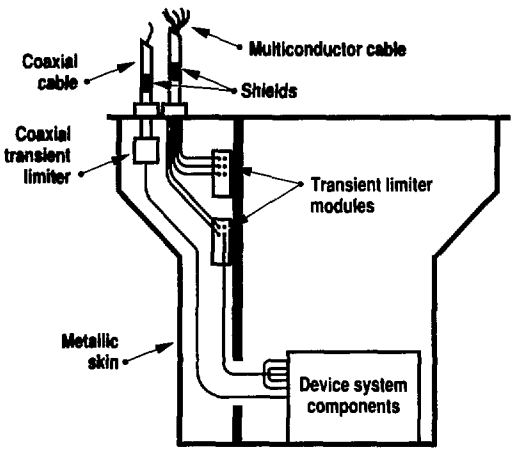

Figure 1. Simplified schematic of the lightning-invulnerable device system (LIDS). A metallic skin surrounds the nuclear device system. Penetrating electrical conductors have external metallic shields and internal transient limiters to isolate the device system from lightning currents.

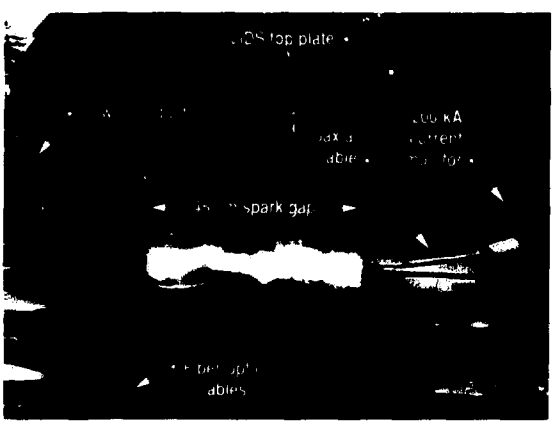

Figure 2. Test setup for high-*di/dt* simulated lightning. Transient limiters connected to the cable conductor were subjected to peak currents of about 50 kA and a *di/dt* of more than 200 kA/μs.

Simulated Lightning Tests

Our first testing of the prototype LIDS canister was done at the Lightning & Transients Research Institute in Florida. After initial low-level tests to determine the electrical charactistics of the system, we ran tests to determine how effectively the transient limiters would protect various system components in the presence of a threat-level *di/dt*.

To do this, we used a Marx generator consisting of forty 1.6-μF, high-energy storage capacitors. After the capacitors were charged in parallel through resistors to 35 kV, triggered spark gaps switched them in series, producing 1.4 MV across a 0.4-μF capacitance. About 40 kJ of energy was discharged into a large wire grid, 6 m overhead and well insulated from ground, which functioned as a peaking capacitor of about 750 pF. A low-inductance down-lead carried the charge to a 48-cm-wide spark gap, which was connected to a cable conductor that led to the transient limiter under test (see Fig. 2). The high-voltage, high-*di/dt* pulse broke down the limiter, allowing the generator charge to flow to the LIDS structure and then to ground.

The resulting input-current waveform consisted of a 145-kHz, underdamped sine wave with a peak of about 50 kA. The effect of the peaking capacitor and down-lead inductance was to produce a 4-MHz damped oscillation, which was superimposed onto the leading edge of the 145-kHz wave. The steep leading edge of the 4-MHz wave produced a *di/dt* in excess of 200 kA/μs. The limiter conducted the full transient current and was subjected to an action integral of 2×10^4 A$^2 \cdot$ s.

We also discharged severe peak currents into the cable's overall shield to determine what portion of the applied

current would actually penetrate into the LIDS and how the limiters would perform. Thirty-nine of the capacitors were relocated close to the LIDS and wired in parallel, providing 62.4 μF. After charging the capacitors to 33 kV (34 kJ of energy), we discharged them into the shield via a remotely operated paddle switch, producing a 20-kHz damped sine wave with a peak current of 200 kA and a *di/dt* of 15 kA/μs. The corresponding action integral was 1.8×10^6 $A^2 \cdot s$, which is somewhat greater than the value associated with a severe lightning stroke.

These tests subjected the transient limiters to hundreds of high-*di/dt* and high-current discharges. All limiters performed as expected, holding voltages to safe levels. The residual currents entering the LIDS were between 10 and 20% of the applied current, well within the capabilities of the limiter components.

Rocket-Triggered Lightning Tests

The next step was to subject LIDS to natural lightning. At the invitation of NASA, we participated in the 1986 Rocket-Triggered Lightning Program (RTLP-86) at the John F. Kennedy Space Center (KSC). The KSC lies in a region where lightning-producing thunderstorms are common.

The RTLP test area includes the Atmospheric Sciences Field Laboratory, a rocket-launch platform, and a control and data-acquisition facility (a surplus, all-metal railroad caboose). The wooden launch platform stands about 4 m above ground and contains 12 launch tubes for 1-m-long, plastic-bodied, black-powder-fueled rockets. Affixed to the tail of each rocket is a spool containing 700 m of small-diameter wire, jacketed with Kevlar to provide strength. The lower ends of the wires are connected to the rocket launch stand, which is tied to the system ground plane. Rocket launching is controlled by pneumatic signals from the control and data-acquisition facility.

For RTLP-86, the lightning-strike object was our 2.7-m-long, 11- × 10^3-kg LIDS canister, which was placed on the platform adjacent to the launch tubes. As shown in Fig. 3(a), a horizontal metal pipe, which functioned as a lightning rod, was suspended 7 m above the canister by a pair of wooden utility poles and a crossbar. A metal pulley was suspended from the center of the crossbar and electrically connected to the rod by a short piece of wire rope. An insulated line was used to haul a test cable (coaxial or multiconductor) up to the pulley. Removal of the cable's insulating jacket allowed its outer shield to be brought

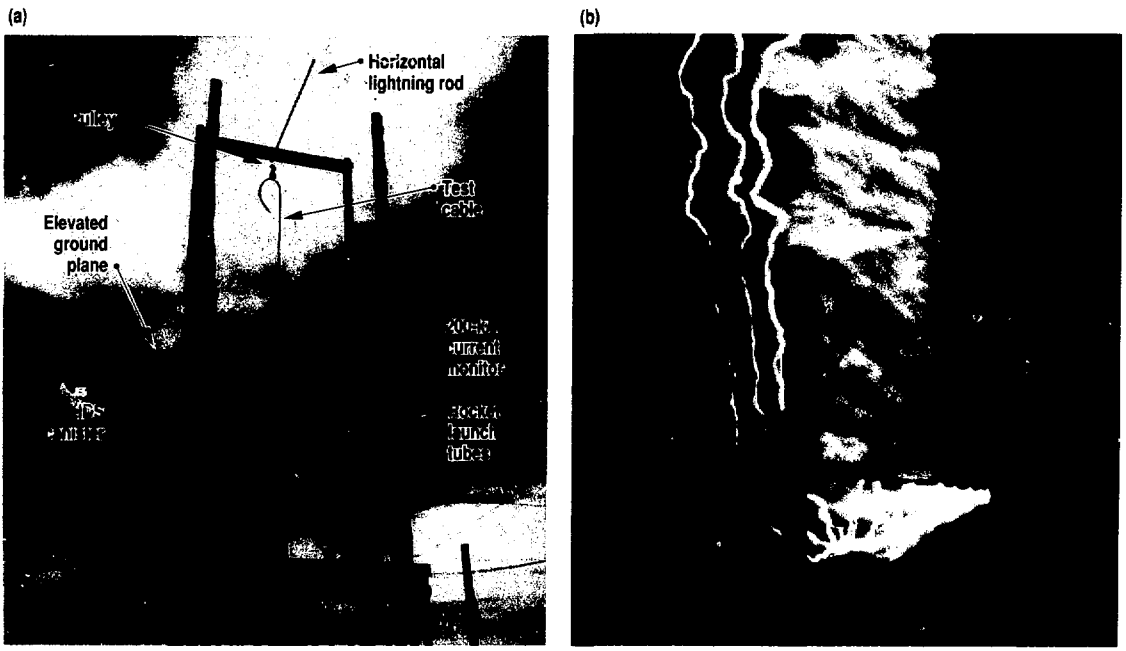

Figure 3. Rocket-Triggered Lightning Program launch platform. (a) Test setup with LIDS as the lightning-strike object. The vaporized wire from a rocket launched into a storm cloud produced an ionized channel. Lightning return strokes flowed from ground via the LIDS, cable shield, lightning rod, and ionized channel to the cloud. (b) Multiple lightning return strokes attached to the lightning rod illuminate the wind-blown vapors (on the right) from a vaporized rocket wire.

into direct electrical contact with the pulley. The cable's upper end, about 1 m beyond the pulley, was terminated by shorting its shield(s) to its conductor(s). The lower end was mated to a LIDS bulkhead feedthrough by means of a 360-degree backshell connector. The base of the canister was connected to the grounding system via the rocket launch stand. The electrical path to ground was expected to consist of the lightning channel, the rod and pulley, the cable shield, and the LIDS metallic skin.

We measured the current applied to the LIDS with a 200-kA toroidal current transformer, which we also used in the simulated lightning tests. Other sensors measured the transient voltages and currents that reached the device system components. All electrical signals were converted to optical signals by the use of battery-powered, fiber-optic transmitters.

Our data-acquisition system consisted of seven dual-channel digital oscilloscopes, which were triggered simultaneously when the lightning input current reached 4 kA. Immediately after data were acquired, a computer system automatically stored all of the scope setup information and data on a floppy disk.

The metal caboose was well-grounded, power-wire penetrations were made via appropriate transient limiters, and all signal and control connections to and from the launch platform used either pneumatic or fiber-optic links. During test periods, a diesel generator located adjacent to the caboose provided ac power. As a result, the triggered lightning strikes, only 50 m away, never upset or damaged our data-acquisition system.

Launch Scenario

As a storm cell approached, we monitored the potential gradient (PG) with a system of instruments known as electric-field mills (EFM). The PG gradually changed from a small, positive fair-weather value to a large negative value. A; first, natural lightning discharges occurred, temporarily reducing the PG. The coincidence of natural lightning with a rocket launch would have eliminated the possibility of triggering lightning. When the frequency of natural lightning flashes fell off and the measured PG remained above -4 kV/m, a launch was feasible.

At launch time, a single rocket was fired after a short (5- to 10-s) countdown. Once the 700-m-long wire was close enough to the storm cell overhead, a discharge current of several hundred amperes flowed through it, vaporizing the wire in a bright flash and leaving an airborne ionized channel close to the horizontal rod. We believe that, since the ionized channel exhibited a significant inductive reactance, the increasing rate-of-rise of channel current soon led to a very high channel-to-ground voltage. The rod-to-ground path via the LIDS canister represented a lower impedance than that provided by the bottom part of the vaporized wire. Thus, when the channel voltage exceeded the breakdown value for air, a channel-to-rod arc occurred and a high-current return stroke flowed. Typically, there was a delay of several hundred milliseconds between the wire burn and the first return stroke.

Test Results

During the test period, five storms passed close enough for us to trigger 22 flashes, producing between 80 and 100 return strokes that were conducted via our LIDS canister. A maximum peak current of 52 kA was recorded. Figure 3(b) shows a closeup of multiple return strokes attached to the rod.

One multiconductor and two coaxial cables were subjected one at a time to these lightning return strokes. As in the simulated lightning tests, the LIDS design provided protection from the effects of a direct strike to the cable. In the case of the multiconductor cable, we measured 3 kA of total internal current in conjunction with a 29-kA stroke. Since the internal current was carried by 36 parallel, 20-kA limiters, the average per-channel transient current was estimated to be less than 100 A.

Because the coaxial cable's solid shield provides nearly perfect shielding, no internal current was detected for even a 40-kA stroke. In all cases, the transient voltages and currents reaching the device system components were limited to absolutely safe amplitudes.

Conclusions

The goal of LIDS was to develop a device system that could sustain a severe lightning strike directly to its cables without exposing its safety-critical components to threat-level energy. We have tested a prototype LIDS against severe levels of simulated lightning and typical levels of natural lightning; it passed all tests.[2] While the rocket-triggered lightning tests used a single cable, NTS downhole device systems typically have eight or more cables. A lightning strike would result in all of the cables dividing the current essentially equally (i.e., a 200-kA stroke would cause each cable to carry 25 kA or less). Thus, the single-cable current of many of our rocket-triggered lightning strokes approached or exceeded an equivalent of 200 kA to an eight-cable bundle.

The major portion of all simulated and natural lightning currents was carried via the cable shield, 360-degree backshell connector, and grounded LIDS skin. Residual currents penetrating into the LIDS were significantly lower than the ratings of the limiters through which they were conducted. Voltage and current transients were held to safe levels. Using techniques generally known to be effective in mitigating hazardous lightning effects, we successfully demonstrated that the LIDS concept will protect a device system from lightning. This concept is now being implemented on all of the Laboratory's NTS tests.

References:

1. R. T. Hasbrouck, J. P. Johnson, R. J. Burton, S. R. Crawford, and J. D. Robb, *Final Report of the Nuclear Explosive Lightning Vulnerability Task Force*, Lawrence Livermore National Laboratory, Livermore, Calif., UCRL-15618 (1984).
2. R. T. Hasbrouck, J. P. Johnson, and B. G. Melander, *Final Report of the Device Systems Lightning Project*, Lawrence Livermore National Laboratory, Livermore, Calif., UCRL-21068 (1988).

We developed and fielded two environmental control systems to maintain a laboratory-like environment in downhole device canisters. The goal was to maintain the same environment for the experiments from their fabrication at LLNL to completion at NTS. Canister temperature had to be kept at 70 ± 2°F and relative humidity at 10 ± 1%. The challenge was to field a system that could meet these requirements for long periods or even indefinitely under varying external temperatures and internal heat loads.

The first environmental control system was fielded on the Delamar Event, the second on the Kernville Event. On Delamar, temperature was controlled by circulating air through a chilled-water heat exchanger or over duct heaters. On Kernville, the circulating air passed through a chilled-water heat exchanger and then was reheated to the desired temperature. Humidity control was similar for both events.

Delamar

For Delamar, temperature was controlled by either heating or cooling the canister air, which was circulated through a cooling coil (air-water heat exchanger) and over duct heaters (Fig. 1). Nine 1-kW duct heaters provided heat. Thirteen tons of ice, which had an operational life of about 40 days, provided cooling. The heating and cooling systems operated independently, but they were not allowed to run simultaneously. This would have reduced the cooling system's operational life.

The amount of energy (heat) that was added or removed from the device canister was governed by its internal heat loads and external ambient temperatures. Heating was controlled by varying the power to the heaters. Cooling was controlled by varying the mass flow rate of a water/ethylene glycol (WEG) mixture that was circulated between the air-water and water-ice heat exchangers.

Humidity was controlled by two methods. The canister air was dehumidified by circulating it over the evaporator coil of a mechanical dehumidifier. The condensate that formed was then captured in a container that used oil as a cork to prevent evaporation. The canister air was humidified by bubbling dry gas through water.

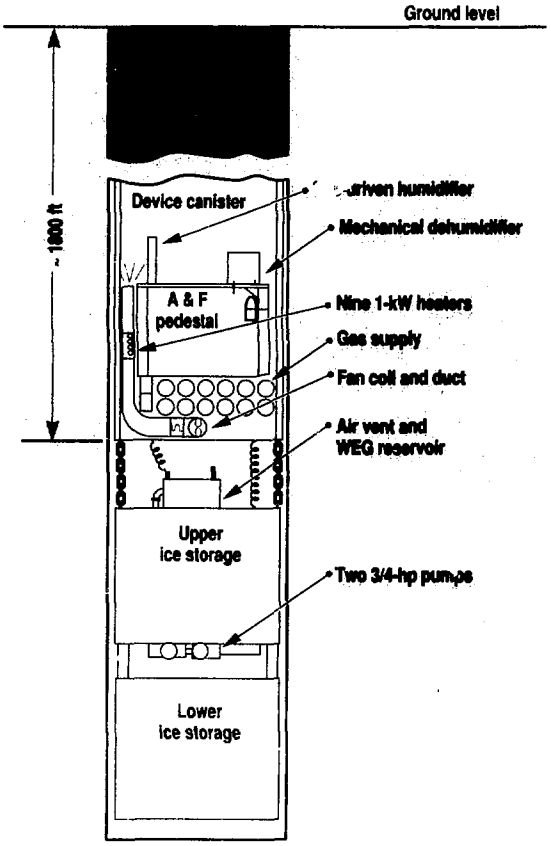

Figure 1. Schematic of the environmental control system fielded on the Delamar Event.

The environmental control system was governed by temperature and humidity sensors placed near the experiments; four process controllers ran the equipment. Proportional integral derivative (PID) logic was used for temperature control, which allowed us to vary the system's power levels. "Bang Bang" (on/off) logic was used for humidity control. System performance was ±1.6°F for temperature and ±0.2% for relative humidity.

Figure 2. Schematic of the closed-loop, split-cascade refrigeration system fielded on Kernville. The downhole unit was directly beneath the device canister.

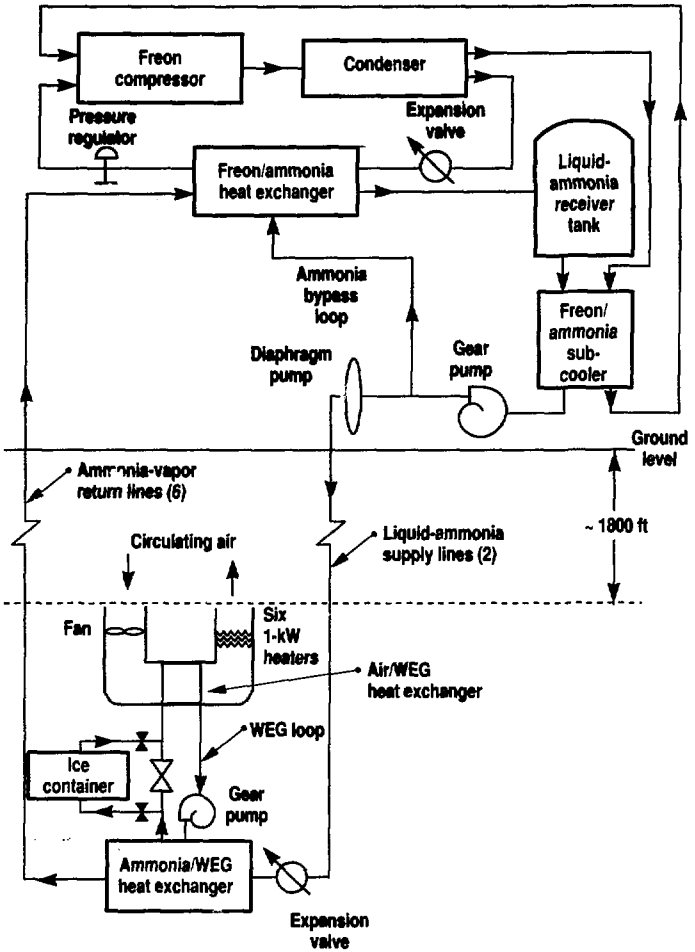

Kernville

The Kernville environmental control system was much more complex because it was designed to operate indefinitely. For temperature control, J. P. Clay, with analytic support from C. S. Landrum and K. A. Thole, designed a unique split-cascade refrigeration system (Fig. 2). The expansion valve and evaporator were downhole, 1800 ft below ground. The bulk of the refrigeration system and its controls were on the surface, another 1200 ft away from the hole, which meant the refrigeration system operated over a 6000-ft closed-loop circuit. The system had four heat-transfer loops for cooling. Seven tons of ice were also sent downhole as a backup to the cooling system. Six 1-kW duct heaters provided heating.

Liquid ammonia, which was stored in an uphole receiver tank, was pumped downhole by a diaphragm pump at a pressure of about 530 psig to maintain saturation temperature. When the ammonia reached the device canister, its operating pressure was approximately 1000 psig owing to the addition of gravity head. The ammonia was then expanded through a needle valve into an ammonia/WEG heat exchanger to an operating pressure of 30–40 psig. The liquid ammonia absorbed the downhole heat, turned to gas, and returned to the surface. There, it was condensed thermally by the freon refrigeration system, which then rejected the downhole heat to the uphole atmosphere.

A water loop transferred heat from the test canister to the ammonia. A WEG mixture was circulated through the ammonia-water and water-air heat exchangers. The water loop also provided a means to ensure that any escaped ammonia gas did not contaminate the experiments. Circulating the canister air through the water-air heat exchanger would sub-cool it; the air was then reheated to maintain the required 70 ± 2°F.

Humidity control was modified slightly for Kernville. The humidifica-

tion process was the same as for Delamar, but the canister was dehumidified by purging it with a dry gas.

Control of the Kernville environmental system was also similar to that used on Delamar. Temperature and humidity sensors were placed next to the experiments, and five process controllers using PID and "Bang Bang" logic ran the equipment. The system performance was ±0.7°F for temperature and ±0.2% for relative humidity.

Summary

The lessons learned from successfully fielding environmental control systems on the Delamar and Kernville events have given us a design basis for fielding future systems. Work is now under way to develop simpler environmental controls for future events. Our goal is to increase overall system reliability by minimizing the number of moving parts.

Timing and Control System at the Nevada Test Site

B. K. Yoon

Accurate timing and control of the command sequence in testing nuclear devices is crucial. Precise, reliable control over the timing signals that arm and fire a device is needed to ensure the success, safety, and security of an event.

Several hours before a scheduled event, an arming party travels to ground zero (GZ) where the device systems engineer connects the command system to the device system. The arming party then returns to the Control Point and the device systems engineer tells the test director that the device has been armed and that the firing sequence can begin. From that point, the test director takes control of the shot and gives the order for the timing and control (T&C) system at the Control Point to send out timing signals via microwave transmission to the timing station. The timing station decodes and distributes these signals to recording trailers in the trailer park near GZ to start the various recording devices where experimental data are collected (see Fig. 1). In addition, some of the decoded signals are sent to a special trailer—called the Red Shack—in the same trailer park. The Red Shack contains the power supplies, trigger generators, and other equipment that use the signals received from the timing station to apply the voltages necessary to generate the final firing command.

Our current T&C system is a mix of 1960s vintage equipment and state-of-the-art upgraded components.[1] Over the past several years, we have been modernizing the entire system. There were two major upgrades in FY88: a new signal programmer was incorporated, and the new microwave link and monitor subsystem became operational. Our main task in FY89 is to improve the command encoding, decoding, and distribution system.

Though we are making great strides in modernizing the technology of the T&C system, its basic architecture remains fixed. For nuclear explosive safety, there will always be human and mechanical links in the command chain. As noted above, a person, not a computer, must actually arm and give the go-ahead for firing a device. This ensures that even in the worst case of computer malfunction, the device cannot be armed and fired without human help. The use of equipment like the scrambler encoder/decoder and of manual controls for critical commands keeps people, not computers, in control.

FY88 Upgrades

Our new signal programmer was designed and developed by Los Alamos

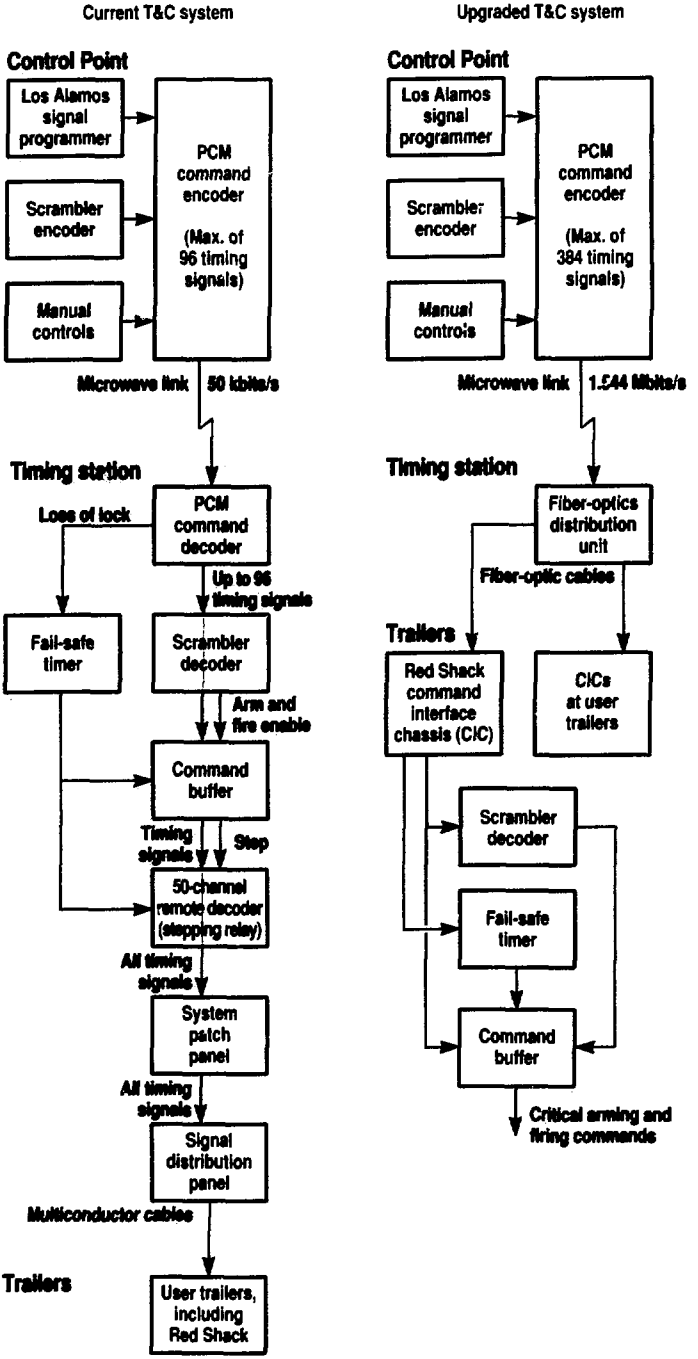

Figure 1. Comparison of current timing and control system (left) and its proposed upgrade (right). The upgraded system features a cleaner, simpler architecture, better timing resolution between signals (<2 ms versus 16 ms), more logical placement of scrambler decoder and command buffer at the Red Shack, and the use of current technology in all equipment. The blue lines in the current timing station are wired through for noncritical commands.

and built for us by EG&G. It generates the automatic timing signals at the Control Point. We found the Los Alamos signal programmer to be suitable for our NTS operations, and it had already been approved by a Nuclear Explosive Safety Study as a critical component. The decision to have it built for us instead of designing our own saved about $500,000 in development costs.

The new signal programmer gives us more flexibility in scheduling automatic timing signals, reduces the amount of setup required, and enhances the overall reliability of the T&C system. It will also let us phase out some of the equipment now in use whose components are no longer available.

The new microwave link consists of state-of-the-art equipment for terrestrial microwave transmission and reception. The link is set up for full duplex operation (i.e., information is sent and received at both ends) with frequency diversity: it sends and receives signals on two channels and can switch between the two channels to obtain the strongest signal. By utilizing hitless switches with automatic signal-quality sensors, the link achieves a throughput bit error rate of zero.

The monitor subsystem keeps track of conditions at GZ, measures the performance of the T&C system, and provides data links between the Control Point and the user trailers at GZ. The new monitor subsystem is fully redundant, and the data it sends are fed directly into the VAX computers at the Control Point for processing. All of the monitor data are sent to the timing station from the Red Shack and user trailers via fiber optics for noise immunity and electrical isolation.

FY89 Upgrades

Beginning in FY89, the command encoding, decoding, and distribution system is the target of our next major overhaul. As we envision the upgraded system, commands will go from the signal programmer through the encoder and microwave transmitter at the Control Point to the timing station, where they will be distributed to the Red Shack and user trailers over fiber-optic cables. Eliminating the currently used multiconductor cables between trailers will result in complete electrical isolation and keep electrical noise from being carried from one trailer to another. A command interface chassis (CIC) at the trailer end of the fiber-optic cables will decode the incoming optical signals into a form compatible with the users' equipment. The line going out to the Red Shack controlling critical operations will be interlocked with the scrambler decoder, as is done in the current system. Figure 1 compares the upgraded and present configurations of the T&C system.

We also want to simplify set-up procedures for an event, reducing the time required. Currently, we must physically wire the patch panels and adjust the output voltages at the timing station to set up for an event. After upgrading, we will only have to program and install a set of programmable read-only memory (PROM) chips in the signal programmer, command encoder, and command interface chassis. The PROMs required for an event can be prepared ahead of time. Once an event is completed, the timing station can be moved to its next location, have its PROMs replaced, and be ready for operation as soon as the microwave link is set up and the fiber-optic cables are attached. Rewiring for an event can take up to two days; reprogramming PROMs will take only two hours.

At this stage, we have begun talking to vendors about the equipment needed for such an upgrade. Pulse-code modulation (PCM) encoders that can be modified to implement the distribution system at the timing station are commercially available, as are PCM decoders suitable for the command interface chassis. Replacements for the monitor subsystem's user encoders and optical modems are also available. By having the manufacturers modify their products, we will avoid the considerable expense of designing from scratch in an area outside of our expertise. We also gain the advantage of drawing upon the manufacturers' experience in putting together a more efficient system.

Summary

The T&C system was designed over 20 years ago. Many of the parts needed in servicing its equipment are no longer available because the technology is obsolete. We are continuing to upgrade the system, modernizing and simplifying its subsystems. These changes will reduce the work required to prepare for an event and, thus, reduce set-up time. Upgrading the T&C system with state-of-the-art technology will also increase the system's reliability and eliminate the maintenance problems encountered when using obsolete equipment.

Reference:

1. *Nuclear Explosive Safety Study of the LLNL Arming & Firing and Timing & Control Systems and Operations at the NTS*, U.S. Department of Energy, Nevada Operations Office, Las Vegas, Nev. (1982).

Kearsarge and Shagan: The Joint Verification Experiment

D. C. Conrad

On August 17, 1988, the U.S. and the Soviet Union conducted a joint underground nuclear test, called Kearsarge, on Pahute Mesa at NTS. Approximately one month later on September 14, 1988, the two countries conducted a second joint underground nuclear test, called Shagan, at the Semipalatinsk Test Site (STS) in the Soviet Union. These two tests constituted the Joint Verification Experiment (JVE), the first instance of collaboration by the Soviets and Americans on underground nuclear tests (see Fig. 1). The JVE was made possible when then U.S. Secretary of State George Schultz and Soviet Minister of Foreign Affairs Edvard Schevardnadze signed an agreement on December 9, 1987, announcing the plans for this undertaking. This agreement represented a major step in the continuing efforts by diplomats from both nations to resolve differences on the issue of yield verification for the Threshold Test Ban Treaty (TTBT) and Peaceful Nuclear Explosives Treaty (PNET), which were written in the 1970s but have never been ratified. The agreement initiated a fast-moving chain of events that included the establishment of the Nuclear Testing Talks in Geneva and reciprocal visits to each other's test sites to explore the logistics for the conduct of the two tests and, finally, culminated in the two tests themselves.

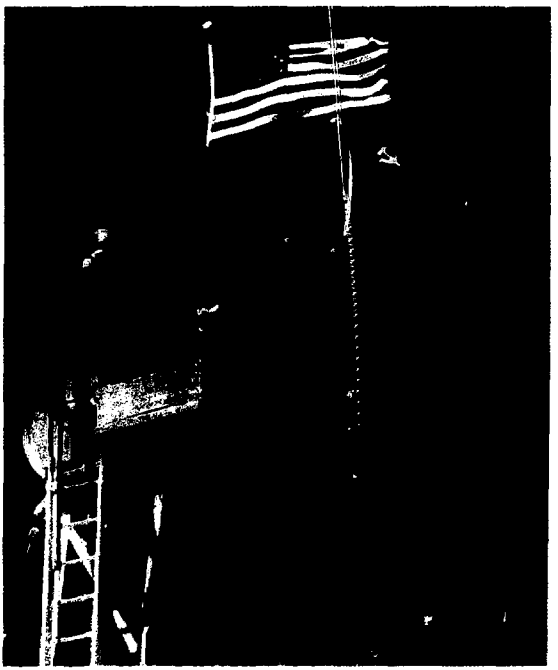

Figure 1. For the first time in history, the flags of the U.S. and the Soviet Union flew jointly over the nuclear ground zeros for Kearsarge at NTS and Shagan at STS. Shown here are the two flags atop a drill rig at the Kearsarge ground zero.

The December agreement stated that the U.S. and the Soviet Union would proceed with the design of the two JVE tests with the following objectives:

- Elaboration of improved verification measures for the eventual ratification of the TTBT and PNET.
- Measurement of event yields using teleseismic and onsite hydrodynamic methods.
- Demonstration of the applicability of standard test practices in a verification experiment.
- Demonstration of the practicality, effectiveness, and nonintrusiveness of the verification methods.

Early Agreements

Just as the concept of a joint experiment between the U.S. and the Soviet Union involving a nuclear explosion was unprecedented in previous treaty negotiations, the execution of Kearsarge and Shagan presented unprecedented challenges, both operational and technical, for the nuclear testing programs in both countries. Although the signed agreement defined the concept of the JVE, it delineated only a few of the technical parameters for its execution. According to the agreement, the yield of the explosions to be verified would not be less than 100 kt and should approach 150 kt. To verify compliance with these requirements, the verifying side

at each test site would be allowed to field hydrodynamic yield measurements in the emplacement hole for each event as well as in a satellite hole within a specified distance of the emplacement hole. Then, the yield determined from the measurements in the emplacement hole would be a "yield standard" for the event. All the remaining technical and organizational parameters associated with conducting the JVE were to be negotiated by *ad hoc* working groups to be established in Geneva.

Elaboration of Improved Verification Measurements

Shortly after the December agreement was signed, technical delegations from both sides met in Geneva to discuss each side's preferred methods for making yield verification measurements for the TTBT and the PNET. The U.S. presented a hydrodynamics technique, called CORRTEX (COntinuous Reflectometry for Radius versus Time EXperiments), that would be used in the emplacement hole or a satellite hole near the event to be verified. The Soviets presented teleseismic measurements as their principal method for yield verification; however, they also presented several techniques for making hydrodynamic measurements, including contact closure pins and a CORRTEX-like measurement called MIZ, that would be used to calibrate the teleseismic measurements. Both sides conducted extensive seminars on the theory of operation, the instrumentation hardware, and the analysis techniques associated with their verification methods. Both sides also exchanged historical data on past events at NTS and STS to substantiate the models on which the analysis codes were based. The U.S. even provided the Soviets with a CORRTEX measurement unit for disassembly and inspection. Even though these talks did not produce a common yield verification technique accepted by both sides, they did develop a better understanding on the part of both the U.S. and the Soviets of the technology associated with the different techniques that were being proposed. This mutual understanding was critical to the success of the JVE and to future negotiations on the TTBT and the PNET.

Measurement of Event Yields on Kearsarge and Shagan

While discussing the merits and problems associated with the various yield verification methods, the working groups in Geneva began planning the actual yield-measurement experiments to be fielded at the two test sites to fulfill the requirements of the JVE. As stated in the agreement, both sides were allowed to make teleseismic and hydrodynamic measurements for both events. The teleseismic measurements would be made from designated stations located farther than a specified minimum distance from the test site being monitored. As discussed previously, the hydrodynamic measurements would be made in the main emplacement hole and in a satellite hole and would be identical for both events. Both sides finally agreed on the hydrodynamic measurement configuration shown below:

- U.S.: six CORRTEX cables in the emplacement hole and six CORRTEX cables in the satellite hole.
- U.S.S.R.: two sets of radio frequency (rf) pins, two sets of logging pins, and two MIZ cables in the emplacement hole; three sets of logging pins and two MIZ cables in the satellite hole.

In support of these measurements, a number of additional agreements were reached regarding the fielding of the two events. After much debate over the size of the emplacement holes, an existing NTS hole, U19ax (96 in. in diameter), was selected for Kearsarge and a Soviet hole, No. 1350 (36 in. in diameter) was selected for Shagan. The depth of the explosion points for the two holes was determined to be 2020 ft for Kearsarge and 2107 ft for Shagan. The host side designed the device and diagnostic canisters for each event. For Kearsarge, the device canister was 88 in. in diameter and 6 ft long and was attached to a short diagnostic canister. For Shagan, the device canister was much smaller, and there was no separate diagnostic canister.

The locations for the measurement recording stations were finally resolved to be 1000 m from ground zero (GZ) for the U.S. station on Shagan and, because of terrain difficulties, 580 m from GZ for the Soviet station on Kearsarge (see Fig. 2).

Figure 2. The remote trailer park containing the Soviet Recording Station and U.S. support equipment. The area inside the orange fence was considered to be Soviet territory until zero time, when it became joint Soviet/American territory until data were recovered.

The density of the stemming material in the hydrodynamic region for each device was a major issue because of the difficulty of matching the density of the stemming material with that of the surrounding rock. On Kearsarge, dry garnet sand was used for stemming 56 ft of the emplacement hole around the explosion point. This was capped with a 200-ft sanded-gypsum concrete plug, a much larger plug than is required for containment. On Shagan, the hole was filled with saturated iron ore in the vicinity of the explosion point. (The Soviets fielded densitometers in each hole to measure the actual density of the materials in the hydrodynamic region.) Stemming the Shagan satellite hole presented an especially difficult problem. Experts from the U.S. and the Soviet Union developed a new pumping technique using Soviet equipment for this operation. It is important to note that the stemming materials used for the two tests were different in part because of the differing geologies at NTS and STS. Because the water table at NTS is so deep, underground tests are conducted in unsaturated media. A higher water table at STS means that most, if not all, tests are conducted wet (in tully saturated media).

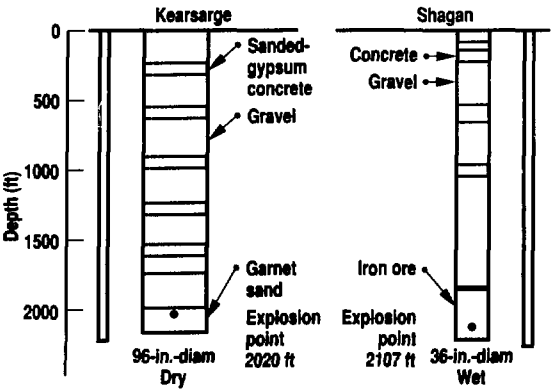

Figure 3. The stemming requirements in the region around the devices were unique for both JVE events in order to optimize the performance of the hydrodynamic systems.

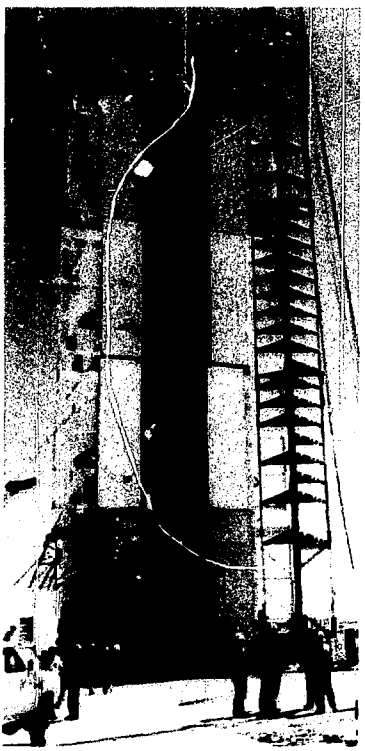

Figure 4. An elaborate array of brackets was used to support the hydrodynamic sensors in the region of the device on both events. Shown here is the first 100 ft of the Kearsarge emplacement pipe with support brackets attached.

Demonstration of Standard Test Practices

In general, the JVE incorporated the standard test practices of the host country. The rules governing nuclear, industrial, and radiological safety were strictly followed at both test sites. Except in the hydrodynamic region around the device, standard containment practices were used on both events (see Fig. 3). (The special stemming features in the hydrodynamic regions in no way compromised the containment safety for the events.) Except for minor modifications to incorporate the extensive array of hydrodynamic sensors in the first 200 ft above the device (see Fig. 4), standard drill-pipe emplacement operations and cable-handling procedures were used at both test sites. Although the command and monitoring systems for the two test sites differed radically in concept and construction, the standard system for the host site was successfully used on each

event. Finally, standard event quality assurance practices for the host site, including signal dry runs and design reviews, were used on each event.

However, to accommodate the unique requirements of Kearsarge and Shagan, each side occasionally had to alter several standard test practices, sometimes radically. At both sites the host side constructed three trailer parks: a host recording station; an event execution park; and the visitor's recording station, which was remote from the host's recording station and event execution parks. Administrative and operational planning meetings were held daily between the visiting and host management teams. The visiting team conducted extensive seminars to explain the design and operation of its measurement systems. All technical communications between the two teams (e.g., countdowns for signal dry runs, seminars, and discussions during stemming and downhole operations) had to be conducted through interpreters, most of whom had limited technical backgrounds. At NTS, the U.S. was required to provide uninterruptible 220-V, 50-Hz electric power for the Soviet recording station and their remote monitoring station. In addition, the U.S. side had to conduct a nonstandard "no hold" 15-min countdown to accommodate the Soviet recording station's standard mode of operation. At both test sites, the visiting side had to endure makeshift field communication systems with limited capabilities that caused many delays and much frustration. And, finally, both test sites faced major changes in procedures and numerous unprecedented problems in logistics and security because of the presence of large numbers of personnel from the visiting side at the base camps and in actual testing areas.

Results of the Joint Verification Experiment

The JVE was born in political negotiations between the U.S. and the Soviet Union and was executed in the field by collaboration between scientists, engineers, technicians, and interpreters from both countries. It was an extremely difficult undertaking that, although introducing unprecedented problems in the nuclear testing programs in both countries, was conducted successfully. It led to an incredible information exchange between the two programs and allowed people within the testing organizations a rare opportunity to interact with their counterparts from the other country in a working relationship.

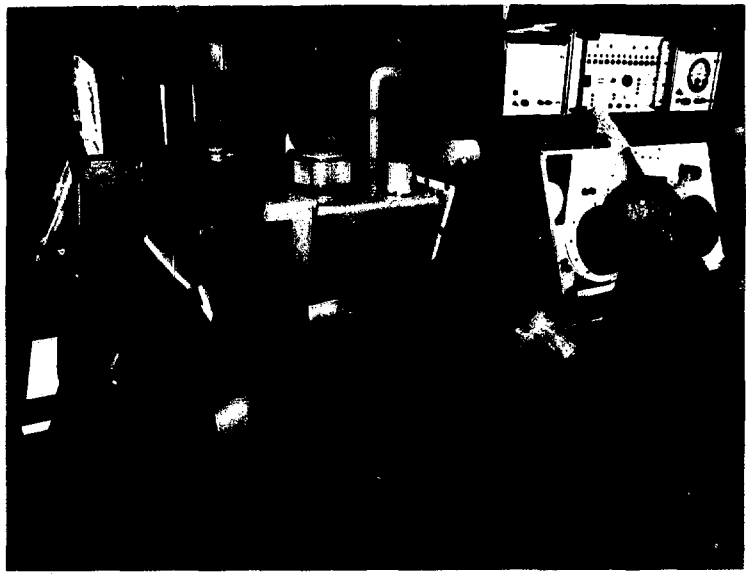

3
Nuclear Chemistry

The main mission of the Nuclear Chemistry Division is to provide experimental data, through the methods of radiochemical diagnostics, with which to understand the performance of nuclear explosives tests. We rely upon nuclear chemistry diagnostics to determine the most basic performance criteria of nuclear tests—total fission and thermonuclear yields. The increasing complexity of these tests and the desire for more detailed data require an ongoing research and development (R&D) program to improve and expand our arsenal of diagnostic techniques.

To understand the physics of a nuclear explosive experiment in detail, we must determine yields of individual parts, burn asymmetries in fissile and thermonuclear fuels, fast-neutron outputs, and the extent of shell instabilities. Firm data on these performance details are needed to verify computational-model predictions or to identify deficiencies in the models, thereby leading to a better understanding of the physics of nuclear explosives. In this chapter, we report R&D in support of the Division's radiochemical diagnostics mission.

The development of new and improved radiochemical diagnostic techniques requires both laboratory and field experiments. We are using this approach to develop charged-particle detectors, based on the conversion of iodine and bromine to xenon and krypton by (p,n) and (d,2n) reactions, and a neutron-fluence detector, based on the production of a series of radioactive bismuth isotopes by successive (n,2n) reactions on stable ^{209}Bi. Evaluations of fission-yield measurements based on noble-gas fission products demonstrate the value of recent improvements in laboratory measurement capabilities applied to nuclear-test diagnostics. Reports in this chapter describe the status of laboratory developments necessary to begin using ^{243}Am as a new radiochemical tracer on nuclear tests and the application of gas radiochemistry to evaluate the effectiveness of containment measures on weapons-effects tests performed by LLNL for the Department of Defense.

Maintaining first-rate laboratory facilities and improving measurement and analysis capabilities are important components of the continuing development of nuclear chemistry diagnostics. The computer data-processing, accelerator mass spectrometry, and x-ray calibration and standards facilities are multiapplication capabilities with important roles in providing and interpreting nuclear-test data. We have also developed a new, mobile, gamma-ray spectrometer system for rapid analysis of radioactive drill-core samples at the Nevada Test Site (NTS). This system provides accurate assessments of core-sample quality within minutes of sample recovery, thus removing much of the guesswork from nuclear-test sampling.

Interpreting radionuclide production data to determine physical performance measures, such as fission yields and neutron and charged-particle fluences, requires the knowledge of a large number of nuclear-reaction cross sections. We determine the required cross sections by experimental measurements, data evaluations, and theoretical model calculations, and then test them against new nuclear-test measurements and improved explosion-code predictions. We have recently measured (n,2n) cross sections for krypton and xenon isotopes—needed for neutron-fluence diagnostics—as well as (p,n) and (d,2n) cross sections for zirconium and europium isotopes—needed for charged-particle fluence diagnostics. We completed preliminary model calculations of a set of cross sections for iridium to improve our interpretation of data from this important, energy-sensitive, neutron-fluence detector.

To process radiochemical data and provide consistent physical interpretations, we need specialized data-analysis and interpretation codes. We have now implemented GOSPEL, a third-generation, radiochemical-diagnostics data-base management and interpretation code, on our VAX computer system. We are also developing codes to take advantage of the accessibility and graphics capabilities of personal computers to enhance some of the data-management processes in our cross-section modeling.

Our theoretical modeling of nuclear-reaction cross sections for radiochemical diagnostics has a natural extension into the field of astrophysics. Following a detailed evaluation and calculation of bismuth-isotope reaction cross sections, we note the possible importance of the long-lived ^{210}Bi isomeric state in the astrophysical s-process production of ^{207}Pb. We also present a new model of the astronomical features known as planetary nebulae in terms of "spheromak" plasma configurations.

Development and Implementation of a Field Gamma-Ray Spectrometer for Onsite Core Analyses at the Nevada Test Site

A. A. Dalecchi, L. A. Maynard, A. L. Prindle, W. D. Rabtor, and A. V. Friemehner

We have developed a new germanium-detector–gamma-ray spectrometer system that measures the fission-product content and sample quality of NTS drillback cores. Following detonation of an underground nuclear test, solid samples of the device debris are returned to LLNL for radiochemical analysis to determine device performance. To address potential sampling errors, we request that these samples be taken from widely separated locations, both vertically and horizontally, in the melt region. We also require that selected chemical elements of diagnostic interest in these samples *not* be chemically fractionated. Chemical fractionation can occur underground during the condensation phase shortly following a test. By measuring the ratio of the fission products ^{95}Zr and ^{140}Ba found in the samples, we are able to select those that have insignificant levels of chemical fractionation.

The traditional system for selecting solid samples from drillbacks at the NTS is as follows:

- A slant hole is drilled to intercept the "puddle" region at some distance out from the shot centerline (see Fig. 1).
- Upon completion of the hole, a high-intensity gamma-ray logging tool is lowered into the drill pipe in order to survey the target zone. The LLNL drilling engineer uses this log to locate where high-radiation fields exist (often hundreds of R/h) and, hence, where good cores might be obtained (see Fig. 1 inset).
- A sidewall sampling tool is used to extract cores from all promising locations, beginning with the deepest locations. Typically, 15 to 20 cores are taken per drillback hole. In a special trailer located at the drillback site, each core that has a high radiation reading is "high-graded" to produce several 10- to 20-g candidate samples.
- The candidate samples are shipped from the remote testing area at the NTS to Mercury, where they are assayed by gamma-ray spectrometry on a Compton-suppressed, germanium-detector system to determine the sample's fission content and the extent of chemical fractionation.
- After sampling of the first hole is finished, the drill pipe and tools are withdrawn, and a sidetrack hole is started several hundred feet higher in the hole and drilled through another part of the target zone. The high-intensity gamma-ray logging, coring, and high-grading are repeated for the sidetrack hole.
- Once assays of the high-graded samples at Mercury have been completed, a selected suite of samples judged to be suitable for more detailed analysis is shipped to LLNL.

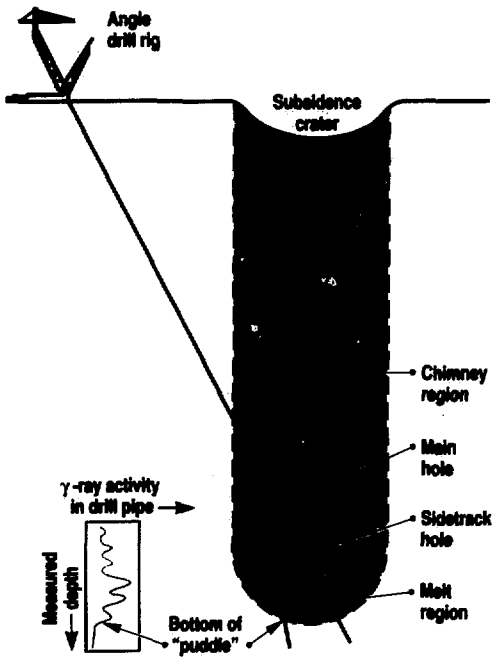

Figure 1. *The drilling configuration used for recovering solid cores from an underground nuclear test. The inset shows a representative log of gamma-ray intensity observed in a drill pipe intersecting the melt ("puddle") region.*

Although in most cases the drillback procedure outlined above successfully satisfies our sample requirements, at times, especially during difficult drillbacks, it would be advantageous to know more about the quality of the cores shortly after they are obtained.

The New Field Gamma-Ray Spectrometer System

During this past year, we designed, built, and used a system that allows us to quickly determine the weight, fission product content, and chemical fractionation of a drillback core within minutes after its retrieval.

A schematic diagram of the principal elements of the system is shown in Fig. 2. A movable germanium detector was installed in the trailer that is used to extract cores. During drillbacks, this trailer is located immediately adjacent to the drill rig. Now, soon after a core is extracted, it is placed into a shielded counting position where a load cell determines its weight (typically 50 to 300 g). An operator in a second trailer located outside the potentially contaminated drillback area can remotely position the detector to be from 0.9 to 3.0 m from the core in order to compensate for variable levels of activity. (Good cores contain fission products from 10^{15} to 10^{16} total fissions and can be retrieved as early as three days after a test.)

Readouts of the core weight and the sample-to-detector distance are available in the second trailer (see Fig. 2), where the data are analyzed. We found that a 4-min count is usually sufficient to establish for the core both the total fission content and the atom ratio of ^{95}Zr to ^{140}Ba from a pulse-height spectrum. Each spectrum is analyzed and interpreted with a code containing yield information regarding detector calibration and fission products; results are stored on a floppy disk and printed out. Generally, quantitative information is available within six to seven minutes after a core has been extracted. However, a semiquantitative measure of core quality is available earlier during the count from the displayed count rates of selected gamma-ray peaks.

Therefore, within a few minutes following core extraction, a decision can be made whether to continue sampling at the current depth or to proceed to a new location.

Drillback Experience

This new field gamma-ray spectrometer system was used for the first time to select cores on the Schellbourne Event (May 11, 1988). Measurements were made on all cores from one drillback hole and from a sidetrack hole, as well as on a number of high-graded samples. Results of the field measurements made on the high-graded samples were in excellent agreement with results of assays done at Mercury. In nearly all ways, the new system performed up to expectations. It provided timely information on the progress of the drillback and, except for some minor operational details, which were quickly worked out, the new measurements did not adversely affect other drillback operations.

The assay of one of the cores taken during the Schellbourne drillback illustrates one advantage of this new capability. Generally, cores taken from the upper region of an underground cavity are highly chemically fractionated, often containing excess amounts of the more volatile elements. Consequently, even though these cores may be highly radioactive, they are not suitable for radiochemical analyses. Moments after we retrieved the uppermost core from Schellbourne's main drillback hole, the core assay showed, to our surprise, that it was the best material retrieved from this hole. If we had needed more material from this hole, we would have been able to mine this location and perhaps even higher locations for additional samples. This information would not have been available to us without the new capability.

During the Schellbourne and the subsequent Comstock drillback operations, we learned that the high-grading process also benefited from having the new core measurement information. Because the

Figure 2. Principal features of the field gamma-ray spectrometer system used to assay drillback cores.

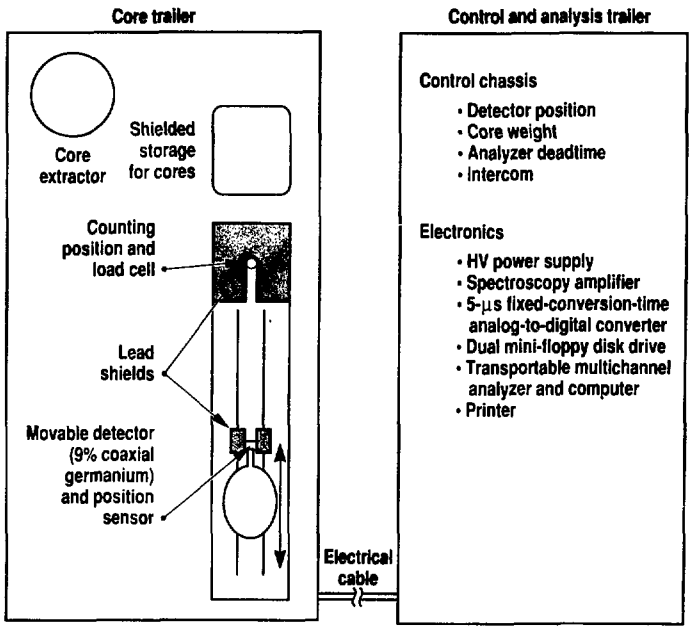

new measurements told us which cores contained good material and which did not, we were able to restrict high-grading to only the more promising cores, thereby reducing personnel radiation exposure. In addition, we were able to ask that more material be selected from cores that we knew contained particularly large amounts of good material.

Additional benefits gained from the new field gamma-ray spectrometer measurements were most clearly demonstrated during the drillback of the Comstock Event (June 2, 1988). The gamma-ray log of the main drillback hole showed high-intensity gamma-radiation fields in only a few narrow regions in the lower half of the underground cavity, and we had little success in retrieving material from these locations. After five hours of sampling, we had too few cores and, unfortunately, the material we had retrieved all came from about the same depth in the hole. Because the new system gave us a clear understanding of the limitations of our cores, we repeatedly tried to obtain cores from two more widely separated locations in the hole. After many attempts, we finally succeeded in getting sufficient material from these locations to satisfy our minimum sampling requirements. A sidetrack hole was then drilled to intercept the puddle region about 60 ft horizontally distant from the main hole. Its gamma-ray log looked very similar to the first. The coring operation had barely started (two samples were retrieved) when the drill string became stuck in the rock formation. During attempts to free the drill string, the drill pipe parted about 700 ft from the bottom. At this point, we had to make a choice: Did we have enough samples to adequately diagnose this test, or should we go for another sidetrack hole? The latter operation would take at least one more day of drilling and delay our post-shot analyses accordingly. In a close decision, we concluded that there was enough material for the required analyses and that the drillback operation could be terminated. Without the new field gamma-ray spectrometer measurements on the Comstock drillback, it would have been necessary to drill an additional sidetrack hole, thus extending the drillback operation by at least one more day and, of course, adding expense.

Conclusion

The capability of this new gamma-ray spectrometer system to assay drillback cores shortly after they are extracted improves our ability to effectively sample underground nuclear tests. Quantitative measurements of the quality of freshly obtained cores can be used to decide which downhole locations should receive the greatest sampling effort and which cores should be high-graded for further analysis. As a result, this system will enable better sampling of underground tests while at the same time reducing both drilling costs and personnel radiation exposure.

A New Approach to Characterizing Nonlinearities in Multiplier Ion-Detection Systems

S. Niemeyer, N. Henry, G. Hunt, and E. H. Wilkes

Experimental instruments used for ion detection frequently use some type of secondary-electron multiplier system to enhance the instrument's signal-to-noise ratio. The introduction of any multiplier detector immediately raises questions regarding the linearity of the total amplification system over the entire range for which the instrument is designed. Here, we specifically address this issue for

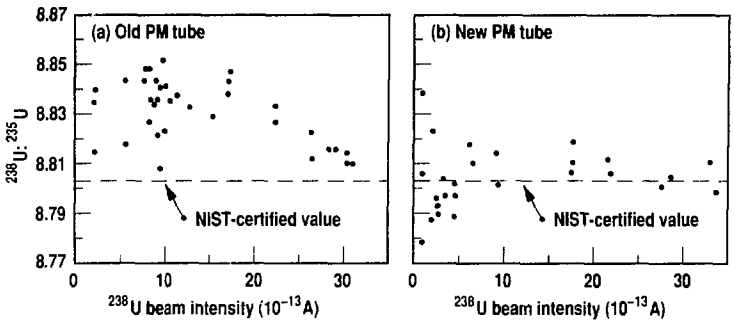

Figure 1. Measured uranium isotopic ratios after correcting for mass-fractionation using the double-spike technique. (a) The nonlinearity of the old photomultiplier (PM) tube is evident; the trend toward the correct value at higher intensities is real and reproducible. (b) The linearity of the new PM tube allowed all data sets to be averaged to obtain a single value for each standard analysis (see Table 1).

thermal-ionization mass spectrometry. The common calibration technique for the ion-detection system in these instruments involves measuring a suite of uranium isotopic standards that are certified by the National Institute of Standards and Technology (NIST). Deviations of measured isotopic ratios from the certified values in excess of the certified uncertainties (typically 0.1% on $^{238}U/^{235}U$ for the NIST suite) indicate a nonlinear system. In addition, if the deviations show a systematic trend that correlates with the magnitude of the ratio, we can also infer a nonlinear response.

Although this calibration scheme has been used extensively and successfully for mass spectrometers, it has two principal drawbacks. First, evaporation of the uranium from the hot filament produces an isotopic spectrum that is mass-fractionated relative to the true isotopic ratios. This effect is usually taken into account by rigorously following an established protocol for filament-loading and mass spectrometric analysis so that the magnitude of the mass-fractionation is the same for all standards. Generally, experimental protocols require loading similar amounts of sample and analyzing at similar ion-beam intensities for the major isotope. In addition, because of the limitations imposed by the need to rigorously account for mass-fractionations in the source, even if nonlinearities are observed, characterizing the nature of the nonlinearity can still be very difficult. Indeed, as detailed here, one of our Daly multiplier systems on a thermal-ionization instrument was quickly determined to be nonlinear at the 0.2 to 1.0% level, but ambiguities introduced by possible mass-fractionation effects prevented our identifying the nature of the nonlinear response until we employed the technique described in this article.

Double-Spike Calibration Technique

In our approach, we add a double spike of ^{236}U and ^{233}U to each NIST uranium standard so that we can directly measure the mass-fractionation via the $^{236}U/^{233}U$ ratio and correct each measured $^{238}U/^{235}U$ ratio for the mass-fractionation measured during the same time period. Nonlinearities in the ion-detection system do not cause systematic errors in the calculated mass-fractionations because the double spike has equal amounts of the two-spike isotopes. An example of data that have been corrected for mass-fractionation is shown in Fig. 1(a) for the system in its nonlinear mode. Each point represents the corrected $^{238}U/^{235}U$ ratio determined by 10 to 30 measurements of each ion beam. Because we can accurately track the changes in mass-fractionation as the filament temperature is varied, we can study the degree of nonlinearity as a function of beam intensity. This constitutes a major advantage over the usual method because in the unspiked analysis, the manner in which the mass-fractionation changes with time and temperature during an analysis is not known well enough to construct this type of plot. Figure 1(a) shows that the measured ratio is about 0.5% too high at a ^{238}U beam intensity of 1.0×10^{-13} A, but as the beam intensity increases, the measured ratios begin to approach the correct value. Other standards with different isotopic ratios demonstrate this same behavior, although the beam intensity at which the nonlinearity disappears changes according to the magnitude of the isotopic ratio.

After several analyses of various standards, we were able to characterize the nature of this detector's nonlinearity. (We noted that even with extensive efforts prior to using the double-spike technique, we were unable to accomplish this characterization.) Figure 2 presents a correction factor (f) that can be used to correct all measured isotopic ratios to an accuracy of ±0.1%. A function of beam intensity f has a constant value of about 1.009% at low beam intensities ($<10^{-14}$ A) and decreases linearly to zero at 5×10^{-14} A. Above this intensity, no correction is necessary. Earlier unpublished unspiked data for these standards are consistent with this correction function. Most notably, this correction scheme accounts for some observations that we found puzzling. That is, NIST U200 ($^{238}U/^{235}U = 3.98$) appeared to give approximately the correct ratio at both very low and high intensities, but in the intermediate range, the measured ratios were too high.

Our implementation of this new technique for calibrating ion-detection systems demonstrates that it does, in fact, overcome the principal drawbacks of the previous approach. In other words, extremely rigorous protocols for sample preparation and loading are no longer required, and a simple correction function can be rather readily constructed. Furthermore, the entire calibration of the mass spectrometer can now be accomplished much more quickly and accurately.

Linear Amplification by Daly Multiplier Systems

Before characterizing the nonlinearity, we attempted to identify the source of the problem in our Daly detector system. In this detector, ions strike a polished metal knob held at about −30 kV relative to the detector enclosure, releasing about eight secondary electrons per incident ion. These secondary electrons are attracted to a scintillator, thereby converting the secondary electron signal to photons, which are transmitted out of the vacuum system

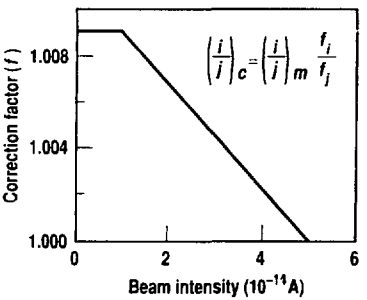

Figure 2. Correction factor for the old, nonlinear PM tube. It can be used to correct previous VG1 mass-spectrometer analyses that used the old PM tube. The ratio $(i/j)_m$ is the measured isotopic ratio; f_i and f_j are the correction factors for the i and j ion beams, respectively; and $(i/j)_c$ is the corrected ratio.

through a transparent window. The transmitted light signal is then amplified by a PM tube. By removing or changing various components in the signal-processing electronics, we determined that none of these electronic elements was responsible for this particular nonlinearity. Finally, we discovered that the PM tube itself was responsible for the nonlinearity. Earlier, this possibility had been discounted because the nature of the nonlinearity is equivalent to a PM-gain curve in which the gain is constant at low beam intensities; then at 10^{-14} A, it begins to increase until it reaches a new gain plateau above 5×10^{-14} A. We expected just the opposite current-gain effect for a nonlinear PM tube.

In Fig. 1, we show some data for a double-spiked NIST U100 standard before and after replacing the PM tube. After replacing it [Fig. 1(b)], no trend relating to beam intensity is apparent, and now the measured values show good agreement with the certified ratio. Because no trend is evident, we can legitimately average the measured values for all beam intensities in order to place the strictest limits on the degree of nonlinearity. The results are shown in Table 1 for two different Daly multiplier systems on two mass spectrometers. For both systems, each standard agrees very well with the certified ratio. We conclude that the upper limit on nonlinearity is about 0.05% for both systems.

Table 1. Calibration data for Daly multipliers.[a]

Mass spectrometer	$^{238}U/^{235}U$ NIST value	$^{238}U/^{235}U$ Measured value	δ (%)[b]
VG1	3.9799 (40)	3.9809 (19)	+0.03 (5)
VG2	8.803 (9)	8.807 (6)	+0.05 (7)
VG1	8.803 (9)	8.805 (3)	+0.02 (4)
VG2	18.956 (19)	18.934 (4)	−0.06 (2)
VG1	18.956 (19)	18.944 (10)	−0.01 (5)
VG2	98.62 (10)	98.58 (11)	−0.04 (11)
		98.64 (08)	+0.02 (8)
		98.70 (11)	+0.08 (11)
VG2	203.3 (2)	203.1 (4)	−0.10 (20)

[a] Measured ratios represent the average of all sets of data for a single sample where ^{238}U was at least 3×10^{-14} A (although no significant deviations were evident at lower intensities); each set of data was separately corrected for mass-fractionation using the double-spike technique. Uncertainties corresponding to two standard deviations are shown in parentheses. The listed average deviation δ between measured and certified values is an unweighted average. VG1 is our production mass spectrometer and the one with the faulty PM tube discussed in this paper. VG2 is our clean-room mass spectrometer.

[b] $$\delta\,(\%) \equiv \frac{(^{238}U/^{235}U)_{\text{measured}}}{(^{238}U/^{235}U)_{\text{NIST standard}}} \times 100\,.$$

Conclusions

The study described here represents the most precise and comprehensive determination to date of the linearity of the Daly type of multiplier system. We conclude that this type of detector has no inherent nonlinearity at the 0.05% level, and any nonlinear response in excess of this limit is probably associated with the PM tube or the electronics used to measure its output. Thus, we have demonstrated that the Daly multiplier is very well suited for analog measurements of ion-beam intensities over its entire working range. The technique we developed to characterize the Daly multiplier nonlinearities is also applicable to other types of multiplier detector used in thermal-ionization mass spectrometers and can be adapted for detector systems in other types of mass spectrometer.

Variation of Fission-Product Yields with Neutron Energy

D. R. Nethaway

We have prepared a preliminary set of fission-product yields for several important nuclides from the fission of ^{233}U through ^{240}U by 0- to 15-MeV neutrons. The use of a complete set will make it unnecessary to rely on the two-group model to characterize the neutron spectrum causing fission and will lead to a more accurate determination of uranium fission yields in device tests. We find

that present uncertainties in fission-product yields place a lower limit of about 3 to 5% on the accuracy of determining device fission yields.

In measuring fission yields for device tests, we use a two-group model to characterize the neutron spectrum causing fission. In this model, we divide the neutrons into two groups called "fission spectrum" and "14 MeV," with the energy division being at about 8 MeV. We have had to use this model because, until recently, we did not know how fission-product yields varied as a function of neutron energy up to 15 MeV (because of the relative difficulty in measuring fission yields in the 2- to 14-MeV neutron-energy range). In essence, then, we calculate the number of fissions in a sample by using the known fission-product yields (atoms/fission) for fission-spectrum and 14.1-MeV fission, together with an assumed two-group fission split and the measured number of fission-product atoms. This "energy split" (fraction of fissions in each of the two groups) usually comes from a calculation with an explosion code like MEG. Or, it can be obtained by adjusting the split so that the calculated yield of an energy-sensitive fission product, such as ^{156}Eu or ^{161}Tb, matches the measured value. We have relied on the effective fission-product yield calculated for the two-group spectrum to approximate the true value for the real spectrum, without actually knowing what error was being introduced.

To further compound the problem, not all fissions of uranium or plutonium are due to a single isotope (e.g., ^{235}U, ^{238}U, ^{239}Pu). Therefore, we group fissions from uranium isotopes 233 through 236 to form a "^{235}U" family, and those from uranium isotopes 237 through 240 to form a "^{238}U" family. Similarly, all plutonium isotopes form a "^{239}Pu" family. From the explosion calculation, we obtain a fission "mass split" for these three families. Finally, we use fission cross sections as a function of energy for only ^{235}U, ^{238}U, and ^{239}Pu to estimate the energy splits, ignoring the differences in cross sections for any other fissioning isotopes, such as ^{236}U and ^{240}Pu.

This is a preliminary report of an effort to develop a complete set of excitation functions for fission-product yields over the energy range from 0 to 15 MeV for all of the uranium isotopes. The use of this set will make it unnecessary to use the two-group model and will allow one to use fission cross sections for all of the uranium isotopes. Enough experimental fission-yield data exist to define reasonably well the variation in fission yield from 2 to 14 MeV for the major fission products of ^{235}U and ^{238}U that we use for yield interpretation. Furthermore, I can reasonably estimate these yields for the other uranium isotopes with masses from 233 to 240, which is the range covered in the explosion codes. So far, this study has covered only the isotopes of uranium; I intend to extend the work to include plutonium. In addition to preparing excitation functions, I also assessed the uncertainty in each fission yield for ^{235}U and ^{238}U over the whole energy range up to 15 MeV. This allowed me to make estimates of the uncertainty inherent in our fission-yield quotations for typical device neutron spectra and fission splits.

Preparation of Fission-Yield Files

We routinely use the fission products ^{95}Zr, ^{144}Ce, and ^{147}Nd to measure fission yields for underground nuclear tests. In addition, the nuclide ^{99}Mo is of interest because of its historic use during atmospheric testing. The nuclides ^{156}Eu and ^{161}Tb are also routinely measured and provide information on the fission split, in terms of both energy and fissioning species. I have used these six nuclides as the basis for this study. I started by making plots of the available fission-yield data for these six nuclides from fission of all of the uranium isotopes with neutron energies from thermal to 15 MeV. As examples, Fig. 1(a), which uses data from Refs. 1 through 3, shows the excitation function for ^{95}Zr from the fission of ^{235}U. Figure 1(b), which uses data from Refs. 1 and 4 through 7, shows the excitation function for ^{147}Nd from the fission of ^{238}U. As can be seen, these two (and other) fission yields are quite well known over the entire energy range. Error envelopes show my estimates of the 1σ uncertainty in the excitation functions, which are just French-curve fits to the data points. Data points for the fission-spectrum (plotted at 1.8 MeV) and 14.1-MeV energies are the values we currently use at LLNL and are taken from the GOSPEL or PROPHET computer codes. (GOSPEL is a computer program that has replaced the PROPHET program for summarizing diagnostic results.)

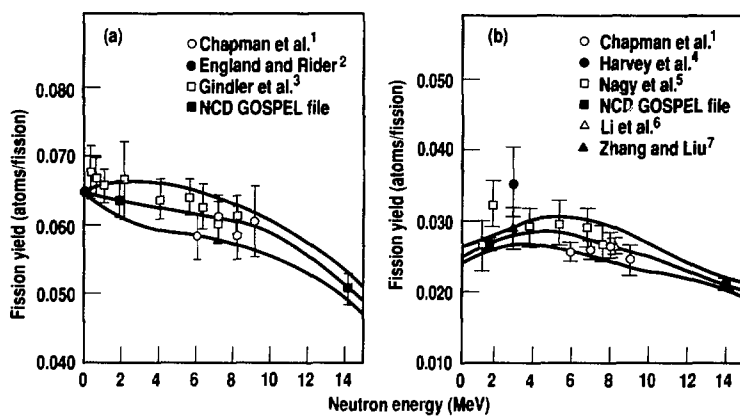

Figure 1. (a) Fission yield of ^{95}Zr from neutron-induced fission of ^{235}U. The outer lines are estimates of the uncertainty (1σ) in the line fitted to the data points. (b) Fission yield of ^{147}Nd from neutron-induced fission of ^{238}U. The outer lines are estimates of the uncertainty (1σ) in the line fitted to the data points.

The next step was to address the fission-product yields for the various uranium isotopes for both fission-spectrum and 14.1-MeV fission. Figure 2 shows the yields of three products for the fission of ^{233}U through ^{240}U with fission-spectrum neutrons. I used curves such as these to estimate missing yields for ^{237,239,240}U fission, for which no data exist, with the assumption that the curves should be smooth, with no odd-even fluctuation. I used many of the evaluated yields from the compilation of Rider[8] in preparing these plots.

In summary, I prepared plots of the yields of the six fission products over the energy range from 0 to 15 MeV for uranium isotopes 233 to 240. For ^{237}U, ^{239}U, and ^{240}U, the plots are based only on the yields at 1.8 and 14.1 MeV, determined from plots such as those in Fig. 2. I estimated the uncertainty in the excitation functions only for ^{235}U and ^{238}U. I prepared a data file for use with the WATUSI computer code containing all of the neutron reactions on uranium for masses 233 to 240, together with explicit cross sections to produce the six fission products. The cross sections were group-averaged in the 53-group structure used in the MEG code, so that fluence files generated by MEG could be used with WATUSI to calculate the number of fissions and the production of the six fission products. This then gives directly the effective fission yield of each product for use in calculating the device yield.

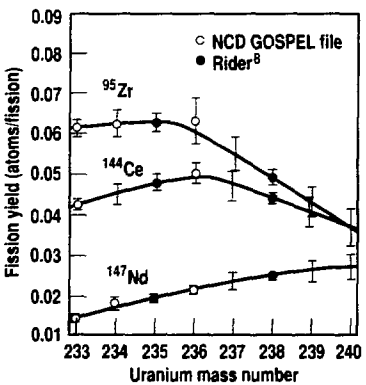

Figure 2. Fission yields of ^{95}Zr, ^{144}Ce, and ^{147}Nd from fission of $^{233-240}$U induced by fission-spectrum neutrons. Error bars mark the estimated yields for fission of ^{237,239,240}U and for ^{144}Ce from fission of ^{234}U.

Discussion

Calculations made for the uranium fission in several devices show that the effective fission-product yields for ^{95}Zr, ^{144}Ce, and ^{147}Nd are about 2 to 3% higher than those previously estimated using the two-group model. Even though the new fission excitation functions are still preliminary, they provide a more accurate method of determining device fission yields. The error introduced by using the two-group model is small but significant. The calculations also show that the yields for ^{156}Eu and ^{161}Tb are about 3 to 6% lower than those estimated with the two-group model. This implies that the energy splits should be softened to include less 14-MeV fission, in agreement with the trend suggested by energy splits inferred from fission gas diagnostics.

I prepared separate cross-section files for the fission of ^{235}U and ^{238}U using the upper and lower bounds to the excitation functions ($\pm 1\sigma$) as shown in Fig. 1. For a typical device neutron spectrum, the yields of the products ^{95}Zr, ^{144}Ce, and ^{147}Nd have an uncertainty of about 2% for ^{235}U fission and 4 to 5% for ^{238}U fission. We can combine these uncertainties with an additional 2% for the uncertainty in measurement due to the detector calibrations. Hence, the minimum uncertainty in our uranium fission-yield results for device tests is about 3 to 5%. The yields of the energy-sensitive products ^{156}Eu and ^{161}Tb have an uncertainty of about 5% and 9%, respectively, for ^{235}U fission and about 5% and 6%, respectively, for ^{238}U fission.

Future Work

I plan to extend the scope of this work to include excitation functions for the fission of ^{238}Pu through ^{243}Pu for the same six fission products. I also intend to try to fit the mass-yield data with an analytical function. By doing this, I expect to better model the change in fission yield for a particular product as either the neutron energy or the mass of the fissioning species is changed. This should improve the accuracy of interpolating between fission-spectrum data and 14-MeV data and of estimating fission yields for target nuclides for which little or no data exist. Musgrove et al.[9] and Dickens[10] have shown that mass-yield data can be well represented by the sum of five Gaussian distributions; their model may be quite appropriate for my work.

References:

1. T. Chapman, G. Anzelon, G. Spitale, and D. Nethaway, *Phys. Rev. C* **17**, 1089 (1978).
2. T. R. England and B. F. Rider, "Status of Fission Yield Evaluations," *NEANDC Specialists Meeting on Yields and Decay Data of Fission Product Nuclides, Brookhaven National Laboratory, Upton, N.Y., Oct. 1983*, BNL-51778 (1984), pp. 33–63.
3. J. Gindler, L. Glendenin, D. Henderson, and J. Meadows, *Trans. Amer. Nucl. Soc.* **39**, 877 (1981).
4. J. Harvey, D. Adams, W. James, J. Beck, J. Meason, and P. Kuroda, *J. Inorg. Nucl. Chem.* **37**, 2243 (1975).
5. S. Nagy, K. Flynn, J. Gindler, J. Meadows, and L. Glendenin, *Phys. Rev. C* **17**, 163 (1978).
6. Z. Li, C. Zhang, C. Liu, X. Wang, L. Qi, A. Cui, H. Lu, S. Zhang, Y. Liu, C. Ju, D. Liu, P. Tang, J. Meng, and K. Jing, *Yuanzihe Wuli* **7**, 97 (1985).
7. C. Zhang and C. Liu, *He Huaxue Yu Fangshe Huaxue* **7**, 1 (1985).
8. B. F. Rider, *Compilation of Fission Product Yields*, Vallecitos Nuclear Center, Pleasanton, Calif., Report NEDO-12154-3(C) (1981).
9. A. R. del Musgrove, J. L. Cook, and G. D. Trimble, "Prediction of Unmeasured Fission Product Yields," *Proc. Panel on Fission Product Nuclear Data, Bologna, Italy, Nov. 1973*, IAEA-169 International Atomic Energy Agency (1974), pp. 163–200.
10. J. K. Dickens, *Nucl. Sci. Eng.* **96**, 8 (1987).

Calibration of Fission-Product Yields for ^{136}Xe and ^{85}Kr

G. B. Hudson

Measurements of fission-produced ^{136}Xe and ^{85}Kr can provide accurate and reliable determinations of the total number of fissions occurring in an underground nuclear explosion.[1] One difficulty in using the ^{136}Xe method is that we lack accurate measurements of the number of ^{136}Xe atoms produced per fission. This measurement is moderately difficult because it requires the neutron irradiation of fissionable materials such as ^{235}U and ^{239}Pu. The U and Pu targets have large alpha decay activities, and the irradiation induces additional gamma and beta decay activity from the mixed radioactive fission products.

While direct measurements of the ^{136}Xe and ^{85}Kr fission-product yields (atoms/fission) are planned, we have calibrated these yields using existing data from underground nuclear explosions. The technique is nearly identical to laboratory-based experiments. In these experiments, we irradiate a sample of Pu or U with neutrons and measure the fission products ^{95}Zr, ^{144}Ce, and ^{147}Nd. Then, on the basis of previous measurements of the atoms/fission for ^{95}Zr, ^{144}Ce, and ^{147}Nd, we can deduce the number of fissions that occurred. We chose these isotopes because they are routinely used in measurements of nuclear explosion fission yields. One goal of the ^{136}Xe calibration is to compare total device fission yields determined by gaseous elements directly with those determined by refractory elements without concern over systematic bias.

In using underground nuclear explosions for the ^{136}Xe (or ^{85}Kr) atoms/fission calibration, we determine the total number of fissions using ^{95}Zr, ^{144}Ce, and ^{147}Nd. Then we measure the total ^{136}Xe produced in the nuclear explosion. This measurement gives the ^{136}Xe fission-product yield (atoms/fission) for the particular mix of fissionable material that went to produce the nuclear explosion. Here lies the chief disadvantage of this method. We cannot measure the ^{136}Xe fission-product yield for a single fissioning isotope or a single neutron energy. Instead, we measure a highly relevant mixture of fissionable materials and neutron energies. By measuring the ^{136}Xe produced on a variety of tests, we can calibrate the ^{136}Xe fission-product yield with enough accuracy for our purposes.

Analysis

To analyze an explosion, we first review the refractory element data and postshot physics modeling to determine the number of fission reactions and the distribution of reactions as a function of parent isotope and neutron energy. Then we review the gaseous element data to determine the number of ^{136}Xe (or ^{85}Kr) atoms produced. Using regression analysis, we determine the ^{136}Xe fission-product yield as a function of the parent isotope—^{239}Pu, ^{235}U, or ^{238}U—and neutron energy. We divide neutron energy into two groups: fission-spectrum energy (1–2 MeV) and energy at 14 MeV. Then we evaluate the agreement between the total number of fission reactions as determined by ^{95}Zr, ^{144}Ce, and ^{147}Nd vs that determined by ^{136}Xe.

Results

We have gaseous and refractory element measurements from 16 nuclear tests. For both gases and solids, the data must be internally consistent; that is, all samples—either gas or solid—of a given event must give the same result. All but one of these 16 tests gave a consistent calibration for the ^{136}Xe fission-product yields. We estimated that the agreement between ^{136}Xe and refractory measurements should be 3.7% (one standard deviation), on the basis of the analytical precision of the data. The standard deviation of our calculated ^{136}Xe fission yields agrees with refractory element data to about 3.7%, indicating that our assignment of analytical errors is correct and no other source of deviation is present. Comparable results are obtained for ^{85}Kr with an uncertainty of 6.0%. The calculated fission-product yields of ^{136}Xe and ^{85}Kr are given in Table 1.

Conclusions

We calibrated the ^{136}Xe and ^{85}Kr fission indicators with sufficient accuracy to make them generally useful in routine radiochemical fission diagnostics. These indicators are attractive because they are easy to measure.

Reference:

1. G. B. Hudson, "Test Diagnostics based on Isotopic Measurement of Xenon," *Nuclear Chemistry Division Annual Report FY83*, Lawrence Livermore National Laboratory, Livermore, Calif., UCAR-10062-83 (1983).

Table 1. Fission-product yields of ^{136}Xe and ^{85}Kr.

Fission product	Fission-product yield (atoms/fission)					
	^{239}Pu at		^{235}U at		^{238}U at	
	FS[a]	14 MeV	FS	14 MeV	FS	14 MeV
^{136}Xe	0.0634	0.0450	0.0615	0.0400	0.0670	0.0500
^{85}Kr	0.00148	0.0023	0.0028	0.0032	0.0014	0.0018

[a] FS = fission-spectrum energies (1–2 MeV).

Using Radiochemical Diagnostics to Evaluate Containment Performance

C. E. Smith

We have applied radiochemical diagnostics techniques to evaluate the performance of containment features installed on tunnel events by the Defense Nuclear Agency (DNA). Containment diagnostics have traditionally been instrumental in nature and observational in practice. Instruments monitoring the tunnel environment faithfully record such things as radiation level, pressure, and temperature of the environment. This information gives an accurate history of the timing and enables us to evaluate the impact of a major failure of the first-line containment systems. Physical effects are also measured by instrumentation to determine stress levels, material motion, and shock propagation. These measurements are useful in the design of future test-bed configurations and serve as a comparison base to link a series of events. In practice, most of our understanding of how containment systems perform has been observational. The DNA literally mines into regions of interest and inspects the systems. These traditional techniques do not directly address the basic question of the nature of the challenge to the containment barriers, nor can they evaluate barrier performance short of failure.

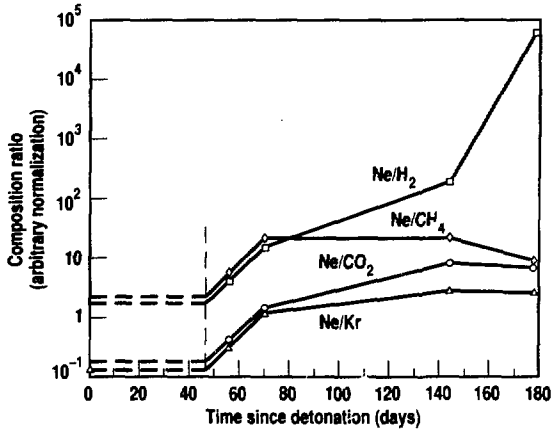

Figure 1. Mission Ghost chimney-gas components show dilution effects when plotted as shown. We adjusted the data by arbitrary scaling factors to create a common display. Krypton added as a tracer serves as a reference, and the initial value of Ne/Kr is known. From the intersection of this value by the extrapolated Ne/Kr measurements, we determined that dilution effectively began on day 46 (vertical dashed line). Similar extrapolation of the reactive-gas data to this time gives an estimate of the initial cavity-gas composition.

We have recently participated in several nuclear tests that were executed in tunnel test beds and have applied radiochemical diagnostic techniques to address questions of concern to the DNA containment program. Our studies have included determining cavity-gas composition and pressure as a function of time, identifying mechanism and time of material transport, and evaluating the performance of containment systems. As we are able to participate more fully in planning and to influence reentry activities, our contributions to the understanding of tunnel containment-system performance will continue to grow. We are now actively involved in the design and execution of an extensive study of cavity-gas phenomenology for a future event. The following examples are drawn from our recent experience and illustrate the scope and nature of the information that can be obtained using radiochemical diagnostics techniques.

Cavity Phenomenology

Our analyses of gas samples obtained from the Mission Ghost chimney region defined the cavity-gas composition and chemical history of this event. The DNA was concerned that the cavity apparently had not subsided and that it might still be pressurized with an explosive gas mixture that could prove hazardous to reentry operations near the cavity. A hole drilled from the mesa penetrated the top of the cavity 42 days after detonation. Four days later, a horizontal hole drilled from the reentry drift penetrated the side of the cavity. The horizontal hole yielded five gas samples between 48 and 178 days after detonation. These samples were sent to us for analysis.

The samples comprised mixtures of oxygen-depleted air and H_2 with small amounts of CO_2, CH_4, and other hydrocarbons. The composition varied significantly with sampling time. H_2,

which was the principal component of the early samples, had all but disappeared by the end of sampling. CO_2 decreased by more than a factor of 3, while CH_4 increased by a factor of 4. Such drastic changes are unprecedented in our experience. The observations are consistent with a model involving hydrogen combustion by oxygen in the air, coupled with CO_2 reduction and conversion to CH_4. We believe that the vertical drillhole first allowed pressure relief into the formation and then supplied air to the cavity as it cooled and lost gases to these reactions.

To test this theory and to obtain an estimate of the original cavity composition, we used neon as an indicator of air. Figure 1 displays normalized ratios of neon to the three principal cavity gases, H_2, CO_2, and CH_4, as a function of sampling time. Also shown is the ratio of neon to krypton, which was added to the preshot cavity as a tracer. Because we know the preshot void volume, we also know the total neon present initially. This ratio is plotted at zero time, and it would have remained constant had air not been allowed to enter the cavity. Changes in composition between 55 and 70 days are caused mainly by air dilution. (Later changes are caused largely by chemical reactions.) We extrapolated the dilution line defined by these two points to intercept the known zero-time neon-to-krypton ratio. The vertical dashed line drawn through this point of intersection is the effective start time for the dilution. Extrapolation of the cavity-gas component ratios to this time gives an estimate of the predilution cavity-gas composition.

Our conclusion from this ar.. .ysis is that the cavity gas was almost pure H_2 at early times. The consequences of this observation, from a containment standpoint, range from awareness of the need to contain this flammable, highly mobile gas to consideration of ways to decrease the amount produced. We expect to provide assistance to the DNA in its evaluation of future containment systems designed to address these needs.

Evaluation of Containment-System Performance

Many DNA-sponsored tunnel events are effects tests in which radiation from a nuclear device is allowed to impinge on various target specimens placed at the far end of a line-of-sight (LOS) pipe. The containment of test debris requires that this LOS be closed and sealed soon after the passage of radiation. To accomplish this, DNA installed a number of rapid-closure systems in the LOS of the Mission Cyber Event.

We studied gas taken from the LOS in the region bounded by the fast-acting closure (FAC) and the tunnel and pipe seal (TAPS). The FAC is a high-explosive machine that collapses the pipe within 1 ms of detonation. The TAPS is a trap-door arranged to close and seat under the influence of gravity within 1 s of detonation. Dividing the LOS between the TAPS and the FAC is the gas-sealing auxiliary closure (GSAC). This is actually two helium-driven doors that occlude the LOS and seat against knife edges to create a gas seal at about 25 ms after zero time.

Early gas samples (1, 15, and 50 s after zero time) were obtained by Sandia National Laboratory using evacuated bottles placed in the Mission Cyber LOS pipe on the working-point sides of the TAPS and the GSAC. The DNA also collected reentry grab samples of gas from within the LOS at these two locations and from the chimney region above the working point. These were sent to us for analysis.

The early samples obtained in the GSAC-FAC volume were all found to contain the fission product ^{85}Kr in small quantities. The concentration was less than 10% of that found in this volume at reentry, and the latter was less than 1% of the concentration in cavity gas. The early samples were taken before complete decay of the ^{85}Br precursor, and the levels were consistent with expectations. The low concentration seen at reentry relative to that found in the chimney indicates a high degree of isolation of the LOS from the cavity. We conclude that a small puff of cavity gas passed the FAC at very early times, that little subsequent influx occurred, and that the FAC performed its function well.

The gas collected at early times from the GSAC-FAC region consisted largely of high-explosive detonation products (from the FAC) and helium (from the GSAC). A little oxygen-depleted air was also present. Pressure was about 1 atm. Early gas in the TAPS-GSAC region was largely helium and oxygen-depleted air with a few high-explosive gases and reached a pressure of only 0.2 atm. This difference was expected because the GSAC is designed to close before good mixing can occur. However, at reentry, we found that the gases from these two regions were of intermediate concentration, were both at atmospheric pressure, and both contained additional air. This finding indicates that the GSAC allowed gas to flow from the FAC toward the TAPS. Furthermore, this flow was fast relative to subsequent air influx. We conclude, therefore, that the gas-seal performance of the GSAC was below design level.

Late-Time Gas Generation

The grab samples from the Mission Cyber LOS amply illustrate the nature of late-time gas generation. In Fig. 2, we have plotted the volumes of several gases contained in the TAPS-FAC region as a function of sampling time.

The total of most gases had stabilized by 50 s after zero time and did not change significantly in the 2 to 3 months prior to reentry. H_2, however, increased by about 50%. This is a lower limit to the amount of H_2 generation for two reasons. First, the gas is quite oxygen depleted. Less than half as much O_2 is present as would be expected from normal air on the basis of argon present in the samples. Most likely, the "missing" O_2 reacted with H_2 to form water. Second, the absence of CO_2 is strong evidence of the occurrence of the water-gas reaction ($CO_2 + H_2 \rightarrow CO + H_2O$). CO_2 is produced in the high-explosive charge that drives the FAC. It was never present at the expected level. Quantitation of this effect is made difficult by the presence of

additional reactions that remove CO from the gas (e.g., disproportionation and reduction to graphite).

Late generation of H_2 in regions not directly connected with the cavity (a problem of concern to the DNA because of the explosive nature of H_2) is probably caused by reduction of water by various metals in the construction materials and surrounding media. Our observations are among the first to demonstrate the nature and extent of H_2 production. We will be working with the DNA to evaluate alternative construction materials and emplacement techniques to alleviate the problem.

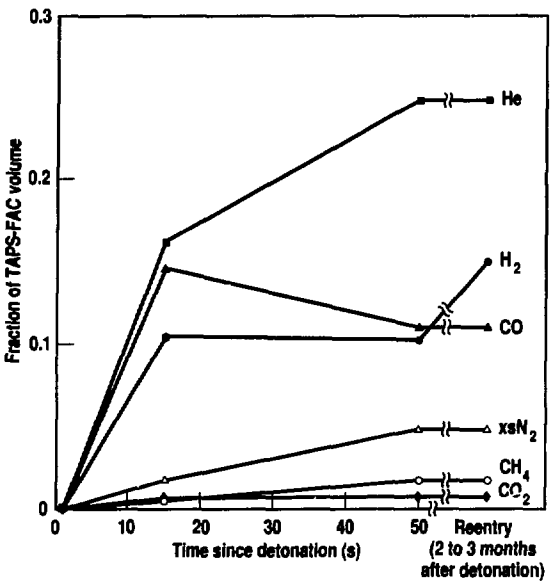

Figure 2. Temporal history of the volumes of several gases contained within the TAPS-FAC region of the Mission Cyber LOS pipe. Helium was the drive gas for the GSAC. CO, CO_2, and excess N_2 (xsN_2) were residual products of the FAC high explosive. H_2 and CH_4 were reaction products of water, metals, and the other gases. Early samples were poorly mixed, but by 50 s the mixture had stabilized, and only continued production of H_2 changed the composition at late times.

Summary

Radiochemical diagnostics techniques have been used to address a wide variety of containment-related concerns for the DNA. Future involvement not only will continue to address questions similar to those discussed here but also will extend to questions of cavity-gas composition, materials transport, and the performance of additional containment structures. An extensive cavity-phenomenology experiment planned for a future nuclear event will determine the relative amounts of rock and grout that are incorporated into the early cavity.

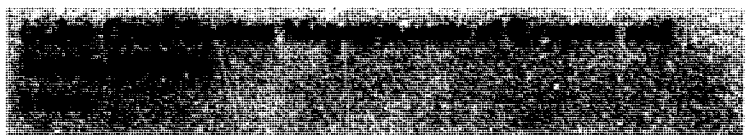

As part of our research in developing gas detectors for test diagnostics, we irradiated gas samples of ^{78}Kr, ^{80}Kr, and ^{124}Xe and measured the (n,2n) cross sections of these isotopes at three neutron energies between 14 and 15 MeV. We obtained results that are higher than those previously measured.

Isotopic gases such as ^{78}Kr, ^{80}Kr, and ^{124}Xe have been used as radiochemical detectors in several nuclear devices in order to measure the fluence of 14-MeV neutrons. Unfortunately, the cross sections are not very well known, which makes the interpretation of the results less accurate. For this reason, and as part of our research to develop gaseous detectors, we have measured the (n,2n) cross sections for three gases using enriched targets of ^{78}Kr (99%), ^{80}Kr (92%), and ^{124}Xe (40%).

In the application of gas detectors to device diagnostics, it is very important to know the half-lives of the activated products as accurately as possible. During the course of this work, we determined the half-life of ^{123}Xe to be 2.04 ± 0.01 hours, which is shorter than the previously

accepted 2.08 hours; the half-life of ^{77}Kr is 71.7 minutes; and that of ^{74}Kr is 34.9 hours (Ref. 1).

Experiment

We irradiated gas samples of ^{78}Kr, ^{80}Kr, and ^{124}Xe at the Rotating Target Neutron Source (RTNS-2) accelerator at LLNL. The 14-MeV neutrons were produced by the reaction of 360-keV deuterons on a tritium target. Four separate irradiations were performed during a period of 14 days; the third and fourth irradiations were used to repeat the measurements on the ^{78}Kr and ^{124}Xe samples. The ^{80}Kr samples were irradiated only one time because the half-life of the activated ^{79}Kr product is 34.9 hours.

The gases were contained in cylindrical quartz capsules 1 cm high by 1 cm in diameter, with a volume of approximately 0.8 cm^3. These quartz capsules were filled with about 1 atm of krypton or xenon gas and were irradiated for 1 hour at a fixed distance of 20 cm and at angles of 30, 60, and 90 degrees with respect to the deuteron beamline. A semicircular plastic hoop that held the capsules was positioned with the center of curvature at the neutron source.

Aluminum foils were used in front and back of the quartz capsules to monitor the neutron flux. We measured ^{24}Na from the ^{27}Al(n,α)^{24}Na reaction and calculated neutron fluences from the known cross sections of aluminum, as given by Tagesen and Vonach.[2]

Nickel foils were used to determine the energy of the incident neutron beam. These foils were also positioned in front and back of each capsule. In the 14- to 15-MeV range, the ^{58}Ni(n,p)^{58}Co cross section increases with energy, while the ^{58}Ni(n,2n)^{57}Ni cross section decreases. Therefore, the ^{58}Co:^{57}Ni ratio becomes a sensitive indicator of the neutron energy, and we can easily determine the incident beam energy by referring to the measured cobalt:nickel ratio.

We measured the activated products from the above reactions and the (n,2n) products of the three target gases with Ge(Li) detectors. In the case of the ^{78}Kr and ^{124}Xe samples, we made six successive 1-hour counts to follow the decay of ^{77}Kr ($t_{1/2}$ = 1.19 hours) and ^{123}Xe ($t_{1/2}$ = 2.04 hours). In the case of the ^{80}Kr samples, we made four successive 5-hour counts to follow the decay of ^{79}Kr ($t_{1/2}$ = 34.9 hours). All of the counting data were reduced with the GAMANAL computer code.

Results

Using the measured (n,2n) product, the gas loading in the quartz capsule, and the neutron flux generated by the aluminum foils, we calculated the cross section for each isotope at a particular energy determined by the position of the gas target with respect to the deuteron beam. These cross sections are listed in Table 1 as a function of energy for each of the three gases. Besides the individual measurements, we show an average cross section at each energy with a standard deviation, which represents the uncertainty of each value with respect to the mean of the replicate analysis. This uncertainty, which is a result of counter calibrations and counting statistics, is less than 5% in all cases.

The only previously measured cross sections for ^{78}Kr, ^{80}Kr, and ^{124}Xe are by Kondaiah.[3] The reported values at 14.5 MeV are 245 ± 20 mb, 810 ± 60 mb, and 1130 ± 110 mb, respectively. In comparison, our values are 321 ± 26, 797 ± 40, and 1585 ± 33, respectively.

References:

1. F. F. Momyer, "Gaseous Neutron Detectors and Detector Products," *Nuclear Chemistry Division FY84 Annual Report*, Lawrence Livermore National Laboratory, Livermore, Calif., UCAR-10062-84-1 (1985), p. 3-3.
2. S. Tagesen and H. Vonach, "Evaluations of the Cross-Sections for the Reaction ^{27}Al(n,a)^{24}Na," *Phys. Data* **13**, 3 (1981).
3. E. Kondaiah, "(n,2n) Cross Sections and the Statistical Model Predictions," *J. Phys. A* **7**, 1457 (1974).

Table 1. Measured ^{78}Kr, ^{80}Kr, ^{124}Xe (n,2n) cross sections.

RTNS No.	Target gas	Product	Neutron energy (MeV)	Cross section (mb)	Averaged cross section (mb)
	^{78}Kr	^{77}Kr			
9-87			13.98	239	233 ± 9
9-89			13.97	227	
9-87			14.41	339	321 ± 26
9-89			14.42	302	
9-87			14.70	376	
9-87			14.69	364	376 ± 11
9-89			14.69	376	
9-89			14.72	392	
	^{80}Kr	^{79}Kr			
9-87			13.98	688	—
9-87			14.44	797	—
9-88			14.69	934	895 ± 56
9-88			14.68	855	
	^{124}Xe	^{123}Xe			
9-88			13.93	1393	
9-88			13.97	1474	1436 ± 35
9-90			13.98	1426	
9-90			14.00	1453	
9-88			14.38	1608	1585 ± 33
9-88			14.45	1561	
9-90			14.78	1594	1618 ± 33
9-90			14.73	1642	

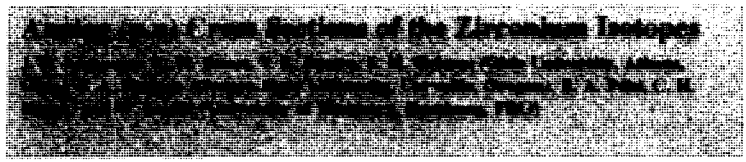

The isobaric analog of the ground state of a nucleus with neutron and proton numbers (N,Z) is that excited state of the isobar $(N-1,Z+1)$ of identical configuration to the (N,Z) ground state but with a neutron exchanged for a proton. We can easily identify the (p,n) charge-exchange reaction[1] on the nucleus (N,Z) by observing the prominent peak in the energy spectrum of the outgoing neutrons that corresponds to a reaction Q-value equal to that leading to the $(N-1,Z+1)$ ground state minus the Coulomb energy difference between the adjacent isobars (N,Z) and $(N-1,Z+1)$. The isobaric analog state is the lowest state in $(N-1,Z+1)$ with isospin T equal to the isospin of the (N,Z) ground state. Typically, that state occurs at an excitation energy such that it is superimposed on a continuum of states of isospin T-1.

The excitation of isobaric analog states in (p,n) reactions has generally been interpreted in terms of a direct charge-exchange process. Lane[2] has described this in terms of quasi-elastic scattering in which the optical model potential contains a term proportional to the scalar product of the isospin operators of the incident nucleon and the target nucleus. As a result, the Lane model predicts that the cross section for the (p,n) analog reaction should be proportional to the neutron excess of the target, $(N-Z)$. In a study of the (p,n) reaction on the isotopes of molybdenum,[3,4] however, the analog cross sections were found to depart considerably from the Lane model prediction. For the even-A isotopes, coupled-channel calculations[5] demonstrated that the deviation from the Lane model was the result of couplings to low-lying collective states and their analogs.

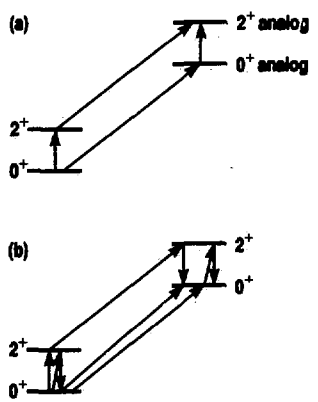

Figure 1. Results from coupled-channel calculations for the (p,n) reactions. (a) The primary mechanisms to analogs of excited states are the two 2-step mechanisms. (b) These three 3-step processes reduce the ground-state analog cross section.

The coupled-channel calculations[5] demonstrated that the isobaric analogs of strong collective states proceed primarily by two 2-step mechanisms, the direct 1-step process being negligibly small. The 2-step mechanisms are shown in Fig. 1(a). Consequently, for the excitation of the 0^+ ground-state analog, the dominant 1-step charge-exchange process is reduced by the destructive addition of three 3-step amplitudes [see Fig. 1(b)] that are nearly in phase with each other. If this is the case, then when 2^+ collective states are coupled, the cross section for the 0^+ analog state should decrease by an amount that is roughly proportional to the inelastic (p,p') 2^+ cross section. This was verified in Ref. 5 for the even molybdenum isotopes, where the dependence of the analog cross sections on the inelastic scattering deformation parameter was clearly reproduced by the coupled-channel calculations.

Our purpose in this experiment was to extend the molybdenum measurements to lower-deformation parameters in the same mass region, thereby further testing the influence of collective states on the charge-exchange process. In addition, measurements of the (p,n) analog cross section at 18 and 25 MeV allowed

confirmation of the previously observed anomalous energy dependence of the analog excitation function.[3,4,6,7]

Experimental Results

We used proton beams of 25.0 ± 0.1 and 18.0 ± 0.1 MeV from the LLNL Cyclograaff accelerator and the 16-detector fast-neutron time-of-flight (TOF) spectrometer to obtain the (p,n) neutron spectra. These facilities and the experimental method have been described in detail elsewhere.[8,9] We measured neutron TOF spectra at each detector angle and extracted the analog peak from the underlying continuum of T-1 states. By fitting the resulting analog angular distributions with a Legendre polynomial expansion, we obtained the integrated cross sections, σ. These cross sections divided by the corresponding neutron excess are plotted against the neutron excess in Fig. 2(a).

Discussion

Figure 2(a) clearly demonstrates that excitation of the isobaric analogs of the zirconium isotopes by the (p,n) reaction does not follow the simple prediction of the Lane model. In order to see if the deviation from the Lane model is the result of coupling to low-lying collective states, as was the case for the molybdenum isotopes, we adopted the following procedure: The 18-MeV zirconium data were normalized to the 25-MeV data in order to remove the anomalous energy dependence. The resulting reduced cross sections, σ/(*N*–*Z*), were then plotted [see Fig. 2(b)] against the square of the deformation parameter, β^2, for inelastic scattering to the lowest 2^+ collective state for each even zirconium target. The corresponding data from molybdenum[3,4] are also plotted in Fig. 2(b), as are the results of the coupled-channels calculations[5] for the molybdenum isotopes. The zirconium data clearly follow the trend of the molybdenum data and the calculations and confirm the steeper variation with deformation parameter at lower energy. Even though the variation in the deformation parameter for the zirconium isotopes is small, the result of the coupling on the ground-state analog cross section is as large as 30%.

This experiment confirms the importance of the coupling of excited states and their analogs in understanding the mechanism for the (p,n) charge-exchange reaction.

References:

1. J. D. Anderson and C. Wong, *Phys. Rev. Lett.* **7**, 250 (1961).
2. A. M. Lane, *Phys. Rev. Lett.* **8**, 171 (1962); *Nucl. Phys.* **35**, 676 (1962).
3. C. H. Poppe, S. M. Grimes, J. D. Anderson, J. C. Davis, W. H. Dunlop, and C. Wong, *Phys. Rev. Lett.* **33**, 856 (1974).
4. S. M. Grimes, C. H. Poppe, J. D. Anderson, J. C. Davis, W. H. Dunlop, and C. Wong, *Phys. Rev. C* **11**, 158 (1975).
5. V. A. Madsen, V. R. Brown, S. M. Grimes, C. H. Poppe, J. D. Anderson, J. C. Davis, and C. Wong, *Phys. Rev. C* **13**, 548 (1976).
6. G. W. Hoffmann, W. H. Dunlop, G. J. Igo, J. C. Kulleck, C. A. Whitten, Jr., and W. R. Coker, *Phys. Lett. B* **40**, 453 (1972).
7. C. Wong, J. D. Anderson, J. C. Davis, and S. M. Grimes, *Phys. Rev. C* **7**, 1895 (1973).

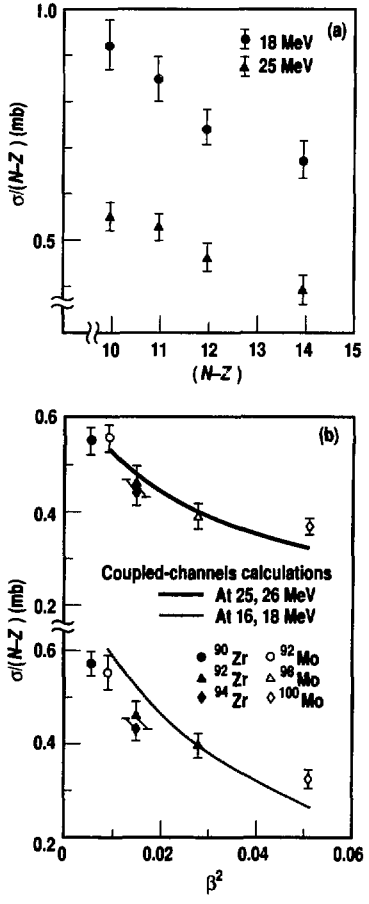

Figure 2. (a) Values of the reduced cross sections, σ/(*N*–*Z*), plotted as a function of neutron excess, (*N*–*Z*). The deviation from a horizontal straight line indicates failure of the Lane model. (b) Values of the reduced cross sections, σ/(*N*–*Z*), plotted as a function of the square of the deformation parameter, β, and for selected proton energies, E_p. These data show the effect of a variation in the deformation parameter on the 0^+ analog cross section. The molybdenum data and calculations are from Ref. 5.

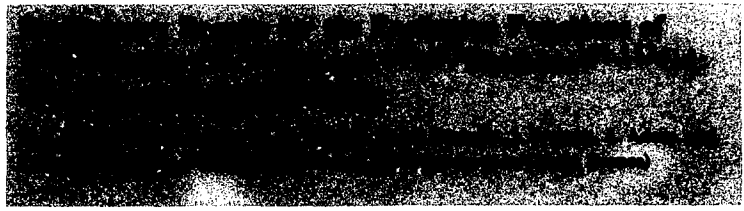

An interest exists at both LLNL and the Centre d'Etudes Bruyeres-le-Chatel, France (CEB) in obtaining accurately measured excitation functions for $^{151,153}Eu(p,n)^{151,153}Gd$ and $^{151,153}Eu(d,2n)^{151,153}Gd$. Here, we report our initial measurements made at the French laboratory's Van de Graaff accelerator for energies up to 12 MeV. Installation of the new Van de Graaff at LLNL will allow us to extend the measurements to 20 MeV.

Experimental Procedures

We used the activated-foil technique to determine the cross sections of the two stable europium isotopes. Europium in metallic form oxidizes rapidly (ignites in air at 150 to 180°C); thus, we looked for a method of target preparation that uses a compound of the element europium. The method established was to mix Eu_2O_3 with a polyimide resin that when polymerized forms a plastic similar to Kapton (a du Pont de Nemours product). The polyimide plastics we used will tolerate irradiation dosages of 3000 to 10,000 $\mu C/cm^2$. Total areal densities were about 15 mg/cm^2, one-third of which was europium. All of the foils were intercompared using x-ray fluorescence spectrometry. We used ^{241}Am radiation to excite the europium K x rays and used the fact that their measured intensities were proportional to the amount of europium present. These foils were assayed for europium content by burning representative foils to ash and then weighing them as Eu_2O_3. The foil densities were known to better than ±1%.

During an irradiation, the beam incident on a target was swept in a square pattern approximately 8 by 8 mm to ensure that no small nonuniformity in the foil would cause undue error in the cross-section measurement and to minimize heat loading. As a further check, we used only those foils shown by x-ray fluorescence to be uniform to better than 2%.

The activities from the foils were counted on large-volume germanium detectors installed in the gamma-ray counting facility at CEB, and the data were analyzed by computer-aided techniques. Some of the foils were sent to LLNL in order to cross-calibrate the detectors at the two laboratories.

The data were analyzed using the decay-scheme parameters listed in Table 1. The half-lives are from Nethaway.[1] The value of I_γ for the 153.6-keV gamma ray of ^{151}Gd was determined by averaging the value of 6.1 (5%) from Gregorich et al.[2] and the value of 6.3 (4%) from Voth et al.[3] I_γ for the 97.43-keV gamma ray of ^{153}Gd was taken from the *Table of Radioactive Isotopes*.[4] The other gamma-ray intensities were adjusted slightly from those in the literature to fit the relative intensities measured at CEB. The isotopic abundances

E (keV)	153.6	174.7	243.2	97.43	103.18
I_γ(%)	6.20	2.98	5.58	27.60	20.45

used for natural europium are 47.8% for ^{151}Eu and 52.2% for ^{153}Eu.

Because of the foil thicknesses, the energy loss for protons in a foil varied from 0.4 to 0.6 MeV, and for deuterons, it varied from 0.8 to 1.2 MeV. The energy losses in a stack of foils, which consisted of aluminum degraders (which also served as heat sinks) and Eu_2O_3-loaded Kapton, were calculated by our FELOSSK code, which was adapted to run on CEB's IBM computer. We were concerned about the accuracy of our calculations, so we performed some energy-loss experiments at CEB using protons and deuterons on selected foil combinations. Our preliminary analysis of these data indicates the error to be less than 3%. The maximum error in the reported energy for a cross section from such a source could be about 90 keV. These data also show marked effects of straggling and should afford us an opportunity to improve our calculations of this effect.

Because of the wide energy bite used in each cross-section measurement, significant corrections to the data were required in the rising portions of the excitation functions [the measured excitation functions are shown in Fig. 1(a) through (d)]. The method is described in our papers.[5,6] (Reference 6 is especially pertinent because it shows the results of corrections necessary for a relatively thick stack of foils. For protons, the corrections were less than 10%. For deuterons, the corrections were larger.) The lowest data point in Fig. 1(c) was adjusted from 0.49 to 0.18 mb; for the two data points at about 5.9 MeV, the corrections were approximately 35%. Few corrections were needed at energies higher than 7 MeV.

Results and Modeling

The measured excitation functions are given in Fig. 1, with STAPRE calculations for comparison. Some earlier measurements of the cross sections are available,[7,8] and they are in fair agreement with the present results when all necessary corrections are made. The data were modeled using the current LLNL version of the STAPRE code of Uhl and Ströhmaier,[9] which is based on the Hauser-Feshbach evaporation formalism plus the exciton preequilibrium model. Since these are preliminary calculations, the physics inputs are largely global values. However, 12 to 15 discrete levels from the current literature were used for each compound and residual nucleus (except for ^{150}Eu) involved in these calculations. For the deuteron-induced reactions, the theory is shown with and without deuteron breakup in the

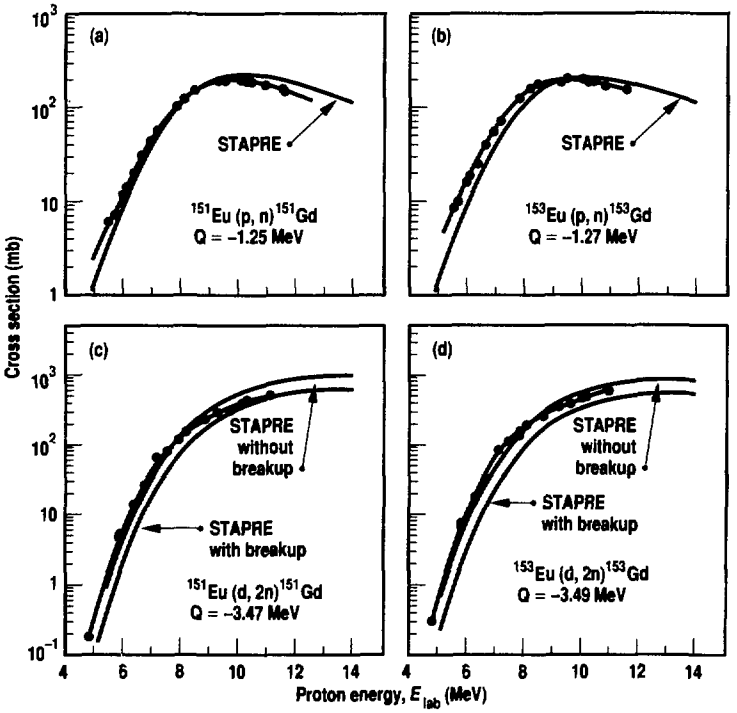

Figure 1. (a) The ^{151}Eu(p,n)^{151}Gd excitation function. The results of a STAPRE calculation are shown for comparison. (b) The ^{153}Eu(p,n)^{153}Gd excitation function. There appears to be a systematic difference between STAPRE calculations and experiment that requires explanation. (c) The ^{151}Eu(d,2n)^{151}Gd excitation function. STAPRE calculations are shown with and without deuteron breakup. The comparisons at low energy indicate the need for major changes in the calculations. (d) The ^{153}Eu(d,2n)^{153}Gd excitation function. STAPRE calculations are shown for comparison. Again, note the systematic difference between theory and experiment.

entrance channel. The breakup calculation follows methods reported in our earlier work.[10]

Global optical potentials were used. We used the Moldauer[11] potential for neutrons below 1 MeV and the Rapaport[12] and Varner et al.[13] potential for those above 1 MeV. For protons, we used the potential of Perey,[14] for alpha particles, the McFadden-Satchler potential,[15] and for deuterons, the potential of Perey and Perey.[16]

For level densities, we used the composite nuclear-level-density formalism of Gilbert and Cameron with shell and pairing corrections, the parameters being taken from Rose and Cook[17] as adjusted to known low-energy discrete levels.

The preequilibrium model parameters were taken from the work of the Milano[18] group with 2p-1h initial configuration for the (p,n) reactions and 3p-1h for the (d,2n) reactions.

Discussion

The STAPRE results for ^{151}Eu(p,n)^{151}Gd agree with the data reasonably well. For the ^{153}Eu(p,n)^{153}Gd reaction, there appears to be a systematic difference that must be explained. Note the calculations for the (d,2n) cross sections both with and without deuteron breakup [Fig. 1(c)]. At first glance, one could interpret the results as meaning breakup does not occur at the lower energies. However, we think the answers to the disagreements seen in Fig. 1(c) and (d) lie elsewhere. To good order, we would expect the ^{151}Eu and ^{153}Eu (p,n) and (d,2n) reaction data, respectively, to have the same excitation functions. Indeed, we can get perfect matches by adjusting the energy and amplitude scales appropriately. Agreements can also be achieved between theory and experiment by the same sort of adjustments. Thus, we are led to believe that the problem lies either in the available mass data or in the optical potentials. ^{151}Eu has a deformation parameter of $\beta = 0.13$ and so is nearly a spherical nucleus, whereas ^{153}Eu has a deformation of $\beta = 0.28$ and so is highly prolate.[19] We are looking for optical potentials that reflect this difference.

References:

1. D. R. Nethaway, private communication, Lawrence Livermore National Laboratory, Livermore, Calif. (1988).
2. K. E. Gregorich, J. J. Moody, and G. T. Seaborg, *Radio. Chemie. Acta.* **35**, 1 (1984).
3. E. Voth, W.-D. Schmidt-Ott, and H. Behrens, *Zeit. f. Phys. A: Atoms and Nucl.* **313**, 167 (1983).
4. E. Brown and R. B. Firestone, *Table of Radioactive Isotopes*, V. S. Shirley, Ed. (John Wiley & Sons, New York, N.Y., 1986).
5. M. G. Mustafa, H. I. West, Jr., H. O. Brien, R. G. Lanier, M. Benhamou, and T. Tamura, "Measurements and Direct Reaction Plus Hauser-Feshbach Analysis of ^{89}Y(p,n)^{89}Zr, ^{89}Y(p,2n)^{88}Zr, and ^{89}Y(p,pn)^{88}Y Reactions up to 40 MeV," *Phys. Rev. C* (in press). Also, Lawrence Livermore National Laboratory, Livermore, Calif., UCRL-98444 (1988).
6. H. I. West, Jr., R. G. Lanier, M. G. Mustafa, and H. O'Brien, *The Excitation Function for ^{48}V from Tritons on Natural Titanium*, Lawrence Livermore National Laboratory, Livermore, Calif., UCID-20163 (1987).
7. K. Komura, S. Tanaka, M. Uesugi, and M. Sakanoue, *J. Inorg. Nucl. Chem.* **38**, 2157 (1976).
8. N. A. Konyakhin, I. O. Konstantinov, P. P. Dimtriev, N. N. Krasnov, and V. M. Tuev, *Sov. Atom. Energy* **27**, 944 (1969).
9. M. Uhl and B. Ströhmaier, *A Computer Code for Particle Induced Activation Cross Sections and Related Quantities*, Institut für Radiumforschung und Kernphysik, Vienna, IRK 76/01 with Addenda (1976).
10. M. G. Mustafa, T. Tamura, and T. Udagawa, *Phys. Rev. C* **35**, 2077 (1987).
11. P. S. Moldauer, *Nucl. Phys.* **47**, 65 (1963).
12. J. Rapaport, *Phys. Rep.* **87**, 25 (1982).
13. R. L. Varner, T. B. Clegg, T. M. McAbee, and W. J. Thompson, *Phys. Lett. B* **185**, 6 (1987).
14. F. G. Perey, *Phys. Rev.* **131**, 745 (1963).
15. L. McFadden and G. R. Satchler, *Nucl. Phys.* **84**, 117 (1966).
16. C. M. Perey and F. G. Perey, *Phys. Rev.* **132**, 755 (1963).
17. E. K. Rose and J. L. Cook, *An Evaluation of the Gilbert-Cameron Level Density Parameters*, Australian Atomic Energy Commission, Australia, AAEC/E419 (September 1977).
18. G. M. Braga-Marcazzan, E. Gadioli-Erba, L. Millazzo-Colli, and P. G. Sona, *Phys. Rev. C* **6**, 1398 (1972).
19. R. G. Lanier, L. G. Mann, G. L. Struble, I. D. Proctor, and D. W. Heikkenen, *Phys. Rev. C* **18**, 1609 (1978).

Low-energy nuclear cross sections usually are calculated by the Hauser-Feshbach (HF) evaporation formalism,[1] where the main ingredients are the nuclear-level densities and optical-model potentials. However, when the bombarding energies are increased (for example, above 10 MeV for neutrons and above 15 MeV for protons), direct reactions (DR) start to play an important role and eventually become the dominant reaction process at higher energies. In this article, we briefly describe the physics of our DR code, which now runs on a Cray computer, and its application to the (p,n) and (p,2n) reactions on ^{89}Y (Ref. 2).

Physics in the MSDR Code

Our DR code is based on the multistep direct reaction (MSDR) formalism of Tamura, Udagawa, and Lenske.[3] Our version of the code works for the one- and two-step reactions. For example, for the (p,n) reaction, we can calculate the one-step (p,n) cross section or the two-step (p,p′n) plus (p,n′n) cross sections, where p′ and n′ represent the intermediate states of the projectile-target composite system. A formal theory of multistep reactions is presented in Ref. 3, but the essential physics is described here by the one-step (p,n) cross section[4]

$$\sigma_{pn}(\theta;E_p,E_n) = \sum_l \rho_l(E_p + Q - E_n) \times \sigma_l(\theta;E_p,E_n) \,. \quad (1)$$

In Eq. (1), $\rho_l(E_p + Q - E_n)$ is the spectroscopic density and $\sigma_l(\theta;E_p,E_n)$ is the standard distorted-wave Born approximation (DWBA) cross section for the (p,n) process. The quantity E_p is the proton bombarding energy. E_n is the energy of the outgoing neutron at an angle θ, Q is the Q-value of the (p,n) reaction, and l denotes the transferred angular momentum. The DWBA calculation is well known,[5] and the physics lies in the choice of the form factors. The form factors are usually taken to be proportional to the optical potential or its radial derivative. The spectroscopic density $\rho_l(E_p + Q - E_n)$ is obtained from the random-phase approximation[6] and constructed out of the Nilsson single-particle levels. This quantity describes how the strength of a given particle-hole state is distributed over the excitation energy $E_x = E_p + Q - E_n$. (For a more complete discussion of the DWBA part of our calculation and of the spectroscopic density, see Refs. 2 through 5.)

The two-step cross section is somewhat more complicated, but it is a straightforward generalization of the one-step process. In the past, the calculations were limited mostly to the one-step process because of computational difficulties. With Cray computers, however, the two-step calculation is now performed easily.

Results and Discussions

The details of our calculations and the results have been reported in Ref. 2. Here, we illustrate the application of the DR theory for the two reactions: ^{89}Y(p,n)^{89}Zr and ^{89}Y(p,2n)^{88}Zr. In Fig. 1, we show the (p,n) calculations. The DR cross sections are shown together with the HF calculation, and the sum of the two (HFDR) is compared with the data of O'Brien et al.[7] The HFDR calculations fit the data quite well over the whole energy range, showing that a combined use of the HF and DR theories adequately explains the data. We should also point out that, as expected, the HF calculational result alone fits the data for the lower energies, but the direct reaction dominates at higher energies and must be included to fit all of the data.

The ^{89}Y(p,2n)^{88}Zr cross sections are shown in Fig. 2. This time, the HF cross section fits the data up to about 30 MeV, but beyond that the remaining

Figure 1. Cross-section data and calculations for the ^{89}Y(p,n)^{89}Zr reaction. The HF, DR, and HFDR cross sections are shown and compared with experimental data.[7]

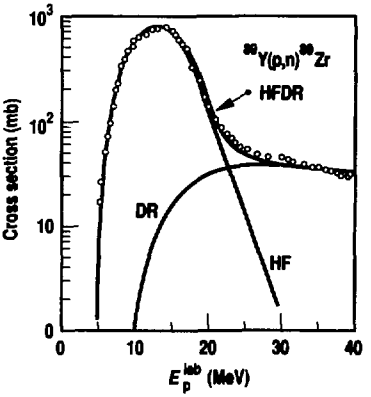

cross section in the range of 30 to 40 MeV is explained better by the DR theory. Again, without giving the details of the calculation, we show that the *HFDR* cross section improves the fit to the data.[7] Note the dominance of the DR cross section at 40 MeV. Note also that, in combining the HF and DR cross sections to obtain HFDR, we have reduced the HF cross section by the ratio of the sum of all direct-reaction cross sections [(p,n), (p,p′), ...] relative to the optical-model reaction cross section. This is done to account for the reactions that do not lead to the formation of a compound nucleus. This kind of scaling was not done for the (p,n) reaction because the scaling is important only at higher energies where the HF contribution to the (p,n) cross section is small.

Conclusion

In summary, we can do one- and two-step DR calculations in a routine fashion. We have shown that the measured (p,n) and (p,2n) cross sections for ^{89}Y are well reproduced by the HF formalism and DR, thereby providing a quantum-mechanical understanding of the low-energy activation cross sections. We should also add that, with some adjustments of the model parameters, a good fit to the data can be achieved by the semiclassical preequilibrium models.[8] These results are reported in Ref. 2. Finally, although the *HFDR* calculations are somewhat more complicated than the usual HF-plus-preequilibrium models, we expect the quantum-mechanical HFDR approach to be used routinely in future modeling of low-energy cross sections.

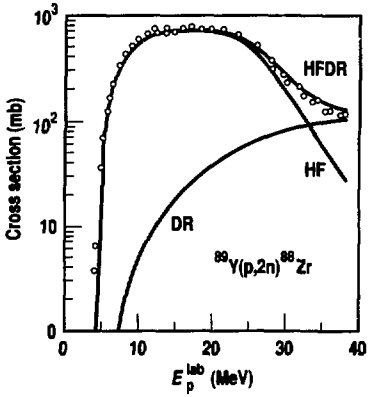

Figure 2. Cross-section data and calculations for the ^{89}Y(p,2n)^{88}Zr reaction. The HF, DR, and *HFDR cross* sections are shown and compared with experimental data.[7]

References:

1. W. Hauser and H. Feshbach, *Phys. Rev.* **87**, 336 (1952).
2. M. G. Mustafa, H. I. West, Jr., H. O'Brien, R. G. Lanier, M. Benhamou, and T. Tamura, "Measurements and a Direct Reaction Plus Hauser-Feshbach Analysis of ^{89}Y(p,n) ^{89}Zr, ^{89}Y(p,2n) ^{88}Zr, and ^{89}Y(p,pn) ^{88}Y Reactions up to 40 MeV," *Phys. Rev. C* **38**, 162 (1988).
3. T. Tamura, T. Udagawa, and H. Lenske, *Phys. Rev. C* **26**, 379 (1982).
4. T. Tamura, T. Udagawa, and M. Benhamou, *Comp. Phys. Comm.* **29**, 391 (1983).
5. G. R. Satchler, *Direct Nuclear Reactions*, Chapter 3 (Oxford University Press, 1983), pp. 78–116.
6. A. Bohr and B. R. Mottelson, *Nuclear Structure*, Vol. II (W. A. Benjamin, Reading, Mass., 1975), p. 436.
7. H. A. O'Brien, H. I. West, Jr., R. G. Lanier, and M. G. Mustafa, *Nuclear Chemistry Division FY86 Annual Report*, Lawrence Livermore National Laboratory, Livermore, Calif., UCAR-10062-86 (1986), pp. 2–26.
8. M. Blann, *Annu. Rev. Nucl. Sci.* **25**, 123 (1975).

There is a need in our nuclear test program for radiochemical detectors (i.e., for specific elements or isotopes) that can sample neutrons of a few MeV for use in measuring fission-spectrum neutrons in nuclear devices. The possibilities are limited by various factors, but one choice is iridium, which has two stable isotopes, ^{191}Ir (37.3%) and ^{193}Ir (62.7%). Iridium used as a detector can provide information not only about midrange neutron energies, via (n,n′) production of the ^{193}Ir isomer, but also about high-energy neutrons via the formation of ^{189}Ir and ^{190}Ir from successive (n,2n) reactions on ^{191}Ir. ^{192}Ir, produced by the two reactions ^{193}Ir(n,2n) and ^{191}Ir(n,γ), gives additional information. Figure 1 shows a total of 22 ground

states and isomeric states (isomers) of 10 iridium isotopes, from ^{187}Ir to ^{196}Ir. These are the states we considered as targets or products in our calculations.

Cross sections were calculated for the following reactions: (n,γ), (n,n′), (n,2n), and (n,3n) for incident neutron energies from $\geq 10^{-5}$ to 20 MeV. We computed 228 excitation functions for partial and total reactions among the iridium states; all were needed because the potential usefulness of iridium in a variety of neutron intensities and energy distributions requires correct accounting of all sources of each product. Further, the products that we measure are either single isomers or sums of the ground states plus one or more isomeric populations. Therefore, it was necessary to consider a large number of isomers since isomeric states can play an important role in the net production of the measurable end products. Yet, for reasons that we will address, these iridium cross-section sets are only preliminary and are used primarily for sensitivity studies until their deficiencies can be corrected.

In some situations, two-step reactions may overwhelm the one-step processes. For example, ^{189g}Ir may be produced by ^{191g}Ir(n,2n) to the ground state and isomers of ^{190}Ir, followed by (n,2n) reactions on the ^{190}Ir states to produce ^{189g}Ir (all of the ^{189}Ir isomers decay by gamma-ray emission to the measured ground state). The ^{191g}Ir(n,3n)^{189g}Ir reaction may contribute little to the measured product except when the neutron fluence is especially low. Because the expected intensity and the energy distribution of the neutron fluence are important considerations in the placement of the iridium detector, an accurate interpretation of the net production of a particular state requires as complete a set of production and destruction cross sections as possible.

Cross-Section Calculations

We used our versions of the COMNUC[1] and STAPRE[2] statistical-model codes to calculate the cross sections and the optical-model code SCAT2[3] to compute the neutron-transmission coefficients. The neutron potential we used had been derived for iridium[4] and modified by Arthur[5]; we added isospin terms to allow for changes in the mass number. Arthur found it necessary to modify the original potential in order to increase the total reaction cross section at energies above 10 MeV. However, we observed in later studies that the original potential achieved better agreement with experiment. We calculated the gamma-ray transmission coefficients based on our systematics for absolute E1 and M1 strength functions.[6]

We described each iridium isotope above the ground state with a preliminary set of about 35 to 70 discrete levels, each having associated gamma-ray-decay branching fractions. Above these levels, we employed a level-density expression in which some of the parameters were modified, based on information we extracted from the discrete levels using statistical analyses. Of utmost importance to the accurate calculation of isomer populations is a complete description of the low-lying discrete-level structure of each nucleus with correct associated gamma-ray branchings. Our analyses showed that our preliminary discrete-level sets were incomplete or uncertain because of experimental and theoretical structure difficulties. All of the iridium discrete-level sets are missing up to half of the levels that our statistical analyses indicate should be present, especially above 0.5 to 1 MeV, and some of the gamma-ray-decay branches from the levels included are open to question. In the case of odd-mass nuclei, we can truncate the incomplete sets at about 1 MeV and normalize our level-density formulae to these truncated sets. For odd-odd nuclei, we estimate that about 50% of the levels are missing below about 0.5 MeV, and truncation is not useful.

The level structure of odd-odd iridium nuclei is very complex, and simple models cannot accurately predict all of the levels present. Odd-odd nuclei with somewhat fewer protons than ^{77}Ir, such as ^{75}Re and ^{73}Ta, are symmetric rotors, whereas heavier nuclei, e.g., odd-odd ^{79}Au, are *not* symmetric rotors. Models that describe well the ^{75}Re or ^{79}Au nuclei fail when used to predict the level structure of ^{77}Ir. The Interacting Boson Fermion Fermion (IBFF) model

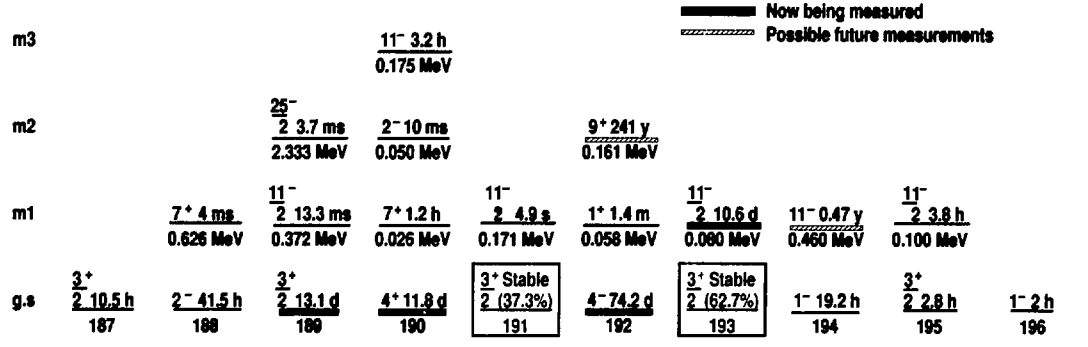

Figure 1. Iridium isotopes and their ground and isomeric states that were used as either targets or products in our calculations.

may provide improved level sets.[7] At present, IBFF yields about 50% more levels for ^{192}Ir.

Results for ^{193}Ir

Several neutron reactions that produce the 10.6-day isomer of ^{193}Ir are shown in Fig. 2(a). Among these, only inelastic scattering from the ground state is a first-order reaction. Unfortunately, because of the high-energy tail of the (n,n′) reaction, the isomer is produced even at 14 MeV, since its cross section decreases only by a factor of about 5 from 3 to 20 MeV. This may present problems if the iridium detector is chosen to sample fission-spectrum neutrons and the actual neutron-fluence energy distribution is different.

All of the ^{193m}Ir neutron destruction reactions shown in Fig. 2(b) are total reactions. The destruction of this isomer via neutron capture is much more important than via inelastic scattering below a few hundred keV. The production and destruction cross sections of this isomer by the (n,n′) reaction are about equal for neutrons of 4 to 8 MeV. At higher neutron energies, the (n,2n) reaction becomes the principal destructive mode. Thus, even for an ideal choice of detector placement and neutron fluence, the destruction of ^{193m}Ir is a serious problem and underscores the need to have the best possible sets of discrete levels and gamma-ray branchings if our calculations are to be reliable.

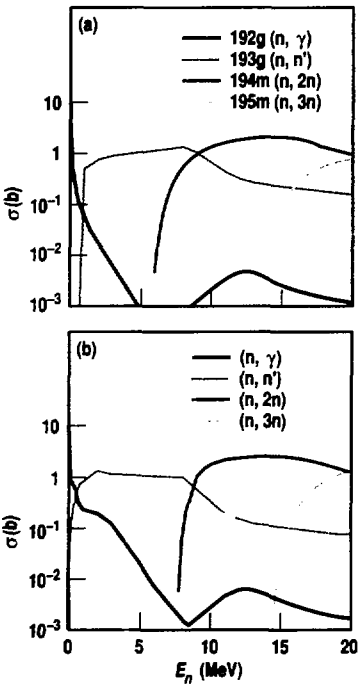

Figure 2. Calculated cross sections, σ, vs incident neutron energy, E_n, for some reactions involving the 10.6-day isomer of ^{193}Ir: (a) production and (b) destruction reactions.

Because of the modeling problems mentioned above, our original description of ^{193}Ir, with 68 discrete levels up to an excitation energy of 1.76 MeV, was severely deficient in levels at energies above 1 MeV. We determined that truncating to 37 levels at 1.015 MeV does not greatly affect the calculated isomer production by inelastic scattering and allows a good prediction of the level spacing, D_{ob}, at the neutron separation energy. This can be seen in Fig. 3, where our calculations with the original and two truncated level sets are compared with the measurements of Bayhurst et al.[8] Further, we can present physics arguments indicating that the measured value at 7.6 MeV must be incorrect. Neither we nor others[5,8] have successfully reproduced the 7.6-MeV value.

Our neutron capture calculations for ^{193g}Ir are compared in Fig. 4 with three experimental results.[9–11] The large spread in the experimental data makes it difficult to evaluate the reliability of our calculations. This measurement should be repeated.

We next illustrate with the ^{193g}Ir(n,2n) reaction the problems involved with the discrete levels and their gamma-ray branches in odd-odd iridium nuclei. Figure 1 shows two isomeric states (m1 and m2) above the 74-day ground state of ^{192}Ir. Only the cross section to the sum of the ground state and m1 has been measured.[8,12] Figure 5 presents our calculations of this partial cross section for three cases using the number of discrete ^{193}Ir levels indicated. Also shown is a total (n,2n) calculation for ^{193g}Ir. In all of the above, ^{192}Ir was described with 37 levels up to 532 keV. Changing the target-level sets produces only a small effect on the (n,2n) cross sections due to the spins available for the (n,n′) competition, but all calculations are low by factors as great as two. Clearly, our calculations are populating the unmeasured m2 isomer far too much. The gamma-ray branchings in our ^{192}Ir level set transfer all of the populations of levels with spins greater than or equal to 5 to m2, the 9$^+$ isomer. We believe that the introduction of the 30 or so missing levels in ^{192}Ir, together with corrected gamma-ray branches for the entire set, will modify our calculations significantly so that they may agree better with experiment. Although we can estimate the number of levels missing from our present ^{192}Ir set and their spins and parities, we cannot deduce the energy of any particular level.

Results for Some of the Other Iridium Isotopes

We shall now discuss our observations on the measured species of ^{189,190,192}Ir and comment briefly on the long-lived isomers of ^{192}Ir and ^{194}Ir. Note that all but ^{189}Ir are odd-odd nuclei and therefore have the most severe nuclear structure problems.

- **^{192g}Ir.** Neutron capture on ^{192g}Ir produces roughly equal amounts of the 3/2$^+$ ground state and the measured 11/2$^-$ isomer of ^{193}Ir, whereas inelastic scattering produces about equal amounts of the 1$^+$ and 9$^+$ isomeric states of ^{192}Ir at energies several hundred keV above their thresholds. Again, accurately calculated isomeric populations are needed.
- **^{190m3}Ir.** The major problem here is the third isomeric state, m3, in ^{190}Ir. This 3.2-hour state decays by electron capture to ^{190}Os about 95% of the time. Our ^{191g}Ir(n,2n) calculations overpredict its population by as much as a factor of 2 compared with experimental data.[12–15] Fortunately, the measured cross section for producing this isomer is less than 10% of the total (n,2n) cross section and thus may

not have too serious an impact on test program diagnostics.

• **^{189m2}Ir.** Again, the high-spin, 25/2$^-$, m2 isomeric state of ^{189}Ir at 2.3 MeV is a problem. If the iridium detector were used in a high-energy, high-intensity neutron fluence region, the amount of ^{189}Ir remaining for diagnostic interpretation might differ significantly from that predicted by our present cross-section library.

• **^{192m2}Ir, ^{194m}Ir.** The long-lived ^{192m2}Ir is populated by reactions on ^{191m}Ir, ^{192g}Ir, ^{193g}Ir, ^{193m}Ir, and ^{194m}Ir. It is destroyed primarily by the (n,2n) reaction at high energies and by the (n,γ) reaction at low energies. Although it is difficult to measure, it may possess diagnostic possibilities since it is not greatly affected by inelastic scattering. Also, measurement of the long-lived ^{194m}Ir could help in the interpretation of low-energy neutron fluences.

Conclusions

Further progress in the calculation of iridium cross sections, especially those to isomeric states, awaits new nuclear-structure theoretical calculations and experimental measurements, some of which are now under way.[7,16] Other useful experiments would be the remeasurement of the ^{193g}Ir(n,n′)^{193m}Ir cross section at energies below 8 MeV; the remeasurement of the ^{193}Ir(n,γ) cross section to resolve the large discrepancies; liquid scintillator measurements of the total ^{191,193}Ir(n,2n) cross sections; and, perhaps, ^{192}Os(t,xn) cross-section measurements.

References:

1. C. L. Dunford, *A Unified Model for Analysis of Compound Nucleus Reactions*, Atomics International, Canoga Park, Calif., AI-AEC-12931 (1970).
2. M. Uhl, *Acta Phys. Austriaca* **31**, 245 (1970).
3. O. Bersillon, *SCAT2: Une Programme de Modele Optique Spherique*, Centre d'Etudes de Bruyeres-le-Chatel, Bruyeres-le-Chatel, France, CEA-N-2227 (1981).
4. O. Bersillon, Bruyeres-le-Chatel, unpublished work (1978).
5. E. D. Arthur, *Calculation of Neutron-Induced Cross Sections on Isotopes of Iridium*, Los Alamos National Laboratory, Los Alamos, N. Mex., LA-7843-PR (1979), p. 4.
6. D. G. Gardner, M. A. Gardner, and R. W. Hoff, "Dipole Strength Functions in the Actinide Mass Region," *Proc. Sixth Conf. on Capture Gamma-Ray Spectroscopy, Leuven, Belgium, 1987*, Institute of Physics Conference Series, No. 88, p. S658 (1988).
7. R. A. Meyer, private communication, Lawrence Livermore National Laboratory, Livermore, Calif. (1988).

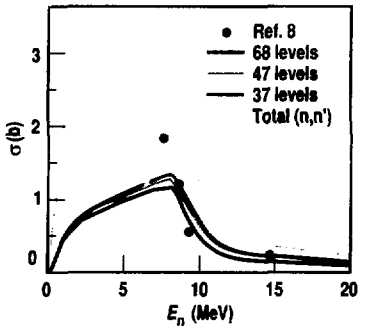

Figure 3. Calculated production of the 10.6-day half-life ^{193m}Ir by inelastic scattering, using three sets of discrete levels in ^{193}Ir, compared with a set of measurements.

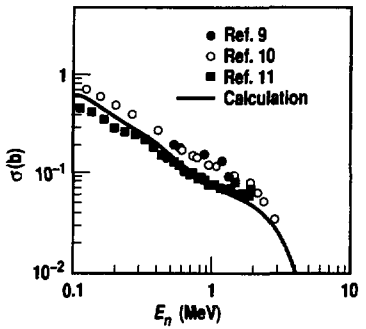

Figure 4. Our calculated (n,γ) excitation function for neutrons incident on ^{193g}Ir, compared with three sets of experimental measurements.[9–11]

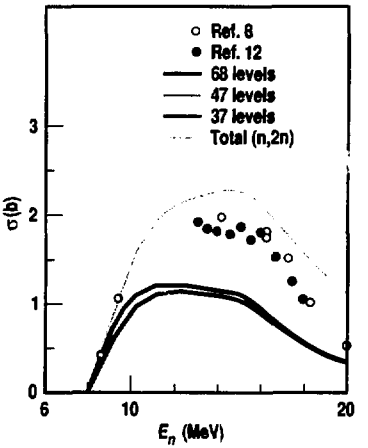

Figure 5. Three calculated (n,2n) excitation functions for neutrons on ^{193g}Ir, together with two sets of experimental measurements.[8,12] See text for details.

8. B. P. Bayhurst, J. S. Gilmore, R. J. Prestwood, J. B. Wilhemy, N. Jarmie, B. H. Erkkila, and R. A. Hardekopf, *Phys. Rev. C* **12**, 451 (1975).
9. M. Herman, A. Marcinkowski, and G. Reffo, *Acta Phys. Polonica* **B16**, 87 (1985).
10. M. Lindner, R. J. Nagle, and J. H. Landrum, *Nucl. Sci. Eng.* **59**, 381 (1976).
11. R. L. Macklin, D. M. Drake, and J. J. Malanify, *Fast Neutron Capture Cross Sections of ^{169}Tm, ^{191}Ir, ^{193}Ir, and ^{175}Lu for 3 ≤ E_n ≤ 2000 keV*, Los Alamos National Laboratory, Los Alamos, N. Mex., LA-7479-MS (1978).
12. M. Herman, A. Marcinkowski, and K. Stankiewicz, *Nucl. Phys. A* **430**, 69 (1984).
13. S. M. Qaim, *Nucl. Phys. A* **185**, 614 (1972).
14. J. K. Temperley and D. E. Barnes, *Neutron Activation Cross Sections for [illegible]ne Isotopes of Ruthenium, Palladium, Indium, Tin, and Iridium*, Ballistic Research Laboratories, Aberdeen Proving Ground, Md., BRL-R-1491 (1970).
15. M. Bormann, H. H. Bissem, E. Magiera, and R. Warnemunde, *Nucl. Phys. A* **157**, 481 (1970).
16. R. Hoff and R. A. Meyer, private communication, Lawrence Livermore National Laboratory, Livermore, Calif. (1988).

New Bomb-Fraction Tracer: ^{243}Am

R. J. Douglass, A. A. Detweiler, R. W. Whitworth, E. J. Moody, and P. E. Berry

In a series of experiments on underground nuclear tests at the NTS begun in 1983, Los Alamos National Laboratory has shown that ^{243}Am can be used both as a tracer and as a valuable neutron detector. Unfortunately, Los Alamos's supply of ^{243}Am has been used up, and there does not presently exist a readily available source of this material of sufficient quantity and purity for future experiments. A large amount of ^{243}Am does exist both in irradiated ^{242}Pu fuel assemblies and in solutions produced from previous chemical processing of fuel assemblies at the Savannah River Plant (SRP). In the last several years, LLNL and Los Alamos have been pursuing ways to make this material available to the weapons program.

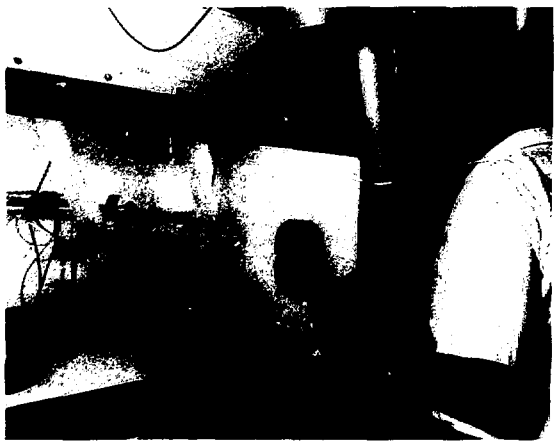

Figure 1. Radiation-shielded manipulator box used for assembling tracer packages of ^{243}Am.

In 1985, a study group consisting of representatives from LLNL, Los Alamos, the Office of Military Application (OMA), the Office of Nuclear Material Production, the Savannah River Laboratory, and the Oak Ridge National Laboratory (ORNL) met to investigate supply options. While technical issues regarding justification and processing of the SRP material were supported, no funding was received, principally because of the large costs that would be incurred in the refurbishing of the Multipurpose Processing Facility (MPPF) at the SRP. The funding situation has not changed significantly in the last two years, despite repeated pleas by the two laboratories for a supply of ^{243}Am.

In January of this year, representatives from LLNL, Los Alamos, and ORNL again briefed OMA staff members at DOE headquarters on the need for ^{243}Am for the weapons program and presented a strategy developed by scientists at the Transuranium Processing Plant at ORNL to use their facilities to recover ^{243}Am from the SRP-irradiated fuel assemblies.

This process would produce adequate yearly supplies of ^{243}Am without incurring the large, up-front costs of refurbishing the MPPF. We hope this more cost-effective approach will receive funding.

Experiment

During the past year, we have developed procedures for using ^{243}Am as a bomb-fraction tracer on underground nuclear tests. We also have prepared tracer packages for two future tests by using a small supply of ^{243}Am oxide in our possession that has chemical and isotopic compositions comparable to those expected from ^{243}Am obtained by processing SRP-irradiated fuel assemblies. The ability to simultaneously field both ^{241}Am and ^{243}Am on these tests will make it possible for us to get new information on the relative volatility of actinide tracers.

A new radiation-shielded manipulator box (see Fig. 1) for assembling tracer packages of ^{243}Am has been developed in the Heavy Element Facility at LLNL, and it will be used solely for this nuclide. This will eliminate the possibility of cross contamination from other tracers. The oxide powder is doubly encapsulated in sealed brass cans, and the packages are leak-tested with liquid nitrogen and alcohol baths.

We analyzed a small fraction of our supply of ^{243}Am oxide to determine the isotopic content of actinium, thorium, uranium, neptunium, plutonium, curium, and americium. The oxide was dissolved, and chemical separations were done to provide samples for alpha pulse-height and gamma-ray spectroscopy. An accurate analysis of all radioactive impurities, especially ^{244}Cm and ^{241}Am, is important because the preshot ^{243}Am content of tracer packages is determined by calorimetry. Because of the small amount of heat generated by the decay of ^{243}Am (<8 mW/g), we could not use the existing calorimeters in the Heavy Element Facility. Instead, a calorimeter with higher sensitivity in the Gaseous Chemistry Facility at LLNL was used. The heat output of each tracer package was measured to within 0.1 mW, and, using the isotopic data, we were able to determine the amount of ^{243}Am in each package to within 2%.

Postshot analysis of ^{243}Am and ^{241}Am from underground tests will be done with a combination of alpha pulse-height and mass spectrometry. Since ^{243}Am is used as a chemical-yield spike in our standard postshot americium chemistry, we must process both spiked and unspiked samples to correct for the ^{243}Am present in the pot solutions. ^{243}Am in unspiked samples will be determined by measuring the ^{243}Am:^{241}Am ratio with mass spectrometry.

Conclusion

The isotope ^{243}Am is expected to be a valuable resource for test diagnostics, both as a detector and as a tracer. In the past year, we have developed and demonstrated the ability to make ^{243}Am tracer packages at the Heavy Element Facility by using a radiation-shielded manipulator box. Two tracer packages have been assembled that will be used in future nuclear tests. We have also developed both preshot and postshot analytical methods for assaying ^{243}Am.

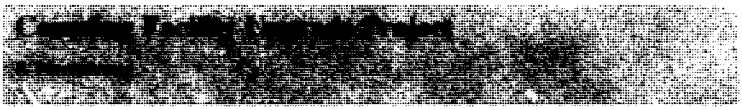

In FY88, we upgraded the Nuclear Chemistry Counting Facility (NCCF) to improve counting, data storage and retrieval, and data analysis capabilities. NCCF includes more than 100 counting stations with various configurations that perform alpha-, beta-, gamma-, and x-ray counting and spectroscopy as well as magnetic mass spectrometry, to analyze isotopic species. During the upgrade project, we replaced obsolete nuclear instrumentation and procedures with an integrated data acquisition and analysis facility, and provided standard mechanisms to control and transfer data to a central data base. To meet our needs at LLNL, we developed the NCCF network (NCCF–NET)—a set of independent computer systems, called workstations, that are networked to a central host computer (Fig. 1). The workstations, which we use to acquire data, control 22 sample changers, 14 pulse-height analyzer (PHA) systems, 2 scaler/timer systems, and 59 detectors. The host computer archives and reduces data. To implement the network, we use a Digital Equipment Corporation (DEC) VAX 11/750 computer and a DEC networking software package, called DECNET.

Counting-System Workstations

At NCCF, each workstation controls the instrumentation for one to eight nuclear counting systems. Workstations are based around an LSI-11/73 microcomputer running the DEC RSX-11M multi-user, multitask operating system. At a workstation, scientists can schedule counts, maintain schedules, control nuclear instrumentation and sample changers, acquire and store data, and transmit data to the host computer.

Workstations attached to NCCF–NET are distributed throughout the building, near the counting stations they control.

Workstations must perform several tasks on all instrumentation to which they are attached. Their major task is to control the nuclear instrumentation, such as scaler/timers, PHAs, and sample changers. Workstations are also programmed to set up, initiate, and terminate counts using the schedule specified by the scientist. In addition, data acquired by the instrumentation must be read by the workstation and stored on its disk unit.

Spectral data from the workstations can be automatically transferred to the VAX using DECNET and stored in a data base by the INGRES data-base management system (DBMS). In addition, data can be stored in the workstation for up to 72 hours, so workstations can operate unattended when the host computer is unavailable. This loose coupling between the host and the workstation also increases the reliability of the network. No single unit—host or workstation—can drastically affect the remainder of the network if the system crashes.

We divided the facility instruments into two types: instruments with an associated sample changer and those without. Thus, we could develop software to control instrumentation and sample changers somewhat independently. We built PHA workstations for alpha and germanium gamma-ray counting systems, and scaler/timer workstations for alpha and beta counting systems. PHA systems provide multichannel analysis, while scaler/timer systems perform integral counting on 1 to n channels. PHA workstations also operate as stand-alone systems. Sample-changer interfaces

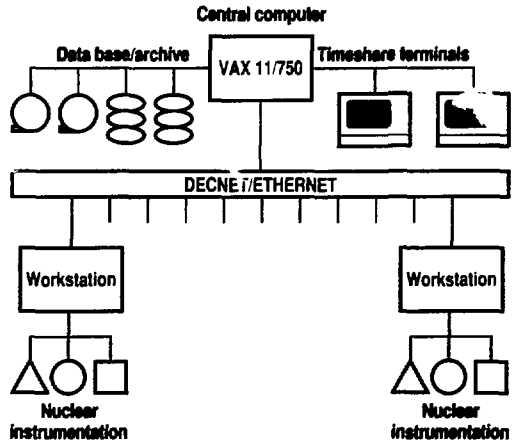

Figure 1. The Nuclear Chemistry Counting Facility network. Data collected on counting-system workstations are transferred to the central VAX processor for archiving and analysis.

Figure 2. A pulse-height analyzer (PHA) data-acquisition workstation. The tall rack contains an LSI-11/73 processor, interfaces to the ND66 PHA, local CAMAC subsystem, and ETHERNET. It also contains a 30-MByte storage device, a nuclear instrumentation module system, and a local CAMAC crate with a communications link to the sample-changer crate system (SCCS). The ND66 PHA provides spectral display, and the VT100 terminal provides a user interface to the menu system. The SCCS controls two 26-position sample changers.

were designed so five types of changers can be controlled from each workstation.

Our standard PHA is the Nuclear Data ND66 (Fig. 2), which can be controlled from its keyboard and from the host computer. Any command that can be invoked from the keyboard can be invoked by the host computer. The ND66 communicates to the workstation via a standard serial line using a link-level digital data communication message protocol to assure reliability. The workstation is connected to the PHA serial line by a programmable serial line card (ISL-11) with direct memory access capabilities. Therefore, the ISL-11 can transfer commands from the memory of the workstation to the PHA and can transfer data from the PHA to the memory of the workstation without a processor.

A library of functional software provides a control path for application codes from the workstation to the ND66. By accessing this library, an application code can perform any desired function on the PHA via standard subroutine calls. The library includes such functions as send a command, dump a spectrum, and load a spectrum.

For gross counting and single-channel analysis, we attached a scaler/timer system (Fig. 3) to the workstation via a computer-automated measurement and control (CAMAC) subsystem—a reliable input/output (I/O) system for data acquisition and control. Packaged as two CAMAC modules, the scaler/timer system is configured from an LLNL-designed master timer module (MTM) and a general purpose scaler module with six scalers. The MTM can accumulate live time, real time, and dead time for long count periods. It has three input channels, three output channels, a gate signal, a reset signal, and an enable signal. The scalers support a maximum count rate of 10 MHz, which allows us to make fast, accurate dead-time correction. Scalers are cascaded in pairs to provide a 48-bit register, which gives a maximum of 2.8×10^{14} counts/pair and, thus, allows count times to exceed several months at the maximum rate.

The display for the CAMAC scaler/timer system is provided by a nuclear instrumentation module (NIM) system scaler/timer, which is local to the counting station and runs parallel to the CAMAC system. The scaler/timer system is controlled from the workstation via the CAMAC subsystem. Software commands terminate counts when they reach a preset time or count in any data channel. A library of software for this system allows us to perform various functions, such as set, start, stop, and read the scaler/timer, using standard subroutine calls.

Eight types of sample changers support the counting stations in NCCF. Changers range from 4 to 200 positions, from a simple turntable to a carousel with 8 stacks of 10 samples. At any workstation, we can control all aspects of the sample changer, including positive-position feedback from the sample changer for monitoring the changer status, as well as counting-system status monitoring. This control capability requires an interface to the workstation and to the sample changer, and functional software to drive them.

The interface to the workstation is a serial line packaged in a commercially available CAMAC module. Each interface to a sample-changer is designed specifically for the changer it controls. The sample-changer interface is controlled via a CAMAC microcrate. This microcrate, known as the sample-changer crate system (SCCS), contains a stand-alone crate controller with an LSI-11/23 processor, an input module, and an output module to provide feedback to and from the sample-changer interface, and to the expansion modules. These expansion

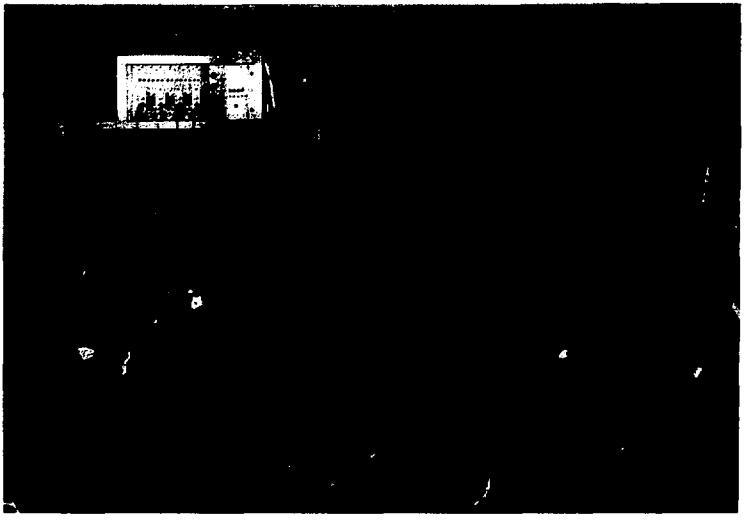

Figure 3. A scaler/timer data-acquisition workstation. The tall rack contains an LSI-11/73 processor, interfaces to the local CAMAC subsystem, and ETHERNET. It also contains a 30-MByte storage device, a VT100 for debug support, and a local CAMAC crate. The local CAMAC crate contains scaler/timer master timer module sets to record data and a communications link to the sample-changer crate system (SCCS). The VT100 on the table provides a user interface to the menu system. The SCCS controls four 4-position sample changers. Above the sample changers are the nuclear instrumentation module scaler/timers, which display count information.

modules house a two-channel serial line card (workstation channel and debug channel), random access memory, and programmable read-only memory firmware to control and interpret workstation commands for the specific changer. All sample-changer systems use the same crate design. Only the custom interface differs according to the specific changer being controlled.

The SCCS operates both in remote and local control, so scientists can control the sample changer from the workstation when necessary. A local control unit allows the user to manipulate the changer only when in local control. A library of software for the sample-changer system allows us to control all sample-changer functions from the workstation, such as move the changer to a specified position, search to a position with sufficient activity, and report current status.

Most instrument control functions performed by the workstation are supported by the CAMAC subsystem. In addition to the crate system, which is directly connected to the workstation, the subsystem also includes the microcrates connected to the sample changers. Most CAMAC module functions that we require are available commercially and are compatible with the CAMAC standard, which allowed us to develop the workstation control more quickly and will facilitate expanding the system. The CAMAC subsystem also is supported by a library of software that allows us to control all functions available from the modules attached to the subsystem. This software supports the crate attached directly to the workstation as well as the modules residing in the microcrates at the sample changers.

System Hardware

Figure 1 shows the major hardware components installed at NCCF. The VAX computer at the hub of the system is used to gather, store, and analyze scientific data. This computer counts and analyzes only those data that require a measure of control and security. It also serves as the host for the counting-system workstations networked to it. We use a second VAX computer to operate in an open environment—one that is used for unclassified projects only. Communication protocols allow us to forward acquired data automatically via the network to the VAX, where they are stored by the INGRES DBMS.

To provide data communications between the various systems associated with the upgrade project, we installed two independent IEEE 802.3 ETHERNET local area networks: one for the secure environment and one for the open environment (Fig. 1). Each workstation can transmit data to its host VAX directly through the ETHERNET link, which eliminates the need for a central data concentrator system.

Workstation Software

Control software for the NCCF workstations operates in the DEC RSX-11M operating system environment. The numbers and types of supported instruments and controllers vary from station to station, so each station must have a set of control software. Our layered software system extends from modules that control the individual hardware components to executive control systems, which manage each counting system. When hardware is added to a workstation, the software modules needed to operate the hardware are easily configured by assembling the independent task modules for the new system. The task modules are, in turn, built from libraries of special subroutines developed to control the individual hardware units.

When a detector is added to a workstation, an executive control system for that detector is automatically generated and activated. The executive control systems operate the different nuclear measurement systems, using local data bases to store parametric and counting data related to samples. Users may access the data bases to enter, alter, or examine information pertinent to counting the samples. The executive control systems also interact with the network to transfer counting data and other relevant information to the control host processor.

Several quality assurance features in the workstation software allow us to monitor equipment status and configurations easily. Many potential problems can be detected automatically and either corrected or flagged for operator action. If fatal errors or damaging conditions occur, the software immediately shuts down the faulty equipment and sends appropriate messages to the operators. The system also protects stored data, control information, and system status against power failures or interruptions. Should such problems occur, an automatic restart program allows workstations to pick up the final status of the samples being processed and resume the counting schedule.

The six major software components for our system are a forms management system, a configuration file handler, a file manager, a data manager, an executive control system, and the instrumentation tasks.

Forms Management System. The forms management system, produced by DEC, provides convenient, consistent menu-driven communication between each user and each executive control system in a given workstation. The menu system allows users to select a measurement system, specify configuration data, receive status reports, and enter and control samples.

Configuration File Handler. The configuration file handler establishes and maintains files on the configuration status and equipment specifications for each workstation. The handler verifies user requests for control-system availability. Internal workstation names maintained by this task communicate with the forms management system and the executive control system.

File Manager. The file manager transmits data files to the host computer using DECNET. It also maintains a file management system of resident data files and makes storage space available on the workstation when it is requested by other tasks.

Data Manager. The data manager converts spectral data from the PHA to a standard DEC form. It then merges spectral and header data from the PHA with schedule file information and other pertinent parameters to form a nuclear chemistry standard data file.

Executive Control System. Each equipment system on a workstation has an executive control system, which directs the flow of information controlling the system. The executive control system accesses the schedule files when prompted by the forms management system or an instrumentation task and initiates the appropriate process as required by status-state flags. The executive control system issues all commands to set up, start, and stop counting operations and to collect and transfer data. It also checks the schedule files to determine the next sample to be counted.

Instrumentation Tasks. All devices are driven by the executive control system, which calls for functional or primitive tasks to initiate action on a device. These functional tasks then process the command and pass control to the device communications handlers. Only two types of communications handler are required: PHA and CAMAC. The communication handlers issue appropriate buffers to the device and acknowledge commands through the functional software. The functional software then returns a command status report (positive or negative acknowledgments) to the executive control system. All task interactions are transmitted via task-to-task communication buffers. For example, an interrupt request is first processed by the device communications handlers; then it is sent to the executive control system. I/O drivers support all interaction between the ISL-11 and the PHA, and between the workstation CAMAC interface and the CAMAC subsystem. The CAMAC controller has a power-up look-at-me (LAM) for interrupt service requests. We also added software to the CAMAC I/O driver to recognize power ups and provide support for recognizing and clearing module LAMs.

Summary

In FY88, we completed the NCCF upgrade project, which improved the counting equipment and our information-gathering techniques. This upgrade includes a distributed control network and a central data base for storing and analyzing data. It also increased data integrity by providing standard, automated data-acquisition instrumentation, data structures, and data flow. This design enhanced the reliability of NCCF, improved our ability to maintain the system, and provided audit trails for quality assurance.

NCD's Computer Capabilities in the Age of Information

D. R. Massett and J. B. Carlson

The many different computer systems used by the Nuclear Chemistry Division (NCD) play a much larger role than just controlling experiments, accumulating experimental data, and performing calculations. In fact, they are vital in all aspects of the scientific process: computer networks (equipment that transfers information between computers) allow collaborators to exchange information without being physically located in one area. Computers are also used by authors to create and publish their papers, and they provide access to library resources and technical data bases that lie at the very heart of modern scientific research.

Our computer requirements are divided into three categories: scientific data analysis, office and administrative support, and personal workstations. The area of scientific computing is served by Digital Equipment Corporation (DEC) computers and is subdivided into three categories reflecting security constraints: SRD (Secret Restricted Data), PARD (Protect as Restricted Data), and unclassified. Office and administrative support are provided by NBI and Data General (DG) computers. Personal workstations (IBM PCs, Apple Macintoshes, etc.) allow individuals to tackle their problems with desktop-computer power.

Most of the Division's data-analysis computing is performed on DEC VAX computers. The first VAX 11/750 was acquired in 1982 for use in automating our counting facilities. An additional VAX 11/750 was acquired in 1984 to

provide for unclassified computing. We now have 12 VAX machines in use, including three VAX 11/750s and nine microVAX IIs.

Administrative and office computing are performed on NBI word processors and on the Data General Comprehensive Electronic Office (CEO) system. The NBI system was chosen in 1986 for technical word processing because of its ability to manipulate mathematical equations. A continuing problem for the Division is the inability to transfer data easily from the CEO office system, used by the scientific staff, to the NBI word-processing systems, used by our administrative staff. Both systems will soon be supported in UNIX environments, and we fully expect the networking capabilities of UNIX to provide the solution to this long-standing problem.

An appealing solution for some information processing applications (e.g., instrument control) is to put computing capability on a user's desk. Many of our staff members have done this with individual choices of different personal computers and workstations. This choice distributes the Division's computing capabilities directly to the area of need but requires additional effort to understand and maintain the many distinct hardware/software combinations.

We maintain three separate network environments, which operate at SRD, PARD, and unclassified security levels, as shown in Fig. 1.

- The SRD environment is our most protected and is used for running our GOSPEL data base code.[1]
- The PARD environment encompasses the Division's extensive alpha-, beta-, and gamma-ray counting facilities. These facilities have been described previously.[2,3]
- Our unclassified network is the largest and is also our most comprehensive. The majority of the scientific computing that supports our research programs is performed here. We also use this environment for testing and prototyping systems for our SRD and PARD environments. Because of the stringent requirements for protecting the information in the SRD and PARD environments, we have no plans to connect them with our unclassified network.

Computer Networking

In the recent past, to move data between two computers required the physical delivery of media (cards, tapes, disks, etc.) from source machine to destination. Modern computer networks now replace the physical movement of media with signals sent between machines. Such networks provide considerable freedom to users, since data are transferred by typed commands.

Originally, these networks were limited to communication between computers of the same manufacturer. But now, with the advent of Ethernet (an industry standard for high-speed signaling on coaxial cable), the rapid transfer of information is feasible between many different vendors' computers.

Staff members of the NCD require access to many different computers, both inside and outside the Laboratory, and require the exchange of information between these systems. However, if we are to avoid confusion, our users need a standard software interface. The UNIX operating system has been developed to meet the need for convenient networking and will run on many different computers. The use of a single operating system requires less effort by users working with different computers and provides easier exchange of information between systems.

We have made extensive use of networking in our unclassified environment. An Ethernet is installed throughout our buildings, allowing us to easily connect our unclassified computers. Users can transfer files, send electronic mail, and establish remote terminal connections among a large number of systems. We are currently working on extending these capabilities to all of our systems. We have also installed Ethernet-based terminal servers that allow users to selectively connect their terminals to any of our computers, eliminating the need for multiple terminals in an office.

We have begun installing UNIX systems within our network to allow users to become familiar with the UNIX environment. These systems also provide a platform to begin the changes needed to make our computer codes run on UNIX systems. One of these new systems, designated as the NCD mail/news gateway machine, provides Division members with a centralized point for electronic information exchange. A block diagram of our unclassified network is shown in Fig. 2.

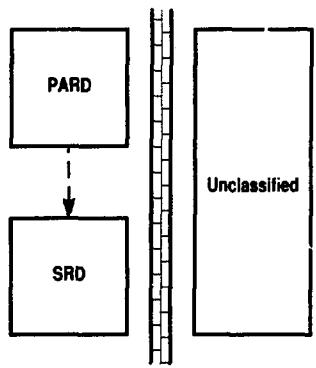

Figure 1. The Nuclear Chemistry Division has segmented its information systems into three distinct areas. We are working on information transfer between the PARD and SRD areas but must isolate both from the unclassified area.

Computer Unification

A single, unified system to handle all our information collection, analysis, and management needs would be ideal. Our data classification requirements may keep us from total unification, but we can develop and implement subsets of such a network.

Our approach is to incorporate our existing computers into an integrated system that provides for extensive exchange through network access. The challenge lies in the combination of dissimilar computers and operating systems: NBI word processors, DEC VAXs running VMS, Data General MVs running DG/UX and AOS/VS, IBM PCs running DOS and OS2, and microcomputers running UNIX. Our solution to integrating this mixture of hardware and software is to use standard network and user interfaces; other possibilities lead to combined systems understandable only to computer experts.

Future Directions

The Division is continuing its efforts to develop a unified information-management system. We expect that standardized operating systems and networks are the keys to such a system. We envision a system that not only will access our locally collected information but also will allow easy access to external data sources. Access to library systems concerning publications, electronic mail to allow collaborators to exchange ideas and scientific data, and administrative information relating to travel, purchase orders, and meeting scheduling are among the goals we are pursuing.

References:

1. A. D. Dougan, W. Buckley, J. B. Carlson, D. R. Manatt, N. L. Smith, and E. H. Willes, "GOSPEL: Our Third-Generation Radiochemical Diagnostics Code," p. 182 of this publication.
2. D. N. Hunt and J. B. Carlson, "The Counting Facilities Upgrade Project," *Nuclear Chemistry Division FY83 Annual Report*, Lawrence Livermore National Laboratory, Livermore, Calif., UCAR-10062-83-1 (1983), p. 14.
3. J. B. Carlson, "Nuclear Chemistry Division Information System Upgrade Project," *Nuclear Chemistry Division FY86 Annual Report*, Lawrence Livermore National Laboratory, Livermore, Calif., UCAR-10062-86 (1986), p. 2-80.

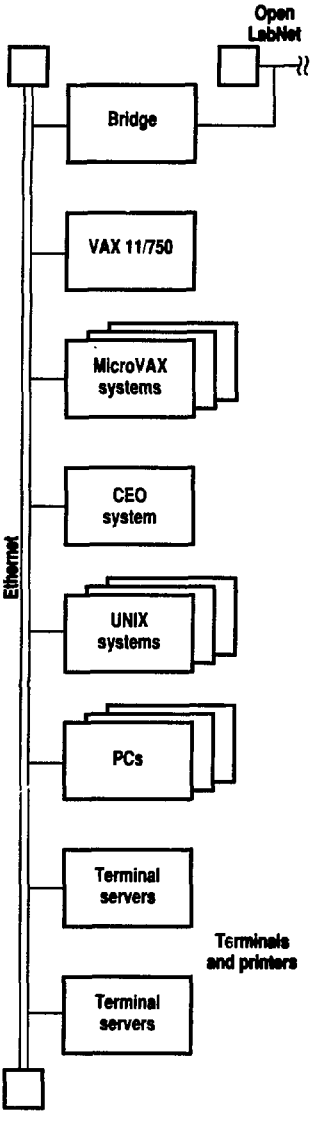

Figure 2. Every box represents one of the NCD's computers. Each one performs a different task, such as data reduction, word processing, or data and information retrieval from data bases; and each can communicate with the others via Ethernet.

GOSPEL: Our Third-Generation Radiochemical [illegible]

A. [illegible], R. Crawford, J. R. Carlson, D. B. Mignerey, N. L. Smith, and E. H. Wilhelmy

GOSPEL, our new, third-generation program for analyzing radiochemical results from nuclear test diagnostics, uses both core- and gas-sampling data. It is a menu-driven application that uses an INGRES data base and runs on a MicroVAX computer. The first working version of GOSPEL went into production May 1, 1988.

GOSPEL replaces two previous codes, PROPHET and OUIJA. We have designed GOSPEL to be more interactive, modular, and reliable than the previous codes; we hope it will take us into the next century of event-data analysis.

OUIJA, developed in 1963, was the first fully integrated analysis of all radiochemical diagnostic data in one code with summary output. It was originally written for an IBM 7090 and was modified and expanded with the advent of each new computer over the years. In 1970, it ran in batch mode on a CDC 6600 computer. In the fall of 1970, the PROPHET Group was formed to extensively rewrite OUIJA to make it more general and interactive. The PROPHET code, written for the CDC 7600 computer, used the interactive capabilities of the LLNL Octopus system, but it retained OUIJA-like hardcopy output. The PROPHET project required approximately 10 man-years of effort.

In 1982, a GOSPEL users' committee and a working group were formed to consider the possibility of developing a new code to replace PROPHET. They decided that a substantial revision of the PROPHET code was needed, and new capabilities of the code were outlined. However, the Nuclear Chemistry Division was involved in an upgrade of its counting facilities, and the GOSPEL project was put on hold.

In 1986, as a proof of principle for GOSPEL, we conducted a test project called Apocrypha,[1] in which we used a VAX computer and a commercial data-base product, INGRES.[2] The work was divided into four tasks: (1) designing data-base structures, (2) implementing the design with a full data set, (3) checking the design by running performance tests, and (4) demonstrating several calculations. The work was completed in October 1986, after six man-months of effort.

In the spring of 1987, work began in earnest on the GOSPEL project. We ordered a MicroVAX computer and prepared a secure room. We drafted specifications for the first running version of GOSPEL. By July 1987, all design features were "locked in," and we started to write the program. In November, we made our first "dry run" test with event data. When the first event data were stored and analyzed in May 1988, we stopped using PROPHET for all of our data storage. In summary, we built a working system with sufficient time to test and implement it before the CDC 7600 computers were scheduled for retirement in mid-July 1988.

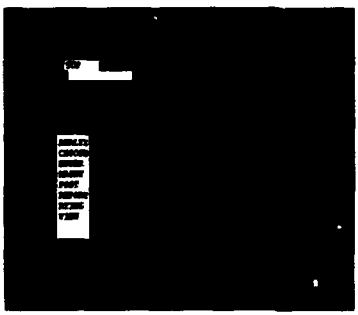

Figure 1. Top-level menu for the GOSPEL program's data-base administrator. Of the eight basic functions listed, the user may select one and run a program or select from another menu.

The GOSPEL Project

The first working version of GOSPEL includes:

- A menu-driven application using an INGRES data base.
- Data-base tables in use for the current data set.
- Methods for inputting preshot and postshot data.
- A file-transfer method for moving data into a spreadsheet.
- Some "canned" algorithms.
- Historical data transferred to the VAX.

GOSPEL is written in VAX-Fortran, with extensive use of Relational Technology's EQUEL (Embedded

QUEL preprocessor commands for data-base access and forms support.

The User Interface. GOSPEL was designed to be modular in form for ease of maintenance and programming. Because we intended to use a large number of options, we chose to display them in a menu. Some menu items would be hierarchical, with further choices or functions from which to choose. To further complicate matters, not all options were to be available to all users. We designed a menu driver with data-base tables to store the relationships between menus and functions.[3]

The present system has 65 menu items, which consist of methods for entering and editing data; 50 forms; 38 data-base tables; 22 views of data; 29 reports; and two analysis options. On-line help is available for each module. A facsimile of the top-level menu is shown in Fig. 1. At the bottom of the figure are listed a number of options. The option "Up" returns the user to the previous screen. "Go" calls the chosen function or displays more menu items. "Jump" allows the user to select any function or menu item in the program. On-line help is available with the "Help" option; "Quit" exits the program; and "Shell" escapes to the operating system.

For security purposes, we have structured several classes of users. One class of users is the data-base administrator, who has full privileges. At the other extreme is a scribe, who may only enter postshot data. In the middle are event nuclear chemists with specific responsibilities and privileges for an event and general users who may view and analyze data.

Preshot Data. Device parts may be entered as specific items. Each item has a location name and an elemental composition. We keep tables of standard atomic weights and natural abundances of all elements. Standard atom and weight percents of compounds that we use often are also stored. When a part contains a standard compound, its isotopic composition is calculated automatically and stored in the data base. All isotopic compositions are converted to atoms and stored for each item. Descriptive information, such as date and time of data entry and who entered the data, is also stored.

Postshot Data. Postshot data are entered from a variety of sources. Most data are transferred on floppy disk from another computer using data-base tables for temporary storage. Some data are typed in by hand. Because a given isotope may be measured in more than one manner, we had to devise a way to distinguish the various types of data. Therefore, each piece of data includes codes for the sample type and analysis method and has a category from "first wild guess" to final. Whenever a scribe makes an entry, it is labeled "uncertified" until the event nuclear chemist reviews and certifies the data. Once certified, weighted averages of replicated data are calculated and stored.

Quality Assurance. We do not allow any preshot or postshot data to be replaced or deleted. We simply flag duplicated data as superseded and append newer data. The certification process described above ensures that the event nuclear chemist is aware when data are added to or changed in the data base. We use INGRES's journaling feature to audit the data base in case we have a problem with data integrity. We frequently back up our program and data in case of unforeseen problems.

Calculations. We have begun rewriting many of the basic algorithms found in PROPHET, have added the Barr-Gancarz analysis,[4] and have updated them with form input and data-base access. Because many users desire to use spreadsheets to analyze their event data, we have created several reports that serve as inputs to a spreadsheet program on either a VAX or a personal computer.

Future Developments

We plan to enhance our calculational capability with graphics and improved error handling. We are in the process of reading the historical data into data-base tables consistent with the new data structure and will develop methods to search these data interactively. Documentation and user training will be necessary shortly. As more users become familiar with GOSPEL and as the data base is used more, we will improve performance where needed.

Summary

GOSPEL went into production May 1, 1988. In its first real use on the Schellbourne Event, the stored data compared favorably to PROPHET results.

The program is modular and menu driven. Compared to its predecessors, it has quicker data-base access and is easier to operate, more extensive, simpler to maintain, and more fail-safe. With the improvements planned, GOSPEL will certainly serve us well for a long time to come.

References:

1. A. D. Dougan, W. M. Buckley, and J. W Meadows, "Apocrypha: Proof of Principle for A New Radiochemical Diagnostics Code," *Nuclear Chemistry Division FY87 Annual Report*, Lawrence Livermore National Laboratory, Livermore, Calif., UCAR-10062-87 (1987), pp. 2–3.
2. INGRES, a product of Relational Technology, Alameda, Calif.
3. D. Coles, "Multiple Level Menus Using EQUEL," *Proc. Spring 1986 Ingres Users Association Meeting*, Relational Technology, Alameda, Calif. (1986).
4. J. F. Wild and H. G. Hicks, "Adaptation of the Barr-Gancarz Fractionation Analysis to Radiochemical Diagnostics of Underground Nuclear Tests," *Nuclear Chemistry Division FY82 Annual Report*, Lawrence Livermore National Laboratory, Livermore, Calif., UCAR-10062-82-1 (1982), p. 48.

Development of IBM PC Codes for Use in our Nuclear Cross-Section Calculational Effort

G. L. Larson, M. A. Gardner, and D. A. Gardner

We are developing three menu-driven, IBM PC codes for use in calculating nuclear cross sections. INDIGO is an interactive graphics routine that makes two-dimensional plots; PC GERALDINE is a graphical processing code that compiles and prepares calculated cross sections; and LCHECK is a code that creates, analyzes, and checks nuclear levels and gamma-ray branching data.

The accuracy of the cross sections that we calculate with our modern nuclear-reaction codes depends on the quality and accuracy of a variety of input parameters. At each step in our calculational procedures, whether it be the development of new parameter systematics, the refinement of parameters for a particular mass region, or the comparison of calculated results with experiment, we need to make graphical analyses. In addition, we think that using preprocessing codes to check and assemble the input and using postprocessing codes to extract, manipulate, and summarize the final results will expedite the work and enhance its accuracy. Therefore, we are developing three menu-driven, PC-based codes: INDIGO, PC GERALDINE, and LCHECK.

Description of the Codes

All three codes are being developed for use on an IBM PC, XT, AT, or compatible clone that has 512 Kbytes of free memory, a colorgraphics or enhanced-graphics adapter board, a color monitor, and a math coprocessor. All are written using MicroSoft C,[1] and both INDIGO and PC GERALDINE are based on the GraphiC graphics library.[2]

Each program provides push-button menu selection and simple, fill-in forms for control and input. The philosophy of "make it user friendly" creates some programming problems and requires more coding than would be necessary if we were concerned only with ease of programming. In fact, most of the problems encountered have been design problems related to interfacing with the user and deciding what type and how many constraints to put on the user or on the program.

INDIGO. INDIGO (INteractive Data Interpretation with Graphical Output) is

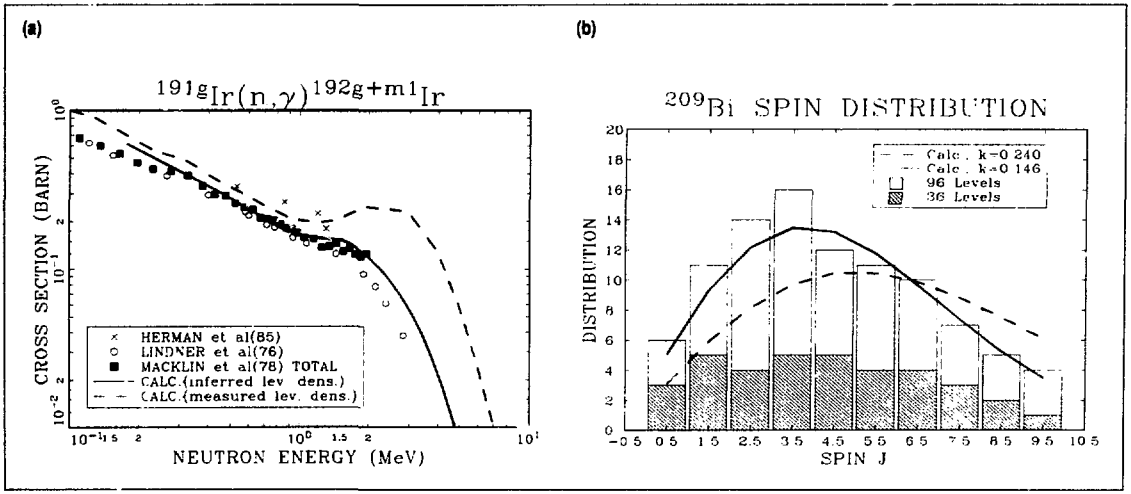

Figure 1. Examples of recent plots made using INDIGO. (a) Our results for the (n, γ) cross section on ^{191}Ir as a function of incident neutron energy, calculated using different level-density parameter sets, compared with several experimental measurements. (b) The distribution of spins in two discrete-level sets for ^{209}Bi, together with calculated spin distributions using different parameters.

an interactive graphics routine that makes two-dimensional plots and is designed to serve a wide variety of scientific graphics needs. It allows the rapid analysis of multiple sets of experimental or calculational data from a variety of sources with almost format-free input. Multiple curves may be plotted, with each curve a different style, thickness, and color. INDIGO allows different curve types such as bar charts, histograms, and text plots for viewgraphs. It supports both log and linear axes and has several fitting routines.

Input to INDIGO can be through the terminal or from disk files; output can be viewed on the monitor or sent to a hard-copy device. We have drivers available for a number of printers and plotters. A limited amount of data manipulation may be done with arithmetic, geometric, and trigonometric functions. We can use different fonts, super- and subscripts, and Greek and math symbols in any text string.

In essence, INDIGO gives the user the power to generate any plot from the very simple to the very complex. Figures 1(a) and (b) are examples of plots made recently with INDIGO.

PC GERALDINE. PC GERALDINE is an emulation of the GERALDINE code[3] now running on the CDC 7600 computers that will soon be phased out. It is a graphical processing code that permits us to compile and prepare calculated nuclear cross-section excitation functions for energy-group averaging and for further use in other codes that make activation calculations for radiochemical device diagnostics.

The original GERALDINE code enables the user to graphically display the calculated cross sections as a function of incident energy, to modify and manipulate these excitation functions where necessary, and then, by means of analytical fitting and interpolating, to construct an output file with a finer energy grid suitable for group averaging. We are rewriting this code using a subset of INDIGO options with more case-specific input and output constraints. We are replacing the polynomial fitting routine used in the CDC 7600 version with a piecewise cubic Hermite interpolation package.[4] We plan to expand the capabilities of PC GERALDINE in order to make the postprocessing of our calculated results more automated.

LCHECK. To obtain accurate results in our calculations, it is necessary to describe nuclei in the first few MeV above their ground states with large, complete, discrete-level sets (and associated gamma-ray branching fractions). Some of this information comes directly from structure-code calculations such as those provided by R. Hoff et al.,[5] where the modeled discrete-level information can be checked, to a large extent, internally by the codes themselves. However, many level sets are assembled "by hand" from a variety of experimental and theoretical sources. Since these data may consist of 100 or so discrete levels, with many levels having five to 10 separate gamma-ray-decay branches, they are particularly prone to typographical and other errors.

To check these data, we are developing the LCHECK code, which has three operating modes:

- Batch mode: analysis of discrete-level and gamma-ray branching input for various errors.
- Interactive mode: creation and preprocessing of this input into the format required by our nuclear-reaction codes.
- Gamma-ray-batch mode: creation or supplementation of the gamma-ray branching information based on our calculational systematics.

In the batch mode, LCHECK analyzes existing sets of discrete levels and their gamma-ray branchings in the STAPRE[6] format for a number of typographical and physics errors. If no errors are found, a table is written containing the initial and final levels, branching fractions, and the possible multipole types for each radiation branch. The branching fraction divided by $E_\gamma^{(2\ell+1)}$ is printed, because this provides information that can be related to relative gamma-ray strength functions and, in some cases, to the Clebsch-Gordon coefficients if several transitions to members of the same rotational band occur. This quantity may be suppressed if only one transition occurs from a given level. If the transition has a multipolarity of $\ell > 3$, it is labeled "other," because STAPRE utilizes only transitions with $\ell \leq 3$. Higher ℓ transitions would be long-lived enough for the parent level to be considered an isomer in most of our applications. Isomers (no branches) are printed as such in the table. The table may be truncated so as to list fewer than the complete set of levels.

Figure 2 shows an example of a partial table that was produced by LCHECK following the analysis of discrete-level information for ^{193}Ir. Here, the spin of level 4 was deliberately mistyped as 8.5 instead of 2.5, and the gamma-ray decay branching of level 4 was incorrectly assigned to level 3 instead of level 1 for illustration purposes.

In the interactive mode, LCHECK allows the user to create sets of discrete levels and associated gamma-ray branching ratios in the STAPRE format while typing in the original information in the format usually used by nuclear-structure personnel. All input information is tested for the errors listed under batch mode, and the opportunity for error correction is provided at the time any errors are detected. When the level set is completed, the constructed STAPRE input file is written into a disk file and then analyzed through the batch mode to produce the output table. One or more level sets may be constructed sequentially in this way, each with a header line containing up to 65 characters of descriptive information.

In the third mode, gamma-ray-batch, the discrete-level set minus the branching information is read and the branching ratios are constructed by LCHECK under one of two possible assumptions: either the levels have no collective character, or the levels are all rotational band heads with the remaining band members deleted. In both cases, the energy dependence

of the gamma-ray transition is assumed to be proportional to $E_\gamma^{(2\ell+1)}$, with the initial constant either supplied by the user or calculated from the Weisskopf assumptions. Only E1, M1, and E2 transitions are permitted; up to 30 branches are calculated per parent level, of which up to 20 can be E1 and M1 transition types and up to 10 can be E2 transitions. From these, the 10 most intense transitions are chosen, normalized to unity, and written into the input file in STAPRE format. If the levels are just collective band heads, the user has the option of using the K-quantum number selection rules. Then the K-quantum numbers must be supplied when K does not equal J for that level. Also, up to six states may be designated as isomers. As in the interactive mode, the newly constructed STAPRE input file is then run through the batch mode, and the output table is written.

Figure 2. A portion of the table produced by LCHECK following the analysis of discrete-level information for ^{193}Ir that contained some intentional input errors. Notation is: N (level number), E (level energy in MeV), J (level spin), P (level parity), EG (transition energy in MeV of gamma ray), and BR F (gamma-ray decay branching fraction). The user has underlined the mistyped spin of 8.5 and has circled the questionable transitions.

GAMMA-RAY TRANSITIONS AMONG DISCRETE LEVELS

Initial Level				Final Level					
N	E	J	P	N	E	J	P	EG	BR F
8	0.362	2.5	1						
	Possible Multipoles			5	0.180	1.5	1	0.182	0.400
	BR F/EG**(2L+1):					M1		E2	M3
						6.64e+001		2.00e+003	6.05e+004
	Possible Multipoles			4	0.139	8.5	1	0.223	0.010
									OTHER
	Possible Multipoles			2	0.073	0.5	1	0.289	0.190
	BR F/EG**(2L+1):					E2		M3	
						9.42e+001		1.13e+003	
	Possible Multipoles			1	0.000	1.5	1	0.362	0.400
	BR F/EG**(2L+1):					M1		E2	M3
						8.43e+000		6.43e+001	4.91e+002
7	0.358	3.5	1						
	Possible Multipoles			4	0.139	8.5	1	0.219	0.410
									OTHER
	Possible Multipoles			1	0.000	1.5	1	0.358	0.590
	BR F/EG**(2L+1):					E2		M3	
						1.00e+002		7.83e+002	
6	0.299	3.5	-1						
	Possible Multipoles			3	0.080	5.5	-1	0.219	1.000
						E2		M3	
5	0.180	1.5	1						
	Possible Multipoles			2	0.073	0.5	1	0.107	0.760
	BR F/EG**(2L+1):					M1		E2	
						6.20e+002		5.42e+004	
	Possible Multipoles			1	0.000	1.5	1	0.180	0.240
	BR F/EG**(2L+1):					M1		E2	M3
						4.12e+001		1.27e+003	3.92e+004
4	0.139	8.5	1						
	Possible Multipoles			3	0.080	5.5	-1	0.059	1.000
						E3			
3	0.080	5.5	-1			***** ISOMER *****			
2	0.073	0.5	1						
	Possible Multipoles			1	0.000	1.5	1	0.073	1.000
						M1		E2	
1	0.000	1.5	1						

References:

1. MicroSoft C, Microsoft Corporation, Redlands, Wash. (1988).
2. GraphiC, Scientific Endeavors Corporation, Kingston, Tenn. (1988).
3. A. A. Delucchi, GERALD'NE, an undocumented computer code written to run on the CDC 7600 computers, Nuclear Chemistry Division, Lawrence Livermore National Laboratory, Livermore, Calif.
4. F. N. Fritsch and R. E. Carlson, *Piecewise Cubic Hermite Interpolation Package*, Lawrence Livermore National Laboratory, Livermore, Calif., UCRL-87285 (1982).
5. R. W. Hoff, R. F. Casten, M. Bergoffen, and D. D. Warner, *Nucl. Phys. A* **437**, 285 (1985).
6. M. Uhl, *Acta Phys. Austriaca* **31**, 245 (1970).

A Preliminary Evaluation of the 3×10^6-Year Isomeric State of ^{210}Bi in Astrophysical s-Process Nucleosynthesis

D. G. Gardner and M. A. Gardner

The last stable nucleus to be produced in the slow (s-process) of nucleosynthesis is ^{209}Bi; when it captures a neutron, both the ground state of ^{210}Bi ($t_{1/2}$ = 5 days) and its long-lived isomer ($t_{1/2} = 3 \times 10^6$ years) are formed. Figure 1 shows two possible paths that may occur at the termination of the s-process. The path usually assumed is that drawn with solid arrows. Here the isomer is coupled to the 5-day ground state; the ground state can beta-decay to ^{210}Po, which either decays via alpha-particle emission to stable ^{206}Pb or undergoes further neutron capture to ^{211}Po, which decays to stable ^{207}Pb. The second, competing, path is indicated by dashed arrows. The isomer is not coupled to the 5-day ground state

and hence will not be destroyed rapidly. It can capture a neutron, making ^{211}Bi, which alpha-decays to ^{207}Tl, and this then beta-decays to ^{207}Pb. Thus, different relative amounts of stable ^{206}Pb and ^{207}Pb will be produced.

Cosmological chronologies of nucleosynthesis that are based on the radioactive parents ^{235}U, ^{238}U, and ^{232}Th and on the relative abundances of their stable daughter isotopes of lead require corrections to be made for the slow and rapid (r-process) contributions to production of the lead isotopes. Presently, these radiogenic chronologies have assumed that the ^{210}Bi isomer does not survive in a stellar environment long enough for the second s-process cycle to be important.[1,2] However, on the basis of our preliminary calculations for the production and destruction of the isomeric state by neutrons and photons, we conclude that the ^{210}Bi isomer may not be destroyed rapidly in certain stellar environments and that the second path shown in Fig. 1 may compete in the s-process nucleosynthesis. If this is true, then the cosmoradiogenic chronologies based on isotopic lead compositions may have to be reexamined.

Calculational Background

In the process of developing a preliminary cross-section set for the ^{209}Bi radiochemical detector (a neutron-fluence monitor for our nuclear test program), we have studied some 165 neutron-induced, partial, and total reactions on 20 ground and isomeric target states from ^{203}Bi to ^{210}Bi (Refs. 3 and 4). Particular attention was given to the cross sections of those reactions involved in the production and destruction of $^{205-208}$Bi, the nuclei we measure for radiochemical diagnostics. Cross sections for the following types of reaction were calculated for incident neutrons in the energy range of 10^{-5} to 20 MeV: (n, γ), (n,n'), (n,2n), (n,3n), and (n,4n). Although of potential future value to nuclear test diagnostics, production and destruction cross sections for ^{210}Bi were not studied in detail since we do not now measure the 3×10^6-year isomeric state. While making these calculations, we were able to determine suitable parameters for this mass region for the following required types of input: neutron optical-model potential, nuclear-level densities, gamma-ray strength functions, and precompound neutron emission. We determined some of the parameters, such as those for the level densities, from the analyses of discrete-level information. We found that this information must be as complete as possible; it not only should consist of those levels obtained from experiment but also be supplemented, by model calculations, with theoretical-level structures known to be present. Furthermore, descriptions of nuclei at low excitation energies with complete sets of discrete levels, together with their associated gamma-ray-decay branching fractions, are mandatory for calculating accurate cross sections and isomer ratios.[5]

For the present astrophysical calculations, the discrete levels in ^{209}Bi are well known, but this is not true for ^{210,211}Bi. Discrete-level information for ^{210}Bi consists of only 28 levels up to 1.585 MeV in excitation and 30 levels for ^{211}Bi up to 1.4 MeV, whereas our present ^{209}Bi set contains 96 discrete levels.[6] In addition, for ^{210}Bi, 26 of the 28 levels have the same parity; this situation means that M1 dipole transitions will be important. Unfortunately, M1 transition strengths as a function of energy are not well understood, either in the continuum above the discrete levels or among the levels themselves. See Fig. 2 for a partial decay scheme of ^{210}Bi.

Results for Incident Neutrons

For the neutron fluxes and the energy range in the typical s-process stellar environment, there is only one way to form ^{210}Bi (and its long-lived isomer) initially—namely, by keV-neutron capture on stable ^{209}Bi. We have calculated the ^{209}Bi total capture cross section for incident neutrons from 1 keV to a few MeV in energy, as well as total capture

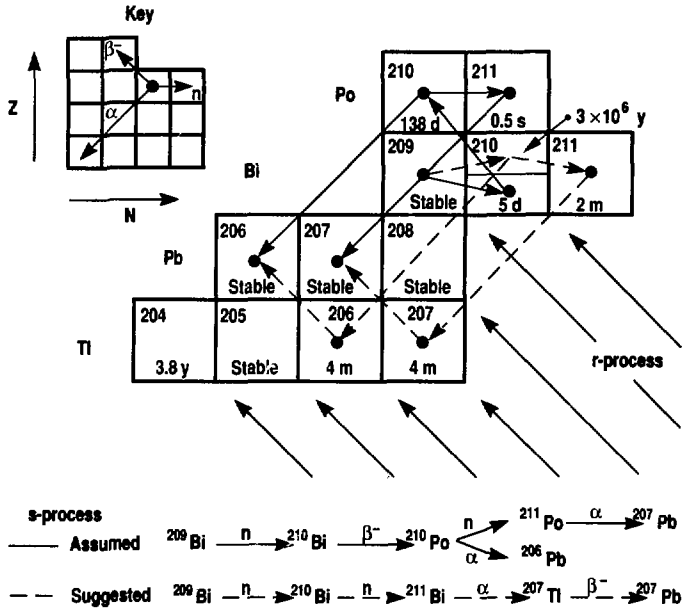

Figure 1. The mass region around bismuth that is involved in s-process nucleosynthesis. Two possible s-process cycles are illustrated.

gamma-ray spectra, and have obtained good agreement with experiment.[7] We also calculated the partial capture cross sections to the ^{210}Bi ground state and the three isomeric states shown in Fig. 2. We observe that the 1$^-$ ground state and the 5$^-$(m3) isomer are populated about equally well and together represent about 60% of the total capture cross section for 10- to 100-keV incident neutrons. Most of the remaining cross section goes to the 7$^-$ (m2) isomer, whereas the initial population of the long-lived, 9$^-$(m1) isomer is only a few percent of the total capture cross section. Under laboratory conditions, 100% of the 5$^-$ isomer population decays via two gamma-ray transitions through the 3$^-$ level to the ground state, while all the 7$^-$ isomer decays proceed to the 9$^-$ state. Thus, in the absence of photons, about 40% of the total capture reaction produces the 9$^-$ isomer.

Once formed, the 9$^-$ isomer is not destroyed, nor is more of it produced, by inelastic neutron scattering until the incident neutrons reach energies in the region of hundreds of keV, well above the conditions considered in this work. However, all of the states in ^{210}Bi are subject to destruction by neutron capture, producing ^{211}Bi with a 2-minute half-life (see Fig. 1). Because of the spins involved and the larger neutron separation energy in ^{211}Bi compared to that in ^{210}Bi, for neutrons in the energy range of interest here, the destruction of the 9$^-$ (m1) isomer of ^{210}Bi is about a factor of 10 greater than its production. These results are shown in Fig. 3.

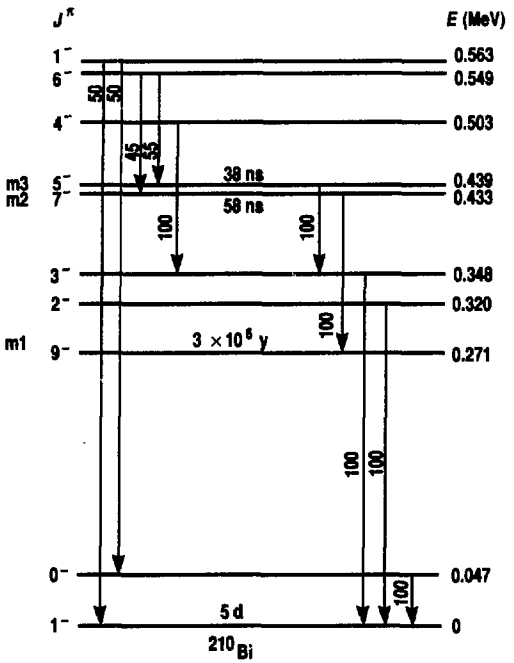

Figure 2. Partial decay scheme for ^{210}Bi, showing the gamma-ray-decay branches and isomeric states used in present work.

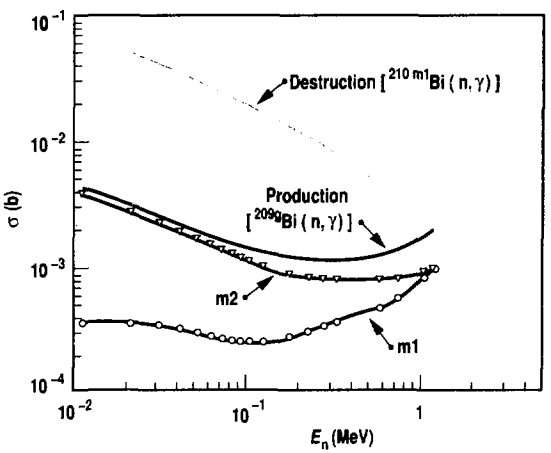

Figure 3. The production and destruction of the 9$^-$(m1) isomer of ^{210}Bi by neutron capture. The line labeled "production" is the sum of the production of the 9$^-$ (m1) and 7$^-$(m2) isomeric states.

Results for Incident Photons

We now consider the response of ^{210}Bi states to incident photons. The 9$^-$ isomer is not produced by photons incident on the 1$^-$ ground state. Furthermore, as shown in Fig. 4, neither is it destroyed appreciably by photons. Photons on the 9$^-$ (m1) target state mainly reproduce that state. The next most likely reaction produces the 7$^-$ isomer, which normally decays completely back to the 9$^-$ state. The destruction reactions, i.e., those that lead to the ground state or the 5$^-$ state, have lower cross sections, down by several orders of magnitude from those of the first two reactions. Thus, the 9$^-$ isomeric state should not be depopulated by photons at any reasonable stellar temperature.

Another way to view this is shown in Fig. 5. Here, the Planck photon-density distributions at various temperatures, from kT = 10 to 50 keV, and the photoproduction cross sections (in nb) of some of the ^{210}Bi states due to photons incident on the 9$^-$ (m1) isomer are plotted vs photon energy. The ordinate scale runs from 10^2 to 10^{25}. Only photons with energies greater than 1 MeV begin to

destroy the 9⁻ isomer directly, and then only to the extent of 0.1 to 1% of the time. Therefore, if the average temperature is 20 keV or less, as suggested by our previous work on ^{176}Lu and its isomer,[8] no direct photodestruction of the ^{210}Bi 9⁻ isomer will occur.

One question remains: What role, if any, is played by the photoproduction peaks below 1 MeV (see Fig. 5)? These primarily reproduce the 9⁻ (m1) target state, but the peaks around 0.3, 0.65, and 0.9 MeV do produce the 7⁻ state to the extent of 15 to 30% of the time. It is conceivable that the photon flux is sometimes great enough to allow a two-step excitation process to occur, where the 7⁻ state is produced and then absorbs another photon before decaying back to the 9⁻ target state.

For photon energies above about 1.1 MeV, the 7⁻(m2) state produces similar amounts of the 9⁻(m1), 7⁻(m2), and 5⁻(m3) states, but very little of the 1⁻ ground state is produced directly. Thus, roughly 1/3 of the 7⁻ state would be prevented from repopulating the 9⁻ isomer. Below 1.1 MeV, there are a few peaks in the photon excitation function curve for the 7⁻ target. One broad peak centered about 100 keV photoexcites the 5⁻ level about 20% of the time. Another peak just below 800 keV populates the 5⁻ level about 75% of the time, while a peak near 900 keV produces the 5⁻ state about 25% of the time. Similar calculations were made with the 5⁻ level as the target, and the photoexcitation results were not greatly different from those for the 7⁻ target. It would seem, therefore, that the photodestruction of the 9⁻ isomer of ^{210}Bi is not a serious problem, even in high photon fluxes where multiple photon absorption may occur.

Conclusions

It appears very likely that the 9⁻ isomer of ^{210}Bi is not destroyed rapidly in the typical s-process stellar environment. Bear in mind that our present calculations are tentative because of the limited amount of discrete-level information available for ^{210}Bi. The second path, neutron capture to form ^{211}Bi with subsequent decays to ^{207}Tl and ^{207}Pb, probably competes well with the usually assumed path. If this is so, then the Pb isotopic abundances will be significantly affected, thereby necessitating a reevaluation of some of the cosmoradiogenic chronometers in current use.

Additional work is required to refine these calculations for use in stellar modeling codes. First, a larger and more complete set of ^{210}Bi levels, together with their gamma-ray branches, must be assembled using structure theory. Then, the sensitivity of the relative isomeric and ground-state productions to the modeling of the M1 and E2 multipole transitions must be investigated. For the purpose of learning more about M1 transition strengths, one should determine the feasibility of making experimental measurements[9] of the primary capture gamma-ray energy spectrum for low-energy incident neutrons on target ^{209}Bi. Also, our current assumptions concerning level densities, spin cut-off parameters, and the neutron optical-model potential must be carefully reviewed.

References:

1. D. D. Clayton, *Astrophys. J.* **139**, 637 (1964).
2. D. D. Clayton and M. E. Rassbach, *Astrophys. J.* **148**, 69 (1967).
3. M. A. Gardner, D. G. Gardner, R. A. Meyer, and M. N. Namboodiri, "Development of a Cross-Section Library for the Ground and Excited

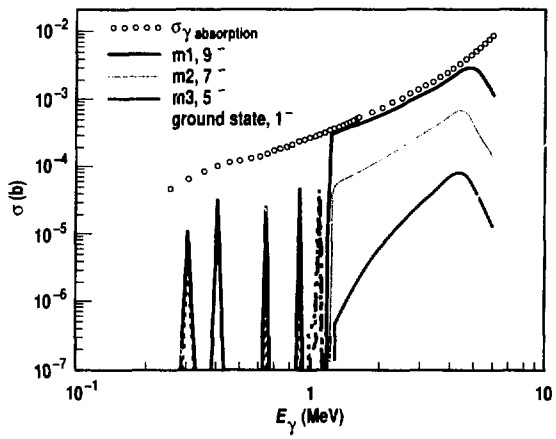

Figure 4. The photoproduction of various states of ^{210}Bi by photons incident on the 9⁻(m1) isomer. The $\sigma_{\gamma\ absorption}$ curve is the calculated total photon-absorption cross section.

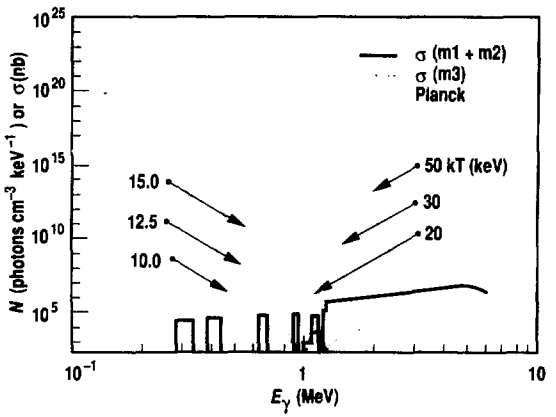

Figure 5. Planck photon-energy distributions at various temperatures, and photoproduction cross sections from photons incident on the 9⁻(m1) isomer plotted vs photon energy.

States of the Bismuth Isotopes," *Nuclear Chemistry Division FY86 Annual Report*, Lawrence Livermore National Laboratory, Livermore, Calif., UCAR-10062-86 (1986), pp. 2-21 to 2-25.
4. M. N. Namboodiri, M. A. Gardner, D. G. Gardner, and D. R. Nethaway, "Inclusion of Isomeric States as Targets in our Bismuth Cross-Section Library," *Nuclear Chemistry Division FY87 Annual Report*, Lawrence Livermore National Laboratory, Livermore, Calif., UCAR-10062-87 (1987), pp. 2-19 to 2-22.
5. M. A. Gardner and D. G. Gardner, "The Importance of Level Structure in Nuclear Reaction Cross-Section Calculations," *Nuclei Off the Line of Stability, ACS Symposium Series 324*, R. A. Meyer and D. S. Brenner, Eds. (American Chemical Society, Washington, D.C., 1986), p. 100.
6. R. A. Meyer, private communication, Lawrence Livermore National Laboratory, Livermore, Calif. (1985).
7. J. Voignier, S. Joly, and G. Grenier, *Nucl. Sci. Eng.* **93**, 43 (1986); corrigendum, *Nucl. Sci. Eng.* **96**, 343 (1987).
8. M. A. Gardner, D. G. Gardner, and R. W. Hoff, *J. Phys. G* **14 Suppl.**; *Institute Phys. Conf. Ser. No. 88* p. S315 (1988).
9. G. Walter, H. Beer, F. Kappeler, G. Reffo, and F. Fabbri, *Astron. Astrophys.* **167**, 186 (1986).

Spheromak Model of Planetary Nebulae

C. L. Bennett

Many stars end their lives by disintegrating; the most massive do so by exploding as supernovas. However, the more common intermediate-mass stars (such as our sun) are destined to spend part of their lives as red giants. During this red-giant phase, some stars eject much of their mass to form a planetary nebula, and the remaining core mass becomes a white dwarf.

The gas ejected to form the planetary nebula consists of hot, rapidly moving plasma, which is observed to form highly symmetrical patterns. Although the high degree of symmetry of the planetary nebulae has long been noted, until now there has been no explanation for these patterns.

The Model

I have found that a very simple model can be used to describe the morphology and velocity distribution of the material in nearly all planetary nebulae.[1] The model is based on several assumptions regarding physical properties:

- First, I assume that the mass current has zero divergence, meaning that only insignificant new mass is being injected into the nebula.
- I also assume that the mass current is proportional to its curl, $\nabla \times j = kj$, implying that the flow is "relaxed" so that there are no Magnus forces acting. (The Magnus force in fluids is given by the vector product of vorticity and velocity.)
- Finally, I assume that the lowest energy configuration consistent with the above constraints is realized.

These three assumptions result in a unique mass current given by

$$j = \hat{r}\,[2\cos(\theta)\, j_1(kr)/kr] - \hat{\theta}\sin(\theta)\,(1/kr)\, d/dr\,[rj_1(kr)] + \hat{\varphi}\sin(\theta)\, j_1(kr), \quad (1)$$

where j_1 is a spherical Bessel function. This configuration is known in plasma physics as a spheromak. It is convenient in discussing morphology to choose $1/k$ as the unit of length. Those orbits in the (cylindrical coordinate) ρ-z plane that are traced out by a particle exactly following these current vectors have constant values for the quantity $rj_1(r)\sin^2(\theta)$. Various examples of such ρ-z orbits are drawn in Fig. 1. A gray-scale map of the magnitude of the current vector in the ρ-z plane is drawn in Fig. 2.

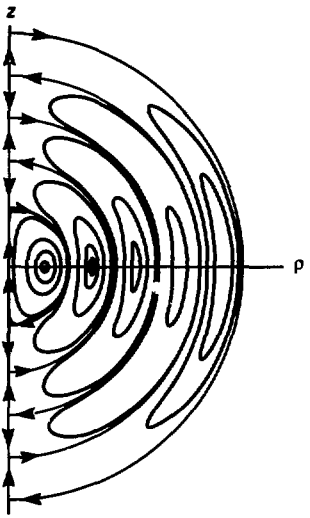

Figure 1. Typical ground-state spheromak orbits in the ρ-z plane.

In Figs. 3 through 7, photographs of various planetary nebulae are compared with various trajectories from the spheromak model. From an examination of each of these figures, it can be seen that the very different detailed spatial shapes or morphologies for these nebulae are very well reproduced by the model trajectories. Correlations with the model include such features as the position of the ansae (handle-like projections) in the Saturn nebula (Fig. 4) and the coiling of the Helix nebula (Fig. 3).

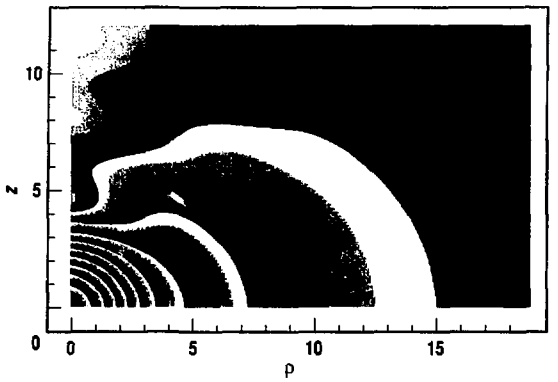

Figure 2. Distribution of ground-state spheromak current vector shown on a gray scale. Each change of scale corresponds to a 2% change in density, with each black band corresponding to a 10% change in density. Nodes along the z-axis correspond to zeros of the spherical Bessel function j_1.

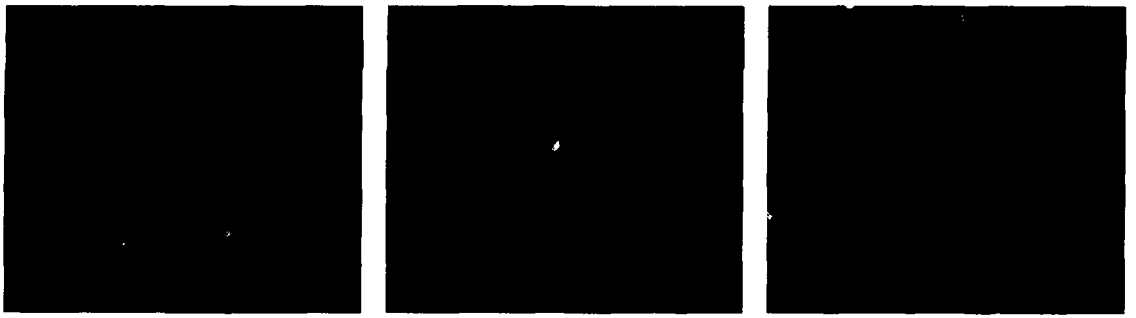

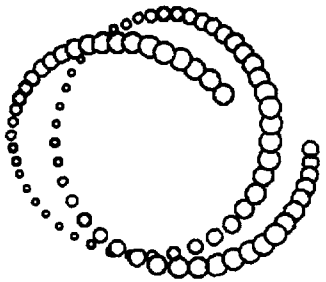

Figure 3. A representation of a spheromak orbit compared to a photograph of the Helix nebula NGC 7293 (Hale Observatories). The circle radii are linearly related to the z coordinate. This orbit is characterized by having an initial dimensionless cylindrical ρ coordinate of 2 for $z = 0$.

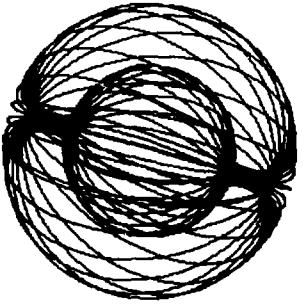

Figure 4. A "wire-frame" figure of revolution corresponding to a ρ-z plane trajectory that begins just outside the innermost spherical separatrix and passes just inside the second innermost separatrix compared to the 1918 appearance[2] of the Saturn nebula NGC 7009. Note that in this drawing the "wires" do not represent individual trajectories.

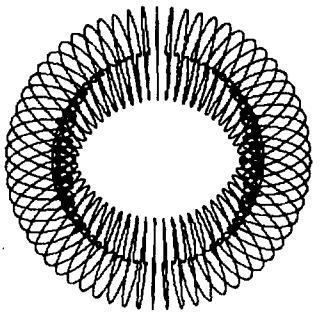

Figure 5. A "wire-frame" figure of revolution compared to a photograph of the Ring nebula M57 (Lick Observatories). Note the similarity in the appearances of the brighter streaks in the photograph and the overlapping portions of the "wire-frame" model.

The model also reproduces the very complex velocity profiles that are seen in many of the planetary nebulae. Figure 8 compares a model slit spectrum from the spheromak model with an experimental slit spectrum from the nebula NGC 7662. Not only is the central elliptical pattern reproduced, but the hitherto mysterious, faint outer extensions are also present.

References:

1. C. L. Bennett, *Astrophys. J.* **323**, L123 (1987).
2. H. H. Curtis, *Lick Obs. Pub.* **13**, 57 (1918).

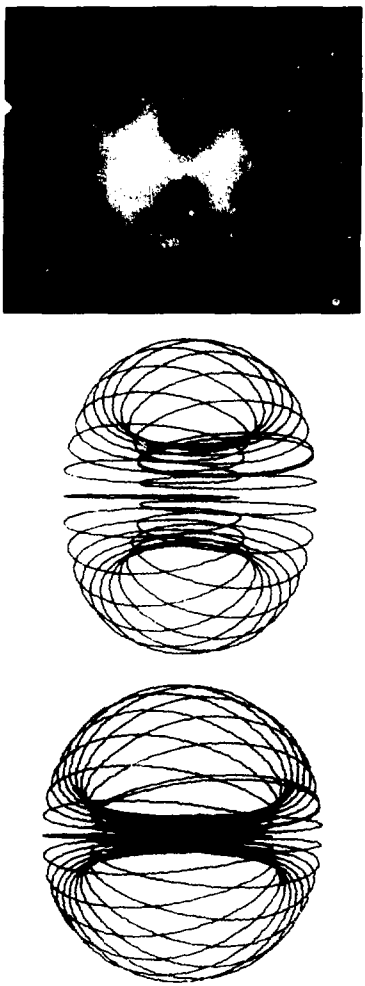

Figure 6. A pair of neighboring models compared to a photograph of the Owl nebula M97 (Hale Observatories).

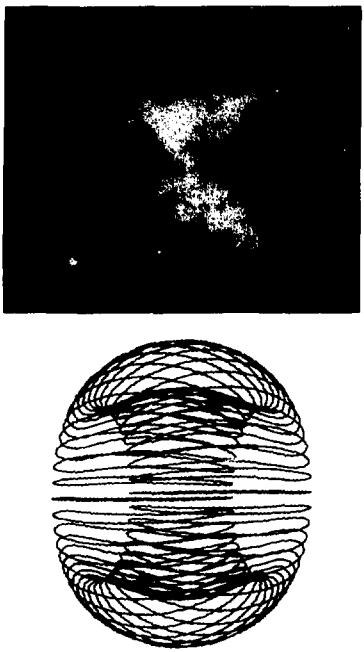

Figure 7. A photograph of the Dumbbell nebula M27 (National Optical Astronomy Observatories) compared to a model whose orbits are located between the first and second nodes in the spherical Bessel functions.

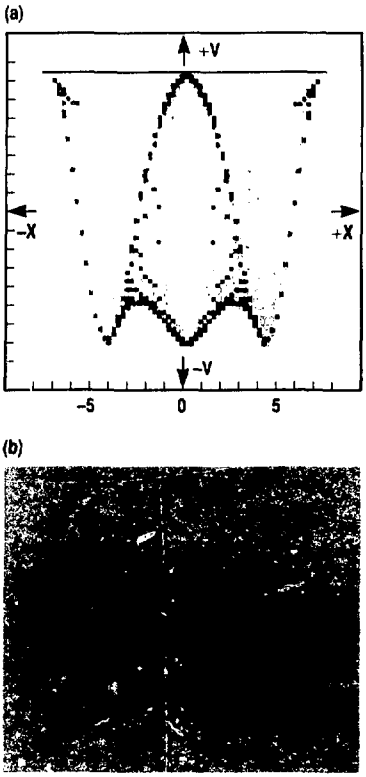

Figure 8. Comparisons between model and experimental slit spectra: (a) A gray-scale representation of the radial-velocity slit spectrum for the innermost two spherical shells of a spheromak. The spatial dimension is oriented horizontally; the velocity relative to the center is plotted vertically. The relative intensity of the plotted gray scale is determined by the relative volume of material with the appropriate velocity. The gray-scale changes occur at relative volumes of 1, 3, 9, and 12. The indicated spatial scale corresponds to values of the dimensionless number kr. (b) An [O III] 5007 slit spectrum for the nebula NGC 7662 (Hale Observatories).

Measuring the Beta-Decay End Point of Atomic Tritium

W. Stoffl, D. Decman, and J. Engelage

The mass of the neutrino is an important parameter in many areas of physics. For example, a mass of even a few electron volts would have a profound effect on cosmology because of the vast number of neutrinos in the universe; the discovery of such a mass would support modern theories of particle physics and set values for some of the parameters.

The mass of the electron antineutrino, in theory, can be determined by careful measurement of the beta decay of tritium. A nonzero neutrino mass alters the shape of the electron spectrum near the end-point energy of the beta-decay process. Researchers in Moscow[1] reported the results of such a tritium beta-decay measurement and claimed evidence for an electron antineutrino mass between 18 and 45 eV. The range comes from uncertainties in the final-state distribution of their source material. In contrast, groups in Switzerland[2] and Tokyo[3] found no evidence for a neutrino mass with upper limits of 18 and 27 eV, respectively. These experiments used sources with the tritium embedded in a solid, a technique that introduces numerous systematic errors.

Our experiment has been designed to eliminate these systematic errors. Electrons from tritium atoms that decay in our cryogenic, gaseous, atomic tritium source are guided into a large, toroidal, magnetic-field spectrometer by a system of five solenoidal superconducting magnets. Only electrons emitted from the gaseous atomic tritium will successfully pass through the high-resolution spectrometer and be detected.

During FY88, we completed the hardware for our experiment. This was often a very complicated undertaking because most of the components required some combination of high-vacuum surfaces, nonmagnetic materials, parts operating at cryogenic temperatures, and high voltage.

We completed the gas-handling system that introduces tritium into the gaseous tritium source and assembled the source. Figure 1 shows the flow of tritium and beta-decay electrons through the source assembly. Although not shown in this simplified diagram, the source tube is encased in a liquid-nitrogen-cooled radiation shield, which is further enclosed in a larger tube that is kept at high vacuum by its own pumping system. This multitube source assembly is positioned inside the bore of five superconducting magnets. Also not shown is the section of the source tube that is lined with charcoal that can be cooled to cryogenic temperatures. The absorption of tritium onto the cold charcoal further inhibits tritium gas from entering our spectrometer tank.

We run the source assembly, including its support table, at 5 kV; therefore, all the power for the source equipment must be obtained through isolation transformers. We use optical-fiber lines for computer control of the source parameters. The source was tested at a 30-kV potential and found to be stable.

The magnetic spectrometer (Fig. 2) is housed in a large (30,000-L) vacuum

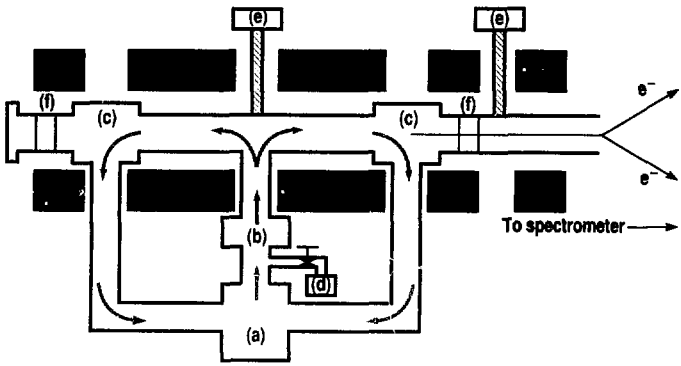

Figure 1. Cross-sectional view of the gaseous tritium source assembly. Tritium flows out of the liquid-nitrogen-cooled cleanup trap (a) and is made atomic in the radiofrequency dissociator (b). The source gas circulates through a 16.4-ft-long, 1.25-in.-diam aluminum source tube until being pumped out by turbomolecular pumps, four at each point (c). These pumps decrease the tritium gas pressure from about 10^{-3} Torr at the center of the source tube to 10^{-7} Torr at its two ends. Tritium gas can be added to the system from a gas bottle (d). The source tube is kept at cryogenic temperatures as low as 10 K by having it in contact with the cold heads of a closed-loop refrigeration unit (e). Electrons from beta decay in the source tube are guided to the spectrometer by the magnetic field of the superconducting magnets (shaded areas). A potential of 5 kV across the acceleration gaps (f) "tags" the electrons from the source with this extra energy for a total of about 23 keV; electrons from tritium that has leaked into the tank have no more than 18.6 keV. The tritium exhausted from the turbopumps is sent back through the trap (a) and reinjected into the source tube.

tank fabricated from nonmagnetic stainless steel. Using two turbopumps and two cryopumps, we achieved a vacuum of less than 5×10^{-9} Torr.

The spectrometer focuses the electrons onto a cylindrical silicon detector that is segmented into 16 independent ring elements. Each element has its own amplifier system. Because the silicon detector has good energy resolution, we can distinguish between good events and background from radioactive decays and secondary cosmic-ray interactions. To avoid thermal stress, the spectrometer will be operated at a constant field and current setting. We will obtain the energy spectrum of the electrons emitted in the source by applying a variable electric potential that accelerates the electrons to the energy that corresponds to the spectrometer's field setting.

We produce the toroidal magnetic field in the spectrometer with a 72-loop system that has a total resistance of about 0.5 Ω and involves more than 700 connections. This low resistance is necessary because each loop must carry 50 A. The outer portions of these loops are 0.5-in.-diam aluminum rods; for the inner part, we use 1-in.-wide, 0.055-in.-thick copper bands. We incorporated ways to ensure that the copper bands inside the loops are straight; this is crucial to the resolution of the spectrometer because the electrons pass close to these bands as they are focused. To make them straight, we stretched each 12-ft band section 1.5 in. with 3000 lb of force. The bands are held straight in the spectrometer by stainless steel springs, each of which applies a 60-lb force.

Among our concerns were compensating for Earth's magnetic field, minimizing the effect of the electric field produced by the conductors, ensuring a stable temperature, and determining the spectrometer's resolution function. The magnetic spectrometer cannot focus the electrons properly unless we cancel Earth's magnetic field. To reduce the field to less than 5 mG, we surrounded the tank with a shield consisting of 30 coils containing approximately 20,000 ft of wire and energized with 17 computer-controlled power supplies.

We also considered the problem of the electric field produced by the conductors. Because the voltage is dropping along the current path of the spectrometer, this electric field varies with position. To minimize the deflection of the electrons by these electric fields, we strung shield wires at ground potential 0.25 in. on either side of the inner conductors. Similarly, we positioned a grounded wire mesh between the outer conductors and the electron paths.

We took several measures that should help keep the temperature of the spectrometer stable to better than 1°C:

- We monitored the temperature of the conductors and the space frame using temperature-sensitive integrated circuits.
- We chemically blackened the conductors so that they can better radiate away the 1.2 kW of heat generated by the current they carry.
- We installed copper lines for cooling water on the space frame to stabilize the temperature inside the vacuum vessel.

We also built in several computer-controlled diagnostic and correction elements that help us achieve the necessary energy resolution. For example, 128 electrostatic deflector plates allow us to tune the spectrometer in 16 different sections. We can isolate the effects of each set of deflector plates by positioning a movable cup over the detector. The cup contains a slit that allows only a narrow range of electron trajectories to impinge on the detector. Similarly, a movable slit installed at the first focus of the spectrometer allows us to study the resolution of the spectrometer as a function of the trajectories accepted from the source. Because the stepping motors for both the detector diagnostic cup and the movable slit are computer-controlled, we can do a very thorough optimization.

An important aspect of our measurement is knowledge of the system's resolution function. The finite resolution of the spectrometer, as well as any energy loss in the source, will smear the shape of the beta-decay spectrum. Therefore, the resolution function must be unfolded from the data in order to extract the value of the neutrino mass. We will measure our resolution function by using the isomeric decay of the 17.8-keV conversion electron line of ^{83}Kr. This isomer, which has a half-life ($t_{1/2}$) of 1.8 hours, is produced by the decay of ^{83}Rb ($t_{1/2}$ = 86 days). Because the isomer is a gas, it mimics exactly the behavior of the tritium in our source, and it gives us a monochromatic line that enables us to measure and tune the resolution of our system. In addition, we can measure the ^{83}Kr line with admixtures of hydrogen, deuterium, or tritium gas at various pressures (the nominal operating pressure is about 10^{-3} Torr in the source tube) to measure the energy loss in the source gas.

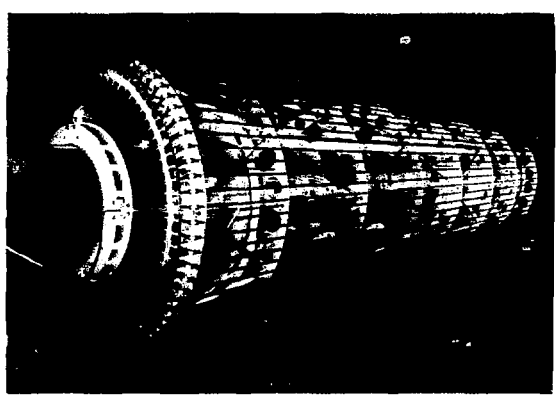

Figure 2. The 26-ft-long toroidal-field electron spectrometer that will be used to measure the tritium beta-decay spectrum near the end point. The large rings that support the 72 current loops are 6.5 ft in diameter.

To ensure that this complicated set of hardware is operating correctly, we developed a sophisticated, computerized, data acquisition and control system for our experiment. The system uses a dedicated VAX 11/750 computer and a commercially available branch driver to interface the computer to several computer-automated measurement and control (CAMAC) crates. To monitor and regulate more than 500 parameters, we developed software that can communicate with a wide range of devices, including digital voltmeters, output registers, valves, pumps, temperature sensors, magnetometers, stepping motors, and high-voltage power supplies. This system has been most useful during the developmental phase of the spectrometer; we expect to use it extensively to optimize the resolution of the spectrometer and to monitor the stability of the system in the final experiments.

In early FY89, we will continue to test and optimize the electron spectrometer by using an electron gun positioned at the entrance of the tank. Later, we will test the entire system using ^{83}Kr in the gaseous source. After these tests are complete, we will begin our first tritium measurements.

So far, we have found nothing that could keep our experiment from reaching the goal of being sensitive to a neutrino mass of 5 eV.

References:

1. S. Boris, A. Golutvin, L. Laptin, V. Lubimov, V. Nagovizin, E. Novikov, V. Nozik, V. Soloshenko, I. Tigomirov, and E. Tretjakov, "The Neutrino Mass from the Tritium Beta Spectrum in Valine," *Phys. Lett. B* **159**, 217 (1985).
2. M. Fritschi, E. Holzschuh, W. Kundig, J. W. Petersen, R. E. Pixley, and H. Stussi, "An Upper Limit for the Mass of the Electron Anti-Neutrino from Tritium Beta Decay," *Phys. Lett. B* **173**, 485 (1986).
3. H. Kawakami, K. Nisimura, T. Ohshima, S. Shibata, Y. Shoji, I. Sugai, K. Ukai, T. Yasuda, N. Morikawa, N. Nogawa, T. Nagafuchi, F. Naito, T. Suzuki, H. Taketani, M. Iwahashi, K. Hisatake, M. Fujioka, Y. Fukushima, T. Matsuda, and T. Taniguchi, "An Upper Limit for the Mass of the Electron Anti-Neutrino from the INS Experiment," *Phys. Lett. B* **187**, 198 (1987).

Laboratory and Field Studies of Radionuclide Transport in Groundwater

K. V. Marsh, J. H. Rego, and R. W. Buddemeier; and J. R. Hunt (Department of Civil Engineering, University of California, Berkeley)

LLNL's Hydrology and Radionuclide Migration Program (HRMP) investigates the subsurface hydrologic transport of radionuclides at NTS. We are continuing our work at NTS on Pahute Mesa where the Cheshire Event was detonated in 1976. The detonation took place 600 m below the water table with an announced yield in the 250- to 500-kt range. The large size of the detonation, its location in a relatively permeable formation, and its proximity to the NTS boundary combine to make this an important location for field studies. Our recent work in that location has shown that several radionuclides in the cavity water are more than 99% adsorbed onto colloidal particles, and considerable laboratory and field evidence indicates that colloidal material is mobile in groundwater.[1] We have been concentrating a large part of our work this past year on understanding the importance of the possible migration of radionuclides off NTS via both colloid- and solution-transport mechanisms.

Field Work at the Cheshire Site

Last year we reported preliminary results from the UE20*n*-1 exploratory hole, also known as the "satellite well," at the Cheshire site.[2] The only data available at that time were tritium and ^{125}Sb concentrations measured in the field during drilling; we had planned extensive large-volume sampling of this new hole once the effects of drilling had dissipated.

The UE20n-1 hole had been drilled by means of an air-foam technique that does not use bentonite clay mud; rather, the cuttings are suspended in a detergent foam and blown out of the hole with compressed air. Lithium bromide was added to the drilling fluid as a tracer, and the detergent itself also served this

purpose. Our intention was to periodically monitor the concentrations of both these tracers because their decrease to undetectable levels would mean the water in the hole was typical of that in the aquifer.

To avoid stressing the aquifer by high-volume pumping, we installed a 14-gal/min pump in the hole.

Unfortunately, because both bromide and detergent were slow to dissipate, the detergent was easily detectable six months later (October 1987), and the bromide was at the limit of detectability. We suspended sampling during the winter and did not resume operations until early February 1988. Then, in addition to the continued presence of the detergent, we discovered high concentrations of iron hydroxide and mud of undetermined origin.

Although these developments precluded any attempts at further studies of colloid-radionuclide associations in the satellite well, we continued to measure concentrations of radionuclides in 1-L unfiltered water samples. These results are given in Table 1, where they are compared to concentrations measured in the cavity and in the formation aquifer 250 m above the estimated upper boundary of the cavity. Although these field data are limited and we do plan to augment them, they tend to confirm our expectations based on previous measurements.

Laboratory studies have indicated that the minerals found in tuff at NTS readily sorb cations but that anionic species exhibit little sorption.[4] Since we expect both technecium and iodine to exist in these aquifers primarily as anionic species, we would also expect them to be quite mobile, and that is what we observe. Both track the tritium concentrations very closely from the cavity to the satellite well. On the other hand, laboratory data[5] have indicated that ^{125}Sb may be slightly sorbed onto colloidal particles (1 to 2%) and that ^{137}Cs is more strongly sorbed (20%). This would qualitatively account for their reduction to 0.14 and 4×10^{-4}, respectively, in the satellite well compared to the cavity (see Table 1). ^{152}Eu, known to be greater than 99% sorbed on colloidal particles,[5] has not been detected in the satellite well, but we would not expect to see it in samples smaller than about 200 L. In 200-L samples of the formation water above the cavity, ^{152}Eu has been measured at a concentration of about 2% of that in the cavity.

In summary, our field data from the new satellite well tend to confirm our previous experimental results and our geochemical expectations. We are gaining experience with a suite of tracers whose mobilities range from high to practically zero and whose physical states range from completely dissolved to completely colloid-associated. As our work progresses, we should be able to develop data concerning both solution- and particle-controlled transport processes.

Table 1. Ratios of radionuclide concentrations in liquid samples from formation aquifer[a] and satellite well[b] to Cheshire cavity concentration as measured in October 1984 (10/84).

Element	Cavity concentration, 10/84 (per mL)[c]	Formation aquifer, 5/85	Formation aquifer, 10-11/85	Satellite well, 7/87	Satellite well, 2/88
^{3}H	0.5 μCi	0.85	0.80	1.15	1.15
^{99}Tc	5×10^{-8} μCi	0.75	—	0.88	—
^{129}I	8.4×10^{12} atoms	—	0.74	1.31	—
^{125}Sb	7×10^{-6} μCi	0.77	0.62	0.22	0.14
^{137}Cs	3×10^{-6} μCi	0.21	0.28	1×10^{-3}	4×10^{-4}

[a] Formation aquifer 250 m above the estimated upper boundary of the cavity.
[b] Exploratory hole UE20n-1 at the Cheshire site.
[c] Tritium concentrations were measured by liquid scintillation counting, ^{99}Tc by radiochemical separation followed by liquid scintillation counting, ^{129}I by accelerator mass spectrometry (discussed elsewhere in this document),[3] and ^{125}Sb and ^{137}Cs by direct gamma-ray spectroscopy of liquid samples.

Laboratory Colloid Studies

Our field studies at NTS have demonstrated that radionuclides associated with colloidal material are mobile in the groundwater. This occurrence is counter to conventionally accepted contaminant-transport models that assume that sorbed species are immobile. Consequently, we are conducting laboratory research into some of the fundamental processes controlling the attachment of colloids onto substrates.

We know that colloid attachment following collision with the surface of a medium is controlled by electrostatic and van der Waals forces between the particles and the surface. In solutions of high ionic strengths, electrostatic forces are masked, and attractive van der Waals forces dominate such that 100% of the particles stick when they collide. As the ionic strength is lowered, electrostatic repulsion increases. Theory predicts that near a critical ionic strength, the sticking efficiency goes to zero over a very small change of concentration. However, sticking-efficiency experiments with well-defined particles flowing past clean media surfaces indicate that sticking efficiencies are rarely less than 0.1%.

Now, for natural groundwater flow, even at a sticking efficiency of 0.1%, colloids should not be transported more than a few tens of meters unless other processes are at work to release them. Experiments have measured colloid release from surfaces only in turbulent environments, where shear stresses from turbulent bursts could cause erosion. Steady-state laminar groundwater flow could not release colloids from a fixed solid surface. In the aquifer above the Cheshire cavity, we detected only 2.5% of the concentration of strongly sorbed radionuclides in the cavity. Therefore, colloids are indeed being removed, but mobility of strongly sorbing species on a scale of hundreds of meters is entirely unexpected.

A major problem at the Cheshire site is first, to identify the mobile colloids and, second, to develop predictive models for their mobility in fractured media. We are working with a group headed by Dr. Roger Jacobson from the Desert Research Institute (DRI) of the University of Nevada to identify the colloidal particles. We have used x-ray diffraction to analyze cavity samples and have found that particles in the 0.05- to 0.003-μm range are dominated by quartz and (Ca, K) feldspars. Approximately 10% of the particles could not be identified by x-ray diffraction; these could be clay minerals formed as secondary minerals during feldspar weathering. Fourier transform, infrared spectroscopic characterizations tend to support the hypothesis that clays are present in the colloid fraction.

We are also working with a group headed by Dr. James R. Hunt at U. C. Berkeley's Department of Civil Engineering to identify the initial experimental measurements needed to quantify colloid migration in fractured media. The physical transport mechanisms of submicrometer colloids to unaltered mineral surfaces are well known and experimentally verified. However, natural fracture surfaces are covered with secondary minerals produced by weathering reactions and thus are not represented well by ideal, flat, mineral surfaces. Colloid deposition on surfaces containing previously deposited colloids on secondary mineral growths is also an important issue in long-term transport in natural environments, but no applicable theory or experimental data are available.

Our experimental approach will be to flow a dilute suspension of known clay colloids between two parallel glass plates separated by, at most, 1 mm. As time passes, a deposit of clay colloids will begin to plug the space between the glass plates until an equilibrium is reached when particles are no longer retained because hydrodynamic shear forces exceed colloid-colloid attachment forces. Colloid retention over time and at different location will be monitored by passing a light beam through the glass plates. The independent parameters of interest are imposed flow rate, aqueous solution composition, and gap width. The measurements will determine colloid mass retention and permeability alteration.

We expect that predictive, although empirical, relationships will be found between these measures of clogging and the structural characterization of colloid aggregates through rheological measurements. We will do the experiment first with a well-characterized clay mineral, such as kaolinite, and then with actual colloids collected from NTS groundwater. The end result will be a mechanistic understanding of colloid retention in fractured media and permeability alteration. Subsequent work can address the important issues of colloid release from fracture surfaces following detonations and of regional colloid migration through fracture networks.

References:

1. L. M. McDowell-Boyer, J. R. Hunt, and N. Sitar, "Particle Transport Through Porous Media," *Water Resour. Res.* **22** (1986), pp. 1901-1921.
2. R. W. Buddemeier, J. H. Rego, R. A. Failor, and K. V. Marsh, "Field Studies of Radionuclide Migration at the Nevada Test Site's Cheshire Site," *Nuclear Chemistry Division FY87 Annual Report*, Lawrence Livermore National Laboratory, Livermore, Calif., UCAR-10062-87 (1987), pp. 3-19 to 3-22.
3. R. C. Finkel, M. W. Caffee, K. V. Marsh, and J. H. Rego, "Accelerator Mass Spectrometry Measurements of ^{129}I and ^{36}Cl in Groundwater from the Nevada Test Site," *Nuclear Chemistry Division FY88 Annual Report*, Lawrence Livermore National Laboratory, Livermore, Calif., UCAR-10062-88 (1988), pp. 94-95.
4. W. R. Daniels, K. Wolfsberg, and R. S. Rundberg, *Summary Report on Geochemistry of Yucca Mountain and Environs*, Los Alamos National Laboratory, Los Alamos, N. Mex., LA-9328 (1982).
5. R. W. Buddemeier and J. R. Hunt, *Radionuclide Transport by Colloids in Nevada Test Site Groundwater*, Lawrence Livermore National Laboratory, Livermore, Calif., UCRL-97111 (1988); *Appl. Geochem.* (in press).

Accelerator-Based Mass Spectrometry At LLNL

M. W. Caffee and R. C. Finkel

Radioactive isotopes are used as tracers of geologic and biologic processes. These isotopes often occur in nature in such low abundances that they are difficult to detect by either decay or conventional mass spectrometry (Fig. 1). For example, ^{10}Be occurs in ice cores with a concentration of only 10^7 atoms/kg. One kilogram of ice would produce only five decays per year. It would be impossible to use such a low rate for detailed geochemical studies using decay-counting techniques. Also, conventional mass spectrometry often fails

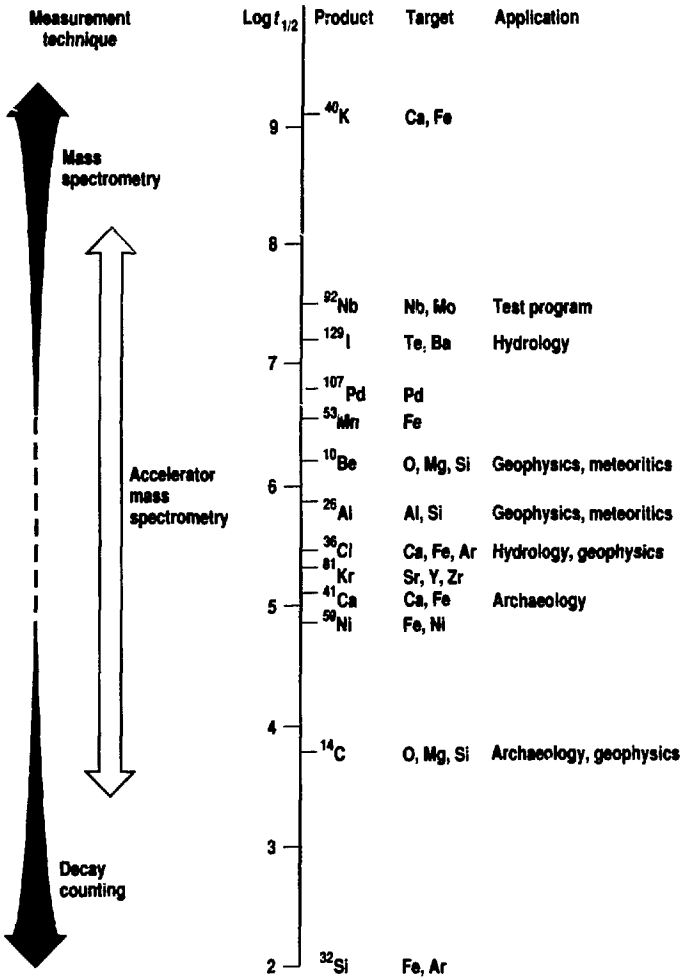

Figure 1. Half-lives of a number of radioisotopes. Those isotopes with short half-lives usually can be detected by conventional counting techniques. Those with long half-lives are generally more abundant and can be determined using conventional mass spectrometry. Between these two groups are a number of rare isotopes that lend themselves to AMS measurement. (Adapted with permission of the originator from a drawing by K. Nishiizumi.)

in such cases because of isobaric and molecular interferences.

The primary limitation of conventional mass spectrometry for very rare nuclides is the interference from isobars. For example, to analyze ^{36}Cl, we must distinguish it from ^{36}S. The mass resolution ($M/\Delta M$) needed for such a separation is about 30,000. *In principle*, it is possible to obtain such mass resolution with conventional mass spectrometry; however, to do so would require very narrow slits, resulting in a loss of most of the ion beam. This approach is self-defeating if the isotope is very rare. A better technique is to maximize the ion-beam transmission while eliminating interfering species by using other means.

These isotopes can be measured by combining particle accelerators, such as those built for research in nuclear physics, with additional magnetic and electrostatic analyzers and energy-loss or time-of-flight detectors.[1] Such an accelerator mass spectrometer (AMS) has been constructed as a combined effort of LLNL's Nuclear Chemistry, Experimental Physics, and Biomedical Sciences divisions.

Facility Description

Figure 2 is a schematic of the AMS facility, and Fig. 3 is a photograph of the tandem accelerator. Its important features are as follows.

Ion Source. Most AMS facilities employ cesium-sputter ion sources. Usually, a solid sample is bombarded by the cesium ions. The cesium-sputtering process produces negative ions with good efficiency, a circumstance that is used to advantage in some instances. Nitrogen, for example, does not readily form a negative ion; thus, the ion source itself enhances the discrimination between ^{14}C and its isobaric interference, ^{14}N. The ion source for the LLNL AMS facility can accommodate up to 60 samples on a computer-controlled cassette. Target weights are generally a few milligrams but can be as small as 20 μg for ^{14}C. This ion source was delivered in late 1988.

Injector. Before the acceleration of the negative ion beam, one stage of mass separation is performed by means of a 90-degree magnet. After separation, the beam is pre-accelerated to several hundred keV.

Tandem Accelerator. The LLNL AMS facility uses a tandem Van de Graaff accelerator, which can charge the terminal up to 11 MV. At the terminal, the ion beam passes through a stripper, either a thin foil or gas. As a result of this stripping, the ions are positively charged, and the centroid of the roughly

Gaussian distribution of charge states depends on the terminal voltage and the element accelerated. Electron stripping largely eliminates molecular interferences because molecules in a charge state of +3 or greater are not stable. Accelerator construction is nearly complete. The only major component remaining to be built is the gas-handling system for the SF_6, the insulating gas.

Positive-Ion Analysis. Two 90-degree sector magnets located behind the accelerator remove scattered particles, molecular fragments, and unwanted charge states by selecting only a specific ratio of *energy* × *mass*/(*charge*^{2}). Installation of these magnets is complete. Analysis of radionuclides heavier than ^{36}Cl, such as ^{129}I, requires further separation of the masses. A Wien filter, which selects particles of the same velocity by using perpendicular *E*- and *B*-fields, accomplishes this separation. This filter will be installed during the summer of 1989.

Detection System. The detection system consists of two elements: that portion used for measuring the stable-isotope beam (^{13}C, for example) and the detector used for measuring the various low-abundance isotopes. Faraday cups placed behind the first magnetic sector on the high-energy side of the accelerator measure the stable-isotope beam current. Presently, we envision three detectors for measuring a radioisotope: a dE/dx gas ionization detector, a time-of-flight detector, and a gas-filled-magnet detector in conjunction with a dE/dx detector. The dE/dX detector[2] has been installed recently. This type of detector works on the principle that isotopes having the same atomic mass but differing atomic numbers have different rates of ionization loss. Thus, this detector can resolve isotopes having isobaric interferences, such as ^{14}C–^{14}N and ^{36}Cl–^{36}S. Development is proceeding on both a time-of-flight detector and a gas-filled-magnet detector.

Research Applications

We are concentrating our efforts in four areas: migration of radionuclides, *in situ* production of radionuclides in terrestrial material by cosmic-ray interactions, Nuclear Test Program applications, and atmospheric dynamics. In some of these areas, there is considerable collaboration among different scientific groups at LLNL. Because the facility at LLNL is not yet operational, we are performing initial experiments at the University of Rochester's AMS facility. Doing some initial experiments there enables us to develop the necessary chemical separation techniques and at the same time develop the needed hardware. We hope that this will allow us to begin work immediately upon completion of our facility. The results of some of our initial measurements are presented elsewhere.[3]

Environmental Issues. The disposal and storage of both low- and high-level radioactive waste are important national concerns. The primary issue in radioactive waste disposal is containment. There are several areas we can address.

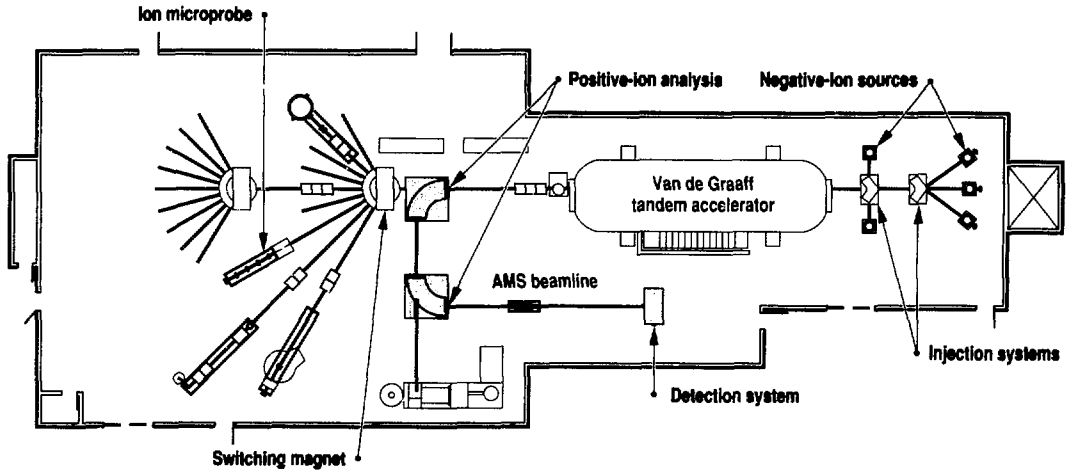

Figure 2.
Schematic view of the new tandem-accelerator laboratory. The components necessary for the AMS beamline are the ion source, injector magnets, accelerator, positive-ion analysis magnets, and a detection system. Also shown are other experimental beamlines completed or under construction.

• An important step in evaluating the viability of disposing wastes at the proposed storage facility in Yucca Mountain, Nevada, is to assess the loss rate of radioactivity from bare nuclear reactor fuel and cladding, particularly if this material were to come into contact with groundwater. Experiments designed to simulate this circumstance are now under way. In the first studies, both the bare fuel and cladding materials are stored in water-filled vessels for up to two years. During this two-year interval, water samples will be drawn and analyzed. Among those radionuclides to be studied are ^{129}I, ^{99}Tc, and ^{14}C. Westinghouse has done some ^{129}I studies using neutron-activation analysis. AMS reduces the time required for an analysis and attains a level of precision that is not possible with neutron activation.

• Once a particular radioisotope enters the environment, it is necessary to predict the rate at which that isotope will migrate. This is one of the criteria to be studied in assessing the suitability of the Yucca Mountain high-level-waste repository. Two possibilities must be considered: the rate of migration of radioisotopes given the prevailing geologic conditions at Yucca Mountain and the possibility that, within several half-lives of the longer-lived radioisotopes, the geologic conditions will change. The migration of radionuclides produced in underground nuclear explosions at NTS can provide some information applicable to evaluating the general problem of radionuclide migration. For example, by comparing the $^{99}Tc/^{129}I$ ratio with the calculated production ratio in the Cheshire device, it will be possible to determine whether iodine and technetium, both of which are believed to be anionic in the Pahute Mesa aquifer, do in fact remain unfractionated during migration, as predicted.

• It is generally accepted that the Yucca Mountain area is geologically stable; however, it is possible that periods of increased hydrothermal activity may lead to a pumping of warm water through the site. Evidence for this comes from mineral assemblages that could form either from meteoric water acting in an arid environment or from hydrothermal activity. If the water responsible for the formation of these phases is simply meteoric in origin, there is little danger of unexpected increased transport of radionuclides. If, on the other hand, these phases form from increased groundwater activity, then it is desirable that any increases be understood. Dating of the mineral assemblages using ^{14}C and ^{36}C may shed some light on one or the other of these hypotheses.

Terrestrial *In Situ* Production. The high sensitivity of AMS makes it possible to consider using terrestrial isotopes produced *in situ* as tracers and chronometers for a wide range of surface processes that occurred during the Pleistocene epoch. Some examples are the emplacement of volcanic flows, the retreat of glaciers, the ages of meteorite craters, the ages of evaporite deposits, erosion rates, and a history of the cosmic-ray flux. The use of such isotopes requires a fresh surface not previously exposed to cosmic rays and not heavily eroded. Production rates for the most suitable isotopes (^{10}Be, ^{26}A, ^{36}Cl) are on the order of 10 atoms/(y · g of rock) at sea level. Since AMS generally permits the detection of 10^6 atoms or better, a 1000-year-old deposit could be measured with 100 g of sample to about 10% precision. Because *in situ* production is a new field, much calibration work must be done before the accuracy of dates deduced would approach the analytical precision. The physics of this phenomenon must be investigated, including the determination of flux profiles (neutrons, μ^-) in different exposure conditions and the measurement of neutron and μ^- cross sections. We will also have to consider the effects of exposure geometry and altitude.

• Dating young volcanism ($<5 \times 10^4$ y) is a difficult geologic problem. If biologic material that is unequivocally associated with the flow can be found, ^{14}C would be useful as a chronometer. If biologic material cannot be found, then cosmogenic isotopes produced *in situ* would hold great promise as a tool to approach this problem. The ability to determine the chronology of recent volcanism has practical as well as basic-research applications. For example, assessing the suitability of the proposed high-level nuclear waste disposal site at Yucca Mountain requires assessing the risk of volcanic activity at the site. Assessing the volcanic risk requires knowledge of any recent (≤200,000 y) volcanic history of the proposed area. We will investigate the applicability of terrestrial, cosmic-ray-produced isotope dating to this problem.

• Terrestrial cosmogenic isotopes produced *in situ* could also form the basis

Figure 3. The tandem-accelerator facility now under construction at LLNL.

for a chronometer for the retreat of mountain and continental glaciers. Rocks showing glacial polish can be sampled to ensure that inherited isotopes have been scraped away and that post-glacial erosion has not been severe. The chronology determined from such a study would be an important contribution to understanding the nature of climate change during the Pleistocene epoch.

• It is also possible to study the cosmic-ray flux in the past. Deposits whose ages can be determined by other dating techniques can be used to determine the production rates of terrestrial in-situ produced isotopes in the past.

Test Program. The role for AMS in the Nuclear Test Program would involve abundance determinations of nuclei with very low natural backgrounds that are difficult to measure by decay counting. The charged-particle-detector pair ^{48}Ti-^{49}V is an example. Separated ^{48}Ti can be loaded on a target to trace deuteron (D) and tritium (T) fluxes, which produce ^{49}V. Because D and T fluxes are localized to specific parts of a device, appropriate placement of the ^{48}Ti will give information about mixing during detonation. The one-year half-life, combined with its decay mode of x-ray emission, makes a ^{49}V difficult to measure by counting. Several other heavy isotopes, either products of high-energy neutron reactions or fission products, are possible candidates for AMS analysis. The principal problem is isobaric interferences at these larger masses. A good example is Nb, which is attractive because it alloys with U.

Atmospheric Dynamics. The global dynamics of the atmosphere influence such widely differing processes as climate change and the dispersal of anthropogenic pollutants. Cosmogenic isotopes produced in the atmosphere are useful as tools for understanding the pathways and time scales associated with global atmospheric mixing. The half-lives available range from days to 10^6 years and allow investigation of a wide range of processes extending from short-term turbulent mixing in clouds to secular changes of atmospheric circulation over geologic time periods. The concentrations of many of the longer-lived isotopes are small, so the only practical approach for analysis of these samples is AMS. Outlined below are two examples of possible fields of investigation.

• The production ratio of ^{10}Be (half-life = 1.6×10^6 y) to ^{7}Be (half-life = 53 d) depends on the cross sections for production (primarily from nitrogen and oxygen) and is about 0.5. Once formed, the ^{10}Be and ^{7}Be nuclei become associated with aerosol particles. The ratio measured in an actual air sample then depends on the "irradiation age" of the air mass (i.e., on the time since the air was last washed clean of its aerosols). Therefore, the ^{10}Be:^{7}Be ratio is an indicator for air-mass lifetimes and mixing patterns, in particular, for identifying the injection of stratospheric air into the troposphere. Such measurements could be used to characterize the structure of the stratosphere and even to examine the possible stratospheric source of species such as ozone and nitrate.

• The mechanisms by which aerosol-bound species are transported through the atmosphere and ultimately deposited are not well understood. An understanding of these mechanisms is important when considering the fate of impurities injected into the atmosphere and is necessary for understanding both pollutant dispersal and the use of naturally occurring radioisotopes as geophysical tracers. For example, we see wide variations of the ^{36}Cl:^{10}Be ratio in polar snow. Because the production of these isotopes is constant, we expect the ratio to remain constant. Its observed variation implies an unknown atmospheric transport or deposition process. For example, the ^{137}Cs:^{131}I ratio in the Chernobyl fallout varies, perhaps reflecting the prevailing deposition condition. Do we observe the same fractionation on a global scale? Is a similar mechanism responsible for the natural ^{36}Cl and ^{10}Be variation? We don't know the answers to these questions. Coupling experimental studies of cosmogenic isotopes by using AMS with model calculations that use global circulation models of aerosol transport could help answer these and other questions.

References:

1. D. Elmore and F. M. Phillips, "Accelerator Mass Spectrometry for Measurement of Long-Lived Radioisotopes," *Science* **236**, 236 (1987).
2. D. Shapira, R. M. DeVries, H. W. Fulbright, J. Toke, and M. R. Clover, "The Rochester Heavy Ion Detector," *Nucl. Instrum. Methods* **129**, 123 (1975).
3. R. C. Finkel, M. W. Caffee, K. Marsh, and J. H. Rego, "Accelerator Mass Spectrometry Measurements of ^{129}I and ^{36}Cl in Groundwater from the Nevada Test Site," p. 202 of this publication.

Accelerator Mass Spectrometry Measurements of ^{129}I and ^{36}Cl in Groundwater from the Nevada Test Site

R. C. Finkel, M. W. Caffee, K. V. Marsh, and J. H. Rego

LLNL's Hydrology and Radionuclide Migration Program (HRMP) monitors the migration of radionuclides through aquifers at NTS. To understand how chemistry and colloid transport might influence the migration of radionuclides, it is necessary to acquire data on a range of chemical species, both anions and cations. We are using accelerator mass spectrometry (AMS) to measure low concentrations of ^{129}I (produced by fission) and ^{36}Cl (produced by neutron activation of Cl) in NTS groundwater samples to determine distances and rates of migration from a nuclear test cavity. Radionuclide migration rates from cavity sites must be understood to better manage their environmental impacts, to develop criteria for disposal sites for high-level nuclear wastes, and to provide information on the chemistry and physics of trace-species movement through aquifers.

Sampling

Initially, we analyzed groundwater from the subsurface aquifer surrounding the site of the Cheshire Event. Cheshire was detonated at NTS on February 14, 1976, in a fractured rhyolitic lava formation 1167 m below Pahute Mesa and 537 m below the water table. The announced yield was from 200 to 500 kt. Sampling was done through a reentry hole that was slant-drilled, cased, and perforated within the cavity.

Cavity water was intermittently sampled from 1983 to 1985. In May 1985, the well was plugged at 860 m and reperforated between 763 and 858 m to sample for radionuclides in formation water outside the cavity. Predetonation investigations had shown that the zone sampled is highly permeable and located in the path of water flow from the cavity. External formation water was pumped out of this location from May to November 1985. Because the presence of radionuclides in the reentry hole strongly suggested that radionuclide migration was occurring, a second satellite test well was drilled during May and June 1987, approximately 100 m farther away along the flow path from the cavity.

Experimental Plan

Our initial determinations of the ^{129}I concentrations in Cheshire-associated waters are about 10^{13} atoms/L. This is equivalent to about 1 dpm/L and would be very difficult to measure by decay counting. However, this atomic concentration can readily be determined by AMS. This new technique is an analytical method that couples particle identification by nuclear-accelerator techniques with conventional mass spectrometry to detect extremely rare isotopes. For those isotopes detectable by AMS, it is usually possible to analyze as few as 10^6 atoms of a rare isotope in the presence of as many as 10^{21} atoms of a stable element. The most frequent application of AMS has been the determination of long-lived radioisotopes such as ^{10}Be, ^{14}C, ^{26}Al, ^{36}Cl, ^{41}Ca, and ^{129}I. The development of LLNL's AMS is described in the article beginning on p. 197.

Pending startup of our AMS facility, we have performed some test measurements at the University of Rochester's tandem Van de Graaff AMS. To allow comparison with other isotope measurements made as part of the HRMP program, we chose to measure three water samples, one from each of the Cheshire pumping sites: the bomb cavity (sampled from the reentry hole); the formation water (sampled from the reentry hole after access to the cavity had been

sealed); and water in a satellite hole (about 100 m farther away from the reentry hole).

Although we eventually want to determine the chemical form of a radionuclide as it migrates through the aquifer, our initial experiments tested extraction efficiency of iodine from water samples, independent of its *in situ* speciation. Therefore, we used the formation water samples to test several chemical separation schemes in order to evaluate the ^{129}I extraction efficiency.

After we added an iodine carrier, necessitated by the low iodine content of the groundwater, we extracted iodine from the water sample as I_2, as ICl, and by ion exchange on a bisulfate column. Earlier work had shown that the ICl extraction was likely to lead to complete equilibration of carrier and fission iodine.[1] After extraction, the iodine was precipitated as AgI and measured using the AMS at the University of Rochester.

In addition to three water samples from the formation water, one water sample from the cavity and one from the satellite hole were analyzed. Even at 10^{12} atoms of ^{129}I per liter, the extraordinary sensitivity of the AMS technique was sufficient to allow quantitative measurements with less than 10 μL of water. This very high sensitivity means that we might be able to extend our measurements to tests of significantly lower yield than the Cheshire test.

Our results (Table 1) show that all three iodine extraction methods gave the same concentration for ^{129}I in the formation water. This result gave us confidence that we extracted all the ^{129}I from the water samples. To confirm this, we are investigating the possibility of carrying out either a neutron activation or an inductively coupled, plasma mass spectrometry (ICP-MS) determination of ^{129}I. Either technique would detect all of the ^{129}I present, independent of its speciation.

We have not yet determined ^{36}Cl in water from the Cheshire Event site. We do have samples on hand, and our first measurements were made in the summer of 1988. Calculations based on ^{36}Cl measurements by the Los Alamos National Laboratory on water samples from the Cambric site indicate that we should have little difficulty in analyzing ^{36}Cl in these samples.[2]

Discussion

In Table 2, our ^{129}I results are compared with preliminary results for ^{99}Tc from Ref. 3 and with results for ^{3}H. (Results from our study are also included in Ref. 4.)

The ^{99}Tc values are preliminary but give a ^{99}Tc:^{129}I atom ratio of 2.1 ± 0.6. By comparing the measured ratio with the calculated production ratio in the Cheshire Event, it will be possible to determine whether iodine and technetium, both of which are thought to be anions in the Pahute Mesa aquifer, remain unfractionated during migration as expected.

Conclusions

We have applied AMS to the measurement of ^{129}I in water samples. Sensitivity is sufficient to allow water from a number of HRMP wells to be analyzed. Our methodology for extracting ^{36}Cl was tested in the summer of 1988 at the University of Rochester AMS laboratory. We expect to continue this work sometime within the next year using the LLNL AMS facility.

References:

1. K. V. Marsh in *Radiochemical Purification Procedures for the Elements*, compiled by Manfred Lindner, Lawrence Livermore National Laboratory, Livermore, Calif., UCRL-14258 (1965), p. 57.
2. A. E. Ogard, J. L. Thompson, R. S. Rundberg, K. Wolfsberg, P. Kubik, D. Elmore, and H. W. Bentley, "Migration in Alluvium of Chlorine-36 and Tritium from an Underground Nuclear Test," *Radiochim. Acta* (in press).
3. R. J. Silva, R. Evans, J. H. Rego, and R. W. Buddemeier, *Methods and Results of Tc-99 Analysis of Nevada Test Site Groundwaters*, Lawrence Livermore National Laboratory, Livermore, Calif., UCRL-96399 (1987).
4. K. V. Marsh, J. H. Rego, R. W. Buddemeier, and J. R. Hunt, "Laboratory and Field Studies of Radionuclide Transport in Groundwater," p. 195 of this publication.

Table 1. Reproducibility of ^{129}I in Cheshire formation water.

Extraction technique	^{129}I concentration (10^{12} atoms/L)
ICl	6.28 ± 0.46
I_2	5.91 ± 0.52
Anion exchange	5.82 ± 0.27

Table 2. Comparison of ^{129}I, ^{99}Tc, and ^{3}H measurements.

Sample location (date)	Isotope concentration		
	^{129}I (10^{12} atoms/L)	^{99}Tc[a] (10^{13} atoms/L)	^{3}H[b] (10^{15} atoms/L)
Cavity (10/23/84)	8.3[c]	1.83	10.4
Formation (11/7/85)	7.17	1.75[c]	8.29
Satellite (7/23/87)	10.9	1.61[d]	12.2

[a] Ref. 3.
[b] Ref. 4.
[c] Sample collected 5/29/85.
[d] Ref. 3.

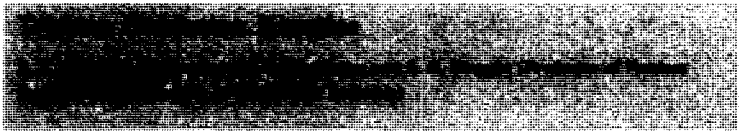

We proposed a sophisticated, computer-modeled mechanism for the formation of tritiated water by the gas-phase reaction of small amounts of tritium in oxygen at one atmosphere and room temperature. We measured the ozone-time profile during this reaction, and our experimental results support the predictions of the model. These experiments are the first time a reaction intermediate of tritiated water formation has been measured.

The biological toxicity of tritium in the form of water (HTO or T_2O) is 25,000 times greater than that of molecular tritium (HT or T_2). It is, therefore, important for the operators of a tritium-handling facility to know what percentage of tritium in the work environment is present as tritiated water and to know the rate of conversion from the molecular form to the water form.

To better understand the formation of tritiated water, we developed a computer model that explains the mechanistic pathways of one of the most basic reactions forming tritiated water—tritium oxidation. Our model's predictions have been discussed elsewhere.[1,2] We are making a series of experimental measurements to test the model's predictions beginning with measurements of the time variation of ozone produced as a by-product of the tritium oxidation reaction.

Model Predictions and Comparison with Experiment

Following the initial phase of the reaction of T_2 and O_2, a point is reached where reactions between four intermediate species dominate the chemistry of the system. The two main sets of reactions incorporate different species but result in the same overall reaction pathway. These reactions are as follows:

$$O_3 + TO_2 \rightarrow OT + 2O_2 \quad (1)$$
$$2TO_2 \rightarrow T_2O_2 + O_2 \quad (2)$$
$$OT + T_2O_2 \rightarrow T_2O + TO_2 \quad (3)$$

$$O_3 + 2TO_2 \rightarrow T_2O + 3O_2 \quad (4)$$

$$O_3 + TO_2 \rightarrow OT + 2O_2 \quad (1)$$
$$OT + TO_2 \rightarrow T_2O + O_2 \quad (5)$$

$$O_3 + 2TO_2 \rightarrow T_2O + 3O_2 \quad (4)\,.$$

Obviously, ozone (O_3) and hydroperoxyl (TO_2) play important roles in the formation of tritiated water.

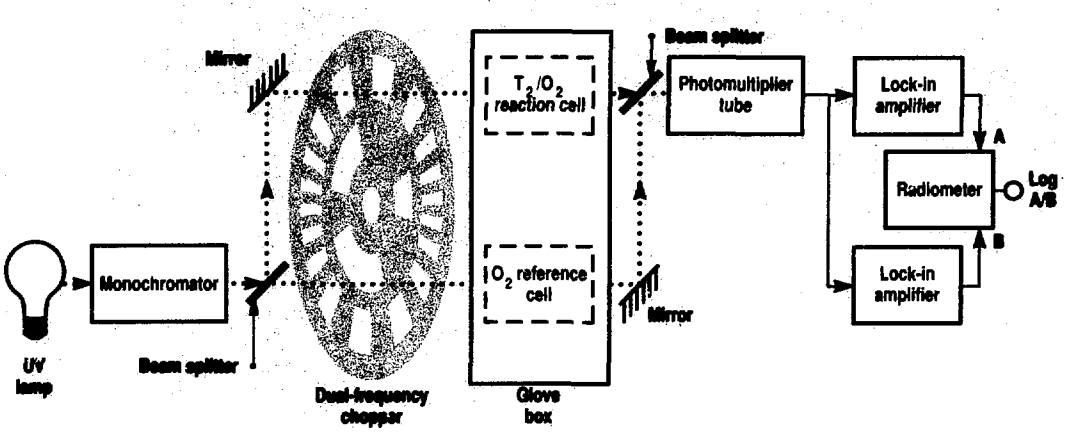

Figure 1. Schematic of the double-beam UV absorption apparatus for ozone detection.

For a variety of reasons,[3] it is very difficult to directly monitor the production of T_2O in a nonintrusive manner at the low concentrations predicted by our model. Since the formation of T_2O is dependent on the ozone concentration, we chose to monitor its formation. Our model predicted that sufficient ozone would be produced so that we could detect it *in situ* using ultraviolet (UV) absorption spectroscopy.

We constructed a UV spectrophotometer that allows us to monitor the ozone concentrations in reaction vessels inside a glove box, which is required for secondary containment because of the high concentrations of tritiated water that may be produced. The main features of the spectrophotometer are shown schematically in Fig. 1.

We have monitored the ozone concentration for initial T_2 concentrations from 0.035 to 1.0% (at a total pressure of one atmosphere and room temperature). Figure 2 shows the variation of the ozone concentration with time for three concentrations. The uncertainties in the ozone measurements are approximately 0.2 parts per million (ppm). The general form of the ozone variation with time is very close to that predicted by the basic model.[4,5] These are the first reported results for the measurement of a reaction intermediate leading to the formation of tritiated water.

We used the reaction-rate constants from literature compilations as input to our model. No adjustments were made to these values to try to fit our predictions to other experimental or theoretical results. Although our model predicted the shape of the ozone profile very well, the actual values of the final predicted ozone concentration were low by as much as a factor of 3. It was evident that we needed to examine our model for a feature that could account for this.

We found that there is one reaction that dominates the removal of ozone from the system:

$$O_3 + TO_2 \rightarrow OT + 2O_2 . \qquad (1)$$

When we reduced the rate constant for just this reaction, our model predictions more closely matched the experimental results. Figure 3 shows ozone concentrations from these adjusted predictions for the three T_2 concentrations shown in Fig. 2. Also included for the 0.035% T_2, for comparison, is the ozone profile case predicted by the model before adjustment of the rate constant for the $TO_2 + O_3$ reaction.

The fact that reducing the rate constant for Rxn. (1) improves the agreement between our model and experiment does not imply that the literature value is inaccurate. Although the accuracy of the rate constants we used varies, the literature rate constant for Rxn. (1) is probably within a factor of 2 of the true value. We do know that the overall rate of Rxn. (1), controlled by the concentrations of the TO_2 and O_3 and the rate constant, is very important to the overall ozone concentration. We will investigate this effect in more detail. However, considering the complexity of the model, the agreement between the model predictions and the experimental results is quite good.

In the reaction of T_2 and O_2, tritium acts in two ways to control the ozone concentration. First, it is the tritium-decay beta particle that radiolyzes the oxygen to form oxygen atoms and, hence, ozone. Second, intermediate species containing tritium, hydroperoxyl, hydroxide, and hydrogen peroxide react with the ozone to control its final concentration. We wanted to find an experimental way to differentiate these two effects.

Since H_2 will undergo the same chemical reactions as the T_2 (though with

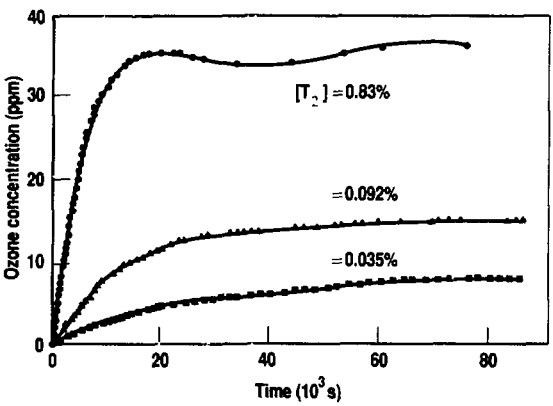

Figure 2. Experimental ozone profiles for three initial concentrations of tritium in oxygen at a total pressure of one atmosphere at room temperature.

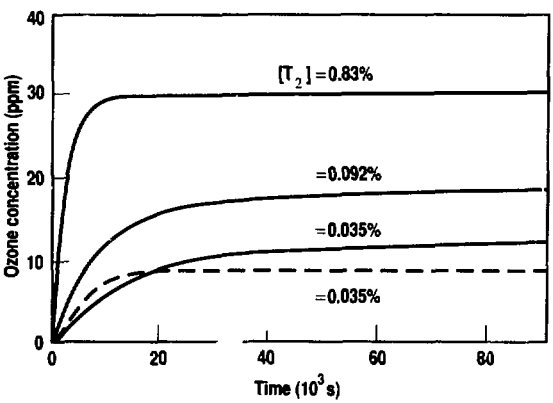

Figure 3. Computer-model-predicted ozone profiles for three initial concentrations of tritium in oxygen. The fourth line (dashed) is the model prediction before adjustment of the rate of the $O_3 + TO_2$ reaction.

accelerated rates as a result of the kinetic isotope effects) but will not introduce any radiolysis, using various mixtures of tritium and hydrogen is a good way to test the relative importance of these two effects on the ozone concentrations. We used the computer model to predict the ozone concentration profile under several combinations of total hydrogen and tritium concentrations and hydrogen-to-tritium ratios. These predictions are shown in Fig. 4.

We expected the change in the ozone concentration with the hydrogen/tritium variation to be a complex function of the effects due to radiolysis versus the effects due to the elementary chemical reactions, such as Rxn. (1). Instead, we find that the ozone concentration depends mostly on the amount of tritium present. Although the reasons for this are somewhat complex, we find the following: When the amount of total hydrogen (combined H_2 and T_2) stays the same but the radiolysis (just T_2) is decreased, species that deplete the ozone are not formed in abundance, and the ozone level remains essentially unchanged.

In our next set of experiments, we will reproduce several combinations of tritium and hydrogen, providing another test of our computer model.

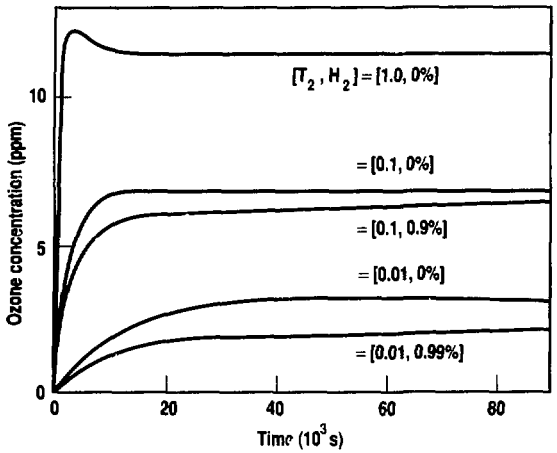

Figure 4. Computer-model-predicted ozone profiles for several combinations of T_2 and H_2. Notice that the final ozone concentration is mostly dependent on the T_2 concentration.

References:

1. R. A. Failor and P. C. Souers, "Tritium Oxidation Kinetics," *Nuclear Chemistry Division FY85 Annual Report*, Lawrence Livermore National Laboratory, Livermore, Calif., UCAR-10062-85 (1985), p. 4-105.
2. R. A. Failor and P. C. Souers, "Tritium Oxidation Kinetics," *Nuclear Chemistry Division FY86 Annual Report*, Lawrence Livermore National Laboratory, Livermore, Calif., UCAR-10062-86 (1986), p. 4-104.
3. R. A. Failor, P. C. Souers, and S. G. Prussin, *Fusion Tech.* (in press); also, *Comments on the Gas-Phase Initial Rate of Tritiated Water Formation*, Lawrence Livermore National Laboratory, Livermore, Calif., UCRL-97411 Rev. 1 (1988).
4. R. A. Failor, P. C. Souers, and S. G. Prussin, *J. Phys. Chem.* **90**, 5974 (1986).
5. R. A. Failor, P. C. Souers, and S. G. Prussin, *J. Phys. Chem.* **92**, 429 (1988).

Weapons Supporting Research

Introduction

The Laboratory's Weapons-Supporting Research (WSR) Program supports fundamental research and preliminary development in disciplines, concepts, and technologies important to LLNL's primary mission of nuclear weapons R&D. As a part of the WSR Program, our Nuclear Chemistry Research Program allows us to maintain a sound intellectual basis for future developments in nuclear-test diagnostics and for contributions to other aspects of nuclear-weapons R&D. The Nuclear Chemistry Research Program, presented in this subsection, embraces four disciplinary research areas—isotope geochemistry, inorganic chemistry, transplutonium element properties, and nuclear structure—and an interdepartmental research collaboration on heavy-ion reactions.

A small disciplinary research project in isotope geochemistry complements our nuclear-test diagnostics mission as advances in the technology of isotope mass spectrometry continue to create new frontiers in both fields. We report on isotopic investigations of gaseous and solid samples from Earth's mantle that provide information about the formation of the atmosphere from the degassing of the solid Earth and about the formation of continental crust from the underlying mantle.

A small research effort in inorganic chemistry provides the scientific foundation for the development of new chemical-separation procedures to meet the requirements of future nuclear-test diagnostics. The research is focused on the behavior of metal ions in solution. FY88's work includes studies of the complexation of lanthanum and thorium ions with multiple fluoride and organic ligands in order to better understand the factors that influence the stability of such complexes in aqueous solution. A newly developed, automated system for rapid chemical separation of actinide elements has been successfully used in studies of the decay properties of berkelium and einsteinium isotopes.

Research on the physical and chemical properties of elements and isotopes heavier than plutonium continues to be a mainstay of the Nuclear Chemistry Research Program. Highlighting FY88's work is the discovery of a new isotope of nobelium (element 102) with 160 neutrons—the largest neutron number of any known nuclide. A study of the chemical properties of lawrencium (element 103) showed that it is unlikely to have a monovalent state in aqueous solution. Also included are a study of the production of the heaviest actinide elements by heavy-ion transfer reactions and investigations of spontaneous fission and other decay modes in heavy actinide and transactinide elements.

Our research on nuclear structure is directed toward a better fundamental understanding of nuclear excitations through comparison of nuclear spectroscopy data with theoretical models. We used in-beam gamma-ray and conversion-electron spectroscopy to identify possible two-phonon octupole states in ^{96}Zr, to help characterize structure symmetries in the platinum region, and to search for a gamma-ray decay branch in the ^{237}Np shape isomer. We used inelastic electron scattering as an electromagnetic probe to investigate the recently discovered M1 scissors mode of nuclear vibration in deformed rare-earth nuclei. Single-proton transfer reactions were used to investigate the proton-shell closure at Z = 64 protons

and to study octupole deformations in ^{227}Ac. Also included are a survey of the nuclear structure of deformed odd-odd nuclei and a new theoretical approach to providing reliable predictions of nuclear properties along the astrophysical r-process path.

In a joint research initiative with the LLNL Physics Department, we are studying nuclear reaction mechanisms and the properties of nuclear matter under extreme conditions produced in heavy-ion accelerator bombardments. Current studies deal with nuclear fragmentation at intermediate and relativistic energies.

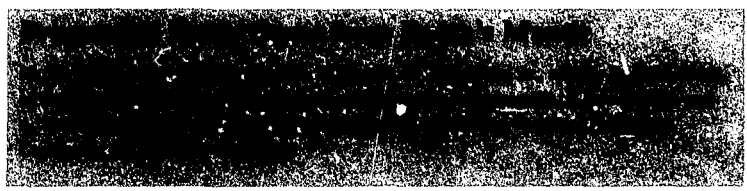

The history of the early solar system, including the formation of the planets, is of considerable scientific interest. To understand the circumstances that led to the formation of Earth, we rely on the chemical and isotopic analyses of solar system materials. We have an assortment of materials to examine: meteorites, lunar samples, and Earth itself. Direct measurements of these samples can be compared with data obtained from the photospheric spectrum of our Sun, from solar-wind data, and from solar-flare data from satellite-based observations. One area where we are lacking is in our knowledge of the chemical and isotopic composition of the entire Earth. This lack of knowledge has less to do with measurement capabilities than with the availability of samples to study.

Earth's mantle and core contain about 99.6% of its mass, leaving less than 1% in the crust and atmosphere. Although the crust is derived from the mantle, it has undergone extensive changes. Thus, it is generally not possible to use crustal material to study the entire Earth and how it formed. Studying material from the mantle would yield better information about Earth's composition as a whole. Unfortunately, it is difficult to obtain mantle material, since the mean thickness of the crust is 17 km. There are, however, two types of mantle samples available to us: igneous rock erupted from the mantle, such as basaltic rocks produced at the midocean ridges, and gaseous emanations from deep wells.

Discussion

The noble gases are useful for studying geologic activity because of their chemical inertness and low abundance. Xenon is especially interesting. The nine stable isotopes of xenon (with masses between 124 and 136) are produced in a variety of ways. The spontaneous fission of nuclei such as ^{238}U produces measurable quantities of the heavier xenon isotopes (masses 131 to 136). Often it is possible to use the relative abundance of the xenon fission products to determine which nuclei fissioned. Early in the history of the solar system, ^{129}I (half-life of 1.6×10^6 years) was sufficiently abundant to produce measurable ^{129}Xe. Most primitive meteorites contain ^{129}Xe from the decay of ^{129}I. Rather surprisingly, some terrestrial samples contain ^{129}Xe from ^{129}I decay.

There are three known reservoirs of xenon in our solar system. The first and

largest is the xenon in our Sun. The isotopic composition of solar xenon is known from studies of solar-wind-implanted xenon in lunar soils and in a few special meteorites.

The second reservoir of xenon, called planetary xenon, is that found in meteorites. The isotopic composition of the light xenon isotopes (masses 124 to 128) of planetary xenon is almost identical to that of solar xenon. This is not the case for the heavy xenon isotopes, which are conspicuously different. The composition differences cannot be explained in a simple fashion and have been a topic of controversy for several decades.

The third reservoir of xenon is found in Earth's crust and atmosphere. The light isotopes in atmospheric xenon are related to the other two reservoirs by mass fractionation. The process of mass fractionation refers to a shift in isotope ratios for a given element that is approximately a linear function of mass difference between the two isotopes used for the ratio. The effect is related to atomic and molecular velocity effects: different masses move at different speeds. Diffusion is an example of a process that produces mass fractionation. When or how the mass fractionation of atmospheric xenon occurred is unknown. Again, the relationship between heavy atmospheric xenon isotopes and heavy isotopes from either of the other two sources is not simple. It is certain, from comparisons with planetary or solar xenon, that atmospheric xenon contains ^{129}Xe from ^{129}I decay. It is also clear that heavy isotopes of atmospheric xenon contain xenon from the decay of ^{244}Pu. Again, this nuclide was present in the early solar system but is now extinct because of its short half-life of 8.2×10^7 years.

The first question to answer is whether the xenon isotopic composition of the mantle differs from that of the present-day atmosphere. There are several reasons why it might. One has to do with the formation of Earth's atmosphere. Earth's present atmosphere is not a primordial atmosphere, as are the atmospheres of the giant gaseous planets. Their atmospheres were gravitationally captured from the presolar nebula during their formation. It is possible that Earth also had such an atmosphere but lost it.

Earth's present-day atmosphere originated from a degassing of the solid Earth. In simple terms, volcanic eruptions brought volatile elements to Earth's surface. These volatiles were gravitationally bound to Earth (except hydrogen and helium), and the gaseous elements formed an atmosphere. By studying the isotopic composition of xenon in mantle-derived samples, we may be able to learn when the mantle outgassed.

Consider the possibility that the atmosphere formed very quickly and that, before all of the ^{129}I and ^{244}Pu decayed, some of the mantle xenon was expelled into the atmosphere. Then, present-day xenon in the mantle would have an excess of ^{129}Xe and ^{244}Pu fission-derived xenon relative to the composition of atmospheric xenon. Both igneous rocks and gases from CO_2 wells would show such excesses of ^{129}Xe.[1,2] In this scenario, we would also expect to find ^{244}Pu-derived xenon, since plutonium has a longer half-life than ^{129}I. However, no clear evidence for ^{244}Pu-derived xenon has previously been reported.

To test our hypotheses, we have analyzed the noble gases (helium, neon, argon, and xenon) from three separate deposits of CO_2 gas: two in Colorado (McElmo Dome and Sheep Mt.) and one in Australia (Caroline).[3] As discussed later, the sample from the Caroline gas well does show evidence for ^{244}Pu fission xenon.

Results

What do noble gases say about the mantle? Because it is neither gravitationally bound nor produced significantly in naturally occurring nuclear reactions, ^{3}He has the smallest concentration of all the stable isotopes in the terrestrial atmosphere. In comparison, ^{3}He is relatively abundant in the solar system as a whole. Thus, the observation of samples with a ^{3}He:^{4}He ratio greater than that in the atmosphere is evidence for the degassing of a primitive composition. The CO_2 samples from the Caroline gas well show a clear enrichment in ^{3}He with a ^{3}He:^{4}He ratio three times greater than the atmospheric ^{3}He:^{4}He ratio.

Neon isotopes tell a similar story. Several types of mantle sample, including diamonds,[4] have ^{20}Ne:^{22}Ne ratios higher than the atmospheric ratio. There are two possible explanations. The first is that the neon is severely mass fractionated. The second is that the mantle contains a reservoir of solar-like neon. All of the CO_2 well gases we analyzed have high ^{20}Ne:^{22}Ne ratios. The measured ^{20}Ne:^{22}Ne ratio for Caroline CO_2 is about 12 compared with ratios for atmospheric neon of 10 and solar neon of 14. The shift from 10 to 12 is too large for mass fractionation to be a reasonable explanation. So, like the helium data, neon-isotope measurements show a significant contribution from solar-like noble gases.

Previous studies of xenon showed excess ^{129}Xe in mantle-derived samples. This may be telling us that Earth's atmosphere formed quickly by degassing of the mantle before all ^{129}I in the mantle had decayed. In the Caroline CO_2 gas sample, the xenon isotopic composition is quite different from that of atmospheric xenon. The Caroline xenon composition closely matches a mixture consisting of 9% planetary xenon and 91% atmospheric xenon. There are fission contributions to the xenon heavy isotopes. These are dominated by ^{238}U spontaneous fission; however, it is possible that about 20% of the fission is due to ^{244}Pu decay. Given their somewhat complementary compositions, the presence of the planetary xenon hides the presence of fission xenon from ^{244}Pu. The observation of only a small amount of excess ^{244}Pu fission xenon in mantle samples, despite the fact the mantle has stayed partially isolated from the atmosphere, shows that degassing occurred after most of Earth's ^{244}Pu had decayed (a few times 10^8 years).

Conclusions

The detection of a source of xenon in the mantle that matches the composition of xenon found in meteorites constrains us to change our view of the formation of Earth's atmosphere. The conventional view is that ^{129}I was incorporated into Earth during its accretion. The decay of this ^{129}I is responsible for the excesses of ^{129}Xe observed in mantle samples. However, the presence of a meteoritic component in the xenon as seen in the Caroline sample presents other possibilities. Earth may have accreted materials already containing ^{129}Xe from the decay of ^{129}I. In this model, we are not required to rapidly degas Earth in order to generate excess ^{129}Xe in the mantle. This scenario would be consistent with a very small effect due to ^{244}Pu, since we can wait for most of the ^{244}Pu to decay before degassing Earth. Accordingly, because of the lack of excessive ^{244}Pu fission xenon, we conclude that the degassing of the mantle must have occurred after most of Earth's ^{244}Pu had decayed, that is, a few times 10^8 years.

References:

1. D. Phinney, J. Tennyson, and U. Frick, *J. Geophys. Res.* **83**, 2313 (1978).
2. C. J. Allegre, Th. Staudacher, Ph. Sarda, and M. Kurz, *Nature* **303**, 762 (1983).
3. A. R. Chivas, I. Barnes, W. C. Evans, J. E. Lupton, and J. O. Stone, *Nature* **326**, 587 (1987).
4. M. Honda, J. H. Reynolds, E. Roedder, and S. Epstein, *J. Geophys. Res.* **92**, 12,507 (1987).

Subcrustal Sources for Basalts and Mantle Pyroxenites from Northern Mexico

G. J. Nimz (Earth Sciences Board, University of California, Santa Cruz, Calif.); S. Niemeyer; and K. L. Cameron (Earth Sciences Board, University of California, Santa Cruz, Calif.)

We are determining the strontium, neodymium, and lead isotopic compositions of northern Mexican volcanic rocks and samples of Earth's upper mantle that were entrained in these lavas. These isotopic measurements test a hypothesis that a major continent-building event occurred 25 to 35 million years ago along southwestern North America. The analyses suggest that, indeed, more than 4 km of continental crustal thickness were added to the continent at that time.

Earth's upper mantle extends from the base of the crust, which in continental areas is typically 30 to 50 km beneath the surface, to a depth of about 650 km. As basaltic magmas pass through the upper 100 km of the mantle, fragments of the mantle are broken from the conduit walls, entrained within the magma, and eventually erupted onto the surface. These fragments are termed mantle xenoliths, and they provide our only direct information on the mineralogic and chemical composition of Earth's upper mantle.

One such eruption occurred at La Olivina, northern Mexico, about 160 km southwest of Big Bend National Park. Two basic types of xenoliths are found: peridotites (in which olivine dominates) and pyroxenites (in which clinopyroxene dominates). Most of the upper mantle consists of peridotite. Pyroxenites occur within the mantle as veins (centimeters to meters thick) formed through precipitation of minerals onto conduit walls by basaltic magmas. We have analyzed pyroxenite xenoliths from this site, their host basaltic lavas [2 million years (Ma) old], and mid-Cenozoic (25- to 35-Ma-old) basalts from northern Mexico for strontium, neodymium, and lead isotopic compositions.

Isotopic Results

We have discovered that two isotopically distinct pyroxenite varieties occur. A clear distinction between them can be seen on all three isotopic systems shown in Fig. 1. On the strontium-neodymium isotope covariation diagram (a), one group of pyroxenites (the "A-type") forms a tight cluster near the host basalts, while the other variety (the

"E-type") forms a more diffuse field, which partially overlaps the field formed by the older, mid-Cenozoic basaltic rocks. The same associations can be seen on the lead-lead isotope covariation diagrams (b). The close association of each pyroxenite group with its respective basalt group clearly suggests that the A-type pyroxenites formed as precipitates from magmas associated with the host basalt, while the E-type pyroxenites formed from the mid-Cenozoic basalts in a similar manner. Preliminary analysis of the La Olivina peridotites suggests that the small displacement observed for each pyroxenite group relative to its associated basalt group on the isotopic diagrams probably results from the reaction of the pyroxenites with the peridotite wallrock they now vein.

Geologic Significance

It has been demonstrated that the entire mid-Cenozoic volcanic sequence in northern Mexico, which contains rocks that range from 48 wt% SiO_2 (basalts) to 76 wt% SiO_2 (rhyolites), could have originated from mantle-derived basaltic magmas.[1–3] The differentiation process, in which the most siliceous lavas formed from the least siliceous through crystal extraction from the magmas, would have added more than 4 km of thickness (crystal segregates) to the crust in northern Mexico.[1] This crustal growth would have occurred within a 10-Ma time span—incredibly rapid by geologic standards. However, if the basaltic magmas did not originate within the mantle but originated within the crust, no material would have been added to the crust. The fact that the E-type pyroxenites formed from the mid-Cenozoic basalts is then highly significant. Geothermometry and geobarometry calculations, which indicate the temperatures and pressures of formation of the E-type pyroxenites, and the association of the pyroxenites with mantle peridotites both indicate that the E-type pyroxenites were formed in the mantle. The mid-Cenozoic basalts that formed them must, therefore, also have originated within the mantle. The existence of the E-type pyroxenites implies that a major mid-Cenozoic crust-forming event did occur in northern Mexico.

Because basalts will have the same isotopic compositions as the mantle rocks that melt to produce them, mantle-derived basalts can be used as probes of

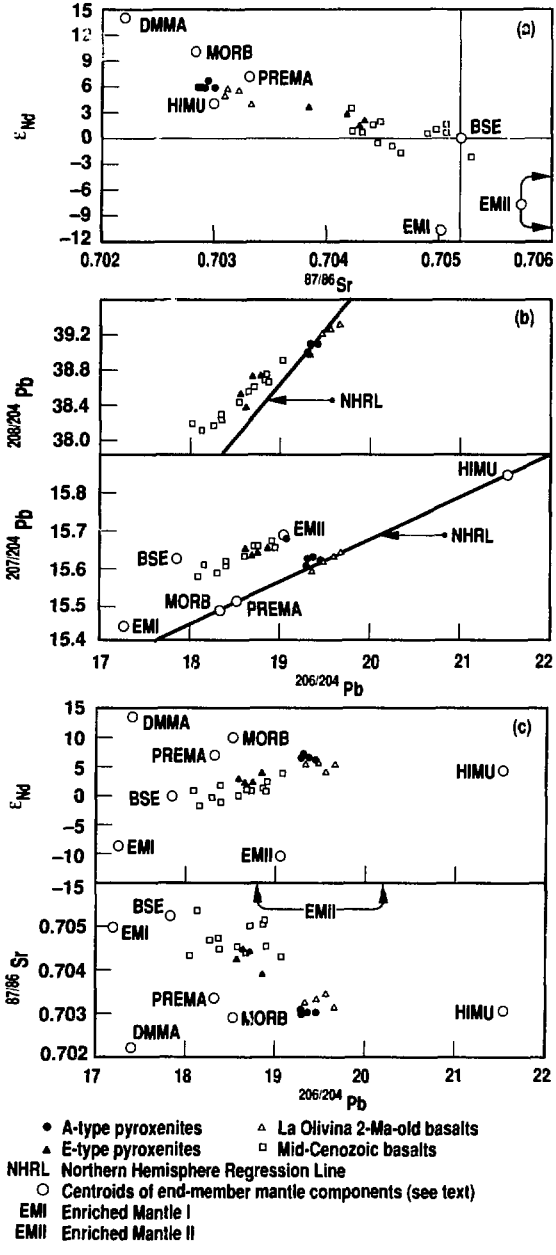

Figure 1. Isotope covariation diagrams for La Olivina pyroxenites and basalts and the northern Mexican mid-Cenozoic basalts. The line labeled NHRL is drawn through data (not shown) for mantle-derived oceanic basalts in the northern hemisphere. For a full discussion of the various mantle components, see Zindler and Hart.[4]

the composition of the mantle. In continental areas, basaltic magmas can be contaminated by crustal rocks as they rise to the surface. The utility of mantle pyroxenites is that they indicate the isotopic composition of the basalts from which they formed before crustal contamination could occur. The pyroxenites can then be used as probes to mantle regions even deeper than those in which they occur.

Because of the broad range of isotopic compositions observed in uncontaminated mantle-derived basalts, it is convenient to discuss the isotopic chemistry of the mantle in terms of end-member components that are present in varying degrees in the source regions of the basalts. Mixtures of the components give rise to the isotopic compositions observed in the basalts. Centroids for the isotopic components commonly discussed in the literature[4] are shown in Fig. 1.

The neodymium isotopic compositions are expressed as ε_{Nd}, where

$$\varepsilon_{Nd} = \left[\left(\frac{^{143/144}Nd_{measured}}{^{143/144}Nd_{CHUR}} \right) - 1 \right] \times 10^4, \quad (1)$$

and $^{143/144}Nd_{CHUR} = 0.512636$. This is an assumed present-day value for a geochemical reservoir with a chondritic samarium:neodymium ratio.

The lead isotopic composition of the E-type pyroxenites indicates that the source region for the basalts that formed them contains the "Enriched Mantle II" (EMII) component. This component shows long-term enrichment in certain trace elements (uranium relative to lead, rubidium relative to strontium, neodymium relative to samarium). Time-integrated radioactive decay has resulted in more radiogenic lead and strontium and less radiogenic neodymium isotopic compositions than are prevalent in the mantle. It is likely that this component was derived from pelagic sediment that was brought into the mantle by a subducting oceanic lithospheric slab. This is a reasonable conclusion because it is commonly believed that the subduction of such a slab caused the mid-Cenozoic volcanism in the region. The utility of examining the E-type pyroxenites in this context is that they indicate that the EMII component is subcrustal and is not a result of contamination of the basalts by continental crust, which would have isotopic compositions similar to those of pelagic sediment.

The A-type pyroxenites and host basalts have unusual lead isotopic values for continental alkali basalts. The compositions require, in their mantle source areas, the presence of a component with an isotopic composition that is the result of time-integrated, very high uranium:lead ratios. This component, which is also seen in certain ocean island basalts (e.g., Azores, Ascension Island), is termed the HIMU component by Zindler and Hart[4] (see Fig. 1). It indicates an old [perhaps 1- to 3-billion-year-(Ga) old] geochemical disturbance in the mantle region that fractionated lead from uranium. The positions of the samples on the strontium-lead and neodymium-lead isotope covariation diagrams in Fig. 1(c) show the necessity of the HIMU component in their mantle source. Mixing between an HIMU component and a depleted mantle component (e.g., mid-ocean-ridge basalts, MORB or prevalent mantle, PREMA) could produce the isotopic source compositions for the A-type pyroxenite-forming basalts. Published lead isotopic data from North American late Cenozoic undersaturated lavas form an array with a higher positive slope than the Northern Hemisphere Regression Line (NHRL) of Hart[5] (Fig. 2). The La Olivina host basalts plot below this array, showing lower $^{207/204}Pb$ values for similar $^{206/204}Pb$ values. A significantly different mantle source is implied for the La Olivina host basalts than for the other late-Cenozoic North American basaltic rocks.

The strontium-neodymium-lead isotopic values for the E-type pyroxenites and mid-Cenozoic basalts are in the same range as late-Cenozoic alkaline basalts from the northern Rio Grande Rift-Southern Colorado Plateau region.[6,7] The strontium-neodymium compositions of the A-type pyroxenites and host basalts are similar to those of late-Cenozoic basalts from the southern Rio Grande Rift-Basin and Range region.[6] La Olivina is within the Basin and Range province and directly south of the Rio Grande Rift. To explain the differences in the strontium-neodymium isotopic compositions between the northern and southern rift basalts, Perry et al.[6,7] have suggested that the northern basalts were derived from old trace-element-enriched mantle directly underlying the crust, whereas in the south, the enriched mantle has been mostly removed by continental rifting processes and replaced with upwelling trace-element-depleted mantle. They suggest that the enriched mantle keel is enriched as a whole because of numerous small pods of pyroxenite or

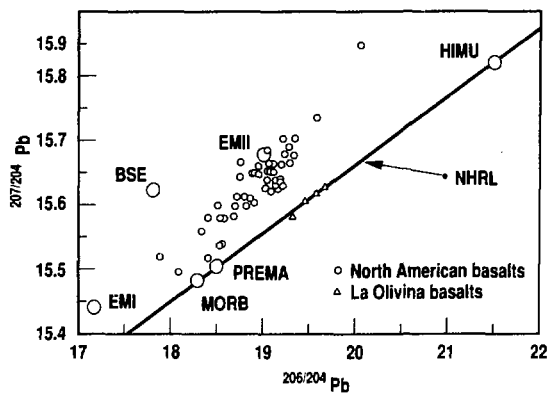

Figure 2. $^{207/204}Pb$ vs $^{206/204}Pb$ for the La Olivina 2-Ma-old basalts compared with other recent (0- to 10-Ma-old) undersaturated basalts of western North America. See Fig. 1 for an explanation of NHRL and other symbols.

chemically altered peridotite that are absent in the underlying depleted mantle. The lower $^{143/144}Nd$ and higher $^{87/86}Sr$ composition of these pods is a time-integrated result of trace-element enrichment that occurred during continent formation in the region (1.7 Ga ago). We instead suggest that the E-type pyroxenites (and perhaps mantle that was chemically altered by interaction with the pyroxenites) may represent these enriched pods and that the enrichment would not, therefore, be a 1.7-Ga event, but mid-Cenozoic. Therefore, the lower $^{143/144}Nd$ and higher $^{87/86}Sr$ values would not have resulted from time-integrated radioactive decay within a mantle keel but would have been derived ultimately from the mantle source(s) that produced the mid-Cenozoic volcanism.

Summary

The isotopic study of the La Olivina mantle pyroxenites undertaken at LLNL is one of the first of its kind. We have demonstrated that mantle pyroxenites can be used to answer difficult questions concerning continental basalt petrogenesis. At La Olivina, the pyroxenite study has demonstrated that the mid-Cenozoic basalts were mantle derived and that, if we assume the entire mid-Cenozoic volcanic sequence was derived from the basaltic magmas, a major crust-forming event did occur in southwestern North America 25 to 35 Ma ago. As probes to the continental mantle, the pyroxenites have demonstrated that mid-Cenozoic basalts had a mantle source region that contained the EMII component and that the 2-Ma-old basalt source contained the HIMU component. Finally, on the difficult subject of the timing of enrichment events in the mantle underlying southwestern North America, the study of the E-type pyroxenites suggests that the enrichment implied by the Colorado Plateau basalts was not a 1.7-Ga-old event but, rather, occurred during the mid-Cenozoic epoch.

References:

1. M. Cameron, W. C. Bagby, and K. L. Cameron, *Contrib. Mineral. Petrol.* **74**, 271 (1980).
2. K. L. Cameron and M. Cameron, *Contrib. Mineral. Petrol.* **91**, 1 (1985).
3. R. Gunderson, K. Cameron, M. Cameron, *Geol. Soc. Am. Bull.* **97**, 737 (1986).
4. A. Zindler and S. Hart, *Ann. Rev. Earth Sci.* **14**, 493 (1986).
5. S. R. Hart, *Nature* **309**, 753 (1984).
6. F. V. Perry, W. S. Baldridge, and D. J. DePaolo, *J. Geophys. Res.* **92**, 9193 (1987).
7. F. V. Perry, W. S. Baldridge, and D. J. DePaolo, *Nature* **332**, 432 (1988).

Hydrolysis of the La[2.2.1] Cryptate

R. A. Torres and P. A. Bulsing

We are studying the properties of the lanthanide ions in aqueous solution and are particularly interested in understanding the factors that influence the stability of the complexes they form with various ligands. The bonding in lanthanide complexes is typically electrostatic since the valence electrons that might participate in covalent (shared) bonds are buried rather deeply in a tripositive lanthanide ion. Because the electrostatic attraction between oppositely charged species is strong, aqueous lanthanide complexes with negatively charged ligands are common. However, for a neutral ligand, the electrostatic attraction is of the weaker ion-dipole type. Since most neutral ligands cannot overcome the ion-dipole interactions between the lanthanide ion and solvent water molecules, which are present in much higher concentration than is the ligand, lanthanide complexes with neutral ligands are relatively rare.

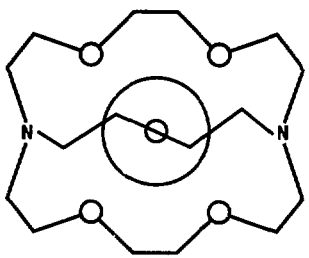

Figure 1. Structure of a metal[2.2.1] cryptate.

Cryptand[2.2.1] (Fig. 1) is an example of a neutral ligand that does form relatively stable lanthanide complexes. It forms *inclusion* complexes, where the metal ion is inside a cavity formed by the nitrogen and oxygen electron-donor groups. Therefore, the metal ion in a cryptate complex is shielded from the solvent water molecules to a larger extent than usual. For this reason, while a lanthanide cryptate irreversibly dissociates to form uncomplexed lanthanide and cryptand in aqueous solution, the kinetics of the dissociation are slow enough (hours to days) to allow us to study the complexes by traditional methods.[1,2]

Because the electron donor groups of the cryptand ligand do not completely saturate the possible number of coordination sites in a lanthanide ion (8 to 10), several water molecules still occupy inner-sphere coordination sites in the complex. Other ligands can displace the water molecules and form *mixed* ligand complexes as shown in the reaction:

$$La[2.2.1](H_2O)_n + X \rightleftarrows La[2.2.1](X)(H_2O)_{n-1} + H_2O \quad (1)$$

We studied the hydrolysis of La[2.2.1] ($X = OH^-$) by potentiometric titration to measure the stability constant and by proton-nuclear magnetic resonance (PMR) spectroscopy to obtain structural information about the hydrolyzed species that form.

Experimental

We synthesized the solid $La[2.2.1](NO_3)_3$ according to the procedure developed by Pruett.[3] We measured the stability constant for the La[2.2.1] hydrolysis reaction by potentiometric titrations with a glass electrode, using sodium hydroxide as titrant. The stability constant was obtained by fitting the experimental hydroxide mass balance, known from the concentrations of the reactants, to the theoretical one calculated from the stability constant and the measured pH. We calibrated the electrode in hydroxide-concentration units (not activity) by titrating standardized HCl with NaOH. All titrations were made at 5°C, and all solutions had an ionic strength of 1.0*M* with NaCl as the inert electrolyte. We chose 5°C as the operating temperature to slow the dissociation kinetics of La[2.2.1] as much as possible. We used NaCl as the supporting electrolyte rather than $NaClO_4$ because La[2.2.1] forms an insoluble species at pH >7 in perchlorate media. We did not encounter any solubility problems when the chloride ion was used.

We monitored the changes that occurred in the PMR spectrum of the La[2.2.1] as titrant was added in parallel experiments. Fourier-transform PMR spectra were measured at 200 MHz with sodium 2,2-dimethyl-2-silapentane-5-sulfonate (DSS) as the internal reference. Except for the use of D_2O rather than H_2O, all experimental conditions were identical to those of the potentiometric titrations.

Results and Discussion

Our potentiometric data indicate the presence of one hydrolyzed species, namely, $La[2.2.1](OH)^{2+}$. The corresponding stability constant, K_{app}, for the hydrolysis reaction (1) is $\log K_{app} = 4.80 \pm 0.02$. A convenient way to compare titrations performed at different La[2.2.1] concentrations is to calculate the average number of hydroxides bound per metal, n_{OH}, which depends only on pH. Figure 2 displays the agreement between the experimental data from three titrations and the speciation calculated using this stability constant. Systematic deviations are present, which could indicate errors in the reactant concentrations or in the speciation model. The inclusion of $La[2.2.1](OH)_2^+$ as an important species does not improve the fit, nor do we obtain a significantly better fit by including a dimer, $La[2.2.1]_2(OH)_2^{4+}$. The dimeric species has been characterized in the solid state and in nonaqueous solution for the analogous praseodymium cryptate.[4] We believe that the deviations occur because of slight concentrations of free lanthanum that are generated by the dissociation of La[2.2.1]. The free lanthanum also reacts with hydroxide and ultimately forms $La(OH)_3$ in the range of pH 8 to 9, causing systematic deviations in this pH region. Analysis by ethylene-dinitrilotetraacetic acid (EDTA) titration showed that about 1% of the La[2.2.1] had dissociated and formed insoluble $La(OH)_3$ by the end of the potentiometric titrations.

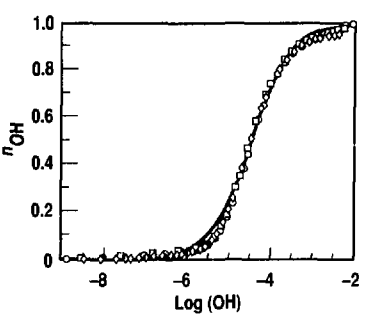

Figure 2. A comparison of the speciation calculated using the hydrolysis constant $\log K_{app} = 4.80$ and experimental data from three titrations of La[2.2.1] with hydroxide. The speciation is expressed as n_{OH}, the average number of hydroxides bound per metal atom.

The PMR spectra of La[2.2.1] at several ratios of total hydroxide added to total La[2.2.1] are shown in Fig. 3. Resonances caused by $N\text{-}CH_2$ protons are upfield (low ppm), and those due to $O\text{-}CH_2$ protons are downfield (high ppm).[5] We clearly see the disappearance of $N\text{-}CH_2$ resonances at 3.2 ppm and the appearance of new $N\text{-}CH_2$ resonances at 3.4 ppm as more hydroxide is added. This indicates the existence of two different La[2.2.1] species that are slow to exchange on the microsecond time scale of the pulsed PMR experiment. The simplest explanation would be that the resonances at 3.2 ppm are those of the unhydrolyzed $La[2.2.1]^{3+}$, while the resonances at 3.4 ppm are those of the hydrolyzed $La[2.2.1](OH)^{2+}$. However, this is not very likely because aqueous lanthanide complexes are usually very labile (i.e., ligand exchange rates are very rapid). Therefore, during the microsecond duration of the PMR experiment, a ligand molecule is complexed to many different metal cations, although the fractions of the

time it is bound and free are directly proportional to the overall macroscopic speciation. Reaction (2) shows one way of writing the ligand exchange reaction for La[2.2.1] hydrolysis:

$$\text{La[2.2.1]} + \text{La[2.2.1](OH)} \rightleftarrows \text{La[2.2.1](OH)} + \text{La[2.2.1]}. \quad (2)$$

Rapid hydroxide exchange would result in a single resonance that is the average of the resonances of the individual species, while slow exchange would cause separate resonances.

Even though our chemical intuition would discard the possibility of slow hydroxide exchange in aqueous solution, we attempted to model the PMR spectra under this assumption. If the assumption is correct, the relative areas of the two resonances at each point in the PMR titration should agree with the relative amounts of $La[2.2.1]^{3+}$ and $La[2.2.1](OH)^{2+}$ predicted by the hydrolysis constant. The blue line in Fig. 4 shows that the PMR data do not agree very well with the speciation predicted by the hydrolysis constant.

Since the two-component model does not agree with the potentiometric data, we must include at least three components, two of which interconvert slowly on the PMR time scale, causing the separate resonances. Furthermore, the three-component model should still allow for the existence of labile aqueous hydroxy complexes. This suggests that the "slow" exchange process is a type of isomerization and not a hydroxide-exchange process between unhydrolyzed and hydrolyzed species. Because the cryptand ligand contains two bridgehead nitrogen atoms, several structures are possible, depending on whether the nitrogen lone pairs are directed inside toward the center of the cryptand (an *endo* conformation) or away from the cavity (an *exo* conformation). Thus, three possible cryptate conformers might exist: *endo-endo*, *exo-exo*, and *endo-exo*. We will denote these conformations as (*i,i*), (*o,o*), and (*i,o*) for *i*nside and *o*utside nitrogen orientations. Therefore, changes in conformation involving nitrogen inversion are a reasonable explanation for the separate resonances we observe in the PMR spectrum as hydroxide is added.

The existence of these different cryptate conformers has long been postulated.[6] Although some kinetic dissociation data indirectly suggest that different metal-cryptate conformers might exist,[7] no direct spectroscopic evidence for their existence has been reported until now. A model that is consistent with all of our data is as follows:

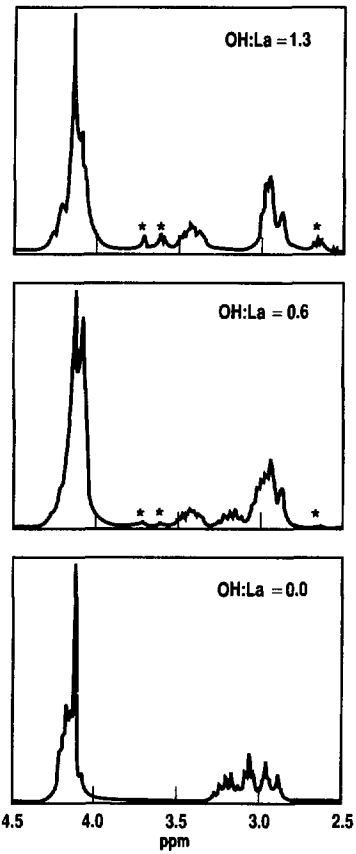

Figure 3. PMR spectra of La[2.2.1] at three ratios of total hydroxide added to total La[2.2.1]. Na[2.2.1] peaks are indicated by an asterisk.

$$\text{La[2.2.1]}_{(i,i)} + \text{OH} \rightleftarrows \text{La[2.2.1](OH)}_{(i,i)} \text{ fast}, \quad (3)$$

$$\text{La[2.2.1](OH)}_{(i,i)} \rightleftarrows \text{La[2.2.1](OH)}_{(i,o)} \text{ slow}. \quad (4)$$

Reaction (3) is a typical hydrolysis reaction, which we expect to be very labile in aqueous solution; Reaction (4) is a conformational change promoted by the hydroxide ion. While nitrogen inversion is severely restricted in the

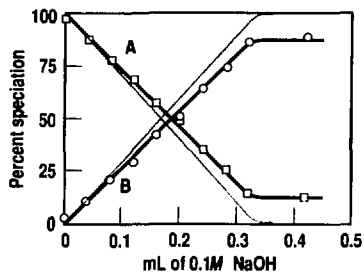

Figure 4. Correlation of the speciation observed by PMR (points) and the speciation predicted by potentiometry (curves) for the La[2.2.1] + OH system. For the fit to two components (blue curve), "A" is La[2.2.1] and "B" is La[2.2.1](OH). For the three-component fit, "A" is $La[2.2.1]_{(i,i)}$ + $La[2.2.1](OH)_{(i,i)}$, and "B" is $La[2.2.1](OH)_{(i,o)}$. [See text for definition of (*i,i*) and (*i,o*).]

unhydrolyzed La[2.2.1], the formation of the lanthanum–hydroxide bond probably weakens the nitrogen–lanthanum interaction and allows the nitrogen to invert.

For this model, the PMR resonance at 3.2 ppm is an averaged resonance from the rapidly exchanging $La[2.2.1]_{(i,i)}$ and $La[2.2.1](OH)_{(i,i)}$, while the new resonance at 3.4 ppm is solely a result of the $La[2.2.1](OH)_{(i,o)}$. The potentiometric titration, which cannot distinguish between the two hydrolyzed conformers, gives an apparent stability constant, K_{app}. This constant depends on the hydrolysis constant, K_1, of Reaction (3) and the equilibrium constant, K_{conf}, for the conformational change of Reaction (4). That is,

$$K_{app} = K_1 \cdot (1 + K_{conf}) . \qquad (5)$$

The solid line in Fig. 4 shows the agreement between this three-component model and our potentiometric data using the fitted values $K_1 = 7.2 \pm 0.3 \times 10^3$ M^{-1} and $K_{conf} = 7.8 \pm 0.5$.

Summary

We have PMR evidence that two conformations of hydrolyzed La[2.2.1](OH) occur in aqueous solution. The interconversion occurs slowly on a microsecond time scale, giving rise to separate PMR signals. We suggest that inversion at one of the nitrogen atoms in the La[2.2.1](OH) complex is the most likely explanation for the conformational difference. We have measured the hydrolysis constant and the equilibrium constant for the conformational change by correlating the PMR data with the apparent hydrolysis constant that was measured by potentiometric titration of La[2.2.1] with hydroxide.

References:

1. R. A. Torres and P. A. Baisden, "Potentiometric and NMR Studies of La[2.2.1] Complexes," *Nuclear Chemistry Division FY87 Annual Report*, Lawrence Livermore National Laboratory, Livermore, Calif., UCAR-10062-87 (1987), p. 4-27.
2. E. L. Yee, O. A. Gansow, and M. J. Weaver, *J. Amer. Chem. Soc.* **102**, 2278 (1980).
3. D. J. Pruett, *Synthesis and Chemical Studies of Some Lanthanide Cryptates*, Ph.D. thesis, Michigan State University, East Lansing, Mich. (1978).
4. J. Rebizant, M. R. Spirlet, P. P. Barthelemy, and J. F. Desreux, *J. Inclusion Phenomena* **5**, 505 (1987).
5. R. A. Torres and P. A. Baisden, "Studies of La[2.2.1] Cryptate Dissociation in Aqueous Solution," *Nuclear Chemistry Division FY86 Annual Report*, Lawrence Livermore National Laboratory, Livermore, Calif., UCAR-10062-86 (1986), p. 4-35.
6. J. Lehn, *Acc. Chem. Res.* **11**, 49 (1978).
7. B. G. Cox and H. Schneider, *J. Amer. Chem. Soc.* **99**, 2809 (1977).

Measurement of the Enthalpies of Complexation of Thorium with Multiple Fluoride Ligands

P. M. Grant and P. A. Baisden; W. F. Kinard (Department of Chemistry, College of Charleston, Charleston, S.C. 29424)

We have studied the complexation of Th^{4+} with the fluoride anion by using a very sensitive solution-calorimeter developed in our laboratory.[1] We are interested in thorium primarily because of its membership in the actinide series. It can serve as a useful analog of Pu(IV) chemistry,[2] and the lower radioactivity and toxicity of thorium facilitate its use in an experimental program. Fluoride is of intrinsic interest in coordination chemistry[3,4] and can also be an important component in applied and environmental studies. For example, F^- is present at parts-per-million concentrations in groundwater from tuff formations in the vicinity of Yucca Mountain at the NTS.[5] At these levels, it must be considered a potentially significant factor in the migration of high-level radioactive waste from a geologic repository over long time periods. The calorimetric investigation of the $Th^{4+} + F^-$ system was a natural extension of recent work in our laboratory on the thermodynamics of lanthanide-fluoride complexation.[6,7]

Formation enthalpies for the second and third complexes of Th^{4+} with F^- at a moderate ionic strength have not previously been reported. However, Baumann[8] does list infinite-dilution values calculated from van't Hoff analyses of stability-constant measurements.

Data do exist in the literature for the formation enthalpy of ThF^{3+} (ΔH_{101}) at an ionic strength (μ) of 1.0*M* ($HClO_4$) and temperature (*T*) of 25°C. Choppin and Unrein[9] measured values of 1.1, 2.3, and 3.0 kJ/mole by means of solvent extraction, potentiometry, and calorimetry, respectively. The most recent evaluation by Martell and Smith inexplicably gives a value of 15 kJ/mole for this enthalpy, but this value may well be a typographical error.[10]

Theoretical considerations can provide some guidance as to what to expect thermodynamically from the formation of the first thorium-fluorine complex. A previously established correlation[3] between Coulomb potential energy and first-complex entropy (ΔS_{101}) for metal-fluoride complexes at μ = 1*M* can be used to predict the formation entropy of ThF^{3+} from the ionic radius of Th^{4+}. These systematics in conjunction with the free energy (ΔG_{101}) lead to a prediction of 1.4 kJ/mole for ΔH_{101}.

Experimental

We prepared a 0.02*M* Th^{4+} working solution from 99.99% pure reagent material (Spex Industries), acidified it to pH 1.1 with $HClO_4$, and adjusted it to μ = 0.5*M* with $NaClO_4$. The titrant was 0.1*M* NaF at pH 6.4 and μ = 0.5*M* ($NaClO_4$). We have presented elsewhere the details of reagent purification, assay, etc.,[6,7] and all materials were of analytical reagent-grade quality or better.

We previously published the description and operation of the adiabatic titration calorimeter used for these experiments.[1] The initial volume of the titrated Th^{4+} solution was 50 mL, and titrant was typically added in aliquots of 0.50 mL. We sampled the entire range of metal-fluoride speciation up to the point of ThF_4 precipitation in this study, and precipitation occurred at an average ligand number (*n*) of about 1.7 in this system.

In addition to $Th^{4+} + F^-$ titrations, we performed experiments in which fluoride was titrated into μ = 0.5*M*, pH = 1.4 $HClO_4$ to measure ΔH_{011} at this ionic strength. We accomplished heat-of-dilution or blank runs by titrating 0.5*M* $NaClO_4$ solution with fluoride.

All calorimetry experiments were performed at 25.00 ± 0.0003°C.

Computations and Data Analysis

At the low pH necessary to prevent Th^{4+} hydrolysis, H^+ successfully competes with the metal for the added ligand, resulting in the formation of HF. The gross calorimeter heat at each titration point must therefore be apportioned between the metal complexation reactions, acid reactions, and the heat-of-dilution of the titrant into a blank, μ = 0.5*M* solution. We subtracted a separately determined dilution heat from the gross heat to give a net reaction heat, and, in order to discern the various reaction modes, we performed detailed speciation calculations to provide knowledge of solution composition at each point of a titration.

We computed general solution speciation by means of unweighted, nonlinear regression with a Basic-language program, CALSPEC, which has the Marquardt algorithm[11] as its basis. Requiring input of initial solution compositions, volumes, and stability-constant data, CALSPEC outputs the change in the number of moles (Δn) of all reactants and products at each titration point. For the present study, all CALSPEC calculations used the literature data summarized in Table 1. Previous investigations of the thorium-fluorine system have shown that neither polynuclear species nor mixed acid-metal complexes require consideration under these experimental conditions.[12]

We corrected calorimeter reaction heats for HF formation from the CALSPEC values of Δn_{011} and a value of ΔH_{011} = (12.38 ± 0.06) kJ/mole. We obtained the latter datum in separate calorimeter experiments in our laboratory, and it is the result of 21 independent measurements. It agrees well with existing literature data of 12.2 (Ref. 13) and 13.0 kJ/mole (Ref. 14) measured by temperature-coefficient methods in μ = 0.5*M* $NaClO_4$ medium.

We calculated the heat change due to metal-ligand reactions, i.e., ΔQ_{ThF_i}, by subtracting the HF heat contribution from the net reaction heat. The equation necessary to compute thorium reaction enthalpies is then

$$\Delta Q_{ThF_i} = \sum_{i=1}^{3} \Delta H_{10i} \cdot \Delta n_{10i} \,. \qquad (1)$$

We obtained the change in moles of a thorium-fluorine complex from CALSPEC, and we calculated values of ΔH_{10i} from a multivariate fit to Eq. (1), using Wentworth's method[15] of weighted (in ΔQ_{ThF_i} only), nonlinear least-squares.

The analysis of these experiments required additional considerations associated with the measurement of very small empirical heats in the thorium-fluoride system. Under the conditions reported here, a titration increment resulted in the generation of approximately 40 mJ of total heat, corresponding to a temperature change (ΔT) of about 100 to 200 µK. This is very close to the calorimeter detection limit and only provided a signal:background ratio of about 1:4, where background refers to the heat-of-dilution measurements. The data, therefore, fall in the nonlinear-response region of the calorimeter below 200 mJ (Ref. 1). Accordingly, we used

Table 1. Stability constants used for the theoretical computation of general solution speciation.[a]

Constant	Value
HF log β_{011}	2.92 ± 0.01
HF_2 log β_{012}	3.51 ± 0.02
ThF^{3+} log β_{101}	7.59 ± 0.04
ThF_2^{2+} log β_{102}	13.44 ± 0.02
ThF_3^+ log β_{103}	17.9 ± 0.1
pK_w	13.74 ± 0.02

[a] From Ref. 10.

the protonation reaction of tris(hydroxymethyl)-aminomethane (TRIS) as a primary calibration standard,[1] and we likewise performed calorimeter titrations of TRIS with HCl to generate 40 mJ of heat. We thus normalized the gross calorimeter heats of the thorium-fluoride runs to the standard value of TRIS ΔH_p = −47.44 ± 0.05 kJ/mole.[16]

We have given more specific detail on analysis techniques and error propagation elsewhere.[1,6] All errors reported in this article are one standard deviation and reflect only the uncertainties in the calorimeter temperature measurements. Uncertainties in the speciation calculation input parameters have not been included. Consequently, the reported errors represent minimum values associated with these experiments.

Results and Discussion

The thermodynamics of the thorium-fluoride system at $\mu = 0.5M$ are summarized in Table 2. The enthalpy data are the results of 85 independent determinations from four calorimeter runs. We fit the calorimetry measurements to one-, two-, and three-complex reaction models by using the Wentworth method, and the three-complex model gave the best fit ($\chi^2_\nu = 2.2$) (Ref. 17) to our experimental data.

We thus measured the formation enthalpies of ThF_x to be small and endothermic, consistent with the creation of inner-sphere complexes.[18] The enthalpy values for the second and third complexes are the first to be reported at $\mu = 0.5M$. The result for ΔH_{101} falls in the range reported by Choppin and Unrein[9] and is in excellent agreement with the theoretical prediction of Hefter's systematics.[3] The correlation calculation of ΔS_{101} predicts a value of 150 J/moleK, precisely the result reported in Table 2.

Much of the bonding of simple metal ions with the fluoride anion is adequately described by simple electrostatic considerations,[3] and we have recently confirmed this finding in studies of lanthanide complexes.[7] The results of the present investigation indicate that the thorium-fluoride system is similarly characterized by predominantly ionic bonding.

Table 2. Thermodynamic parameters for the thorium-fluoride system at $T = 25°C$ and $\mu = 0.5M$ ($NaClO_4$).

Complex	i	$-D G_{i0i}$[a,b] (kJ/mole)	$D H_{i0i}$ (kJ/mole)	$D S_{i0i}$ (J/mole·K)
ThF^{3+}	1	43.3 ± 0.24	1.6 ± 0.03	150 ± 0.8
ThF_2^{2+}	2	76.7 ± 0.12	4.3 ± 0.07	270 ± 0.5
ThF_3^{+}	3	102.0 ± 0.64	7.8 ± 0.9	370 ± 4

[a] The indices "10*i*" refer to the number of atoms of metal, hydrogen, and ligand, respectively, in the complex. Thus, "101" indicates the reaction $M + F \rightleftarrows MF$, "011" indicates $H + F \rightleftarrows HF$, etc.

References:

1. P. A. Baisden, P. M. Grant, and W. F. Kinard, *Rev. Sci. Instrum.* **58**, 1937 (1987).
2. S. Ahrland, in *The Chemistry of the Actinide Elements* (Chapman & Hall, London, 1986), 2nd Ed., Vol. 2, p. 1480.
3. G. Hefter, *Coord. Chem. Rev.* **12**, 221 (1974).
4. A. M. Bond and G. T. Hefter, *IUPAC Critical Survey of Stability Constants and Related Thermodynamic Data of Fluoride Complexes in Aqueous Solution* (Pergamon, Oxford, 1980).
5. D. C. Hoffman and G. R. Choppin, *J. Chem. Educ.* **63**, 1059 (1986).
6. P. A. Baisden, P. M. Grant, W. F. Kinard, and R. A. Torres, *Inorg. Chim. Acta* **128**, 127 (1987).
7. P. M. Grant, P. A. Baisden, W. F. Kinard, and R. A. Torres, *Inorg. Chem.* **27**, 1156 (1988).
8. E. W. Baumann, *J. Inorg. Nucl. Chem.* **32**, 3823 (1970).
9. G. R. Choppin and P. J. Unrein, in *Transplutonium 1975* (North-Holland, Amsterdam, 1976), p. 97.
10. A. E. Martell and R. M. Smith, *Critical Stability Constants* (Plenum, New York, 1982), Vol. 5, Suppl. 1, p. 415.
11. D. W. Marquardt, *J. Soc. Ind. Appl. Math.* **11**, 431 (1963).
12. P. Klotz, A. Mukherji, S. Feldberg, and L. Newman, *Inorg. Chem.* **10**, 740 (1971).
13. S. Ahrland, *Helv. Chim. Acta* **50**, 306 (1967).
14. A. Aziz and S. J. Lyle, *Anal. Chim. Acta* **47**, 49 (1969).
15. W. E. Wentworth, *J. Chem. Educ.* **42**, 96, 162 (1965).
16. I. Grenthe, H. Ots, and O. Ginstrup, *Acta Chem. Scand.* **24**, 1067 (1970).
17. P. R. Bevington, *Data Reduction and Error Analysis for the Physical Sciences* (McGraw-Hill, New York, 1969), p. 89.
18. G. R. Choppin, in *Lanthanide and Actinide Chemistry and Spectroscopy, ACS Symposium Series* **131**, American Chemical Society, Washington, D.C. (1980), p. 173.

Calorimetric Determination of the Enthalpies of Complexation of Thorium with Some Amine-N-Polycarboxylic Acids

W. F. Kinard (Department of Chemistry, College of Charleston, Charleston, S.C. 29424), P. M. Grant, and P. A. Bertsch

The interaction of metal ions with amine-N-polycarboxylic acids is of interest for a number of theoretical and practical reasons. From a theoretical point of view, because these compounds are polydentate in nature, they are capable of forming species with high coordination numbers, which are some of the most stable metal complexes known.[1] In addition, their relatively simple chemical structures allow facile synthesis of analogs to further elucidate the important factors in forming strong metal-ligand complexes.

Since the amine-N-polycarboxylates form such extremely strong complexes, analytical procedures have been developed for many metal ions based on a complexometric titration with these compounds. They also are used extensively as masking agents to bind metal ions that might interfere in other analytical procedures.[2]

In nuclear chemistry and radiochemistry, ethylenedinitrilotetraacetic acid (EDTA) titrations are the method of choice for the quantitative titrimetric analysis of the lanthanide elements in solution. In addition, many decontamination procedures involve the use of EDTA solutions to complex and solubilize metal contaminants. Experience with the disposal of radioactive wastes from laboratories has implicated EDTA as a dispersing agent in the migration of radionuclides from disposal sites.[3,4] Amine-N-polycarboxylate ligands are also used to model metal complexation by trace organics in natural waters to elucidate metal speciation with applications to transport studies.[5]

Experimental

All solutions were prepared from analytical-grade reagents without further purification. Thorium nitrate was used to prepare a 0.10*M* stock solution, and working solutions were made by dilution. The ionic strength of the metal solution to be titrated was adjusted to 0.10*M* with KNO_3 and nitric acid (HNO_3). The HNO_3 adjusted the pH of these solutions to between 1.3 and 2.4 to ensure that no significant hydrolysis of the thorium(IV) occurred.

The 0.15*M* amine-N-polycarboxylate titrant solutions were prepared from reagents of greater than 99% purity by dissolving the appropriate amount of compound in an approximately 1% stoichiometric excess of sodium hydroxide to remove all protons from the ligand. No solubility problems were encountered. The pH of the resulting titrant solution was measured at the appropriate ionic strength.

The highly sensitive LLNL titration calorimeter used to measure the heats of reaction in this study has been described previously.[6] Typically, we made calorimetric measurements at two different metal concentrations having different pH values and at two different titrant addition volumes. We used an extrapolation procedure to obtain the blank correction because there was a mismatch in ionic strengths between the titrant solutions and a 0.10*M* KNO_3 blank. The limiting data, after a number of additions, were extrapolated to zero added titrant to obtain a corrected blank. In the thorium solutions, the endothermic heat of dilution caused by ionic-strength differences was not observed because the reaction of Th^{4+} with Y^{n-} results in only a small change in ionic strength. The resulting corrected heat measurements were combined with speciation calculations in a weighted regression procedure (described in a previous study)[7] to fit the

data. Stability constants for the thorium complexes were taken from data in critically reviewed literature.[8]

Results

Figure 1 shows one of our typical calorimetric titrations with an amine-N-polycarboxylic acid. Since the formation constants of the metal-ligand (ML) complexes are so large ($>10^{18}$), the titration reactions go essentially to completion. In the figure, the first additions represent the exothermic heats caused by the formation of the 1:1 complex with thorium, and a large subsequent increase in the exothermic heat is observed when the ligand begins to protonate. A commensurate increase in the pH of the solution is observed, as expected with this process.

We used four amine-N-polycarboxylic acids in this study. These compounds were EDTA, N-(2-hydroxyethyl)ethylenedinitrilo-N,N′,N′-triacetic acid (HEDTA), diethylenetrinitrilopentaacetic acid (DTPA), and nitrilotriacetic acid (NTA). HEDTA and EDTA are structurally identical, except that one of the acetic-acid functional groups has been replaced by an ethanol group. HEDTA, EDTA, and DTPA provide three, four, and five carboxylate groups, respectively, for bonding to a metal cation, while NTA has three carboxylates attached to a single nitrogen. All of these ligands are polydentate and are capable of wrapping themselves around a metal ion to form extremely stable complexes.

Table 1 contains a summary of our data for the systems studied. Enthalpy of complexation values were calculated from a fit to the equation

$$Q_{meas} = \Delta_{moles}\,ML \times \Delta H_{101} (+ \Delta_{moles}\,MHL \times \Delta H_{111}), \quad (1)$$

where the values of Δ_{moles} ML and MHL (protonated metal ligand) were calculated from literature values of stability constants by using a Newton-Raphson procedure for solving mass- and charge-balance relationships. From an examination of the titration results at two different pH values, it was evident that we had to consider an additional species, MHL, for EDTA and DTPA. The HEDTA titrations showed no pH dependence, indicating no MHL formation. Analysis of the NTA data is complicated by the fact that the thorium-NTA complex is very similar in strength to the protonated species, which means that the ΔH values for the ligand protonation must be known with some certainty if the heat of complexation of thorium is to be extracted from the data.

We attempted to measure the heat of complexation of thorium with ethylenedinitrilodiacetic acid (EDDA), an analog of EDTA with only one carboxylic acid group on each terminal nitrogen. The heats of reaction we observed were only those for the protonation reaction. This observation indicates that, at the low pH values required to prevent hydrolysis of Th^{4+}, the H^+ in solution can effectively compete with Th^{4+} for bonding sites on the EDDA anion.

Our values of −11.5 and −11.9 kJ/mol for ΔH_{101} and ΔH_{111} for EDTA are in reasonable agreement with the values of −12.9 and −12.6 reported previously by Doi, who used a batch titration procedure.[9] Doi's procedure depended on a knowledge of the enthalpy of protonation of EDTA in order to correct for the heats of the protonation when an excess of EDTA was reacted with an acidic thorium solution. Because our procedure involves an incremental titration, we were able to select only those points for analysis where no significant heats of protonation of the ligands were observed.

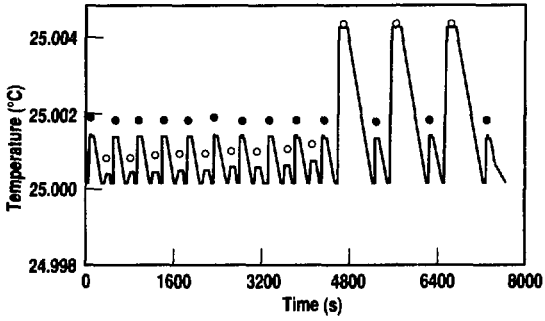

Figure 1. Titration of 50.0 mL of 0.007*M* Th(IV), pH 2.06, with 0.15*M* HEDTA, pH 10.57. The solid circles represent 0.25-J electrical calibration heats, and the open circles identify titration reaction heats. The large increase in the titration heat at the tenth point is caused by ligand protonation after all of the thorium has been reacted.

Discussion

The stability of thorium-amine-N-polycarboxylate complexes is a result of the large entropy effect obtained when the primary hydration sphere of the metal ion is displaced by a single multidentate ligand. Because ΔS_{101} represents

Table 1. Thermodynamics of thorium-amine-N-polycarboxylate complexes.[a]

Ligand	$\log \beta_{101}$	ΔG_{101} (kJ/mol)	ΔH_{101} (kJ/mol)	ΔS_{101} (J/molK)	$\log \beta_{101}$	ΔG_{111} (kJ/mol)	ΔH_{111} (kJ/mol)	ΔS_{111} (J/molK)
NTA	12.4	−70.8	+5.5	256				
HEDTA	18.5	−105.6	−4.4	339				
EDTA	23.2	−132.4	−11.5	406	25.2	−143.8	−11.9	442
DTPA	28.8	−164.4	−12.3	510	30.9	−176.4	−12.3	550

[a] Values determined at 25°C in 0.1*M* KNO_3.

a stabilization gain resulting from the number of water molecules displaced from the hydration sphere by the coordinating ligand, plots of ΔS_{101} and, therefore, log β_{101}, scale linearly with the number of strongly interacting coordination sites available on the ligand. Although relatively small in magnitude, the enthalpy values give a more detailed picture of the bonding process in these species. Figure 2 shows a plot of ΔH_{101} vs the number of carboxylate coordination sites for Th^{4+}, with data for La^{3+} shown for comparison.[10,11] Note that both cations show similar behavior, in that the curves are relatively linear for less than four carboxylate coordination sites (EDTA) and then appear to level off at five (DTPA). The lanthanides may even level off at three (HEDTA), which would be expected upon formation of the noncharged ML complex.

It can be argued from molecular models that, if all three nitrogen atoms in DTPA coordinate with the metal ion, the fifth carboxylate cannot coordinate strongly with the metal ion for geometric reasons. This limitation is not observed in the ΔS_{101} correlation because the nonbonding carboxylate may still be able to cause disruption of the cation hydration sphere, even though it is not strongly bonded to the metal ion.

Another interesting feature of this plot is the anomalous behavior of NTA for both Th^{4+} and La^{3+}. The ΔH_{101} values observed for NTA may indicate that only two of the carboxyl groups coordinate with the metal cation. This is suggested in the plot by the proposed displacement of the NTA data to a carboxylate coordination number of 2.

As mentioned previously, the ΔH_{101} value for the thorium-EDDA complex could not be measured in the strongly acidic solutions required in this study to prevent Th^{4+} hydrolysis. Martell has estimated a log β_{101} for the thorium-EDDA complex to be about 11.9 (Ref. 1). If we use a scaled value of 215 J/molK, obtained from a plot of ΔS_{101} for the thorium-amine-N-polycarboxylate complexes vs carboxylate coordination number and interpolate a value of +2.6 kJ/mol for ΔH_{101} from Fig. 2, we can estimate a log β_{101} of 10.8 for thorium-EDDA.

Summary

This work shows that the thermodynamic parameters obtained for the thorium-amine-N-polycarboxylate complexes follow the same entropy correlations previously observed for the lanthanides. In addition, a closer examination of the enthalpy data gives a more detailed look at the bonding in the amine-N-polycarboxylate complexes.

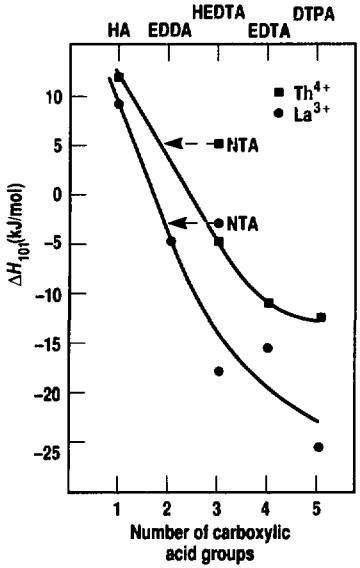

Figure 2. Comparison of ΔH_{101} values for Th^{4+} and La^{3+}. Note that the NTA points should be displaced by one coordination site because NTA has only one highly basic nitrogen coordination site, as compared with two for the other amine-N-polycarboxylates used in this work.

References:

1. R. M. Smith and A. E. Martell, *Sci. Total Environ.* **64**, 125 (1987).
2. C. N. Reilley, *Fed. Proc.* **20**, 22 (1961).
3. J. L. Means, D. A. Crerar, and J. O. Duguid, *Science* **200**, 1477 (1978).
4. J. M. Cleveland and T. F. Rees, *Science* **212**, 1506 (1981).
5. N. Miekeley, R. M. Dotto, I. L. Kuchler, and P. Linsalata, *Mat. Res. Soc. Proc.* **44**, 591 (1985).
6. P. A. Baisden, P. M. Grant, and W. F. Kinard, *Rev. Sci. Instrum.* **58**, 1937 (1987).
7. P. A. Baisden, P. M. Grant, W. F. Kinard, and R. A. Torres, *Inorg. Chim. Acta* **128**, 127 (1987).
8. S. Ahrland, G. R. Choppin, P. A. Baisden, R. A. Torres, and G. Marx, *Gmelin Handbook of Inorganic Chemistry*, 8th Ed., Thorium, Suppl. Vol. D (Springer-Verlag, New York, 1988).
9. K. Doi, *J. Inorg. Nucl. Chem.* **40**, 1639 (1978).
10. G. R. Choppin, M. P. Goedken, and T. F. Gritmon, *J. Inorg. Nucl. Chem.* **39**, 2025 (1977).
11. R. M. Smith and A. E. Martell, *Critical Stability Constants* (Plenum Press, New York), Vol. 1, 1974, Vol. 5, 1982.

Development of an Automated, Chromatographic Actinide Separation System

C. E. A. Palmer and R. A. Boisclair; H. L. Hall, D. C. Hoffman, and D. M. Lee
(Lawrence Berkeley Laboratory, Berkeley, Calif.)

We are interested in the chemical and nuclear properties of the heaviest elements, particularly those formed by bombarding high-Z targets with light-to-heavy ions in accelerators or cyclotrons. To study these short-lived isotopes, high-quality separations of the many reaction products must be performed on a time scale of the half-lives of the isotope of interest, usually several minutes or less. To facilitate this work, we have developed an automated chromatographic chemical element separator system (ACCESS), a computer-controlled separation system that consists of three parts: a sample injection system, a separation system, and a collector. After the sample is injected, the activity is moved, using solvents, through a system of valves and finally onto a chromatographic column. Separated samples are then collected and prepared for radiochemical analyses.

ACCESS has been used in two experiments thus far to study the decay properties of heavy actinides. In the first, chemically separated samples of 7.3-m ^{246}Es and 4.7-m ^{247}Es were collected and analyzed by alpha- and x-ray pulse-height spectra. In the second experiment, we used ACCESS to search for the presumably short-lived, missing isotope ^{241}Bk by means of the ^{241}Am (α, 4n) reaction.

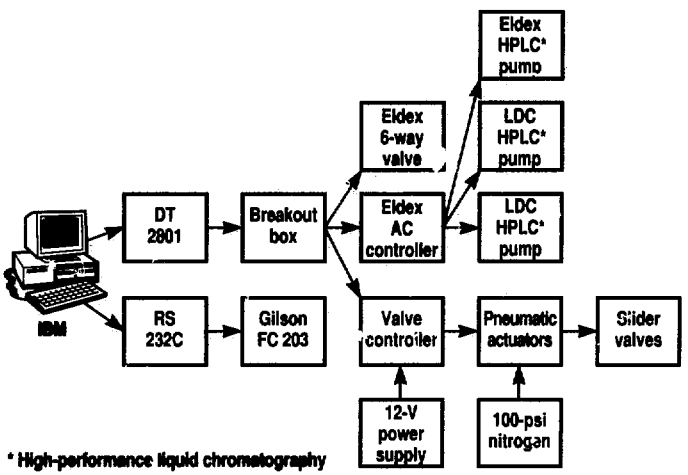

Figure 1. Automated control-system diagram for ACCESS.

Design Considerations

We sought to construct a system that could perform high-quality separations rapidly and reproducibly. To enhance the quality of the separation, we planned to raise the temperature at which the separation would be performed. To increase the speed of the separations, we planned to pressurize the separation column and, to afford reproducible separations, automate the system.

Another consideration was the potential for the system to experience continued exposure to the corrosive solvents used in the chemical procedures. This suggested the use of inert components throughout the system. The limited availability of chemically inert, low-volume, precision pumps constrained us to a pressure of about 500 psi. Operation at this pressure permitted the selection of small-volume (0.3-mm-i.d.) Teflon tubing, fittings, and pneumatically actuated, chemically inert slider valves.

Finally, we wanted the system to be as modular and flexible as possible to permit adaptation to many types of experiments. A variety of separation applications could be envisioned for ACCESS. For example, multiple columns could be used either in parallel or sequentially.

Introduction of Radioactivity. Radioactivity is introduced in one of two ways. In the first configuration, ACCESS is coupled to a target chamber

at the Lawrence Berkeley Laboratory's 88-in. cyclotron via a KCl aerosol-helium–jet transport system. The recoiling products from heavy-ion reactions attach to the KCl aerosols, which are transported to the chemistry area by helium gas. The aerosols are deposited on a coarse filter-paper frit in a pneumatically actuated valve. After a suitable time, solvent is pumped through the frit to dissolve the activity and move it onto the column. This method of trapping the KCl aerosols is inexpensive and makes changing the collection filter easy. Several other frit materials (i.e., ceramic foam, filter cloth, fritted glass, and glass wool) were examined. However, they tended to decrease the helium-jet flow rate and reduce the aerosol collection efficiency. Also, their useful lifetimes were too short for continuous use.

The second way of introducing radioactivity is by the direct-injection configuration. It is essentially the same as the first method except that the activity is introduced via an injection loop rather than from the filter-paper frit. Because this off-line configuration makes the system flexible, ACCESS can also be used as a routine laboratory ion-chromatography system.

Separation. We use well-established liquid-chromatographic techniques such as cation exchange and reverse-phase-extraction chromatography to achieve the desired separation.[1,2] Both these techniques are widely used in studies of the transplutonium elements.

We construct our separation columns from precision-bore glass tubing and chemically inert column end fittings. This permits us to vary the column length and optimize the separation. A typical column resulted in a free-column volume (FCV) of 14 drops (13 μL/drop).

Initially, we used a low-volume precision pump. However, it took several minutes for the pump to reach operating pressure (400 psi). Also, the volume necessary (~8 mL) to change solutions in the pump head was significant in comparison with the desired total elution volume (≤2 mL). To circumvent these constraints, we have installed a second column and pump to maintain the necessary back pressure and to reduce the system's dead volume.

Elevated temperatures permit more favorable exchange kinetics between the resin functional groups and the activity,[3] thereby improving the quality of separation. Therefore, we constructed an aluminum heater block for the analytical column; the block affords uniform and reproducible heating of the column during the elutions and is covered with ceramic paper to insulate it from changes in ambient temperature that may occur during continuous use. Changes in column temperature would alter the separation equilibrium and could alter the elution position and volume of the desired element.

Collection. The volume of eluent containing a separated element varies from element to element. We chose a fraction collector that can independently vary the volume of each fraction it collects. Also, we designed small hot plates to be inserted in the fraction-collector rack in place of tubes. This feature allows fractions to be collected on heated metal foils and evaporated as they are collected. These two features allow us to collect minimum-volume fractions and to start evaporating them immediately after separation.

The downstream end of the analytical column tubing is attached to 0.3-mm-i.d. Teflon tubing, which was cut at a 45-degree angle. This reduced the drop volume by nearly a factor of 2.

Recycling the system requires reconditioning the column between elutions. This was achieved by using a third pump in conjunction with a selector valve able to draw from six reservoirs.

Automation. To control ACCESS, we programmed the process control routines on an IBM PC using Basic. To interface the computer to ACCESS, we selected a multifunction input-output (I-O) board. With the digital outputs, we controlled the pumps and the slider valves used to direct the flow of solution through the system. The fraction collector was also controlled by the PC through an RS-232C serial interface (Fig. 1). The software controlled the conditioning of the column before each separation and during all steps of the separation. We designed the software to be as modular and as flexible as the chromatographic components.

Experimental Results

Our initial work focused on the separation of several lanthanides and involved cation-exchange separation using alpha hydroxyisobutyric acid (alpha-HIB) as the eluent.[3,4] The lanthanides and actinides share similar electronic configurations, oxidation states, and ionic radii. Similar elution behavior is a consequence of these similarities under these chromatographic conditions. Thus, we were able to study the longer-lived, more readily available lanthanides as models for the actinides we wish to study.

Using the lanthanides ^{171}Tm, ^{152}Eu, and ^{166m}Ho, we observed separation factors that were consistent with previous work, although our resolution was improved by using smaller drops (~3 μL vs 45 μL).[3,4] The rapid separation time permits repeated separations, which reduce the errors obtained. We found it useful to assemble a data base of the tracer-elution results. We wrote a computer program that uses this information to predict the separation factors for the lanthanides and actinides eluted with alpha-HIB as a function of pH.

ACCESS has been used in two experiments. The first was a collaboration with a group at Tokyo Metropolitan University. With them, we studied ^{246}Es and ^{247}Es using a ^{249}Cf target bombarded with protons from the LBL 88-in. cyclotron. Samples were collected in 1.1-mL vials directly from the helium jet. The activity was dissolved in 200 μL of 0.5*M* alpha-HIB (pH ~2, not adjusted) and directly injected into ACCESS using the injection loop. A schematic diagram of the system used is shown in Fig. 2.

The column consisted of Hamilton cation exchange resin, AG-50W X-12 (size range 10 to 15 mm) packed in a 2- × 100-mm glass column. The column

was operated at 400 psi and 90°C for 20 hours. The nominal flow rate under these conditions was 17 mL/min/cm^2. Before each elution, the column was regenerated by flushing for 2 min (about 5 FCVs) with pH 4.20, 1*M* alpha-HIB to strip off any residual activity. 1*M* NH_4Cl was pushed through for 2 min to ensure that the resin was fully aminated before the next elution. Steam-distilled water was flushed through the column for 3 min to remove any unexchanged NH_4Cl, and 0.05*M* alpha-HIB was passed through the column until the sample was injected. After elution, the fraction containing the einsteinium was removed from ACCESS, evaporated to dryness, and flamed. The entire process was repeated every 20 min. This repetition rate was determined to be optimum, based on the half-lives and the time required to convert the separated einsteinium fraction to a form suitable for alpha counting. The repetition time could have been shortened to about 4 min in the single-column configuration with minimal degradation of radiochemical purity, but evaporation of the einsteinium fraction for alpha counting was the rate-limiting step, not the separation.

We have also used ACCESS to study the light berkelium isotopes produced in the ^{241}Am (α, xn) reaction, but particularly to search for the missing isotope ^{241}Bk. The recoiling products were swept from the reaction chamber to a collection site via a KCl/helium-jet aerosol and collected in 1.1-mL vials. After a 10-min period, the activity was dissolved in concentrated nitric acid saturated with sodium bromate, which oxidizes the berkelium from the +3 to the +4 oxidation state. This solution was injected directly into ACCESS. The column consisted of bis(2-ethylhexyl) orthophosphoric acid (HDEHP)[2] sorbed on an inert support (Absorbosphere C-18) packed in a 0.5- × 40-mm Teflon column. With high concentrations of nitric acid (>1*M*), all the trivalent actinides will be eluted, while the Bk^{+4} is strongly bound to the column. Two-molar nitric acid was then passed through the column at 400 psi, with a nominal flow rate of 4.5 mL/min/cm^2. Eight 1-min fractions were collected following the injection. Presumably, $^{241}Bk^{+4}$ decays by electron capture to $^{241}Cm^{+3}$ (32.8 d), which is no longer bound to the column under these conditions. Therefore, a plot of ^{241}Cm activity against elution time would yield the parent ^{241}Bk half-life. The results from this experiment are encouraging but as yet are inconclusive as to the identification of ^{241}Bk.

Conclusions

Our automated chromatographic separation system's modular assembly affords maximum flexibility in experimental design. The separation of transplutonium elements can be achieved in as little as one or two minutes or can be varied to meet the specific needs of an experiment. The separations are highly reproducible (within 2%) and can be done in rapid succession. The system can be recycled in about 10 min.

References:

1. J. Korkisch, *Modern Methods for the Separation of Rarer Metal Ions* (Pergamon, Oxford, 1969).
2. E. P. Horwitz, C. A. A. Bloomquist, and D. J. Henderson, *J. Inorg. Nucl. Chem.* **31**, 1149 (1969).
3. G. R. Choppin and R. J. Silva, *J. Inorg. Nucl. Chem.* **3**, 53 (1956).
4. H. L. Smith and D. C. Hoffman, *J. Inorg. Nucl. Chem.* **3**, 243 (1956).

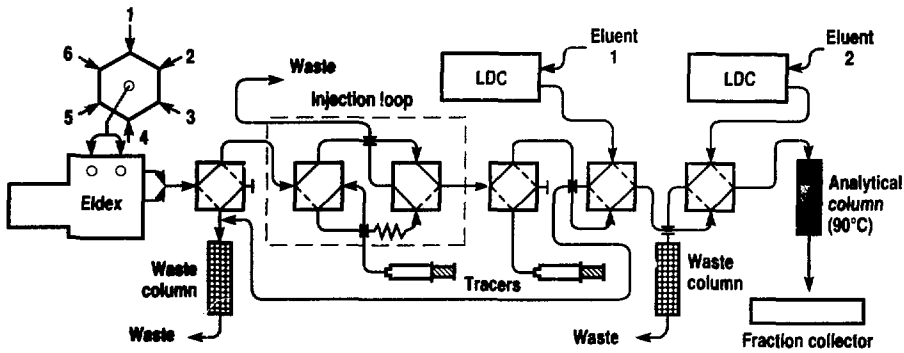

Figure 2.
Schematic diagram of ACCESS in the direct-injection configuration.

Monovalent Lawrencium is Unlikely

R. W. Lougheed, K. J. Moody, R. J. Dougan, J. F. Wild, and E. K. Hulet

Extrapolation of the Periodic Table properties shows a valence electronic configuration for lawrencium of $6d7s^2$ with a filled 5f core. However, estimates and calculations that include relativistic electron velocities[1,2] predict that the ground-state electronic configuration of lawrencium is $7s^27p_{1/2}$. These calculations show a stabilization of the 7s and $7p_{1/2}$ electron orbitals relative to the 6d and an increased radius for the 5f core due to relativistic effects. The ground-state electronic configuration could be directly measured by a Stern-Gerlach experiment as proposed by Hulet[3] or inferred from measurements of the physical properties of atomic lawrencium. One experiment, based on the volatility of atomic lawrencium, showed no evidence for a $7s^27p$ ground state but did not exclude it either.[4]

The chemical properties of lawrencium ions cannot be used to determine the ground-state electronic configuration, but they do provide information on the ionization energies of the valence electrons. The most stable oxidation state of lawrencium was shown by Silva et al.[5] in 1970 to be 3^+ in aqueous solutions, as expected. It may be possible to reduce lawrencium to the 1^+ oxidation state if the 7s electrons are sufficiently stabilized to act as an "inert pair," analogous to unipositive thallium. The inert-pair effect observed in thallium, lead, and bismuth is attributed to relativistic effects[6] that are enhanced for the 6s vs 5s electrons. We would expect Lr^+ to possess chemical properties that are similar to the chemically analogous alkali metals, thallium, and silver.

A limit of ≤ -0.4 V for the reduction potential of Lr^{3+} to Lr^+ in aqueous solution was recently reported.[7] These experiments used the nuclide ^{260}Lr ($t_{1/2}$ = 3 m). We report here measurements obtained using the new, longer-lived lawrencium isotope, ^{262}Lr ($t_{1/2}$ = 216 m).[8] The longer half-life of ^{262}Lr permitted the use of chemical techniques requiring more time.

We chose to use the $Sm^{2+} \rightarrow Sm^{3+} + e^-$ reaction couple for the reduction attempt because of its high potential (1.55 V). We coprecipitated (cocrystallized) a 1^+ fraction using sodium tetraphenylborate or chloroplatinic acid with rubidium carrier. The 2^+ and 3^+ actinides do not precipitate with these precipitating agents; thus, they can be physically separated from the 1^+ ions by centrifugation or filtration. Sodium tetraphenylborate is particularly desirable for precipitating the 1^+ ions because the alkali metals, thallium and silver, are quantitatively precipitated as the tetraphenylborates and because the tetraphenylborate does not rapidly oxidize Sm^{2+}, in contrast to the chloroplatinate.

Experimental

We bombarded a target containing 8.4×10^{16} atoms/cm^2 ^{254}Es with 127-MeV ^{22}Ne ions at the Lawrence Berkeley Laboratory's 88-in. cyclotron and collected the recoil products on 3.5-mg/cm^2 molybdenum foils. Three bombardments, ranging in length from 4 to 8 hours, were made. At the end of each bombardment, lawrencium was chemically purified, as described elsewhere in this report,[9] except that we omitted steps designed only to purify lawrencium from gamma- and beta-emitting isotopes.

The purified lawrencium fraction was transferred to an inert-atmosphere glove box after the sample was fumed with perchloric acid to destroy any organic residues and was then evaporated to dryness with hydrochloric acid under helium flow. All solutions used in the subsequent reduction tests were prepared from either ethanol or hydrochloric acid and water that had been refluxed under an argon atmosphere. The lawrencium sample was then dissolved in a small amount of 0.1 *N* HCl, and a 25% assay sample

was removed for direct counting to establish the lawrencium chemical yield. We added 2 mg of rubidium carrier to the aqueous lawrencium fraction before transferring the resultant solution to a glass cone containing 25 to 50 mg of anhydrous samarium dichloride. Ethanol was used to rinse any lawrencium remaining in the glass planchet to the cone. The final solution contained 0.085 mL of 0.09 *N* HCl and 1.25 mL of ethanol. The reddish purple of the dissolved samarium dichloride was used to indicate the presence of excess reductant.

The mixture was then vigorously stirred for 30 to 60 s, or until the reddish samarium color appeared to have decreased to about half its original intensity. At this point, a precipitating agent for 1^+ ions was added to the mixture. We used sodium tetraphenylborate in two experiments and chloroplatinic acid in one. The solution was quickly centrifuged and the supernate removed. The deep reddish-purple color of the 2^+ samarium was still present after centrifuging when the tetraphenylborate was used but not when we used chloroplatinic acid. This resulted from the reduction of the chloroplatinate ion to $PtCl_4$ and platinum metal by Sm^{2+}.

We then determined the amount of lawrencium that coprecipitated with the rubidium carrier by dissolving and oxidizing the precipitate using nitric and hydrochloric acids. A small amount of ^{249}Cf tracer (10 dpm) was added as a chemical-yield tracer for lawrencium. We then performed cation-exchange chromatography using hydrochloric acid solutions and 80% ethanol-20% water saturated with HCl as eluants to separate lawrencium from the rubidium carrier and residue samarium that had been trapped in the precipitate. Trivalent lawrencium elutes from this column with californium, but on its forward edge. Samples were evaporated on platinum disks and counted for alpha energy and fission events using surface-barrier detectors. The chemical yield was determined from ^{249}Cf alpha events and the lawrencium content from fission events.

Results and Discussion

We observed one fission event from the experiment in which the 1^+ ions were precipitated with chloroplatinic acid. We expected to observe a total of 19 events from all experiments if the lawrencium was 100% reduced to the 1^+ state. Because we expected a few percent of the supernate to be trapped in the precipitate or simply not transferred out of the cone containing the precipitate, it is likely that the observed fission arose from a Lr^{3+} ion rather than a Lr^+ ion. For this reason, we chose to calculate an upper limit for the reduction potential of the $Lr^{3+} \rightarrow Lr^+$ couple based on five events, the 95% confidence limit for the observation of one event. The Nernst equation $E = E^0 - (RT/nF)lnK$ gives the relationship between the standard electrochemical potential and the equilibrium coefficient for a reaction couple. For the reaction

$$Lr^{3+} + 2Sm^{2+} = Lr^+ + 2Sm^{3+} ,$$

we can derive the expression $E^0(Lr^{3+} \rightarrow Lr^+) = E^0(Sm^{3+} \rightarrow Sm^{2+}) + 0.0127lnK$, where $K = (Lr^+)(Sm^{3+})^2/(Lr^{3+})(Sm^{2+})^2$, assuming that the ratio of the activity coefficients is unity. From our visual observation of the color change, we estimated that the Sm^{3+} and Sm^{2+} concentrations were about equal. Then, using five Lr^+ atoms as the 95% confidence level for the upper limit and 14 Lr^{3+} atoms, we calculated an upper limit for the reduction potential of lawrencium of −1.56 V. Even if we were a factor of 10 low or high in our visual estimates of the samarium-ion concentrations, the upper limit would change by only ±0.06 V, respectively. We conclude that it is unlikely that Lr^+ can exist in aqueous solutions.

References:

1. L. Brewer, *J. Opt. Soc.* **61**, 1101 (1971).
2. J. P. Desclaux and B. Fricke, *J. Physique* **41**, 943 (1980).
3. E. K. Hulet, "Proposed Atomic-Beam Instrument for Determining the Atomic Structure of New Elements," *Nuclear Chemistry Division FY84 Annual Report*, Lawrence Livermore National Laboratory, Livermore, Calif., UCAR-10062-84 (1984), pp. 6-19 to 6-22.
4. D. T. Jost, H. W. Gäggeler, C. Vogel, M. Schädel, E. Jäger, B. Eichler, K. E. Gregorich, and D. C. Hoffman, *Inorg. Chim. Acta* **146**, 225 (1988).
5. J. Silva, T. Sikkeland, M. Nurmia, and A. Ghiorso, *Inorg. Nucl. Chem. Lett.* **6**, 733 (1970).
6. K. S. Pitzer, *Acc. Chem. Res.* **12**, 271 (1979).
7. U. W. Scherer, J. V. Kratz, M. Schädel, W. Brüchle, K. E. Gregorich, R. A. Henderson, D. Lee, M. Nurmia, and D. C. Hoffman, *Inorg. Chim. Acta* **146**, 249 (1988).
8. R. W. Lougheed, K. J. Moody, R. J. Dougan, J. F. Wild, E. K. Hulet, R. J. Dupzyk, C. M. Henderson, C. M. Gannet, R. A. Henderson, D. C. Hoffman, D. M. Lee, K. Sümmerer, and R. L. Hahn, *Nuclear Chemistry Division FY 87 Annual Report*, Lawrence Livermore National Laboratory, Livermore, Calif., UCAR-10062-87 (1987), p. 4-2.
9. R. W. Lougheed, E. K. Hulet, J. F. Wild, K. J. Moody, R. J. Dougan, C. M. Gannett, R. A. Henderson, D. C. Hoffman, and D. M. Lee, "Discovery of 5-ms ^{254}No and the Study of Its Spontaneous Fission Decay Properties," p. 229 of this publication.

Neutron Emission as a Function of Fragment Energy in the Spontaneous Fission of ^{260}Md

J. F. Wild, R. W. Lougheed, E. K. Hulet, K. J. Moody, and R. J. Dougan; J. van Aarle, W. Westmeier, R. Brandt, and P. Patzelt (Philipps Universität, D-3550, Marburg/Lahn, FRG)

In nuclear fission, the total energy released, known as the Q-value for fission, is determined by the mass difference between the fissioning species and the fragments. A large part of this total energy is given up as kinetic energy of the fragments (total kinetic energy, TKE). The remainder exists in the form of excitation energy of the fragments and is dissipated mostly with the emission of gamma rays and the evaporation of prompt neutrons.

The number of prompt neutrons emitted in a fission event is directly related to the excitation energy of the fragments. The fragments at scission are deformed to some degree; following scission, the potential energy of deformation is rapidly converted to internal excitation energy. The closer the TKE of a fission event is to the fission Q-value, the lower is the amount of energy available for fragment excitation. The spontaneous fission (SF) of ^{260}Md offers the first good test of this relationship in the regime of low-fragment excitation energies.

The SF of ^{260}Md is markedly bimodal,[1] with about two-thirds of the fissions having TKEs in a distribution that peaks at 235 MeV, while the remainder peak at lower TKEs (see Fig. 1). The low-TKE fissions are expected to arise from elongated scission shapes in which the fragments are highly deformed. The high-TKE fissions are expected to arise from more compact scission shapes in which the fragments are nearly spherical.

Because of this compact scission shape, the Coulomb repulsion between the fission fragments is greater, which results in a higher TKE. There is less fragment deformation energy at scission and, hence, less excitation energy available for the emission of neutrons and gamma rays. Consequently, a measurement of the number of neutrons emitted at the time of fission should show an inverse relationship with fragment kinetic energy.

Experimental

Because ^{260}Md provides a major proportion of high-energy fission events in which the fragment excitation energy should be low, we wanted to determine if this manifested itself in a substantially lower neutron-emission rate. In 1986, we sent a sample of ^{260}Md to Philipps Universität, Marburg, FRG, for counting in their neutron counter.[2] For various reasons, the measurement was unsatisfactory, and we wanted to repeat it.

This year we produced a second sample of about 3000 atoms of ^{260}Md from the bombardment of ^{254}Es with ^{22}Ne ions. After extensive chemical purification, we electroplated the mendelevium on a thin (25- to 30-μg/cm^2) polyimide

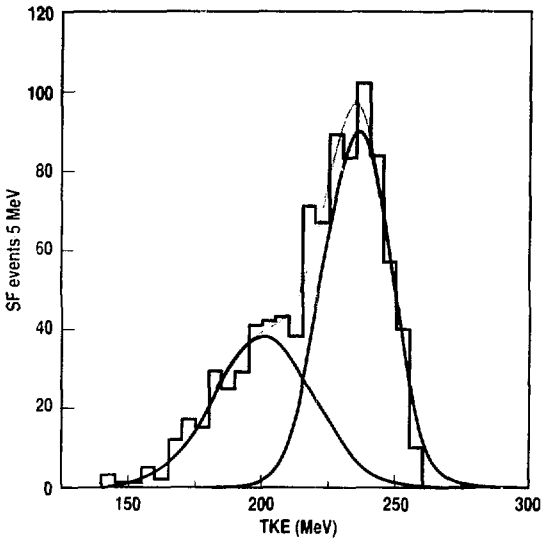

Figure 1. The TKE distribution for the SF of ^{260}Md obtained from this experiment. The two Gaussian curves represent the low- and high-TKE regions of bimodal fission: the high-TKE region contains approximately 63% of the events.

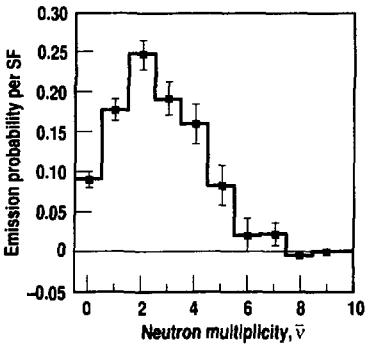

Figure 2. The total neutron-multiplicity distribution from the SF of ^{260}Md, corrected for background, dead time, and counter efficiency. The average multiplicity is 2.58 ± 0.05 neutrons per fission.

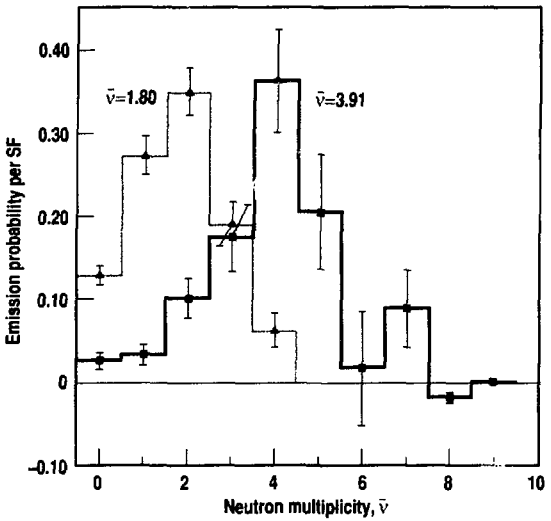

Figure 3. Partial neutron-multiplicity distributions from the SF of ^{260}Md. The blue histogram (triangular data points) is derived from fission events in the upper 63% of the TKE distribution, while the black histogram (square data points) is obtained from fission events in the lower 37% of the kinetic-energy distribution.

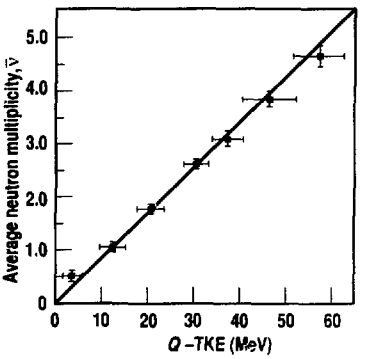

Figure 4. A plot of neutron multiplicity, $\bar{\nu}$, vs Q–TKE (fragment-excitation energy) for the SF of ^{260}Md shows the linear relationship between available fragment-excitation energy and neutron emission.

film and sent it to Marburg for the neutron-multiplicity measurement. This sample was counted for about three months without mishap. We made background, dead time, and counter-efficiency corrections to the observed neutron-multiplicity distribution from 1211 fission events, according to the method outlined by Spencer et al.[3] We used a standard of ^{252}Cf, mounted in a manner identical to that of the mendelevium sample, to calibrate the response of surface-barrier detectors to the fission-fragment energy and to determine the efficiency of the neutron counter.

Results and Discussion

The corrected (true) neutron-multiplicity distribution is shown in Fig. 2. We found the average multiplicity to be 2.58 ± 0.05 neutrons per fission. This number is more than one neutron per fission lower than that of other nuclides in the heavy-actinide region for which neutron measurements have been made. More than 25% of the SF events from ^{260}Md emit fewer than two neutrons while, in comparison, only about 3% of fissions from ^{252}Cf emit fewer than two neutrons. The distribution variance, 2.58 ± 0.11, is considerably higher than that of ^{252}Cf (1.62). This is a result of the sum of the breadths of the individual distributions from the two modes of fission from ^{260}Md.

The bimodal nature of the SF of ^{260}Md is amply demonstrated by the data in Fig. 3, which shows two partial neutron-multiplicity distributions. The blue histogram fitted to the triangular data points was obtained from SF events with TKE values in the upper 63% of the energy distribution, with an average TKE of 235 MeV. This distribution has a low average multiplicity of 1.80 ± 0.05 neutrons per fission. This indicates that there cannot be much fragment excitation energy and strongly suggests that the fragments at scission must be nearly spherical. The black histogram that fits the square data points represents the

remainder of the TKE values, which have an average TKE of 195 MeV and an average multiplicity of 3.91 ± 0.09 neutrons per fission. This latter distribution is more typical of the heavier actinides that undergo "conventional" unimodal SF, such as ^{252}Cf ($\bar{\nu}$ = 3.773) (Ref. 3), and indicates the presence of considerably more fragment-deformation energy from an elongated scission shape.

The fragment-excitation energy for fission can be estimated by calculating the Q-value for a given distribution of fragment masses and subtracting from it the measured average TKE for events with the same mass distribution. We calculated Q values and determined the average TKE for several ranges of TKE in the SF of ^{260}Md and plotted Q–TKE against the average number of neutrons emitted by fissions in each energy range (see Fig. 4). Higher values of Q–TKE result from the lower-TKE fission events and indicate fragments with higher excitation energies that emit more neutrons per fission. The direct linear relationship between excitation energy and neutron multiplicity is quite evident in Fig. 4; the line was force-fitted through the origin and has a slope corresponding to about 12 MeV per neutron emitted.

Conclusion

We have shown that the lower average neutron multiplicity from the SF of ^{260}Md indeed results from the lower average excitation energy of the fragments because the high TKE fissions have nearly spherical fragments. We have extended the relationship between excitation energy and the number of neutrons emitted to a much lower range of excitation energies than previous experiments had revealed.

References:

1. E. K. Hulet, J. F. Wild, R. J. Dougan, R. W. Lougheed, J. H. Landrum, A. D. Dougan, M. Schädel, R. L. Hahn, P. A. Baisden, C. M. Henderson, R. J. Dupzyk, K. Sümmerer, and G. R. Bethune, *Phys. Rev. Lett.* **56**, 313 (1986).
2. J. F. Wild, J. V. Aarle, W. Westmeier, R. W. Lougheed, E. K. Hulet, K. J. Moody, R. J. Dougan, R. Brandt, and P. Patzelt, "Neutron Multiplicity from the Spontaneous Fission of ^{260}Md," *Nuclear Chemistry Division FY87 Annual Report*, Lawrence Livermore National Laboratory, Livermore, Calif., UCAR-10062/87 (1987), p. 4-12.
3. R. R. Spencer, R. Gwin, and R. Ingle, *Nucl. Sci. Eng.* **80**, 603 (1982).

Discovery of 5-ms ^{262}No and the Study of Its Spontaneous-Fission Decay Properties

R. W. Lougheed, E. K. Hulet, J. F. Wild, K. J. Moody, and R. J. Dougan; C. M. Gannett, R. A. Henderson, D. C. Hoffman, and D. M. Lee (Lawrence Berkeley Laboratory, Berkeley, Calif.)

The predicted spontaneous-fission (SF) half-lives and total kinetic-energy (TKE) distributions of the neutron-rich heavy actinide nuclides are extremely sensitive to calculations of the potential-energy surface and inertial mass. Recent theoretical calculations[1–3] allow two or more fission paths in the potential-energy surface leading to bimodal fission[4] (both high and low TKE symmetric fission from the decay of the same isotope) but fail to explain the observation of nearly equal branching ratios for the fission paths. Further, SF half-lives calculated from these new paths in the potential-energy surface are inconsistent with the newer measured half-lives. Our aim, in measuring the fission properties of the heavy, neutron-rich isotopes, is to confront theory with additional experimental information in the hope that the physics of the fission process will eventually be clarified.

From experiments conducted in 1985 and 1987, we discovered two long-lived isotopes of lawrencium, ^{261}Lr and ^{262}Lr, with half-lives of 39 and 216 m, respectively.[5] The SF activities we observed did not necessarily arise from the lawrencium isotopes but could have come from the decay of ^{261}No or ^{262}No formed by electron capture (EC) from the longer-lived lawrencium parents. Q-value predictions for the EC decay of

^{262}Lr are about 2 MeV, making EC decay of the 216-m ^{262}Lr a strong possibility. In the experiments reported here, our goals were to determine if ^{262}Lr decayed by EC and to measure the half-life and SF decay properties of it or its daughter, ^{262}No, by measuring the time intervals between nobelium K x rays and subsequent SF events in samples of chemically purified lawrencium.

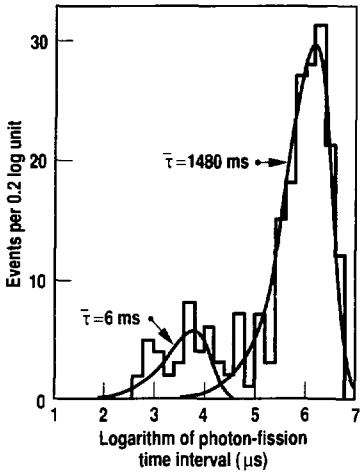

Figure 1. The logarithmic distribution of time intervals between the last photon with nobelium K x-ray energies preceding a spontaneous fission event. The smooth curves are exponential fits to the measured data shown by the histogram.

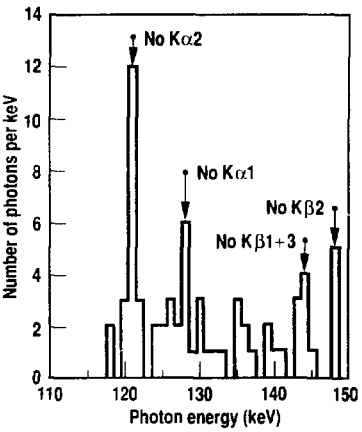

Figure 2. The energy spectrum for photons preceding fission by 50 ms.

Experimental

We bombarded a target containing 1.4×10^{17} atoms/cm^2 of ^{254}Es with 127-MeV ^{22}Ne ions at the Lawrence Berkeley Laboratory's 88-in. cyclotron and collected the recoil products on molybdenum foils. We performed a series of bombardments ranging in length from 1.5 to 9 hours. At the end of each bombardment, we dissolved the foil with HNO_3 and HCl in the presence of the rare earth tracers ^{171}Tm and ^{166m}Ho and passed the resultant solution through a Dowex 1×8 anion exchange column to remove the molybdenum and unwanted reaction products.

To remove interfering gamma-ray activities, we then performed a cation-exchange chromatographic separation of the actinides from the lanthanides using a mixture of ethanol and water saturated with HCl.

We separated lawrencium from interfering actinides using solutions of ammonium α-hydroxyisobutyrate to elute the trivalent actinides from cation-exchange resin.[6,7] Actinides and holmium and thulium tracers were eluted from the column through a 0.8-mm-i.d. Teflon capillary tube that was placed directly against the face of an intrinsic germanium detector. Because lawrencium elutes between thulium and holmium, we were able to reliably collect a single lawrencium fraction by starting the collection as the thulium activity decreased, as detected by the germanium detector. We stopped the collection at the first indication of holmium activity. Mendelevium elutes at almost exactly the same position as holmium and, hence, is efficiently separated from lawrencium by this procedure. We evaporated the lawrencium fraction to dryness with additional ^{166m}Ho tracer and then performed a second separation of lawrencium from trivalent actinides, as above.

We prepared the counting sample by electroplating the lawrencium onto 27-μg/cm^2 polyimide films that were overplated with 25 μg/cm^2 of gold. The chemically purified lawrencium fraction was first evaporated to dryness, fumed with perchloric acid to destroy organic residues, and then transferred to an electroplating cell using dilute HNO_3 and isopropyl alcohol.

We measured the energies of fission fragments and of photons in the nobelium K x-ray region using surface-barrier and intrinsic germanium detectors in a specially built, high-geometry counting chamber.[8] The energies of SF events and photons and the time intervals between the five preceding photons were recorded in list mode using computer-operated measurement and control (CAMAC) modules interfaced to an LSI-11/73 computer.

Results and Discussion

The mean lifetime of ^{262}No and confirmation of ^{262}Lr EC decay to ^{262}No are derived from the distribution of logarithmic time intervals between photons having nobelium K x rays and fission events as shown in Fig. 1. Two distributions, which follow Poisson statistics, are resolved in the figure. The larger peak, with a mean lifetime of 1480 ms, results from background photons preceding a fission event. We attribute the smaller peak, with a mean lifetime of 6 ms, to nobelium K x rays from the EC decay of ^{262}Lr and some tailing from background events. A similar plot with all photons in the 118- to 150-keV region has a background peak with a mean lifetime of 883 ms and a smaller peak with a mean lifetime of 11 ms. From these distributions of time intervals, we calculate a weighted average of 5 ms for the half-life of ^{262}No.

Considering the efficiency of the germanium detectors (34%) and the fraction of K x rays per EC decay, we expected to observe only one nobelium K x ray preceding every four fissions. However, we observed only about 65% of the nobelium K x rays that we expected. Because the decay scheme of ^{262}Lr is unknown, it is quite possible that the missing K x rays can be accounted for by summing of the K x rays with gamma-ray transitions or L x rays arising from internal conversion in the ^{262}Lr decay scheme.

This is especially probable because of the large counting efficiency of the germanium detectors and because ^{262}Lr is likely to have a 3^+ ground state that would decay to excited levels in ^{262}No.

The energy distribution of photons in the 118- to 150-keV window for those events that are within 50 ms of a fission event is shown in Fig. 2. The distribution is about that expected for a nobelium K x-ray distribution, plus some background, except that the ratio of Kα2:Kα1 events is about three times too high. We attribute the excess events in the 120-keV peak to a gamma ray in the ^{262}No decay scheme.

The fission-fragment mass and TKE distributions are shown in Fig. 3. The mass distribution is sharply symmetric (FWHM ≈12 amu), but the TKE distribution is asymmetric, peaking at 237 MeV, with a lower-energy component near 200 MeV. This distribution is similar to that of other nuclides in which we have observed bimodal fission. The fraction of high-energy symmetric fission in ^{262}No is greater than in ^{258}No, the other nobelium isotope for which we have made TKE measurements. This is consistent with our measurements of the fission properties of fermium and mendelevium isotopes, which show the fraction of the high-energy component increasing with neutron number.

Summary

The presence of two almost equally populated fission paths in the neutron-rich fermium, mendelevium, and nobelium isotopes does not have a satisfactory explanation. Calculations by Möller et al.[1] indicate a lower inertial-mass path for very heavy nuclides as they approach ^{264}Fm, which can fission into two doubly magic ^{132}Sn nuclei. This low inertial-mass path for compact shapes produces much shorter half-lives than previously estimated. Möller explains the experimental observation of bimodal fission by a switchback path (also predicted by Brosa et al.[2]) in which the nucleus initially follows the new, lower-inertia path but then can go either into the new valley (high energy symmetric fission) or the old valley (low-energy symmetric fission). However, this model does not predict the observation of nearly equal branching ratios for the two paths we find in so many isotopes. Möller's calculated SF half-life[9] for ^{262}No is 10^{11} less for the lower inertia path vs the old path and is 10^2 shorter than our measured value. The half-life of an even-even nuclide like ^{262}No is one of the simplest to estimate, yet recent calculations from the same author[1,10] vary by a range of 10^9. Even the trend of estimated half-lives with neutron number for the even-even nobelium isotopes is incorrect. Möller overestimates the SF half-life of ^{256}No by several orders of magnitude; he is very close at ^{260}No, and he underestimates the ^{262}No half-life. Although theory now provides qualitative explanations for bimodal fission, accurate quantitative predictions for both half-lives and fission paths are still not obtainable. Finally, we do not observe the predicted trend of increasing stability against SF upon approaching the 162 neutron subshell.[11–13] This may be owing in part to the high-energy fission path observed in bimodal fission.

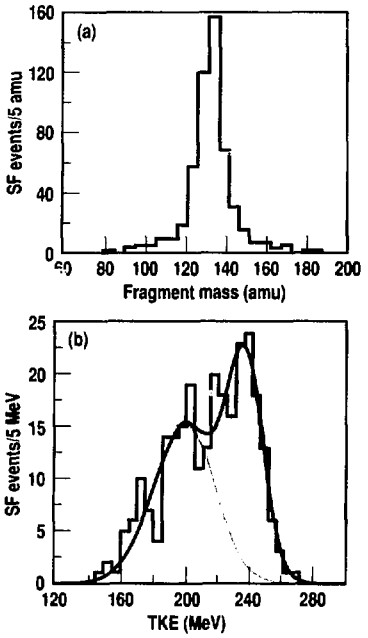

Figure 3. The fission-fragment mass and energy distributions for ^{262}No. (a) The fission-fragment mass distribution, and (b) the TKE distribution. The higher-energy peak comprises 65% of the events.

References:

1. P. Möller, J. R. Nix, and W. J. Swiatecki, *Nucl. Phys. A* **469**, 1 (1987).
2. U. Brosa, S. Grossmann, and A. Müller, *Z. für Phys. A* **325**, 241 (1986).
3. V. V. Pashkevich, *Nucl. Phys. A* **477**, 1 (1988).
4. E. K. Hulet, J. F. Wild, R. J. Dougan, R. W. Lougheed, J. H. Landrum, A. D. Dougan, M. Schädel, R. L. Hahn, P. A. Baisden, C. M. Henderson, R. J. Dupzyk, K. Sümmerer, and G. R. Bethune, *Phys. Rev. Lett.* **56**, 313 (1986).
5. R. W. Lougheed, K. J. Moody, R. J. Dougan, J. F. Wild, E. K. Hulet, R. J. Dupzyk, C. M. Henderson, C. M. Gannet, R. A. Henderson, D. C. Hoffman, D. M. Lee, K. Sümmerer, and R. L. Hahn, *Nuclear Chemistry Division FY 87 Annual Report*, Lawrence Livermore National Laboratory, Livermore, Calif., UCAR-10062-87 (1987), p. 4-2.
6. G. R. Choppin, B. G. Harvey, and S. G. Thompson, *J. Inorg. Nucl. Chem.* **2**, 66 (1956).
7. H. L. Smith and D. C. Hoffman, *J. Inorg. Nucl. Chem.* **3**, 243 (1956).
8. E. K. Hulet, R. W. Lougheed, J. F. Wild, R. J. Dougan, K. J. Moody, R. L. Hahn, C. M. Henderson, R. J. Dupzyk, and G. R. Bethune, *Phys. Rev. C* **34**, 1394 (1986).
9. P. Möller, private communication, Lawrence Berkeley Laboratory, Berkeley, Calif. (July 1988).
10. P. Möller, private communication, Lawrence Berkeley Laboratory, Berkeley, Calif. (May 1988).
11. P. Möller, J. R. Nix, W. D. Meyers, and W. D. Swiatecki, *Proc. 4th Winter Workshop on Nuclear Dynamics, Copper Mt., Colorado, February 22–28, 1986*.
12. K. Boning, Z. Patyk, A. Sobiczewski, and S. Cwiok, *Z. Phys. A* **325**, 479 (1986).
13. S. Cwiok, V. V. Pashkevich, J. Dudek, and W. Nazarewicz, *Nucl. Phys. A* **410**, 254 (1983).

Investigations of the Decay Properties of ^{263}[105] and ^{264}[105]

E. K. Hulet, R. J. Dougan, K. J. Moody, R. W. Lougheed, and J. F. Wild; K. D. Sümmerer (Gesellschaft für Schwerionenforschung, Darmstadt, FRG); G. R. Bethune (Deceased, Bethune-Cookman College, Daytona Beach, Fla.); R. L. Hahn (Oak Ridge National Laboratory, Oak Ridge, Tenn. Current address, Brookhaven National Laboratory, Upton, N.Y.); J. van Aarle (University of Marburg, Marburg, FRG); K. E. Gregorich and D. C. Hoffman (Lawrence Berkeley Laboratory, Berkeley, Calif.)

Decay properties of nuclides with neutron numbers greater than 257 are pivotal in determining future trends in the stability of nuclei beyond the upper bounds of the nuclide charts. Theoretical estimates, as we are discovering, offer neither the accuracy nor the trends needed to provide confidence in their reliability. Without accurate estimates of these nuclear properties, our attempts to bridge this unknown sea of nuclides in order to reach islands of expected stability at the superheavy elements or at a strong 162-neutron subshell have failed. These failures can be attributed mainly to the long extrapolations of the decay properties of the known nuclides in order to estimate those in these islands. For the moment, it seems that only isotope-by-isotope experimental steps upward might tell us where nuclear stability ends and if superheavy elements are a possibility. As part of this quest, we have undertaken studies aimed at determining the decay modes and half-lives of nuclides just beyond the outer border of the known ones, including two unknown isotopes of element 105, ^{263}[105] and ^{264}[105], which we discuss here.

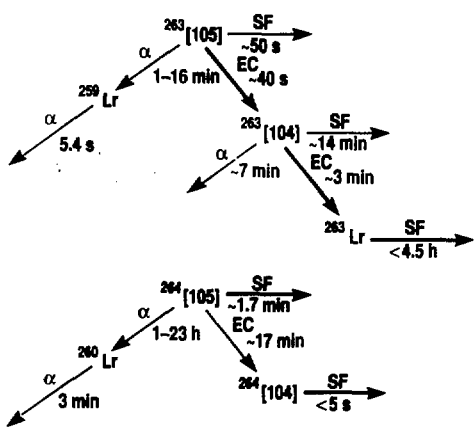

Figure 1. Half-lives predicted from mass tables and SF systematics for the decay chains originating from ^{263}[105] and ^{264}[105]. The SF estimates are quite uncertain.

Experiment and Results

Figure 1 shows our most recent estimates of the partial half-lives for each of the possible decay paths. Those for the alpha and beta decay modes were derived from a set of mass predictions and level schemes described by Moody elsewhere in this report.[1] The estimates for spontaneous fission (SF) half-lives were made from extrapolations of systematic trends. Our first experiments to detect ^{263}[105], made in 1984, were based on the expectation that alpha decay would be the dominant decay path. In those experiments, we bombarded ^{254}Es with 98.5-MeV ^{16}O ions to produce ^{263}[105] by an incomplete fusion reaction and searched for a mother-daughter sequence of alpha decays.[2] Within 3σ limits (95% confidence level), such a sequence was not observed in the half-life range of two seconds to tens of minutes, provided that the formation cross section was greater than 5 nb. This cross section is well below the 15 to 20 nb we would expect from (α,3n) emission reactions (25 to 30 nb for heavy nobelium and lawrencium isotopes).

Still believing that alpha emission would be the main decay mode, in 1986 we made a further attempt at searching for the alpha decay of ^{263}[105]. The strategy was the same, namely, looking for alpha decay of its daughter, the known isotope 4-s ^{259}Lr, within 20 s

after observing an alpha-particle in the appropriate energy range from decay of the parent ^{263}[105]. However, the reaction to produce ^{263}[105] was changed to one of complete fusion by using 71.8-MeV ^{13}C ions as the projectile to bombard ^{254}Es. In the meantime, we had revised our predictions for the alpha energy of ^{263}[105] downward and the half-life correspondingly upward. Thus, the energy window set for ^{263}[105] alpha particles was between 7.9 and 8.65 MeV, rather than the 8.32 to 8.8 MeV used in 1984.

After bombarding with a total of 1.07×10^{17} particles of ^{13}C, we found no evidence for the alpha decay of ^{263}[105] to ^{259}Lr within the half-life range of several seconds to tens of minutes. No mother-daughter pairs of events were observed in the case where the daughter might be deposited on the face of an opposing detector by recoil from the alpha particle emitted by the parent. In the case where the daughter did not leave the sample by recoil, the background essentially equaled the number of pairs of time- and alpha-energy-correlated events that potentially qualified as mother-daughters. Assuming the observation of three pairs (95% confidence), we established an upper limit for the formation cross section of 2.7 nb, whereas we would expect a cross section of 6 to 10 nb.

Having ruled out alpha emission as a major decay mode for ^{263}[105] and also finding that electron capture (EC) was now more favorable (Fig. 1), we performed a new experiment this past year to look for this latter decay mode. The strategy was to bombard for some 12 hours, allow the ^{263}[105] to decay to its EC granddaughter, lawrencium, chemically isolate lawrencium, and examine the lawrencium sample for the decay of ^{263}Lr by SF. This plan assumes that we are correct in our assessment that the daughter, ^{263}[104], decays primarily by EC and not rapidly by SF. The SF half-life estimate of 4.5 hours for ^{263}Lr that we show in Fig. 1 can be considered reasonable in light of the lower limits we have set: 40 min for ^{261}Lr and 8 hours for ^{262}Lr. The outcome of our experiment is shown in Fig. 2, where the upper limits for the formation cross section of ^{263}[105] from the bombardment of ^{254}Es with 71.8-MeV ^{13}C ions is shown as a function of half-lives for SF by ^{263}Lr. The curve was derived by assuming we found three SF events (95% confidence) attributable to ^{263}Lr, although, in fact, none were. From this experiment, it appeared that EC decay of ^{263}[105] was very unlikely to be the main decay mode.

In our attempts to identify ^{264}[105], we thought EC decay to ^{264}[104] might be a viable alternative to SF because of the uncertainty in predicting its SF half-life. If true, we would then expect, with a high degree of certainty, that the even-even daughter isotope would decay within a few seconds by SF. Our experiment, which we carried out this past year, consisted of a series of short (30-min) bombardments of ^{254}Es with 71.8-MeV ^{13}C ions followed by fast (10- to 15-min) chemical separations of element 105 and then examination of the separated samples for SF activity. The chemical separations included a cation-exchange column in which the V-B series of elements (niobium, tantalum, and element 105) were eluted from the cation resin with 0.5*M* HF, which was then followed by extraction of the V-B elements from a mixture of 6*M* HCl-6*M* HF into 4-methyl-2-pentanone. With the use of added tracers, niobium and tantalum were separated with a 50 to 60% yield, while interfering actinides were reduced by about a factor of 10^8. However, the yield of element 105 is unknown because we did not observe fission activity in the samples that we could attribute to its daughter, ^{264}[104]. If we assume the same chemical yield as for niobium and tantalum, that the half-life is 17 min and that EC predominates, we arrive at an upper limit of about 6 nb for formation of ^{264}[105].

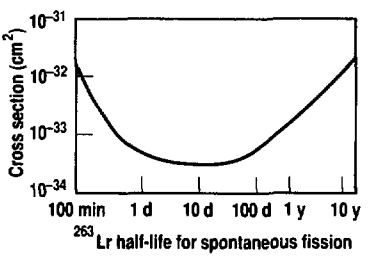

Figure 2. Upper limits for the formation cross section of ^{263}[105] as a function of the SF half-life of ^{263}Lr. It was derived on the basis of all ^{263}[105] decaying by two electron capture steps to ^{263}Lr.

Conclusions

In the case of ^{263}[105], we believe we have virtually eliminated alpha and EC as possible decay modes. We would have to conclude that the most likely possibility is SF decay with a half-life of well under one minute. Drawing a firm conclusion from our experiment on possible EC decay by ^{264}[105] is chancier because of ambiguities concerning the element's chemical properties and because the upper limit for the cross section is not as low as we might wish to measure. Nevertheless, the information we have now favors short SF by this nuclide. Unfortunately, any attempts to search for these isotopes through their SF decay are seriously hampered by the abundance of other SF emitters coproduced in other nuclear reactions used in making isotopes of element 105.

References:

1. K. J. Moody, R. W. Lougheed, E. K. Hulet, R. J. Dougan, J. F. Wild, K. Sümmerer, R. L. Hahn, J. van Aarle, and G. R. Bethune, "Actinide Cross Sections from the Reaction of ^{13}C-ions with ^{254}Es," p. 236 of this publication.
2. R. J. Dougan, E. K. Hulet, R. W. Lougheed, J. F. Wild, K. D. Sümmerer, G. R. Bethune, and R. L. Hahn, "Our Search for ^{263}[105] with the MAD Wheel," *Nuclear Chemistry Division FY 85 Annual Report*, Lawrence Livermore National Laboratory, Livermore, Calif., UCAR-10062-85 (1985), p. 4-50.

Half-Life Calculations for Actinide and Transactinide Nuclides

K. J. Moody

It is important to have reasonable estimates of the life times and decay modes of unknown nuclei before designing experiments that are aimed at producing and detecting those nuclei. These calculations are particularly difficult for the region of the chart of the nuclides that includes the heaviest known elements. Estimates of the partial spontaneous-fission (SF) half-lives for these nuclei are extremely uncertain; nevertheless, it is possible to make reasonable estimates of alpha, beta, and electron capture (EC) partial half-lives.

The most important parameter in half-life calculations is the energy available for decay via a particular process. The ground-state spin and parity of the parent nucleus, and the low-lying excited states of the daughter nuclei, are also important. Möller et al.,[1,2] among others, have performed calculations that indicate the presence of a nuclear subshell near neutron numbers 162–164. This subshell perturbs the systematics of ground-state masses and decay energies (Q-values). Because it owes its existence to the presence of deformations of higher order than quadrupole, the assignments of low-energy nuclear states on the basis of the Nilsson diagram are not feasible.

Using the calculated masses given in Ref. 1 for nuclei near and beyond the 162–164 neutron shell and the results of single-particle calculations with hexadecapole deformations,[3] I have calculated partial half-lives for alpha, beta, and EC decays of both known and unknown actinides and transactinides.

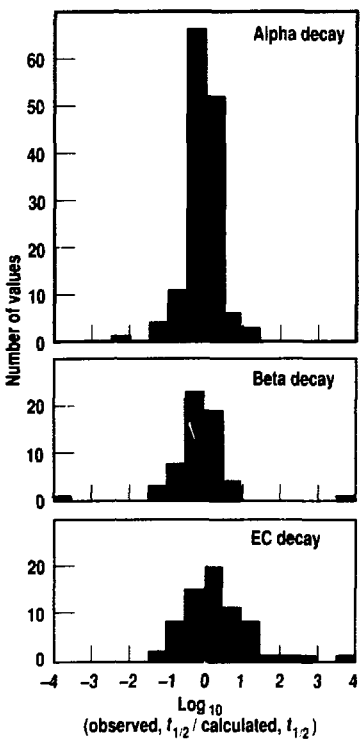

Figure 1. A comparison of calculated partial half-lives for alpha, beta, and EC decays with those observed experimentally, for nuclides with $Z \geq 89$ and $N \geq 133$. A perfect fit gives an abscissa value of zero. The poorest comparisons are for half-life estimates of odd-odd nuclei.

Calculations

I generated a set of reasonable masses by extrapolating the differences between several mass calculations[4] and masses derived from the decay properties of known nuclei[5] into the region of unknown nuclei. I expressed these differences in terms of Q-values for beta and alpha decays, the neutron separation energies, and the mass excesses themselves; then, I extrapolated at constant neutron number, at constant proton number, and at constant mass number. This generated as many as 12 "corrected" mass excess values from each mass formula for each unknown mass excess. I averaged all of these to give a result that was used in further extrapolations. I used this technique for nuclei with as many as 158 neutrons. Beyond that, I used the masses from Ref. 1, which were required to merge smoothly with the extrapolated masses.

I estimated the single-particle levels for unknown nuclei by extrapolating the levels of known nuclei according to the trends predicted by Möller and Nix.[3] The results of the Möller and Nix calculations reproduce only poorly the absolute energies of the excited states of known nuclei, but the relative energy spacings track fairly well. The energy levels of odd-odd nuclei were estimated by coupling the single-particle levels while assuming a splitting of parallel and antiparallel states of about 100 keV. Above excitation energies of 400 keV (or above the pairing gap of even-even nuclei), I used the normalized level-density expression of Lang[6] to generate the number of energy levels with a given spin and parity in each 100-keV interval of excitation energy.

Partial alpha-decay half-lives were calculated by using even-even decay rates and applying hindrance factors extracted from decay systematics. Using empirical log *ft* values, which are somewhat smaller than those of Viola and Seaborg,[7] I calculated the partial beta and EC half-lives.

Results

From these newly estimated decay energies and level structures, I generated partial half-lives for more than 400 nuclides with atomic numbers between $Z = 89$ (actinium) and $Z = 110$. Figure 1 gives a measure of the accuracy of the calculations for those nuclides whose partial half-lives are known. In all three cases (alpha, beta, and EC decay), the greatest discrepancies occurred for odd-odd nuclei. In addition, many high-multipolarity EC and beta decays of low energy (less than 100 keV) were poorly reproduced by the calculation.

In the region of the heaviest elements, between the most neutron-rich known nuclei and the 162–164 neutron shell, the most noteworthy result of the calculations is that EC decay almost always dominates over alpha decay. In many interesting cases, alpha decay does not occur until after several EC steps, resulting in nuclides near the line of beta stability. Several such decay sequences are shown in Fig. 2.

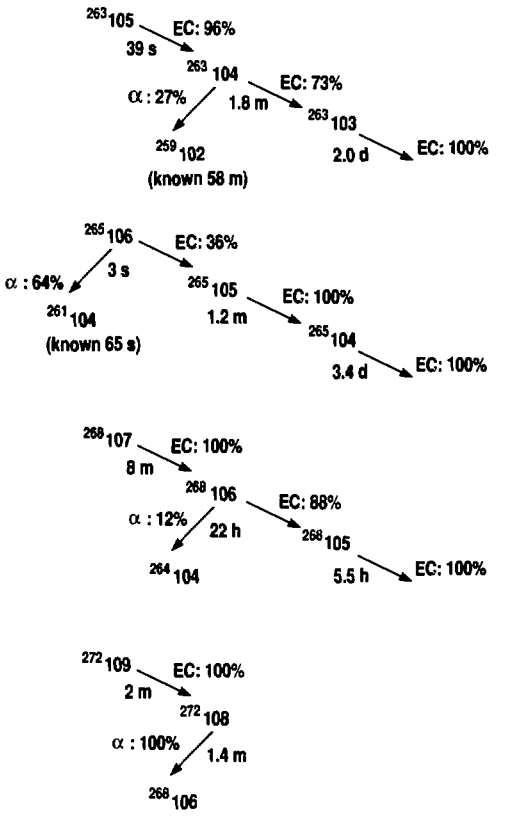

Figure 2. Four examples of calculated decay properties for unknown heavy nuclei, assuming no competition from SF decay.

It should be remembered that SF decay has not been considered in determining these decay modes. Several recent calculations[8,9] have indicated that half-lives for SF decay in the region of shell closure may be quite long; however, SF decay must always be considered, particularly for even-even nuclei.

References:

1. P. Möller and J. R. Nix, *At. Data Nucl. Data Tables* **26**, 165 (1981).
2. P. Möller, G. A. Leander, and J. R. Nix, *Z. Phys. A* **323**, 41 (1986).
3. P. Möller and J. R. Nix, private communication, Lawrence Berkeley Laboratory, Berkeley, Calif. (1986).
4. S. Maripuu, *At. Data Nucl. Data Tables* **17**, 477 (1976).
5. A. H. Wapstra and G. Audi, *Nucl. Phys. A* **432**, 1 (1985).
6. D. W. Lang, *Nucl. Phys* **77**, 545 (1966).
7. V. E. Viola, Jr. and G. T. Seaborg, *J. Inorg. Nucl. Chem.* **28**, 741 (1966).
8. P. Möller, J. R. Nix, and W. J. Swiatecki, *Nucl. Phys. A* **469**, 1 (1987).
9. Z. Lojewski and A. Baran, *Z. Phys. A* **329**, 161 (1988).

Actinide Cross Sections from the Reaction of ^{13}C Ions with ^{254g}Es

K. J. Moody, R. W. Lougheed, E. K. Hulet, R. J. Dougan, and J. F. Wild; K. Summerer (Consultant, Siemens Aktiengesellschaft, Darmstadt, FRG); R. L. Hahn (Chemistry Department, Brookhaven National Laboratory); J. von Aarle (Philips Universiteit, Nijmegen, Netherlands); and G. Bollmann (Deceased; Bethune-Cookman College, Daytona Beach, Fla.)

In the past several years, we have used targets of ^{254g}Es to explore and produce new nuclides in a region of the chart of the nuclides that is inaccessible by any other target/projectile combination.[1–3] The ^{254g}Es target material is the heaviest nuclide obtainable in quantities sufficient to be useful in heavy-ion reactions where beam intensities are limited. Transfer reactions, in which part of the heavy-ion projectile is transferred to the target nucleus, have a special advantage in producing these very heavy isotopes because many more of the products survive fission de-excitation than do the products of heavy-ion fusion reactions. This is due to the lower excitation energies of the primary reaction products.

Transfer reactions with various actinide targets have been studied with projectiles ranging from ^{16}O to ^{238}U (Refs. 1, 4–6). Transfer reactions with the heaviest projectiles (at energies near the interaction barrier) produce broad distributions of nuclides with atomic numbers both above and below that of the target. If a projectile of lower mass is used, the cross-section distributions narrow, and the production of above-target nuclides dominates over below-target production.

We report preliminary results for actinide cross sections from the reaction of ^{13}C ions with ^{254g}Es. This is the first comprehensive measurement of actinide transfer products with a projectile as light as ^{13}C.

Experimental

Targets of 40 to 50 $\mu g/cm^2$ of ^{254g}Es were bombarded at Lawrence Berkeley Laboratory's 88-in. cyclotron with 71.8-MeV ^{13}C ions. Reaction products recoiling out of the target passed through a 50-$\mu g/cm^2$ aluminum cover foil and were either stopped in molybdenum catcher foils mounted close to the target or were attached to KCl aerosol particles that were swept along a capillary and deposited on polypropylene foils. We counted some of these samples without further processing; others, we dissolved and chemically processed, isolating fractions of Es, Fm, Md, and Lr. We stippled these fractions on platinum disks for counting.

Using surface barrier detectors, we counted all samples for alpha particles and spontaneous-fission events. The pulse-height spectra were recorded periodically for as long as eight months after the irradiations. The yields we obtained from decay-curve analyses were used to calculate the cross-section set given in Table 1.

Table 1. Cross sections for heavy nuclide production from 71.8-MeV ^{13}C ions on ^{254g}Es.

Nuclide	Cross section (cm^2)[a]
^{252}Es	$(3.64 \pm 0.51) \times 10^{-27}$
^{253}Es	$(1.32 \pm 0.17) \times 10^{-26}$
^{254g}Es[b]	$(4.63 \pm 0.54) \times 10^{-25}$
^{254m}Es	$(8.42 \pm 1.24) \times 10^{-27}$
^{255}Es	$(1.79 \pm 0.19) \times 10^{-26}$
^{256g}Es	$(7.3 \pm 2.6) \times 10^{-30}$
^{256m}Es	$(1.54 \pm 0.42) \times 10^{-29}$
^{253}Fm	$(3.0 \pm 0.5) \times 10^{-28}$
^{254}Fm	$(1.76 \pm 0.24) \times 10^{-27}$
^{255}Fm	$(2.47 \pm 0.34) \times 10^{-27}$
^{256}Fm	$(7.77 \pm 0.82) \times 10^{-28}$
^{257}Fm	$(1.84 \pm 0.29) \times 10^{-28}$
^{256}Md	$(4.13 \pm 0.42) \times 10^{-29}$
^{257}Md	$(6.79 \pm 0.68) \times 10^{-29}$
^{258g}Md	$(2.11 \pm 0.21) \times 10^{-29}$
^{260}Md	$\leq 1.7 \times 10^{-31}$
^{261}Lr	approx. 3×10^{-32}
^{262}Lr	approx. 1.5×10^{-33}

[a] The cross sections have been corrected for ingrowth from parent activities and for contributions from reactions with impurities in the target.

[b] This cross section does not include reaction products with total recoil energies less than approximately 1.5 MeV.

Discussion

From previous work with heavier projectiles,[5] we are able to exclude the possibility of significant production of nuclides with atomic numbers less than that of the target. We were able to measure the cross sections for all important reaction products. The cross section for ^{254g}Es, which was calculated on the basis of five experiments that gave the same result, has contributions both from nuclear scattering and from elastic (Rutherford) scattering at larger impact parameters. On the basis of the other einsteinium cross sections, we estimate the nuclear contribution to be about 3×10^{-26} cm^2. The total transfer yield is therefore about 80 mb.

A bombarding energy of 71.8 MeV is only about 1 MeV over the reaction barrier. At this energy, we calculate[7] the

total reaction cross section to be about 270 mb. Fusion accounts for about 60 mb, leaving 210 mb available for transfer reactions. The observed transfer yield is more than a third of this value, indicating that a significant fraction of the primary reaction products is formed with little more excitation energy than their fission barriers. This is typically about 5.5 to 6.5 MeV for these nuclides.[8]

In the upper portion of Fig. 1, we plot the observed yields for mendelevium isotopes against their mass numbers. In the lower portion of the figure, we show the Q-values for their formation via binary reactions. The most probable primary mendelevium product mass, about 258 mass units, is determined by the transfer of two protons and a number of neutrons defined by the N/Z of the projectile. Because of the low reaction energy, at most only 22 MeV can be supplied by the collision to make mendelevium isotopes; the binary Q-values allow only mass numbers between 257 and 259. We would expect the primary product distribution to be narrow, peaking at mass 258; however, our observed distribution peaks at mass 257. This indicates that on the average only one neutron is emitted in the de-excitation of the primary products that form the mendelevium isotopes. This corresponds to an average excitation energy of about 7 MeV.

Lawrencium isotopes can be produced in two ways. First, there is sufficient energy in the difference between the entrance-channel energy and the Coulomb repulsion in the exit channel to provide for the formation of these nuclides via transfer reactions. Second, it is possible to form these products via the precompound emission of an alpha particle during the formation of the incomplete fusion nucleus $^{263}103$. In this process, an alpha particle emitted from the projectile carries away substantial excitation energy before complete fusion of the projectile residual with the target nucleus. Then, de-excitation via the emission of neutrons results in the observed reaction products. The magnitudes of the cross sections we observed are consistent with what we would expect from either mechanism.

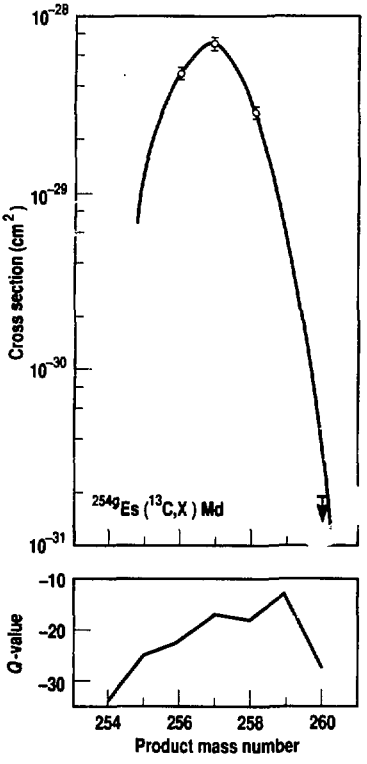

Figure 1. The observed cross sections for the production of mendelevium isotopes in the reaction of 71.8-MeV ^{13}C on ^{254g}Es, and the Q-values for their formation via a binary process. The curve through the cross sections is Gaussian, with FWHM = 2.25 mass units, which fits similar products of the reaction of other heavy ions with ^{254g}Es (Ref. 1).

References:

1. M. Schadel, W. Bruchle, M. Brugger, H. Gaggeler, K. J. Moody, D. Schardt, K. Sümmerer, E. K. Hulet, A. D. Dougan, R. J. Dougan, J. H. Landrum, R. W. Lougheed, J. F. Wild, and G. D. O'Kelley, *Phys. Rev. C* **33**, 1547 (1986).
2. R. W. Lougheed, E. K. Hulet, R. J. Dougan, J. F. Wild, R. J. Dupzyk, C. M. Henderson, K. J. Moody, R. L. Hahn, K. Sümmerer, and G. Bethune, *J. Less-Common Metals* **122**, 461 (1986).
3. E. K. Hulet, R. W. Lougheed, J. F. Wild, R. J. Dougan, K. J. Moody, R. L. Hahn, C. M. Henderson, R. J. Dupzyk, and G. R. Bethune, *Phys. Rev. C* **34**, 1394 (1986).
4. D. Lee, H. R. von Gunten, B. Jacak, M. Nurmia, Y.-F. Liu, C. Luo, G. T. Seaborg, and D. C. Hoffman, *Phys. Rev. C* **25**, 286 (1982).
5. K. J. Moody, D. Lee, R. B. Welch, K. E. Gregorich, G. T. Seaborg, R. W. Lougheed, and E. K. Hulet, *Phys. Rev. C* **33**, 1315 (1986).
6. M. Schadel, W. Bruchle, H. Gaggeler, J. V. Kratz, K. Sümmerer, G. Wirth, G. Herrmann, R. Stakemann, G. Tittel, N. Trautmann, J. M. Nitschke, E. K. Hulet, R. W. Lougheed, R. L. Hahn, and R. Ferguson, *Phys. Rev. Lett.* **48**, 852 (1982).
7. W. W. Wilcke, J. R. Birkelund, H. J. Wollersheim, A. D. Hoover, J. R. Huizenga, W. U. Schroder, and L. E. Tubbs, *At. Data Nucl. Data Tables* **25**, 389 (1980).
8. S. Cwiok, Z. Lojewski, and V. V. Pashkevich, *Nucl. Phys. A* **444**, 1 (1985).

Possible Two-Phonon Octupole States in ^{96}Zr

E. A. Henry, R. A. Meyer, L. G. Mann, and A. Aprahamian; K. H. Maier (Hahn-Meitner Institute, West Berlin, FRG); and N. Roy (San Jose State University, San Jose, Calif.)

We have examined our in-beam gamma-ray and conversion-electron data on the nuclear structure of ^{96}Zr with the aim of identifying candidates for two-phonon octupole states in that nucleus. A two-phonon octupole excitation would consist of a quartet of levels with spin/parity values of 0^+, 2^+, 4^+, and 6^+ at about twice the excitation energy of the one-phonon 3^- state in nuclei. Searches have been conducted for this fundamental nuclear excitation in nuclei such as ^{146}Gd and ^{208}Pb that have 3^- states at relatively low energies.[1,2] Evidence for such states has been generally inconclusive, although the coupling of one and two particles to two-phonon octupole states has been observed.[3]

Nazarewicz et al.[4] predict softness toward octupole deformation in transitional nuclei near $N = 56$, including ^{96}Zr. In ^{96}Zr, the 3^- level is at 1897 keV, only somewhat higher than the 2_1^+ level and lower than the collective 2_2^+ level. In the heavy zirconium nuclei, the 3^- level is reasonably collective [B(E3) ≈ 20 Weisskopf units (W.u.)], and the collectivity increases somewhat as neutron pairs are added to ^{90}Zr (Ref. 5). In addition, a 5^- level exists at 3120 keV that decays mainly to the 3^- level, and it is probably a quadrupole-octupole two-phonon state. A signature of the two-phonon octupole quartet would be fast E1 transitions to these 3^- and 5^- levels. The number of other levels in ^{96}Zr with spins and parities 0^+, 2^+, 4^+, and 6^+ is low because of its double subshell closure and the relatively high energy of the collective quadrupole state. Thus, ^{96}Zr is an attractive nucleus in which to search for the two-phonon octupole states.

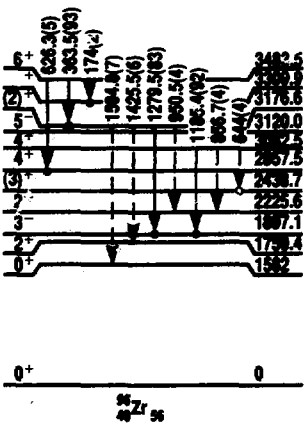

Figure 1. Selected levels for ^{96}Zr (Ref. 6). Excited levels at 3082, 3176, and 3483 keV are candidates for two-phonon octupole states. Transitions indicated by dashed lines are placed on the basis of energy only.

Data and Discussion

We have previously reported on our data and level scheme for ^{96}Zr (Ref. 6) and proposed the existence of a two-phonon octupole multiplet in ^{96}Zr (Ref. 7). Our conversion-electron data revealed three intense E1 transitions with energies of 1185, 1279, and 363 keV. These three transitions establish positive parity for the excited levels at 3082, 3176, and 3483 keV, respectively. The spins of the 3082- and 3483-keV levels are constrained by various other data to be 4 and 6, respectively. We believe the level at 3176 keV may have a spin of 2 because we observe a weak 1595-keV gamma ray that could be a transition from the 3176-keV level to the 0^+ level at 1582 keV. Although other spins are possible if the placement of the 1595-keV transition is incorrect, a spin of 2 is assumed in this discussion. A partial level scheme showing levels and transitions important in the analysis of possible two-phonon octupole states is shown in Fig. 1. In addition to the more intense transitions that have been previously placed by coincidence relationships,[6] several weak transitions are included which are placed only by energy sums. Their placement is not definite, but their intensities at least provide an upper limit for potential transitions.

Collected in Table 1 are data pertinent to the characterization of the 3082-, 3176-, and 3483-keV levels as possible two-phonon octupole states. These data include transition branching ratios, reduced E1 and E2 transition rates for those levels with measured lifetimes,[8] and the reduced transition-rate ratios B(E1):B(E2). In the actinide nuclei and heavy barium nuclei, a value of 10^{-6} fm^{-2} for B(E1):B(E2) is regarded as a good indication of octupole deformation.[9] The B(E1):B(E2) ratios for the 3082-, 3176-, and 3483-keV levels are up to 40 times those found in actinide and barium nuclei. However, the measured half-lives for the 3082- and 3176-keV levels reveal that the E2 transitions depopulating these levels

have approximately single-particle strength, whereas those in the actinide and barium nuclei are highly collective. Nevertheless, the E1 transition rate for the 3176-keV level is greater than 10^{-4} W.u., and the E1 transition rate for the 3082-keV level could be greater than 10^{-4} W.u. The absolute E1 transition rate for depopulation of the 3483-keV level requires a measurement of its half-life. However, the B(E1):B(E2) ratio for the 3483-keV level is similar to that of the 3176-keV level, suggesting that the E1 decay from the 3483-keV level could be fast.

Absolute E1 transition rates have been compiled[10] for nuclei with masses from 90 to 150. Few values are known for E1 transitions from positive to negative parity levels. Those that are known all have B(E1) values less than 10^{-4} W.u. Values for E1 transitions from negative to positive parity levels (e.g., $3^- \rightarrow 2^+$, or $1^- \rightarrow 0^+$) are typically 10^{-3} to 10^{-4} W.u. The latter transitions are generally concentrated in nuclei between barium and gadolinium, where the low-lying negative parity levels are regarded as arising from octupole vibration or deformation, and the influence of octupole deformation on collective band structure is suggested.[9] Thus, one signature of the two-phonon octupole states is their decay by E1 transitions with transition rates greater than 10^{-4} W.u.

We see, by comparing E1 transition rates in ^{96}Zr to the systematics just described, that the 3176-keV level and possibly the 3083-keV level are good candidates for two-phonon octupole states. A half-life measurement is needed for the level at 3483 keV to determine the E1 decay rate from that level. However, the large B(E1):B(E2) ratio of the 3483-keV level, similar to that of the 3176-keV level, suggests that it is also a good candidate.

Conclusion

We have identified three positive parity levels in ^{96}Zr that are possible candidates for two-phonon octupole states. If this identification can be strengthened and confirmed, it would be the first time that more than one member of the two-phonon octupole quartet has been identified. Further experimental work in this direction would include a measurement of the half-life of the 3483-keV level; improved half-life values for the 3176- and 3082-keV levels; confirmation of placement of the weaker transitions; a definitive spin assignment for the 3176-keV level; a search for collective E3 transitions in favorable cases (e.g., from the 6^+ 3483-keV level to the 3^- 1897-keV level); and reaction studies such as (d,d'), which can be used to identify and study octupole states.

Table 1. Characterization of levels in ^{96}Zr as possible two-phonon octupole states.

Initial level (keV)	Final level (keV)	Transition	Branch (%)	$t_{1/2}$[a] (ps)	B(Eλ)[b] (W.u.)	B(E1):B(E2)
3082(4⁻)	1897(3⁻)	1185(E1)	92	2	$<1.3 \times 10^{-4}$	1.2×10^{6}
	2225(2⁻)	857(E2)	4		<1.4	
3176((2)⁻)	1897(3⁻)	1279(E1)	83	$0.56^{+0.85}_{0.41}$	$3.3^{+9.0}_{2.0} \times 10^{-4}$	45×10^{6}
	1582(0⁺)	1595(E2)	7		$0.38^{+1.4}_{0.23}$	
3483(6⁻)	3120(5⁻)	361(E1)	93			29×10^{6}
	2857(4⁻)	626(E2)	5			

[a] Taken from Ref. 8.

[b] B(E1) values greater than 10^{-4} W.u. suggest the influence of octupole vibration or deformation.

References:

1. S. W. Yates, L. G. Mann, E. A. Henry, D. J. Decman, R. A. Meyer, R. J. Estep, R. Julin, A. Passoja, J. Kantele, and W. Trzacka, *Phys. Rev. C* **36**, 2143 (1987).
2. R. Julin, J. Kantele, J. Kumpulainen, A. Passoja, W. Trzaska, E. Verho, and J. Blomqvist, *JYFL Annual Report*, University of Jyvaskyla, Jyvaskyla, Finland (1987), p. 81.
3. S. Lunardi, P. Kleinheinz, M. Piiparinen, M. Ogawa, M. Lach, and J. Blomquist, *Phys. Rev. Lett.* **53**, 1531 (1984).
4. W. Nazarewicz, P. Olanders, I. Ragnarsson, J. Dudek, G. A. Leander, P. Möller, and E. Ruchowska, *Nucl. Phys. A* **429**, 269 (1984).
5. D. Rychel, R. Gyufko, V. van Kruchten, M. Lahanas, P. Singh, and C. A. Wiedner, *Z. Phys. A* **326**, 455 (1987).
6. E. A. Henry, A. Aprahamian, K. H. Maier, L. G. Mann, R. A. Meyer, and N. Roy, *Nuclear Chemistry Division FY 87 Annual Report*, Lawrence Livermore National Laboratory, Livermore, Calif., UCAR-10062-87-1 (1987), p. 4-47.
7. R. A. Meyer and E. A. Henry, *Inst. of Physics* **88**, 458 (1988).
8. T. Belgya, G. Molnar, B. Fazekas, A. Veres, S. W. Yates, and R. A. Gatenby, in *Nuclear Structure of the Zirconium Region*, J. Ebert, R. A. Meyer, and K. Sistemich, Eds. (Springer-Verlag, Heidelberg, FRG) (in press).
9. W. R. Phillips, I. Ahmad, H. Emling, R. Holzmann, R. V. F. Janssens, T.-L. Khoo, and M. W. Drigert, *Phys. Rev. Lett.* **57**, 3257 (1986).
10. P. M. Endt, *At. Data and Nucl. Data Tables* **126**, 43 (1981).

Single-Proton Transfer Experiments on a ^{148}Gd Target

L. G. Mann, D. J. Decman, H. E. Martz, and T. N. Massey; P. Kleinheinz (Institut für Kernphysik, Kernforschungsanlage Jülich, Jülich, FRG); H. J. Scheerer (Physik Department, der Technischen Universität München, FRG); and D. G. Burke (McMaster University, Hamilton, Ontario, Canada)

Studies of ^{146}Gd and neighboring nuclei suggest a double-shell closure at $Z = 64$ protons and $N = 82$ neutrons.[1] The proton shell, or subshell, closure at $Z = 64$ results from a larger energy gap between the $1g_{7/2}$ and $2d_{5/2}$ orbitals, which are filled at 64 protons, and the higher-lying $h_{11/2}$, $d_{3/2}$, and $s_{1/2}$ orbitals below the $Z = 82$ shell closure. A direct way to investigate the 64-proton shell closure is by single-proton transfer reactions, which probe the occupancy of the five proton orbitals between the 50 and 82 magic numbers. These experiments would be most valuable if performed on the 82-neutron target nucleus ^{146}Gd because the strength of the proton-shell closure deteriorates rapidly as the neutron number deviates from $N = 82$. However, it is unlikely that useful targets of ^{146}Gd can be fabricated because of its short (48-d) half-life. Therefore, the best available target is ^{148}Gd.

Several years ago, we fabricated two targets of radioactive ^{148}Gd for use in charged-particle spectroscopy experiments.[2] The ^{148}Gd, which decays by alpha emission with $t_{1/2} = 75$ y, was produced by spallation reactions in tantalum at the Isotopes Production Facility of the Los Alamos Meson Physics Facility (LAMPF).[3] After chemical purifications at Los Alamos and LLNL, target spots of approximately 1 μg of ^{148}Gd were deposited directly onto 50-μg/cm^2 carbon foils by the LLNL isotope separator.

In proton-stripping experiments with the ^{148}Gd(^{3}He,d)^{149}Tb reaction, we clearly identified[4] the five low-lying levels in ^{149}Tb that are produced by proton transfer to the five shell-model orbitals between $Z = 50$ and 84. The spectroscopic factors showed that the $g_{7/2}$ and $d_{5/2}$ orbitals are

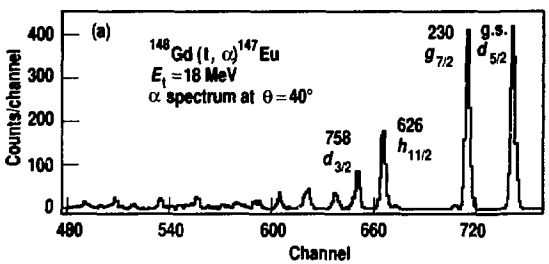

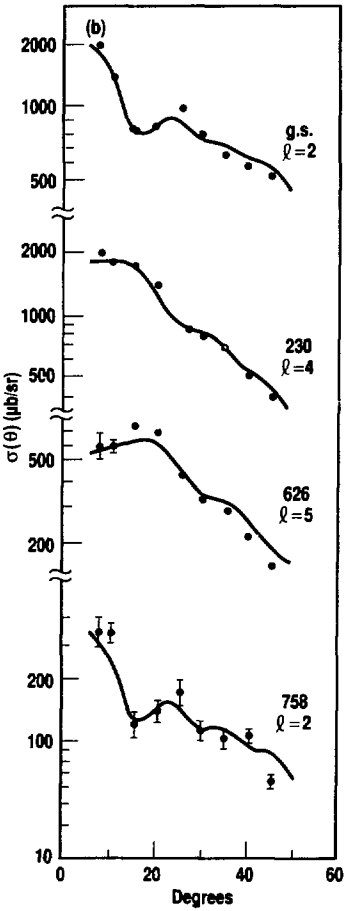

Figure 1. Experimental results for the ^{148}Gd(t,α)^{147}Eu reaction: (a) Alpha spectrum at 40 degrees. Peaks are labeled by the excitation energy (keV) above the ground state in ^{147}Eu and by the proton orbital. (b) Angular distributions of alpha particles. The solid curves are theoretical distributions from a DWBA calculation.

nearly full in ^{148}Gd, and the $h_{11/2}$, $d_{3/2}$, and $s_{1/2}$ are nearly empty, indicating that proton-pair correlations across the $Z = 64$ gap are quite weak in this $N = 84$ nucleus. In this article, we will compare the results from the stripping experiments with new data from the complementary ^{148}Gd(t,α)^{147}Eu pickup reaction.

Experimental

The ^{148}Gd(t,α) experiments were performed with 18-MeV tritons at the tandem Van de Graaff Laboratory at McMaster University. We obtained alpha-particle spectra at nine angles between 7.5 and 45 degrees. The analyzer was an Enge split-pole spectrograph, which provided an overall energy resolution of 22 to 25 keV full width at half maximum (FWHM). The integrated triton beam current on target, needed for obtaining absolute cross sections from the alpha spectra, was monitored by counting elastically scattered tritons from Gd in a Si(Li) detector subtending a known solid angle. The ^{169}Tm(t,α) reaction provided the data for energy calibration of the spectrometer.

Figure 1(a) shows the alpha spectrum obtained at an angle of 40 degrees. We used a spectrum-fitting code, FITEK, and the spectrometer calibration curve to obtain relative intensities and the ^{147}Eu excitation energies associated with each peak. The intensities were converted to absolute cross sections by comparing the counting data with the elastic-scattering cross sections calculated in the distorted-wave Born approximation (DWBA) by the DWUCK code.

Figure 1(b) shows the angular distributions of the (t,α) cross section for the four lowest energy levels in ^{147}Eu. For these four levels, the comparison with the calculated angular distributions from DWUCK clearly establishes the angular momentum transfer (ℓ-value) and, hence, the orbital from which the proton was picked up. These orbitals and ℓ-values, as labeled in Figs. 1(a) and (b), agree with results from other recent work[5] on ^{147}Eu. (No evidence exists for the $s_{1/2}$ state in ^{147}Eu.)

Discussion

The relation between the differential (t,α) cross section for a particular state in the residual nucleus and the cross section σ_{DW} calculated in the DWBA is

$$\frac{d\sigma(\theta)}{d\Omega} = N S_{j\ell}\, \sigma_{DW}(\theta)\,. \qquad (1)$$

The constant N is a normalization factor which, for the (t,α) reaction, has values of about 23, but which requires empirical adjustment for the target and energies used. The spectroscopic factor $S_{j\ell}$ is the fraction of the total cross section σ_{DW} associated with a particular state. For states of the same spin j populated by the pickup reaction, the quantity $\Sigma(2j+1)S_{j\ell}$ gives the number of particles (protons) for the (j,ℓ) orbital in the target nucleus. Thus, the pickup and stripping reactions are sensitive measures, respectively, of the particles or fullness, V^2, and the vacancies or emptiness, U^2, for the orbitals of the target nucleus.

Table 1 summarizes the proton pickup and stripping results for ^{148}Gd. We have normalized the (^{3}He,d) and (t,α) results so that $\Sigma(2j+1)S_{j\ell}$ for the levels shown equals 18 (the number of vacancies) and 14 (the number of protons), respectively, in the 50–82 shell. Thus, we ignore possible weak populating of higher-energy states of the same (j,ℓ). The (^{3}He,d) and (t,α) results are in excellent agreement, as shown by the fact that $U^2 + V^2 \approx 1$ for each of the orbitals.

References:

1. P. Kleinheinz, R. Broda, P. J. Daly, S. Lundardi, M. Ogawa, and J. Blomqvist, *Z. Phys. A* **290**, 279 (1979).
2. R. G. Lanier, T. N. Massey, E. A. Henry, D. H. Sisson, and C. M. Henderson, "Preparation of ^{148}Gd(75y) Targets for Nuclear Spectroscopy Experiments," *Nuclear Chemistry Division FY 84 Annual Report*, Lawrence Livermore National Laboratory, Livermore, Calif., UCAR-10062-84/1 (1984), pp. 6-62 to 6-64.
3. K. E. Thomas, *Radiochim Acta* **34**, 135 (1983).
4. D. J. Decman, L. G. Mann, T. N. Massey, G. L. Struble, D. H. Sisson, C. M. Henderson, K. E. Thomas, H. A. O'Brien, Jr., H. J. Scheerer, and P. Kleinheinz, "Single-Proton States in ^{149}Tb from the ^{148}Gd(^{3}He,d) Reaction," *Nuclear Chemistry Division FY 84 Annual Report*, Lawrence Livermore National Laboratory, Livermore, Calif., UCAR-10062-84/1 (1984), pp. 6-68 to 6-70.
5. R. Julin, A. Pakkanen, M. Piiparinen, B. Rubio, and P. Kleinheinz, "Non-yrast States in ^{147}Eu," *JYFL Annual Report 1985*, Dept. of Physics, University of Jyväskyla, Jyväskyla, Finland.

Table 1. Spectroscopic factors $S_{j\ell}$ for single-proton transfer (^{3}He,d) and single-proton pickup (t,α) on a ^{148}Gd target.

Proton orbit	Excited-state energy in residual nucleus (keV) (^{3}He,d)	(t,α)	Spectroscopic strength $(2j+1)S_{j\ell}$[a] (^{3}He,d)	(t,α)	$U^2 + V^2$
$2d_{5/2}$	207	0	1.6	4.1	0.95
$1g_{7/2}$	460	229.3	1.3	7.1	1.05
$1h_{11/2}$	36	625.3	10.2	2.2	1.04
$2d_{3/2}$	101	755.1	3.3	0.6	0.98
$3s_{1/2}$	0	—	1.6	—	0.8 + ?
		Σ = 18.0	14.0		

[a] Normalized so that the sum of $(2j+1)S_{j\ell}$ equals 18 and 14 for the (^{3}He,d) and (t,α) reactions, respectively.

Measurement of Magnetic Dipole Ground-State Transitions in ^{148,150}Nd and ^{152}Sm by Using Inelastic Electron Scattering

A. Nitsch, K.-G. Dietrich, and A. Richter (Institut für Kernphysik, Darmstadt Technische Hochschule, Darmstadt D-6100, FRG); R. A. Meyer and E. A. Henry

In 1984, a hitherto unknown orbital-magnetic-dipole mode was discovered in deformed rare-earth nuclei by using high-resolution, inelastic electron scattering.[1] This orbital-magnetic-dipole (isovector M1) mode can be visualized by analogy to the electric giant dipole resonance (E1 mode). The E1 mode is caused by translational oscillation of neutrons against protons, while the M1 mode can be visualized as a scissor-like configuration (see Fig. 1). The orbital M1 mode is excited strongly by magnetic-dipole radiation through coupling to the proton convection current and has been called the "scissors mode."[2] Such modes have been found in deformed nuclei ranging from ^{44}Ti to ^{238}U. For even-even nuclei, we can expect $J^{\pi} = 1^+$ states with energy that scales as $E_x \approx 66\delta A^{-1/3}$ MeV, where δ is the mass-deformation parameter.[3] For nuclei near $A \approx 150$, this leads to $E_x \approx 3$ MeV.

Since the experimental discovery of this excitation mode, various theoretical models have been developed to describe it.[3] A systematic study of neodymium nuclei and nearby nuclei presents the opportunity to compare theory with the experimentally determined development and behavior of the scissors mode from the $N = 82$ closed neutron shell to ^{150}Nd, a nucleus that is deformed. This orbital M1 mode is detected best by electromagnetic probes such as (e,e′) and (γ,γ′); they are usually unobserved, or only weakly observed, with hadronic probes such as (p,p′). Thus, preliminary identification of the scissors-mode states can be made simply by comparing (e,e′) and (p p′) scattering experiments. In order to study the distribution and variation of strength in nuclei that are not purely rotational, we have searched for the scissors mode in ^{148}Nd and ^{152}Sm and have complemented these measurements with measurements in the almost purely rotational nucleus ^{150}Nd, which is an isotone of ^{152}Sm. Since the experiments and their detailed analyses are still in progress, we present here only preliminary results.

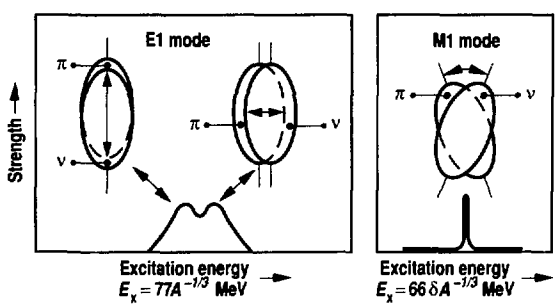

Figure 1. Classical two-fluid picture of collective vibrations of neutrons, ν, against protons, π, leading to isovector E1 and M1 modes, respectively (see Ref. 3 for details).

Experiment

The (e,e′) experiments are being carried out at the Darmstadt Technische Hochschule, Darmstadt, FRG, electron linear accelerator (DALINAC) facility. Isotopically enriched targets 10 mg/cm^2 thick have been used. To date, two spectra for each target have been measured at a scattering angle of 165 degrees, one at a bombarding energy of 25 MeV and the other at an energy of 30 MeV. Total beam time needed for these measurements has amounted to six weeks.

Simultaneously with the (e,e′) experiments, (γ,γ′) experiments have been performed at the new superconducting accelerator at Darmstadt.[4] These experiments have identified 1^+ states at excitation energies of $E_x = 2.931$ (^{152}Nd), 2.992 (^{150}Nd), and 3.090 (^{148}Nd) MeV with excitation strength of $B(M1)\uparrow \approx 0.5$, 0.2, and 0.2 μ_N^2, respectively.

The preliminary analysis of the experimental data that we have collected so far for the series $^{148}Nd_{88}$, $^{150}Nd_{90}$, and $^{152}Sm_{90}$, which bridges the transition

from nonsymmetric-rotor ground state to a fully rotational symmetric rotor, has yielded the background-subtracted spectra shown in Fig. 2. The line shapes are determined with elastically scattered electrons. Although more statistics will be required, these very preliminary spectra already show the expected growth in scissors mode resonance from nearly zero in ^{148}Nd to an identifiable strength in ^{152}Sm. Even though more spectra at different momentum-transfer values must be taken, the form factors obtained so far yield results that are in agreement with the results from the (γ,γ') experiments.

Conclusion

We have identified 1^+ states in ^{148}Nd, ^{150}Nd, and ^{152}Sm nuclei that can be identified as belonging to the M1 scissors mode of nuclear vibration. Further data will be taken for these nuclei and other lighter neodymium nuclei. These data will characterize the systematic development of this excitation mode in nuclei from the $N = 82$ closed neutron shell to the nearly completely symmetric rotor nucleus ^{150}Nd. Once they are well characterized, these results will form a basis for in-beam gamma-ray and conversion-electron studies of the same nuclei. These studies will focus on exploring the electromagnetic de-excitation of these scissors modes and their development (e.g., see Ref. 5).

References:

1. D. Bohle, A. Richter, W. Steffen, A. E. L. Dieperink, N. Lo Iudice, F. Polumbo, and O. Scholten, *Phys. Lett. B* **137**, 27 (1984).
2. N. Lo Iudice and F. Polumbo, *Phys. Rev. Lett.* **41**, 1532 (1978).
3. A. Richter, in *Interactions and Structures in Nuclei* (Institute of Physics, London, 1988), p. 25.
4. V. Aab, K. Alrutz-Ziemssen, R. Amend, D. Flasche, H. D. Graef, V. Huck, K. D. Hummel, M. Knirsch, F. Linqvist, W. Lotz, A. Richter, and K. W. Shepard (Eds.), *The Super. onducting 130 MeV Accelerator at Darmstadt*, Darmstadt Technische Hochschule, Darmstadt, FRG, IKDA 87/30 (1987).
5. R. A. Meyer, E. A. Henry, A. Aprahamian, L. G. Mann, S. Brant, V. Paar, and O. Scholten, *Nuclear Chemistry Division FY 86 Annual Report*, Lawrence Livermore National Laboratory, Livermore, Calif., UCAR-10062-86 (1986), p. 4-58.

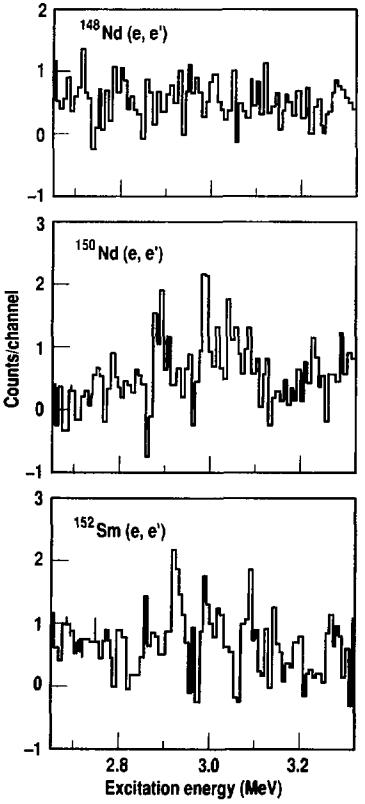

Figure 2. Preliminary (e,e′) spectra taken at 25 MeV and θ = 165 deg.

The Nuclear Structure of Deformed Odd-Odd Nuclei: Experimental and Theoretical Investigations

R. W. Hoff; A. K. Jain (University of Roorkee, Roorkee, India, on leave at Florida State University, Tallahassee, Fla.); P. C. Sood (Banaras Hindu University, Varanasi, India, on leave at Florida State University, Tallahassee, Fla.); and R. K. Sheline (Florida State University, Tallahassee, Fla.)

Among several papers that have treated the calculation of Gallagher-Moszkowski (G-M) matrix elements and Newby shifts in odd-odd rare-earth nuclei, two of the more comprehensive are those of Boisson et al.[1] and Elmore and Alford.[2] Because we are not aware of the publication of similar surveys since the mid-1970s and because neither of these papers treated actinide nuclei, we have begun an effort to update these data.

Data Compilation and Update

A summary of experimentally determined G-M matrix elements for odd-odd nuclei in the actinide region is given in

Table 1. Eighteen different proton-neutron configuration pairs are represented in this data set. Recent experimental data were taken from Refs. 3–6. Matrix elements for a given configuration pair that are observed in two or more nuclei tend to show good agreement; there does not appear to be any strong dependence on mass number. These replicate data are not listed in the table, but the nuclei in which replicates occur are indicated, and the $E_{G\text{-}M}$ entry in the table is an average of the experimental values.

In the two far-right-hand columns of Table 1, the experimental data are compared with theoretical calculations. In the first of these, the calculations[7] were made by assuming a simple zero-range force (ZRF) between the unpaired nucleons and using harmonic-oscillator wave functions for the unpaired nucleons. The single adjustable parameter, $\alpha_0 W$, that characterizes the ZRF is obtained from a fit to the data set. For these actinide data, a value of $\alpha_0 W = 1.03$ MeV was derived.

Boisson et al.[1] reported on G-M matrix elements for a set of 27 different proton-neutron configuration pairs in rare-earth nuclei. These experimental data are labeled "Set A" in their report (see Fig. 1). They calculated matrix elements in the same manner as indicated above, assuming a ZRF and using harmonic-oscillator wave functions, and derived a value of $\alpha_0 W = 0.79$ MeV. As can be seen in Fig. 1, where data from both the rare-earth and actinide regions are plotted, an almost equally good fit to the rare-earth experimental data can be made if one assumes an $\alpha_0 W$ of 1.03 MeV. It appears that the constant that characterizes the ZRF in these two regions need not take on different values. The data in Fig. 1, which are plotted in approximate fashion according to increasing mass number (from left to right), indicate no trend with mass number. This latter observation apparently supports the concept that G-M matrix elements are independent of pairing effects.

Table 1. Gallagher-Moszkowski matrix elements for actinide nuclei.

Configuration			$E_{G\text{-}M}$ (keV)		
			Experi-	Calculated	
Proton	Neutron	Nucleus	mental	ZRF[a]	HF[b]
1/2+400↑	1/2+631↓	^{238}Np	88.0	31.7	8
1/2 530↑	7/2 743↑	^{234}Pa	78.9	116.6	84
	1/2+631↓	^{238}Np	101.8	109.6	52
5/2+642↑	1/2+631↓	^{238}Np	82.4	69.8	51
	5/2+622↑	^{238}Np, ^{242}Am	36.2	39.7	70
5/2 523↓	1/2 501↓	^{240}Am, ^{242}Am	45.4	43.8	40
	1/2+631↓	^{238}Np, ^{240,242}Am	55.0	60.3	71
		^{244}Am	70.0	63.6	69
	1/2+620↑	^{242}Am	21.9	116.4	22
	5/2+622↑	^{238}Np, ^{240}Am	6.1	95.2	12
		^{242}Am, ^{244}Am			
	7/2+624↓	^{244}Am	200.2	207.7	341
3/2 521↑	9/2 734↑	^{248}Bk	186.5	134.4	116
	7/2+613↑	^{250}Bk	66.4	60.0	105
	1/2+620↑	^{250}Bk	110.3	114.9	139
7/2+633↑	9/2 734↑	^{248}Bk	122.0	188.6	344
	7/2+613↑	^{250}Bk	135.0	46.6	72
	1/2+620↑	^{250}Bk	83.6	60.4	57
	3/2+622↓	^{250}Bk	91.2	68.8	37
	1/2 761↓	^{250}Bk	38.0	—	41
			rms deviation:	46	71

[a] From Ref. 7.

[b] From Refs. 8 and 9.

Bennour et al.[8,9] modeled the levels of odd-odd nuclei using the Hartree-Fock approximation. They determined the ingredients of a Bohr-Mottelson unified-model description from the Skyrme III interaction through the adiabatic limit of a time-dependent Hartree-Fock-Bogoliubov approximation. This effective nucleon-nucleon force has been derived from the saturation properties (energy, radius) of closed-shell nuclei such as ^{16}O, ^{40}Ca, ^{48}Ca, ^{90}Zr, and ^{208}Pb.[10] In their description of nuclear states in a deformed nucleus, the single-particle wave functions and energies, the static-equilibrium core properties, and the residual neutron-proton interaction are all determined from the same effective interaction. In a detailed comparison of the experimental levels schemes of ^{160}Tb, ^{174}Lu, and ^{238}Np, Bennour et al.[8] found good correspondence with their calculations. Their calculated G-M matrix elements are compared with experimental data from actinide nuclei in Table 1. The agreement with experiment is really quite remarkable, considering the absence of any *ad hoc* renormalization. The root-mean-square (rms) deviation for this set of calculations vs experiment is 71 keV.

Calculation of the other readily observable manifestation of the neutron-proton

residual interaction, the Newby shift seen in $K = 0$ bands, has traditionally yielded results that were at odds with experiment. Varying assumptions regarding the parameters that describe a finite-range central force between the unpaired nucleons have not provided adequate descriptions of the Newby shifts, as compared with the reasonably satisfactory fits to the G-M matrix element data. Several authors have concluded that an interaction much different from that obtained from fitting experimental G-M matrix elements is required in order to predict the Newby shifts more accurately. The tensor part of the residual interaction is known to be of importance for the Newby shifts in triplet configurations.

Frisk[11] has recently examined this problem of calculating Newby shifts. He has fit the parameters in a phenomenological type of residual neutron-proton force to experimental Newby shifts for 20 "most reliable" bands and obtained an rms error of 16 keV. This force is described by six parameters and includes a tensor-force contribution. The most striking difference between the parameter set he derived and other sets fitted to G-M splittings is the strongly attractive space-exchange term. On the other hand, this parameter set is not useful when calculating G-M splittings, and the reason for this is not understood. Frisk has proposed an empirical rule for the sign of Newby shifts for $K = 0$ rotational bands from pure j-shells. His rule is the following: the favored spins in a $K = 0$ band, I_F, where the angular momentum of the proton and neutron orbitals (j_p, j_n) are good quantum numbers, are given by the expression $I_F = (j_p + j_n) \bmod 2$. The rule seems to work well, with 14 of 22 configurations conforming to it. One of the exceptions, the p1/2⁻[530] – n1/2⁺[631] band that occurs in ^{234}Pa, ^{236}Pa, and ^{238}Np, is listed in Table 2. A careful reexamination of the experimental data for these nuclei has not produced any reason to change the sign (or value) of the experimental Newby shifts. In the rather limited number of examples given in Table 2, the rms error for Frisk's results is no better than for those calculated using a zero-range[7] or the Hartree-Fock approximation.[9]

In calculating G-M matrix elements, several authors have assumed a finite-range central force for the residual interaction. The usual result was only a modest improvement in the correspondence with

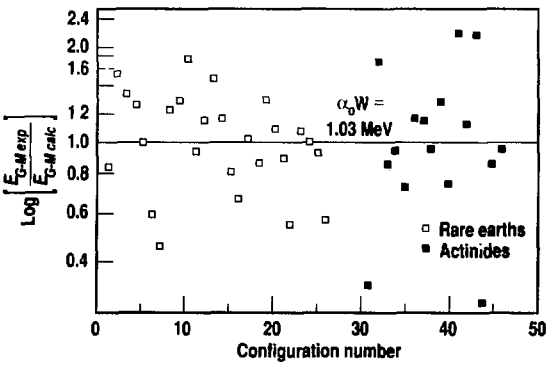

Figure 1. Comparison of experimental and calculated G-M matrix elements assuming a zero-range force for odd-odd nuclei in the rare-earth and actinide regions.

Table 2. Newby terms for $K = 0$ bands in actinide nuclei.

Configuration			E(N) (keV)			
				Calculated		
Proton	Neutron	Nucleus	Experimental	ZRF[a]	HF[b]	Frisk[c]
1/2+400↑	1/2+631↓	^{238}Np	–3.1			–17
1/2-530↑	1/2+631↓	^{234}Pa	–42.5	–44.2	12.5	27
		^{236}Pa	–45.9	–44.2	16.4	26
		^{238}Np	–44.2	–43.1	17.0	25
5/2+642↑	5/2+622↑	^{238}Np	–49.3	–59.1	–73.0	–29
		^{242}Am	–59.4	–59.1	–73.0	–29
5/2-523↓	5/2+622↑	^{238}Np	23.3	–15.2	13.0	27
		^{240}Am	28.0	–14.7	13.2	27
		^{242}Am	27.3	–14.6	13.4	27
		^{244}Am	25.7	–14.5	13.0	27
7/2+633↑	7/2+624↓	^{244}Am	33.1		14.9	63
	7/2+613↑	^{250}Bk	–25.0	–58	–63.2	–19
			Mean deviation:	20	30	24
			rms deviation:	26	53	53

[a] From Ref. 7.
[b] From Refs. 8 and 9.
[c] From Ref. 11.

experiment, as compared with the zero-range calculations (e.g., a reduction of the rms deviation from a typical value of 40 to 45 keV by only about 5 keV). In contrast, Boisson et al.[1] produced a very significant improvement in the rms deviation, bringing it down to 17 keV for their data Set A, by introducing some effects of the polarization of the core by the odd particles. These effects were introduced by polarizing the intrinsic-spin operators and by adding a long-range central force, as well as including a tensor force. With these modifications, the total number of adjustable parameters was increased to seven. A comparison of their calculations with experiment for data Set A is shown in Fig. 2. We have applied the predictions obtained from this force [designated CPTL (for central-polarized-tensor, long-range) in Table 3] to five new G-M matrix elements that have been measured in the rare-earth region. The results are given in Table 3, along with those for a ZRF and a central force (CF), all taken from the calculations of Boisson et al.[1] It can be seen that for these configuration pairs, the predictive power of the various forces are all about the same, with rms deviations of 100 keV. This result is somewhat surprising, in view of the previous results with the CPTL force. Of course, the data sample in Table 3 is quite limited and cannot be assumed to provide a meaningful test of predictive power.

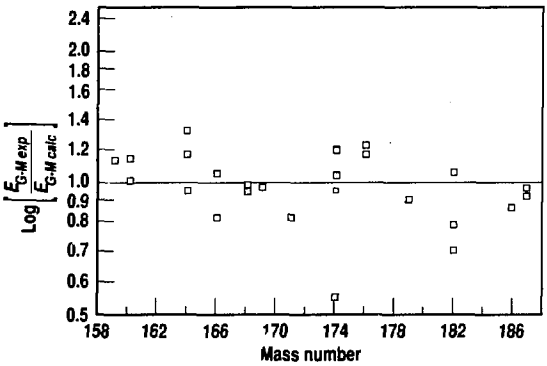

Figure 2. Comparison of experimental and calculated G-M matrix elements for rare-earth odd-odd nuclei where a finite-range (long and short) central force that includes core polarization effects is assumed in the calculation (data Set A from Ref. 1).

Table 3. G-M matrix elements, rare-earth region, predicted values for newly measured cases.[a]

Configuration			$E_{G\text{-}M}$ (keV)			
			Experi-	Calculated values		
Proton	Neutron	Nucleus	mental	ZRF	CF	CPTL
3/2+411↑	7/2+633↑	^{166}Ho	191.2	87	94	146
1/2+411↓	1/2 521↓	^{158}Tm	192.5	130	150	94
1/2+411↓	7/2 514↓	^{176}Lu	122.9	180	171	321
9/2 514↑	7/2 514↓	^{176}Lu	−68.2	−260	−239	−141
5/2+402↑	5/2 512↑	^{174}Lu	129.0	150	145	169
		Data listed above rms deviations:		105	95	108
		No. of entries:		5	5	5
		Data Set A (Ref. 1) rms deviations:		43	40	17
		No. of entries:		27	27	27

[a] From Ref. 1.

References:

1. J. P. Boisson, R. Piepenbring, and W. Ogle, *Phys. Rpts.* **26**, 99 (1976).
2. D. Elmore and W. P. Alford, *Nucl. Phys. A* **273**, 1 (1976).
3. V. A. Ionescu, J. Kern, R. F. Casten, W. R. Kane, I. Ahmad, J. Erskine, A. M. Friedman, and K. Katori, *Nucl. Phys. A* **313**, 283 (1979).
4. J.-L. Salicio, S. Drissi, M. Gasser, J. Kern, H. G. Börner, G. G. Colvin, K. Schreckenbach, R. W. Hoff, and R. W. Lougheed, *Phys. Rev. C* **37**, 2371 (1988).
5. T. von Egidy, R. W. Hoff, R. W. Lougheed, D. H. White, H. G. Börner, K. Schreckenbach, D. D. Warner, G. Barreau, and P. Hungerford, *Phys. Rev. C* **92**, 124 (1984).
6. R. W. Hoff, R. W. Lougheed, G. Barreau, H. G. Börner, W. F. Davidson, K. Schreckenbach, D. D. Warner, T. von Egidy, and D. H. White, "Neutron-Capture Gamma-Ray Spectroscopy and Related Topics 1981," *Proc. IOP Internat. Symp.*, Grenoble, France, von Egidy, Gönnenwein, and Maier, Eds., Conf. Proc. No. 62 (Institute of Physics, London, 1982), p. 250.
7. R. W. Hoff, J. Kern, R. Piepenbring, and J. P. Boisson, "Capture Gamma-Ray Spectroscopy and Related Topics 1984," *Proc. AIP Internat. Symp.*, Knoxville, Tennessee, S. Raman, Ed. (Conf. Proc. No. 125, American Institute of Physics, New York, 1985), p. 274.
8. L. Bennour, J. Libert, M. Meyer, and P. Quentin, *Nucl. Phys. A* **465**, 35 (1987).
9. L. Bennour, Ph.D. Thesis, Univ. de Bordeaux, 33170 Gradignan, France (1987).
10. M. Beiner, H. Flocard, Nguyen Van Giai, and P. Quentin, *Nucl. Phys. A* **238**, 29 (1975).
11. H. Frisk, *Systematics of Rotational Bands with K = 0 in Odd-Odd Nuclei*, Lund Inst. of Tech., Lund, Sweden, Lund-MPH-88/5 (1988).

Predictions of Nuclear Properties on the Astrophysical r-Process Path

A. Aprahamian and E. A. Henry

Neutron-capture processes on various time scales have been shown[1,2] to be of utmost importance in the description of the observed abundances of elements heavier than iron. The time scales can be roughly separated into slow (s-) and rapid (r-) processes. The s- refers to a capture process which is slow compared to the beta-decay lifetimes (10^5 y); whereas the r- refers to those which are rapid in comparison (1 to 1000 ms). The key to understanding either process lies in the microscopic nuclear physics of the elements involved. The s-process is quite well understood since the nuclei involved are longer lived and closer to stability. However, the r-process environment has remained a mystery because the nuclei involved are generally far from stability on the neutron-rich side and therefore extremely difficult or (at times) altogether impossible to measure. It is, therefore, necessary to determine crucial information on nuclear binding energies, excited states, beta-decay rates, fission barriers, and yields either by extrapolation from the known properties of nuclei closer to stability or by predictions resulting from model calculations. Both approaches have their inherent limitations since measured values or parameters of the models act only as a crude guide to unknown nuclei. Figure 1 shows[3] a comparison of calculated nuclear masses from three different mass equations and newly measured values where disagreements are easily of the order of several MeV.

A new approach has recently been developed[7-9] for uniformly viewing large regions of nuclei. The basis of the approach is to view various nuclear properties as a function of the valence neutron-proton product (N_pN_n) instead of N, Z, or A. In this way, complex nuclear systematics can be greatly simplified. The purpose of the work we report here is to exploit this idea by applying it to the parametrization of collective-model calculations and thereby to predict the properties of unknown nuclei (with known N_pN_n products) on the r-process path near the elemental-abundance peaks at $A = 150$ and 190.

Calculations

The essence of the N_pN_n scheme is the neutron-proton interaction and the role it plays in the determination of structure in heavy nuclei. A number of recent studies have shown that the n-p interaction is the controlling agent for the onset of deformation and the development of collectivity. The point is illustrated in Fig. 2. A traditional plot of the first 2^+ energies for a series of nuclei in the $A = 150$ region is shown in Fig. 2(a). What is observed is a complicated function of Z. Figure 2(b) shows the same data as one smooth function of N_pN_n, the product of the number of valence protons and neutrons (counted as holes past midshells or midsubshells where appropriate). Similar simplifications occur for various other nuclear-structure properties, including $4_1^+:2_1^+$ energy ratios, B(E2)s, etc. Furthermore, comparisons of similar properties in vastly different nuclear regions yield similar results. That is, the curves for five different nuclear regions ($A = 100$, 130, 150, 190, and 230) are nearly identical. These results have several significant implications.

First, the existence of a single smooth curve for a given region facilitates making predictions even if only a few points are known. Often, the N_pN_n values of many nuclei far off stability are less than those of some well-known nuclei close to stability. For example, the ^{166}Ba nucleus is 28 neutrons away from the last stable barium isotope, but it has an N_pN_n value of 96, which lies in a well-defined region of Fig. 2. In this way, the properties of unknown nuclei can be determined by interpolation rather than extrapolation of known values.

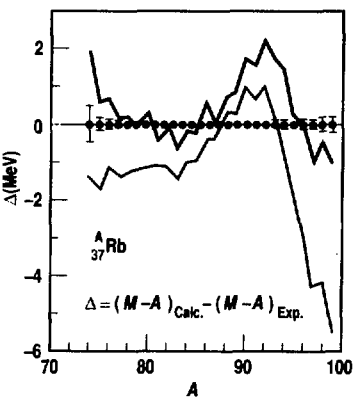

Figure 1. Comparison of experimental and calculated mass excesses for Rb nuclei. The black, blue, and gray curves are the predictions of mass equations by Myers,[4] Liran and Zeldes,[5] and Möller-Nix,[6] respectively.

The second implication is the possibility of parameterizing model calculations in terms of N_pN_n. If a nuclear region can be described so simply, then the parameters of any model may be simply written as a function of N_pN_n and allow a unified description of a whole region.

The latter point was tested for approximately 100 known nuclei from $A = 100$ to 200 within the IBA framework[10] using six parameters. Comparisons of empirical and calculated values for nuclear-structure indicators, such as the energy of the first 2^+, the ratio of the $4_1^+:2_1^+$, and the $B(E2)$ transition strengths, show excellent agreement. The calculations clearly reproduce empirical trends.

We, therefore, selected two regions of nuclei that correspond to elemental abundance peaks of the r-process ($A = 150$ and 190). In these regions, the proton number, Z, falls between the 50–82 shell, and the neutron numbers are in the 82–126 shell. The sequences of unknown nuclei that have been calculated are shown in Fig. 3. Both of the chosen regions correspond to shape transitions from spherical to deformed. This type of a region is particularly simple to describe within the IBA. The Hamiltonian simply contains two terms,

$$H = \varepsilon n_d - \kappa Q \cdot Q , \qquad (1)$$

where

$$Q = (s^+\tilde{d} + d^+s) + \sqrt{1/5}\,\chi(d^+\tilde{d})^2 . \qquad (2)$$

The spherical and deformed limits arise from the absence of the second and first term, respectively. The transitions between the two regions are determined by the size of the parameter ε. In these calculations, we write ε as a function of N_pN_n in the following way:

$$\varepsilon = \varepsilon_0 e^{\frac{-\theta(N_pN_n - N_0)}{4}} , \qquad (3)$$

with the parameters ε, θ, and N_0. In each region, we keep all five parameters (κ, χ, ε_0, θ and N_0) constant and simply vary ε as a function of N_pN_n. In this way, for each nucleus, we get energies of excited states, spins, $E2$ strengths, and the structure contribution to the binding energy.

Figure 2. Systematics of the first 2^+ energies in the $A = 150$ region as a function of (a) N,Z and (b) N_pN_n.

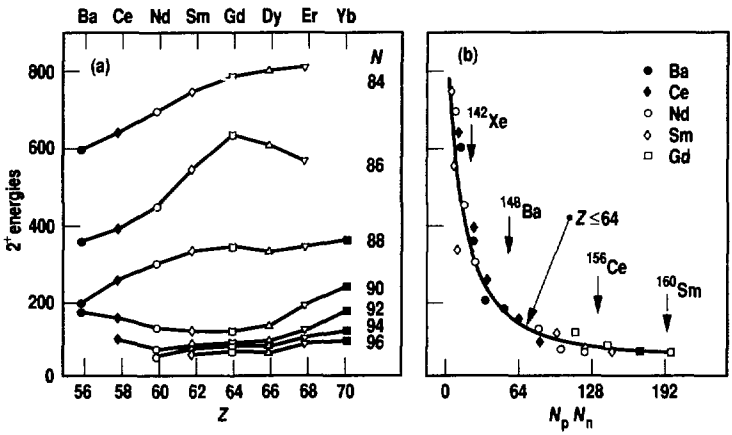

Figure 3. The area of interest from the chart of nuclides. The shaded area indicates known nuclei in the N-Z plane. The × symbols show the calculated nuclei.

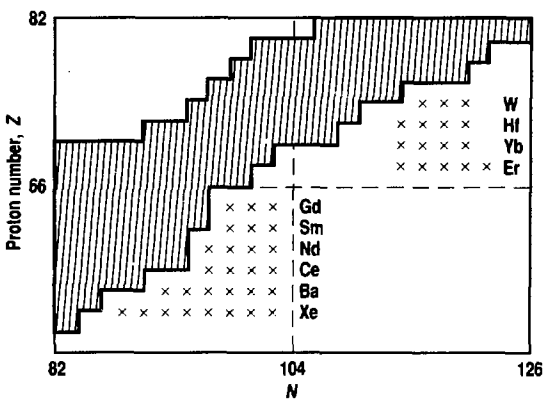

Results and Discussion

Nuclear binding energies are on the order of a thousand MeV. The total binding energy of a nucleus is conventionally expressed as a sum of macroscopic and microscopic terms. The macroscopic component results mainly from liquid-drop properties of the nucleus. This term is by far the larger component, but it is fairly well understood. The microscopic component is typically 10 to 15 MeV in magnitude, and it depends on subtle nuclear-structure effects that have been very difficult to predict.

We calculate the microscopic contribution to the total binding energy. The remaining challenge, then, is to determine the direct relation of calculated microscopic effects to total binding energies. One approach is to write the binding energy for a given isotopic chain as

$$\text{binding energy} = C + AN_n + BE_{\text{IBA}} , \qquad (4)$$

where C and A are constants, N_n is the number of valence neutrons, and BE_{IBA} is the calculated structure contribution. The parameters C and A can be determined from measured total binding energies and then used along with the

calculated BE_{IBA} values to yield the binding energies of isotopes far from stability. The results of such a comparison in the $A = 150$ region are shown in Fig. 4. The calculated and measured values for this region are in good agreement. These predictions, however, represent only a preliminary attempt at calculating crucial nuclear properties along the r process path. The relation of calculated microscopic values to total binding energies is worthy of further investigation.

In conclusion, the N_pN_n approach represents a unique tool for the parameterization of nuclear models and therefore provides a reliable method for the prediction of nuclear properties far from stability.

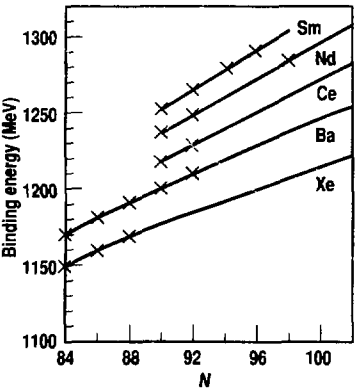

Figure 4. The total binding energies for select nuclei from the $A = 150$ region. The data points indicate measured values; the solid lines are the predictions.

References:

1. G. J. Mathews and R. A. Ward, *Rep. Prog. Physics* **48**, 1371 (1985).
2. G. R. Burbidge, E. M. Burbidge, W. A. Fowler, and F. Hoyle, *Rev. Mod. Phys.* **29**, 547 (1957).
3. D. S. Brenner, M. K. Martel, A. Aprahamian, R. E. Chrien, R. L. Gill, H. I. Liou, M. Shmid, M. L. Stelts, A. Wolf, F. K. Wohn, D. M. Rehfield, H. Dejbakhsh, and C. Chung, *Phys. Rev. C* **26**, 2166 (1982).
4. W. D. Myers, *At. Data Nucl. Data Tables* **17**, 411 (1976).
5. S. Liran and N. Zeldes, *At. Data Nucl. Data Tables* **17**, 431 (1976).
6. P. Möller and J. R. Nix, *At. Data Nucl. Data Tables* **26**, 165 (1981).
7. R. F. Casten, *Phys. Lett. B* **152**, 145 (1985).
8. R. F. Casten, *Phys. Rev. C* **33**, 1819 (1986).
9. R. F. Casten, W. Frank, and P. Von Brentano, *Nucl. Phys. A* **444**, 133 (1985).
10. A. Arima and F. Iachello, *Ann. Phys.* **99**, 253 (1976); *Ann. Phys.* **111**, 201 (1978); *Ann. Phys.* **123**, 468 (1979).

Nuclear Structure of ^{200}Pt from In-Beam Conversion-Electron and Gamma-Ray Spectroscopy

S. W. Yates and E. M. Baum (Univ. of Kentucky, Lexington, Ky.); E. A. Henry, L. G. Mann, N. Roy, A. Aprahamian, and R. A. Meyer; and R. Estep (Los Alamos National Laboratory, Los Alamos, N. Mex.)

The nuclear structure of the platinum region has proven difficult to interpret in terms of traditional descriptions. Studies have shown[1-3] that this complex nuclear region can be interpreted successfully in terms of the O(6) limit of the interacting boson approximation (IBA) model. The IBA model is based in group theory, and it involves a six-dimensional s-d boson space, which is represented by the group U(6). The bosons are valence nucleons treated as correlated pairs of angular momentum 0 and 2. The decomposition of the U(6) group leads to three symmetries—U(5), SU(3), and O(6)—which correspond to the spherical vibrator, the symmetric rotor, and the asymmetric or gamma-soft rotor, respectively. The U(5) and O(6) limits of the IBA arise from a common O(5) group; thus, many properties of low-lying states that have been viewed as evidence for O(6) also apply for the U(5) scheme.[4] Many of the attempts to characterize this region have focused on a single nucleus, ^{196}Pt. The motivation for the work described here was to extend our knowledge of the level properties and systematics in this region by studying the previously unexamined electromagnetic decays of states in ^{200}Pt.

The ^{198}Pt(t,p) reaction, with detection of the emerging protons, was used in the only previously reported study of the structure of ^{200}Pt (Ref. 5). We have also employed the (t,p) reaction to populate excited states in ^{200}Pt; however, to investigate the electromagnetic decay properties of these states, we chose to detect gamma rays and internal-conversion electrons.

Experimental Procedures

The (t,p) reaction was performed on 1.45-mg/cm^2 metallic-foil targets, enriched to 95.8% in ^{198}Pt, with 16-MeV triton beams from the Los Alamos Ion Beam Facility's tandem Van de Graaff accelerator. All spectra were recorded in coincidence with the emitted protons to select the (t,p) reaction from competing neutron-emission channels having higher cross sections. The details of the reaction chamber and the detector system employed for p-γ and p-γ-γ coincidence measurements are given in Ref. 6. In this arrangement, the protons are detected in an annular plastic scintillator (the resulting geometric solid angle is about π steradians), which is lined with a tapered aluminum absorber that stops scattered tritons and reaction-produced deuterons but allows the protons to penetrate through to the scintillator. Because protons pass through the absorber and may not be stopped in the scintillator, individual proton groups are not resolved in this detector. The scintillator is effective in reducing the contributions from neutron-emission channels by a factor of more than 20.

Conversion electrons were detected with a lens-type superconducting solenoidal spectrometer with the experimental arrangement described in Ref. 7. Gamma-ray spectra were recorded simultaneously with a high-purity germanium (HPGe) detector, but, because of the high beam currents necessary for the conversion-electron measurements, the HPGe detector was placed approximately 50 cm from the target. The gamma-ray spectra were recorded in coincidence with protons detected by an annular silicon detector. This spectrum has considerably lower contributions from other sources than those taken in coincidence with the scintillator, primarily because of the better proton selection of the silicon detector, but it is of much poorer statistical quality.

The electron spectra revealed a line at 1583 keV, which likely corresponds to the ground-state decay of the 0$^+$ state observed by Cizewski et al.[5] at 1579 keV. A weak line at 1118 keV that had no corresponding gamma ray was also identified and suggests a 0$^+$ state at that energy. Without additional information on the origin of this peak in the electron spectrum, however, it is impossible to make a firm placement. We deduced internal conversion coefficients for intense transitions from the measured gamma-ray and electron intensities, assuming that the 470-keV 2$^+ \rightarrow$ 0$^+$ transition is of pure E2 multipolarity.

Results and Discussion

The level scheme of ^{200}Pt obtained from our measurements is shown in Fig. 1. All level placements, except for those indicated as E0 decays, are based on observed p-γ-γ coincidences; and the multipolarities indicated were

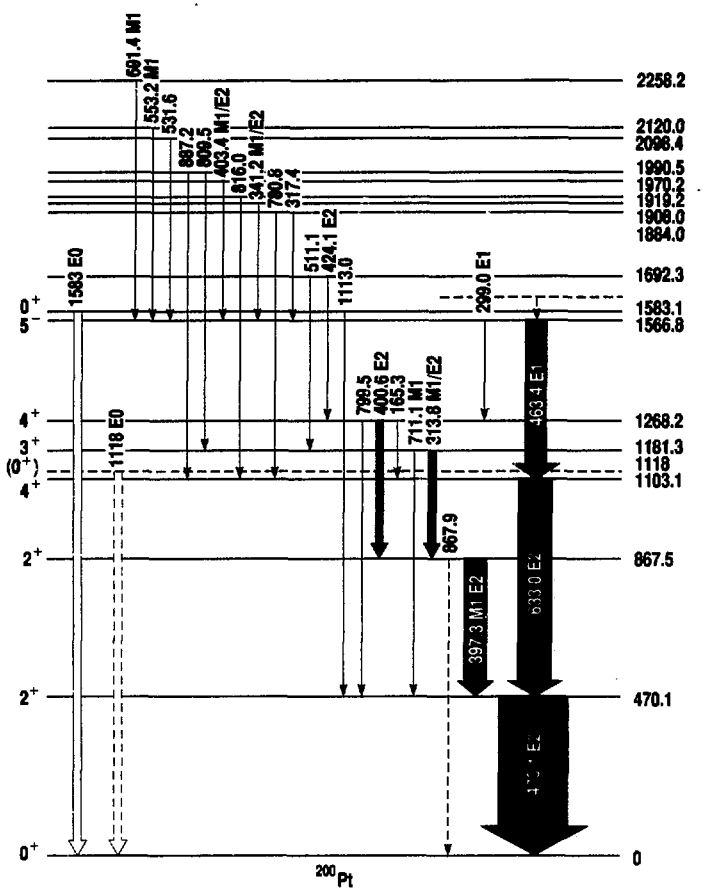

Figure 1. The level scheme of ^{200}Pt deduced from this work. The widths of the solid arrows are proportional to the transition intensities observed with the ^{198}Pt(t,pγ) reaction at E_t = 16 MeV. The widths of the open arrows representing the two observed E0 transitions are not indicative of their intensities. The dashes at the 1118-keV level and the 1118-keV E0 transition indicate tentative placement.

obtained from the measured internal conversion coefficients.

In general, our results support the level assignments of Cizewski et al.[5] for the low-lying states. Of the lowest-lying levels observed in this study, only the unnatural-parity 3^+ state at 1181 keV and the tentatively placed 1118-keV 0_2^+ state were not observed by Cizewski et al.[5] It is surprising that a low-lying 0^+ state would not be observed in the (t,p) reaction; however, the 0_2^+ state in ^{198}Pt was similarly unobserved with this reaction.[5] We have also established several new levels at excitation energies greater than 1.6 MeV, which seem to have no corresponding levels in the proton spectra of Cizewski et al.

Gamma rays that result from feeding by the 299.1- and 463.5-keV E1 transitions from the 1567-keV 5^- level were observed in the delayed gamma-ray spectra with characteristic half-lives of 14.3 ± 0.6 ns. It is possible that a retardation of these E1 transitions by greater than 10^6 with respect to the Weisskopf estimates could be the source of the observed isomerism, but it seems more likely that the 5^- level is populated by a low-energy (<100-keV), unobserved isomeric transition. The low-energy region of the gamma-ray spectrum showed no evidence of a delayed transition, but this is not unexpected, considering that the low-energy radiations were severely attenuated by absorbers, and most low-energy photons were rejected by the timing discriminators. The internal-conversion electron spectra did not extend to energies low enough to provide any useful evidence on this transition.

The negative-parity states in the even-mass platinum isotopes have been interpreted[8,9] as semidecoupled states involving a fully aligned $i_{13/2}$ neutron with a poorly aligned low-j partner. A perusal of the systematics of negative-parity excitations in the even-A platinum nuclei suggests that it is the low-energy $7^- \rightarrow 5^-$ E2 transition that is responsible for the isomerism observed[10] in the lighter nuclei. The reduced E2 transition rates in Weisskopf units (W.u.), along with the predictions by Toki et al.,[9] are shown in Fig. 2 for these transitions. For comparison, we have assumed that the unobserved $7^- \rightarrow 5^-$ transition has an energy of 50 keV and have determined the value of B(E2; $7^- \rightarrow 5^-$) to be 15 W.u. in ^{200}Pt. Thus, the observed trend of decreasing collectivity for this transition with increasing mass is reproduced, as expected, for a transition from rotation-aligned to single-particle structure.

To date, detailed calculations within the IBA model for ^{200}Pt have not been performed, probably for two reasons. First, extensive data for this nucleus were previously unavailable, and second, one must question whether this nucleus has too few valence bosons for this description to be applicable.

Fewell[11] and Leviatan et al.[4] have pointed out the difficulties in distinguishing between the U(5) and O(6) symmetries when only the low-lying states are considered. For the states for which data exist in ^{200}Pt, the relative B(E2)s are identical in the U(5) and O(6) symmetry limits. In Table 1, we compare our measured B(E2) values with those of ^{196}Pt and of the U(5) and O(6) limits. Except where noted, the experimental values for ^{200}Pt have been corrected for the measured M1 mixtures. The presence of large M1 amplitudes indicates a significant degree of symmetry breaking, and, as expected, the degree of symmetry breaking in ^{200}Pt is much greater than that observed in the lighter platinum nuclei. The small value of the ratio, B(E2; $2_2^+ \rightarrow 0_1^+$):B(E2; $2_2^+ \rightarrow 2_1^+$), is consistent with both the U(5) and O(6) limits of the IBA model.

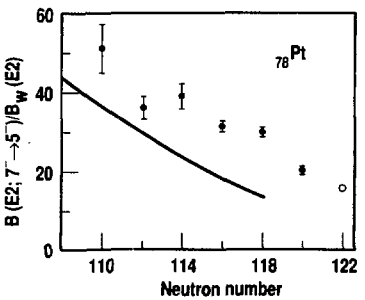

Figure 2. Reduced E2 transition probabilities, in Weisskopf units, for the $7^- \rightarrow 5^-$ transitions of the semidecoupled negative-parity bands in the even-mass platinum isotopes (adapted from Ref. 10). The open point is the value deduced for ^{200}Pt from this work, and the line illustrates the available theoretically calculated values.[9]

Table 1. Relative B(E2) values in ^{196}Pt and ^{198}Pt compared to values calculated with the IBA model in the U(5) or O(6) limit.

Transition	U(5) or O(6)	^{196}Pt[a]	^{200}Pt
$2_2 \rightarrow 0_g^+$	0	0.001	<0.10
$\rightarrow 2_1^+$	100	100	100
$3_1 \rightarrow 2_1^+$	0	0.13	0.19
$\rightarrow 2_2^+$	100	100	100
$\rightarrow 4_1^+$	40	95	—[b]
$4_2 \rightarrow 2_1^+$	0	1.8	0.66
$\rightarrow 2_2^+$	100	100	100
$\rightarrow 4_1^+$	91	109	1100[c]

[a] Data from Ref. 1.

[b] Unobserved low-energy transition.

[c] Pure E2 multipolarity assumed.

Conclusion

Although the occurrence of a triplet of states in ^{198}Pt has been taken[12,13] as an indication of the onset of vibrational structure in the heavier platinum nuclei, we see little evidence of such behavior in ^{200}Pt. The level structure of ^{200}Pt is, in fact, more similar to ^{196}Pt than to ^{198}Pt. Therefore, an O(6) structure, rather than a vibrational or U(5) structure, is suggested. Comparisons of available relative E2 transition probabilities do not, however, permit a clear distinction between the O(6) and U(5) symmetry classifications to be drawn for ^{200}Pt.

References:

1. R. F. Casten and J. A. Cizewski, *Nucl. Phys. A* **309**, 477 (1978).
2. R. F. Casten and J. A. Cizewski, *Nucl. Phys. A* **425**, 653 (1984).
3. R. Bijker, A. E. L. Dieperink, O. Scholten, and R. Spanhoff, *Nucl. Phys. A* **344**, 207 (1980).
4. A. Leviatan, A. Novoselsky, and I. Talmi, *Phys. Lett. B* **172**, 144 (1986).
5. J. A. Cizewski, E. R. Flynn, R. E. Brown, D. L. Hanson, S. D. Orbesen, and J. W. Sunier, *Phys. Rev. C* **23**, 1453 (1981).
6. D. J. Decman, R. J. Estep, E. A. Henry, R. W. Hoff, J. Kantele, L. G. Mann, R. A. Meyer, W. Stöffl, and L. E. Ussery, "Use of the (t,p) Reaction and Coincidence Techniques to Study Neutron-Rich Nuclei," *Nuclear Chemistry Division FY84 Annual Report*, Lawrence Livermore National Laboratory, Livermore, Calif., UCAR-10062-84-1 (1984), p. 6-84.
7. D. J. Decman, E. A. Henry, J. Kantela, L. G. Mann, W. Stöffl, R. J. Estep, and L. E. Ussery, *Nucl. Instrum. Methods* **219**, 523 (1984).
8. S. W. Yates, J. C. Cunnane, R. Hochel, and P. J. Daly, *Nucl. Phys. A* **222**, 301 (1974).
9. H. Toki, K. Neergaard, P. Vogel, and A. Faessler, *Nucl. Phys. A* **279**, 1 (1977).
10. P. Schüler, J. Recht, H. Wilzek, K. Hardt, C. Günther, K. P. Blume, K. Euler, and V. Kölschbach, *Z. Phys. A* **317**, 313 (1984).
11. M. P. Fewell, *Phys. Lett. B* **167**, 6 (1986).
12. S. W. Yates, A. Khan, M. C. Mirzaa, and M. T. McEllistrem, *Phys. Rev. C* **23**, 1993 (1981).
13. S. W. Yates, A. Khan, A. J. Filo, M. C. Mirzaa, J. L. Weil, and M. T. McEllistrem, *Nucl. Phys. A* **406**, 519 (1983).

The Study of Octupole Deformation in ^{227}Ac by Single-Proton Transfer Reactions: ^{226}Ra(d,p)^{227}Ac and ^{226}Ra(α,t)^{227}Ac

[illegible]

When very low-lying negative-parity states were discovered in the radium region[1] during the mid-1950s, the possibility of nuclei having stable octupole deformation was considered.[2] In the region of nuclei just beyond the double-closed shells of ^{208}Pb, the $g_{9/2}$ and $j_{15/2}$ neutron and the $f_{7/2}$ and $i_{13/2}$ proton levels are energetically very close together. Couplings among these orbitals give rise to low-energy ($I^{\pi} = 3^-$) two-quasi-particle configurations, and a superposition of these configurations could form the microscopic basis for stable octupole deformations.[3]

In 1980, Chasman[4] showed that incipient octupole-deformation effects give rise to parity doublets in many odd nuclides of this mass region, including ^{227}Ac. Subsequently, Möller and Nix[5] calculated a minimum in the nuclear potential-energy surface for nonzero octupole deformation. The lowering of the ground-state energy because of additional stability coming from octupole deformation improved the agreement between calculated and experimental masses in the region around ^{222}Ra.

These theoretical studies inspired several experimental searches for evidence of stable octupole deformation in the mass region $220 < A < 230$, even though target materials are unstable and radioactive sources have short half-lives. The first experimental confirmation of

octupole deformation came from the observation[6] of the predicted ground-state parity doublet in ^{229}Pa. This was soon followed by a study of ^{227}Ac (Ref. 7). In the present study, we tested the postulate of a stable octupole deformation with new information from one-particle transfer-reaction experiments.

Details of the experiment and a comparison of the experimental level structure with model calculations of Leander and Chen[8,9] were presented in Ref. 10. In this article, we show that the experimental cross sections derived from our data provide a sensitive test for the presence of stable octupole deformation in ^{227}Ac.

Experimental Nuclear Structure Factors

Using a one-nucleon transfer reaction, one can assign specific bands in reflection-symmetric deformed nuclei. This is because the cross section for populating each member of a rotational band can be calculated with reasonable accuracy. The addition of octupole deformation to the nuclear potential affects the wave functions of the states and, hence, the spectroscopic strengths for populating members of a rotational band. Thus, as a test of the existence of octupole deformation in ^{227}Ac, one can compare the nuclear-structure factors of the present work with those predicted for various magnitudes of β_3, the parameter that provides a measure of static octupole deformation.

The differential cross section for a stripping reaction with an even-even target, exciting a state with spin I, is given by

$$d\sigma/d\Omega = (2I + 1)N\, S_{j\ell}\phi_\ell(\theta)\,, \qquad (1)$$

where N is a normalization factor, $S_{j\ell}$ is the spectroscopic factor, $j = I$, and $\phi_\ell(\theta)$ is the intrinsic single-particle cross section for the transfer of a nucleon with orbital angular momentum ℓ. The spectroscopic factor, which contains all the nuclear-structure information about the final states populated in the reaction, is expressed as follows:

$$S_{j\ell} = \frac{2}{2j+1}\left(\sum_{\Omega} a_\Omega C_{j\ell\Omega} U_\Omega\right)^2, \qquad (2)$$

where the $C_{j\ell\Omega}$ are the spherical amplitudes of the Nilsson states, the a_Ω are the mixing amplitudes, and the U_Ω are the pairing factors. In studies of deformed nuclei, the squared quantity in Eq. (2) is often called the nuclear-structure factor.

The computer code DWUCK[11] was used to calculate the various single-particle cross sections, $\phi_\ell(\theta)$, necessary to describe the (α,t) and (^{3}He,d) reactions on ^{226}Ra. The optical-model parameters were taken from Ref. 12. Normalization factors of N = 6.14 and N = 1.04 were adopted for the (^{3}He,d) and (α,t) reactions, respectively.

Nuclear Reaction Spectroscopy to Test Models for ^{227}Ac

Data from the present work are compared with two sets of theoretically calculated structure factors. The first set is obtained from a reflection-symmetric Nilsson model calculation, with pairing and Coriolis effects included. The parameters used for the Nilsson calculation were $\kappa = 0.058$, $\mu = 0.646$, $\beta_2 = 0.17$, $\beta_3 = 0.0$, and $\beta_4 = 0.09$. Emptiness factors, U^2_Ω, for the various orbitals in the ^{226}Ra target were estimated from the observed excitation energies in ^{227}Ac, assuming that the Fermi surface for ^{227}Ac was at the position of the 3/2⁻[532] orbital and for ^{226}Ra was approximately 250-keV lower. The pairing strength parameter was $\Delta = 0.79$ MeV. Coriolis-mixing calculations were performed for both the positive- and negative-parity bands. For positive-parity levels, the calculations included all rotational bands based on the spherical $i_{13/2}$ level. For K = 7/2 and greater, the bandhead energies were estimated from harmonic oscillator calculations and systematics. For the three experimentally known bands, a least-squares fit was made to all of the levels of the 3/2⁺[651] band, to the I = 5/2 and 13/2 members of the 5/2⁺[642] band, and to the I = 5/2, 9/2, and 13/2 members of the 1/2⁺[660] band. Variables in the calculation were the unperturbed bandhead energies of the three bands, a common moment of inertia, and a decoupling parameter. The Coriolis matrix elements were fixed at 50% of their theoretical values.

For the negative-parity levels, the Coriolis-mixing calculations included the three experimentally observed bands, plus the K = 7/2 and 9/2 bands from the $h_{9/2}$ spherical state with estimated excitation energies. A least-squares fit was made to all of the negative-parity experimental levels except the I = 9/2 and 11/2 members of the $K^\pi = 1/2^-$ band. Variables in the calculation were treated just as in the calculation for positive-parity bands.

The second set of nuclear-structure factors was predicted using the adiabatic reflection-asymmetric rotor model of Leander and Chen.[8] There was no reduction of Coriolis matrix elements in this calculation. Inclusion of a standard reduction factor would substantially lower the calculated structure for the 13/2⁺ level at 211 keV and 9/2⁻ level at 127 keV, as well as change other structure factors. Values for the $K^\pi = 3/2^\pm$ bands are from Ref. 8, while those for the 5/2± and 1/2± bands have been obtained more recently.[9] The two theoretical sets are compared with experimental values in Fig. 1.

Note that there have been no arbitrary adjustments or renormalization in either the measured or calculated results. The comparisons involve absolute values. Also, in extracting the experimental values from the measured cross sections, we assumed that the reaction process is described by a single-step distorted-wave Born approximation process. It is well known, however, that multistep processes in the reaction mechanism can be significant, particularly for weakly populated members of bands. Therefore, consideration should be restricted to the half-dozen or so levels for which the strengths shown in Fig. 1 are reasonably large (e.g., at least 10 to 20% of that for the most strongly populated member of the band).

From Fig. 1 it is seen that a better overall description of the observed spectroscopic strengths is obtained with the Nilsson model for $\beta_3 = 0$, with Coriolis-mixing effects included. The adiabatic reflection-asymmetric rotor model of

Leander and Chen underestimates most of the largest strengths by an approximate factor of 2 to 3. (The excellent agreement in Ref. 8 was obtained by renormalizing the experimental strengths to agree with the calculated values.)

Figure 1. The experimental and calculated structure factors for states in ^{227}Ac. The proposed experimental energies are noted above each state. An asterisk (*) shows that some or all of the measured strength may be the result of another state or states that cannot be experimentally resolved; a question mark (?) denotes that no assignment has been made on the basis of this research.

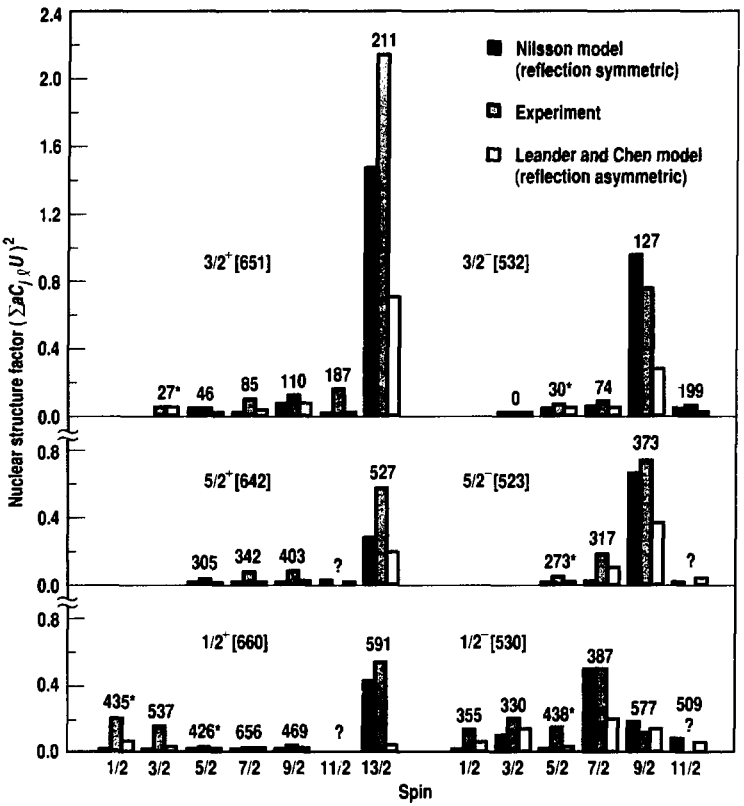

Conclusions

Earlier papers have shown that octupole effects provide a better description of certain nuclear properties, such as level ordering and spacing, decoupling parameters, magnetic moments, etc. However, the present experiment shows that the spectroscopic strengths for single-proton stripping reactions are in better agreement with predictions of the Nilsson model with no octupole deformation. Although the model of Leander and Chen can reproduce the correct level order and account for the observed parity doublets, the calculated nuclear-structure factors for most of the strongly populated levels tend to be too small by a factor of 2 to 3.

References:

1. F. Stephens, F. Asaro, and I. Perlman, *Phys. Rev.* **96**, 1568 (1954).
2. F. Stephens, F. Asaro, and I. Perlman, *Phys. Rev.* **100**, 1543 (1955).
3. K. Alder, A. Bohr, T. Huus, B. Mottelson, and A. Winther, *Rev. Mod. Phys.* **28**, 432 (1956).
4. R. R. Chasman, *Phys. Lett. B* **96**, 7 (1980).
5. P. Möller and J. R. Nix, *Nucl. Phys. A* **361**, 117 (1981).
6. I. Ahmad, J. E. Gindler, R. R. Betts, R. R. Chasman, and A. J. Friedman, *Phys. Rev. Lett.* **49**, 1758 (1982).
7. R. K. Sheline and G. A. Leander, *Phys. Rev. Lett.* **51**, 359 (1983).
8. G. A. Leander and Y. S. Chen, *Phys. Rev. C* **35**, 1145 (1987).
9. G. A. Leander and Y. S. Chen, Oak Ridge National Laboratory, Oak Ridge, Tenn., private communication (1986).
10. H. E. Martz, R. K. Sheline, R. G. Lanier, R. W. Hoff, G. L. Struble, D. J. Decman, D. K. Burke, R. Chasman, and R. A. Naumann, "The Study of Octupole Deformation in ^{227}Ac by Single-Proton Stripping Reactions: ^{226}Ra(α,t) ^{227}Ac and ^{226}Ra(^{3}He,d)^{227}Ac," *Nuclear Chemistry Division FY 87 Annual Report*, Lawrence Livermore National Laboratory, Livermore, Calif., UCAR-10062-87 (1988), pp. 4-84 to 4-88.
11. P. D. Kunz, University of Colorado, Boulder, Colo., computer code DWUCK, private communication (1972).
12. T. W. Elze and J. R. Huizenga, *Phys. Rev. C* **1**, 328 (1970).

Conversion-Electron Experiment to Characterize the Decay of the ^{237}Np Shape Isomer

E. A. Henry, R. W. Hoff, D. G. Gardner, D. J. Decman, and R. A. Meyer; J. A. Becker, N. Roy, and K. E. Sale (San Jose State University, San Jose, Calif.)

Nuclear isomerism plays a key role in the current conceptual designs of a gamma-ray laser.[1] In these designs, the isomeric state stores a large amount of energy that would be released to provide a coherent beam of electromagnetic radiation. Nuclear isomerism results from one or a combination of nuclear structure factors: a small energy difference between nuclear energy levels, a large spin change between levels, K-forbiddenness of the transition connecting levels in the case of deformed nuclei, or a large difference in nuclear shape between the isomer and lower-energy levels. Of these factors, nuclear shape isomerism (major-to-minor-axis ratio of 2:1) is the least studied, and virtually no systematic experimental information exists on isomer occurrence as a function of nuclear mass and charge, isomer decay modes, isomer spin and parity, or other properties.

We are studying the gamma-ray decay of shape isomers in light actinide nuclei to extend the systematic knowledge of their properties and to develop techniques and strategies to identify shape isomers in nuclei where the fission decay mode does not occur.

The nucleus ^{237}Np is known from fission studies[2] to have a shape isomer at 2.85 ± 0.4 MeV with a half-life of 45 ns. Based on the fission half-life systematics of Metag,[3] this isomer decays mainly by gamma-ray emission, with the gamma-ray branch being about 99.9%. With the ^{238}U(p,2n) reaction we used in the experiment, the shape isomer is formed with a total cross section calculated to be 40 μb. We have previously obtained an upper limit of 5.3 μb (2σ standard deviation) for any single gamma ray with an energy between 1600 and 3300 keV associated with the decay of the isomeric state back to the first well.[4] Subsequent statistical model calculations suggested to us that the decay of the shape isomer by a single, intense gamma ray might not be the dominant de-excitation mode. Rather, up to 10 or more primary transitions in that energy range might depopulate the isomeric level, with virtually none of them having a cross section of as much as 5.3 μb. These calculations suggested, however, that the ^{237}Np shape isomer would decay up to half the time to certain less-deformed, low-lying levels, depending on the isomer's spin and parity. These low-lying levels generally have short half-lives or decay promptly. Thus, a 45-ns component in their decay curve would indicate that they are probably populated by the gamma-ray decay of the shape isomer. We report here on the experiment designed to search for this process.

Experimental Procedure

In this experiment, we exploited the capabilities of our solenoidal conversion-electron spectrometer, which is described in detail in Ref. 5. A thin target of uranium oxide (300 μg/cm^2 of ^{238}U) mounted on a carbon foil (30 μg/cm^2) was bombarded with 12-MeV protons from the tandem Van de Graaff accelerator at Los Alamos National Laboratory. Conversion electrons were transported by the solenoidal magnetic field through a baffle system to a 200-mm^2 Si(Li) detector, the energy-dispersive element in the spectrometer. A 100-mm^2 Si(Li) fission-fragment detector monitored the prompt fission fragments and, together with the measured fission cross section for this reaction,[6] determined the number of prompt fissions that occurred in the target. This value served to calibrate the other reaction cross sections.

Low-energy transitions of interest in ^{237}Np included the 208-keV transition between the 3/2$^-$ level at 267 keV and

Figure 1. A time-integrated conversion-electron energy spectrum. The 208-keV transition L and M conversion-electron peaks originating from the 267-keV level in ^{237}Np are identified. The peaks observed in this spectrum arise mainly from the direct reactions. The insert shows a schematic representation of a shape isomer such as ^{237}Np that decays by both fission and gamma-ray decay. Gamma rays emitted during the shape isomer decay are either primary (directly from the shape isomer) or secondary (from lower-lying levels). The 208-keV transition is a secondary transition.

the 5/2$^-$ level at 59 keV, and the 96-keV transition between the 11/2$^+$ level at 129 keV and the 7/2$^+$ level at 33 keV. The K conversion electrons from the 208-keV transition and, particularly, the L conversion electrons from the 96-keV transition occur at low energies where the spectrum is dominated by electrons from the interaction of the proton beam with the atomic electrons of the target nuclei. Therefore, the spectrometer transmission was adjusted to detect the 208-keV-transition L conversion electrons, since in this region the electron background falls rapidly with increasing energy. Data for this higher-energy region were accumulated for 82 hours; 1.41×10^{10} fissions occurred in the target during that time.

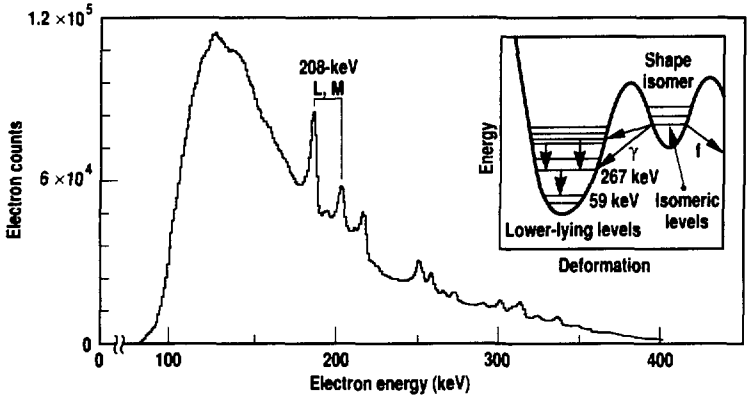

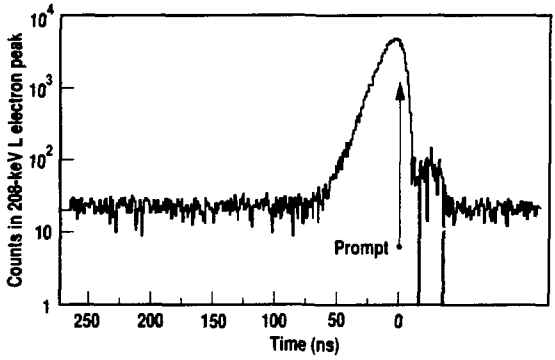

Figure 2. Decay with time of the 208-keV-transition L peak. A time spectrum from a nearby background region has been subtracted and 20 counts added to each channel. The 267-keV level from which this transition originates has a 5.2-ns half-life that is clearly observed. No 45-ns component, indicative of population from the isomer decay, is observed in this spectrum.

Data Analysis

The 208-keV-transition L and M conversion electron peaks are clearly visible in the time-integrated spectrum shown in Fig. 1. This transition, and others visible in the spectrum, result mainly from direct population by the (p,2n) reaction. If a portion of the counts from these transitions is due to decay of the ^{237}Np shape isomer, that portion will be characterized by the 45-ns half-life of the isomer. Figure 2 shows the time distribution of the 208-keV-transition L peak after 10 hours of data accumulation. A background has been subtracted and 20 counts added to all channels to display the statistics at late times. The 208-keV transition originates from a level that has a half-life of 5.2 ± 0.2 ns.[7] A preliminary value for that half-life extracted from the data of Fig. 2 is 5.4 ns, in excellent agreement with the accepted value. A component with a 45-ns half-life cannot be seen in this spectrum or in the summed time spectrum.

To examine the time distribution of the 208-keV-transition L peak in detail, the electron spectrum was projected from the two-dimensional data for two time periods: 67 to 157 ns and 157 to 255 ns after the beam pulse. After 67 ns, all but 0.019% of the 267-keV level, populated directly or through other states, had decayed. Thus, only about 200 counts occur in the 208-keV-transition L peak during the 67–157-ns time period unless the shape isomer decays to the 267-keV level. The electron spectrum for the first time period is shown in Fig. 3. As can be seen, several weak, long-lived peaks in the region of interest complicate the data interpretation. Careful fitting of the spectrum indicates that the multiplet near 186 keV consists of two unidentified peaks, with one 1.4 keV below and the other 1.4 keV above the energy of the 208-keV-transition L peak. These two peaks are also observed in the later time period. The ratio of counts in the two time periods indicates that the half-lives of these

periods indicates that the half-lives of these two peaks are greater than 60 ns. No peaks are detected in this energy region when 6.4 μs has elapsed after the beam pulse. From these considerations, we conclude that a 45-ns component was not observed for the 208-keV-transition L peak.

We can calculate an upper limit for the decay of the shape isomer to the 267-keV level from an analysis of the background counts in the vicinity of the 208-keV-transition L peak. The two-sigma upper limit obtained is 17 μb. This value includes the combined two-sigma uncertainty of 24% in the central values of the various parameters of the cross-section calculation.

We emphasize that the upper limit deduced above is valid only for a truly structureless background. The fact that long-lived small peaks exist in the spectrum during the important time period makes it difficult to rule out the possibility of some isomer feeding to the 267-keV level at about the value deduced above for the limit. Further analysis is required to elucidate the limitations of these data.

Calculations

We have performed calculations using the STAPLUS code[8] to study the gamma-ray decay of the shape isomer. It is assumed that the population of the isomeric state "tunnels" through the potential barrier by mixing with states at nearly the same energy in the normal ground-state potential well. The admixed isomeric level can then decay by dipole electromagnetic transitions in the normal way through low-lying discrete levels to the ground state.

The shape isomer decay calculations for ^{237}Np were carried out with the populated level at three different energies—2.4, 2.8, and 3.2 MeV—since the isomer energy has an uncertainty of 0.4 MeV. Because the isomer's spin and parity are unknown, the populated level was assigned spin values from 1/2 to 15/2. For each of these eight spin values, the production cross section was calculated under two sets of level conditions and for both positive and negative parity. Each set of discrete levels contained 110 energy levels. The two sets differed only in the completeness of the branching-ratio information.

The first set included branching ratios reflecting the assumption that levels in a rotational band decayed to lower levels of the same band until the bandhead level was reached. The decay of the bandhead level to levels in other rotational bands was then calculated using a rotational model. The second set of discrete levels included all the experimentally known branching ratios. The branching ratios of about 20% of the levels were modified in the second set compared to the first.

The calculation of the population of a low-energy discrete level depends significantly on the branching-ratio information. Figure 4 shows the population of the 267-keV level (which is depopulated mainly by the 208-keV transition) when the two sets of discrete-level information

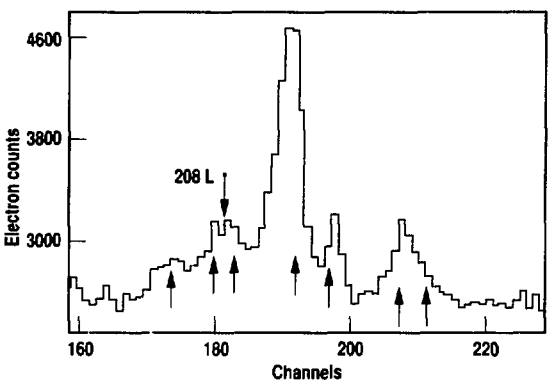

Figure 3. Electron energy spectrum for a time period 67 to 156 ns after the beam pulse. Delayed peaks of unknown origin are indicated by arrows below the histogram. Two such peaks bracket the expected position of the 208-keV-transition L electron peak. Both peaks have a half-life greater than 60 ns. The small peaks make identification of low-level population of the 267-keV level difficult.

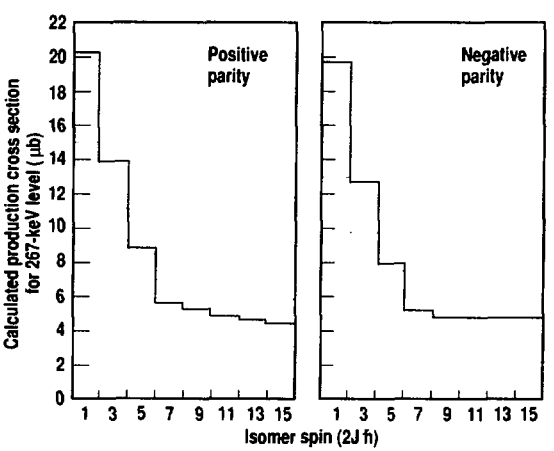

Figure 4. Calculation of the production cross section of the 267-keV level from the shape isomer decay as a function of the isomer spin and parity. The calculation of the cross section is done with two sets of discrete-level information: the set with calculated branching ratios (blue histogram), and the set that contains the known experimental data (black histogram). In these calculations, the production cross section for the shape isomer is assumed to be 40 μb. These calculated cross-section histograms are to be compared to the measured upper limit of 17 μb.

are used. The cross section for population of the 267-keV level by isomer decay is about 50% of the isomer population (assumed to be 40 μb) when the isomer spin is 1/2 and the discrete-level set containing the measured data is used. The cross section of Fig. 4 is to be compared with the experimental upper limit of 17 μb, assuming that other delayed transitions do not mask evidence of real population by the isomer.

Conclusions

Our present experiment is the first reported attempt to identify shape isomer gamma-ray decay by characterizing its population of low-lying discrete levels. Analysis of data so far indicates that the cross-section upper limit for population of the 267-keV level is near the cross section that a calculation would predict. Other electron peaks observed in the experiment have not yet been subjected to detailed analysis and may yield information about the shape-isomer decay.

References:

1. G. C. Baldwin, J. C. Solem, and V. I. Gol'danskii, *Rev. Mod. Phys.* **53**, 687 (1981).
2. E. Migeco, G. Russo, R. DeLeo, and A. Pantaleo, *Phys. Rev. C* **16**, 1919 (1977).
3. V. Metag, *Nucleonica* **20**, 789 (1975).
4. E. A. Henry, J. Kantele, D. J. Decman, J. A. Becker, W. Stoeffl, and L. G. Mann, "Search for the gamma-ray decay of the ^{237}Np fission isomer," *Nuclear Chemistry Division FY 86 Annual Report*, Lawrence Livermore National Laboratory, Livermore, Calif., UCAR-10062-86 (1986), p. 2-48.
5. W. Stöffl and E. A. Henry, *Nucl. Instr. Meth.* **227**, 77 (1984).
6. J. R. Boyce, T. D. Hayward, R. Bass, H. W. Newson, E. G. Bilpuch, and F. O. Purser, *Phys. Rev. C* **10**, 231 (1974).
7. Y. A. Ellis-Akovali, *Nucl. Data Sheets* **49**, 181 (1986).
8. STAPLUS is a version, under development, of the STAPRE statistical model nuclear reaction code by M. Uhl and B. Strohmaier, described in H. Vanoch, *Users Manual for the Code STAPRE as Implemented at Lawrence Livermore National Laboratory*, Lawrence Livermore National Laboratory, Livermore, Calif., UCID-19549 (1982).

Fragmentation Studies Using Niobium + Gold Reactions at 50, 75, and 100 MeV/A

D. J. Fields, T. C. Sangster, H. C. Britt, L. F. Hansen, R. G. Lanier, J. E. Larkin, D. J. Massoletti, R. R. Marquardt, M. N. Namboodiri, B. A. Remington, G. L. Struble, and M. L. Webb; M. Begemann-Blaich, T. Blaich, M. M. Fowler, and J. Wilhelmy (Los Alamos National Laboratory, Los Alamos, N. Mex.); Y. D. Chan, A. Ducal, A. Harmon, J. Poullot, and R. G. Stokstad (Lawrence Berkeley Laboratory, Berkeley, Calif.)

Collisions of energetic heavy ions provide the best tool for studying the nuclear equation of state. By varying such parameters as the projectile and target masses and the incident projectile energy, we can examine the nuclear response to high energy densities and temperatures and to compressional and high spin effects. These studies are made by measuring and comparing particle-production cross sections, particle masses and energies, and total charged-particle multiplicities observed in heavy-ion reactions. However, differences in the nuclear responses are often subtle and require precise measurements, which are difficult to make in an accelerator environment. Furthermore, large multiplicities often impose staggering requirements on detector granularity and dynamic range for complete measurements. However, complete measurements are not always necessary when studying specific

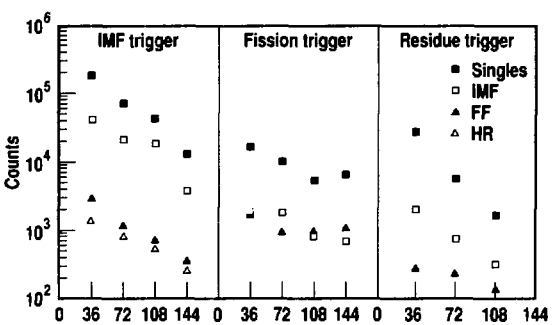

Figure 1. Singles and coincidence rates in the gas counters for 100-MeV/A niobium + gold as a function of laboratory angle. The solid squares represent the total number of events of each classification (FF, HR, or IMF) at the specified angle. The other symbols represent the number of those detected in coincidence with an IMF.

effects in heavy-ion reactions. With appropriate choices for target, projectile, and incident energy, exclusive measurements over a fraction of 4π can yield sufficient information to make a detailed analysis of specific nuclear responses or reaction mechanisms.

We have chosen to study the niobium + gold system at bombarding energies of 50, 75, and 100 MeV/A. In this energy range, the reaction mechanisms are changing rapidly from those that dominate at low energies (e.g., fusion-fission, compound-nucleus decay, and evaporation) to those associated with higher energies (e.g., multifragmentation and single-particle interactions). The large projectile allows us to explore any collective dynamic effects that might influence the collision process and the observed angular distribution of reaction products, while the large projectile energy range allows us to explore the incident-energy dependence of the measured cross sections in this low- to high-energy transition region.

Experimental Apparatus

The complex nature and high charged-particle multiplicities associated with heavy-ion reactions require very sophisticated detector systems that are capable of particle identification with high granularity over broad ranges in particle mass and energy. The Pagoda detector array has been described in detail in a previous report.[1] The array has been upgraded during the past year to increase the solid-angle coverage and dynamic range and to improve the light-particle trigger response. However, the basic design criteria and operational characteristics remain unchanged.

The Pagoda detector array consists of three subsystems:

- A cylindrically oriented, eight-element array of identical, position-sensitive gas counters, which provide energy loss (dE/dx and E) and time-of-flight measurements.
- A large-angle array of fast/slow plastic phoswich detectors, which are sensitive to light particles (p, d, t, and alpha) and to energetic, intermediate-mass fragments that pass through the gas counters. (These new fast/slow plastic detectors replaced the CaF_2/fast plastic modules used last year.)[1]
- An array of similar fast/slow plastic phoswich detectors placed at forward angles to identify projectile-like (i.e., beam velocity) particles. (These detectors were discussed previously.)[2]

The number of large-angle phoswich detectors was increased from 44 to 54, which increased our solid-angle coverage for light particles to backward angles (the CaF_2 detectors covered only forward angles) and lowered the light-particle trigger thresholds to between 4 and 5 MeV/A. This improves our ability to understand the reaction mechanisms that occur in heavy-ion collisions, since light-particle production is a dominant part of the total reaction cross section.

We also performed a number of additional calibration experiments during the past year at LBL's 88-in. cyclotron and the Los Alamos Van de Graaff. The data are now sufficient for final detector calibrations, which will give us total kinetic energies, mass identification, and velocities for virtually all of the detected particles within the limits imposed by detector resolution.

Preliminary Results

Although our final detector calibrations are not available at this writing, we have made a number of preliminary observations that are not dependent on specific detector responses. All the data presented below are from our 100-MeV/A niobium + gold experiment completed in December 1987.

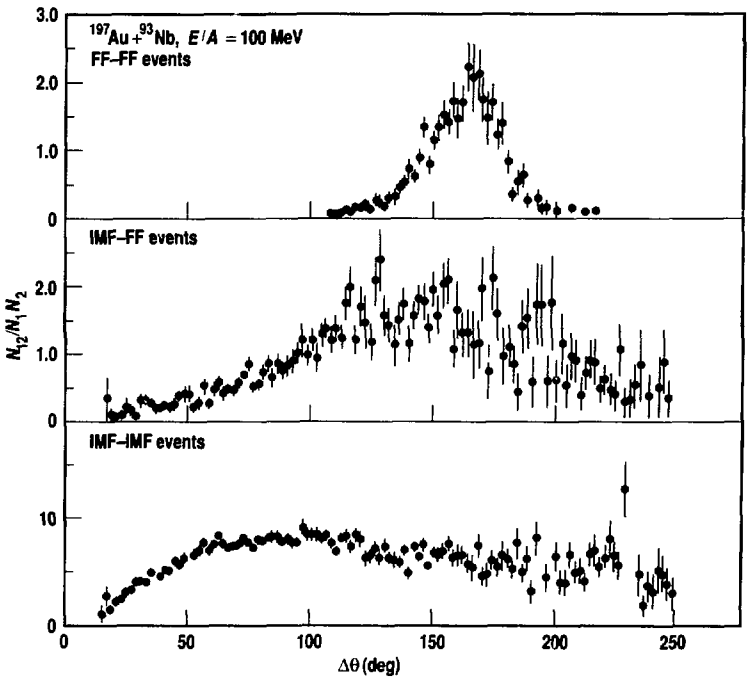

Figure 2. The correlations between two FFs (top), IMF and FF (middle), and two IMFs (bottom) as a function of the relative angle between the fragments for 100-MeV/A niobium + gold. The normalizations are arbitrary.

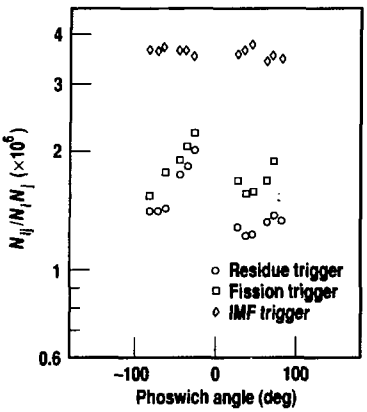

Figure 3. The correlations between coincident, light, charged particles in the large-angle phoswich detectors and an FF, HR, or IMF trigger in one of the gas counters located at 36 degrees. Zero degrees represents the beam direction; positive angles are on the right-hand side of the beamline, and negative angles are on the left-hand side.

The relative numbers of events for fragments detected in the gas counters are shown in Fig. 1. (The angles in the figure are the centers of the gas modules measured from the beam direction.) A preliminary classification of events, based on timing information and ion-chamber pulse height, has been made to facilitate the precalibration data analysis; particles in the gas counters are tagged by mass as an intermediate-mass fragment (IMF), $4 < A < 70$; a fission-like fragment (FF), $70 < A < 110$; or a heavy residue (HR), $A < 110$. These mass assignments are approximate and arbitrary, pending the more detailed mass calibrations. Notice that the IMF cross sections decrease monotonically with increasing detection angle and that the HR cross sections decrease even more rapidly. As expected, fission-like fragments show a somewhat flatter distribution. The FF-FF coincidence probability appears to be lower by a factor of 2 (based on Monte Carlo estimates) than the expected fission-fission coincidence rate, suggesting that a large fraction of the particles identified as fission-like are not, in fact, products of symmetric gold fission.

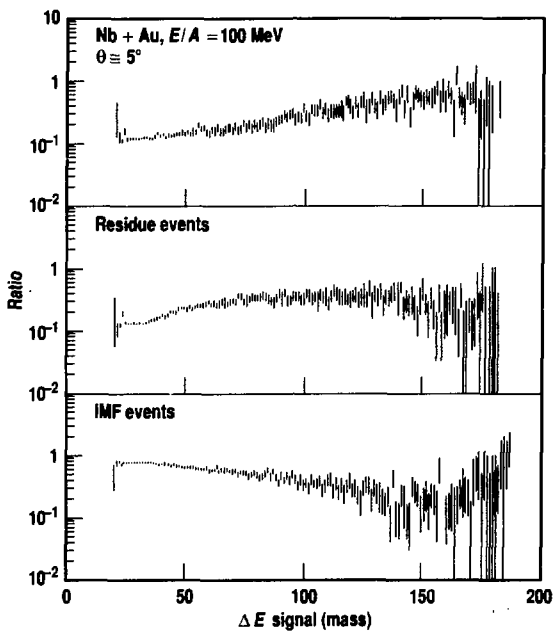

Figure 4. The ratio of all hodoscope events—measured at $\theta \approx 5$ degrees in coincidence with FFs (top), HRs (middle), and IMFs (bottom) in the gas counters—to the inclusive hodoscope spectra. This ratio is plotted as a function of the ΔE signal of the hodoscope, which is roughly proportional to the mass of the detected particle. The rise in the upper spectrum indicates that when an FF is identified in the gas counters, there is a preference for larger fragments (i.e., larger ΔE signals) in the hodoscope.

Angular correlations between particles detected in the gas counters are produced by dividing the spectrum of relative angles between coincident particles by the corresponding spectrum produced with noncoincident particles. Figure 2 shows the relative angle correlations between FFs and IMFs. The correlation between two fission fragments shows a narrow distribution, with the peak corresponding to a momentum transfer of about 3% of the beam momentum (3% of 41 GeV/c, where c is the speed of light), with significant cross sections for momentum transfers up to about 10% of the beam momentum. The correlation between an IMF and an FF exhibits a broad peak on the opposite side of the beam (probably a result of asymmetric fission) and a broader distribution covering all angles (probably a result of actual FF-IMF coincidences or IMF-IMF coincidences where the FF has been improperly identified). The correlation between IMFs is essentially flat, except at small angles where Coulomb repulsion suppresses the correlation. We expect this small-angle suppression to provide information on the time scale of fragment emission.

Correlations between light particles detected in the large-angle phoswich arrays and fragments detected in the gas detectors are shown in Fig. 3. While the correlations with the IMFs are virtually independent of the light-particle detection angle (the data points lie along a horizontal line), those associated with FFs and HRs are forward peaked. This indicates that these fragments are primarily associated with peripheral collisions. Light-particle multiplicities are frequently used to determine or define the centrality or violence of a collision. The measured multiplicities in the 54 large-angle phoswich detectors indicate that the FFs and HRs are indeed associated with more peripheral reactions than the IMFs.

We introduced the forward-angle hodoscope into the PAGODA array to allow a more precise determination of the impact parameter by measuring projectile-like fragments. A single large fragment in the hodoscope ($A = A_{projectile}$) would indicate a peripheral collision

because it is expected that the more central reactions would break up the projectile (as well as the target) into smaller pieces. Preliminary correlations do indeed associate FFs with the larger fragments in the hodoscope and, hence, the most peripheral reactions (see Fig. 4). IMFs are associated with the most central collisions (smallest fragments in the hodoscope), and HRs with more intermediate impact parameters.

The analysis of the niobium projectile data will continue through the end of calender year 1988. A proposal to continue our fragmentation studies with lighter beams (iron and neon) was accepted by the Bevalac Program Advisory Committee in June. This final experiment should be completed by early 1989.

References:

1. T. C. Sangster, D. J. Fields, H. C. Britt, L. F. Hansen, R. G. Lanier, M. N. Namboordiri, B. A. Remington, G. L. Struble, T. Blaich, M. M. Fowler, J. Wilhelmy, S. Kaufman, and F. Videbaek, "The Pagoda Detector System for Heavy-Ion Reaction Studies at Intermediate Energies: Design Improvements and Calibration Experiments," *Nuclear Chemistry Division FY87 Annual Report*, Lawrence Livermore National Laboratory, Livermore, Calif., UCAR-10062-87 (1987), p. 4-51.
2. M. L. Webb, Y.-D. Chan, H. C. Britt, A. Dacal, D. J. Fields, L. F. Hansen, A. Harmon, R. G. Lanier, D. J. Massoletti, M. N. Namboodiri, J. Pouliot, B. A. Remington, T. C. Sangster, R. G. Stokstad, and G. L. Struble, "A Forward-Angle Hodoscope for Use in Heavy-Ion Reaction Studies," *Nuclear Chemistry Division FY87 Annual Report*, Lawrence Livermore National Laboratory, Livermore, Calif., UCAR-10062-87 (1987), p. 4-55.

Fragmentation in Peripheral Collisions of Relativistic Heavy Ions

B. Christie and C. Tull (University of California, Berkeley, and Lawrence Berkeley Laboratory); **J. Davis, L. Greiner** (University of California, Berkeley); **H. Crawford** (University of California, Space Sciences Laboratory, Berkeley, Calif.); **L. Flores, P. J. Lindstrom, V. Perez-Mendez, and D. Stevens** (Lawrence Berkeley Laboratory, Berkeley, Calif.); **R. L. Olsen** (University of Colorado, Boulder); **J. Babcock** (University of New Hampshire, Durham, N.H.); **C. Parks** and **M. L. Webb**

Single-particle inclusive measurements in high-energy nuclear physics have provided the foundation for a number of models of interacting nuclei.[1] Such measurements yield information on the endpoints of the evolution of highly excited nuclear systems. However, they suffer from the fact that the observed particles can be formed in a large number of very different evolutionary paths. To learn more about how relativistic heavy ions (RHIs) proceed, we are performing a series of experiments in which all nuclear fragments issued from the projectile are analyzed for each individual interaction.

Present theoretical models for RHI collisions can be distinguished by their prediction of the excitation phase of the reaction.[2] The distinction is in the energy- and momentum-transfer spectra to the projectile or prefragment before dissociation. We have designed our experiments so that all the original nucleons in the projectile can be accounted for. This enables us to reconstruct the transfer spectra for all decay channels to an accuracy of a few MeV. Hence, we are able to distinguish the reaction mechanism (or mechanisms) responsible for the fragmentation of any particular channel.

Experimental Procedure

We are making these measurements at Lawrence Berkeley Laboratory's Bevalac with the Heavy Ion Superconducting Spectrometer (HISS).[3] The HISS system, shown in Fig. 1, consists of a large (1-m-gap, 2-m-diam) superconducting dipole (30-kG maximum field) and a set of facility detectors. These detectors include two sets of drift tubes and one drift chamber for measuring particle trajectories and a large multisegmented scintillation array for velocity, β, and charge, Z, measurements. We are able to

calculate the rigidity, R, for each projectile fragment by coupling each fragment's trajectory with a predetermined set of Chebychev coefficients that characterize the field of the magnet.[4] We then combine these rigidities with the charges obtained from the scintillation array to obtain the vector momentum, $(\mathbf{p} = Z\mathbf{R})$, for each particle. Complete particle identifications are accomplished using the velocity and the momentum to obtain the mass, A, for each particle.

Results and Discussion

We completed measurements with ^{12}C and ^{16}O projectiles at 2.1 GeV/A on carbon, CH_2, beryllium, and uranium targets in 1983. We have concentrated a major portion of our analysis efforts since that time on individual decay channels in which the projectile nucleus can be completely reconstructed. These investigations, both singularly and collectively, have yielded a wealth of information on the reaction dynamics involved in peripheral collisions. The first decay channel we completed was $^{12}C(^{12}C,3\alpha)X$ (Ref. 5). We found that both the excitation spectrum and the transferred momentum distributions were consistent with a collectively excited ^{12}C nucleus decaying into three alpha particles. Unexpectedly, we found that the 3α channel was not a major contributor to the large cross section for alpha particles seen in the single-particle inclusive measurements. These results were made more interesting with the completion of the work on the (^{12}C, ^{11}B + p) decay channel.[6] We found that this channel not only included the low-energy, excitation-decay spectrum found in the 3α channel, but also a high-energy tail. As shown in Fig. 2, our dissection of this spectrum uncovered three distinct mechanisms:

- An excitation-decay peak at beam velocity and low transverse momentum.
- A quasi-elastic nucleon-nucleon scattering ridge lying along the nucleon-nucleon elastic scattering line.
- An inelastic nucleon-nucleon scattering plateau in the region of high transverse momentum and below beam velocity, which is indicative of π production.

The character of the excitation-decay peak was further clarified with the investigation of the (^{16}O, ^{15}N + p) on beryllium and uranium targets. As shown in Fig. 3, we found that the low-energy peak could be completely explained by a combination of diffractive dissociation[7] and electromagnetic dissociation (EMD).[8]

At the present time, we are investigating the (^{12}C,^{10}Be + 2p) and (^{12}C,^{3}He + 2α) dissociation channels. We should be able to determine the maximum contribution to the spectrum from the nuclear Wiesacker-Williams phonon model[9] by inspecting the momentum distributions of the two protons in the (^{12}C,^{10}Be + 2p) events. The energy spectrum of the two alpha particles in the (^{12}C,^{3}He + 2α) channel will determine if the final fragment spectra are populated by means of a sequential or a multipronged type of process.

Meanwhile, the analysis of the collective or general effects of all channels is beginning to yield information on more central collisions. From a study of the relative populations of projectile fragmentation patterns and their associated internal excitation energy spectra, we know that a simple abrasion picture is sufficient to describe the surviving mass fraction.[10] Further, a clear correlation exists with threshold energy, suggesting that the process is dominated by phase space. In other studies, we are investigating all reactions in which the entire mass of the original projectile has been accounted for, but the observed charge sum has changed by one or more charge units. These "charge exchange" reactions should yield a complete picture of the pion exchange process involved in the inelastic nucleon-nucleon mechanism.[11] This work should yield important information on the nuclear equation of state, and possibly elucidate the quark modeling of the nucleus.

Summary

Through these studies, we see a "picture" of relativistic nucleus-nucleus

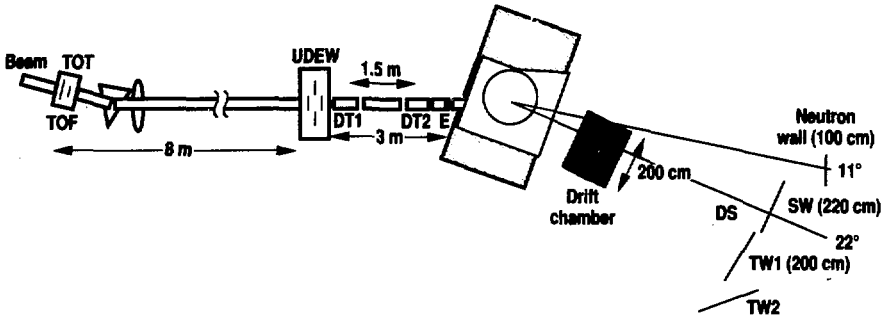

Figure 1. Layout of HISS for the June 1988 running of the RHI projectile fragmentation experiment. Beam scintillators (TOF, TOT, UDEW, E, and DS) define the trigger with logic (TOF·TOT·E_{lo}·E_{hi}·UDEW·DS). Drift tubes (DT1 and DT2) determine the incoming beam particle's trajectory, while the drift chamber determines the charged projectile fragment's trajectories. The time-of-flight (SW, TW1, TW2) scintillation array determines the charge and time of flight for all projectile fragments.

collisions starting to materialize. The picture suggests that:

- For interactions just outside the combined radii of the two nuclei, the nuclei are able to capture virtual quanta from the coulomb field surrounding the other participating nucleus.
- For interactions on the order of the combined radii of the two nuclei, single nucleons in a participating nucleus can pass through the nuclear "skin" of the other nucleus and be diffracted away from the parent nucleus.
- For interactions closer than the combined radii of the two nuclei, a "participant/spectator" type of mechanism is dominant, with the participant part being well described by an intranuclear cascade process and the spectator part being well represented by a statistical decay type of process.[12]

The Future

We have completed a second set of measurements this summer with ^{4}He and ^{20}Ne projectiles at 2.1 GeV/A. We expect the analysis of the ^{4}He data sample to supply an exact characterization of the diffractive scattering mechanism and to provide the best possible data with which to study the quasi-elastic and inelastic nucleon-nucleon scattering processes. In contrast, the ^{20}Ne data sample should supply more information on collective or bulk effects. The integration of these two data sets with the ^{12}C and ^{16}O data should supply a complete picture of the evolution of peripheral RHI collisions, from simple "skin" effects experienced in the collisions of light ions to the hydrodynamic mechanisms witnessed in the interactions of larger nuclei.

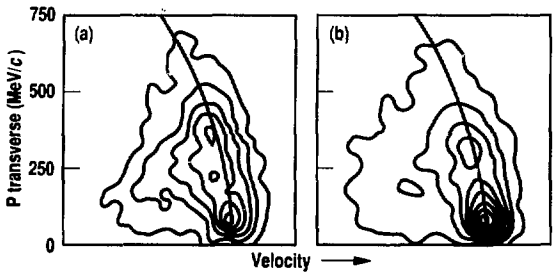

Figure 2. Velocity vs transverse momentum for protons from (a) H(^{12}C, ^{11}B + p)X and (b) ^{12}C(^{12}C, ^{11}B + p)X. Note the peak at low transverse energy and beam velocity. The line shows the location of nucleon-nucleon quasi-elastic scattering.

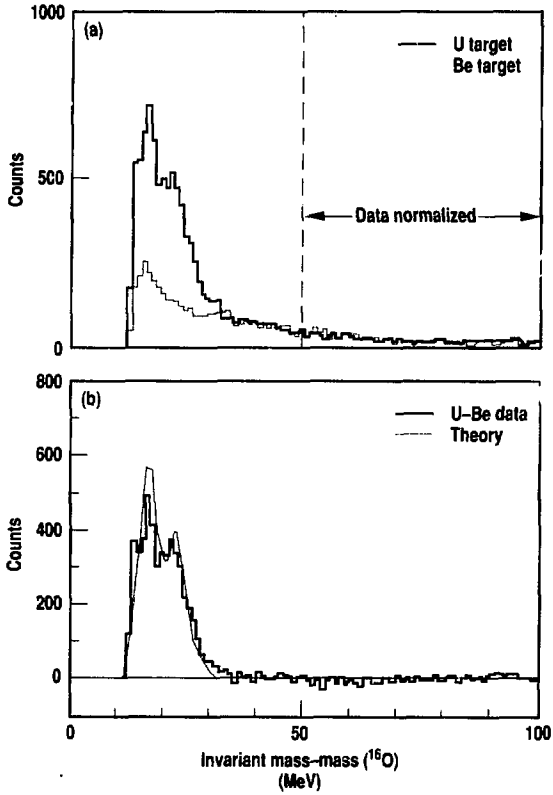

Figure 3.
(a) Excitation energy spectra for U(^{16}O, ^{15}N + p)X and Be(^{16}O,^{15}N + p)X normalized in the region between 50 and 100 MeV. (b) The spectra from (a) subtracted and compared to theoretical EMD calculations. The low-energy data lying to the left of the expected EMD peaks are consistent with the diffractive dissociation model.

References:

1. J. A. Maruhn and W. Greiner, in *Treatise on Heavy Ion Science*, **4**, D.A. Bromley, Ed. (Plenum Press, New York, 1985), p. 565.
2. D. E. Greiner, *Nucl. Phys. A* **400**, 325c (1983).
3. J. Engelage, M. E. Boumgartner, E. Beleal, et al., Lawrence Berkeley Laboratory, Berkeley, Calif., LBL-23867 (1988).
4. H. Wind, CERN 72-21 (1972).
5. J. Engelage et al., *Phys. Lett. B* **173**, 34 (1986).
6. M. L. Webb et al., *Phys. Rev. C* **36**, 193 (1987).
7. K. Goulianos, *Phys. Rep.* **101**, 169 (1983).
8. D. L Olson et al., Lawrence Berkeley Laboratory, Berkeley, Calif., LBL-25318 (1988).
9. H. Feshbach and M. Zabek, *Ann. Phys.* **107**, 110 (1977).
10. H. J. Crawford et al., Lawrence Berkeley Laboratory, Berkeley, Calif., LBL-24380 (1988).
11. P. J. Lindstrom, in *Proceedings of the Eighth High-Energy Heavy Ion Study*, Lawrence Berkeley Laboratory, Berkeley, Calif., LBL-24580 (1988), pp. 397–412.
12. B. G. Harvey, H. J. Crawford, P. J. Lindstrom, and A. J. Cole, Lawrence Berkeley Laboratory, Berkeley, Calif., LBL-25806 (1988).

4

Containment

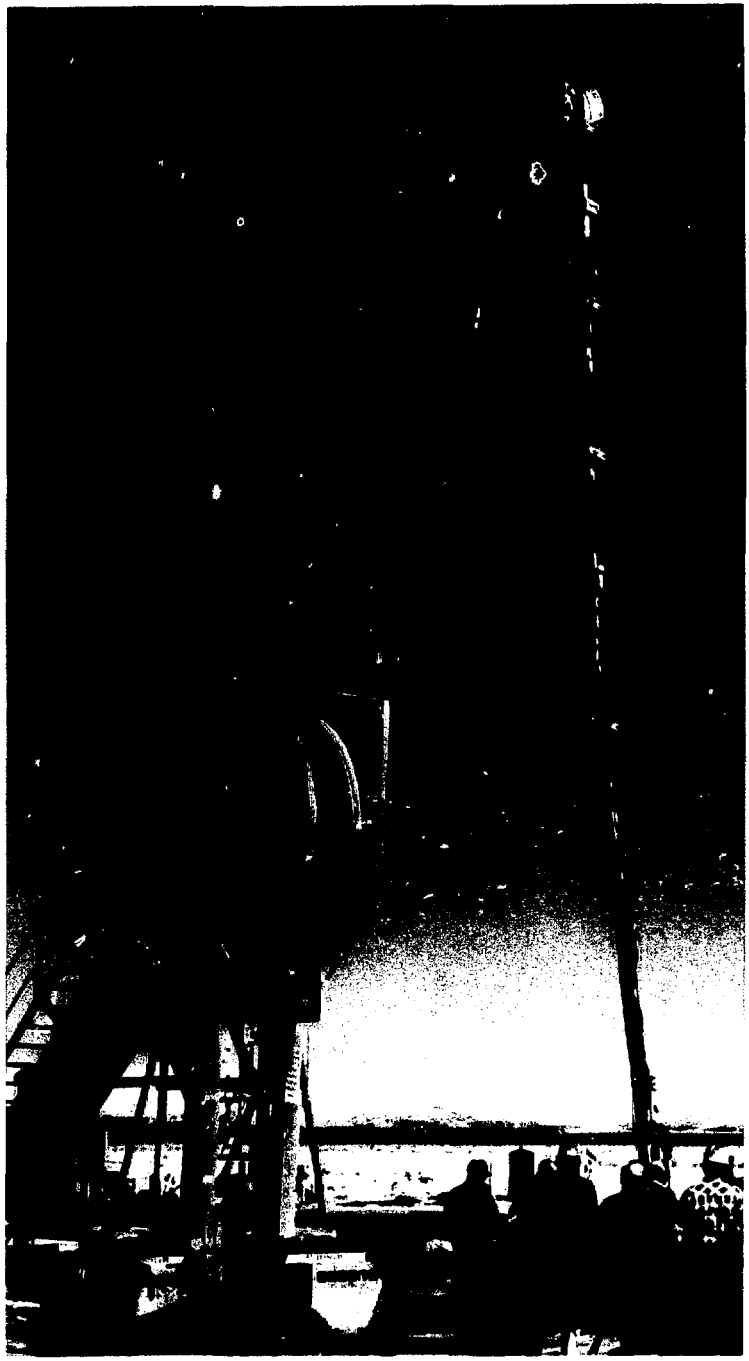

Since the U.S. and the Soviet Union signed the Partial Nuclear Test Ban Treaty in 1963, all U.S. nuclear tests have been conducted underground. This treaty not only precludes atmospheric testing of nuclear explosives but also prohibits the crossing of international borders by detectable quantities of radioactive material from nuclear tests. In addition, it is federal policy that quantities of radioactive material above strictly defined guidelines should not exit the boundaries of the Nevada Test Site (NTS) and should not be inadvertently released on the NTS. The Laboratory's Containment Program is responsible for preventing the release of radioactivity and radioactive debris from LLNL's underground nuclear tests. To this end, we play many roles in the conduct of a nuclear test, from the planning stages through the analysis of data gathered during and after detonation.

When a nuclear test is first placed on the test schedule, it is sited, in conjunction with representatives of LLNL's Field Operations Program, in the most appropriate existing drill hole (there is a stockpile of holes that have already been drilled at NTS). The depth of a hole that has already been drilled determines, in large part, the yield of the event that can be expended in that hole. If no suitable hole exists, a new hole must be drilled.

Whether an existing hole is chosen or a new hole must be drilled, the Containment Program carefully reviews each proposed site, paying particular attention to the geologic setting, adjacent drill holes, and containment experience in the area. The selection of a suitable depth of burial (DOB) to optimize both containment prospects and use of available test areas is based on these factors.

A containment scientist assigned to each event is responsible for assembling all relevant geologic, geophysical, engineering, historic, and computational information. The containment scientist chooses a final DOB and designs a stemming plan—the plan for filling and plugging the hole after the experiment has been emplaced. The containment scientist prepares the Containment Prospectus, a comprehensive document that presents all relevant information, expected event phenomena, and justification for the conclusion that the event will be satisfactorily contained. Each event is presented to the Containment Evaluation Panel (CEP), a group of specialists who advise the Manager of the Nevada Operations Office of the U.S. Department of Energy on the containment prospects of every proposed event. No event can proceed unless the CEP concurs with the test sponsor that the likelihood of successful containment is high.

During FY88, all LLNL events were presented to the CEP, and all events conducted were successfully contained. In addition to preparing LLNL events for the CEP, our containment personnel carefully reviewed the tests proposed by the Los Alamos National Laboratory and the Defense Nuclear Agency to determine the adequacy of their containment designs.

The Containment Program also has the responsibility for determining the hydrodynamic yield of some nuclear tests. The Kearsarge Event in August 1988 presented a unique opportunity for conducting hydrodynamic yield measurements using CORRTEX (COntinuous Reflectrometry for Radius versus Time EXperiment) techniques. (Kearsarge was part of the Joint Verification Experiment conducted by LLNL, Los Alamos, and the Soviet Union as part of the continuing negotiations to ratify the Threshold Test Ban Treaty. See more about Kearsarge in the chapter on Field Operations.) Both the U.S. and the Soviet Union decided to field CORRTEX cables and sensors to determine the practicability of using this technique for measuring hydrodynamic yield. Kearsarge was located in a drill hole that had been sited and drilled by Los Alamos. Because of the CORRTEX yield experiments, the stemming plan was modified so as to provide a suitable environment for the sensors, as determined by both the U.S. and the Soviet Union. In addition to these unique features, Kearsarge was prepared and presented by the Containment Program on an accelerated time scale to meet political requirements. The containment objectives in this experiment were achieved: Kearsarge was satisfactorily contained, and very high quality CORRTEX data were obtained.

In addition to these test events, the Containment Program was involved in other specific tasks related to different facets of testing such as the development of a fast, high-explosive- (HE) driven pipe closure. This device is for a planned future test involving exposure of a target to prompt radiation followed by rapid closure of the line-of-sight pipe between the source and the exposed target. We tested a closure that sealed a 0.46-m-diam pipe in less than 1 ms. The sealed plug was more than 1 m in length and was composed of aluminum, steel, and copper driven on axis by about 300 lb of HE.

Containment Program personnel have also been working on several projects in support of specific test work, including certifying a new computer code for containment calculations; providing faster, more efficient data processing for log processing and data-base retrievals; testing a carbon-oxygen well-logging tool; evaluating a new containment stemming plug diagnostic system; and measuring cavity pressure histories from nuclear tests. Work on these projects is described in more detail in the articles that follow. Progress on these projects enables us to evaluate sites faster and more effectively and to better determine the effectiveness of our containment plans.

Measuring Cavity Pressure in Nuclear Tests

B. C. Hudson

An underground nuclear test is typically conducted in an emplacement hole hundreds of metres deep that has been back-filled with sand, gravel, and concrete plugs. These plugs, which vary in thickness and strength, serve not only to prevent radioactive material from reaching the surface but also, ideally, to constrain it to a region near the explosion cavity. When we determine the appropriate depth of burial (DOB) for a device, we have to make it shallow enough to be economical but deep enough to reasonably ensure containment given the expected yield of the device and the particular geology of the hole. To do this, we have developed sophisticated computer models that consider each site's geologic structure and physical properties to predict explosion effects such as ground motion, confining stresses around the cavity, and cavity pressure. However, to be able to assess the performance and relative accuracy of these computational models, we must develop a data base of the measured values for each of these effects that can be compared with predictions.

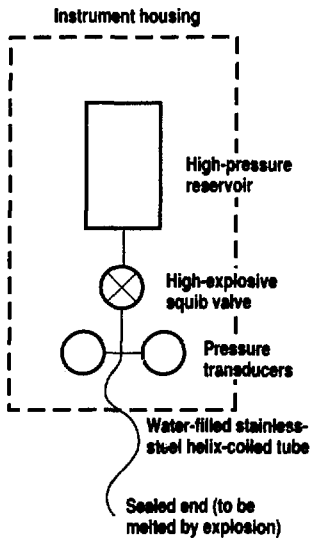

Figure 1. Schematic diagram of the apparatus (one of three) used for measuring cavity pressure on the Cornucopia Event.

Over the past 25 years, many attempts have been made to measure a cavity pressure history. Unfortunately, few attempts have succeeded in giving even partial pressure histories. Furthermore, it has been difficult to establish the validity of data from supposedly successful measurements. In the mid-1980s, we devised a new scheme based on the results of past attempts and phenomenological observations from reentry studies of events detonated in tunnels under Ranier Mesa at NTS. This new scheme was designed to optimize chances of maintaining pressure communication with a nuclear cavity. The essential elements of the new design included a fluid-filled, helically coiled capillary tube and a reservoir containing high pressures (up to 12,000 psi) for blowing the fluid from the tubing after cavity formation (see Fig. 1). Three separate but identical systems were fielded on the Cornucopia Event at Yucca Flat in 1986.[1] Figure 2 shows a plot of the three resulting pressure traces. The agreement between channels was extremely good, giving a believable pressure record that extended from zero time through cavity collapse. A similar measurement set was fielded on a Defense Nuclear Agency (DNA) tunnel event (Mission Ghost) under Ranier Mesa in 1987.[2] Figure 3 shows the two complete data sets in a log-log format. Although the absolute levels are quite different, these data suggested three separate stages of cavity pressure decay. The absolute differences in the traces of the two events are not particularly surprising because there were significant differences in material properties, geologic structure, and yield, each of which is believed to play a role in developing the initial pressure. Following a study of

Cornucopia data, we concluded that pressure decay could be described in terms of three stages[1]:

- Stage I—Initial pressure is either much lower than predicted or hydrofractures allow the initial cavity pressure to drop to a level controlled by non-event-related confining stresses within a very short time (about 50 s on Cornucopia).
- Stage II—The addition of mass combined with additional hydrofractures maintains a nearly constant pressure for a relatively long period (about one hour on Cornucopia) while the temperature drops to near the melting point of rock (about 1400 K).
- Stage III—Heat conduction and Darcian flow out of the cavity cause a monotonic pressure decay until collapse.

Although our conclusions concerning the last two stages seemed fairly well based in theory, we were not as comfortable with our conclusions concerning the first stage, as a result of the uncertainty in time required by the high pressure (7000–11,000 psi) to remove the fluid from the capillary tubing. (This time was impossible to calibrate because we do not know the exact configuration of the tubing after detonation.) In an attempt to obviate this difficulty, we fielded a modified measurement set on the Rhyolite Event in Yucca Flat in 1988. This configuration differed from the previous ones in that it did not have a pressure reservoir for blowing out the fluid. Figure 4 contains the pressure data from this event. Although there is now an uncertainty of up to about 100 psi because of the fluid in the tubes, we believe that the Rhyolite data are representative of cavity pressure from after about 2 s.

The Rhyolite data suggest that the pressure histories determined from Cornucopia and Mission Ghost are not representative of cavity pressure during the period called Stage I and that the beginning of the relatively constant Stage II is probably representative of the initial cavity pressure, which is controlled by cavity growth, prompt-shock-induced mixing of material, and the possible occurrence of hydrofracture. If these interpretations are correct, there is a qualitative difference between Cornucopia, which had an initial pressure of less than half the overburden, and the more recent Mission Ghost and Rhyolite events, which had initial pressures considerably greater than overburden pressure. More data are needed to determine whether this difference is indicative of measurement or modeling difficulties.

Current plans include fielding of similar measurement sets on one DNA and one LLNL event.

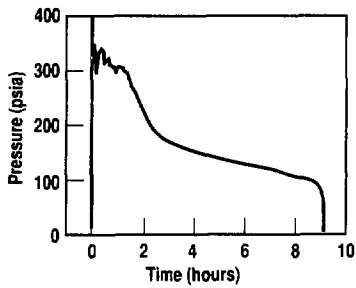

Figure 2. Plot of three pressure traces, which gives a complete pressure history of the Cornucopia Event cavity from the explosion to cavity collapse about nine hours later. (The first minute is obscured by the thickness of the traces and is clipped at 400 psia.) Agreement between the three traces is extremely good. High pressure was applied to the fluid in the helix tubes about 2 s before detonation. The increased rate of pressure drop in the minutes before collapse strongly suggests that reduced cavity pressure brought on, rather than resulted from, cavity collapse.

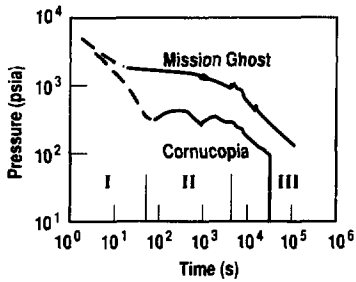

Figure 3. The Mission Ghost cavity pressure appears to have distinct stages of decay, similar to those of Cornucopia. The pressure histories suspected of being the result of fluid "blow-out" are shown as dashed lines.

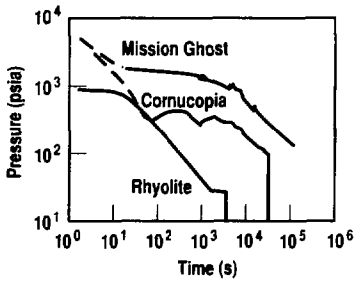

Figure 4. Pressure data from the Rhyolite Event are believed to be representative of cavity pressure from less than 2 s on, suggesting that the "plateaus" seen on Cornucopia and Mission Ghost are the initial starting pressures, while the pre-plateau pressures are artifacts of the fluid removal process.

References:

1. B. C. Hudson, C. Cordill, and L. Starrh, *Recent Nuclear Cavity Pressure Measurements*, Lawrence Livermore National Laboratory, Livermore, Calif., UCRL-96354 (1987).
2. C. Sisemore, B. C. Hudson, C. Cordill, and C. Smith, *Cavity Pressure Measurements and Gas Sampling for MISSION GHOST*, Lawrence Livermore National Laboratory, Livermore, Calif., UCID-21295 (1987).

Adapting Carbon/Oxygen Logging for Use at the Nevada Test Site

J. R Hearst

When a nuclear explosive is tested underground at NTS, rock in the immediate vicinity of the explosion is heated to very high temperatures. If any of that rock contains carbonates (dolomite or calcite), they are dissociated, and the carbon combines with oxygen to form carbon dioxide. When the rock cools, the carbon dioxide remains a gas, increasing both subsurface pressure and the possibility of a delayed leak. Consequently, the process of evaluating potential test sites includes checking for substantial amounts of carbonates. Carbonate content is expressed as equivalent carbon dioxide (CO_2), the amount of CO_2 that would be generated if all the carbon in the cavity region combined with oxygen after the explosion.

At present, we estimate the rock's carbonate content as a function of depth by chemically analyzing drill cuttings or sidewall samples obtained after the borehole has been drilled. Estimated accuracy as stated by the contractor performing these analyses is 0.01 weight fraction CO_2, corresponding to about 0.0225 weight fraction calcium carbonate. Evidence suggests this claim is optimistic. In addition, neither drill cuttings nor sidewall samples are fully representative of the surrounding rock because some rock is washed out during drilling and sampling. Finally, sidewall sampling is costly in our larger-diameter boreholes since the drill rig must sometimes remain onsite. For these reasons, we are working to adapt a commercial neutron-induced gamma-ray spectroscopy log for estimating carbonate content. Such a log would test a much larger (and presumably more representative) sample than the few grams used in chemical analyses and would be continuous rather than discrete.

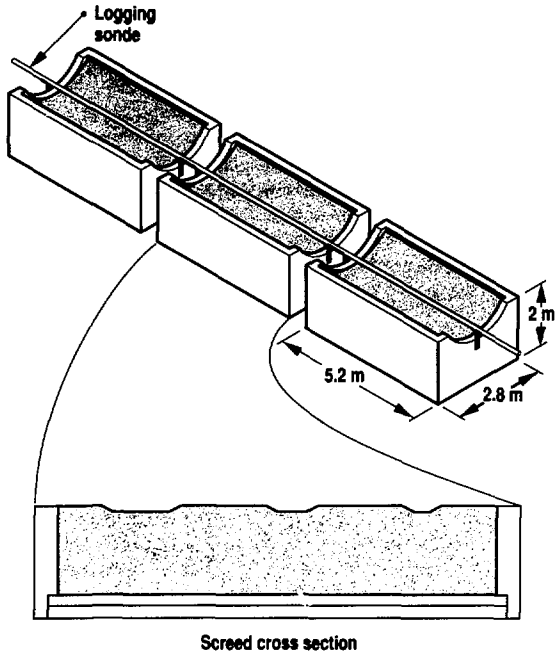

Figure 1. Laboratory experiment for simulating NTS borehole conditions. A logging sonde was pulled the length of three boxes filled with silica sand and limestone mixtures. Tests were run with both constant and varying gaps between sonde and sand mixtures and with both dry and saturated mixtures. Center box shows simulated washouts used for tests with varying gaps.

Neutron-induced gamma-ray spectroscopy logging, commonly called carbon/oxygen (C/O) logging, is used routinely in the petroleum industry. The rock is irradiated with 14-MeV neutrons, and the gamma-ray spectra resulting from inelastic scattering are recorded as a function of borehole depth. The ratio of the number of gamma rays in an energy window appropriate to scattering from carbon to the number in a window appropriate to scattering from oxygen (the C/O parameter) is used as a measure of the ratio of carbon to oxygen in the rock.

Conditions at NTS are very different from those encountered in the petroleum industry. Boreholes are usually air-filled with diameters frequently between 2 and 3.5 m. The walls are often rough; 2-cm rugosity is common over much of a borehole's length. Obviously, the standard petroleum industry calibrations and correction algorithms for small-diameter, liquid-filled, smooth-walled holes are not

necessarily appropriate for our conditions. We, therefore, conducted a series of experiments to determine whether commercial C/O logging could be adapted and calibrated to accurately estimate the carbonate content around NTS boreholes.

Laboratory Experiments

A laboratory experiment was designed to simulate the wall of a 2.4-m-diam borehole. It uses three reinforced-concrete boxes, each having inside dimensions of about 4.9-m length, 2.4-m width, and a minimum of 1.2-m depth. One box is filled with silica sand, and the other two contain mixtures of silica sand and ground limestone. The three boxes are about 0.01, 0.12, and 0.24 by weight limestone, which is equivalent to 0.004, 0.052, and 0.104 by weight CO_2. The ends of the boxes are circular arcs, so that their contents can be screeded (graded) with a long rod to simulate a section of a cylindrical borehole (Fig. 1). The absence of an opposing borehole wall introduces some error, and computer modeling is needed to get a better estimate of this error.

The three test boxes are aligned with a common longitudinal axis to allow the logging sonde to be pulled their full length. A logging winch is used to pull the sonde slowly over the boxes, providing a continuous log. At the ends of each box, an adjustable support gives a gap or standoff between the sonde and the cylindrical test surface. A commercial sonde (a cylindrical tool about 12.5 cm in diameter and 3 m long) was fitted with extensions at each end to keep it well supported while being pulled. The boxes are watertight so that after experiments with dry material are completed, each box can be saturated with water. Since the silica sand and ground limestone both contain roughly the same range of particle sizes, the water content of the saturated mixtures should be approximately the same; in our tests it was about 16% by weight for all boxes.

The first set of experiments was performed with dry test material screeded into a smooth concave arc with a radius of 1.2 m. Runs were made at 0.3 and 0.6 m/min at uniform gaps of 0, 2.5, 5, 8, 13, and 20 cm. Gamma-ray energy spectra were recorded approximately every 8 cm along the boxes. For each gap run, we averaged the resulting C/O parameter over the central 4 m of each box and plotted the C/O parameter against CO_2 content. The C/O parameter increased with CO_2 content and decreased with increasing gap. We obtained parallel lines with the position of their intercepts approximately linear with gap.

The boxes were then saturated with water and the tests repeated. The C/O parameter decreased markedly in the water-saturated material. The fit to straight lines is good, and the lines are nearly parallel.

We obtained an algorithm for calculating carbonate content from the C/O parameter, gap, and water content by least-squares fitting to our data. The good quality of the fits led us to conclude that we can correct the C/O parameter for a constant (known) gap. An important question was whether the same correction would be valid for a varying gap, representing washouts. Consequently, we ran experiments similar to those described above but with the sand screeded into varying gap configurations by a notched template attached to the screed rod.

For these experiments, we used only the middle box. Four templates varied the washouts from 2.5 to 7.5 cm deep. We found that when we corrected the C/O parameter as a function of position for a varying gap, our algorithm did not give as good agreement with measured carbonate content as we obtained for a uniform gap. In other words, a plot of C/O parameter against position does not track the varying gap in a reproducible way. However, if we averaged the varying gap and the C/O parameter over the central 4 m of the box, agreement between calculated and true average carbonate content was good.

Figure 2 shows the difference between the average CO_2 calculated from the algorithm and the true average value of 0.052 (dry weight fraction) as a function of average gap for each of the four washouts. For most gaps, the difference is within our tolerance of 0.01; it is best for an average gap of between 6 and 12 cm. The results were very similar for saturated experiments.

Field Experiments

Two logs were run in 2.4-m-diam boreholes at NTS. The commercial sonde was mounted on a large steel skid to force its face toward the borehole wall. Since the gap discrepancy is at a minimum between 6 and 12 cm, we installed a spacer to create a nominally constant gap of about 7.5 cm from a smooth borehole wall. We also used an aluminum caliper arm to measure the true value of the gap midway between source and detector. The measurement, averaged over an appropriate depth range, was used to apply a gap correction. The

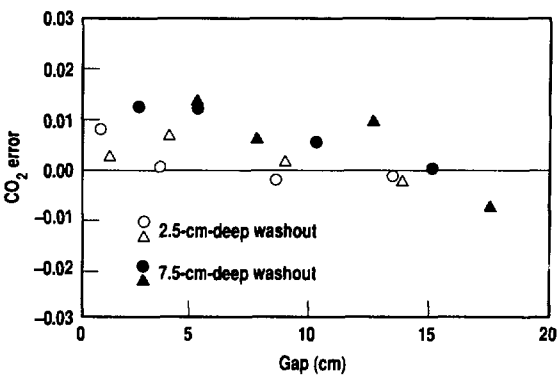

Figure 2. Difference between true CO_2 content (0.052 weight fraction) and that calculated from the C/O log versus gap for four washout configurations in dry material.

skid, as deployed, increased the C/O parameter by approximately 0.016; this number was subtracted from the raw parameter for a skid correction.

Figure 3(a) shows the weight fraction of CO_2 equivalent from the raw log corrected for gap and skid versus that obtained from sample measurements for one of the holes. When a water correction was attempted, the log was severely overcorrected [Fig. 3(b)]. The neutron log used to obtain the water content was run six years before the C/O log, and it is quite possible that the rock near the borehole wall dried out in the interim. This hypothesis is supported by the capture spectra obtained from the log. The 2.2-MeV hydrogen peak is much smaller in these spectra than in the spectra obtained from the saturated laboratory experiments. We plan to use the capture spectrum, rather than the neutron log, to obtain the water correction.

Conclusions

Laboratory tests of a commercial neutron-induced gamma-ray spectroscopy logging system adapted to NTS conditions indicate that the C/O parameter is affected not only by the carbonate content of the material used to simulate the borehole wall but also by its water content and by the gap between the sonde and the wall. For a given water content, an algorithm can be constructed to calculate carbonate content from the C/O parameter and the gap.

In tests with material that had a CO_2 content of 0.052 (dry weight fraction), our algorithm gave the CO_2 content averaged over depth correctly within 0.01 for both dry and saturated material, with the average gap between sonde and sample as large as 12.5 cm and varying by as much as 7.5 cm. Although our tests were not so comprehensive at other carbonate contents, the results suggest that the corrections will be satisfactory.

Preliminary field logging results appear to agree fairly well with data from chemical analyses. Of course, if the latter data were wholly satisfactory, the log would not be required. The agreement, at least, tells us that nothing is seriously wrong with our procedure.

At this point we have gone nearly as far as we can with physical modeling and must turn to computer simulations for further information. In particular, such simulations will be useful in characterizing what happens when some or all of the calcite in a rock formation is replaced by dolomite. Computer simulations will also be useful in helping to develop a water correction based on the capture spectrum. There is evidence that this effect is significantly nonlinear, but we are optimistic that a suitable correction can be developed.

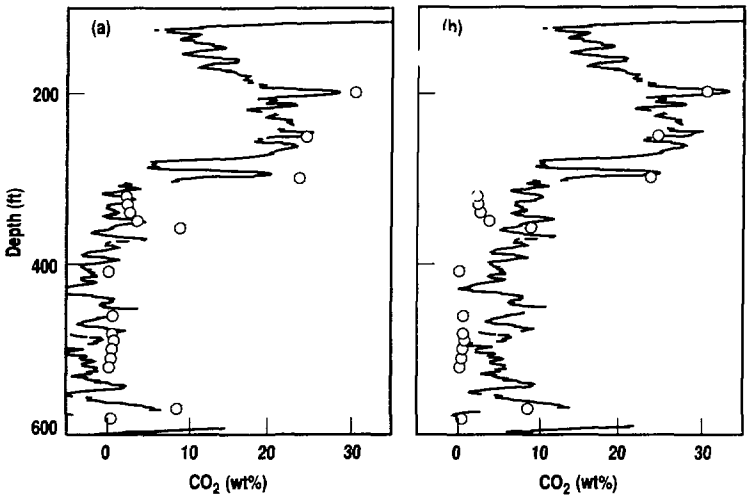

Figure 3. Comparison of CO_2 content in borehole U9cv at NTS as determined from chemical analysis of samples (data points) and from logging values that are (a) gap- and skid-corrected and (b) gap-, skid-, and water-corrected. Water values were chosen to be 0.18 by volume above 300 ft and 0.29 below 300 ft, corresponding to attempts at averaging a neutron log.

Plug Evaluation Diagnostics Systems

B. C. Hudson

The primary responsibility of the Containment Program is to ensure that all reasonable actions have been taken to prevent the accidental release of radioactive material and radioactivity to the atmosphere. Because we do not have unlimited resources, containment systems must be designed to be practical as well as adequately conservative. This requires the development of models that are containment-related and cost-effective means for stemming emplacement holes. This, in turn, requires an aggressive measurement program to determine whether stemming design criteria are met, determine the effectiveness of containment systems, and create a phenomenology data base for the development and validation of containment models.

To gather stemming plug emplacement and performance data in a cost-effective manner, we have developed an electronic multiplex system for plug evaluation diagnostics (PED). The PED multiplex system can gather up to 24 data channels from various instrument locations deep in an emplacement hole and transmit those data to a surface recording trailer via a single coaxial cable. In practice, the PED system now replaces one coaxial and three multiconductor cables with a single coaxial cable or, alternatively, allows us to perform a much more extensive set of measurements using the same number of cables. The PED system gathers data from each of 16 switches, 4 temperature sensors, 2 pressure transducers, and 2 radiation-level monitors at the rate of once each per second (see Fig. 1).

In addition, monitoring the length of the coaxial cable extending from the deepest PED system to the surface allows us to measure the rate and extent of chimney formation during collapse. Monitoring the length of a coaxial cable extending from the PED system to the device position allows us to measure strong shock position versus time immediately following detonation. The latter measurement can be used to derive the hydrodynamic yield of the nuclear device.

Figure 2 illustrates PED data from a typical set of gypsum concrete level switches during plug installation. The switches are designed to indicate the level of gypsum slurry and give an indication of its ability to flow into narrow regions, such as between cables. The temperature histories can be compared with those of other plugs installed in similar settings to give a qualitative indication of plug competency.

Figure 3 shows a typical set of pressure and radiation data. Note that the radiation level remains at background. The pressure trace shows a sharp increase at zero time as a result of ground-motion-induced compaction of the stemming, followed by

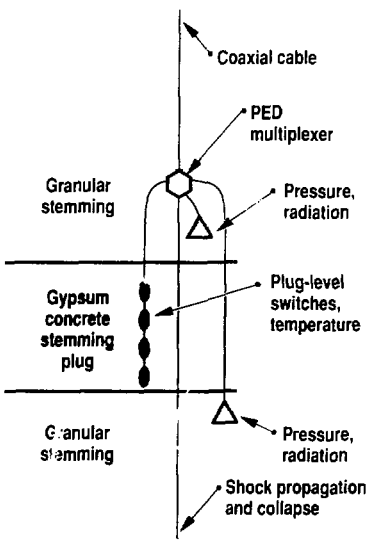

Figure 1. A typical PED system as installed in a sanded-gypsum concrete stemming plug.

a slow decay toward pre-zero-time levels. Both radiation and pressure measurements indicate the successful performance of the deeper gypsum plugs on this event—no radioactive cavity material reaches the level monitored.

The PED system has now been used successfully on several events, and we expect to use it routinely on most future events.

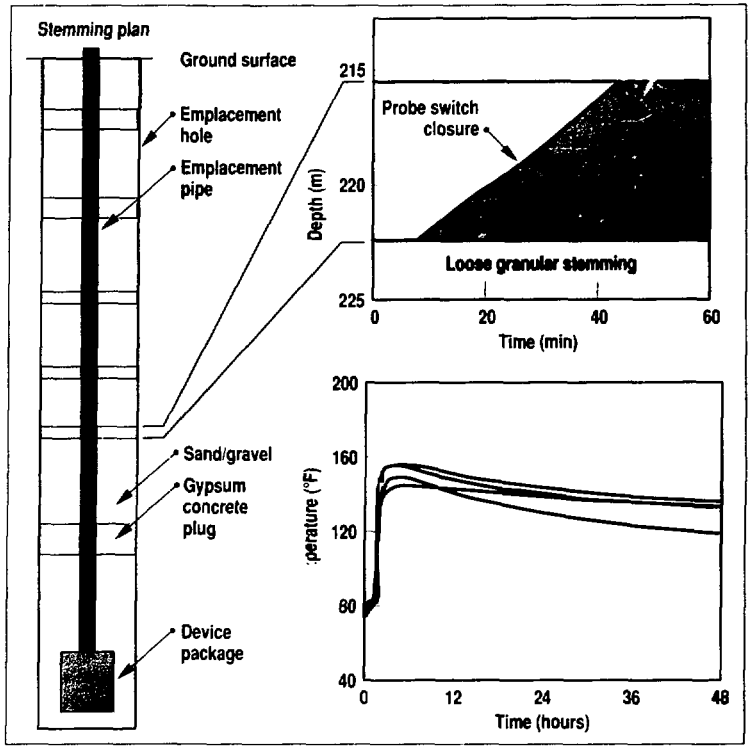

Figure 2. Both the measured temperature histories and the switches showing the gypsum levels indicate a typical stemming plug.

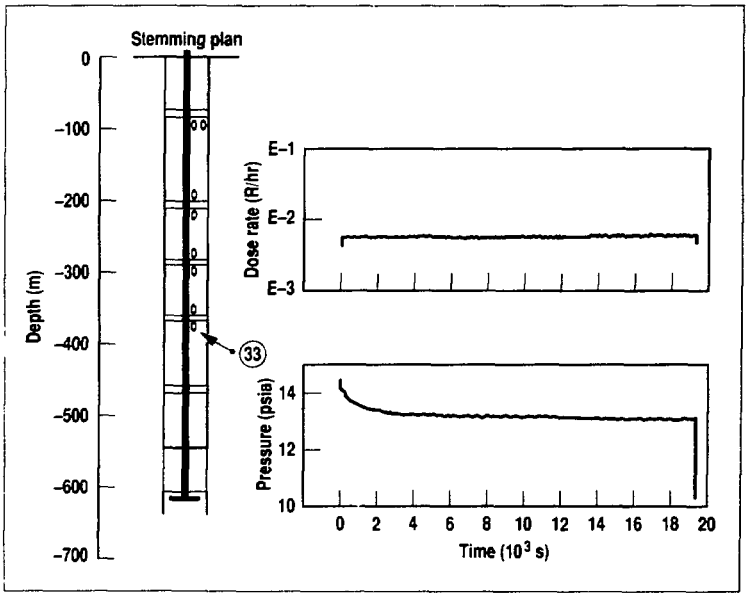

Figure 3. Pressure and radiation data from station 33 relayed via the PED system indicate that no radioactive gases were present above the two deepest gypsum plugs.

Calculations of Underground Nuclear Explosions Using DYNA2D

W. C. Moss and J. T. Rambo

In the U.S., nuclear tests are conducted underground to prevent the release of radiation and radioactive debris. The geologies in which these tests are conducted can be complicated—they often consist of many layers of material with different tensile strengths, bulk and shear responses, water saturation and porosity, as well as faults and cracks. Failure to recognize the effects of different material properties and geologic features on the shock wave generated by the explosion could lead to a containment failure, as exemplified by the Baneberry Event in 1970, which released radioactive debris to the atmosphere through shock-generated cracks that extended from the working point to the surface. Following the Baneberry Event, numerical simulations of underground nuclear explosions (including Baneberry) were performed to identify potential containment weaknesses.

Until October 1988, the numerical simulations were done using TENSOR, which is a two-dimensional, Lagrangian, finite-difference hydrocode. TENSOR was operational only on the CDC 7600 computers, which were shut off in October 1988. Efforts by others to make a version of TENSOR run on the Cray computers were initiated in anticipation of the shutdown of the CDC 7600s but were unsuccessful. Consequently, we chose to use DYNA2D,[1] which is a two-dimensional, Lagrangian, finite-element hydrocode. We selected DYNA2D because it is a state-of-the-art hydrocode that is used worldwide. It is approximately six times faster than TENSOR, has slide-lines, color graphics, and portability (it is easily transferred to other machines). There is also a three-dimensional version that will allow analyses of very complex geologies.

Our immediate goals were to duplicate TENSOR's capabilities. The reasons for this were practical, not technical. The Containment Evaluation Panel (CEP), which approves events for detonation based on probability of successful containment, had developed confidence in TENSOR's calculations over the past 15 years. We did not want to weaken this confidence, so we added those features of TENSOR to DYNA2D that are necessary to do geologic problems: geologic material models, dezoning, and overburden. We also modified the DYNA2D post-processor to produce graphical output of quantities relevant to containment so that TENSOR and DYNA2D output could be compared. In this article, we will show the results of our efforts by comparing calculations done with DYNA2D and TENSOR. We demonstrate that both codes produce similar results.

What Is A Containment Calculation?

A typical numerical simulation of an underground nuclear explosion consists of constructing a two-dimensional representation of the test geology, as shown in Fig. 1. The results of well loggings, analyses of cuttings, and geologic surveys are used to construct the numerical representation of the test geology. The colors represent different materials. Although the geology is three-dimensional, two-dimensional (axisymmetric about the z axis) representations have been found to be adequate (to date). The geology is divided into small, discrete elements (see Fig. 1) in which the equations of motion (conservation of mass, momentum, and energy) are differenced and solved. The parameters for the material model are obtained from experimental data when possible, or from theoretical models when data are not available. The cavity, centered at $r = 0$, $z = 0$, contains the device, which is modeled as a gas with an appropriate

Figure 1. Typical computational mesh used in containment calculations.

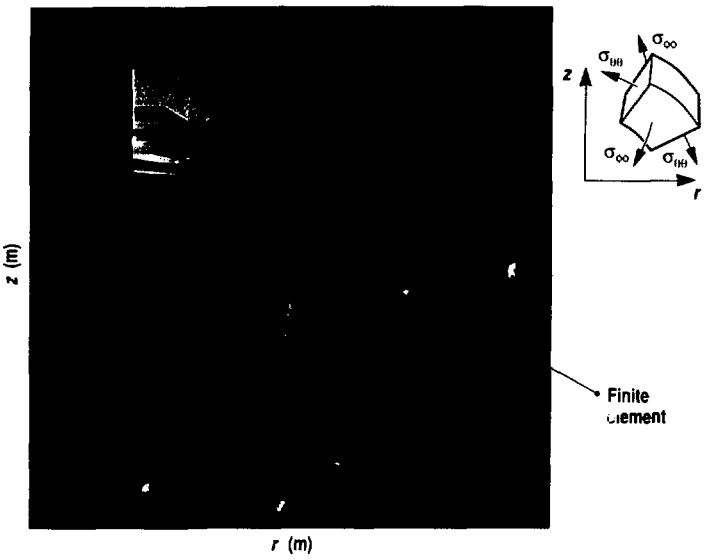

pressure-volume relation. Typically, the calculation begins at approximately 3 ms (0.1 Mbar cavity pressure) so that radiation can be neglected. The calculation is terminated at approximately 1 s, which is usually long enough for the dynamic solution to approach static equilibrium. In order for there to be "good numerical containment," we examine the stress field around the cavity and the spatial extent of material that has failed in tension during the calculation. We look for a spatially thick region around the cavity in which the in-plane ($\sigma_{\theta\theta}$) and out-of-plane ($\sigma_{\phi\phi}$) hoop stresses are compressive (see Fig. 1) and exceed the cavity pressure. We also require a thick region of uncracked material between the cavity and the surface; that is, we do not want to see a pattern of cracks (even if they are currently closed) that extend from the cavity to the surface. In general, interpreting the results of numerical calculations and making conclusions about containment is subjective and difficult. The numerical calculations are useful because they allow us to do controlled sensitivity studies to address particular containment issues that arise. These sensitivity studies can be done quickly and easily with DYNA2D because it is extremely fast and user-friendly.

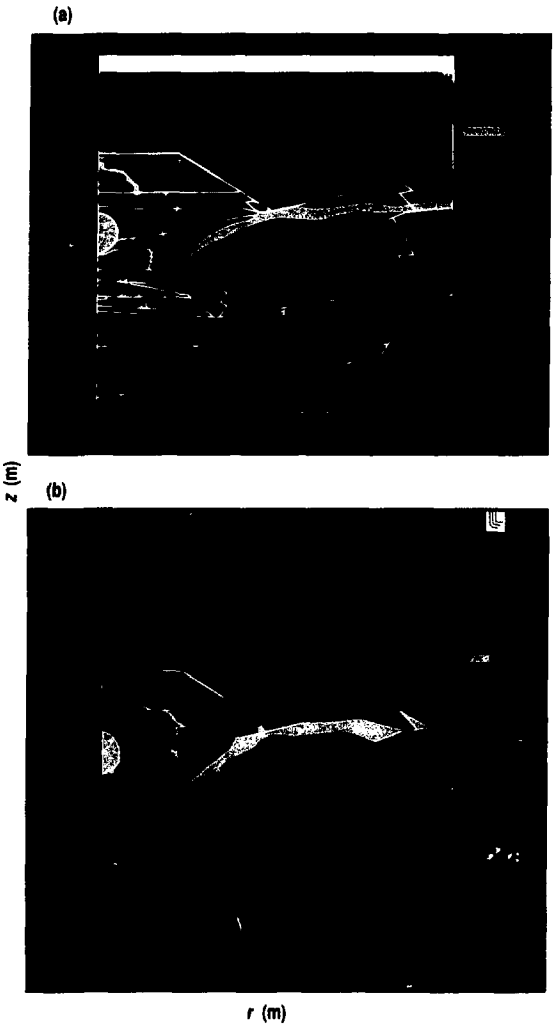

Figure 2. Out-of-plane hoop stress at 800 ms for an event planned for hole U8n, as calculated by (a) TENSOR and (b) DYNA2D.

Comparisons of DYNA2D and TENSOR

Figure 2 shows contours of the out-of-plane hoop stress at 800 ms for an event planned for hole U8n, as calculated by DYNA2D and TENSOR. Identical meshes, boundary conditions, and material properties were used in the calculations. The contour levels (colors) are identical in both calculations, increasing from dark blue to red. Compressive stresses are positive. The calculations are very similar and show "good numerical containment." The complicated material geometry and large number of materials (14) with different material properties assures us that the agreement is not fortuitous and that we have incorporated the relevant features of TENSOR's geologic model in DYNA2D. We have compared other DYNA2D and TENSOR simulations of events that showed good, marginal, and poor compressive stress fields around the cavity at late times. These simulations also were in agreement. Consequently, DYNA2D is a reliable tool for doing containment calculations and can be used for all future LLNL containment calculations.

Reference:

1. J. O. Hallquist, *User's Manual for DYNA2D—An Explicit Two-Dimensional Hydrodynamic Finite Element Code with Interactive Rezoning and Graphical Display*, Lawrence Livermore National Laboratory, Livermore, Calif., UCID-18756, Rev. 3 (1987).

Containment Program personnel collect rock samples and geophysical log data to use for evaluating a drill hole as a site for a proposed nuclear test. The data permit us to characterize the site itself and make comparisons to similar types of data from other drill-hole locations to help determine if anything unusual is present at the proposed site. Rock samples give us three types of data: CO_2

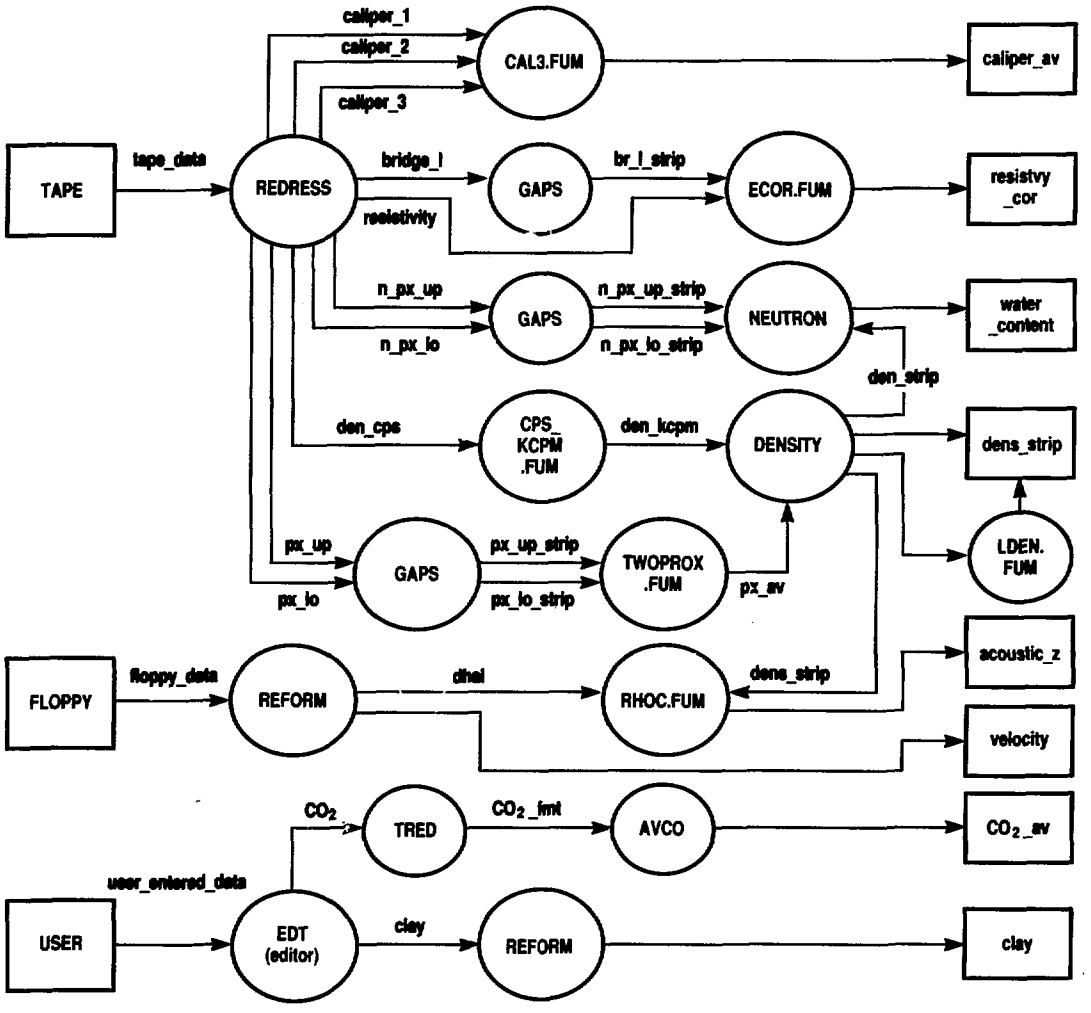

Figure 1. Processing flow diagram of data to be plotted by CEPP.

Figure 2. CEPP input form requesting data file names.

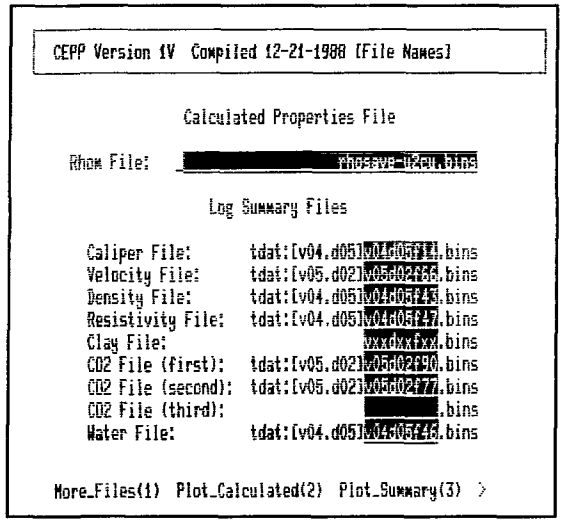

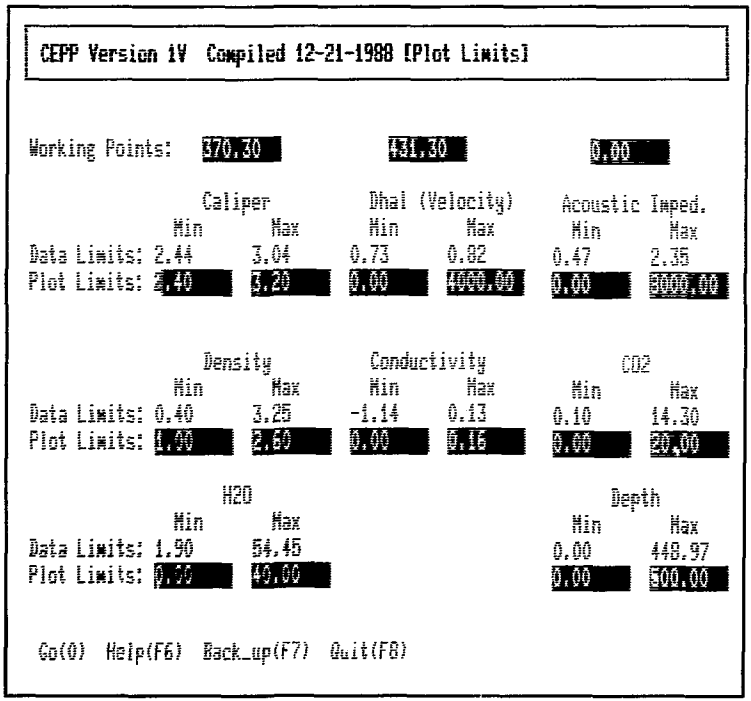

Figure 3. CEPP input form requesting data plotting limits.

content, grain density, and mineral content. Geophysical logs provide us with eight different types of data: acoustic impedance, density, hole diameter, natural gamma radiation, remanent magnetic field, resistivity, velocity, and water content. There may be more than one log for a data type; for example, we obtain density data from both a gamma-gamma log and a gravimeter. We use 10 codes to process the sample and log data. Also, the epithermal neutron log, from which we obtain water content, requires calibrations for correct interpretation, so we have two calibration codes to process these data. Two codes allow us to model the geologic setting and correct density data for the effects of nearby structure. Another code uses measured data to calculate physical properties, porosity, gas porosity, and saturation, all of which we use to help predict the phenomenology of an event.

In the past, these codes were run on CDC 7600 computers. However, we have recently completed a large project in which all of these codes were converted to an in-house VAX. This conversion included packaging the codes more efficiently by encapsulating multiple smaller routines (modules) into parent codes, adding forms that make operating the codes straightforward and simple, and adding a history file of all actions taken on a data set (for quality assurance purposes). The codes meet the Containment Program's software specifications, which were set to produce high-quality, maintainable production software. This includes structured Fortran coding and analysis as well as design reports and documentation including programmers' and users' manuals. Command files for each code link and compile modules and libraries to create an executable file when changes are made.

This conversion project gave us an opportunity to make the codes operate

more efficiently. Before, processing a log consisted of running many small codes, taking output from one code and using it as input for another. Now, related codes are linked as one general code with modules, requiring no operator interaction after starting. The addition of forms to the front of the codes allows the user to supply all necessary information for running the code at the beginning of the session. Initiation of the form starts the code, and the operator is free to work on something else as data processing progresses. Finally, history files keep records of all actions taken on a data set. This is an excellent means of retracing steps to determine how a data set was manipulated.

During the conversion, we also wrote several special-purpose codes to give us some of the capabilities we had on the CDC 7600s that were unreasonable to port and convert. For example, we now have codes to read the geophysical data from magnetic tape, change the format of data when necessary, create (digitize) data, and display data. An example is CEPP, which was written on the VAX to allow us to make log summary plots for presentation. CEPP plots eight data types (not counting lithology) on one page. Similar plots were made on the CDC 7600s but were actually drawn and pieced together using a graphics editor. The flow chart in Fig. 1 shows how the data plotted by CEPP are processed. The data types are shown in the boxes on the right side of the figure. Input forms used for CEPP are shown in Figs. 2 and 3. The first form asks for the names of files to be plotted; these are structured file names from our data base. The second form appears when one chooses the menu option "plot_summary." It requests working-point information and shows the ranges of the data along with the plotting limits t. which the code defaults. The ope ator can override the defaults to c tm custom plotting limits. Figure 4 shows the final plot, which can be sent to a laser printer as a paper copy or viewgraph. It used to take at least one day to generate this plot on the CDC 7600s; we can now produce it in minutes.

The code conversion project is completed, which has given the Containment Program streamlined data processing, resulting in more efficient use of personnel and computer time.

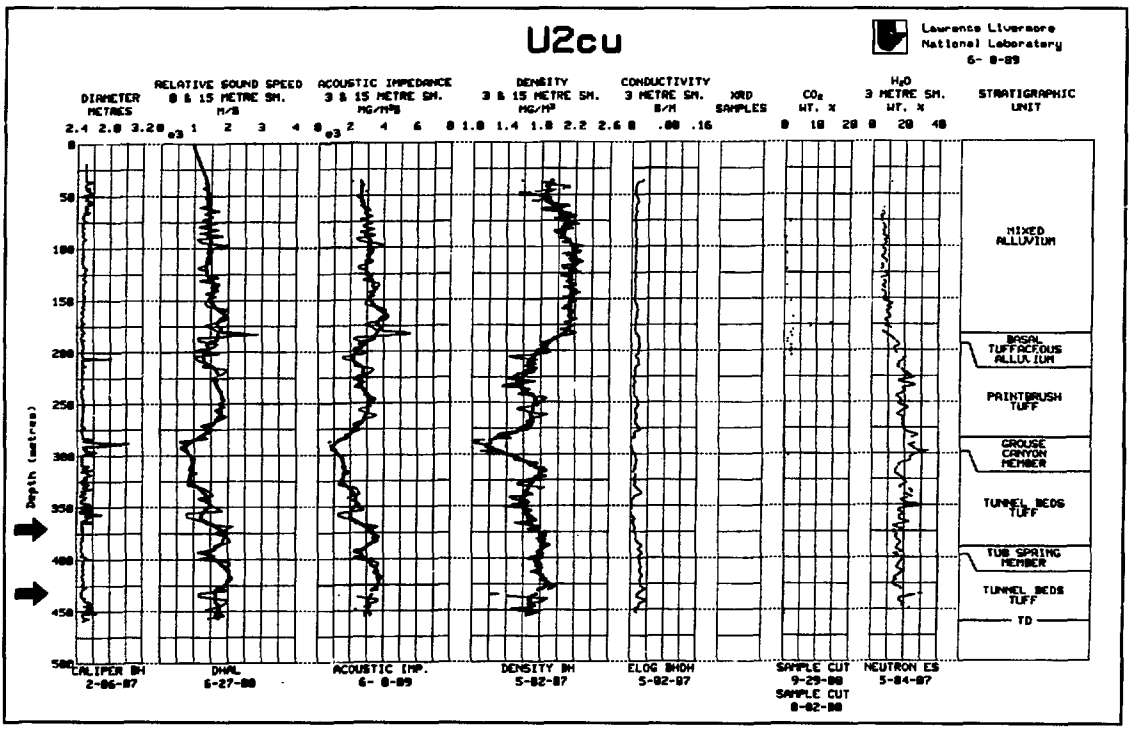

Figure 4. Log summary plot produced by CEPP.